ifas Institute for Fluid Power Drives and Systems | RWTH AACHEN UNIVERSITY

11!FK 11!FK

Global Fluid Power Society

hp

VDMA

GENERAL

Matthias Petry

+49 (0) 241 - 80 47 733
general@ifk2018.com

TRADE EXHIBITION

Jutta Zacharias

+49 (0) 241 - 80 47 711
exhibition@ifk2018.com

CONTRIBUTORS

Stephan Merkelbach

+49 (0) 241 - 80 47 722
papers@ifk2018.com

ADDRESS

Campus-Boulevard 30
D-52074 Aachen

+49 (0) 241 - 80 47 711
+49 (0) 241 - 80 6 47 712
post@ifas.rwth-aachen.de
www.ifas.rwth-aachen.de

11TH IFK | CONFERENCE PROCEEDINGS

FLUID POWER NETWORKS

19th - 21st MARCH 2018 | PROCEEDINGS

11TH INTERNATIONAL FLUID POWER CONFERENCE

Vol. 2



Vol. 2

VOLUME 2 - CONFERENCE: TUESDAY, MARCH 20TH + SCIENTIFIC POSTER SESSION

11TH INTERNATIONAL FLUID POWER CONFERENCE

19th - 21st of March 2018
Aachen, Germany

Volume 1 - Symposium: Monday, March 19th
Volume 3 - Conference: Wednesday, March 21st

WELCOME TO THE 11th IFK!

Fluid Power Networks has drawn a lot of attention and the organizing team and all collaborators at IFAS are proud that you followed our invitation to join the 11th International Conference on Fluid Power in Aachen. Welcome to the academic and truly intercultural city in the heart of Europe!

The traditional IFK is one of the world's largest scientific conferences on fluid power and unites scientists with industrial delegates at an international forum to exchange knowledge in the area of fluid power drives and systems. The first conference (1. AFK, Aachener Fluidtechnisches Kolloquium) was conducted in 1974 by Prof. Wolfgang Backé. Since 1998 the Institute for Fluid Power Drives and Controls (IFAS) at RWTH Aachen University and the Institute of Fluid Power (IFD) at TU Dresden alternately organize the International Fluid Power Conference (IFK) every two years. This year we host 141 scientific contributions and speakers. Attendees from 30 countries are registered. 36 companies exhibit their products in a designated floor area in the Eurogress. A special highlight of the 11th IFK is the 50th anniversary of Fluid Power Research at RWTH Aachen University which will be celebrated on Wednesday, March 21st. It is accompanied by a change in directorship at IFAS. Prof. Katharina Schmitz will be introduced as my successor.

The program starts on Monday morning with a symposium where researchers from mainly universities and other research facilities but also from companies have the opportunity to present their research projects to a wide international community of scientists. In the evening of the first day all participants are invited to the opening event that marks the start of the exhibition.

The second day begins with the opening address of Mr. Christian Kienzle of VDMA followed by two plenary lectures to actual IoT subjects as they concern fluid power. On Tuesday there are six groups in two parallel sessions of presentations covering a wide variety of application and technology oriented topics in the time of digitalization. The banquet is held at the Coronation Hall of the Aachen town hall and will be followed by an after show in the Aula Carolina. On Wednesday the program continues in three parallel sessions. The Rector of RWTH, Prof. Schmachtenberg will talk in the concluding plenary session, arrange the hand over in the directorship of IFAS and initiate the anniversary events.

A traditional cultural program will be offered in the surrounding of Aachen as well as an excursion following the conference on Thursday and Friday.

Finally, we would like to express our thanks to all members of the program and organizing committee, scientific advisory board, plenary and keynote speakers, speakers, reviewers, chairmen and exhibitors for their time and commitment helping to conduct another successful conference and we hope that you will enjoy the 11th IFK in Aachen.



H. Murrenhoff

PROGRAMME COMMITTEE

Achten, Peter	Dr. ir., INNAS B.V., Breda, NL
Bauer, Frank	Dr.-Ing., Hydac International GmbH, Sulzbach
Boes, Christoph	Dr.-Ing., Moog GmbH, Böblingen
Faß, Ulrich	Dr.-Ing., Volvo Construction Equipment, Konz
Fedde, Thomas	Dr.-Ing., Claas Tractor, Paderborn
Fiedler, Maik	Dr.-Ing., IMI Norgren, Fellbach
Fischer, Marcus	Dr.-Ing., Argo-Hytos GmbH, Herdorf
Gauchel, Wolfgang	Dr.-Ing., Festo AG & Co. KG, Esslingen
Hahmann, Wolfgang	Dr.-Ing., Hydac International GmbH, Sulzbach
Hunger, Ingrid	Lic. Oec., Hunger DFE GmbH, Lohr am Main
Huster, Gernot	Dipl.-Ing., KraussMaffei Technologies GmbH, München
Jähne, Hilmar	Dr.-Ing., Hydrive Engineering GmbH, Freital
Kempermann, Christoph	Dr.-Ing., Fluitronics GmbH, Krefeld
Klug, Dirk	Dr.-Ing., Schuler Pressen GmbH, Waghäusel
Knobloch, Michael	Dipl.-Ing., HAWE Hydraulik SE, München
Krallmann, Jens	Dr.-Ing., Thomas Magnete GmbH, Herdorf
Krieg, Mark	Dr.-Ing., Bosch Rexroth AG, Lohr am Main
Krüßmann, Martin	Dr.-Ing., Bosch Rexroth AG, Elchingen
Legner, Jürgen	Dipl.-Ing., ZF Friedrichshafen, Friedrichshafen
Lindemann, Lutz	Dr., Fuchs Petrolub SE, Mannheim
Lüüs, Holger	Dipl.-Ing., Bucher Hydraulics GmbH, Klettgau
Martens, Oliver	Dr.-Ing., Mining Germany GmbH, Düsseldorf
Mundry, Sebastian	Dr.-Ing., Caterpillar Global Mining Europe GmbH, Lünen
Murrenhoff, Hubertus	Prof. Dr.-Ing. RWTH Aachen University
Rahmfeld, Robert	Dr.-Ing., Danfoss Power Solutions, Neumünster
Roosen, Klaus	Dr.-Ing., Parker Hannifin GmbH, Kaarst
Saffe, Peter	Dr.-Ing., Aventics GmbH, Laatzen
Schmitz, Johannes	Dr.-Ing., Linde Hydraulics GmbH & Co. KG, Aschaffenburg
Schultz, Albert W.	Dr.-Ing., MBA, Magnet-Schultz GmbH & Co. KG, Memmingen
Schulze Schencking, Dirk	Dr.-Ing., Hauhinco Maschinenfabrik GmbH & Co. KG, Sprockhövel
Sondermann, Götz	Dipl.-Ing., Siempelkamp Maschinen- und Anlagenbau GmbH & Co. KG, Krefeld
Synek, Peter	Dipl.-Ing., Fachverband Fluidtechnik im VDMA, Frankfurt am Main
van Bebber, David	Dr.-Ing., Ford Research and Innovation Center Aachen, Aachen
Weber, Jürgen	Prof. Dr.-Ing. TU Dresden

INTERNATIONAL ADVISORY COMMITTEE

Bideaux, Eric	Prof., INSA de Lyon
Chiang, Mao-Hsiung	Prof., National Taiwan University
Hong, Yeh-Sun	Prof., Korea Aerospace University
Huhtala, Kalevi	Prof., Tampere University of Technology
Ivantysynova, Monika	Prof., Purdue University
Krus, Petter	Prof., Linköping University
Plummer, Andrew	Prof., University of Bath
Sanada, Kazuschi	Prof., Yokohama National University
Scheidl, Rudolf	Prof., Johannes Kepler University Linz
Stelson, Kim	Prof., University of Minnesota
Yang, Huayong	Prof., Zhejiang University

CONFERENCE ORGANISATION

Petry, Matthias	RWTH Aachen University
Merkelbach, Stephan	RWTH Aachen University
Zacharias, Jutta	RWTH Aachen University

11:00 - 12:30 a.m.

GROUP 1 - DIGITALIZATION, CONNECTIVITY & COMMUNICATION

Raphael Alt	A survey of „Industrie 4.0“ in the field of Fluid Power – challenges and opportunities by the example of field device integration	14
Tapio Torikka	Predictive Maintenance Service Powered by Machine Learning and Big Data	26
Oliver Breuer	From Big Data to Smart Data	34
Prof. Peter F. Pelz	Towards digitalization of hydraulic systems using soft sensor networks	40

GROUP 2 - COMPONENTS

Galina Haidarschin	Benchmarking of potential substituents for leaded bronze in axial sliding bearings for mobile hydraulic applications	54
Roman Ivantysyn	Investigation of the Thermal Behavior in the Lubricating Gap of an Axial Piston Pump with Respect to Lifetime	68
PhD Peter Achten	Reducing the wall thickness of the cups and pistons in floating cup pumps and motors	84
Anton Gaile Emmanuel Viennet	Noise and vibration reduction for an aerospace secondary controlled hydraulic motor	96

01:30 - 03:00 p.m.

GROUP 3 - INDUSTRIAL APPLICATIONS

PhD Bastian Beckmann	myCro – Downsizing of hydraulic power units by revolutionizing the design	108
Marcus Helmke	Computer-assisted modeling and automatic controller adjustment based on an innovative non-parametric identification method	116
Wilhelm Hagemeister	Dynamic High-Torque Test Stand with Hydrostatic Drive	130
Ekhard Siemer	Electro-Hydrostatic Drive Concept for the Ring Rolling Process	144

01:30 - 03:00 p.m.

GROUP 4 - MOBILE APPLICATIONS

PhD Milos Vukovic	Systematic Data Analysis for Optimal System Design	154
Marani Pietro	Experimental Evaluation of the New Meter Out Sensing Architecture	164
Lorenzo Serrao	Adaptive Park Brake Technology to Improve Stability of Wheeled Excavators	176
PhD Martin Inderelst	Quantification of Energy Saving Measures in a 21t Excavator Hydraulic System – A Holistic Investigation?	184

03:30 - 05:00 p.m.

GROUP 5 - ENERGY MANAGEMENT

Sebastiaan Mulders	Control design and validation for the hydraulic DOT500 wind turbine	200
Prof. Kim Stelson	Characterization and Calibration of a Power Regenerative Hydrostatic Wind Turbine Test Bed using an Advanced Control Valve	210
PhD Mirjana Ristic	Electrification of hydraulics opens new ways for intelligent energy-optimized systems	218
Tobias Pietrzyk	Design study of a high speed power unit for electro hydraulic actuators (EHA) in mobile applications	232

GROUP 6 - COMPONENTS

Peter Tappe	High-dynamic Proportional Solenoid on the basis of Established Production Technologies	246
PhD Jörg Schneider	Proportional pressure reducing valves with intrinsic fail safe function	254
Christian Stauch	Proportional Leak-Free Pressure Control Valve	266
PhD Roman Weidemann	Smart hydraulic cylinder with force measurement system	274

SCIENTIFIC POSTER SESSION

GROUP PA - COMPONENTS

Gonzalo A. Barillas	Sealing Systems for Hydraulic Cylinders	SP1	282
Ervin Strmčnik	The improvement of the total efficiency of the gerotor orbital hydraulic motor	SP2	294
Cheng-long Wang	An Active-control digital hydraulic damper: Design, modeling and simulation	SP3	306
PhD Lucian Năşcuţiu	A control approach for fast voice coil actuators for servo valve applications in mobile and industrial hydraulics	SP4	318

GROUP PB - DESIGN PROCESS

Jiaming Wang	The optimization design algorithm of hydraulic components under multiple operating conditions	SP5	330

GROUP PC - INDUSTRIAL APPLICATIONS

PhD Taher Salah El-Din	The Development of an integrated monitoring and filtration system for performance assurance of hydraulic mould oscillation systems used in continuous casting machines at flat steel plants	SP6	338
PhD Tatiana Minav	Experimental Investigation of a Directly Driven Hydraulic Unit in an Industrial Application	SP7	348
Prof. Lijie Zhang	Reliability Evaluation of Hydraulic Pump Based on Performance Degradation	SP8	362

GROUP PD - MOBILE APPLICATIONS

PhD Tatiana Minav	Efficiency Study of an Electro-Hydraulic Excavator	SP9	372

GROUP PE - NEW & SPECIAL APPLICATIONS

Prof. Željko Šitum	Wireless Control of an Electro-hydraulic Robotic Manipulator	SP10	386
Wei Cai	A new type of hydraulic swing drive with integrated motion sensor for narrow spaces	SP11	396
Prof. Mao-Hsiung Chiang	Hydraulic Multi-axial Levelling Control for Turbine Access System of Offshore Wind Farm	SP12	404

GROUP PF - PNEUMATICS

Prof. Jyh-Chyang Renn	Application of Pneumatic Muscle Actuator to Pulse Diagnosis System of Chinese Therapy	SP13	412
Prof. Wanlu Jiang	Fault Diagnosis of Pneumatic Actuator Based on Virtual Prototype Fault Simulation	SP14	420
Prof. Viktor Sverbilov	On Stability of the Two Stage Piloted Gas Pressure Control Unit	SP15	432

GROUP PG - SYSTEMS

Wei Cai	Principle and Application in FAST of Parallel Reliability Test Bench	SP16	442

GROUP PH - TRIBOLOGY & FLUIDS

Jiming Ma	Oil film characteristics and failure mechanism analysis of one kind of mechanical seal under the effect of fluid-structure-thermal coupling	SP17	448
Lingxiao Quan	Innovative Structural Design and Coupled Vibration Analysis of the Bionic Hydraulic Pipeline	SP18	460
PhD Corneliu Cristescu	Experimental Researches to Measure the Total Resistance Forces that Appear at the Switching Process of Directional Control Valves	SP19	472
Marcel Rückert	Surface tension of fuels – Analysis of measurement methods and applicability on high-pressure surroundings	SP20	482

REVIEWED

A survey of “Industrie 4.0” in the field of Fluid Power – challenges and opportunities by the example of field device integration

Raphael Alt *, Hubertus Murrenhoff * and Katharina Schmitz *

RWTH Aachen University, Institute for Fluid Power Drives and Systems (IFAS),
Campus-Boulevard 30, D-52074 Aachen, Germany*
E-Mail: Raphael.Alt@ifas.rwth-aachen.de

This contribution gives a brief introduction to general aspects of “Industrie 4.0”. Besides basic strategies to improve the added value and flexibility of a production, challenges of the transformation, which have to be overcome by the companies, are shown. The commissioning of production machines gains more significance in a dynamic production of a smart factory, so that in consequence the automation of the commissioning would bring significant advantages. Current fluid power systems are not excluded, since most steps of the commissioning are still done manually by the technician. By analysing the integration of a linear electro-hydraulic actuator into a production machine, limitations and problems of current systems are identified and related to the field of fluid power. The analysis of possible solutions is leading to methods and modern information and communication technology, introduced by the “Industrie 4.0”.

Keywords: Cyber-physical system, intelligent field device, plug and produce, plug and play, commissioning, Industrie 4.0, Industrial Internet of Things, electro-hydraulic actuator
Target audience: Fluid Power, Automation, Production

1 Introduction of the Industrial Internet of Things (IIoT)

1.1 Motivation

The Internet of Things (IoT) is affecting everyone. It describes the fusion of computational power (embedded systems), mechatronic systems and their interconnection via internet. Various industrial branches are influenced, reaching from the energy sector (smart grids) over the field of consumer products (smart home, smart phone, etc.) to the manufacturing industry. Within this branch, the “Industrial Internet of Things” (IIoT) or “Industrie 4.0” (German) was firstly introduced as part of the German high-tech strategy in 2011 at Hannovermesse with its goal to master upcoming challenges and to meet new requirements in times of market globalization /1/.

The greater number of competitors, the demand of cheap, individualised goods and the shorter time-to-market sets up new requirements to the manufacturing industry in terms of flexibility, dynamics and adaptability besides the classical ones such as a high quality and low costs.

In order to achieve the ambitious and partly classically contradictory goals, the German organisation “Plattform 4.0” outlined a roadmap to deploy the Industrial Internet within the next 10 to 20 years. Based on the first three industrial revolutions, shown in figure 1, mechanisation, electrification and automation by computational power, the enabling technologies of the fourth industrial revolution are all related to the field of Information and Communication Technology (ICT) such as Net Communication, Data Analysis, Microelectronic, Safety & Security and Semantic Communication /2/.

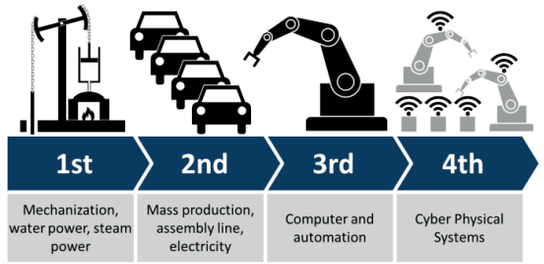


Figure 1: Industrial revolutions /3/

1.2 Basic Concepts

Key concept of “Industrie 4.0” is to make relevant information available in real-time by linking all participating instances of the whole production process and to derive the ideal value-added flow for any step of the production at any time /4/.

Current strategies for implementing IIoT in the manufacturing industry are focusing on four dimensions as shown in figure 2 /5/.

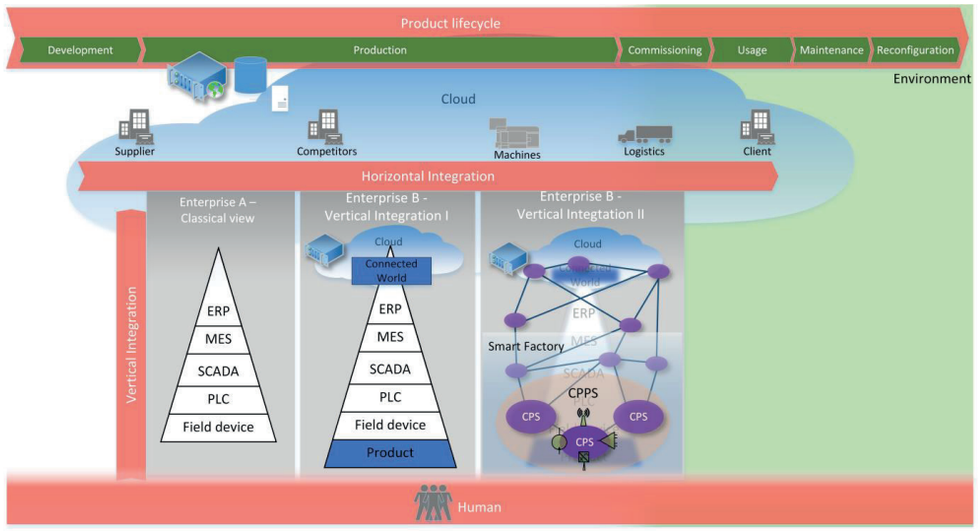


Figure 2: Four dimensions of “Industrie 4.0” in the industrial environment (referring to /5/)

By **Vertical Integration**, components and IT-Systems of different hierarchy levels are linked together. The classical hierarchy of the automation system pyramid, reaching from the field device to the enterprise systems, gets reduced through a decentralised production network composed of intelligent production units, so called cyber-physical systems (CPS). As the product is choosing its own path through the cyber-physical production system (CPPS), it can be added to the automation system pyramid. “Connected World” is representing outside connections via the internet. /6/

Horizontal Integration addresses the interconnection of all participants across the value-added chain of the production process and creating value adding networks, for example different production machines in the enterprise, as well as participants outside the enterprise. In this field, many digital business models are arising. /6/

Integrated Engineering describes a digital consistency of information across the whole **product lifecycle**. Relevant information is recorded and transferred continuously to be able to retrace every step of the tool chain within the different phases of engineering and production. /6/

The **human** role in the professional environment changes from being deeply integrated into the production process to higher planning and guiding tasks due to more intelligent production and personalised assistance systems. Fast changing environments and systems require high flexibility and continuous readiness to learn. Technicians specialised on a single domain are becoming systems engineers. /6/

Although current developments differ in many aspects, they all match in significant increasing internal system complexity. Tasks of the intelligent production systems will be handling this complexity and making essential functions much easier to use for operators, clients and everybody interacting with the systems.

1.3 Economic Benefits

The economic benefits of the fourth industrial revolution are predicted to affect the whole value-added chain of a new product from the development, to manufacturing process, up to its usage and reconfiguration. New profitable and highly scalable business models, strongly based on using and sharing real-time data and information are currently arising /4/. The promised benefits for the manufacturing industry are represented by Wieselhuber as following /7/:

- higher efficiency of production (quality, output, availability)
- higher effectivity of production (flexibility, changeability, adaptability)
- reduced capital costs for production goods (XaaS - Everything as a Service)

WGP estimates a reduction of costs of up to 70% in parts of the production /4/.

1.4 General challenges

Although the predicted benefits are very promising, a few people in the field of Fluid Power seems to know exactly how to deal with the changing circumstances resulting in new requirements imposed to their future products and enabling new potential digital business models. Studies show that especially small and medium-sized enterprises, four out of ten are not following any implementation strategies or taking part in the development and application of IIoT-technologies /8/. One explanation can be found in very diverse understandings of “Industrie 4.0” due to the confusing promotions by the media and marketing divisions, which are labeling anything “IIoT ready”, legitimate or not. Other challenges are seen in high investments /4/ to compensate the lack of technical expertise and infrastructure /4/ on the one hand and to quantify the resulting benefits on the other hand. As well as concerns about Cyber Security /4/, another problem in the classical field of mechanical engineering is the understanding of the correlation between abstractly discussed digital business models and thus necessary design modifications to the components and machines in a company. Condition Monitoring (CM) and Predictive Maintenance (PdM) are broadly recognised future applications and accepted business models related to the Industrial Internet, but for many parties they are the only ones.

2 Commissioning of a linear electro hydraulic actuator

To examine another point of view to the current technologies of “Industrie 4.0” and to relate them to the field of fluid power systems, the following part presents the conducted analysis of the commissioning of an electro-hydraulic-actuator (EHA) which could be integrated by the Original Equipment Manufacturer (OEM) into a machine. As depicted in this section, a majority of the commissioning process is still done manually. Within the settings of a smart factory, plug and play or plug and produce usually combines the installation and commissioning of a system. As part of plug and produce, the goal is to facilitate, speed up and maximise automation of the integration process of a new system for production.

2.1 Commissioning state of the art

2.1.1 Definition

Goal of the commissioning process is to set up the functionality and prove its performance to fit its design requirements. To do so, different tasks need to be done (referring to /9/):

- Setting up and checking the functionality of single components and their interacting behaviour
- Adjusting and optimising parameters
- Eliminating failures and mistakes
- Completion of the documentation

2.1.2 Structure and connections

Figure 3 shows the EHA built into a machine and other interacting systems. The vertical hierarchy of the automation pyramid and the differences in communication can be stated as following. The hydraulic system is composed of a proportional valve, pressure sensors, a cylinder, a position sensor and hoses, all connected to a simplified constant pressure source. The valve is linked to a valve controller and an axis motion controller. Signals in this presented hierarchy level of the field devices are mainly transmitted analogue. Without the correct settings, those transmitted voltages and currents do not represent usable information. The programmable logic controller (PLC) is connected via fieldbus. To obtain a safe functionality of the drive, the mentioned connections need to meet real-time communication (RTC) requirements. Higher hierarchy level systems (Enterprise-Ressource-Planning (ERP), Manufacturing Execution System (MES), Supervisory Control and Data Acquisition (SCADA)), are connected to the PLC by using the Local Area Network (LAN) and have non-real-time communication (NRT).

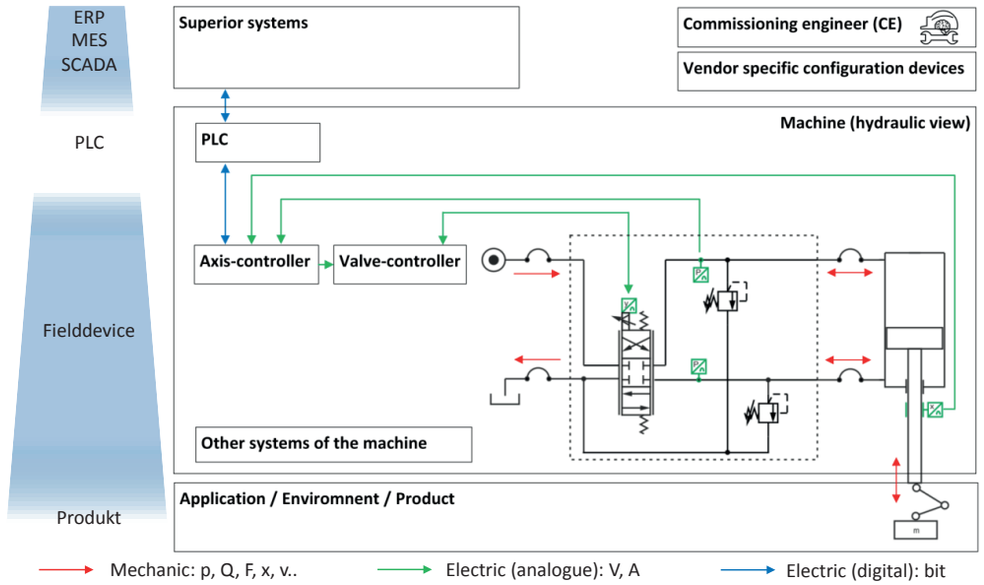


Figure 4: Components and connections of a linear electro-hydraulic actuator

2.1.3 Steps of the Commissioning

After installation, the ramp-up process of the EHA carried out by the OEM can be divided into following phases:

- Validation of the assembly
- Setting up IT-Systems
- Integrating field devices
- Configuring Human-Machine-Interface (HMI)
- Activating the System (Modes: Fail-Safe, Open-Loop, Closed-Loop)
- Testing
- Completion of the documentation

After setting up the system, the commissioning engineer (CE) needs to check the assembly of all hydraulic and electric parts and their connections. Firmware on the PLC as well as on configuration devices needs to be installed or updated. Afterwards, every broadcasting and receiving device needs to be configured to make them understand their communication partner (analogue current and volt or fieldbus). The variety of existing signals and their mapping into higher hierarchy levels makes this step very time consuming and prone to failure in complex systems. The CE uses various data-sheets and his technical knowledge to execute this task. Additional functions for different operating modes, safety and diagnosis are implemented in the PLC. Valve and axis controller are configured and parameterised by plugging-in an additional vendor-specific configuration device. Configuration and mapping of signals for the HMI need to be carried out as well.

To obtain a safe first activation of the drive, the maximum input values of the valve need to be limited, pressure relief valves and the pressure source are set manually to a low level by the CE. In manual or open-loop control mode, tests for the correct direction of the drive and a corresponding position signal are part of the plausibility routine. Checks for mechanical collusions are carried out as well. Dissolved gas is released out of the system, oil gets refilled and the fail-safe system limitations are set back to the desired operating values. As the controller gets activated, parameters are optimised during reference runs in closed-loop control mode. Finally, a test cycle is executed and the results are added to the documentation. The machine is ready to be integrated into the client´s production process.

2.2 Analysis of the Use-Case

As described in the section above, most of the commissioning steps are done manually by the CE or the technician. Only in modern systems, a few steps are executed semi-automatically by the support of assistant systems. A detailed analysis of every single step referring to the following criteria has been carried out:

- Involvement of technical domains (mechanics & hydraulics, electronics, information technology)
- Necessary knowledge and information
- Source and transfer of the information
- Type of execution (manual, semi-automatic, automatic)

Several results can be summarised as following.

2.2.1 Involved technical domains and type of execution

To automate a specific task, it needs to be connected to information technology. In the analysed use-case, around three-quarter of the steps of the commissioning are somehow related to information technology (see Figure 5). In many cases, almost every step is directed to the manual action of a commissioning engineer or technician. Only about one quarter of the steps exclude any relation to information technology.

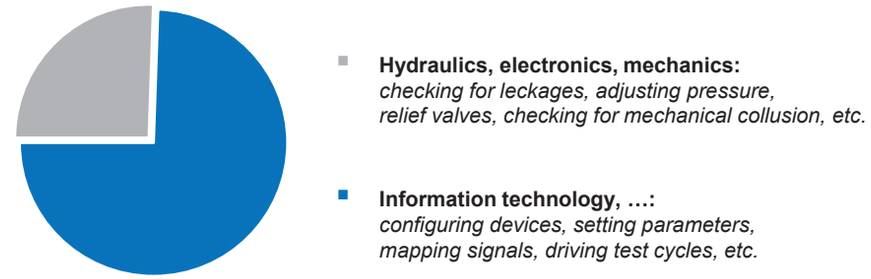


Figure 5: Involved technical domains by the analysed commissioning steps

2.2.2 Necessary knowledge

Much knowledge is applied and a lot of information is needed during the commissioning process. The model pyramide of knowledge (“Wissenspyramide”) of Fuchs-Kittowski /10/, describes the creation of knowledge by linking different information together. Figure 6 gives an example of required information and knowledge for the commissioning process. Classicaly, knowledge is mostly created by the commissioning engineer to derive and execute correct actions.

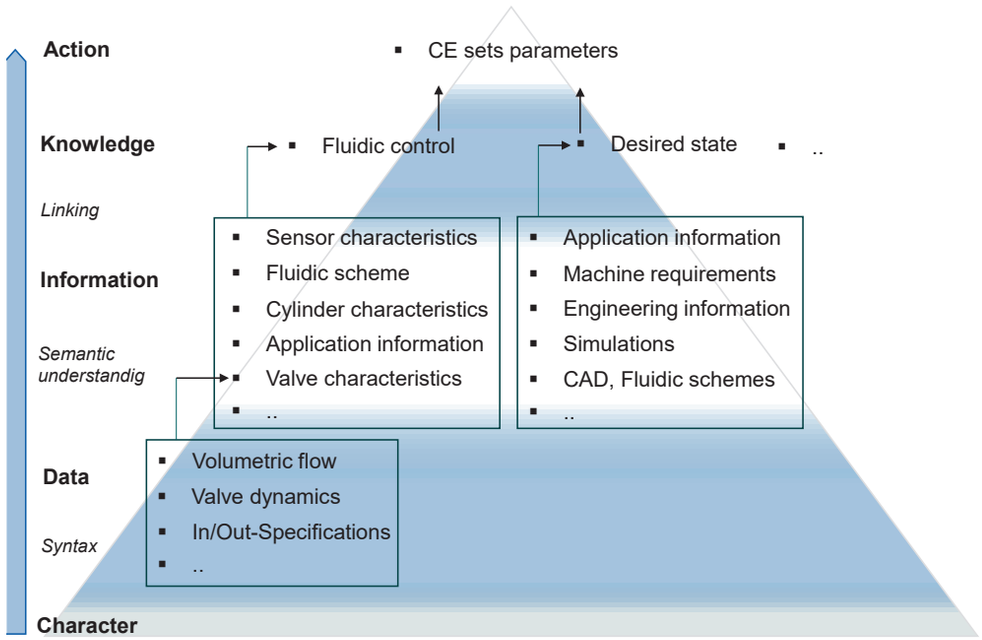


Figure 6: Exemplary necessary knowledge and information for the commissioning (according to /10/)

2.2.3 Source and format of information

Information has no specific structure. It can be represented in lists, diagrams, tables, free text, figures, data bases and many more. In practice, a large amount of information is transferred analogue, via sheets of paper (e.g. manuals, valve diagrams, catalogues, etc.) or during conversations for example between the commissioning technician and the development engineer of the machine. Even the format of information of digital sources is

various, too. Information is stored in configuration files, digital datasheets, simulation models or simple pdf-files, which can be downloaded from the manufacturer´s homepage.

2.3 Evaluation of the Use-Case

The various relations of commissioning steps to information technology shown in figure 4 are representing third industrial revolution technology (automation through computational power) in fluidic production machines. At the same time, the conducted use-case analysis illustrates limitations of "Industrie 3.0" referring to the automation of individual tasks. Figure 7 lists those challenges and relates them to possible technological solutions of "Industrie 4.0" to solve the problems by automating individual tasks as well, represented by the automated commissioning.

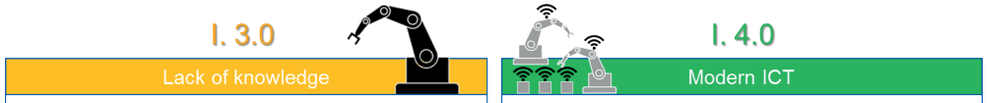


Figure 7: Challenges of "Industrie 3.0"-systems and technological solutions of "Industrie 4.0" by the example of commissioning

2.3.1 Knowledge

One major problem is the insufficient knowledge of the machine. Being caused by multiple reasons, one is the incompatibility of the various communication paths between systems of different hierarchy levels, different functionality or different manufacturers as described in the section above. To achieve a good interoperability, basic standardised communications for the manufacturing industry like for example OPC-UA and AutomationML are introduced /11/.

Unstructured and undefined information, i.e. a mix of numbers, diagrams and drawings on a datasheet, cause problems in terms of machine based processing and effective usage of information. Today, humans interpret the variety of data and input individual required values into the machine. As consequence experts in multiple working groups among different branches are defining basic attributes in order to describe useful properties and features of components and whole systems to increase its computational processability with minimum effort. Current interim results are continuously being integrated in eCl@ss Standard /12/.

Access to information is limited by its local and temporal range which is defined by the source of information. For example, information that was created during the phase of engineering can provide added value two years later for the ramp-up process of machines in another country. Cloud-technology enables worldwide availability of information by connecting via internet for an unlimited period of time. In other local approaches, useful information, which is generated along the whole product lifecycle, gets stored on the product or a virtual data space directly linked to the product. Current generated information can also be sent to other places in real-time.

Currently, technical, organisational and structural knowledge concerning the commissioning is largely based on human experience and provided by specialised technicians and engineers. In order to handle correlations and dependencies, data models of different perspectives are built up and combined in Virtual-Machine-Models (VMM) /13/. The digital twin is one among others discussed. It describes a virtual representation of the real machine which can be analysed in terms of actions and reactions. Additionally, analysing collected data of many commissioning processes (Big Data) and applying machine learning algorithms can build up information technological machine experience and thus improve future ramp-ups.

2.3.2 Action

Based on the latest knowledge, different actions are conducted. Bigger tasks, like the automation of commissioning, are divided into small tasks, solved by functions and services, provided by the available smart components in the system. This can be achieved by a service-oriented architecture (SoA) which had been initially applied in the field of distributed IT-Systems /13/. Referring to the "Industrie 4.0" the service oriented architecture is based on CPS which are the enabling elements to increase the interoperability of systems. They provide encapsulated services and functions that can be executed independently of each other. The flexible arrangement of independent services makes the system adaptable to different configurations and other changing constraints. Automated tuning of the integrated axis controller would be a service in the commissioning process, offered by a smart valve. In several branches, typical descriptions, operational modes and functions of machines are currently being standardized via the OPC-UA Companion Specifications. "AverageCycleTime" and "MachineCycleCounter" for example, represent supplier and machine independent functions, defined in EUROMAP 77 /14/ and EUROMAP 83 /15/ by the branch of Plastic and Rubber Machinery to increase the interoperability of injection moulding machines.

To communicate available services and relevant information right after connecting the devices to the system, a basic communication is another obligatory feature of a CPS.

Several steps of the commissioning might still be executed manually by the technician. Those steps rely on elements that cannot be manipulated via information and communication technology (ICT) since they are not integrated into the system, some not even electrified. Besides adding on-board electronics (OBE) to passive elements, other smart components in the system might provide the required functionality. For example a cylinder does not need to be connected necessarily to the IT-system, if the attached valve provides additional functionality.

2.3.3 General aspects

The classical commissioning process is very reliant on the performing commissioning engineer or technician. Knowledge and manual actions are related directly to this person and thus they are very limited regarding their local and temporal availability. Skills of a single person are not scalable compared to software and furthermore a technician can leave the company with its valuable knowledge and experiences. Different abilities of humans and non-transparent ramp-ups cause unpredicted results in quality, duration and costs of the process which makes it hard for a company to calculate without risking production delays or having resources overhead.

In the scenario of a smart factory, commissioning is becoming very important. The highly flexible production and the reduction of capital costs by temporary renting a production machine (Pay-per-Use) is causing plenty of reconfigurations and repeated commissioning of the machines.

Consequently, mostly automated commissioning (Plug-and-Produce) is the desirable method in a smart factory. People in the production are helping out when the machines action is limited or unexpected errors occur. Modern assistant systems with a personalised human-machine-interface based on visual guidance technology, like augmented reality is supporting non-specialised personal in different execution tasks. If expertise is required, engineers or specialised technicians can support via remote assistant systems.

3 Summary and Outlook

This paper describes basic limitations of the automated integration of current fluid power field devices by the example of a linear electro-hydraulic actuator. As a result of the technological achievements of the third industrial revolution, many commissioning steps and components are already related somehow to information technology. Still, most steps during the commissioning are conducted manually by a commissioning engineer. This can be explained by the individual and changing character of specific tasks, such as a commissioning, that is not feasible for classical automation technology. Due to continuously changing circumstances, knowledge and experience is required to conduct the correct actions.

Developments of "Industrie 4.0" are tackling this problem. On the one hand basic definitions of functions and standardisation of information are improving the computational understanding and interoperability of individual machines. On the other hand, the availability of data and information is improved massively by modern information and communication technology, for example via global accessible clouds. Data is collected consistently across the whole product lifecycle. Through powerful algorithms and increasing computational power, knowledge is generated via big data analysis and machine learning.

Increasing the flexibility of actions and improving the interoperability of different systems can be achieved by the service-oriented architecture. It makes it possible to processes bigger tasks, like the automation of commissioning, by executing distributed functions and services, provided by the system. Cyber-physical systems are the basic element due to their embedded intelligence, basic communication and encapsulated services and functions.

Current research is focusing on the vertical integration of field devices in the defined use-case by implementing a service-oriented architecture of cyber-physical systems. Another digital concept like Assed Administration Shell (AAS) /16/ has the potential to enable horizontal integration, to improve vertical integration and to achieve a consistency of data across the whole product lifecycle.

Furthermore, more use-cases can be analysed in a similar way to complete the picture of future requirements to consider services and attributes in current standardisations.

4 Acknowledgements

The survey on the industrial Internet of Things is in the field of fluid power is funded by FKM - Forschungsfonds Fluidtechnik. The authors thank all experts who enriched the study with their expertise in the conducted interviews in order to reflect the current state of the art of commissioning in the field of fluid power.

Nomenclature

Abbreviation	*Description*
AAS	Assed Administration Shell
CE	Commissioning Engineer
CM	Condition Monitoring
CPPS	Cyber-physical production system
CPS	Cyber-physical system
EHA	Electro-Hydraulic Actuator
ERP	Enterprise-Ressource-Planning
HMI	Human-Machine-Interface
ICT	Information and Communication Technology
IIoT	Industrial Internet of Things
IoT	Internet of Things
LAN	Local Area Network
MES	Manufacturing Execution System
NRT	Non-real-time communication
OBE	On-board electronics
OEM	Original Equipment Manufacturer
PdM	Predictive Maintenance
PLC	Programmable logic controller
RTC	Real-time communication
SCADA	Supervisory Control and Data Acquisition
SoA	Service-oriented Architecture
VMM	Virtual-Machine-Model
XaaS	Everything-as-a-Service

References

/1/ Kagermann, H., et al., *Industrie 4.0: Mit dem Internet der Dinge auf dem Weg zur 4. Industriellen Revolution*, In: VDI Nachrichten, Nr. 13-2011, VDI Verlag GmbH 2011

/2/ acatec, Arbeitskreis smart service Welt, *SMART SERVICE WELT - Umsetzungsempfehlungen für das Zukunftsprojekt Internetbasierte Dienste für die Wirtschaft*, Abschlussbericht, 2015

/3/ Wikipedia, *Industrial revolutions and future view*, https://en.wikipedia.org/wiki/Industry_4.0#/media/File:Industry_4.0.png, visited on October 1, 2017

/4/ Wissenschaftliche Gesellschaft für Produktionstechnik (WGP), *WGP-Standpunkt Industrie 4.0*, 2016

/5/ VDI/ VDE, *Statusreport - Referenzarchitekturmodell Industrie 4.0 (RAMI4.0)*; 2015

/6/ BITKOM, VDMA, ZVEI, *Umsetzungsstrategie Industrie 4.0*, 2015

/7/ Dr. Wieselhuber & Partner GmbH, Fraunhofer IPA, *Geschäftsmodell-Innovation durch Industrie 4.0 Chancen und Risiken für den Maschinen- und Anlagenbau*, 2015

/8/ Schröder, Christian, *Herausforderungen von Industrie 4.0 für den Mittelstand*, Friedrich-Ebert-Stiftun 2016

/9/ Wünsch, G., *Methoden für die virtuelle Inbetriebnahme automatisierter Produktionssysteme,* Dissertation Universität München, Herbert Utz Verlag, 2007

/10/ Fuchs-Kittowski, K., *Wissens-Ko-Produktion – Organisationsinformatik*, Gesellschaft für Wissenschaftsforschung, Berlin, 1. Auflage, 2001

/11/ Schleipen, M., Lüder, A., Sauer, O., et al., *Requirements and concept for Plug-and-Work*, Automatisierungstechnik, DE Gruyter, Band 63, Heft 10, 2015

/12/ eCl@ss classification and product description, http://www.eclasscontent.com/ , visited on October 1, 2017

/13/ Abel, M., *Automatisierte Inbetriebnahme von rekonfigurierbaren Bearbeitungsmaschinen mit serviceorientierten Paradigmen*, Dissertation Universität Stuttgart, Fraunhofer Verlag, 2017

/14/ EUROMAP 77, http://www.euromap.org/euromap77, visited on October 1, 2017

/15/ EUROMAP 83, http://www.euromap.org/euromap83, visited on October 1, 2017

/16/ Plattform Industrie 4.0, ZVEI, *Struktur der Verwaltungsschale–Fortentwicklung des Referenzmodells für die Industrie 4.0-Komponentem*, Berlin, 2016

Predictive Maintenance Service Powered by Machine Learning and Big Data

Dr. Tapio Torikka and Dr. Steffen Haack

Bosch Rexroth AG, Zum Eisengießer 1, Lohr am Main, Germany

E-Mail: tapio.torikka@boschrexroth.de , steffen.haack@boschrexroth.de

We present a service for Predictive Maintenance in which existing machine data from control units or data from retrofitted sensors can be acquired from industrial machines by various gateway solutions. These gateways preprocess the data onsite and transmit it securely to a cloud-based Big Data system without impacting the production process of the industrial machine. Additional servers run Machine Learning algorithms to analyze the incoming data and generate data-based models representing the machine behavior. Results from existing applications show that significant benefits can be created for our customers and that Machine Learning algorithms demonstrate superhuman performance in detecting anomalous machine behavior.

Keywords: big data, digitalization, connectivity, machine learning, predictive maintenance
Target audience: mobile hydraulics, industrial hydraulics, industrial internet

1 Predictive Maintenance

The goal of Predictive Maintenance is to increase the availability of machines by recognizing failures or problems before significant damage is cause to the equipment. With advance information of developing failures, the machine operator is able to prepare required maintenance activities well in advance and avoid unplanned downtime. This is particularly beneficial on mission critical machines in 24/7 operation where downtime is very costly. Predictive Maintenance builds up on Condition Monitoring practises, traditionally carried out using threshold monitoring based on signal analysis: Thresholds for alarms levels are set on individual sensor signals. Also, predefined rules can be used for more complex systems. The interpretation of the data rests on human experts. A Predictive Maintenance system will add an analytics component to assist a human expert in detecting possible failure patterns and maintenance recommendations. This increases the level of automation and accuracy of the predictions. The Predictive Maintenance service presented in this paper uses Machine Learning to reach the required prediction accuracy and to provide an easily observable metric for decision making by human experts. Advantages of this approach, a high prediction accuracy and the reduction of manual setup work, have been demonstrated in academia /3/. The requirement of such an approach is a large volume of data in order for Machine Learning algorithms to learn typical failure patterns. Modern Big Data IT systems are capable of handling huge data volumes and although adoption in traditional industry is not yet common, this is commonplace in IT industry especially among popular cloud services like Facebook and Twitter. At the same time, advances in Machine Learning methods and computing, especially GPU computing, has made the required computing resources available. The platform developed by Rexroth, ODiN, uses these technologies to collect and analyze data from a growing worldwide network of connected machines.

2 Machine Learning

Machine Learning is a field of Artificial Intelligence in which an algorithm constructs a model based on input data in order to make predictions. No explicitly programmed instructions are used to create the model, which enables problems to be solved where limited or no domain knowledge is available. The flow chart in figure 1 shows the process of training and applying a Machine Learning algorithm. After acquisition of data from a selected data source it has to be preprocessed, e.g. by scaling the data and imputation of missing values. After preprocessing a Feature Extraction step extracts significant information from the data in order to improve the following training step. During the training phase a learning algorithm is used to iteratively adjust the internal parameters of the Machine Learning model to improve itself. Once a desired accuracy or a preset training time has been reached, the model can be saved and later used to make predictions with unknown data. /1/

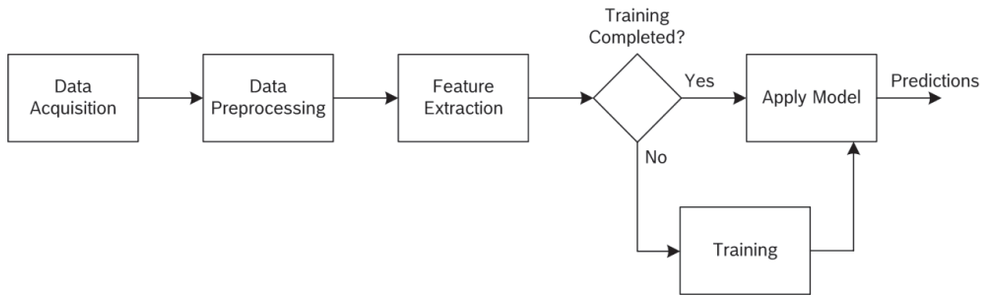


Figure 1: Data flow in a Machine Learning process

In Predictive Maintenance, the goal of a trained Machine Learning model is to predict failures, i.e. assign a known failure category to a presented data set. Two distinct types of learning are of particular interest in this application: Unsupervised and Supervised learning.

2.1 Unsupervised Learning

When no example data of failures is available, unsupervised learning can be used for anomaly detection, i.e. to detect unusual patterns in the data by comparing newly acquired data to previously observed reference data. These patterns can later be labelled and used as input data for a classifier trained via supervised learning.

2.2 Supervised Learning

Supervised learning is preferred when labelled data from known failure patterns is available either through experiments or collection of field data. Also, unsupervised learning can be used for data exploration on unknown data sets to assist the labelling process. The data is labelled with the target category for prediction and used in the training process. After training, a classifier will attempt to classify unknown data to these predefined categories.

2.3 Advantages of Machine Learning

Many machines are purpose built for a specific application and therefore exhibit a unique behavior. Additionally, environmental effects like temperature variations, noise, vibrations, etc. influence the sensor signals. To make matters worse, the data volumes produced by industrial machines are often very large. One reason for this is the need for high frequency measurements due to highly dynamic production cycles of the machine. These characteristics make the assessment of the health state of the machine based on manual inspection of individual sensor signals or simple rules next to impossible. For a Machine Learning algorithm such characteristics do not pose a problem. Learning patterns in the data is possible as long as there is enough data for the algorithms to work with. An example illustrates the capability of this approach: A Machine Learning algorithm reaches a prediction accuracy of over 95% predicting failures on an axial piston pump /3/. The data was collected on a series of test bench experiments by collecting vibration data from accelerometers mounted on a pump. Measurements were carried out on a Good pump as well as after introduction of built in failures. Additional measurements were conducted by running the pump out of specifications. The high variation in the vibration signal which is caused by a different setup of the test bench and maintenance work was taken into account by repeating the measurements after adjustments in the piping of the test bench and after performing a series of simulated maintenance steps on the pump. When the data is presented to a human expert for manual classification, the prediction accuracy drops to 43%.

3 Big Data

Regardless of the definition of the term Big Data based on the data itself (e.g. 3 V:s, 4 V:s), efficiently handling a data set exceeding the storage capacity of a single computer requires the use of a distributed computing framework like Apache Hadoop /2/. In Hadoop each node in a cluster of servers contains storage and computation resources and jobs on the complete data set can be performed using the combined computation and storage capacity of the cluster. Access to the data at the lowest level is provided by a file system, HDFS (Hadoop Distributed File System). Minimal structuring of the data is needed when stored in HDFS, which allows various types of data to be stored as collected from data sources (text files, images, measurement data, logs etc.). Various additional modules in the Hadoop framework allow for data to be structured and processed as required by the use case, e.g. Spark (computation), Hive (data warehouse) and HBase (data structuring into tables). Hadoop contains a management system, YARN, to manage resources and jobs on the cluster. Data on the cluster is typically replicated on several servers/racks. In case of a problem, e.g. hard drive failure, the copies of the data on other hard drives will ensure that no data is lost. This is all managed automatically and is an essential feature for clusters containing thousands of servers. The following chapter shows the architecture of such a system.

4 ODiN Platform

4.1 Architecture

Rexroth has developed a cloud-based Big Data platform, ODiN, in which existing machine data from control units or data from retrofitted sensors can be acquired from industrial machines by various gateway solutions. These gateways collect the data parallel to the control unit of the machine, preprocess the data onsite, prepare it for transmission and forward it to the centralized ODiN Big Data system. The data collection does not impact the production process of the industrial machine since no control functions are performed by the gateway. A secure https data transmission over the Internet is realized in parallel to the existing machine network typically via a cell phone network in order to avoid interference with the onsite network infrastructure.

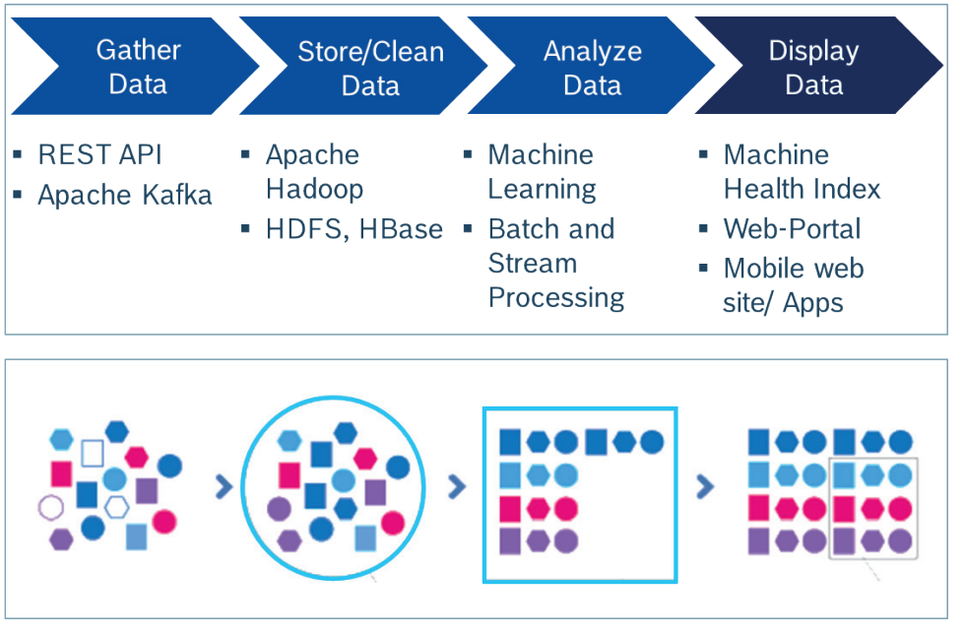


Figure 2: Data processing in ODiN platform

Figure 2 illustrates the data processing within the ODiN system. The cloud-based Big Data system consists of a cluster of servers for hosting data from all connected machines worldwide. The data ingestion is carried out by servers running Apache Kafka receiving data from the gateways on machines via a REST API. These servers feed the data to a Hadoop system where data is stored in HDFS. HBase stores the data in a more structured form for easier access by visualization and analytics processes.

The system implements the lambda architecture consisting of a stream and batch processing part. Stream processing uses Apache Spark and carries out simple statistical calculations (e.g. mean) directly on the input data stream. The results are pushed towards a web portal for fast data visualization purposes. Tasks requiring more computing power, e.g. Machine Learning, are carried out by the batch processing part. Dedicated analytics servers access data in HBase or HDFS, perform predictions on the data and output the results back into these data stores.

The web portal visualizes the results of both stream and batch processing. Quick status information is available on a dashboard and a charting tool gives the users a more detailed access to data and a look at long term trends. The web portal also includes tools for maintenance report generation, accessing equipment information including sensors, a message feed and gateway connection status. Administrators have the possibility to manage users and organizations. A mobile website for handheld devices contains basic information (dashboard and messages) for a quick status check.

4.2 Machine Health Index

The status of machines is displayed using a dedicated metric, the Machine Health Index. Where traditional signal analysis with threshold monitoring involving dozens or hundreds of sensor signals from each connected machine would be laborious, the Machine Learning algorithms condense all input signals from a component or a larger system to a single value, thus simplifying the monitoring of applications. The Machine Health Index quantifies the behavior of the machine or component ranging from 0 to 100 (0 = poor health, high failure probability, 100 = good health, low failure probability). Figure 3 shows a large number of input sensor signals available for monitoring in a traditional approach. The condensed information out of these signals in a Machine Health Index is shown in figure 4.

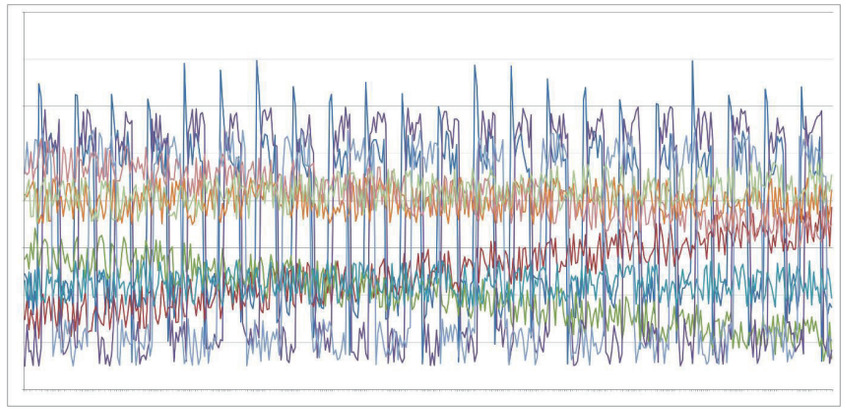


Figure 3: Example sensor signals from industrial equipment

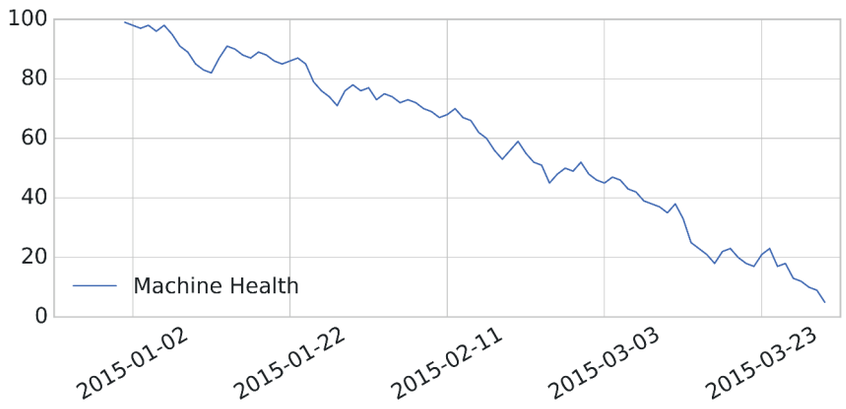


Figure 4: Example of a Machine Health Index with a failure developing over time

In the case of unavailable failure data, the Machine Health Index is based on known failure free reference data from the machine in question. This data is typically collected after installation of the system. In a retrofitted machine a fitness check ensures that the equipment is running nominally. An unsupervised Machine Learning algorithm will then compare incoming data to the reference state, the Machine Health Index will represent the deviation from the reference state. On large machines with a high number of sensor signals the Machine Health Index can be calculated for each component in the machine enabling a more detailed overview of the health of the machine. If known failure data is available, a more precise calculation of the Machine Health Index including the probabilities for the known failures with supervised learning is possible.

4.3 Predictive Maintenance Service

The presented ODiN platform is the basis for a Predictive Maintenance service. This service is offered to customers as a complete package containing data collection, analysis, status reporting and implementation of service actions when necessary. The following chapter shows examples from implemented real life applications.

5 Examples

A break disc manufacturer is using the Predictive Maintenance service presented in the last chapter to increase the availability of a mission critical hydraulic power pack in the production process. The Predictive Maintenance solution would complement an existing scheduled maintenance to further reduce the risk of unplanned downtime. Since no redundancy is built into the power unit, a breakdown of the pump will lead to downtime of the power unit and affect the production process. The power unit was retrofitted with sensors and a gateway collecting data and sending it into the cloud for analysis. After a fitness check the system went live and a Machine Health Index is calculated for each component in the power unit (pump, oil, filters, cooling system). Figure 5 shows an excerpt or the data showing the Machine Health Index for the pump developing over time. After running 70% longer than a scheduled maintenance would have allowed, the behaviour of the pump suddenly changed as indicated by the significant drop in the Machine Health Index. The customer was contacted after a detailed diagnosis by human experts and a replacement of the pump was scheduled a week later. Production continued normally until the replacement. A bearing failure was detected at the inspection of the replaced pump. Due to the advance warning the customer was able to improve organization of the maintenance stop and subsequently cut the maintenance time by 50%.

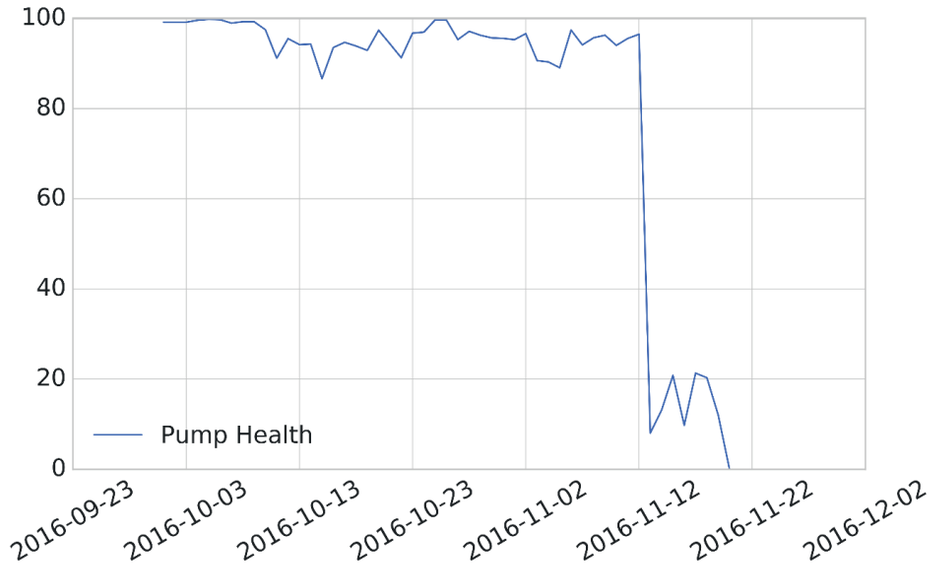


Figure 5: A sudden decrease of the Machine Health Index in early November indicated a significant deterioration of the pump. The customer was immediately notified and maintenance work could be carried out a week later.

A sudden change in machine behaviour like in the example above requires maintenance actions to be taken fast. An example of a slowly developing failure can be shown in figure 6. There is a slowly developing trend in the Machine Health Index several weeks before a serious problem arises. This enables machine operators to be notified well in advance. In the example below, the pump is deteriorating slowly and as soon as a more significant drop to 60 in the Machine Health Index occurred, the customer was notified to schedule maintenance. This time, maintenance could be scheduled three weeks later. During these three weeks the Machine Health Index kept deteriorating but the pump was still operating nominally. This time a less dramatic failure was detected at inspection after pump replacement. However, a failure process was ongoing and the pump would have failed in the near future.

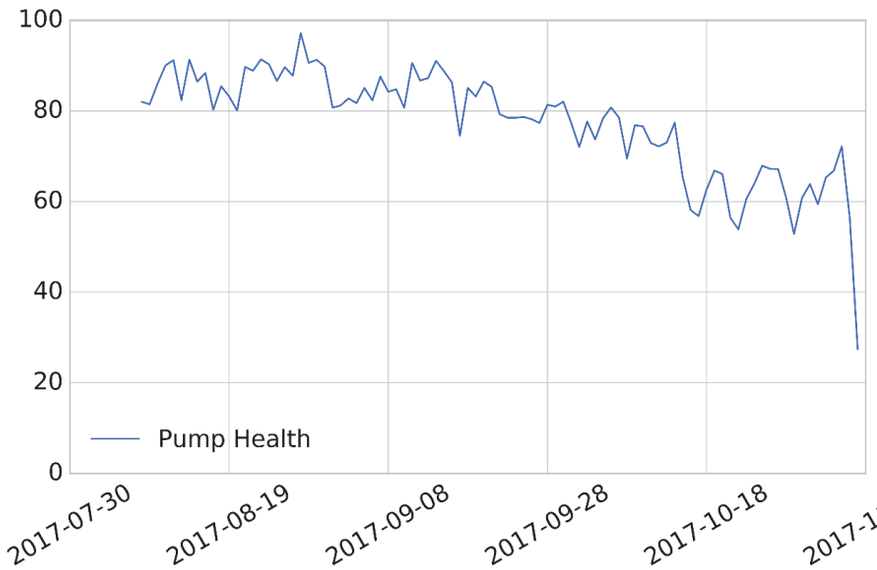


Figure 6: Health of the pump over time. A clear downward trend can be observed. The customer was notified in the middle of October to schedule maintenance. Maintenance was carried out three weeks later.

In the examples above, the Machine Health Index serves as the first indicator of an anomaly in the application and removes the need for humans to continuously analyse the incoming data. Human experts are still needed when an anomaly occurs to decide the correct action to be taken.

With an increasing number of machines connected to the ODiN system the data store is growing rapidly and generating the basis for more detailed failure diagnosis further automating the analytics process.

6 Conclusions

Maximizing availability on industrial machines with Predictive Maintenance requires a higher degree of automation for data analysis when compared to traditional condition monitoring systems. The examples presented in this paper show that Machine Learning algorithms provide this capability by accurately predicting patterns that represent sudden as well as slowly developing failure processes in fluid power equipment without significant human involvement. The required Big Data system containing data from all Predictive Maintenance applications worldwide can be implemented using state of the art software solutions.

When included in a maintenance contract, this solution can significantly reduce downtime on customer machines as demonstrated on real life examples. Due to advance planning, savings of up to 50% in maintenance costs could be achieved. Additionally, lifetime utilization of equipment can be significantly increased in applications where scheduled maintenance is currently used (by up to 70%). Once in place, the data in such a platform can be used by data scientists for the development of additional data based services for end customers as well as component and system manufacturers further increasing productivity.

References

/1/ Duda, H., Hart, P., Stork, D., *Pattern Classification 2nd Edition*, Wiley, 2000.

/2/ N, N., *Apache Hadoop*, http://hadoop.apache.org/, visited on December 12, 2017.

/3/ Torikka, T., *Bewertung von Analyseverfahren zur Zustandsüberwachung einer Axialkolbenpumpe*, Shaker Verlag, Reihe Fluidtechnik, Aachen, Germany, ISBN 978-3844003420, 2011.

From Big Data to Smart Data

Oliver Breuer*

FLUIDON GmbH, Jülicher Str. 338a, 52070 Aachen, Germany*
E-Mail: oliver.breuer@fluidon.com

Industrial Internet of Things (IIoT) and Industry 4.0 are very popular buzz words today. The „me too" factor is pretty high and attracted companies are faced with an overwhelming market of data management solutions. But despite the large amount of data that can be collected from industrial facilities, the real benefit is behind colourful graphics and charts. To get there, the data provided by the connected components of an IIoT capable system has to be analysed and put into context. So, the question is not what can be done with all the collected data but how to generate useful information.

Keywords: Digital Twin, Simulation, IIoT, Model-based Systems Engineering
Target audience: Digitalization, Connectivity and Communication, Design Process

1 Introduction

Monitoring industrial systems is no new invention at all. Equipping a system with a few sensors and logging their data has been best practice for decades. A more sophisticated approach is condition monitoring as an early approach for predictive maintenance, years before it became one of the most popular catch phrases for IIoT.

The real differences between conventional and smart systems are their grade of connectivity and the simple existence of certain sensors due to their integration just into the used components. It means that more components have more to say and are provided with a forum to do just that. That sounds quite simple, but distributing data in an industrial environment is a challenge for various reasons, including security restrictions.

Beyond the challenges that data acquisition entails, data processing is the key to further benefits. IIoT provides contextual analysis of the same data in different domains and levels.

2 Smart Data

Frequently, measured data only becomes useful information in the broader context. This transition requires some kind of intelligent processing.

2.1 A trivial analogy

A car driver is an excellent example of a human data processor. His task is to use all relevant information provided by his senses to drive the car safely. The differences between experienced and unexperienced drivers are

- the definition of "relevant information",
- the definition of "safe operation" and
- the individual grade of control over the system.

Unexperienced drivers are often overwhelmed by the amount of available information. Traffic, road condition, weather, traffic signs, pedestrians, buildings, even the radio programme – all this will be noticed by this driver and taken into account. The data analysis is very time-consuming, and hopefully his skills are sufficient to react adequately.

By contrast the experienced driver is able to filter the incoming information a lot better. He knows the relevant bits in the data stream that affect the behaviour of his vehicle. The reason for that is that he has got a much better idea of how his car reacts and what the requirements for a safe journey are. Objects beneath to the road are, for example, no threat as long as they do not intend to move towards the car's heading. Moisture on the road is more dangerous in leafy corners than on motorway straights, and so on.

The experienced driver has developed a model of his environment and the objects he uses and is able to feed it with current data. He knows how slippery a wet, leafy road is and when his car begins to lose wheel grip. Having analysed the relevant data and applied that to his model, he is able to predict how fast he can drive through the next corner without hitting anything.

2.2 Analysing data

As shown in 2.1, the quality of prediction depends on current data, knowledge about the behaviour of a system (the model) and experience. Screening the relevant data and assessing it manually is an appropriate way for a manageable amount of data and simple systems, but it reaches its limits with increasing data amounts and system complexity as occurring when the full potential of new technologies like IIoT is to be exploited. Referring to the driver example, even experienced drivers get overstrained sometimes if the needed information cannot be recognized at once. So, there is the need for an experienced driver with very quick comprehension who can analyse data based on his earned knowledge.

A promising approach to a quick and complete examination of data is automated data processing. A contemporary data processing system can observe millions of values in fractures of seconds, compare them with thresholds and display warnings to the operator. Despite its performance, this approach alone would be insufficient having the large amount of data in mind that can be provided by IIoT systems, at least if one would like to tap the full potential. If the correct relations are established in the system, the correlation of all this data unveils a deeper information layer. The instance that can make these relations is the model.

2.3 Digital Twin

Using a model in automated analysis allows estimating the condition of a subsystem or component, even though it is not directly monitored by dedicated sensors. It acts as a virtual experienced maintenance engineer who can diagnose a system from many malfunctions by just listening to his machine's noises because of the knowledge-based model in his mind. Beyond that, the approaches of both the maintenance engineer's mind model and the digital model can be used for "what-if" scenarios. It means that it is possible to use a model for extrapolating current data based on a behavioural description. An obvious use case is predictive maintenance. This method tries to avoid unexpected system downtimes due to worn-out components by monitoring the trend of certain indicators and providing an estimated remaining runtime until the need for maintenance. The indicators are calculated by a simulation model that is a replica of the real system – a digital twin.

Real-time data processing for a huge amount of data, a digital twin of the whole system – that offers a whole bunch of new possibilities, doesn't it? Being able to predict every future development of any component in the facility sounds tempting but, in fact, that is not the way it goes.

A major critique on simulation is often the lack of completeness. Simulation models are just as accurate as the behavioural description behind and only within its validity range. To achieve a sufficient grade of accuracy, the model has to be very precisely defined. This is directly related to the computational power required for acceptable calculation times. Such an accurate model representing a whole facility with all aspects would therefore be way too slow to provide the current state of the system in time.

At this point, the car driver example in 2.1 could be helpful a last time. The purpose of the driver's model is to ensure a safe journey. That does not include any other coherence like the photosynthetic uptake of the tree beneath the wet corner while the car passes by, emitting carbon dioxide, although this is of course also an important issue.

But the environmental model of our driver has to include the tree's effect on his car when he hits it in case of a miscalculation, not the biological processes of the wooden plant.

This strategy of simplification and concentration on the relevant things can be transferred to the concept of the digital twin. The guiding principle should not be "Process all of the available data". In fact, a definition of what information is useful for an additional benefit should come first. A simulation model for exactly this purpose is most likely computable in reasonable times and much more maintainable because of its size.

2.4 Use case

Suppose a system contains hydraulic cylinder drives. The drives are position controlled and used for material processing where accuracy and speed have top priority and machine downtime has to be absolutely minimized. Power supply is provided by an adjustable pump unit. The layout of the cylinder drive is shown in Figure 1.

The subsystem is equipped with the common sensors that can be found in many similar systems. A PLC processes the relevant sensor data and activates the pump and the servo valve. The operator is quite up to date and has established a pool for all the accumulating data of his facilities, catchy related to as the cloud. Although the components of the described subsystem have been provided by different manufacturers, they are all able to transmit data to the cloud, either via the PLC or via their own interfaces.

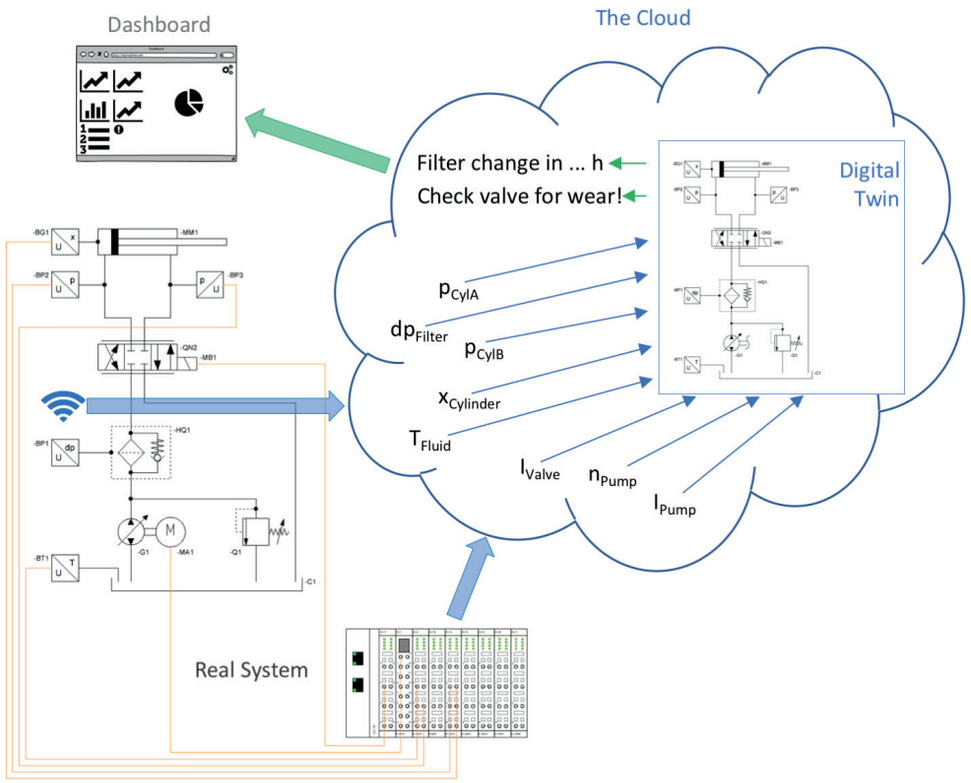


Figure 1: The digital twin as data analyser

As mentioned, the operator is especially interested in keeping the machine running and remaining a high standard of accuracy. Concentrating on the exemplary cylinder drive, there are at least two components that can be related to these requirements: the high-pressure filter and the servo valve.

Some operator's questions could therefore be

- When does the filter have to be changed if we keep the current operating conditions?
- When will the servo valve be too worn-out to keep the tolerances while maintaining the current speed?

or maybe even

- With the current system condition, how fast can we produce without affecting quality?

The filter is a component that has to be maintained frequently, depending on run-time, fluid contamination, or even sudden stress failures, so monitoring this component closely could reduce machine downtime. The servo valve suffers from wear of its metering edges, which has an impact on system performance and accuracy. The similarity between both components is that they cannot simply raise their arm and say "Hey, operator, I'm tired!".

The condition of these components can only be determined by context. The valve control signal value, for example, has to be checked against the current cylinder movement profile and the differential pressure over the filter depends on filter load as well as fluid viscosity. These dependencies are described within the model of the hydraulic part of the cylinder drive, the digital twin, and it is part of the cloud.

3 The Value Chain

The creation of digital twins, as well as the creation of simulation models in general, requires know-how and data. That can be a problem in terms of intellectual property, because the plant manufacturer is not necessarily the manufacturer of the used components and could therefore have limited access to required data. One way to deal with this information gap is to estimate the missing data based on experience or context. Another way is to add new processes to the component manufacturer's value chain.

3.1 Model Exchange

An obvious alternative is the deployment of the physical component along with the corresponding digital twin by the component manufacturer (Figure 2). In this case the twin is technically a boxed simulation model with a defined interface. This is not a new approach to the exchange of models, in fact it is one of the initial drivers for the Functional Mock-up Interface (FMI):

> "The FMI development was initiated […] with the goal to improve the exchange of simulation models between suppliers and OEMs." (Modelica Association, /1/)

So, using the FMI protects intellectual property but allows the usage of a model that has been created by the manufacturer itself and should therefore be as accurate as possible. The model, according to the FMI standard called a FMU (Functional Mock-up Unit), becomes part of the digital twin that is located in the plant operator's cloud.

3.2 Component as a Service

The new flexibility offered by IIoT also allows an outsourced analysis. The component manufacturer gets access to certain values in the cloud of the plant operator and analyses the data using his own component twin. This approach works best when the component does not have too many logical dependencies on the rest of the system.

Combined with a maintenance contract, the plant operator actually pays more for the function provided by the component than for the component itself (Figure 3). A further aspect is the possibility of continuous adaptation and improvement of the component due to the manufacturer's access to real-time operating conditions. He could

therefore install an improved version of his component at the next maintenance appointment. So, although the exchange of data with third parties is a major problem for many companies, both sides can benefit.

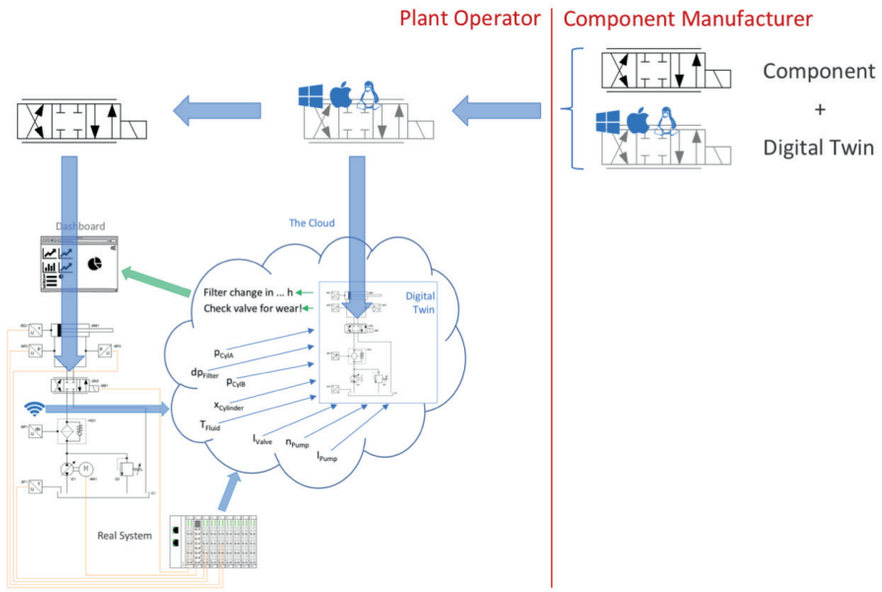


Figure 2: Model Exchange

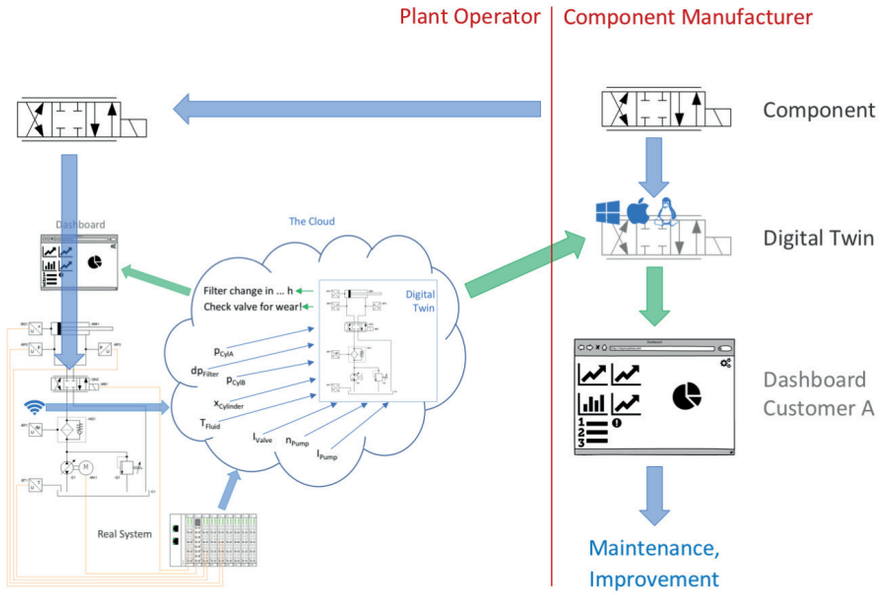


Figure 3: Component as a Service

4 Digital Thread

Working with digital models is an enabler for a connected data flow through design, development and operation of a system. In the past, simulation models where mostly used during the product development phase. Digital twins remove this limitation. Not only that these particular models are used in parallel to the real system's operation phase, they can also serve as prototype for a new clone to be used for future developments, being constantly fed with real-time process data. This opens up the possibility of being able to carry out performance and wear behaviour studies during development on the basis of current data.

5 Conclusion

Simulation models are no longer just development tools. They can accompany their real counterpart over its entire lifetime. The digital twins serve as reference and test bench, they transform raw data into useful information. The particular challenge with digital twins is not so much the creation of accurate models as the derivation of current states based on measured data. The biggest challenge, however, is to even get close to data, at least for third party cloud services. The distribution of data to the other side of the company site wall causes an uneasy feeling for many plant operators.

References

/1/ Modelica Association, *Functional Mock-up Interface*, <http://www.fmi-standard.org> (11.01.18).

Towards digitalization of hydraulic systems using soft sensor networks

REVIEWED

Peter Pelz*, Ingo Dietrich*, Christian Schänzle* and Nils Preuß*

Institut für Fluidsystemtechnik, Technische Universität Darmstadt
Otto-Berndt-Str. 2, D-64287 Darmstadt, Germany*
E-Mail: Peter.Pelz@fst.tu-darmstadt.de

Today buzzwords like “smart machine” and “intelligent component” dominate the discussion about digitalization in the fluid power domain. However, the engineering fundamentals behind the words “smart” and “intelligent” often remain unclear. A common and target-oriented discussion needs transparent approaches including the applied technical system understanding. Therefore, this paper presents new concepts of soft sensor networks which allow the aggregation of information about fluid systems from heterogeneous sources. Soft sensors presented in this paper are physical models of system components that ensure transparency. Soft sensors and soft sensor networks are applied on exemplary hydraulic systems on three different levels: (i) the sensor level, (ii) the component level and (iii) the system level.

Keywords: soft sensor network, digitalization, condition monitoring, predictive maintenance
Target audience: mobile and stationary hydraulics, component manufacturers, system operators

1 Introduction

As the motto of the 11th IFK „Fluid Power Networks“ states, the digitalization in the fluid power industry is becoming more and more important. New applications and functionalities are developed and may be a competitive advantage on the market. At the same time, hydraulic systems are characterized by their high power density, high reliability and good controllability for varying load requirements. Typically, such systems contain positive displacement pumps, hydraulic motors for energy conversion, accumulators for energy storage and valves to realize the control.

Despite of the high technical demands, hydraulic systems usually face a high cost pressure because of strong competition. Thus, implementing new digital features, such as integrated sensors, condition monitoring and predictive maintenance solutions are challenging. Integrating expensive hardware and sensors into hydraulic components can only be considered for high-end applications due to financial reasons. Furthermore, today’s discussion about digitalization of the fluid power domain is dominated by buzzwords like “smart machine” or “intelligent component”. However, the engineering fundamentals behind the word “smart” and “intelligent” often remain unclear and the conflict between cost pressure and the realization of new features is neglected. Given this background, soft sensors are a promising and cost effective solution.

Soft sensors are models of system components that allow the calculation of system variables. In control theory, soft sensors are usually called “observer”. For their implementation, affordable computer hardware is necessary. The recent price drop of electronic hardware offers possibilities for a wide range of applications. The Raspberry Pi zero is a representative example. The fully equipped computer is half the size of a credit card and available for 5 $.

This paper presents new concepts of soft sensor networks combining multiple soft sensors to exchange and to gain information about technical systems derived from heterogeneous sources. All presented soft sensors are based on physical modelling and, thus, on clear fundamentals of engineering. The capability of soft sensors to contribute to the digitalization in hydraulic applications is demonstrated in this paper by focussing on three different levels: (i) the sensor level, (ii) the component level and (iii) the system level. Each application level is motivated by its own research question: (i) How can costs of hardware measurement equipment be reduced? (ii) How can components become self-aware and environmental-aware? (iii) How can additional information on system level be generated and used for predictive maintenance?

To address these research questions, in section 2 this paper gives a brief literature review on soft sensors and presents the further development based on hybrid soft sensors. Section 3 presents the soft sensor application on sensor level and discusses cost reduction as well as the calculation of immeasurable system variables by means of a pressure accumulator. Section 4 focuses on the soft sensor application on component level. Based on a simple fluid the implementation of a self-aware pump that recognizes its or the system’s changing characteristic due to wear is discussed. Section 5 presents the soft sensor application on system level where each component is represented by a soft sensor. In this way, a redundant data acquisition based on different soft sensors is possible and allows data induced conflicts. Data induced conflicts are used as an indicator of changed system behaviour and provide an approach for predictive maintenance. Finally, section 6 gives a conclusion and an outlook on future research.

2 Soft sensors and soft sensor networks

Literature review

Soft sensor is the abbreviation of “software sensor” and represents a cyber physical system that measures a subset of system variables $X_{i,m}$ of a process and, on this basis, computes unknown system variables $X_{i,c}$ of this process. For this purpose, process models are needed to describe the relation $X_{i,c} = f(X_{i,m})$. These models can be subdivided into the following three main categories: (i) physical models, (ii) empirical models and (iii) data-driven models based on machine learning algorithms (e.g. artificial neural networks) /1/ /2/ /3/.

Initially, the process industry, with its challenging conditions like plant size, rough environment for measuring equipment and high costs concerning machine downtime, motivated the usage of soft sensors in the 1990s. Facing the high complexity of technical processes, an analytical description often is not possible. Hence, given the availability of historical plant data, most of the soft sensors in the process industry are based on data-driven models and artificial neural networks. Their main use is to back-up measuring devices, to replace hardware sensors, to estimate system variables for condition monitoring and controlling as well as to detect failure. In this context, Fortuna et. al. /4/ and Desai et. al. /5/ prove the use of soft sensors in distillation columns and batch bio-reactors, respectively. Furthermore, Kadlec et. al. /6/ give a detailed overview of further applications of soft sensors in the process industry.

Nowadays, soft sensors can be found in various fields of applications, e.g., manufacturing or chemical industry. A new field of application are fluid systems. Here, soft sensors are mainly used to replace the volume flow measurement, since flow metering entails high acquisition and installation costs. Concurrently, flow control is the most important control strategy in industrial applications /7/. Against this background Ahonen /8/ and Leonow et. al. /9/ present soft sensor approaches that are based on physical and empirical models of single centrifugal pump units representing the following pump characteristics: Q-H characteristic, Q-P characteristic or Q-I characteristic, where Q is the volume flow rate, H is the pressure head, P is the power consumption and I is the stator current of the electric drive of the pumps. Yong-feng et. al. /10/ describe a method to estimate the volume flow rate of a gear pump, depending on the load pressure, rotational speed and varying viscosity of the hydraulic oil. Their experimental analysis shows, that their soft sensor can achieve an accuracy of ±2 % concerning the relative error. Beside the scientific publications, soft sensors have already entered the centrifugal pump industry. The pump manufacturers Grundfos and KSB developed the Alpha 3 series /11/ and the PumpMeter /12/, respectively. Both soft sensors allow the model based determination of the volume flow rate in the current operating point of the pump.

New view on soft sensors

In contrast to the reviewed literature, a classification of soft sensors in distinct models needs to be overcome. Instead it is useful to combine different approaches developing hybrid soft sensors. Hybrid soft sensors are characterized by the combination of methods of problem condensation, e.g. dimensional analysis, cf. Pelz et. al /13/, domain specific knowledge (axiomatic and empiric models) and data-driven models. Figure 1 illustrates a generic hybrid soft sensor as a stack of filter disks representing the capability to combine, exchange and expand different approaches.

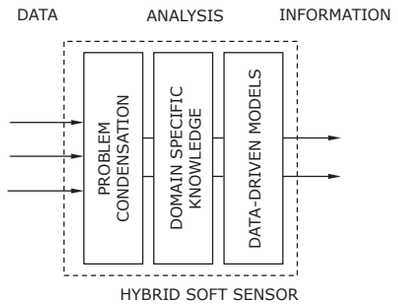


Figure 1: "Filter disks" of a hybrid soft sensor.

From this perspective, a soft sensor needs to be implemented as a digital twin of a respective component. In order to create synergies and to gain information, the exchange of information of the multiple soft sensors is necessary and useful. Consequently, this leads to soft sensor networks. Figure 2 shows the generic approach of a soft sensor network applied on the example of a hydraulic drive system. In the first step, electric signals are measured that are used by soft sensors to gain data based on their implemented models. In the second step, all data of the soft sensors needs to be merged. This allows a detailed analysis to gain information on system level and forms a basis for applications like predictive maintenance.

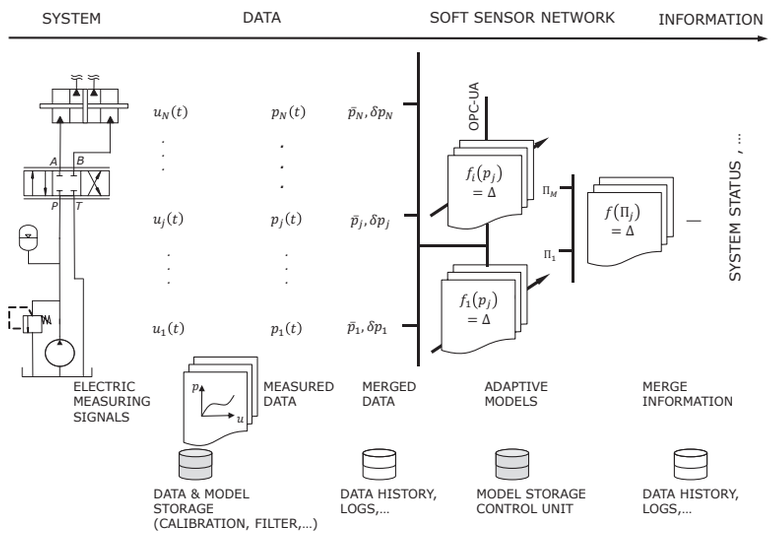


Figure 2: Generic approach to aggregate system information based on a soft sensor network.

3 Sensor level – cost reduction in hydraulic systems

As mentioned above, high cost pressure often prevents the use of expensive measurement equipment in hydraulic applications. From this perspective, the use of soft sensors provides a useful opportunity to realize the determination of desired system variables. Particularly in regard to hydraulic components, a large number of models already exists and is given by well-known literature /14/ /15/. On this basis, the application of soft sensors in the hydraulic domain suggests itself. In the following, the model of a pressure accumulator given by Pelz and Buttenbender /16/ serves as an illustrative example of a soft sensor application and its advantage usage.

The knowledge of the time-dependent energy content of a pressure accumulator during operation is often desired, but the metrological determination is costly and, thus, usually not considered. However, applications like the *Hybrid Air* of the PSA Group /17/ require the quantification of the energy content. As shown by Pelz and Buttenbender /16/, this is possible with axiomatic description of the time-dependent behaviour of a pressure accumulator by means of only three equations:

1. The equation of continuity that considers the temporal change of the density ϱ and the volume V, the mass flow rate at the inlet $\dot{m}$, i.e. the product of the density ϱ and the volume flow rate Q, and the mass flow rate due to permeability $\dot{m}_{perm}$

$$V\frac{\mathrm{d}\varrho}{\mathrm{d}t} + \varrho Q + \dot{m}_{perm} = 0. \tag{1}$$

2. The equation of energy that considers, firstly, temporal change of the volume specific inner energy, i.e. the product of the density ϱ, the isochoric heat capacity c_V and the gas temperature T, secondly, the enthalpy flow due to mass flows at the inlet and due to permeability, multiplied with the isobaric heat capacity c_p and gas temperature T, and thirdly, the heat flow due temperature difference between gas temperature T and ambient temperature T_U with the accumulator surface A and the heat transfer coefficient k

$$V\frac{\mathrm{d}\varrho c_V T}{\mathrm{d}t} + (\varrho Q + \dot{m}_{perm})c_p T + kA(T - T_U) = 0. \tag{2}$$

3. The thermal equation of state of an ideal gas considering the pressure p as a function of the density ϱ, the gas constant R and the temperature T

$$p = \varrho R T. \tag{3}$$

With known initial conditions $p(0) = p_0,\ T(0) = T_0$ and the integrated volume flow Q that gives the time-dependent volume V

$$V = V_0 + \int_0^t Q\mathrm{d}t\,, \tag{4}$$

the solution of the non-linear equation system (1) to (3) is possible and all remaining unknowns, i.e. the pressure p, the temperature T and the density ϱ, can be calculated. Pelz et. al. /16/ proof a good correlation between the numerical solution and the solution of the linearized description. Given the transmission function, the description of the time-dependent behaviour of a pressure accumulator including the energy content only needs the measured volume flow rate at the inlet. At this point, calculated values of the volume flow rate (see section 5) may also serve as input and can replace the rather costly measurement of the volume flow rate. As the example shows, the implementation of soft sensors on the sensor level can reduce the expenses for measuring equipment.

4 Component level – self-aware and environmental-aware components

During operation, components of a fluid system will change their characteristics due to wear. However, the operator must ensure that the fluid system still fulfils its function permanently or needs to identify the worn out component in the case of a malfunction. On the other side, it is in the interest of each component manufacturer to be aware if his component or another system component, i.e. the system environment, caused a malfunction of the system. From both points of views, a self-aware and environmental-aware component that detects its changing characteristic and describes it quantitatively is of high interest. Consequently, this leads to the research question *how can components become self-aware and environmental-aware*?

Soft sensors are able to provide a solution, which is demonstrated on an exemplary generic fluid system, shown in Figure 3. This case example considers the perspective of a pump manufacturer whose pump is used in an unknown fluid system. From this point of view, only parameters of the pump, e.g. size, control, power supply and the working fluid are known. Regarding the pump, the complete environment, e.g. valves, filters or similar, can be described as one generalized resistance. Furthermore, the pressure and temperature are measured at the outlet of the pump. The function of the fluid system is to realize a specified volume flow rate.

In the case of wear, three scenarios are possible: Firstly, the pump characteristic changes, secondly, the system environment characteristic changes or, thirdly, both characteristics change. In either case, the function, i.e. the volume flow rate, will change and must be controlled, e.g. via the pumps rotating speed. At this point, the manufacturer needs a soft sensor of his pump and a soft sensor of the system environment monitoring the pump's conditions. In the following subsections, both soft sensors and their fusion to a self-aware and environmental-aware pump are presented and discussed.

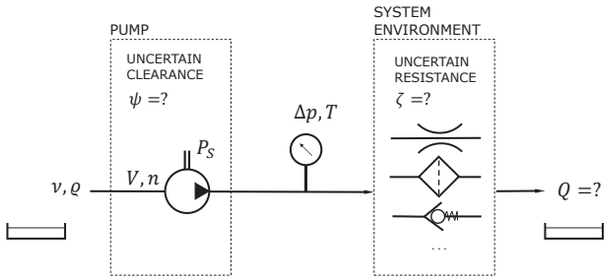


Figure 3: Schematic view of a generic fluid system.

4.1 Soft sensors of the pump and the system environment

The function of the exemplary fluid system shown in Figure 3 is to realize a specified volume flow rate. The volume flow rate is a conservation variable that is equal for the pump and the environmental system. Hence, it is the starting point of both soft sensors.

Considering the pump, the volume flow rate Q is the difference between the theoretical volume flow Q_{th} and the internal leakage Q_{l}. The theoretical volume flow Q_{th} is the product of the geometric volume V and the rotation speed n that lead to the description of the volume flow rate

$$Q = nV - Q_l. \tag{5}$$

The internal leakage $Q_l = Q_l(\Delta p, \nu, \varrho, V, \psi,)$ is derived by Pelz et. al. /13/ to be a function of the pressure Δp, the working fluid properties, i.e. kinematic viscosity ν and density ϱ, and the geometric parameters of the machine, i.e. the geometric volume V and the relative gap ψ. Taking dimensional analysis into account, Pelz et al. /13/ develop a semi-analytical model of the volumetric efficiency η_{vol}

$$\eta_{vol} = 1 - \frac{1}{Re}\ Q_l^+(\psi, \Delta p^+), \tag{6}$$

with the Reynolds number Re and the specific internal leakage Q_L^+. The specific internal leakage Q_L^+ is a function of the specific pressure Δp^+ and relative gap ψ. The mentioned dimensional numbers are defined as

$$\eta_{vol} \coloneqq \frac{Q}{nV}, \qquad Re \coloneqq \frac{nV^{2/3}}{\nu}, \qquad Q_L^+ \coloneqq \frac{Q_L}{\nu V^{1/3}}, \qquad \Delta p^+ \coloneqq \frac{\Delta p}{\nu^2 \varrho V^{-2/3}}. \tag{7}$$

Equation (2) represents a soft sensor for the pump characteristic and is mathematically described by

$$\eta_{vol} = 1 - \frac{L}{Re}\ (\Delta p^+ \psi^3)^m \tag{8}$$

with the empiric pump parameters L and m. Hence, the volume flow rate is represented by the dimensionless volumetric efficiency of the pump. Furthermore, the effect of wear in the pump can be described by an increase of the relative gap ψ, that leads to a higher internal leakage. Consequently, the relative gap ψ is uncertain and needs to be determined during operation.

At the same time, the unknown system environment of the pump can be modelled by a generic resistance

$$\Delta p = \frac{\varrho}{2} \zeta' \left(\frac{Q}{A}\right)^2 \tag{9}$$

with a loss coefficient ζ' and the unknown cross section A. Equation (5) describes the pressure loss in the system environment as a quadratic dependence of the volume flow rate. By means of dimensional analysis the generalized loss coefficient is defined as

$$\zeta \coloneqq \zeta' \frac{V^{4/3}}{A^2} \tag{10}$$

and leads to a dimensionless representation of the generic resistance

$$\Delta p_+ = \frac{1}{2} \zeta\ Re^2 \eta_{vol}^2 \tag{11}$$

with the known dimensionless numbers of equation (7). The unknown cross section A does not occur anymore. The effect of wear in the system environment can be described by a change of the generalized resistance ζ. Like the relative gap ψ of the pump, the generalized resistance ζ is uncertain and needs to be determined during operation.

At this point, there are two soft sensors, equation (8) and equation (11), that contain the three unknowns: Firstly, the volume flow rate Q or volumetric efficiency η_{vol}, secondly, the relative gap ψ and, thirdly, the generalized resistance ζ.

Thus, one further equation is necessary to complete the equation system allowing the calculation of the three unknowns during operation. For this purpose, the model of the hydro-mechanical efficiency η_{mh} of the pump by Pelz et. al /13/ can be applied

$$\eta_{mh}^{-1} = 1 + \frac{2\pi}{1 - \kappa_+}\left(C + R_\mu \frac{Re}{\Delta p^+ \psi} + R_\varrho \frac{Re^2}{\Delta p^+}\right) \tag{12}$$

with the known dimensionless compressibility κ_+ of the working fluid. The dimensionless numbers are defined as

$$\eta_{mh} \coloneqq \frac{\Delta p V n}{P_S}, \qquad \kappa_+ \coloneqq \kappa \Delta p / 2. \tag{13}$$

C, R_μ and R_ϱ are empiric pump parameters. The relative gap ψ occurs in the model of the hydro-mechanical efficiency as well, as equation (12) shows.

4.2 Fusion to a self-aware and environmental-aware pump

The soft sensor network based on the three soft sensors, i.e. equation (8), (11) and (12), now allows the sequential calculation of the three unknowns, the volumetric efficiency η_{vol}, the relative gap ψ and the generalized resistance ζ during operation. The approach is as follows:

4. The relative gap ψ is calculated from equation (12) on the basis of the known empiric pump parameter, the geometric volume, the measured quantities, i.e. pressure, temperature, rotating speed and shaft power. The working fluid properties, i.e. viscosity, density and compressibility, have to be calculated from rheological models, e.g. the Arrhenius law, and the temperature.
5. The volumetric efficiency η_{vol} is calculated from equation (8) and the known relative gap ψ.
6. The generalized resistance ζ is calculated from equation (11) and the known volumetric efficiency η_{vol}.

Within this framework, the pump manufacturer is able to monitor and describe the condition of his pump quantitatively by means of the relative gap ψ and, at the same time, knows if the pump or the system environment causes a malfunction, i.e. providing an unspecified volume flow rate.

In summary, the presented soft sensor network consists of five layers and represents the above presented approach from simple data measurement to a self-aware and environmental-aware pump. According to Figure 4, the five layers of the soft sensor network are (i) the supply of additional information, eq. rheology, (ii) the problem condensation by means of dimensional analysis, (iii) the domain specific knowledge of fluid systems, (iv) the equation solver and (v) the presentation of problem specific key performance indicators (KPI) in a cockpit to the manufacturer or operator.

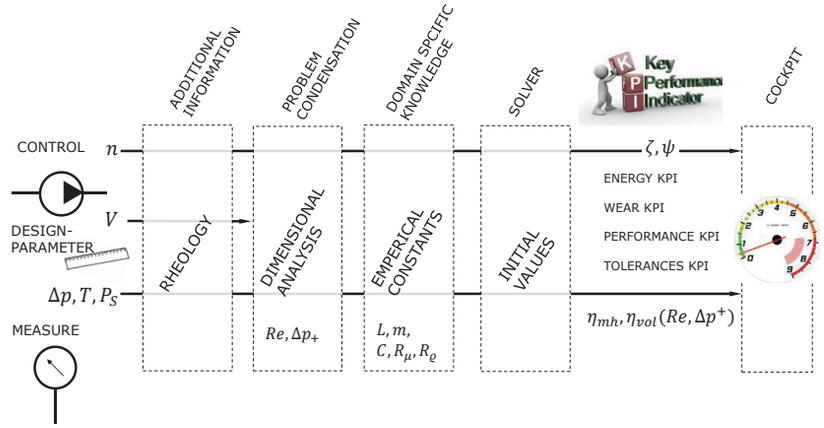


Figure 4: Application of the filter disks (Figure 1) resulting in five layers of a soft sensor network for ζ and ψ.

The approach to a self-aware pump was also examined experimentally on a test bench by means of two identical screw pumps: One screw pump without wear and one screw pump with modified gaps, according to typical signs of wear /18/. The examination includes the measurement of characteristic curves, i.e. pressure and volume flow rate, at a constant rotating speed for two different oils. Furthermore, the sequential calculation of the two unknowns of the worn out pump, i.e. the relative gap ψ and the volume flow rate Q, is performed. On this basis, a validation of presented approach according the self-aware pump is possible. Figure 5 shows the validation results by means of the measured characteristics curves of both, the screw pump without wear and the worn out screw pump, and the calculated characteristic curve of the worn out pump by the soft sensor. The soft sensor and measured values show a very good correlation in the case of an oil with a kinematic viscosity of 22 cSt, as shown in Figure 5a). The calculated and measured values in the case of an oil with a kinematic viscosity of 54 cSt show a slight deviation, but still underline the application ability of the approach under the named conditions.

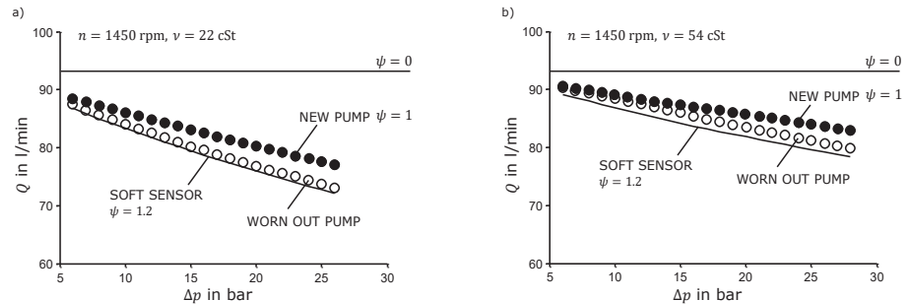


Figure 5: Validation of soft sensor network approach on screw pump with and without wear.

5 System level – data aggregation in hydraulic systems using soft sensor networks

As already mentioned, hydraulic systems face a high cost pressure on the market. Installation and maintenance require highly qualified professionals. Thus, not only the initial purchase and installation costs, but also the operating and maintenance costs are of high interest. Against this background, predictive maintenance is closely connected to significant cost saving potential /19/. Since these cost saving will occur over the operating time, the advantage is not directly seen by the customer. Thus, additional costs for predictive maintenance solutions are rarely accepted on the market.

While section 4 is discussing the use of soft sensors on the component level, for fluid systems containing multiple hydraulic components, the application and connection of soft sensors on every component, i.e. a soft sensor network, is useful. As Aristotele's proverb has it "the whole is greater than the sum of its parts", data of all single soft sensors need to be merged and are supposed to generate additional information. This is of high interest, since additional information on the system level comes "for free" without the need of additional sensor equipment. Consequently, the question raises "how can additional information on the system level be generated and used for predictive maintenance?"

Under the assumption of a constant density of the working fluid and no external leakage, the volume flow rate represents a conservation variable of each fluid system. Thus, the volume flow rate is an information carrier between the corresponding soft sensors and allows its redundant calculation by different soft sensors. Now two scenarios are possible: Firstly, the calculated data is consistent and verified. Secondly, contradictory statements about the volume flow rate occur. Such contradictory statements are called data induced conflicts and can have different reasons: (i) A measuring sensor breaks down or becomes defective. (ii) The inconsistent data results from model uncertainties of the soft sensors. (iii) Single system components characteristics change due to wear. Hence, a data induced conflict is an indicator for uncertainty in the fluid system. On the other side, the resolution of a data induced conflict provides a basis for predictive maintenance, e.g. the identification of a worn out component before breakdown.

The following approach is developed within the Collaborative Research Center 805 "Control of Uncertainties in Load-Carrying Structures in Mechanical Engineering" at the Technische Universität Darmstadt. The first step is obvious. Data induced conflicts have to be allowed by means of redundant data acquisition of a soft sensor network. In the second step, the cause of the data induced conflict has to be classified into (i) sensor break down, (ii) soft sensor uncertainty or (iii) component characteristic change. The following action depends on the classification of the conflict. In the first case, a sensor breakdown is usually identified by the time history of the sensor. If the signal suddenly changes or interrupts, either the sensor needs to be replaced or the soft sensor must ignore it. In the second case, soft sensors need to be based on validated models meaning the model uncertainty is

known and quantified. Thus, a data induced conflicts caused by model uncertainty can be identified and has to be accepted. The third case occurs as soon as the two previous cases are excluded. The worn out component needs to be identified, monitored and replaced or repaired before its breakdown. At the same time, its soft sensor model needs to be adapted to the changed characteristic (as shown in section 4 of this paper). The identification process of the worn out component requires the resolution of the data induced conflicts, which is still a subject of current research.

As a proof of concept for data induced conflicts, the change of a component characteristic due to wear is discussed by means of a simple fluid system consisting a pump and a valve. The data induced conflict due to wear in the valve is illustrated in Figure 6. Figure 6 shows the qualitative characteristics of the pump and the valve which are used to calculate the volume flow rate as a function of the measured pressure. In addition, the known measurement and model uncertainties are taken into account. Without wear the intersection of the model curves will determine the operation point. In this case, the calculated flow volume rate of both pump and valve model will be equal. However, if wear occurs in the valve, its characteristic curve will change, and, consequently, the operation point will change as well. The volume flow rate increases and the initial model curve will not represent the valve behaviour anymore. This leads to an incorrect calculation of the volume flow rate by the soft sensor of the valve. Consequently, the calculation of the volume flow rate based on the pump Q_P and the valve Q_V will differ and a data induced conflict occurs.

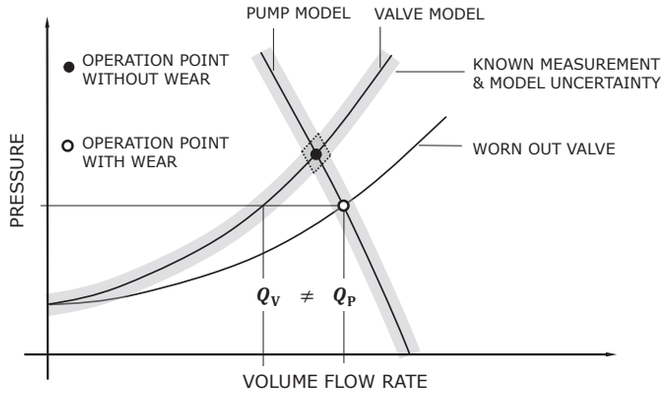


Figure 6: Data induced conflict due to a worn out valve.

The presented approach was applied on a hydraulic test bench at the Chair of Fluid System at the Technische Universität Darmstadt. The test setup contained a screw pump operating against a worn out manual throttle valve. The measured variables are the rotating speed of the pump, pressure differences of the pump and the valve, valve lift as well as the working fluid temperature. The working fluid is a hydraulic oil (ISO VG 22).

The models used at the test bench are shown in Figure 7. The pump model (Fig 7a)) calculates the internal leakage of pump (see Section 4.1.). Taking the rotating speed and geometric volume into account, equation (5) determines the volume flow rate. Pelz et. al show the derivation and calibration of the model in /13/. Figure 7b) shows the characteristic curve of the valve for different valve lifts h. Figure 7 c) and d) illustrate the dependence of the viscosity and density from the temperature, respectively. The viscosity is calculated by the Arrhenius law and the density is calculated by a trivial interpolation of measured values.

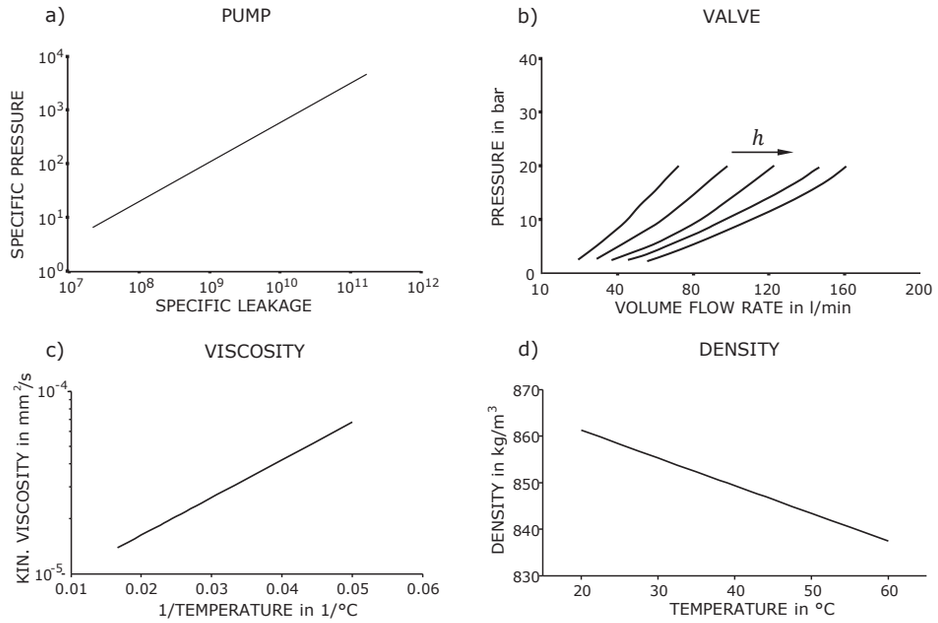


Figure 7: Models used at the test setup.

The measured volume flow rate of both soft sensors, the pump and the valve, for different operating points is shown in Figure 8. The error bars describe the model and measurement uncertainty. For the operating points 1 to 4 the difference between the two soft sensors exceeds the corresponding uncertainty and, thus, a data induced conflict occurs and indicates a worn out component, which, in this example, is the valve. Consequently, the measurements show, that the concept of data induced conflicts is applicable to hydraulic systems.

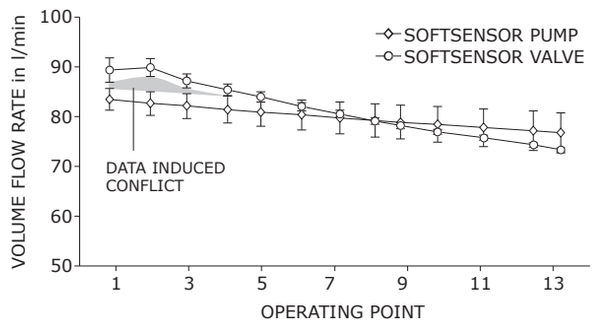


Figure 8: Measurement results for two different soft sensors, describing a pump and a valve.

However, in the experimental setup the worn out component is known and the resolution of the data induced conflicts is not necessary. In a predictive maintenance context, the solution of the data induced conflict is the key. That is why the collaborative research center 805 is carrying out further research on this subject focusing on the three promising approaches: (i) identification of anomalies in data time series, (ii) enabling further redundancies by other hydraulic components (e.g. accumulators, filters) and (iii) voting logics, as known from the aviation industry.

6 Conclusion

This paper presents new concepts of soft sensor networks demonstrating the capability of soft sensors to contribute to the digitalization in hydraulic applications. Hence, soft sensor network applications on three different levels, (i) sensor level, (ii) the component level and (iii) the system level, are presented by means of exemplary fluid systems. All soft sensors are based on physical modelling and, thus, clear fundamentals of engineering. On the sensor level, the focus is on the cost reduction saving expensive measurement equipment. On the component level, the implementation of a self-aware and environmental-aware pump is presented. Finally, on the system level, the advantageous use of data induced conflicts for predictive maintenance is discussed.

Following the presented concepts, the next steps are further experimental investigation of soft sensor networks as well as research on the resolution of data induced conflicts. Furthermore, an operational predictive maintenance application by means of an exemplary fluid system needs to be developed. To do so, further filter disks are applied to form a hybrid soft sensor, as shown in Figure 1. In this way, transparent and implemented approaches will support a common and target-oriented discussion. These investigations will be carried out within the framework of the Collaborative Research Centre (CRC) 805 “Control of Uncertainty in Load Carrying Structures in Mechanical Engineering” of Technische Universität Darmstadt.

7 Acknowledgements

The authors would like to thank the German Research Foundation (DFG) for funding this research within the Collaborative Research Centre (SFB) 805 “Control of Uncertainties in Load-Carrying Structures in Mechanical Engineering” (TU Darmstadt, speaker Prof. Dr.-Ing. Peter F. Pelz).

Nomenclature

The first column of the following table shows the symbols utilized for physical and mathematical quantities. The second column shows the meaning of each quantity. The dimension of each physical quantity is denoted in the third column, based on the generic quantities length (L), mass (M), time (T) and temperature (Θ).

Variable	*Description*	*Dimensions*
V	Volume	L^3
ϱ	density	ML^{-3}
t	Time	T
Q	Volume flow rate	$L^3\,T^{-1}$
$\dot{m}_{perm}$	Mass flow rate due to permeability	MT^{-1}
c_v	Heat capacity	$L^2T^{-2}\Theta^{-1}$
T	Temperature	Θ
c_p	Isobaric heat capacity	$L^2T^{-2}\Theta^{-1}$
k	Heat transfer coefficient	$MLT^{-3}\Theta^{-1}$
A	Surface Area	L^2
T_u	Ambient Temperature	Θ
p	Pressure	$ML^{-1}T^{-2}$
R	Gas constant	$L^2T^{-2}\Theta^{-1}$
n	Rotational speed	T^{-1}
Q_l	Internal leakage flow rate	L^3T^{-1}
ν	Kinematic viscosity	L^2T^{-1}
ψ	Relative gap	1
η_{vol}	Volumetric efficiency	1
Re	Reynolds number	1
Q_l^+	Specific internal leakage	1
Δp^+	Specific pressure difference	1
m	Empiric parameter	1
L	Empiric parameter	1
ζ'	Loss coefficient	1
η_{mh}	Hydro-mechanical effiency	1
κ_+	Dimensionless compressibility	1
C	Empiric pump parameter	1
R_μ	Empiric pump parameter	1
R_ϱ	Empiric pump parameter	1
P_S	Shaft power	ML^2T^{-3}
κ	Compressibility	$M^{-1}L^1T^2$
Q_P	Volume flow rate of the Pump	L^3T^{-1}
Q_V	Volume flow rate of the valve	L^3T^{-1}
h	Valve lift	L

References

/1/ Fortuna, L., Graziani, S., Rizzo, A., Xibilia, M. G., *Soft Sensors for Monitoring and Control of Industri Processes*, Springer, London, 2007.

/2/ Chéruy A., *Software sensors in bioprocess engineering*, In: Journal of Biotechnology, 52, pp. 193-199, 1997.

/3/ Luttmann, R., Bracewell, D. G., Cornelissen G, Gernaey, K.V., Glassey, J., Hass, V. C., Kaiser, C., Preusse, C., Striedner, G., Mandenius, C., *Soft sensors in bioprocessing: A status report and recommendations,* In: Biotechnology Journal, 7, pp. 1040-1048, 2012.

/4/ Fortuna, L., Graziani, S., Xibilia, M. G., *Soft sensors for product quality monitoring in debutanizer distillation columns,* In: Control Engineering Practice, 13, pp. 499-508, 2005.

/5/ Desai, K., Badhe, Y., Tambe, S. S., Kulkarni, B.D., *Soft-sensor development for fed-batch bioreactors using support vector regression*, In: Biochemical Engineering Journal, 27, pp. 225-239, 2006.

/6/ Kadlec, P., Gabrys, B., Strandt, S., *Data-driven Soft Sensors in the process industry*, In: Computers and Chemical Engineering, 33, pp. 795-814, 2009.

/7/ Leonow, S., *Nutzung des Energiesparpotentials von Kreiselpumpen durch szenarienbasierte Regelung*, Dissertation, Ruhr-Universität Bochum, Germany, 2015.

/8/ Ahonen, T., *Monitoring of centrifugal pump operation by a frequency converter*, Dissertation, Lappeenranta University of Technology, Finland, 2011.

/9/ Leonow, S., Mönnigmann, M., *Soft sensor based dynamic flow rate estimation in low speed radial pumps*, In: European Control Conference (ECC), pp. 778-783, 2013.

/10/ Yong-feng, J., Li-chen, G., Qingqing, T., *Soft-sensing Method for Flow of the Variable Speed Drive Constant Pump*, In: Applied Mechanics and Materials, 318, pp. 55-58, 2013.

/11/ http://de.grundfos.com/about-us/news-and-press/news/grundfos-alpha3.html, 16.10.2017.

/12/ KSB AG, Betriebs-/Montageanleitung PumpMeter, Frankenthal, Germany, 2015.

/13/ Pelz, P. F., Schänzle, C., Corneli, T, *Ähnlichkeitsbeziehungen bei Verdrängermaschinen - eine einheitliche Wirkungsgradmodellierung*, In: O+P – Ölhydraulik und Pneumatik, 1-2, pp. 104-113, 2016

/14/ Murrenhoff, H., *Hydraulik,* Shaker, Aachen, 2016.

/15/ Findeisen, D., *Ölhydraulik: Handbuch der hydraulischen Antriebe und Steuerungen*, Springer, Berlin, 2015.

/16/ Pelz, P. F., Buttenbender, J., *The dynamic stiffness of an air-spring,* In: ISMA2004 International Conference on Noise & Vibration Engineering, Leuven, Belgium, pp. September 20-22, 2004.

/17/ Hybrid Air of Peugeot, P. F., Buttenbender, J., *The dynamic stiffness of an air-spring,* In: ISMA2004 International Conference on Noise & Vibration Engineering, Leuven, Belgium, pp. September 20-22, 2004.

/18/ Klein, O., Hoffmeister, H., *Corrosive, erosive and abrasive wear in twin screw multiphase pumps*, In: EMBT Conference – Evolving Multiphase Boosting Technology Conference 2, pp. 119-126, 2008.

/19/ 109. O+P Gespräche, *Chancen und Herausforderungen von Industrie 4.0 für die Fluidtechnik – Teil 2*, In: O+P – Ölhydraulik und Pneumatik, 3, pp. 28-28, 2016.

Benchmarking of potential substituents for leaded bronze in axial sliding bearings for mobile hydraulic applications

Galina Haidarschin*, Mareike Hesebeck*, Eddy Su* and Marc Diesselberg*

*Danfoss Power Solutions, Krokamp 35, D-24537 Neumünster, Germany
E-Mail: ghaidarschin@danfoss.com

This study comprises testing of RoHS-compliant axial sliding bearing materials, including bronzes, brasses, thermally sprayed coatings and PVD coatings, in a pin-on-disc tribometer and bench testing in an axial piston pump. The aim was to compare and benchmark these materials against commonly utilized leaded bronze with respect to durability and tribological mechanisms and to derive principles for axial sliding bearing material suitability in hydrostatic components. By evaluating the test results, some fundamental understanding was gained about characteristics which materials must exhibit to achieve sufficient tribological performance and durability in hydrostatic components including, but not limited to resistance against friction-induced material transformation and sufficient ductility to withstand pressure-induced part deflection.

Keywords: Axial piston pumps and motors, axial sliding bearing materials, RoHS-compliance, tribology
Target audience: Mobile Hydraulics, Machine Manufacturers, Bearing Material Suppliers

1 Introduction

Leaded bronze has been a long-established material applied in axial sliding bearings for hydraulic applications due to its outstanding performance under starved, mixed, and fully lubricated conditions. However, among other things, environmental restrictions described for example in EU directive 2011-65-EU (*Restriction of Hazardous Substances Directive* aka. RoHS2) drive the substitution of leaded bronze by novel materials in certain applications. For automotive applications, alternative materials like non-leaded bronzes and brasses, thermally sprayed coatings and physical-vapour deposited thin films have been already successfully implemented. Nonetheless, for hydrostatic components, a potential substitute with equal or better wear protection like leaded-bronze is still being pursued. The aim of this study was to compare and benchmark these materials against commonly used leaded bronze with respect to durability and tribological mechanisms and to derive principles for axial sliding bearing material suitability in hydrostatic components.

2 State of the art

In a hydrostatic axial piston pump, in particular a swashplate type, there are several interfaces that are tribologically loaded during operation, i.e. several parts are sliding and/or rolling against a counterpart while being fully or partially separated by a (usually fully formulated) hydraulic fluid. For those interfaces, which might see severe metal-to-metal contact during operation, sufficient wear resistance of the material is needed for both normal operating conditions like break-in as well as in abnormal conditions, i.e. intermediate local fluid film breakdown because of fluid foaming or else. One of these bearing interfaces is the pair comprising the rotating piston-containing cylinder block and the valve plate (sometimes called differently depending on component design and manufacturer). As the (slightly tilted) block is rotating with rotational velocity of up to several thousands of rpm, corresponding to a speed of up to 40 m/s, and as an intermediate fluid film breakdown can happen in certain conditions, the valve plate material must withstand very high metal-to-metal sudden impact energies without losing its bearing function for the rest of the component's lifetime.

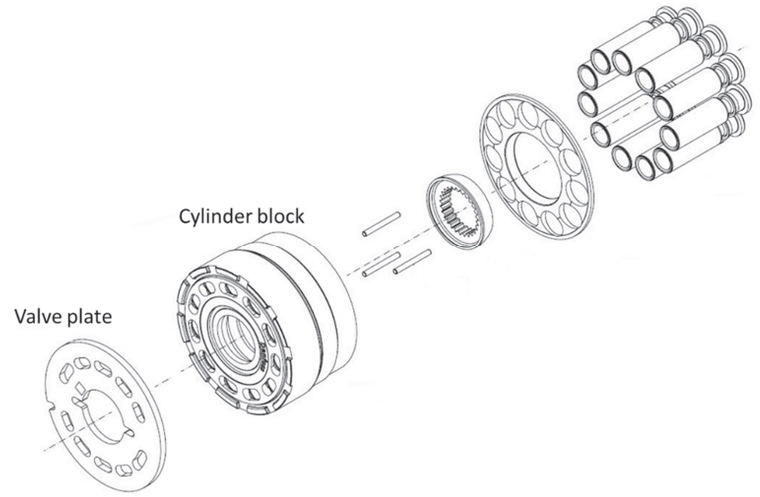


Figure 1: Exploded view of the rotational kit of a swashplate type axial piston pump

A material that has been successfully used for decades to fulfil this emergency bearing function is leaded bronze, sometimes as bulk material, often as thick layer on a steel part. The copper in that alloy exhibits good oxidation resistance, sufficient strength and ductility. The function of lead itself in bronze is not fully understood in detail, but several hypotheses have been published. The solid insolubility of lead within a copper microstructure, leads to segregations of large lead particles along the grain boundaries. /1/ Due to the low melting point of lead of 327.5°C, near-surface particles will melt under frictional heating and smear across both tribological partners, thus separating the solid metal parts from each other and preventing fatigue wear. /2/ At the same time, the near-surface removal of lead leaves voids which can act as supplemental fluid reservoirs in addition to the existing valleys of the original surface finish. Despite the excellent tribological properties as axial sliding bearing material in axial piston pumps, lead exhibits some disadvantages of which especially the environmentally hazardous properties have gained significant attention in the recent past, as mentioned in the introduction.

For many years, alternative materials have become commonly available and are being successfully utilized, for example, by the automotive industry. However, these materials have not reached full market penetration in the mobile hydraulic machinery yet. As an example, amorphous carbon coatings commonly known as diamond-like-carbon (DLC) are widely used in industry as coating for tappets, piston pins, and in diesel injection systems. /3/ However, DLC films have shown issues when applied on hydrostatic components. Besides common and potentially resolvable technical problems such as ductility to withstand the pressure-induced part deflection or substrate bonding issues, other obstacles including the insufficient heat transfer capability, the low thermal stability up to 300°C /4/ and the resulting heat-induced graphitization with accompanying low wear resistance, have principally prevented a successful application in hydrostatic components thus far.

Further examples of substitutes for leaded bronze are lead-free bronzes and brasses. Several groups are investigating the performance of different lead-free bronzes in comparison with leaded bronze, showing e.g. for CuSn12Ni2 a lower wear level /5/ or a strong speed/pressure dependency on the performance of aluminium bronze. /6/ However, previous tests (not published) did also show that some of these materials did not achieve similar performance levels while tested in hydrostatic components. To improve the performance level of lead-free copper alloys and to mimic the beneficial effect of lead described above, several groups have published experiments with bismuth containing bronze. /7/ On a laboratory scale, some promising results were achieved, however no experience is currently available with applications in actual hydrostatic components or even field use.

Other lead-free materials such as polymers or composite materials have several issues with the thermal stability as well. Polyetheretherketone (PEEK) is a high-performance polymer with excellent mechanical, chemical and

thermal properties. Additionally, this material exhibits low coefficient of friction and low wear rate in comparison to other polymers. Its properties allow an application in journal bearings and piston rings. However, its low glass transition temperature of 143-162°C and melting temperature between 343-387°C are limiting factors for its application as a valve plate component. /8/

Another wear resistant material system that is being utilized successfully in automotive applications are thermally sprayed coatings based on iron and molybdenum. This coating system is used in internal combustion engines as liner materials that carries piston and piston ring loads./9/ It has not been tested as an axial sliding bearing material thus far.

3 Experimental details

3.1 Materials

10 different materials from three different classes have been chosen (ref. Table 1) for the purpose of comparison with the leaded bronze.

Class	Designation	Material type	Processing type	Hardness	Layer thickness	Carrier material
Cu-based	CuSnPb	Leaded bronze	Sintering on steel strip	106.0 ± 4.0 HBW 1/5/30	358 ± 8 µm	C22
Cu-based	CuNiSi	Copper alloy	Casting on steel strip	117.0 ± 2.5 HBW 1/5/30	1032 ± 4 µm	C22
Cu-based	CuSn	Tin bronze	Sintering on steel strip	78.9 ± 1.3 HBW 1/5/30	540 ± 5 µm	C22 or similar
Cu-based	CuSnBi	Bismuth bronze	Sintering on steel strip	75.7 ± 2.6 HBW 1/5/30	504 ± 7 µm	C22 or similar
Cu-based	CuZn	Brass	Ingot casting	92.1 ± 0.5 HRB	-	-
Cu-based	CuZn+MoS_2	Brass with coating	Ingot casting + cold spraying	92.1 ± 0.5 HRB (CuZn)	8 µm	CuZn
Thermal Spray	Fe-base	Thermally sprayed coating	Atmospheric plasma spray on steel substrate	436 ± 22 HV0.3	131 ± 7 µm	C22
Thermal Spray	Mo-base	Thermally sprayed coating	Atmospheric plasma spray on steel substrate	573 ± 43 HV0.3	102 ± 5 µm	C22
PVD coating	Cr-base	Nitride multilayer	Cathodic arc deposition on steel substrate	19GPa	5.4 µm	42CrMo4 HH+QT
PVD coating	Ni-base	Metal layer	Cathodic arc deposition on steel substrate	7 GPa	5.9 µm	42CrMo4 HH+QT
PVD coating	Al-base	Oxide layer	Cathodic arc deposition on steel substrate.	25 GPa	4.6 µm	42CrMo4 HH+QT

Table 1: Overview of tested valve plate materials

Based on the investigated material, different carrier materials are selected, depending on the requirements of each bearing material. The influence of the backing material on the performance of the material is not part of this study. The roughness of the tested hardware is adjusted to the current standards in the automotive and bearing application and thus is not comparable among the samples. The same is valid for physical properties, such as the hardness of the coating.

The counterpart for the valve plate is a cylinder block, manufactured out of powder metal material, infiltrated with copper. Some of the parameters of the steel surface are listed in Table 2.

Hardness	Rpk [µm]	Rk [µm]	Rvk [µm]
89 HRB	1.3	0.65	0.55

Table 2: Parameters of the cylinder block

3.2 Testing procedure

According to DIN 50322, every test can be categorized into one of six classes, depending on their complexity. Field-testing in real machines as the test with the highest comparability to the real application is considered as category one. On the other end of the scale (category six), tribometer tests show the lowest comparability as simplified special parts and test conditions are used. These tests are conducted to understand the material properties in loaded conditions and to become a first indication of the performance in real application by comparing with the known material. The test stand is located between the field-testing and the tribometer testing in category three. With this test, real components under laboratory conditions on a test stand are tested.

For this study, pin-on-disc tribometer tests and full-sized Danfoss pump tests are used for benchmarking the alternative materials against the standard leaded-bronze.

3.2.1 Tribometer tests

For the comparison of the materials properties such as abrasive and adhesive wear resistance, a pin-on-disc tribometer setup with a UMT-3 tribometer (Bruker) is taken. The tested material is applied on discs. The surface parameters of the tested materials are listed in Table 3.

Material	Rpk [µm]	Rk [µm]	Rvk [µm]
CuSnPb	0.55 ± 0.1	1.18 ± 0.05	0.69 ± 0.06
CuNiSi	0.56 ± 0.08	1.10 ±0.03	0.62 ± 0.06
CuSn	0.45 ± 0.03	0.96 ± 0.02	0.51 ± 0.03
CuSnBi	0.42 ± 0.06	0.95 ± 0.07	0.60 ± 0.07
CuZn	0.16 ± 0.04	0.7 ± 0.1	0.5 ± 0.2
CuZn+MoS_2	21 ± 3	18 ± 5	2.8 ± 0.5
Fe-base	0.008 ± 0.001	0.028 ± 0.001	0.8 ± 0.1
Mo-base	0.008 ± 0.001	0.026 ± 0.001	0.8 ± 0.3
Pin	2 ± 1	3 ± 1	2 ± 2

Table 3: Surface roughness of the tested tribometer samples

For the counterpart, pins manufactured from powder metal material, similar to the material of the cylinder blocks are manufactured. To ensure that no rapid contact area changes due to a tilting of the pin are possible, and to increase the contact pressure by reducing the contact area, a half-sphere shape with a diameter of 10 mm is fine-turned at the test end of the pin. Lubricated conditions during the test are realized by a splash lubrication with a non-additivated group II mineral oil based hydraulic fluid VG 46. Using the base oil excludes the impact of the additives, which might influence the performance of various material classes differently. To analyse the steady-state behaviour of a tested material, a long-term test under a steady load is carried out. The test conditions are shown in Figure 2.

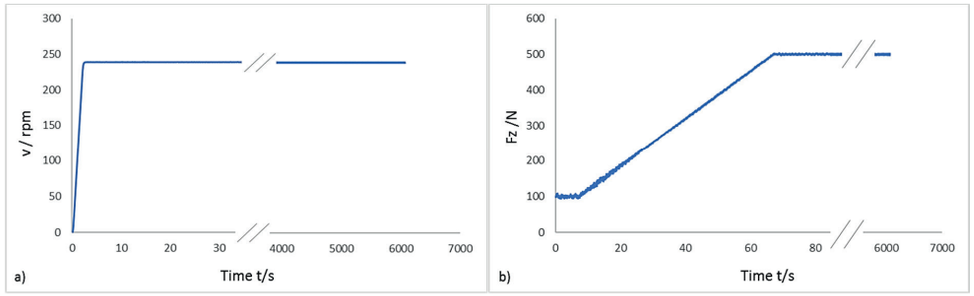


Figure 2: Test conditions of the tribometer steady state test

After a 10 s running-in period at a load of 100N, the load is increased to 500 N within 60 s and then held for 6000 s at a circumferential speed of about 0.5 m/s. The rotational speed is chosen to ensure mixed lubrication conditions during the test. The tests starts at ambient temperature (22±1°C). The temperature is neither controlled nor tracked during the tests.

One of the main results from the tribometer testing are the *Coefficient of Friction* (COF) curves. The COF of a system depends on many parameters, such as surface roughness, hardness of contact partners, chemical bonding, etc. The behavior of the COF curve during the test indicates the performance of the material and the stability of the chosen pairing. A high coefficient of friction in a real component causes decreased efficiency and additionally, increase of frictional heat, which consequently results in shrinkage of the fluid film separating the surfaces, subsequent breakdown of lubrication and at the end, damage of components.

3.2.2 Component testing procedure

For component testing, axial piston pump was utilized and operated with the same conditions at the same test bench for each material. In every test run, the complete rotating kit, including the stationary valve plate, copper-infiltrated steel cylinder block and the pistons, were replaced to avoid influences from previous test runs (e.g. break-in, contamination). The test sequence consisted of ten consecutive steps of pressure and speed increase, finally exceeding rated values by approximately 20%. During the test, several parameters were observed to be able to stop the test in case of detected irregularities. The component testing sequence was considered as successfully passed, if all steps of pressure and speed increase had been executed without any occurrence of abnormal pressure drop or case-flow increase during the overall testing time of 90 min, which would indicate leakage between valve plate and cylinder block due to wear. For statistical analysis of the results, three tests for each material were performed. For the comparison of the results, PV-factors for different materials achieved during the test were calculated. Therefore, for materials with strong variation of the test results, the minimum achieved value is selected. The PV factor represents the product of the pressure P (case pressure during the test) with the sliding velocity V (rotational speed of the kit) of the latest successfully passed testing stage and gives information regarding the contact lubrication severity. /10/

3.3 Wear characterization

For evaluation of the wear volume on the tribometer samples, 2D and 3D profilometry is used for the discs and pins, respectively. Thereby measurements with a tactile profilometer are taken perpendicular to the wear track using a Zeiss Surfcom 5000. For the calculation of the total wear volume over the disc, the wear area, determined on the 2D wear profile, shown in red in Figure 3, is multiplied with the total length of the wear track (eq. 1).

$$V_w = 2\pi R \cdot A \quad (1)$$

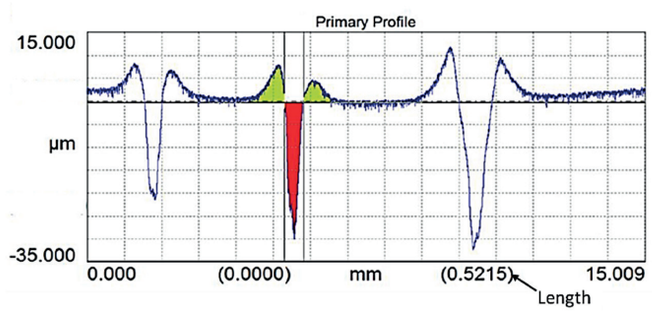


Figure 3: Wear area measurement

For statistical evaluation, the wear area is measured on three different positions of the wear track. For calculation of the wear volume, which is defined as the total material loss, the material accumulations at the edges of the wear track need to be subtracted from the calculated value (see green areas in Figure 3). For the pins, the wear volume was calculated using the confocal microscope Neox-S of Sensofar and by using the software SensoMaps. Therefore, the measured wear area at the tip of the pin is converted into a cavity and the volume of it is calculated (see Figure 4).

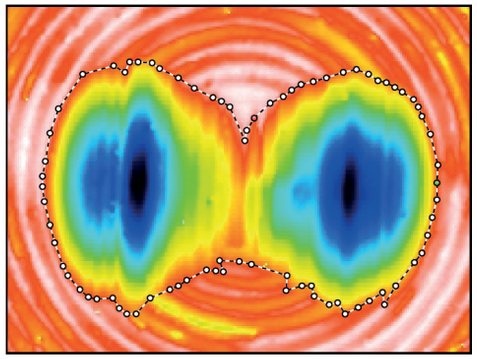


Figure 4: 3D wear volume measurement on the pin

Regarding the tribological analysis of the component hardware, both valve plate and cylinder block were analysed using a Zeiss-made Scanning Electron Microscope (SEM) with Oxford-brand Energy Dispersive X-ray detector. Deep dive analysis of the microstructure is carried out by using the Leica DMi 8 A optical microscope.

4 Results and Discussion

4.1 Tribometer test

One key response from the tribometer testing was the coefficient of friction (COF) during the constant load test. The summary of all curves is shown in Figure 5. The pin-on-disc test has shown significant principal differences in the progression of the COF of above mentioned materials.

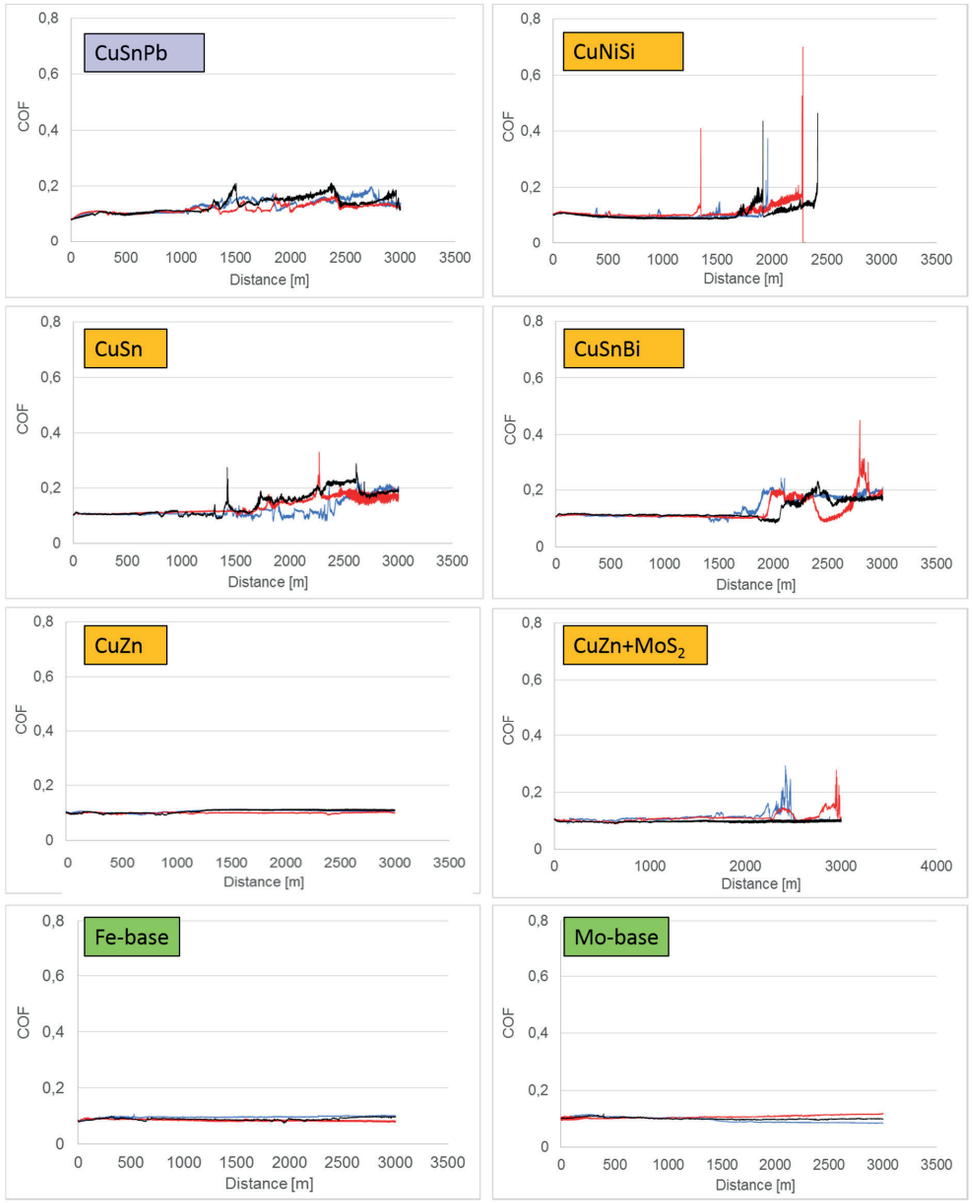


Figure 5: Coefficient of friction curves for different materials

The reference CuSnPb shows a continuous increase of the COF up to 0.2 and some fluctuations of the curve. CuNiSi material, in contrast, shows very stable COF progressions until a sudden increase to over 0.5 occurs, which triggered a stop of the test, indicating adhesive wear and tribological failure. CuSn and CuSnBi have comparable behaviour as the leaded bronze with slightly higher increase of the COF up to 0.3 during the test. The fluctuations of the curve, which can be seen as a sudden increase of the COF with immediate decrease are interpreted as a result of temporary welding of the two contact partners or temporary accumulation of larger amounts of wear debris in front of the pin. CuZn and CuZn+MoS_2 show different results respectively. While the CuZn samples have a stable behaviour throughout the test with a constant COF of 0.1, the CuZn+MoS_2 samples show a strong increase of COF at the end of the test but without exceeding a value of 0.3, which is likely attributed to larger amounts of wear debris of the topmost MoS_2 coating. Thermal sprays of Fe-base and Mo-base show, in addition to uncoated brass, demonstrated the most stable behaviour of the COF in comparison with other tested materials, reaching a maximum value of 0.1 and 0.12 respectively, indicating only a very slight change in material or surface properties. In case of the PVD coatings, the test had to be halted after only a few seconds due to premature coating failure, which is related to the initially contact pressures applied during this test. Therefore, these coatings needed to be excluded from evaluation.

The respective calculated wear volumes for the discs and the pin are shown in Figure 6. The reference bronze shows the highest average wear of the pin of 0.27 mm^3, compared to other tested materials. The calculated value for the average wear on the disc amounts to 1.31 mm^3. Other copper-based materials, besides the manganese silicide fortified brass materials, show similar wear volumes as the reference. It must be noted that the calculated wear volume of CuNiBi is not comparable with the other samples, since the tests were prematurely stopped and are marked red for this reason. CuZn and CuZn+MoS_2 show different wear volumes, of which CuZn shows a lower materials loss compared to the reference. Even if the composite hardness of CuZn was measured to be lower than that of the leaded bronze, the embedded (hard) manganese silicide particles, which are oriented parallel to the running surface, significantly improve the wear resistance. CuZn+MoS_2, including soft carbon-based coating at the top apparently shows the highest material removal on the surface. However, this result is misleading because it includes material removal of the sacrificial MoS_2 layer, which is intended. This soft layer is easily removed by abrasive wear due to the locally applied initial high contact pressure by the pin. The two thermal sprays (Fe-base and Mo-base) resulted in the lowest material loss in this study as well as for the disc (0.43 mm^3 and 0.35 mm^3) as for the pin (0.01 mm^3 and 0.03 mm^3). This is mainly related to relatively high hardness, resulting in high abrasive wear resistance (Archard's law), smoother surfaces, causing less material removal during break-in and manufacturing-process-related high density of pores in the surface, which act as fluid reservoirs thus improving the lubrication.

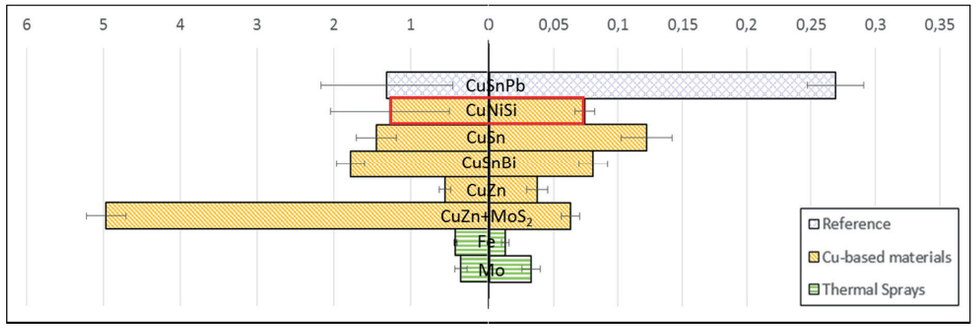


Figure 6: Wear volumes after the constant load test for Disc (left) and the Pin (right, different scale)

4.2 Component test

As described in the experimental details, all materials were benchmarked against the leaded bronze by calculating the PV factor of the last sequence step prior to test abort, if occurred. The bi-metal leaded bronze reference valve plate was one of the materials that successfully passed the sequence, therefore achieving the highest possible PV factor in the last step of this test sequence. The normalized PV factors for all tested materials are shown in Figure 7.

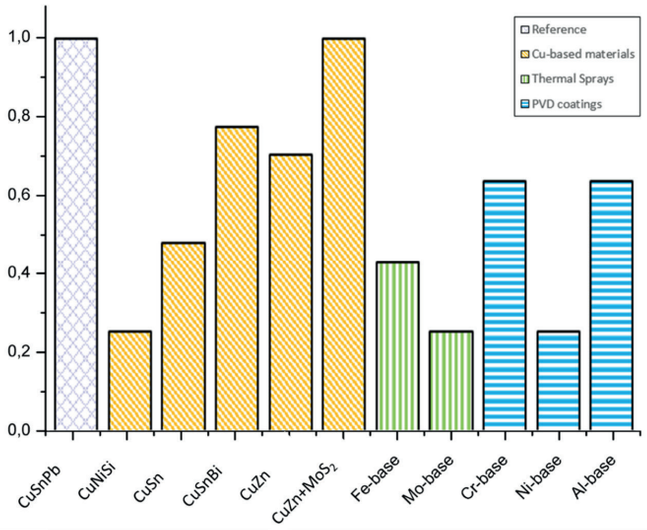


Figure 7: PV factors reached before test stop/abort (normalized)

All copper-base materials, highlighted in orange, are showing large variation in achieved PV factors, ranging from 25 to 100% of the reference bronze, i.e. only one material (brass+MoS_2) besides leaded bronze ran though the complete testing sequence without test abort. Both thermal sprays, shown in green, remain below 43%, while the PVD coatings, highlighted blue, range from 25 to 64%. To interpret this high variation of results, which is not meeting the performance expectations based on successful usage in automotive and other bearing applications, a detailed analysis of the wear tracks on the valve plate and the cylinder block was performed.

Therefore, scanning electron images of the plates' raceways are shown in Figure 8. The reference bronze CuSnPb shows only mild polishing with removal of some surface peaks. The valleys of the initial surface finish are still present. No other major wear mechanisms beside minor abrasive wear (scratches) were detected.

For all other copper-based material, except the MoS_2-coated version, strong deformation, material transfer, chunk formation and signs of fatigue were detected. For non-coated CuZn brass and CuNiSi, clear indications of adhesive wear were observed. In these cases, the original surface was no longer even partly visible. The cross-sectional microstructure analysis of these parts (Figure 10) shows a material transformation below the raceway, resulting in finer grains. In the case of CuSn and CuSnBi, this transformation leads to embrittlement of the microstructure, formation of microcracks and subsequent delamination of the transformed sublayer. Alloying with bismuth, which arranges along the grain boundaries is said to weaken those and enhances the forming of microcracks additionally. /11/

This detrimental friction-induced material transformation happens in metal-to-metal contact situations, because the (naturally slightly tilted) rotating cylinder block locally touches the (naturally slightly deflected) valve plate with speed of several thousand rpm (up to 40 m/s) and high resulting contact energy that converts very locally into friction, heat and/or material deformation. This detrimental effect has been earlier identified for amorphous carbon coatings (DLC) as well which transform to graphite under frictional heating within seconds.

The addition of MoS_2 coating to the brass material surface results in a significant improvement of the performance over the non-coated brass, also seen in the achieved PV factor. The raceway shows only a slight decrease of the film thickness in areas of the highest contact.

For the Fe-based thermal spray, the appearance of the affected surface does not indicate any enhanced wear. Only a mild polishing of the surface can be observed, which is corresponding to the results from tribometer testing. However, on a macroscopic scale, this coating exhibited a significant issue with the coating bond to the substrate at the edges of the kidneys in the high-pressure area of the valve plate, leading to partial coating delamination (not shown) finally resulting in a significant change in hydrodynamic/hydrostatic balance and leakage.

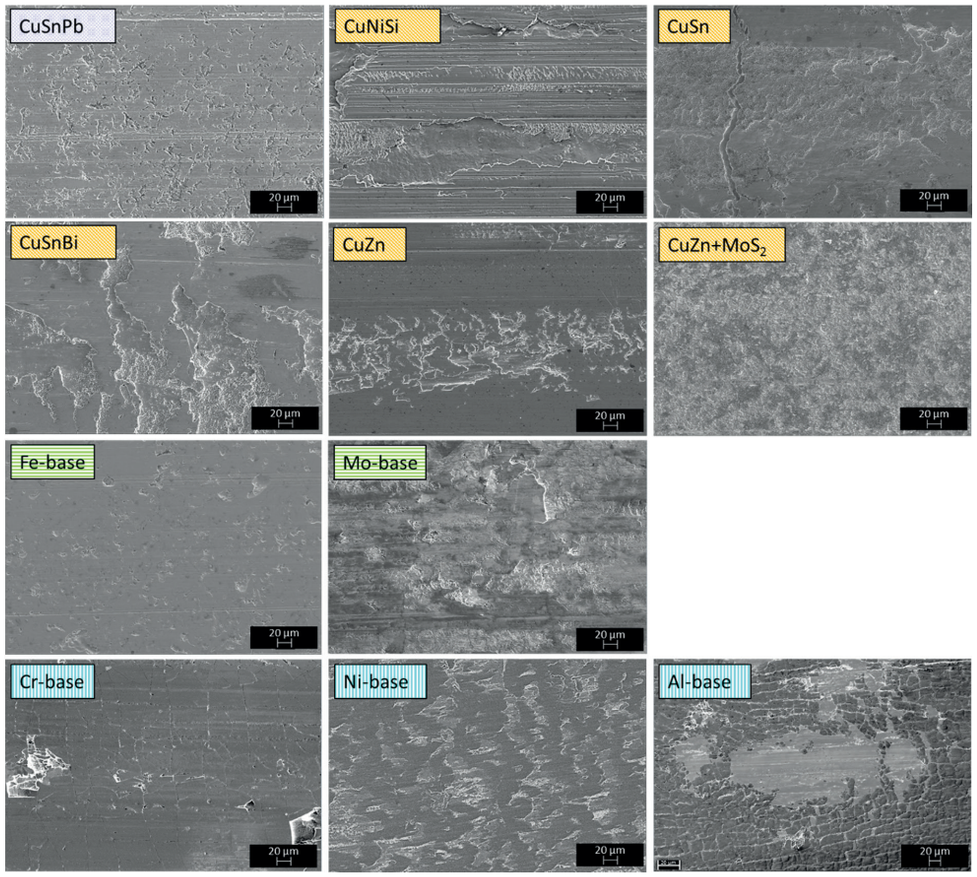


Figure 8: SEM images of the wear tracks

Concerning the Mo-based thermal spray, adhesive wear can be detected in the wear track. Additionally, delamination in the edge areas of the kidneys (shown in Figure 9) is observed for this coating as well.

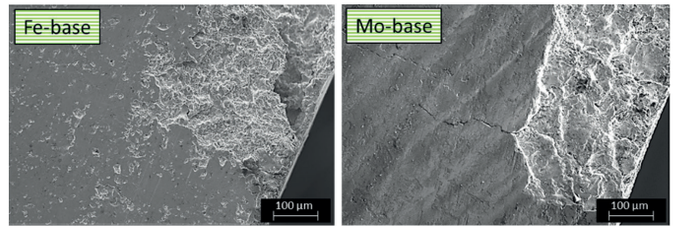


Figure 9: Delamination in the edges of the kidneys for thermal sprays

The investigated three PVD coatings are showing different wear mechanisms in this application.

In the case of the Cr-based nitride PVD coating, cracks were observed all over the raceway. This is in relation to shear stresses caused by a high coefficient of friction exceeding the coatings ductility. In addition, the relatively low temperature resistance of this coating (300°C), which is exceeded in certain spots of the surface, will likely lead to a detrimental change of coating intrinsic properties.

For the Ni-based PVD coating, a strong adhesion tendency to the counterpart has been detected, leading to massive material transfer, surface roughening (formation of scales) and wear of the counterpart.

The Al-based oxide PVD coating shows formation of very fine floes that are separated by fine cracks or larger voids of absent coating. These voids expose the underlying substrate and lead to subsequent adhesive wear (present in other locations of the valve plate, not shown). It is believed that this failure mode is a direct consequence of insufficient substrate hardness for this coating leading to an eggshell effect, which might be improved by modifying the substrate material or heat treatment.

Summarized and categorized, several main failure mechanisms were identified:

- Insufficient shear stress stability due to weakened grain boundaries and/or transformed material
- Insufficient bonding strength of coatings on the substrate resulting in delamination of the coating
- Insufficient ductility of coatings leading to crack formation and subsequent delamination of the coating

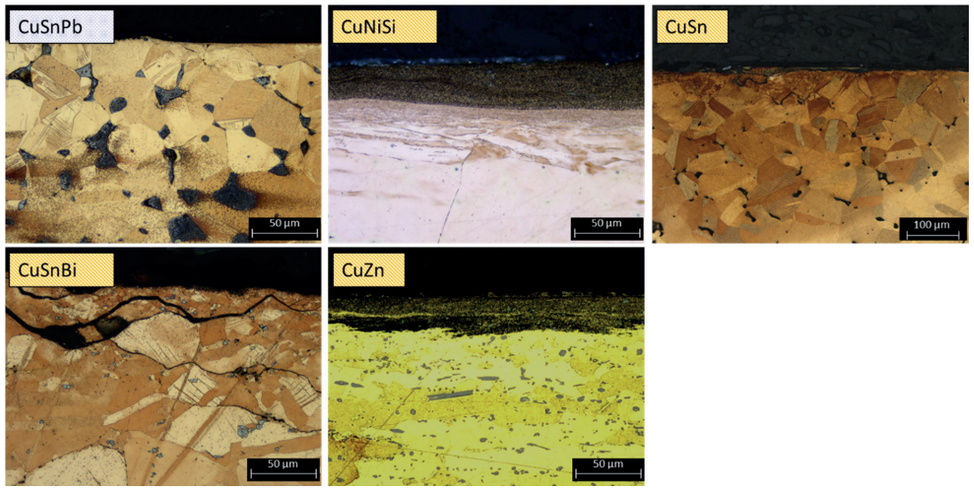


Figure 10: Microstructure of the copper-based tested materials

Comparing these results with the pin-on-disc tribometer results, a significant difference becomes obvious. Even if statements concerning materials-related coefficient of friction will remain identical, the component tests showed a completely different wear performance and durability, e.g. thermally sprayed coatings which have shown excellent performance during the tribometer test, failed in very early load stages of the component test. This can be explained by the higher grade of complexity of the dynamic system and contributing factors like fluid pressure-induced part deflection, tribological interface geometry with resulting break-in behaviour and fully formulated HLP-class fluid usage in comparison with the static system of a tribometer.

5 Summary and Conclusion

One goal of this study was to benchmark commonly available RoHS-compliant bearing materials against the current state-of-the-art leaded-bronze for application in hydrostatic axial piston pumps and motors. In addition to that, indications towards a more systematic approach to optimize that interface by materials choice were needed. Therefore, the tribological performance and durability of leaded-bronze (CuSn10Pb10) on a steel backing has been compared with the behaviour of potential substitutes, namely lead-free copper-based bi-metals and bulk materials, thermally sprayed coatings and PVD coatings, in a pin-on-disc tribometer and a full-sized axial piston pump test rig. For both testing methods, a major focus was on the actual wear mechanism and progression to identify principally influencing (and limiting) factors on durability in hydrostatic components.

The pin-on disc test results are strongly dependent on material properties such as hardness and surface roughness of both contact partners and can successfully be applied to determine basic material properties. During this study, the pin-on-disc test has shown significant principal differences in the progression of the coefficients of friction of different materials, which are explained by sample properties like hardness and surface texture. In the end, however, indications for superior wear performance, like constantly low coefficients and minor wear of wear tracks, were not transferable to component tests. This was explained by the higher grade of complexity of acting factors like fluid pressure-induced part deflection, tribological interface geometry with resulting break-in behaviour and fully formulated HLP-class fluid usage. For future material developments to be used in hydrostatic components, it is therefore almost mandatory to increase the complexity level of tribometers from level three (DIN 50322) to a higher level by adapting component properties like similar interface geometry (i.e. ring-on-ring instead of pin-on-disc to mimic the valve plate / cylinder block interface) and maybe even including the balancing of hydrodynamic and hydrostatic lubrication by adding kidneys into the rings and pressurized lubrication. By doing that, the tribological conditions in such a tribometer would become more similar to the actual conditions in a hydrostatic pump or motor. Then, in the end, the high effort and costs of component tests would be lessened or could even be completely avoided when testing alternative materials for the axial sliding bearing interface to improve durability.

From a wear analysis perspective, the component tests resulted in a new fundamental understanding of critical characteristics that materials must exhibit to achieve sufficient tribological performance and durability in hydrostatic components, including, but not limited to low adhesive wear tendency and low coefficient of friction in mixed lubrication conditions, sufficient bonding strength in the case of coatings and certain fatigue resistance. One big difference to automotive bearings, which explains important additional requirements, is the fact that the tribological interface not only functions as a sealing and lubricating gap but also as a load-carrying element, which results in parts deflection and very high metal-to-metal contact pressures in case of fluid-film break-down. One of these additional requirements was found to be the material's ability to withstand detrimental friction-induced material transformation in high-speed metal-to-metal contact situations, already known from amorphous carbon coatings (DLC), but now also shown for certain copper-based bearing materials. Another key element identified is the material's ductility to withstand high stresses caused by pressure-induced parts deflection and vapour cavitation effects.

All findings together generally, show the difficulty to directly transfer well-established bearing material solutions from automotive applications to hydrostatic pumps and motors. However, with further holistic optimization of all the above-mentioned factors and therefore tailoring of material properties to the demands of axial sliding bearings in hydrostatic pumps and motors, it will become possible to fully substitute and even outperform the leaded bronze in the long term for even the most demanding operating conditions. As an outlook that would finally enable component and machine manufacturers to further optimize machine performance and efficiency while using environmentally acceptable materials at the same time.

Nomenclature

Variable	*Description*	*Unit*
V_w	Wear Volume	[mm^3]
R	Radius of the wear track	[mm]
A_w	Wear area	[mm^2]
PV	PV factor	$[\frac{N}{m \cdot s}]$

References

/1/ Hutching, I., Shipway, P., *Tribology: Friction and Wear of Engineering Materials*, 2nd edition, p.316, 2017.

/2/ Davis, J. R., *Copper and Copper Alloys*, ASM Specialty Handbook, ASM International, Ohio, United States of America, p. 91, 2001.

/3/ Donnet, C., Erdemir, A., *Tribology of Diamond-Like Carbon Films*, Springer, New York, USA, 2008

/4/ Jung,H. -S., Park, H. -H., Pang,S. S., Lee, S.Y., *Thin Solid Films*, 355-356, pp.151-156, 1999

/5/ Paulus, A., *Tribolayer Formation on Bronze CuSn12Ni2 in the Tribological Contact between Cylinder and Control Plate in an Axial Piston Pump with Swashplate Design*, 10th international Fluid Power Conference, 10. IFK, Dresden, Germany, March 8-10, 2016

/6/ Prasad, B.K., *Sliding wear behavior of bronzes under varying material composition, microstructure and test conditions*, Wear 257, pp. 110-123, 2004

/7/ Oksanen, V.T., Jehtovaara, A.J., Kallio, M.H., *Load capacity of lubricated bismuth bronze bimetal bearing under elliptical sliding motion*, Wear, Vol.388-389, pp. 72-80, 2017

/8/ VICTREX® PEEK, Properties Brochure, © Victrex plc March 2016

/9/ Barbezat, G., *Advanced thermal spray technology and coating for lightweight engine blocks for the automotive industry*, Surface and Coatings Technology, Vol. 200, Issues 5-6, pp 1990-1993, 2005

/10/ Totten, G.E., *Handbook of Hydraulic Fluid Technology (Mechanical Engineering)*, Marcel Dekker, Inc., New York, USA, p. 387 , 1999

/11/ Y. G. Yin et al., *Study on Mechanical Properties of Cu-Bi Bearing Materials*, Advanced Materials Research, Vols. 756-759, pp. 89-92, 2013

Investigation of the Thermal Behaviour in the Lubricating Gap of an Axial Piston Pump with Respect to Lifetime

Roman Ivantysyn, Prof. Dr. Jürgen Weber

TU Dresden, Institute of Fluid Power (IFD), Helmholzstr. 7a, D-01062 Dresden, Germany
E-Mail: ivanty@msx.tu-dresden.de, fluidtronik@mailbox.tu-dresden.de

Axial piston pumps are universal displacement machines that are used in a vast variety of applications. Their high pressure resistance and ease of operation make them very popular, especially in mobile applications and aerospace. The lifetime of axial piston pumps is depending on the design of the rotating kit, the application and its overall robustness to external loads. The fluid film between the moving parts is responsible for bearing the loads and sealing the displacement chambers. Its design is the most complicated part for a pump designer. All pumps to this date have been designed in a trial and error process, which is not only costly, but doesn't yield an optimum in terms of efficiency and robustness. This paper aims to investigate the influence the fluid film has on the lifetime of the pump. From the three main lubricating interfaces of an axial piston pump, two - cylinder block / valve plate and slipper / swash plate - were analysed in terms of temperature for both interfaces and gap height for slipper only by means of measurements and simulation. The simulation tool that was used for the analysis is called Caspar FSTI, developed by Purdue University. It is capable of calculating the resulting gap height between all three main interfaces resulting from force balance calculations between external and fluid film forces due to the pressure distribution in the gap and taking both deformation due to temperature and pressure into account. The simulation will be used to understand the behaviour of the pump while the measurements will give a deeper look into the actual steady state conditions as well as transient behaviour of the parts including wear in.

Keywords: Axial Piston Machines, Lifetime, Lubricating Gap Design, Temperature Field
Target audience: Mobile Hydraulics, Mining Industry, Component Design, Design Process

1 Introduction

Axial piston pumps are positive displacement machines that are used in a vast variety of applications. Their high pressure resistance and ease of operation make them very popular, especially in heavy duty applications. Some applications require more robust pumps with an extended lifetime, particularly those that operate in remote environments such as the marine type or mining operations.

To understand the physical phenomena that can cause premature failure, it is necessary to take a closer look on the sealing gaps in these positive displacement machines. The lubricating gaps in piston pumps are the primary source of the power losses and also produce particles due to wear. These gaps have been in the focus of many researches over the last 30 years /1, 2, 3/. In the last 15 years vast improvements in the computational power have paved the way to more complex simulation models of these lubricating gaps /4, 5, 6, 7, 8/. One particular simulation model, Caspar FSTI, has proven itself to be a highly reliably and capable model for swash plate type axial piston pumps /5, 6, 7/. The model predicts the lubricating film thickness in all major lubricating gaps and considers all major physical effects such as deformation of the parts due to temperature and pressure. This simulation model was used in this research to evaluate the pump before any measurements were done, in order to place the sensors at the right locations, as well as to understand the measured phenomena including the gap height. The authors published two previous publications, validating the software for both interfaces /9, 10/.

For this research, a unique test stand has been developed, which is capable of measuring fluid film thickness using eddy current gap height sensors, while simultaneously measuring temperature using thermocouples, which were placed directly in the sealing interface of the valve plate and the swash plate (see Figure 3). Previous researchers have measured gap height or temperature in these interfaces before /6, 7, 8, 11, 12/. However, none have measured both the temperature and the fluid film thickness at the same time, and none have looked at two interfaces simultaneously. The two most noteworthy were Zecchi /7/ and Schenk /6/. Zecchi placed 22 thermocouples directly underneath the running surface of the valve plate and used it to validated his research work, which ended up being the cylinder block/valve plate model in Caspar FSTI. The slipper/swash plate model of Caspar was developed by Schenk, who validated his model using fluid film measurements using eddy current mounted in the swash plate, measuring the gap to the slippers across the entire shaft rotation.

Building on all of this prior work, the "transparent pump" test stand was developed, which enables a deeper look into the inner workings of an axial piston pump. The goal of this paper is aimed to show how the pump reacts to different operating conditions both in transient and stationary form, as well as how the wear-in can change the pumps behaviour. This was determined using measurements and simulation. In this paper, the measurement results will be in the primary focus.

2 Research goal and approach

As described in the introduction, there are many publications that performed research in the area of lubricating gaps within piston pumps. The goal of this research is to build on those and develop a holistic approach for the lifetime prediction and eventually life time extension of axial piston pumps. In order to achieve this, the lifetime limiting factors such as wear, were observed during measurements and analysed using different parameters such as temperature and particle generation. As already described, this paper focuses on two of the three main interfaces of axial piston pumps, as shown in yellow and red in **Figure 1**.

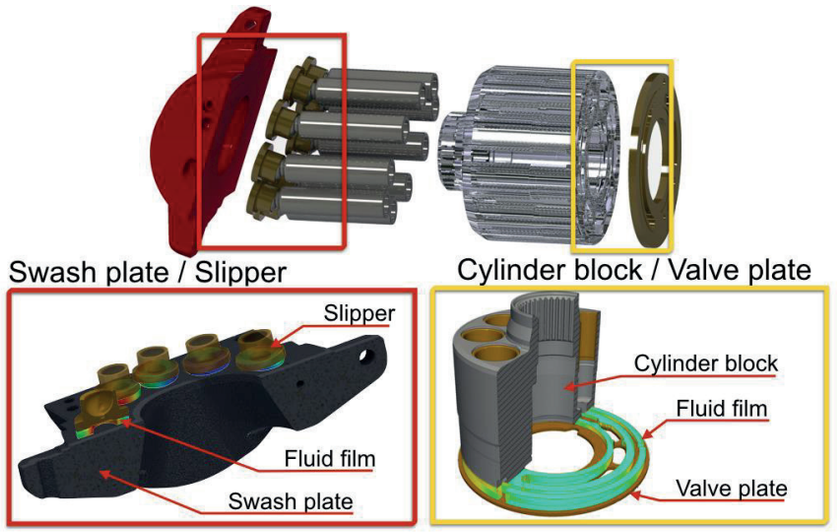


Figure 1 – Studied sealing gaps in the axial piston pump

The measurements will have two purposes, one to measure transient behaviour, and second measure steady state conditions, which can then be used to validate the simulation. The simulation model was used to place the sensors in the appropriate positions, predict problematic operating conditions, and explain observed phenomena. In addition, the measured wear-in behaviour was used to improve the simulation model, by incorporating a simulation based wear prediction /3/. The used test rig set up is shown in **Figure 2**. The pump's outlet and drain port are equipped with temperature, pressure and particle sensors. The inlet port is also equipped with

temperature and pressure sensors, as well as two filter elements, one fine 4 µm filter as well as a metal filter, which works with permanent magnets. The purpose is to be able to measure the particles generated by the pump itself, without recirculating the particles through the tank. The inlet line is pressure controlled by a supply pump, which guarantees a cavitation free environment, by keeping the pressure at 1.8 bar. The pump is a 92 cc open circuit axial piston pump, rated to 350 bar nominal and 420 bar peak pressures with a maximum speed of 2300 rpm. The test conditions were chosen to be 500-1800 rpm and pressures up to 300 bar. A full list of the measured operating conditions can be seen in the bottom of Figure 5.

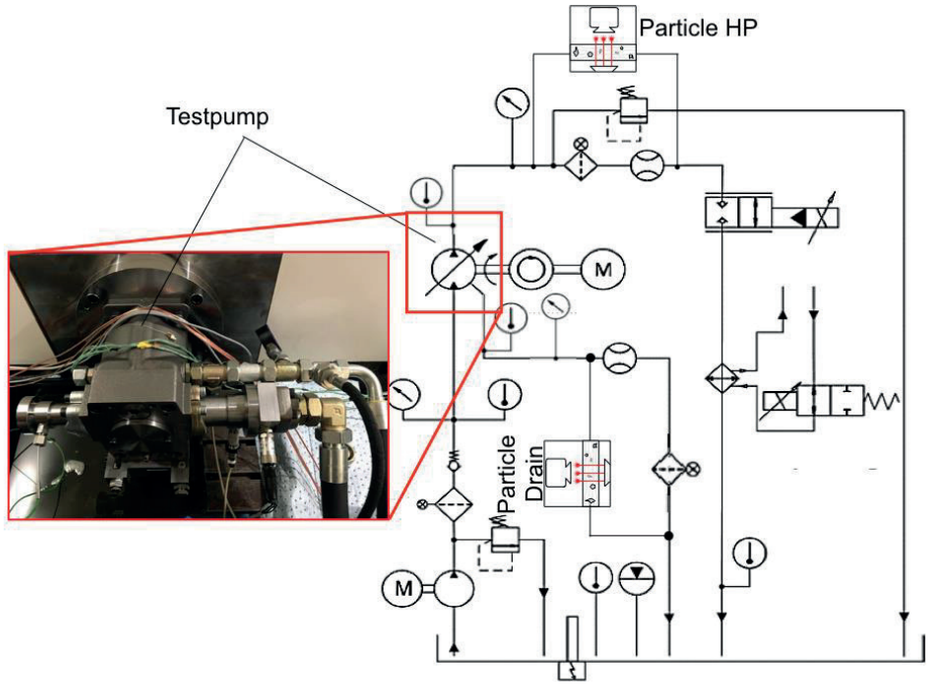


Figure 2 – Test stand "Transparent Pump" schematic

3 Prediction of lifetime affecting conditions with respect to temperature

The next section shows the measurements results over various operating conditions. The pump was tested in stationary as well as in transient conditions. In order to reach true stationary conditions, each temperature gradient was zero while the tank temperature was at 40±1°C. This took about 30 min per operating condition.

3.1 Measurement set up

A total of eight measurement series were performed. The first four measurement series were focusing on capturing the slipper gap height and swash plate temperature. The slipper measurement set up is shown in **Figure 3** on the right. The shown sensor plate (outlined in red) was removable and axis symmetric, therefore there were two positions this plate could be mounted. The first position (oriented as shown in Figure 3) captured the gap heights on the high pressure side, and the second position the gap heights on the low pressure side. Series 1 & 2 were measuring with the sensor plate in position I and the series 3 & 4 in position II. The way the temperature sensors were located, a complete temperature field could only be achieved using data from both plate positions, totalling in 28 unique measurement spots, where some locations were measured in both plate positions in order to compare the measurements.

Series 5 & 6 focused on the temperature measurements on the valve plate only, here no slipper measurements were performed. A total of 26 thermocouples were placed 0.5 mm underneath the running surface at the locations shown in Figure 4 top left. Series 7 and 8 were used to repeat the run-in process for the cylinder block valve plate interfaces. Series 7 used a different run-in pattern (only low pressures), whereas Series 8 repeated the measurement order of Series 5 and 6. In Series 8 both interfaces, slipper / swash plate and cylinder block / valve plate were analysed. Therefore 2 of the 3 main lubricating gaps were measured at the same time, giving a deep look into the pumps performance and being able to estimate the power loss contribution of each interface. An overview of all 8 series can be seen in **Table 1**.

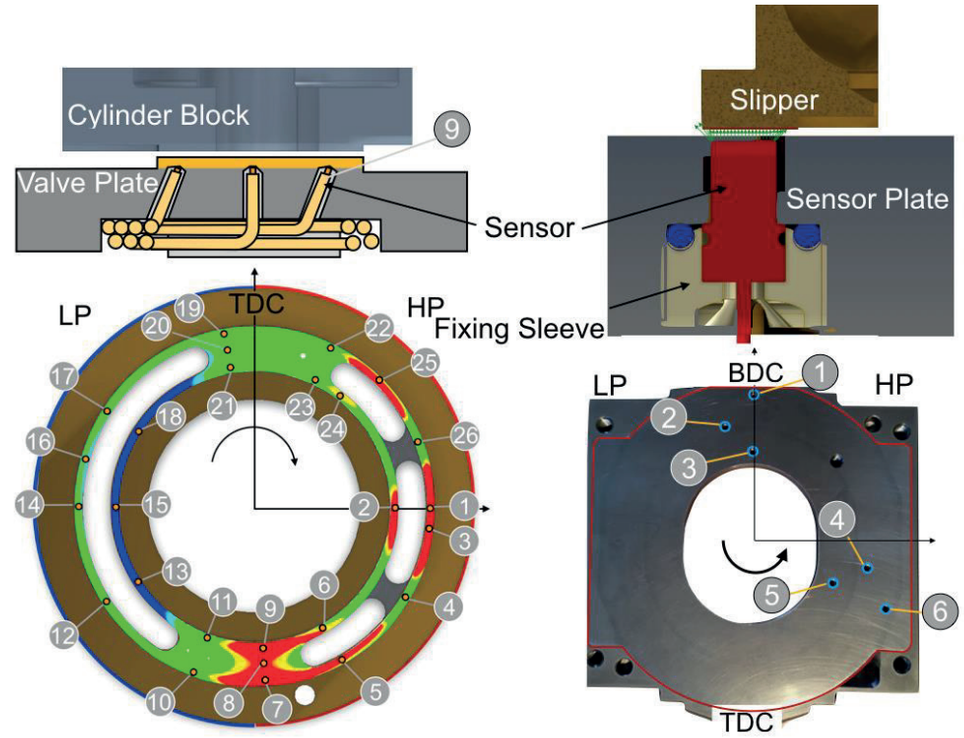


Figure 3 – Sensor instalment for the two interfaces:
Temperature on valve plate (left), gap sensor swash plate (right)

Table 1 is listing the measured interfaces, the sensors used, as well as the new parts if any were exchanged. It also shows the Swash Plate Position (Position I – gap measurements on the high pressure side and BDC or Positon II – gap measurements on the low pressure side and TDC).

In addition, starting at Series 5 particle sensor were placed in the high pressure and drain line as shown in Figure 2. These particle sensors were Argo-Hytos OPComII sensors, capable of measuring particles ranging from 4 µm to 21 µm in size. They are mounted in a by-pass configuration and output oil cleanliness and particle concentration in particles/ml. The

Table 1 - Overview of the measurement series

Series	Measured Interface	Swash Plate Position	Measured Sensors in Pump	New Pump parts
1	Slipper / Swash Plate	Position I	6 Eddy Current, 17 Thermocouples (TC)	Everything new, but run-in by the manufacturer, besides the swash plate
2	Slipper / Swash Plate	Position I	6 Eddy Current, 17 TC	N/A
3	Slipper / Swash Plate	Position II	6 Eddy Current, 17 TC	One new slipper
4	Slipper / Swash Plate	Position II	6 Eddy Current, 17 TC	N/A
5	Cylinder Block / Valve Plate	N/A	26 TC, Particle Sensors	New valve plate, new cylinder block
6	Cylinder Block / Valve Plate	N/A	26 TC, Particle Sensors	N/A
7	Cylinder Block / Valve Plate	N/A	26 TC, Particle Sensors	New valve plate. New Block
8	Slipper + Cylinder Block	Position I	6 Eddy Current, 17 + 26 TC, Particle Sensors	New valve plate

Based on the previous publications /9, 10/, it can be concluded that the temperature field captures the gap behaviour in an excellent fashion. Problematic areas are where high temperatures occur, which indicate low fluid film thickness, high viscous friction and low leakage, whereas lower temperatures are due to higher gaps when higher leakage occurs. A sample temperature field for a low speed high pressure applications can be observed in the top of **Figure 4**. Here the temperature field is shown for both interfaces at 300 bar, 500 rpm and 100 % displacement. The swash plate temperature is shown on the top right. It can be seen that the there is a region of higher temperature shortly after the transition from low to high pressure (Top Dead Centre – TDC), indicating that in this region the gap height is low. Then there is a region of low temperature at the bottom dead centre (BDC), indicating higher gap heights and higher leakage. The corresponding simulated and measured gap heights are shown in the figure in the middle of Figure 4. The simulated fluid film at φ = 180˚ is shown on the bottom with the three sensor positions. The min and max gap heights are a simulation output, whereas the blue, red and green lines are measured outputs for sensor 1-3 or sensor 5-6 correspondingly.

Similarly, the valve plate temperature, gap height and simulated fluid film is shown on the left side of Figure 4. Here the highest temperatures are around the outer sealing land of on the high pressure side, as well as at both TDC and BDC. On the low pressure side, the gaps are larger and therefore less heat is being generated while more cooling through leakage is introduced. From Figure 4 it becomes clear that the gap height measurements only give a small glimpse at the overall picture, they don't capture the maximum or minimum gap height, rather they output a snapshot of the orientation of the measured part at one instance in time. This is true for both interfaces. The temperature field however delivers a great overview of potentially life time critical conditions.

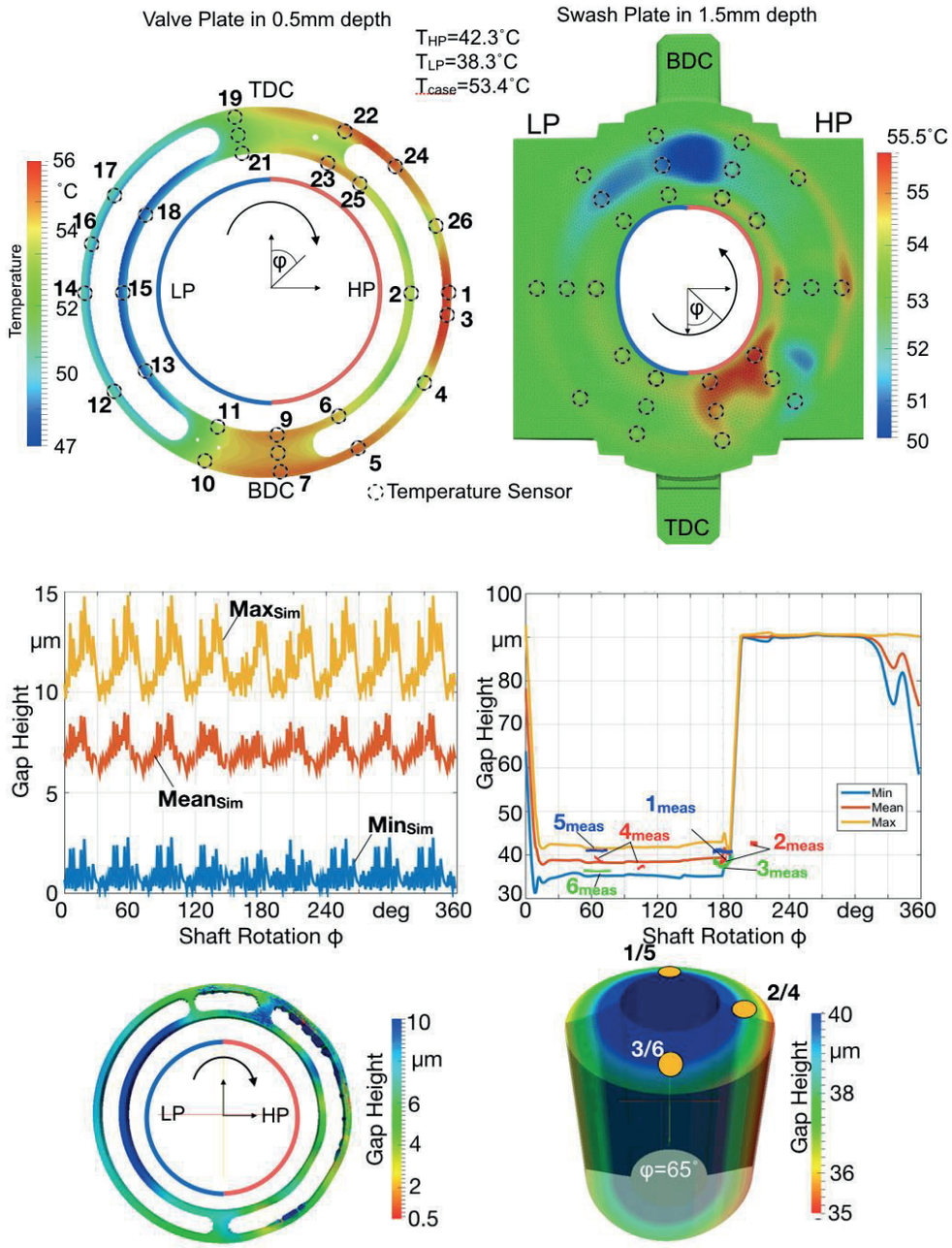


Figure 4 – Example Temperature field (top), measured and simulated gap height (middle) and 3D fluid film (bottom) at 300 bar, 500 rpm and 100% displacement for both interfaces along with the thermocouple placement.

3.2 Steady State Temperature Trends

This section discusses the measured temperature trends, across the entire operating field of the pump. A total of 30 operating conditions were measured in each series, varying pressure, speed and displacement of the pump. Each operating point was held constant until no changes were observed in any of the temperature sensors. The temperatures were then recorded for 2 minutes and averaged over the steadiest period in these 2 minutes. To achieve repeatability between each measurement, the tank temperature was regulated to be 40˚C, yielding in roughly 35-38˚C inlet temperature, depending on the operating condition. It is also necessary to mentioned, that the measurements were afterwards adjusted to an inlet of 35˚C, to make them comparable to each other. The 30 operating conditions can be seen in the bottom of **Figure 5**. Here the minimum (blue), mean (green), median (black) and maximum (red) valve plate temperatures of the 26 thermocouples are shown across all operating conditions. The shown values are average values from series 5 & 6. It can be observed, that the mean temperature level of the valve plate increases with speed and pressure. The median temperature level is very close to the mean, indicating an evenly distributed temperature field, rather than a few outliers. The effect of the displacement change on the mean temperature level is small, but can be observed. Larger displacements tend to have lower temperature levels than lower displacements. This effect can be explained by rather steady losses but lower volumetric flow, which yields to less cooling of the valve plate. This is confirmed by the fact, that the difference between the min and max temperature stays almost the same when displacement changes occur, indicating that the temperature distribution remained similar, just with a different temperature level. However, there are also other influences on the mean temperature level during the displacement changes besides the change in flow. By taking a look at 500 rpm, 300 bar and 25%, it can be seen that the temperature lever is higher than the general trend. Here the influence of the other interfaces can be observed. At this particular point, the slippers generate higher losses (see Figure 6), which increase the case temperature and therefore influences all parts of the rotating kit. Higher case temperature means that the parts such as the valve plate can dissipate less heat towards the surrounding oil, increasing their temperature. This illustrates the complexity of the physical phenomena that occur in these pumps, and how important it is to take all influences into regard when trying to model these gaps.

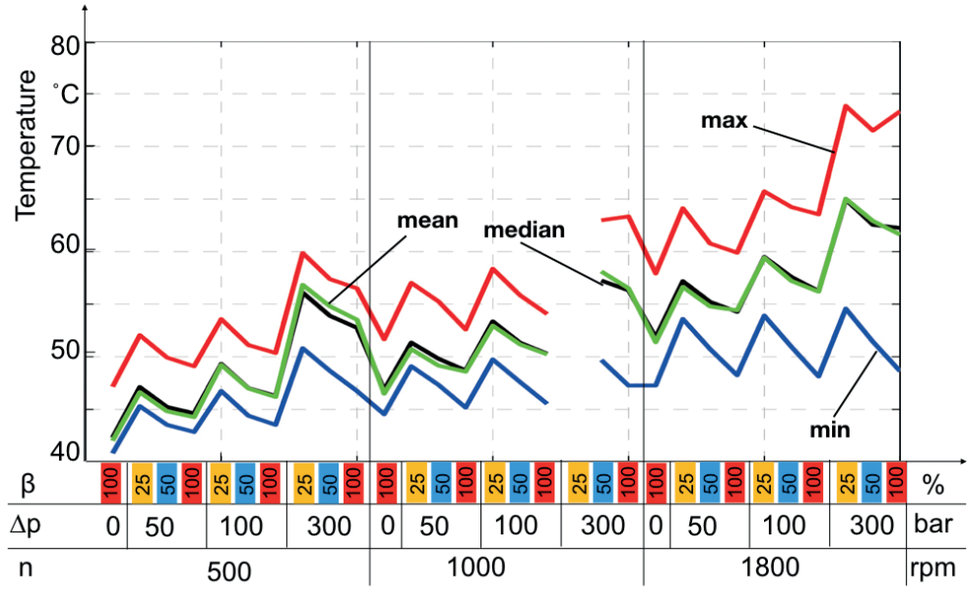


Figure 5 – Min, mean, median and max temperature of the valve plate across 30 operating conditions

Another trend that can be observed in Figure 5, is that the temperature spread, the difference between min and max, increases with pressure but more so with speed. The larger the spread, the higher the thermal strain on the valve plate and the larger the gap height difference.

Figure 6 shows the temperature distribution of the swash plate in a similar fashion. The shown values are the average of Series 1 - 4. It can be clearly observed, that the trends are different on this interface than on the cylinder block valve plate. What is the same is the general trend that the mean temperature increases with speed, with a few outliers. However, the pressure dependence is different. Medium pressure levels tend to have lower temperatures than higher or lower pressures. The influence of the displacement angle is also not as clear. For some pressure and speed levels the lower displacements have higher temperatures than at higher displacements, but this is not true for all operating conditions.

The spread between min and max varies drastically between operating conditions, with no clear trend visible. The highest spread seems to be at low displacements with a high or low pressures. The missing points for the three 25% displacement operating conditions are due to faulty or incomplete data at these points.

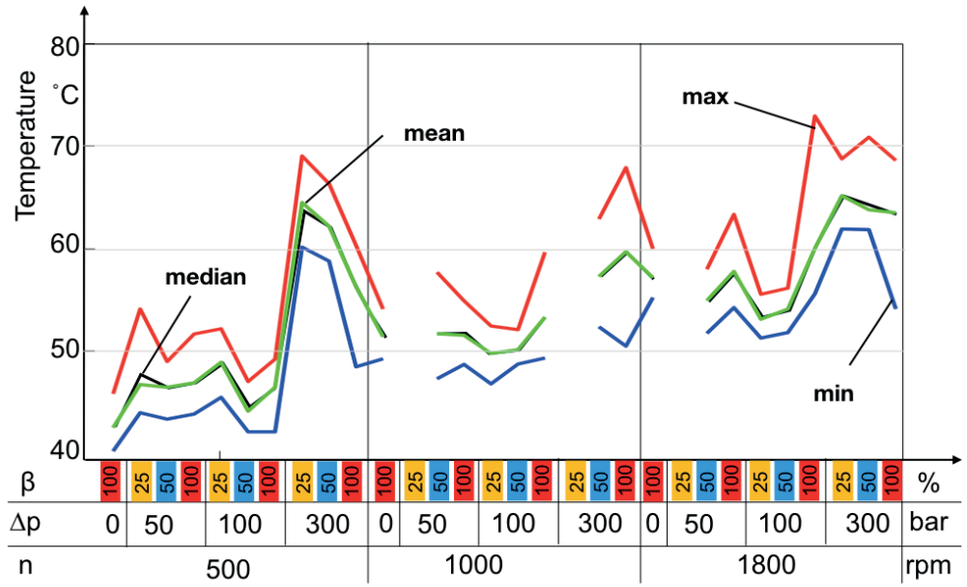


Figure 6 – Min, mean, median and max temperature of the swash plate across 30 operating conditions

In general, these temperature trends can be used to analyse the behaviour of the interfaces at each operating condition. For example, it becomes clear that 500 rpm 300 bar and 25% displacement is a difficult condition for the slippers, while 1800 rpm 300 bar and 100 % displacement is a tough one for the cylinder block / valve plate. Overall the slippers of this pump tend to work better at medium pressure levels.

A different analysis of these temperature trends can be seen in **Figure 7**. Shown on the left is the maximal measured valve plate temperature for varying pressures and speeds at 100% displacement. The grey lines indicate the measured power lines. It becomes obvious that the temperature contour lines are crossing the power lines, which means that the cylinder block valve plate heat generation varies within the same power output. In case of the 20 kW power line for example, the highest point is at 1800 rpm 80 bar with 64˚C (purple circle), while the lowest temperature occurs at 750 rpm 200bar with 56˚C (green circle), a delta of 8K.

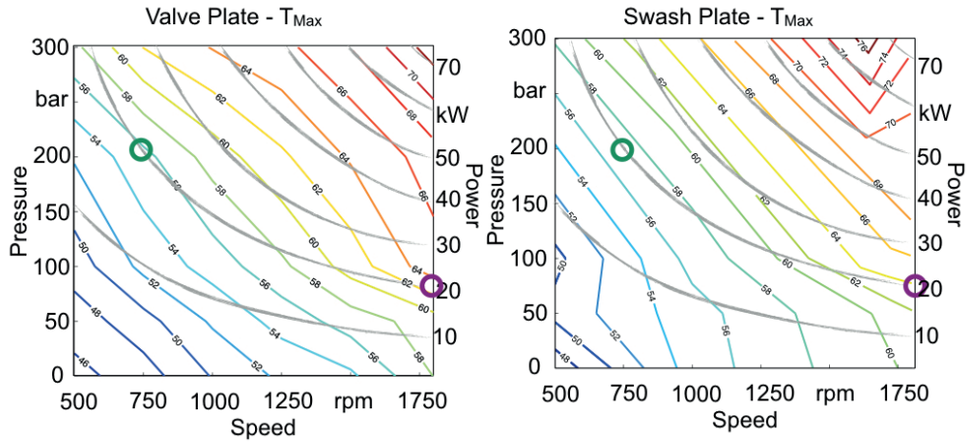


Figure 7 – Max. temperature contour field with measured power lines for both valve plate and swash plate

The right side of Figure 7 shows the maximum temperature on the swash plate also at 100% displacement. The trend is very similar. For example, looking at the 20 kW power line the lowest temperature is at 57˚C (green circle) at 200 bar 750 rpm, while the highest is at 64˚C (purple circle) at 80 bar and 1800 rpm, yielding a 7 K temperature difference.

Looking at both interfaces, it can be concluded that this particular pump should be operated rather in lower speeds and higher pressures in order to keep the maximum temperatures lower. These shown maximum temperatures were measured at steady state, the transient temperatures were usually higher. Higher hot spots (max temp) usually mean higher viscous friction, which can lead to higher wear. Therefore, if life time extension is desired, lower temperature levels are desirable. For this particular pump, this means running at lower speeds and higher pressures is advantageous.

3.3 Transient effects

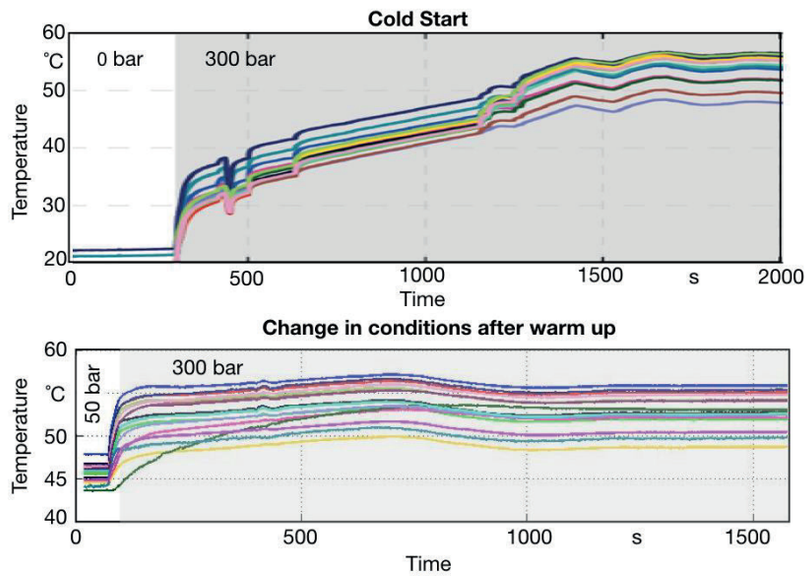


Figure 8 – Transient valve plate temperature for 500 rpm from a cold start and warm transient change

Next to the steady state findings, the transient measurement data gives great insight into dynamic effects such as wear. In contrast to the steady state temperature measurements, during dynamic conditions, such as pressure changes, the pump parts do not have time to heat up or cool off from the previous operating condition. Therefore, it does play a role in which order these measurements have been taken. For the initial run-in phase, the first couple of operating conditions, the order for each series was kept the same. The difference in terms of maximal temperature occurring in the cylinder block / valve plate gap can be seen in **Figure 8**. The upper part of the figure shows a cold start, meaning it's the first operating point of the day, when the oil is still cool. Shown is the pump running at 500 rpm 0 bar with a sudden increase to 300 bar. A steep increase in temperature by roughly 20 K can be observed. The final steady state temperature was reached after 2000 s. Note that the temperature spike during a cold start did never surpass the steady state temperatures. The ups and downs after roughly 1300 s are due to cooling of the tank. The bottom of Figure 8 is the same operating condition, but when the pump is already heated up. The initial spike is lower, however the temperature level is already at or even higher than the steady state level. For this particular operating point the impact of the initial temperature spike doesn't seem too obvious, however during some operating conditions the initial spike is very high, which can indicate wear as shown in the next section.

3.4 Wear in behaviour of the valve plate

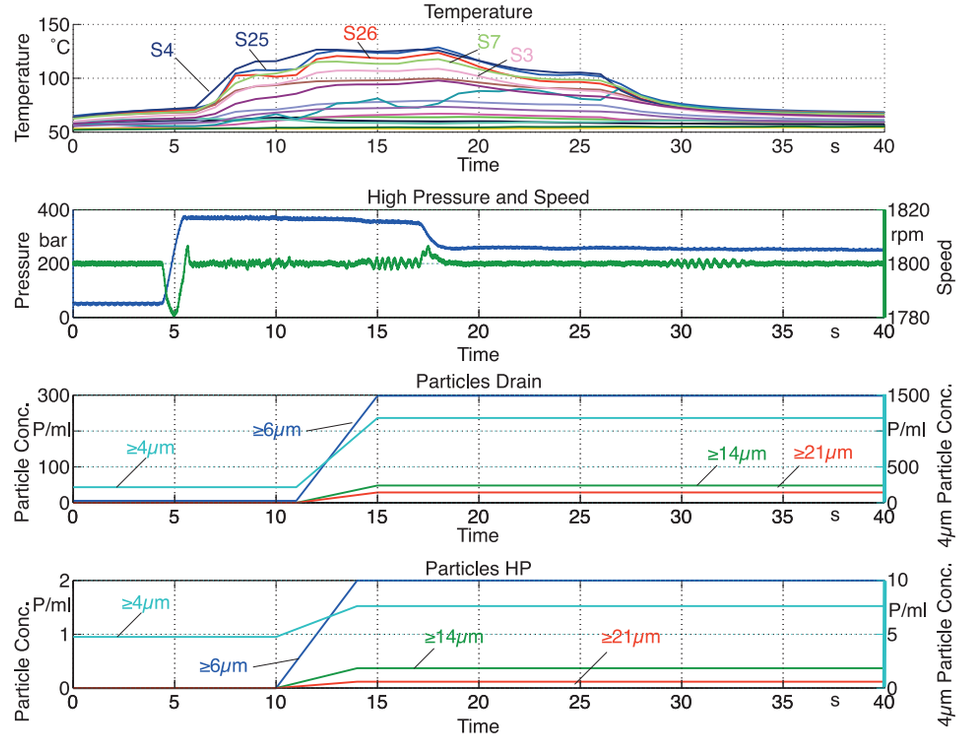


Figure 9 – Valve plate temperature at first time wear in along with particle generation in series 8

Figure 9 shows the measured transient data for a change in pressure at 500 rpm 100 % displacement, going from 50 to 360 bar. The top figure shows the temperature curves, the one below that the high pressure signal, and the bottom two figures show the data from the particle monitors both in the drain and the high pressure line. They output the particle concentration in parts/ml for four particle sizes: ≥4 µm, ≥6 µm, ≥14 µm and ≥21 µm. The ≥4 µm is shown on the right y-axis due to a different scaling. The important detail here is that both the cylinder block and valve plate have never seen a pressure above 300 bar before this.

The first thing that is quite astonishing, is that temperatures of multiple temperature sensors drastically increased to well above 100˚C, as soon as the pressure was increased. After about 12 seconds at this high pressure the pressure was reduced to 300 bar. After that the temperatures dropped again to a normal level. During this period of very high temperature the particles increased drastically in all four particle sizes in both the high pressure and drain line. This behaviour was document before in this pump and published /9/, the resulting temperature curve can be seen in Figure 12 on the left. The previous trend was measured during series 5, when both valve plate and block were new and the pressure was raised to 300 bar for the first time. Unfortunately, during that measurement series the particle monitors were not set up correctly and it was not possible to record the shown particle trend. However, the pump was opened afterwards and the locations that experienced these high temperature levels had significant wear. The above trend in Figure 9 occurred by accident in series 8, it was never planned to increase pressures above 300 bar, however an error in the load valve controller cause this pressure spike. This time the particle sensors were working properly and gave the shown trends.

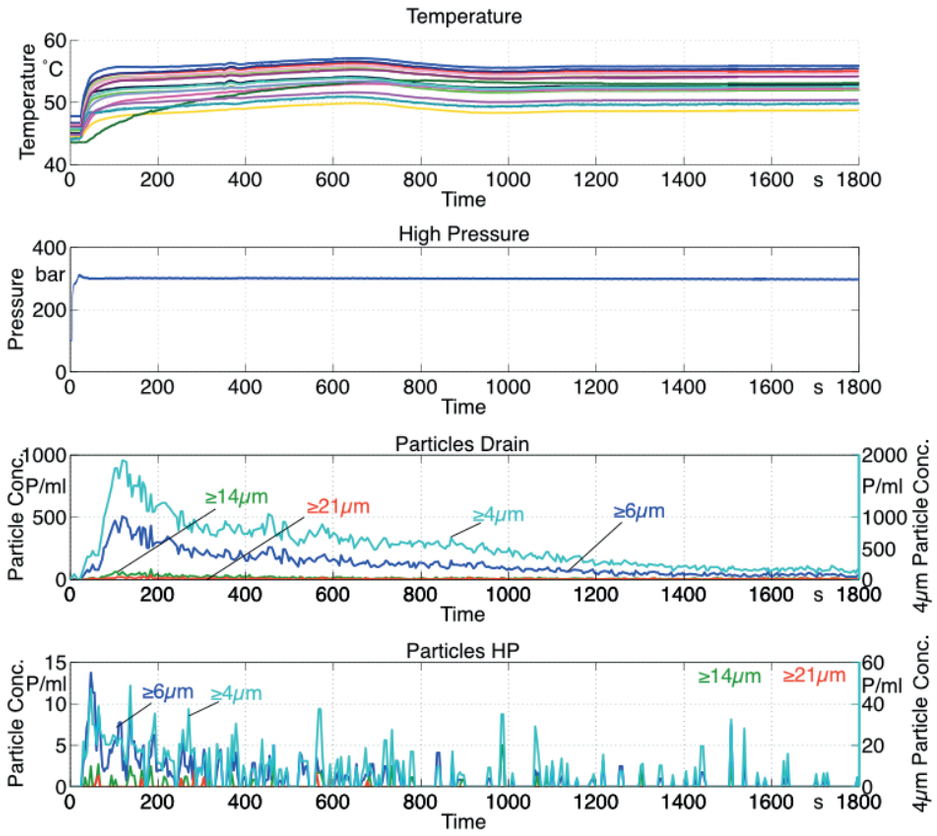


Figure 10 – Wear in temperature in series 8 for valve plate only

The mentioned temperature spike at 300 bar, which occurred during series 5, was not repeatable in series 5 nor 6. This suggested that it was due to a one-time wear-in process. Series 8 had a new valve plate installed, hence it was expected that a similar effect can be observed. The measured valve plate temperature and high pressure as well as drain particle concentration can be seen in **Figure 10**. Clearly the temperature spike was not nearly as hot as in Figure 9 or the previously published temperature spike, however the particles monitors in both lines clearly saw a large spike, which slowly decreased with time. The particle concentration levels are very comparable to the ones in Figure 9 and even higher. The fact that there was significant wear but the temperature rise was not above 60˚C needs to be further investigated. One theory is that the temperature increase in Figure 9 resulted from both brass and steel wear, where steel wear would only occur at the cylinder block since the valve plate is made from brass. The cylinder block was not replaced for series 8, therefore the cylinder block should be already run-in. Another interesting aspect in Figure 10 is the duration of the particle generation. Even after 1600 s (30 min) and with a steady state temperature level reached, the particle generation has not completely ceased. When the operating point was repeated for a second time in series 8, the particle generation died down significantly, as can be seen in **Figure 11**.

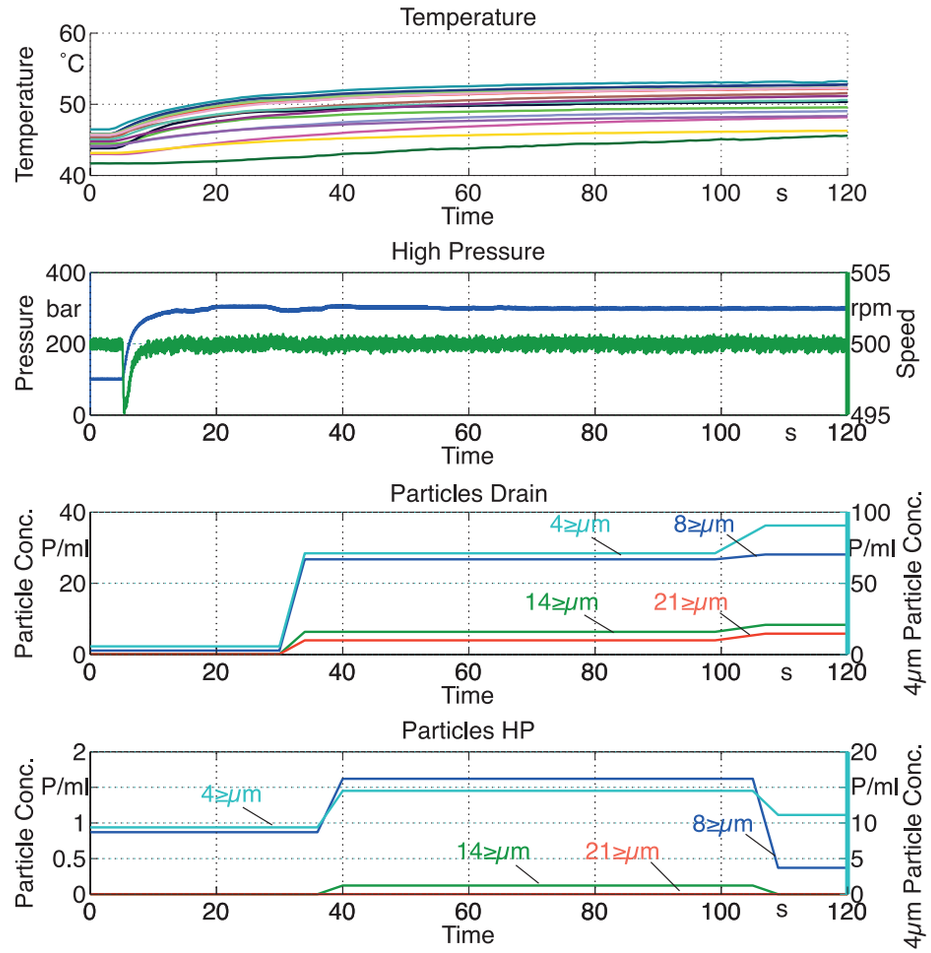


Figure 11 – Valve plate temperature and particle wear for re-rerun of 500 rpm 300 bar 100% in series 8

The initial temperature rise for the re-run is not as high as in the first run (Figure 10), even though the steady state temperature level of the previous operating condition had similar temperature levels. There still is a spike in particle generation, however the concentration levels are much lower than in the first run. A more detailed temperature analysis of the three transient measurements for 500 rpm 300 bar is shown in **Figure 12**. The figure shows 3 temperature graphs from left to right: The temperature transient temperature for the new valve plate (VP) and new cylinder block (CB) from series 5, the measurement for a new VP from series 8 and the second time the new VP from series 8 experienced the 300 bar. The temperatures are shown for the same time frame,

which makes them more comparable. What becomes obvious is that the temperature levels are different and the sensor that experiences the max. temperature change as well. Above the three graphs is the top 3 max temperature after stationary conditions were reached (adjusted to 35˚C inlet). The physical sensor locations are shown in Figure 4 top left.

For the new VP and CB (left graph) the top 3 transient temperature sensors are S5, S7 and S3. After roughly 30 min run-in the max stationary temperature top 3 are: S5, S25 and S3. In series 8 the transient and stationary order changed to: S25, S26 and S4. One outlier is S5 in the right graph, which has here the highest temperature, however this is due to the fact that S5 was the highest in the previous operating condition. Not only the transient temperatures levels are different between the three measurements, but also the final stationary temperature levels, which are decreasing from left to right. The cylinder block is the same for all 3 measurements, therefore it is possible that the more the cylinder block wears-in, the colder the temperatures on the valve plate become.

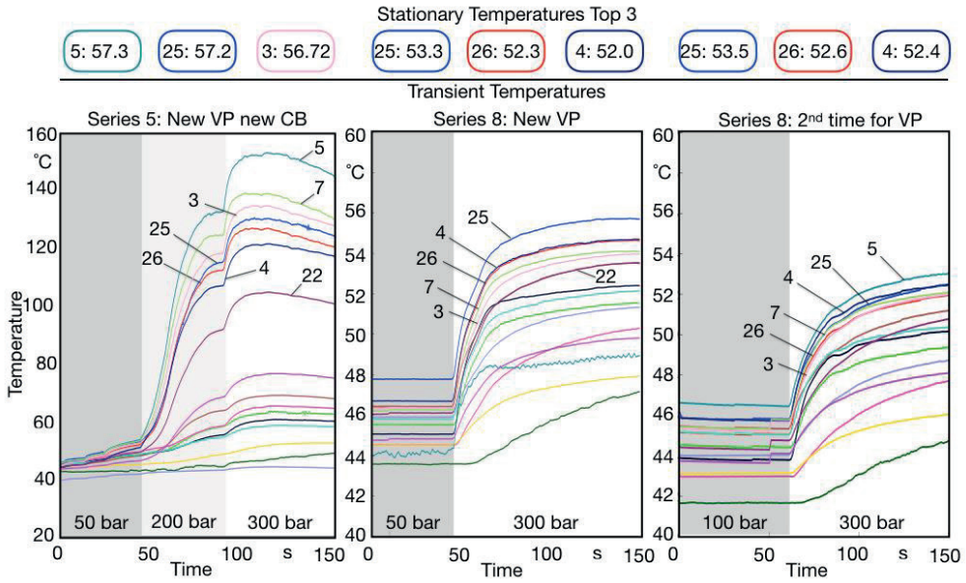


Figure 12 – Transient valve plate temperature rise for 500 rpm 300 bar 100%

Another interesting trend that was noticeable, was that not every operating condition experienced such a strong run-in. It rather seemed that each pressure level independent of speed had to be run-in, as well as every speed level independent of the pressure. For example, after completing the run-in for 500 rpm 300 bar, the effect of increasing the speed to 1800 rpm caused more particle generation, than increasing the pressure from 50-300 bar at the higher speed level. This effect is shown in **Figure 13**. Here the initial condition is 750 rpm, 50 bar and 100% displacement. Then the speed is increased to 1800 rpm while maintaining the pressure level. After the speed is reached the pressure is increased to 300 bar. This is the first time the valve plate has seen this high speed and high pressure, however the effect on the particle generation by increasing the speed is larger than the pressure increase.

An overview of the max particle concentration for each of the four shown cases, can be seen in **Figure 14**. The two bar charts show the max. recorded particle concentration for the different particle sizes. The blue bar represents the first time the new valve plate in series 8 has experienced 300 bar. The green bars show the max particles for the second time the valve plate experienced 300 bar in series 8. The orange shows the 360 bar case (first for both valve plate and cylinder block see Figure 9) The red bars show the additional particle concentration caused by the pressure increase from 50-300 bar at 1800 rpm as seen in Figure 13. The trend shown is that the particle generation drastically decreases after the first time the pump parts have experienced a new pressure level. This is true even if the speed changes.

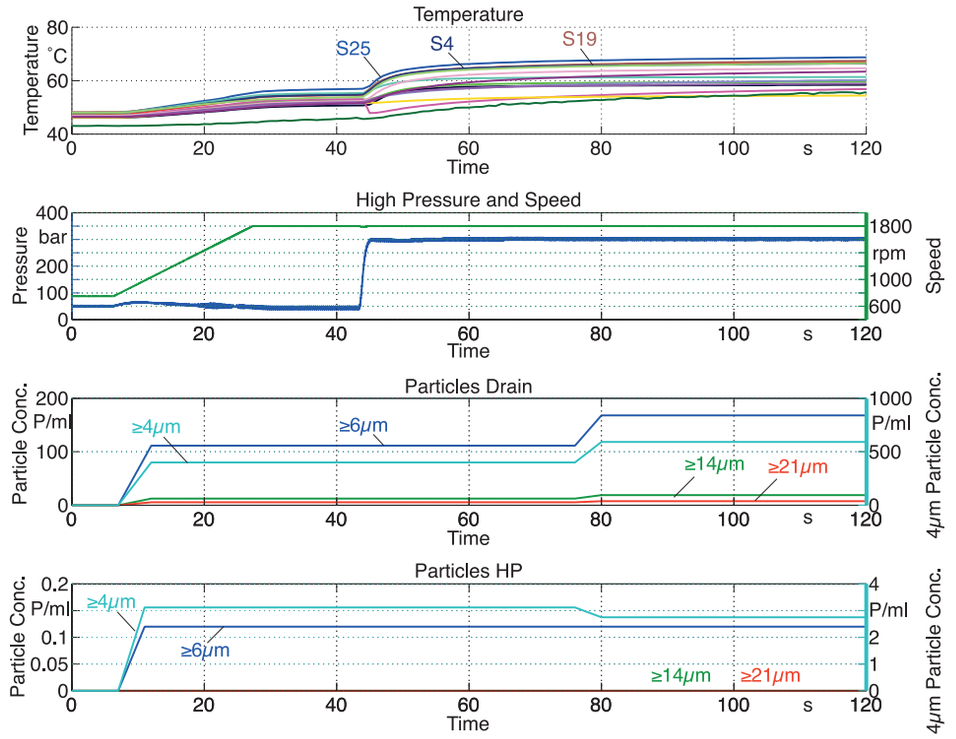


Figure 13 –Valve plate temperature and particles for speed and pressure change – first 300 bar pressure at high speed

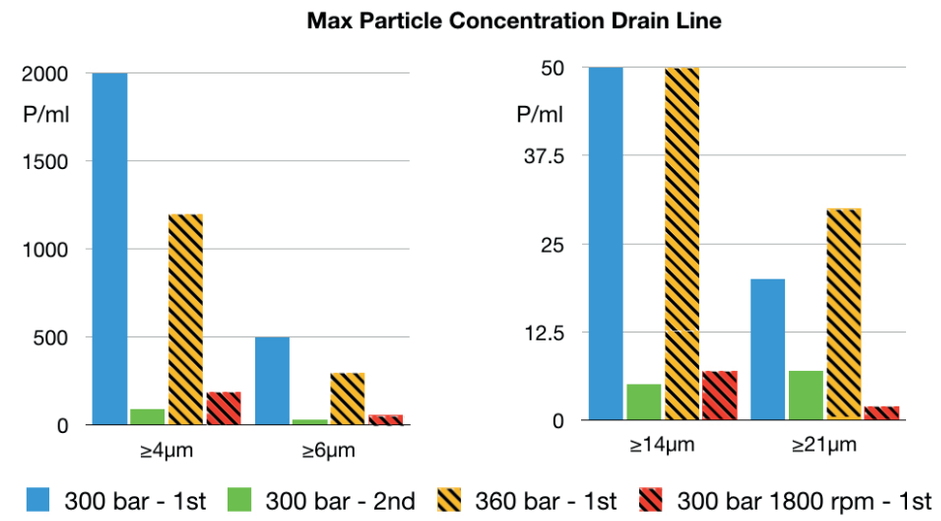


Figure 14 – Overview max. particle concentration for 500 rpm 100 % displacement.

To conclude, it can be said that a run-in occurs every time the pump either experiences a never-before seen pressure or speed level. However, the two can be seen independently from each other. The pump run-in can take about 30 min per operating condition for the cylinder block valve plate interface. A direct connection between temperature rise and particle generation can be seen, but cannot be quantified at this point, since a similar particle generation caused two different transient temperature curves.

4 Summary and Conclusion

This paper presented both transient and steady state measurement from a novel “transparent pump” test rig. The measurements included surface temperature measurements of the valve plate, swash plate as well as the fluid film thickness of the slipper. Combined with particle sensors the data was used to analyse wear patterns and the run-in of the valve plate interfaces. A state of the art simulation program was used to analyse the pump and interpret the measured data. Especially the gap height measurements are greatly enhanced when combining them with the simulation findings.

The novel findings are that changes in pressure and speed have significant impact on the valve plate surface temperatures, whereas changes in displacement are rather insignificant. The surface temperature of the swash plate has a similar speed dependency; however, the slippers react differently to pressure or displacement changes than the cylinder block. Medium pressures tend to have lower temperatures than very high or low pressures. It was also shown that the CB/VP interface can be influenced by the other interfaces, by being affected of elevated case temperatures, which were caused by increased slipper losses. Figure 7 illustrated that the examined pump operates at lower temperature levels at low speed and higher pressure for both the slipper/swash plate and CB/VP interface.

It was also shown that the run-in of the cylinder block and valve plate are accompanied by temperature changes in the transient regime. It was also shown that the run-in is not always the same and is influence by other factors that need to be studied in more detail. A typical run-in phase was about 30 min, after that time the particle generation was significantly reduced.

The next steps in this research are to show the slipper wear and its effect on the performance of the slipper / swash plate interface. The fluid film measurements of the cylinder block / valve plate will be published in future publications. The slippers experience a much longer run-in period than the cylinder block. Furthermore, the simulation tool will be further enhanced by incorporating the wear-in, something that showed already tremendous potential for the cylinder block / valve plate interface.

5 Acknowledgements

This research was funded by the German Federal Ministry of Economic Affairs and Energy (Ref. No. 03SX382B). The authors are responsible for the content of this publication.

Special thanks to Argo-Hytos and Micro-Epsilon for their support of this research with their donation of measurement equipment.

Supported by:
Federal Ministry for Economic Affairs and Energy
on the basis of a decision by the German Bundestag

Nomenclature

Variable	*Description*	*Unit*
β	Pump Displacement	[%]
BDC	Bottom Dead Centre	
CB	Cylinder Block	
Δp	Difference between High and Low Pressure	[bar]
HP	High Pressure	[bar]
LP	Low Pressure	[bar]
n	Rotational Speed	[rpm]
φ	Shaft Rotational Angle	[°]
T_{Case}	Temperature in Drain Line	[°C]
T_{HP}	Temperature in High Pressure Line	[°C]
T_{LP}	Temperature in Low Pressure Line	[°C]
T_{Max}	Maximum Temperature	[°C]
TC	Thermocouple	
TDC	Top Dead Centre	
VP	Valve Plate	

References

/1/ IVANTYSYNOVA, MONIKA: *An investigation of viscous flow in lubricating gaps*, SVST Bratislava, Czechoslovakia, 1983

/2/ WERNECKE, P.W.: *Messung physikalischer Größen im Dichtspalt*. In: o+p ölhydraulik und pneumatik (1982), Nr. 26

/3/ WINNER, D.: Verschleißempfindlichkeit von verschiedenen Verdrängereinheiten. In: *o+p ölhydraulik und pneumatik* Bd. 28 (1984), Nr. 4

/4/ DEEKEN, MICHAEL: *Simulation of the tribological contacts in an axial piston machine*. In: IMECE04, 2004, S. 1–5

/5/ PELOSI, MATTEO: *An Investigation on the Fluid-Structure Interaction of Piston/Cylinder Interface*, Purdue University, 2012

/6/ SCHENK, ANDREW: *Predicting Lubrication Performance Between the Slipper and Swashplate in Axial Piston Hydraulic Machines*, Purdue University, 2014.

/7/ ZECCHI, MARCO: *A novel fluid structure interaction and thermal model to predict the cylinder block/valve plate interface performance in swash plate type axial piston machines*, Purdue University, West Lafayette, IN, 2013

/8/ WEGNER, STEPHAN: *Experimental investigation of the cylinder block movement in an axial piston machine*. In: FPMC2015 -9529, 2015

/9/ IVANTYSYN, ROMAN ; SHORBAGY, AHMED: *An Approach to Visualize Lifetime Limiting Factors in the Cylinder block / Valve Plate Gap in Axial Piston Pumps*. In: *FPMC2017-4327*, 2017, S. 1–12

/10/ IVANTYSYN, ROMAN ; WEBER, JÜRGEN: *“Transparent Pump” – An approach to visualize lifetime limiting factors in axial piston pumps*. In: *ASME 2016 9th FPNI Ph.D Symposium on Fluid Power*. Florianapolis, Brazil, 2016

/11/ BERGADA, J. M. ; DAVIES, D. L. ; KUMAR, S. ; WATTON, J.: *The effect of oil pressure and temperature on barrel film thickness and barrel dynamics of an axial piston pump*. In: *Meccanica* Bd. 47 (2012), Nr. 3, S. 639–654

/12/ KIM, JONG-KI ; JAE-YOUN, JUNG: *Measurement of Fluid Film Thickness on the Valve Plate in Oil Hydraulic Axial Piston Pumps (Part I)* Bd. 17 (2003), Nr. 2, S. 246–253 — ISBN 8263270391

Reducing the wall thickness of the cups and pistons in Floating Cup pumps and motors

Peter Achten, Sjoerd Eggenkamp, Jeroen Potma

INNAS BV, Nikkelstraat 15, 4823AE Breda, The Netherlands
E-Mail: pachten@innas.com

The rotational speed of slipper type, axial piston pumps and motors is limited. One of the most important reasons for this limitation is the barrel tipping torque, which is (amongst others) affected by the centrifugal forces of the pistons. The force of the barrel spring is needed to overcome the tipping of the barrel, and thus preventing the malfunction of the pump or motor. The hydrostatic pressure can create an additional hydrostatic force, pushing the barrel to the port plate, and thereby preventing the barrel to tip. But, at low operating pressures, the hydrostatic force is insufficient, and the tipping torque can only be counteracted by the central barrel spring. Due to the limited strength of this spring, the barrel will tip above a certain operating speed. At that point, the face seal of the barrel will no longer make a full contact with the port plate, and the pump or motor cannot any longer be operated, due to excessive leakage and wear.

Floating cup (FC) pumps and motors have the advantage that the pistons are press-fitted into the central rotor. Therefore, the pistons can't create anymore any tipping torque load on the barrel. But, unlike in conventional axial piston designs, in FC-machines, the cylinders are no longer integrated and machined inside the cylinder block or barrel. Instead, they are separated and have become cup-like cylinders which are floating on, and supported by the remaining barrel plate. Being isolated from the barrel itself, these 'cups' will create another tipping torque load on the barrel. The weight of the cups is however small, much smaller than the weight of the pistons in an equally sized slipper type machine. Furthermore, the centrifugal tipping torque is reduced by the short cup-stroke in the floating cup machine.

Nevertheless, it is desirable to further reduce the mass of the cups, not only to increase the maximum operating speed, but also to reduce the force of the central barrel spring, which would further increase the overall efficiency. The best way to reduce the mass of the cups, is by means of a reduction of the wall thickness of the cups. It needs to be considered that the cups expand when being pressurized. Therefore, in order to maintain a tight sealing between the cups and the pistons, the piston crown needs to expand as well, thereby following the radial expansion of the cup. Consequently, the wall thickness of the piston crown needs to be reduced as well.

The question is whether these conditions can be met when the wall thickness of the piston crown and cup wall is reduced. In this paper, the effects of a 50% reduction of the wall thickness are investigated and described. The deformation is calculated by means of FEM analysis of the piston and the cup.

Keywords: Floating cup, FEM-analysis, barrel tipping torque
Target audience: Hydrostatic pump and motor designers and manufacturers

1 Introduction

Hydrostatic piston pumps and motors are positive displacement machines. In Floating Cup (FC) pumps and motors, the displacement is created by cup-like cylinders. These 'cups' are translating on pistons, which have a ball shaped, spherical piston crown. Unlike in other axial piston designs, the pistons are press-fitted into the rotor. Compared to slipper type and bent axis machines, the FC-design is therefore more or less inverted: the pistons are locked, and the cylinders, the 'cups', are free to move on the barrel plate. One of the advantages of the new design is, that the centrifugal forces of the pistons no longer create a torque load on the barrel. This so-called 'tipping torque' is one of the most important reasons why axial piston machines cannot be driven above a certain operating speed [1-3].

However, in the FC-principle, the cylinders are isolated from the barrel. The 'cups' can slide and translate on the remaining barrel plate. But, due to their degree of freedom, they will also create a new tipping torque on the barrel. To make things even worse, the FC-principle is a multi-piston principle, typically having around 12 pistons and cups per barrel. This is more than the average 9 pistons, that cause a tipping torque load in slipper type machines, and the larger number of cups will increase the tipping torque load. The barrel tipping torque is also strongly influenced by the radius of the pitch circle of the pistons. However, the FC-principle does not increase this radius [4], and therefore there does not have any effect on the tipping torque in comparison to slipper type machines having the same geometrical displacement.

On the positive side, the FC-principle has a swash angle of around 8°, which is less than halve the swash angle of most slipper type machines. This is advantageous for reducing the tipping torque, since the small swash angle results in a small stroke of the cups. In other words: the center of mass of the cups is always close to the midpoint of the piston head, which results in a smaller arm for the centrifugal forces to create a torque load.

But the most important effect is the difference between the mass of the cups and the mass of the pistons of a comparable slipper type machine. Figure 2 shows the cup of a floating cup machine and the piston of a slipper type machine, both having a displacement of 28 cc. The mass of the cup is 13.1 gr, being only 23% of the weight of the piston of the slipper type pump, which has a mass of 56.2 gr.



Fig. 1.: Piston of a 28 cc slipper type pump (56.2 gr) and cup of a 28 cc FC-pump (13.1 gr)

The combined effect of the reduced stroke and the lower mass of the cups results in a strong reduction of the tipping torque [3], even including the detrimental effect of the large number of cups. Nevertheless, at some point, the centrifugal forces of the cups still limit the maximum operating speed of the FC-pumps and motors. In order to further reduce the tipping torque load, i.e. to increase the maximum rotational speed, this study investigates the opportunity to reduce the mass of the cups by means of a reduction of the wall thickness. In a 24 cc prototype, the wall thickness of the cups has been reduced from 2.25 mm to 1.1 mm, a reduction of about 50%. FEM-analysis have been performed to calculate the effect of the reduced wall thickness on the deformation of both the cup and the piston crown.

2 The effects of centrifugal forces on the tipping torque

The cups create several loads on the barrel, many of which result in a tipping torque load on the barrel. Figure 2 shows the forces acting on the cup, excluding the hydrostatic forces. The most dominant forces are the centrifugal force F_{centr} and the friction force $F_{fr,1}$ between the cup and the piston. The last-mentioned friction force is an indirect effect of the centrifugal force. The centrifugal force creates a lateral reaction force in the contact between the piston and the cup, thus causing a friction force. Since the centre of mass of the cup (point B in Figure 2) differs from the point A of rotation, there is a reaction force $F_{r,2}$ in the contact between the cup and the barrel plane. All these reaction forces of the cups together create a tipping torque on the barrel.

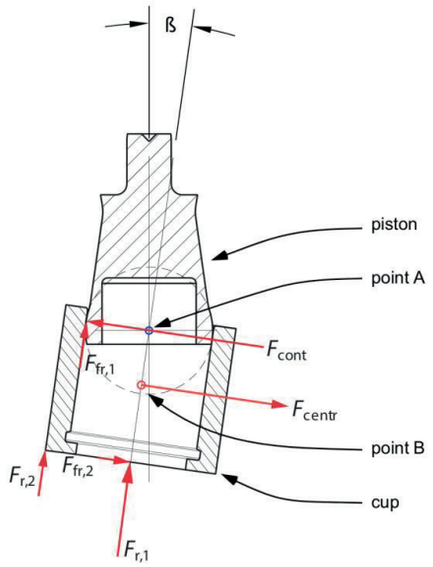


Fig. 2: Forces acting on the cup. Point A is the center of the sphere of the ball-shaped piston crown. Point B is the center of mass of the cup and ots oil contents.

The effects of these forces on the tipping torque can be calculated. First of all, there is the direct effect of the centrifugal forces of the cups on the tipping torque. These create a torque load on the barrel in the x-direction (see Figure 3). In the y-direction, the sum of all centrifugal torque loads amounts to zero: the torque loads are cancelled internally. Figure 3 also illustrates how the torque vector is influenced by the cup position on the piston crown. In the Top Dead Centre (TDC) the centre of mass of the cup, point B, is to the right of the point of rotation A. In the Bottom Dead Centre (BDC), point B has shifted to the left of the point of rotation A. The result is that all torque vectors are pointed towards the minus-x-direction. The resulting torque tends to tip the barrel towards the TDC. This is independent of the direction of rotation of the pump or motor.

The second cause for the tipping torque is the friction between the cups and the pistons. This force is directly related to the centrifugal force. In the case of solid or mixed friction, the centrifugal load of the cups is taken in the contact between the cup and the piston, thereby creating a friction force. Even when hydrodynamic lubrication is assumed, the centrifugal force will push the cup towards one side of the piston, thereby reducing the gap height of the oil film, and increasing locally the viscous friction.

It is important to realize that the FC-principle does not create any hydrostatic load between the piston and cylinder, as is the case in slipper type machines. The only remaining lateral load on the piston is created by the centrifugal force of the cup. Although the magnitude and direction of the centrifugal load can be calculated accurately, the magnitude of the friction force very much depends on the unknown tribological conditions. However, the direction of the friction force is well defined: when moving from TDC to BDC, the friction force pushes the cups onto the barrel plate. From BDC to TDC the friction force is in the opposite direction. The resultant tipping torque will therefore be on the y-axis. The direction of this torque vector is dependent on the direction of rotation of the main shaft. The magnitude of the friction tipping torque strongly depends on the friction coefficient. Assuming a value of around 0.1, the friction force itself is much smaller than the centrifugal force. But, since the friction force creates a tipping torque around an arm which is about 10 times larger than the centrifugal tipping torque, both tipping torques have about the same magnitude.

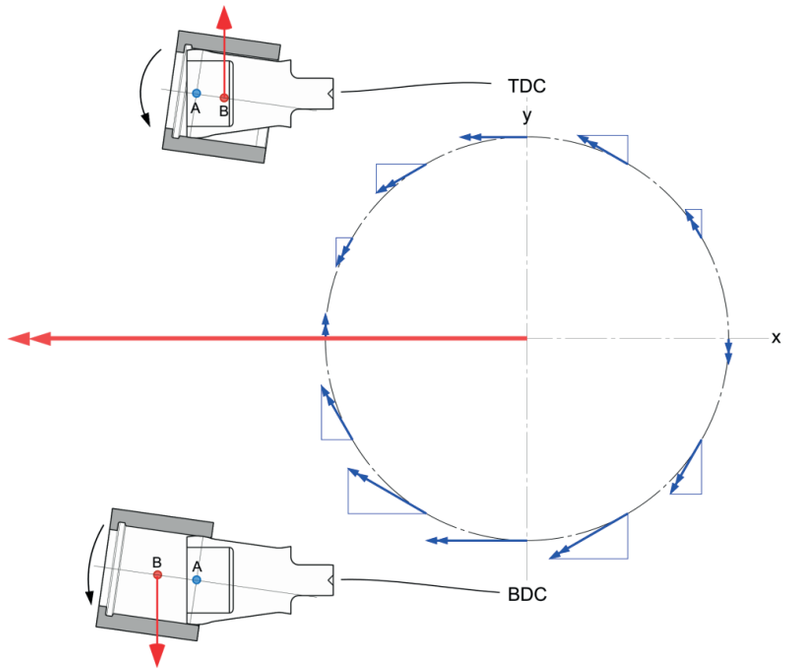


Fig. 3: Barrel tipping torque generated directly by the centrifugal forces of the cups (TDC = Top Dead Centre, BDC = Bottom Dead Centre)

The third tipping torque is caused by the friction between the rotating barrel and the stationary port plate. Due to the previous two torque loads, the barrel will already slightly incline towards a certain direction. At the point where the gap height is smallest, the friction between the barrel and the port plate will be higher, which will generate another tipping torque.

Figure 4 shows all three torque vectors, as is calculated in the simulation model for pump operation and projected on top of the port plate. The high-pressure side is on the right side of the port plate. The calculation has been performed assuming a near to zero pump pressure. Pressure dependent torque loads are therefore not included. The figure shows that the resultant torque load tends to tip the barrel towards the high-pressure side of the port plate, having the smallest gap height around 45° before the TDC. If a barrel would start tipping, this is where it would make contact with the port plate.

This has been confirmed with a number of experiments. Figure 6 shows a test of about 5 minutes, in which a 24 cc constant displacement pump has been operated at the lowest possible pump pressure, while gradually increasing the speed. At around 250 seconds, the pump reached a speed of 4920 rpm. At that point, the case drain flow suddenly increased and the pump pressure dropped to zero. The test was performed on a 4-quadrant hydrostatic machine which demanded a pre-charge pressure level at the supply side during pump operation.

After inspection of the pump, a clear mark of the barrel edge was found (see Figure 5). This mark can only be explained by the tipping of the barrel. The mark was visible on both port plates of the floating cup pump, indicating that the critical tipping speed was the same for both barrels. Since both barrels are identical, this was expected.

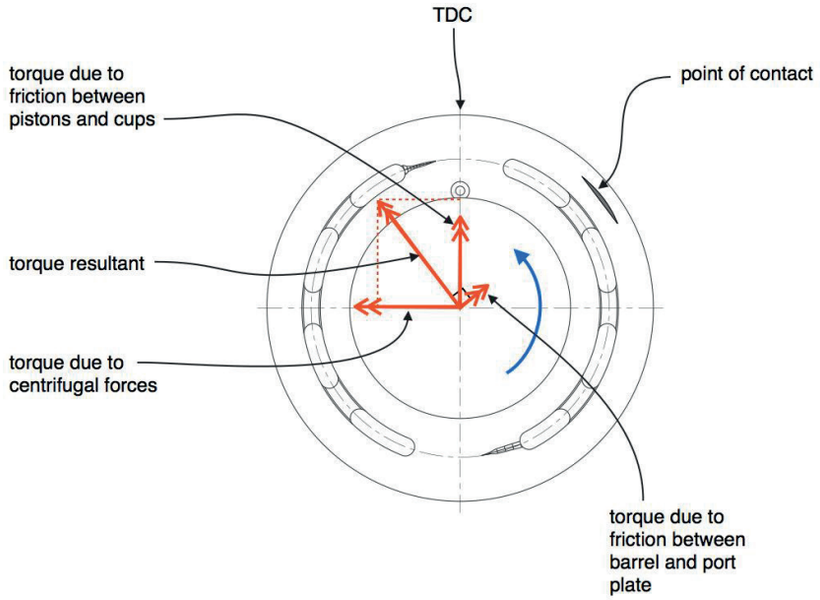


Fig. 4: Centrifugal and friction tipping torque acting on the barrel



Fig. 5: Port plate showing the tipping mark of the barrel

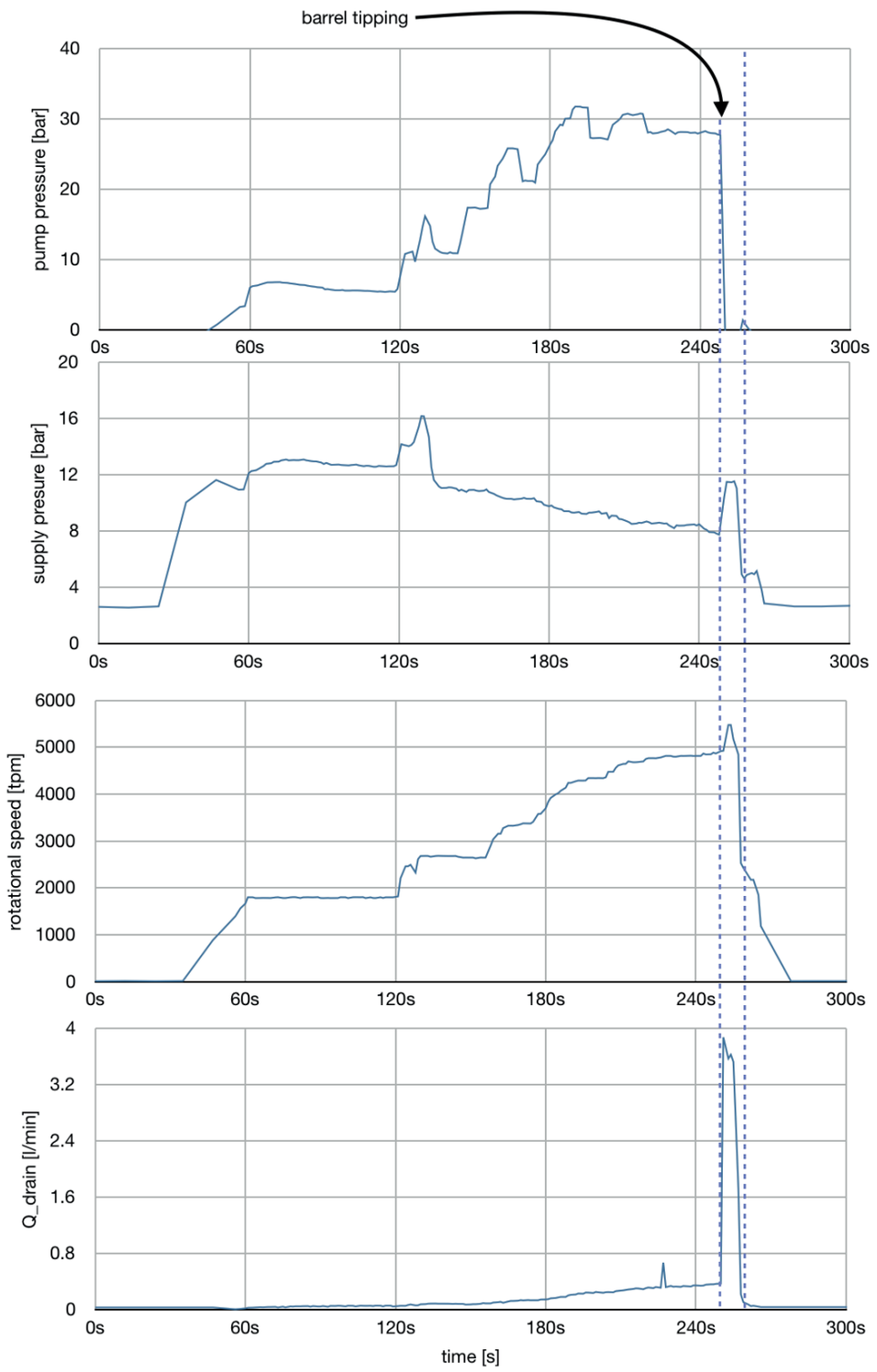


Fig. 6: Test of a 24 cc constant displacement FC-pump at low operating pressures (Oil temperature 40°C, HLP46)

3 Reducing the wall thickness of the cups

The centrifugal force of the cups is the root cause of the barrel tipping at low operating pressures. The barrel tipping could be reduced by increasing the strength of the central spring, which pushes the barrel towards the port plate. But this would create an additional bearing load in the contact between the barrel and the port plate, thereby increasing the friction losses. The most adequate way to reduce the centrifugal tipping torque is to reduce the mass of the cups.

The centrifugal tipping torque T_{ct} is linearly dependent on the mass of the cups:

$$T_{ct} \equiv m_{cup} \cdot n^2 \tag{1}$$

Without a hydrostatic load, the tipping torque can only be counteracted by the central barrel spring, which has a certain spring force F_{sp}. The barrel will tip whenever the centrifugal tipping torque is larger than the counteracting torque generated by the barrel spring. Consequently, there is a critical rotational speed n_{cr}, which is dependent on the spring force and the cup mass:

$$n_{cr} \equiv \sqrt{\frac{F_{sp}}{m_{cup}}} \tag{2}$$

In this study, the mass of the cups of a 24 cc FC-pump is reduced from 12.3 gr to 5.16 gr, a reduction of 61.3%. This would result in an increase of the maximum speed of 54.4%. With the original cups, a critical tipping speed of 4920 rpm has been measured. With the new, light cups, the critical speed would (in theory) be increased to 7600 rpm.

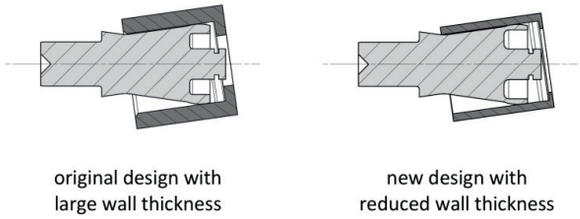


Fig. 7: Old and new designs of piston and cup

The weight reduction has been achieved by reducing the wall thickness of the cups. Figure 7 shows the original and the new design, side by side. The thickness of the wall has been reduced from 2.25 mm to 1.1 mm. The cups have an inner diameter of 12.5 mm. Also, the thickness of the cup base has been reduced from 1.5 mm to 1 mm.

Figure 7 also shows, that, aside from the cup design, also the piston design has been adapted. This is necessary to keep the gap between the piston crown and the cup small, even when the components are being pressurized [4]. The reduced wall thickness reduces the stiffness of the cup. Consequently, the thin-walled cups will expand more in the radial direction when being exposed to the internal hydrostatic pressure. In order to follow this expansion, the stiffness of the piston crown needs to be reduced as well.

4 FEM-analysis

FEM-analysis have been performed to investigate the deformation of the new cup and piston design. Several designs have been reviewed. Each design configuration requires a number of FEM-analysis at various positions of the cup on the piston crown. The analysis not only involves the radial expansion of the cup and the piston crown, but also calculates the axial deformation of the cup base. The cups are floating on the barrel plate (hence the name Floating Cup), and the cup base acts as a face sealing and bearing interface. The deformation of the sealing area strongly influences the sealing and bearing capacity between the cups and the barrel plate. Figure 8 shows the (enlarged) calculated deformation of two different cup designs. In the left design, the deformation of the cup base results in a convergent gap profile, whereas the right design creates a divergent gap profile. Both calculations are made for the same piston position and pressure load.

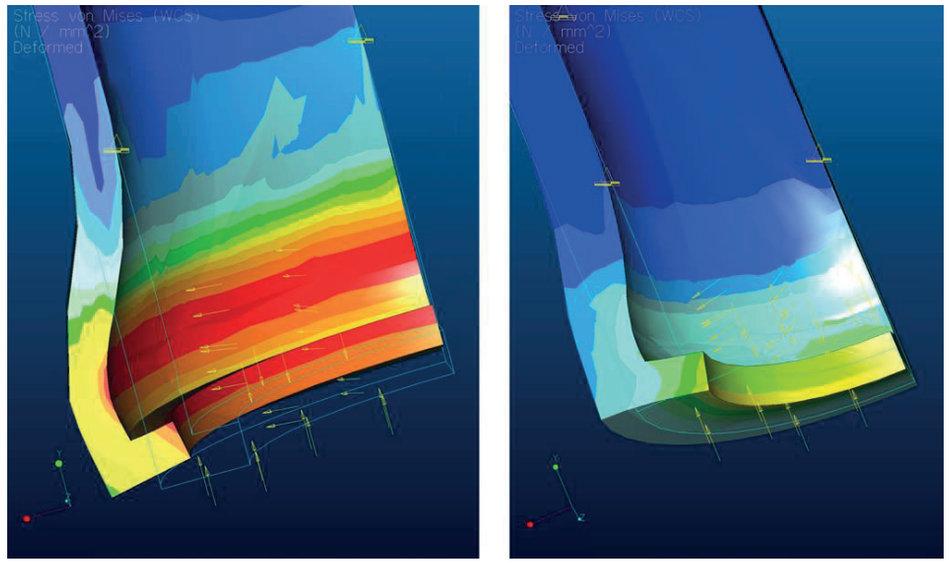


Fig. 8: Local deformation of two cup designs

The deformation of the cup changes with the position of the cup on the piston crown:

- The part of the cup cylinder which is pressurized depends on the position of the sealing line between the piston crown and the cup. The pressurized area of the cup wall is therefore variable;
- The inner shoulder of the cup base increases the stiffness of the cup. Therefore, the cup expansion is smaller close to the TDC-position.

By means of the FEM-analysis, a number of piston and cup designs have been evaluated for a 24 cc pump, being operated at a maximum pressure of 500 bar. Figures 9, 10 and 11 show the axial deformation of the inner diameter of the cup base shoulder, the radial expansion of the cup at the sealing line, and the maximum Von Mises stress. In each diagram, the final new design is compared to the original design having a wall thickness b of the cups of 2.25 mm, at various positions of the piston crown inside the cup.

The FEM-analysis clearly shows the larger expansion and the deformation of the thin walled cups. The mechanical stress is also increased. The axial deformation of the cup shoulder is somewhat less, especially between the BDC-position and half of the piston stroke. In this part of the stroke, the axial deformation has a positive value, meaning that the shoulder is bent away from the cup base, thus resulting in a divergent gap profile.

The most important result is the radial expansion of the cup at the location of the sealing line with the piston crown. Obviously, the thin walled cup expands considerably more than the heavier original design. The maximum value is increased from 2.8 µm to 4.6 µm, which corresponds to an increase of 66%.

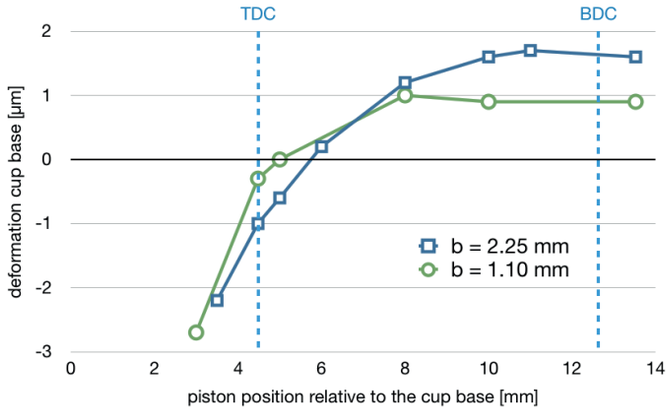


Fig. 9: Axial deformation of the cup base at p =500 bar (positive values result in a divergent gap profil

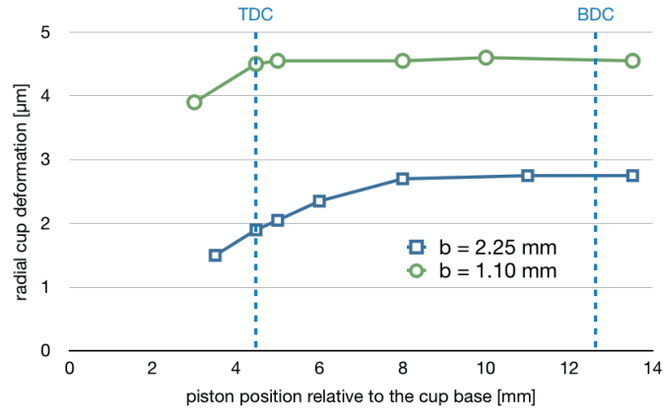


Fig. 10: Radial deformation of the cup cylinder at the sealing line with the piston (p = 500 bar)

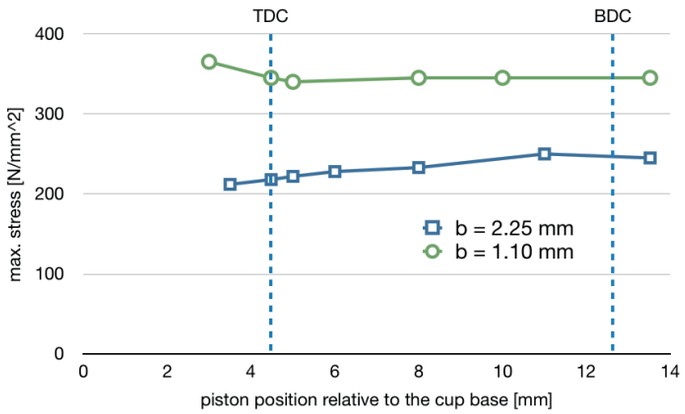


Fig. 11: Maximum value of the calculated Von Mises stress (p = 500 bar)

One of the advantages of the thin walled cups is that the radial expansion of the sealing line is almost constant during the entire stroke. In the original cup, the radial deformation varies between 1.9 and 2.75 µm. It is important to consider that the pressurized area of the piston crown is independent of the cup position. Furthermore, at any position of the cup, the piston expansion should be smaller than the cup expansion. Hence, the piston crown must be dimensioned as such that it matches the smallest radial expansion of the cup, i.e. the radial expansion at the TDC-position. Consequently, the gap between the expanded cup and the expanded piston crown widens when the cup moves to the BDC-position, since the cup expansion will become larger, whereas the piston deformation stays the same.

This effect cannot be seen with the new, thin walled cups, for which the radial expansion stays almost constant. This helps to reduce the gap height between the piston crown and the cup, but also creates the opportunity to shift the stroke closer to the cup base, thereby reducing the cup length. The shift will also improve the average position of the centre of mass of the cup, bringing it closer to the midpoint of the piston crown. This will further reduce the centrifugal tipping torque.

The reduction of the wall thickness will also create new opportunities for cost reduction, since the reduced wall thickness facilitates the use of mass production manufacturing technologies, such as deep drawing and stamping. The reduced tipping torque allows the pumps and motors to be operated at higher rotational speeds. This is important for many motor applications, but it also allows the application of high speed electric motors in electro-hydraulic actuators.

5 Test of the new cups and pistons

The original thick-walled cups and pistons have been replaced by the new cups and pistons having a smaller wall thickness. As before, the pump has been tested at minimum pump load in a speed range up till the point where the pump operation is no longer stable, or the maximum speed of the test bench has been reached. Unlike with the original cups, the pump operation remained stable. Due to the electric motor of the test bench, the pump could not be operated at higher rotational speeds than 5000 rpm. It is therefore not possible to verify whether, with the new cups and pistons, the pump can be operated up to the theoretical limit of 7600 rpm.

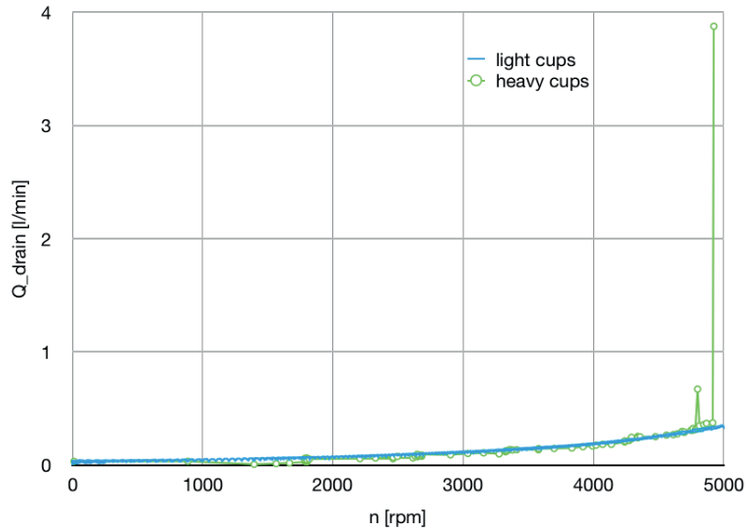


Fig. 12: Measured drain flow at minimum pump pressure

6 Conclusions and further outlook

This study investigates a subtle, but nevertheless important design change of the floating cup pumps and motors: the wall thickness of the cups has been reduced by about 50%, resulting in a weight reduction of 61%. Simultaneously, the wall thickness of the piston crown has been reduced as well. This was needed in order to maintain a tight sealing between the piston crown and the cup when being pressurized. The new cups and pistons have been successfully implemented in a 24 cc prototype. With the new cups and pistons, pump operation has been stable across the entire speed range up till 5000 rpm.

Aside from the improved high-speed stability, the new design offers a number of additional advantages:

- The new cup design has a more constant radial expansion, allowing a better match between the expansion of the piston crown and the expansion of the cup, even when getting close to the TDC;
- The new cup design reduces the outer diameter of the cups, thereby allowing a smaller pitch circle of the pistons i.e. a smaller design of the pump or motor;
- The reduced mass of the cups reduces the centrifugal tipping torque, thus allowing a higher rotational speed of the pump or motor;
- The new design allows a reduction of the wall thickness of the cup base, thereby reducing the length of the cup and thus the length of the entire machine;
- The reduced wall thickness reduces the width of the sealing land of the cup base, thereby allowing a larger diameter of the bore in the base of the cup, and thus a reduction of the flow losses;
- The reduced cup mass reduces the lateral centrifugal load of the cups. This reduces the friction between the cups and the pistons.

The reduced wall thickness also paves the way for further improvements of the cup and piston design. The aim is to produce these components by means of deep drawing, stamping and other low-cost, large series production and manufacturing technologies.

Nomenclature

Variable	*Description*	*Unit*
β	Swash angle	[°]
b	Wall thickness	[mm]
F_{centr}	Centrifugal force	[N]
F_{cont}	Contact force between cup and piston	[N]
$F_{fr,1}$	Friction force between cup and piston	[N]
$F_{fr,2}$	Friction force between cup and barrel plate	[N]
$F_{r,1}$	Reaction force between cup and barrel due to the hydrostatic balance	[N]
$F_{r,2}$	Reaction force between cup and barrel due to the cup tipping	[N]
F_{sp}	Force of the barrel spring	[N]
m_{cup}	Mass of the cup	[N]
n	Rotational speed	[1/minute]
n_{cr}	Critical rotational tipping speed	[1/minute]
p	Pressure	[bar]
T_{cr}	Critical rotational tipping torque	[Nm]

References

1. Manring, N.D., *Tipping the Cylinder Block of an axial-piston swash-plate type hydrostatic machine.* Transactions of the ASME, 2000. **122**: p. 216-221.
2. Manring, N.D., et al., *Scaling the Speed Limitations for Axial-Piston Swash-Plate Type Hydrostatic Machines.* Journal of Dynamic Systems, Measurement, and Control, 2014. **136**(3): p. 031004.
3. Achten, P. and S. Eggenkamp, *Barrel tipping in axial piston pumps and motors.* Proc. 15th Scandinavion International Conference on Fluid Power SICFP17, June 7-9, 2017, 2017.
4. Achten, P.A.J., *Power density of the floating cup axial piston principle.* Proc, of IMECE2004, November 13-19, 2004, Anaheim, California, USA, IMECE2004-59006, 2004.

Noise and vibration reduction for an aerospace secondary controlled hydraulic motor

Emmanuel Viennet*, Anton Gaile**, Tobias Röben**

University of Applied Sciences, Department of Mechanical Engineering, 1700 Fribourg, Switzerland*
Liebherr-Aerospace Lindenberg GmbH, Flight Controls and Actuation Systems,
Pfänderstraße 50-52, Germany**
E-Mail: anton.gaile@liebherr.com

During flight, passenger comfort is affected by noise emissions from various aircraft systems. Apart from jet engines one of the main sources of noise within the fuselage is the power control unit (PCU) for high-lift actuation. In preparation for take-off and landing this hydraulic motor is responsible for the extension and retraction of the slats and flaps. Along with the increase in operating pressure from 206bar (3,000psi) to 345bar (5,000psi) noise and vibration induced by fluid power systems became more striking. Consequently the aim of the BMWI founded research project “Move On” was to reduce the emissions of Liebherr’s power control unit. The results of these research activities are presented within this paper. It is shown how the noise emissions could be reduced in a secondary controlled hydraulic motor by means of a valve-plate and structure optimization. In addition the results of a noise measurement campaign, conducted by Airbus on an A350, are presented.

Keywords: Noise, vibration, hydraulic motor, fluid power systems, axial piston motor, valve-plate optimization
Target audience: Aerospace application, commercial aircraft, pumps & motors

1 Introduction

Fluid power systems are used on Aircraft (AC) since many decades. They drive actuation systems, such as primary flight controls, secondary flight controls, landing gear and utility actuation, e.g. door actuation. Fluid power systems on AC are well proven for excellent reliability, low weight and reasonable cost.

In order to further benefit from its high power density, the working pressure of fluid power systems within some commercial AC was recently raised form 206bar (3,000psi) to 345bar (5,000psi). This shift has made two of the main drawbacks of fluid power systems, namely noise and vibration, even more noticeable. At the same time the noise requirements have become more restrictive. Therefore jet engines as the main source of noise on AC have made advancements in noise reduction. As a consequence, the noise emitted by the fluid power system has become more relevant as regards passenger comfort. One of the components responsible for cabin noise is the hydraulic motor driving the high-lift system. Slats extension and retraction are driven with Slat Power Control Unit (SPCU). The investigated SPCU is a hybrid design and comprises an electric and a hydraulic motor.

Within the BMWI founded research project “Move On” Liebherr-Aerospace Lindenberg GmbH and Liebherr Machines Bulle SA together with Airbus Deutschland GmbH have developed a noise reduced variable displacement hydraulic motor. As a boundary condition for this project the weight of the hydraulic motor should not increase, the envelope should not be affected and the performance characteristics should be equal or better compared to the reference motor.

Accordingly in section 2 the considered type of hydraulic motor and possible means for noise reduction are described in detail.

In a next step several concepts for noise reduction have been analysed with the aid of a simulation models. Results of the simulative analysis are given in section 3.

Subsequently the most promising concepts have been realized within a prototype PCU /2/. This prototype was then tested in a laboratory environment at Liebherr-Aerospace, Lindenberg GmbH in comparison with a reference PCU. Test data is provided in section 4.

Finally a noise and vibration test was conducted inside an AC cabin, which exemplifies the improvements within a real AC environment. Airbus performed these vibro-acoustic measurements on an A350 test AC in July 2015. Respective results are depicted in section 5.

2 Means for noise reduction

In axial piston pumps and motors the timing and the geometry of the swash plate are crucial for noise generation. A careful design of the swash plate is therefore one of the most important ways of reducing noise /1/. However, the performance that can be achieved by only optimizing the swash plate is highly sensitive to any variation in operational conditions. One way to mitigate this sensitivity is to use a design with a cross-angle. Johanson et al. /2/ describe the cross-angle as “a fixed small (~1-4°) displacement angle of the swash plate in the direction perpendicular to the traditional displacement [implying] that the piston top and bottom dead-centres […] vary as functions of the displacement angle, which gives varying cylinder pre-compression and decompression”. While cross-angle designs have been mainly used in pumps, it is also mentioned in the literature as a mean to reduce noise of hydraulic motors /3/.

The swash plate axial piston motor developed by Liebherr takes advantage of both a cross-angle and an optimized valve plate geometry to achieve significant noise reduction. It features a maximum displacement of 16cc/rev that can be adjusted in both positive and negative directions.



Figure 1a : picture of the 16cc/rev Liebherr aerospace hydraulic motor

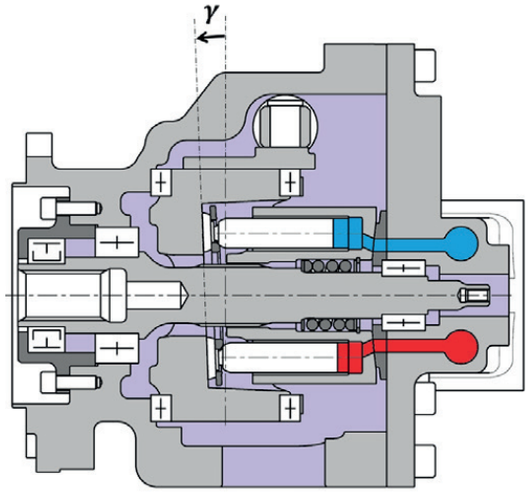


Figure 1b : cross-angle γ machined in the bearing supported swash plate

As shown in Figure 1b, the cross-angle is machined directly in the swash plate of the Liebherr motor. The cross-angle is compatible with both pumping and motoring modes, this as long as the high- and low-pressure ports remain fixed. Actually, if the high and low pressure ports were reversed, the cross-angle direction would have to be reversed as well. The Liebherr motor is therefore particularly well suited for secondary control with one port being supplied by a constant pressure network.

3 Simulation of motor-induced excitations

3.1 Simulation model

The goal of the simulation is to model motor-induced excitations that may lead to noise emissions in order to minimize them. Due to fluid compressibility and dynamic effects taking place in the piston chambers, the pressure profiles are not trivial to describe analytically, therefore a simulation model is used, based on a control volume approach that is common in literature; see for instance /4/ and /5/. The simulation model has been developed with the commercial simulation package Amesim /6/.

From the kinematics of the hydraulic motor, the model first computes the piston stroke y_i and the fluid volume V_i of the ith piston chamber as a function of angular position ϕ_i.

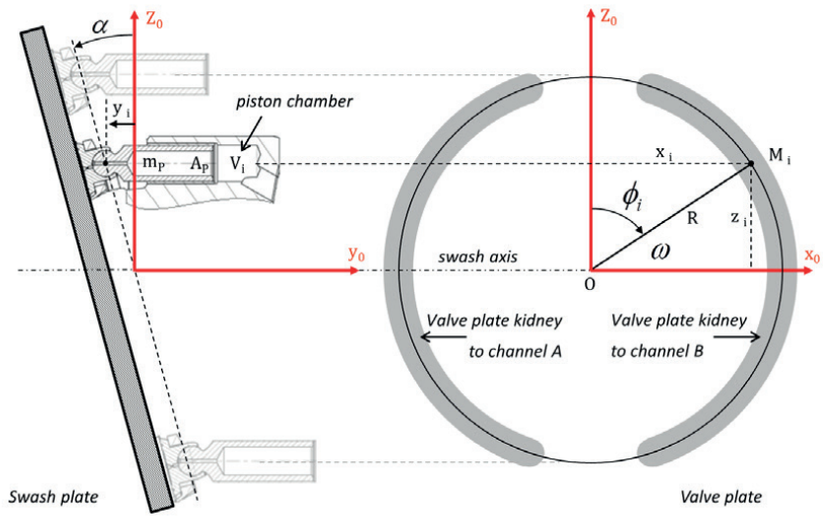


Figure 2: Sketch of motor kinematics (cross-angle not represented)

The displacement angle is referred to as the angle α around the x_0 axis. This first rotation transforms (x_0, y_0, z_0) into an intermediate coordinate system (x_1, y_1, z_1). Then the cross-angle is referred to as the angle γ around the axis z_1 and transforms (x_1, y_1, z_1) into (x_2, y_2, z_2).

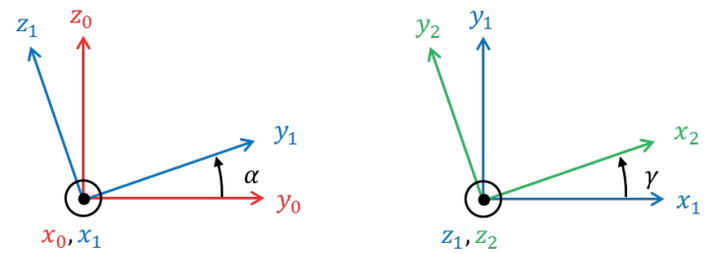


Figure 3: displacement angle (left) and cross-angle (right)

The piston stroke, i.e. the displacement of the piston along the y_0 axis, follows as:

$$y_i = R \cdot \frac{tan\gamma}{cos\alpha} \cdot sin\phi_i - R \cdot tan\alpha \cdot cos\phi_i \tag{1}$$

Then the model computes the pressure-rise rate in the piston chamber as:

$$\frac{dP_i(\phi_i)}{dt} = \beta \cdot \frac{Q_{iA} + Q_{iB} + Q_{iKIN}}{V_i(\phi_i)} \tag{2}$$

This quantity is integrated to get the pressure profile for each piston at each simulation time step. It is then possible to compute Q_{iA} and Q_{iB}, the flow rates exchanged between the control volume of the ith piston and the channels A and B respectively. It is assumed that these flow rates occur in turbulent regime and can be computed as:

$$Q_{iA} = sign\,(P_A - P_i) \cdot C_q\, A_{iA} \sqrt{\frac{2\,|P_A - P_i|}{\rho}} \;\; and \;\; Q_{iB} = sign\,(P_B - P_i) \cdot C_q\, A_{iB} \sqrt{\frac{2\,|P_B - P_i|}{\rho}} \tag{3}$$

Q_{iKIN} is the piston motion-induced flow rate that relates to the piston axial velocity $\dot{y}_i$ according to

$$Q_{iKIN} = A_p\, \dot{y}_i \tag{4}$$

In Equations (1) to (4):

P_A and P_B are the pressures in the channels A and B respectively.

β and ρ are the bulk modulus and the density of the hydraulic fluid respectively.

C_q is the flow coefficient of the considered flow rate.

A_{iA} and A_{iB} are the flow areas between piston chamber and channels A and B.

3.2 Optimization objectives

We are primarily concerned about the audible noise in the cabin of the aircraft. However this sound can be generated through two main paths:

- Through pressure pulsations generated by the hydraulic motor and transferred to the hydraulic circuit, also known as “fluid borne noise”
- Through the vibrations of the motor structure, transferred to the rest of the aircraft structure, also known as “structure borne noise”

Since the noise transfer path is typically difficult to identify in an aircraft and because the developed hydraulic motor should not be aircraft-specific, both pressure pulsation and vibrations have to be optimized at the same time.

Unfortunately, both pressure pulsation and vibrations are system dependent. Exactly like positive displacement pumps, positive displacement motors generate a flow rate pulsation, the pressure pulsation being only the consequence of the flow pulsation for one given hydraulic circuit. Similarly, the motor generates forces and moments pulsation. The vibration of the motor itself is depending on its own structure but also on the impedance of the structure it is mounted on.

Therefore the value to be monitored for assessing the general tendency of a hydraulic motor to generate pressure pulsation is the flow pulsation at its inlet port (high pressure port). Assessing its tendency to generate vibration is slightly more complicated because forces and moments in all three spatial directions are involved. Nevertheless Skaistis has shown that the swash plate moment M_{X_0} typically shows the greatest potential as a noise source /1/ and to the best of our knowledge, this proved to be true for many practical cases.

Choosing which quantity to monitor is still not enough and precise optimization objectives should be determined both for flow pulsation and swash plate moment pulsation. Again, since the quietness of the motor should not depend on the system it is used in, it is not possible to target amplitude reductions at specific frequencies and we chose two equally weighted optimization objectives consisting of the normalized peak-to-peak amplitude of time signals simulated for the consumed flow-rate Q_A and the swash plate torque M_{X_0}.

$$objective = \frac{\left(\max\left(Q_A(t)\right) - \min\left(Q_A(t)\right)\right)}{mean\left(Q_A(t)\right)} + \frac{\left(\max\left(M_{X_0}(t)\right) - \min\left(M_{X_0}(t)\right)\right)}{mean\left(M_{X_0}(t)\right)} \quad (5)$$

Following constraints have been added to the optimization objectives to avoid cavitation resp. low efficiency:

- Minimum acceptable pressure in the piston chamber
- Maximum acceptable internal leakage due to valve plate underlap

3.3 Simulation results

A set of optimal parameters for both the cross-angle value and the valve plate geometry has been obtained by running the optimization on the simulation model described earlier.

In the figures below, simulation results show the comparison between the reference motor initially used for the high lift actuation and the Liebherr motor presented in this document in terms of flow rate and swash plate moment pulsations.

Figures 4a and 4b show that the choice of the flow rate peak-to-peak amplitude as an optimization function has given very good results in the time domain with a reduction of a factor 2.0 of the peak-to-peak amplitude compared to the reference. In frequency domain, it is interesting to see that it has led to significant improvements at harmonic frequencies but not necessarily at the fundamental frequency.

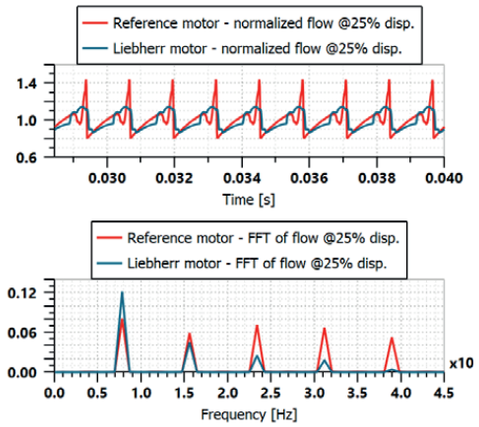


Figure 4a: Normalized flow rate generated by motors at inlet port in time and frequency domain for 25% of max. displacement

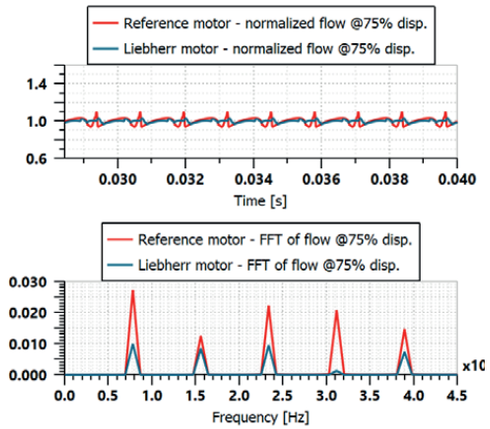


Figure 4b: Normalized flow rate generated by motors at inlet port in time and frequency domain for 75% of max. displacement

The figures 5a and 5b show a massive improvement for the peak-to-peak amplitude of the swash plate moment with a reduction of the peak-to-peak amplitude by a factor 4.0 to 7.0. It indicates that the swash plate moment was most probably not considered when the reference motor was designed, thus probably leading to important vibration of the surrounding structure and consequent audible noise emission.

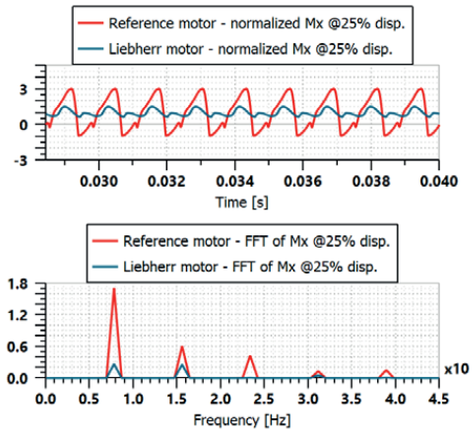


Figure 5a: Normalized swash plate moment generated by motors in time and frequency domain for 25% of max. displacement

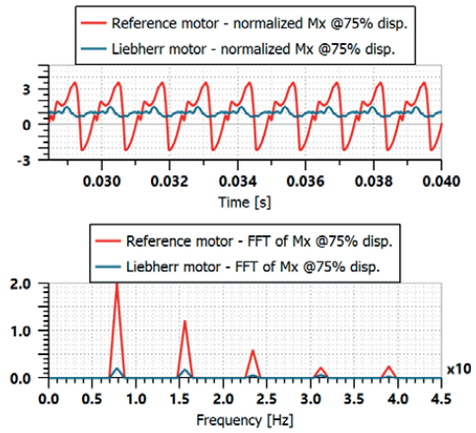


Figure 5b: Normalized swash plate moment generated by motors in time and frequency domain for 75% of max. displacement

4 Noise and Vibration Reduction in Laboratory Environment

In the following test data is presented which demonstrates the achieved reduction regarding noise and vibration. In a laboratory environment the noise emission of the PCU is compared to the reference device /7/. It is further clarified to what extend the improvements affect passenger comfort.

4.1 Structure borne noise

In order to measure the structure born noise emitted during operation, both PCU have been equipped with six tri-axial acceleration sensors. In figure 6 the positioning of these sensors is illustrated. The spectrum of vibration was then measured in various load conditions /8/.

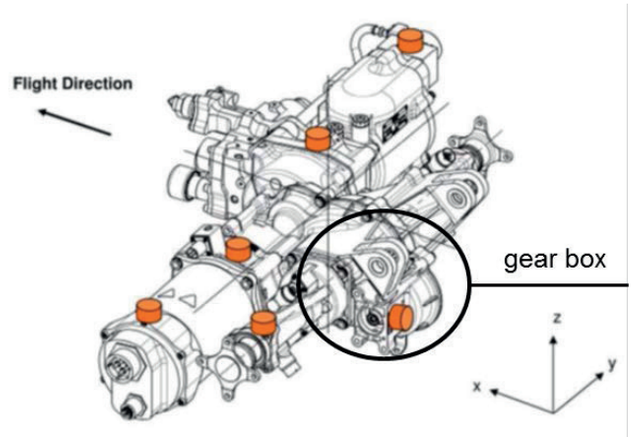


Figure 6: Positioning of acceleration sensors.

Basically all sensors indicated similar characteristics regardless of the sensor position and axis of motion. Therefore the results shall be discussed using the example of the y-axis of the sensor located on the gearbox (refer to figure 6).

The frequency spectrum that occurs during operation of both PCU is depicted in figure 7. While the characteristic frequencies of both units are similar, the vibration amplitude of the Reference PCU (red) exceeds the Liebherr PCU (blue). Both devices are characterized by a fundamental frequency of 790Hz and a first harmonic at 1590Hz. In general the Liebherr hydraulic motor has significantly decreased the structure borne noise for the fundamental and the following harmonics.

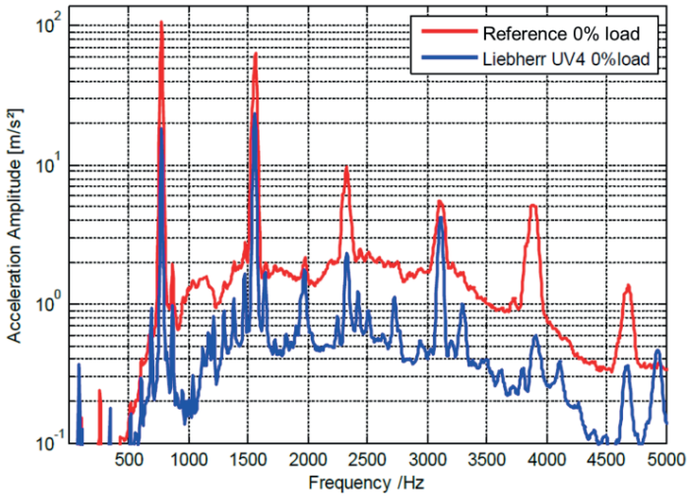


Figure 7: Acceleration amplitude over frequency range of 10Hz-5kHz for varying load conditions.

4.2 Air borne noise

In addition to the structural vibration the sound pressure amplitude spectrum emitted by the PCU was recorded. Microphones were installed at a distance of 1m from the unit. The results are illustrated in figure 8. Thereby the sound pressure was A-weighted according to the international standard IEC 61672:2003, in order to account for the relative loudness perceived by the human ear, which is indicated by the unit dB(A).

Similar to the vibration data a fundamental frequency of 779Hz and a first harmonic at 1558Hz are apparent. Again there is a reduction in the signal amplitude of the Liebherr PCU in comparison to the reference unit.

It is further noted that a sound pressure amplitude increase of 10dB is equivalent to a doubling of the subjective sound level. Therefore according to figure 3 the fundamental frequency with 103dB(A) and its first harmonic with 90dB(A) will have the most disturbing impact to the human ear. The sound pressure of the subsequent harmonics does not increase past 75dB(A). Hence the subjective sound level will be less than half compared to the first harmonic frequency.

Consequently in figure 9 the focus is on the fundamental frequency and its first harmonic. Here the A-weighted sound pressure level of both PCU is depicted in dependence on the load condition. Apparently the Liebherr hydraulic motor has significantly decreased the air borne sound pressure for both the fundamental and the first harmonic frequency. Corresponding to the difference of more than 10dB(A) a subsequent reduction of the sound level in AC environment is expected.

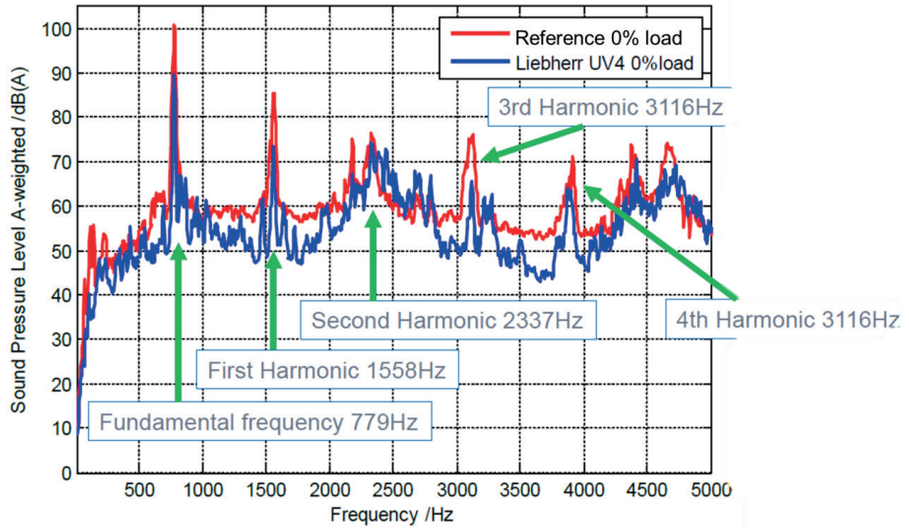


Figure 8: Sound pressure level (A-weighted) over a frequency range of 10Hz-5kHz for varying load conditions.

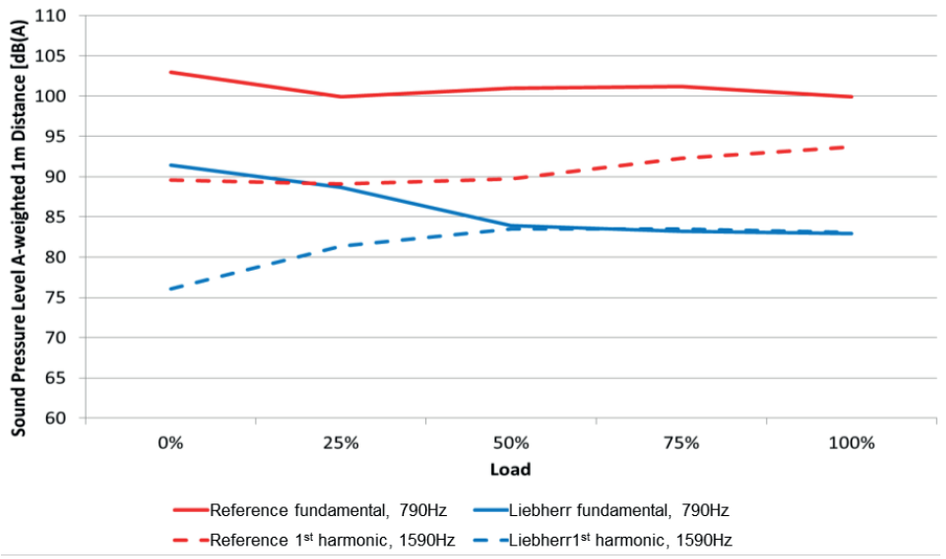


Figure 9: Comparison of sound pressure levels (A-weighted) for different load conditions.

5 Noise and Vibration Reduction in Aircraft Environment

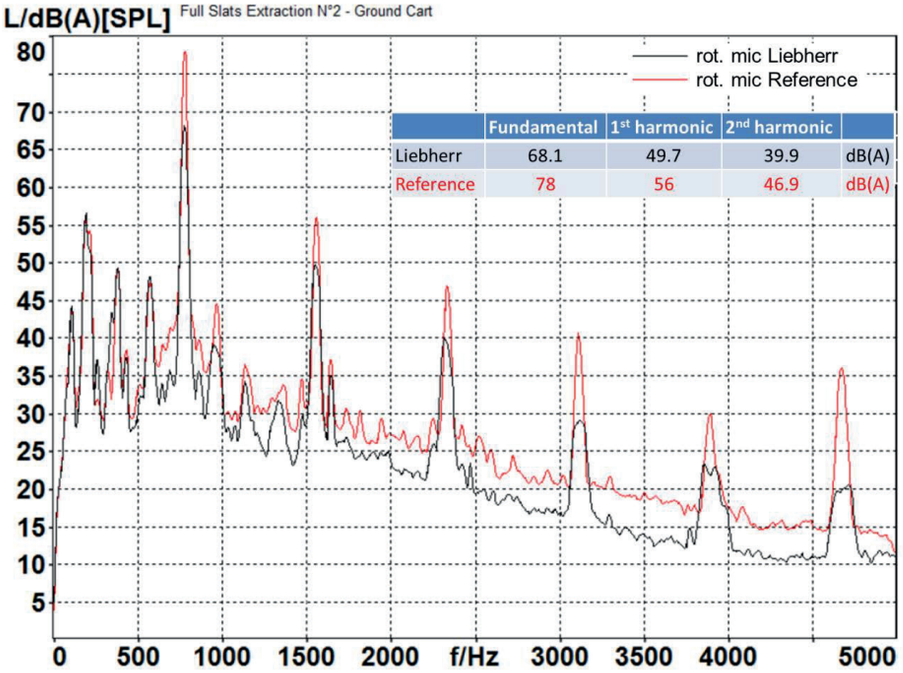
Based on the results in laboratory environment in July 2015 Airbus performed vibro-acoustic tests on an A350 test AC comparing the Liebherr hydraulic motor with the reference unit /9/. Therefore nine microphones have been installed in the cabin for this test campaign (refer to figure 10). Additionally one rotating boom microphone is positioned in the aisle between row 10 and 11.



Figure 10: Microphone test setup for sound pressure level measurement within an A350.

Afterwards several configurations have been tested featuring slat extension and retraction in both a stepwise and complete progression /9/. Thereby the PCU has been powered alternatively by the ground cart and an electromotor pump (EMP). In the following test data with ground cart is presented.

In figure 11 the A-weighted frequency spectrum of the cabin sound pressure level recorded with the rotational boom microphone is illustrated for full slat extension. Again the fundamental frequency in the region of 800Hz and a first harmonic in the region of 1600Hz are apparent. Beyond 500Hz there is a difference in sound pressure level of about 5dB(A) between the Liebherr PCU and the reference unit. This visualizes the subjective perception of noise within the cabin, which is lower when the Liebherr PCU is used.



	Fundamental	1st harmonic	2nd harmonic	
Liebherr	68.1	49.7	39.9	dB(A)
Reference	78	56	46.9	dB(A)

Figure 11: Static sound pressure level (A-weighted) for the rotating boom microphone during slat extension.

Furthermore compared to the laboratory measurements, which have been recorded at a distance of 1m from the source, the sound pressure in the cabin is reduced. Especially higher frequencies are naturally damped, while low frequencies are better transmitted though the fuselage. As mentioned above the subjective perception of sound level is logarithmic to the sound pressure level. Hence again the sound pressure at the fundamental frequency was considered for a detailed comparison between the Liebherr PCU and the reference. The resulting difference of 10db(A) correspond to a subjective sound level reduction by a factor of two.

In figure 12 a surface map illustrates the noise reduction in the A350 cabin and the specific seats. The sound pressure recorded by the rotating boom microphone is indicated by the circle in the aisle between row 10 and 11. The colour scheme represents a pressure between 55dB(A) and 80dB(A) by colours of blue to red. Except for seats 10A and 11D a significant reduction of noise of 5-10dB(A) is apparent. The numeric difference in sound pressure is given in table 1.

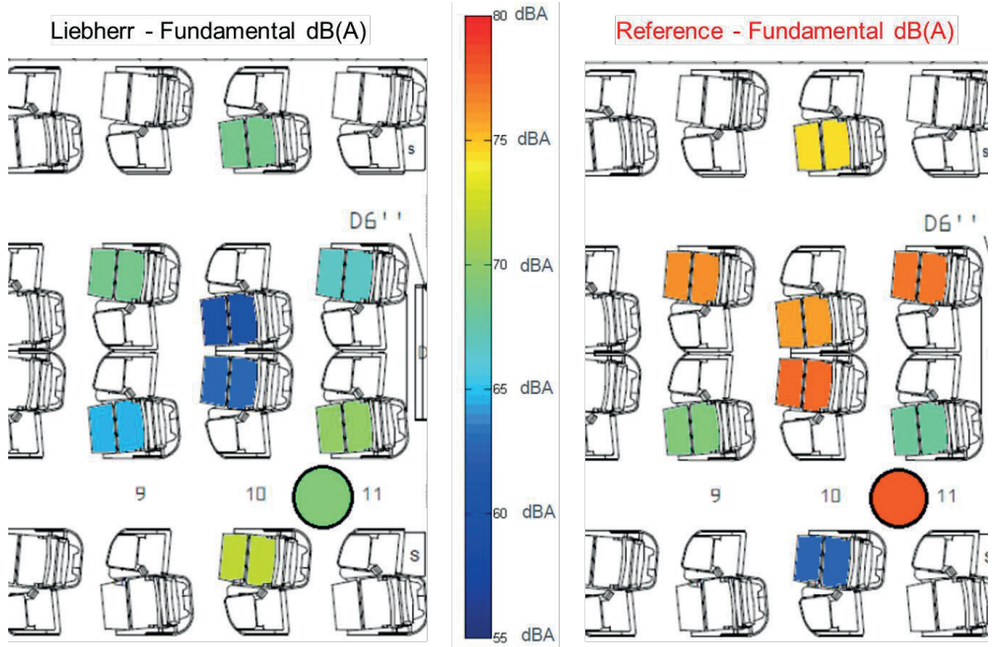


Figure 12: Surface map: Comparison of cabin sound pressure level (fundamental, A-weighted, slat extension).

Microphone	Difference - dB(A)
Seat 11D	0.4
Seat 10A	8.6
Seat 11H	-10.5
Seat 10G	-15.5
Seat 10E	-14.9
Seat 10L	-6.4
Seat 9D	-5.0
Seat 9H	-8.4
Rot. boom mic	-9.9

Table 1: Difference in cabin sound pressure (fundamental, A-weighted, slat extension).

6 Conclusion

It has been demonstrated that effective noise reduction of a hydraulic motor is possible without affecting weight, cost or performance. As the vibration level of the motor was also reduced together with the reduction of the noise emission, the reliability of the unit was improved.

This improvement was not achieved by the typical secondary means, for instance rubber isolation or thicker or more noise absorbing housings; it was achieved by reduction of hydraulic pressure variation between the primary parts of the motor, which are cylinder-block, swash plate and pistons. Thereby the optimized motor produces less noise and vibrations compared to the reference motor. Since no additional parts are necessary, this is the favoured method of noise reduction.

Such an improvement is only possible if the physics inside the motor is properly understood and a verified simulation model is available to support the development activities. Therefore appropriate simulation models are the key for the next generation of low noise, high efficiency hydraulic pumps and motors.

7 Acknowledgements

The noise reduced variable displacement hydraulic motor, whose test data is presented within this paper has been developed within the BMWI founded research project “Move On”. The project was realised in cooperation with Liebherr-Aerospace Lindenberg GmbH and Liebherr Machines Bulle SA together with Airbus Deutschland GmbH. Airbus was mainly responsible for the test campaign within the A350.

Nomenclature

Variable	*Description*	*Unit*
γ	Cross-angle	[rad]
α	Displacement angle	[rad]
x_i	Displacement of the ith piston on x axis	[m]
y_i	Displacement of the ith piston on y axis	[m]
z_i	Displacement of the ith piston on z axis	[m]
V_i	Fluid volume of the ith piston chamber	[m^3]
ϕ_i	Angular position of the ith piston	[rad]
m_P	Mass of piston	[kg]
A_P	Area of piston	[m^2]
R	Cylinder-block pitch radius	[m]
P_i	Pressure in ith piston chamber	[bar]
Q_{iA}	Flow rate between piston chamber and port A of motor	[m^3/s]
Q_{iB}	Flow rate between piston chamber and port B of motor	[m^3/s]
P_A	Pressure in port A	[bar]
P_B	Pressure in port B	[bar]
β	Bulk modulus of fluid	[bar]
ρ	Density of fluid	[kg/m^3]
C_q	Discharge coefficient of valve plate opening	[-]
A_{iA}	Valve plate opening area between piston chamber and port A of motor	[m^2]
A_{iB}	Valve plate opening area between piston chamber and port B of motor	[m^2]
M_{X0}	Swash plate moment around the X_0 axis	[N.m]

References

/1/ Skaistis, S., *Noise Control of Hydraulic Machinery*, Marcel Dekker Inc., New York, 1988.

/2/ Johansson, A., Övander, J., Palmberg J-O., *Experimental verification of cross-angle for noise reduction in hydraulic piston pumps*, in Proc. of the Inst. of Mech. Eng., Part I: Journal of Systems and Control Engineering, Vol 221, Issue 3, pp. 321 – 330, 2007.

/3/ Ericson L., Ölvander J., and Palmberg J-O., *Flow Pulsation Reduction for Variable Displacement Motors Using Cross-angle*, in Proc. of Power Transmission and Motion Control (PTMC 2007), pp. 103-116, Bath, UK, 2007.

/4/ Manring, N.D., *Hydraulic Control Systems*, John Wiley & Sons, New York, 2005.

/5/ Ivantysyn, J. and Ivantysynova, M., *Hydrostatic Pumps and Motors: Principles, Design, Performance, Modelling, Analysis, Control and Testing*, Tech. Books International, New Delhi, India, 2001.

/6/ LMS Imagine.Lab AMESim, User Manual rev 14

/7/ Sinz, G., *VD PCU Noise Reduction - Concepts to Reduce PCU Noise*, internal document, Liebherr-Aerospace, Lindenberg , Germany 2013.

/8/ Ayme, F., Parisot-Dupuis, H., Villard, M., *A350 MSN5 – Vibro-acoustic ground test on FPCU* , technical report, Airbus, France, 2015.

/9/ Heise, U., *Move.On - Comparision of hydraulic motors regarding fluid borne, structure borne & air borne noise*, technical report, Airbus, Germany 2015.

myCro

Downsizing of hydraulic power units by revolutionizing the design

Dr.-Ing. Bastian Beckmann, Dipl.-Ing. Martin Laube
Bosch Rexroth AG, Zum Eisengießer 1, 97816 Lohr am Main
Email: Bastian.Beckmann@boschrexroth.de

Industrial technology is confronted with the constant demands for a reduction in investment and operating costs. Especially hydraulic power units as a core element for supply of flow and pressure for hydraulic actuation systems have a big influence by minimization of the required oil quantity used as well as by optimizing the targeted fluid condition. In addition to the reduction in the required size and weight, the cost of steel fabrications can also be significantly reduced by a smaller tank and the oil quantity during initial filling and maintenance can be reduced. With the innovative engineering-package "**myCro**" presented here, these advantages can be exploited by the customer.

Keywords: Downsizing, Hydraulic power unit, Degassing, Oil conditioning
Target audience: Design, engineering and usage of hydraulic power units

1 Introduction

Hydraulic power units (HPU´s) represent as capital goods the energy or power supply of hydraulic drive technology where low initial and operating costs are an important main focus. The initial costs of an HPU are, in addition to the attached and built-up components, largely influenced by the hydraulic oil tank and the amount of oil stored there, while the maintenance and repair costs make up a large part of the operating costs. In both cases, the percentage of initial or operating costs varies depending on the requirements of an HPU and can therefore not be generalized.

HPU´s are generally characterized by a large variety of sizes and shapes that arise from the requirements they need to meet such as the available footprint or space, the hydraulic power to be provided, the pendulum volume or attached peripherals. In the following picture, three different HPU´s are shown in order to make the broad variance clear.



Figure 1: Variance of HPU´s in terms of size and shape

In order to use hydraulic units in confined spaces in manufacturing plants or to apply them in narrow installation spaces of higher-level machines, the demand for a further increase in the power density of HPU´s (downsizing) is made more frequent.

2 State of the art in the consideration of the oil conditioning by the design of HPUs

Since the size and shape of HPU´s – and therefore also costs - are very much influenced by the tank, it is advantageous to size this as small as possible. In addition to the reduced initial costs due to the smaller tank, there are also lower costs for the initial oil filling. The quantity of hydraulic oil to be used also has a recurring aspect, since it occurs during the initial filling and at the change intervals.

For the regeneration of the fluid (e.g. degassing), a necessary resting time in the tank is usually defined in order to allow the air bubbles in the oil to rise from out of the fluid and to outgas. This process can be relatively slow depending on the size of the air bubbles as well on physical and chemical properties of the fluid. The necessary tank size is thus derived from approximately 3-5 times the circulated oil volume flow /1/. For example, in the current state of the art in the engineering of HPU´s, this would result in a minimum size of the oil tank of 600-1000 l in an HPU capable of permanently delivering a maximum flow rate of 200 l / min.

If the relationship between the circulated oil volume flow and the size of the tank and a corresponding oil conditioning are not taken into account, damage - and thus increased maintenance and repair costs – will result. In addition to contamination of the oil with solid particles, the contamination with air and water must be considered.

Air that is in dissolved form in the hydraulic oil is bound in the molecular structure which is initially unproblematic. The proportion of air dissolved in oil is largely dependent on pressure, less on temperature and viscosity, and not on base oil, refining or additives /2/. Major problems are caused by undissolved air that forms - depending on the type and viscosity of the oil - in a proportion of about 10% in the form of bubbles. For example, it leads to foaming at a proportion of about 30% /2/, which among other things adversely affects the dissipation of heat from the oil and worsens the lubrication of friction surfaces. Other negative characteristics due to undissolved air are accelerated oil aging due to the diesel effect or cavitation phenomena in hydraulic components. The same applies to water in hydraulic oil, which can also occur in dissolved form - bound in the molecular structure of the oil - or undissolved in the form of water droplets. The negative effects of water in hydraulic oil are corresponding to the problem with air.

3 New approach for the efficient design of HPU´s

However, the reduction of the required amount of oil represents an extraordinary challenge, since the hydraulic oil is a decisive factor for meeting demanding tasks in addition to power transmission, such as lubrication and corrosion protection of moving parts. Water and air deteriorate the required properties of the fluid by phenomena such as e.g. oxidation, corrosion, and diesel effect which reduces the life of oil and components and leads to undesired effects such as noise, erosion damage and a lack of system stiffness during operation.

From this it can be concluded that HPU´s can be dimensioned much smaller in principle if the above described phenomena can be treated by suitable fluid conditioning. This can be achieved by controlling the air and water content, the cooling and filtration or by a targeted management of the oil flow or tank design. Since these measures can vary greatly depending on the area of application and the application of the unit, Bosch Rexroth has developed the complete engineering package **myCro** - consisting of active and passive measures - to counteract the complex and multi-layered problems and reliably ensure appropriate oil conditioning. The following table shows the definition of **myCro**.

my	individual
Customized	Customer specific engineered
reduction	to build small and cost-efficient power units
option	Via optional add-on equipment

*Table 1: Definition of **myCro***

As shown in the following illustration, the modular engineering package **myCro** essentially consists of 4 different approach categories, which must be used according to the individual application.

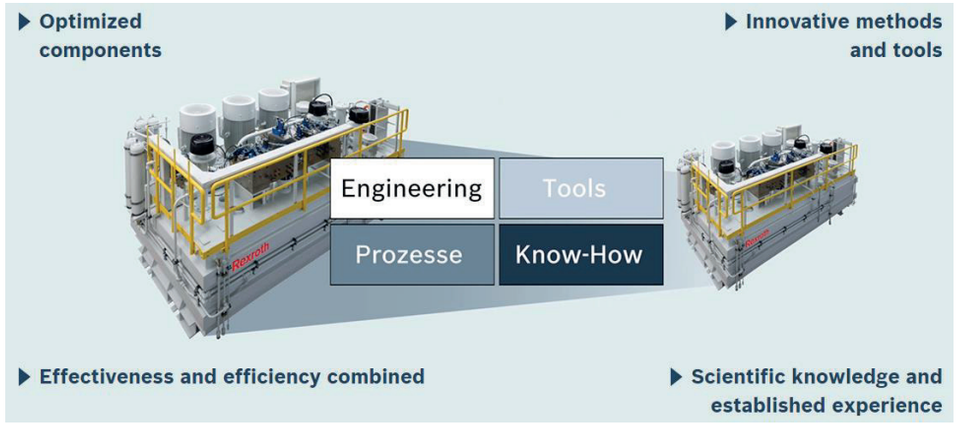


*Figure 2: **myCro** enhanced intelligent fluid management and downsizing of HPU´s*

In principle, **myCro** can be divided into measures for active oil conditioning and measures for passive oil conditioning. For a suitable oil conditioning by means of active measures, the desired parameter to be conditioned in the oil must be measured / interpreted and then possibly improved.

Here systems are available with **myCro** which operate a controlled degassing and dewatering of the hydraulic oil by means of suitable sensors. The systems work independently of the pendulum volume and have a scalable degassing and dewatering rate which makes a wide range of applications possible. In the same way, the filtration can be solved as usual via the secondary circuit. As an example, the degassing of an oil volume can be seen in the following picture.

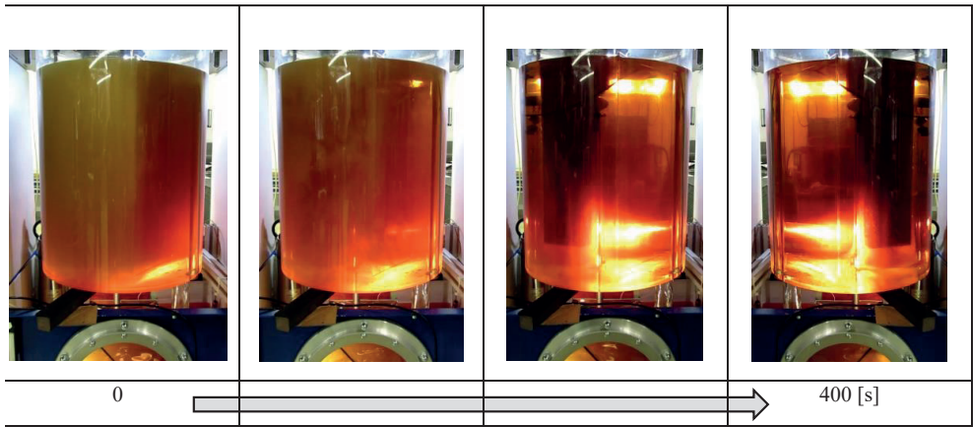


*Figure 3: Exemplary degassing of an oil volume as an active **myCro** measure*

In passive measures, the HPU is designed in such a way that by means of a targeted flow characterization or guidance an enrichment of the hydraulic oil with air or water is prevented or at least slowed down. For an optimized flow and the resulting tank design, modern simulation methods such as 3D CFD simulation are available.

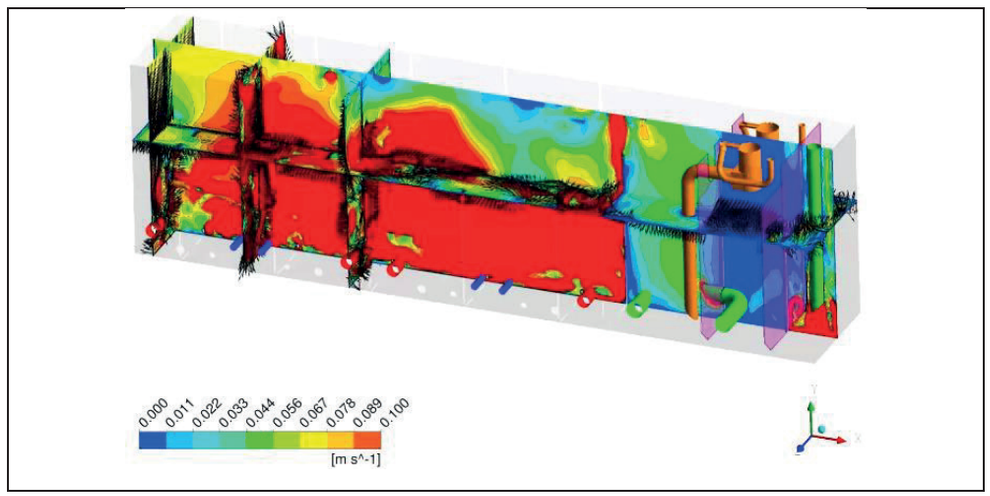


*Figure 4: Exemplary 3D-CFD-Simulation of tank interiror as an passive **myCro** measure*

The effort for the additional hardware or the intelligent tank design is often not justified, why trained and experienced sales staff carry out a corresponding initial evaluation and plausibility check. Thus, in the beginning technical discussions with the customer decisions in favor of smaller and cheaper HPU´s can be made.

Since all elements in **myCro** are modular and flexible (e.g. tank design using 3D CFD simulation, degassing module, etc.) they can be used optionally as needed, depending on the requirements of the HPU and the customer. Although the usage of further elements increases the effort - and thus the production costs - it opens up further potentials for miniaturization of the unit - and therefore a reduction of the production costs. Thus, the technical / economic optimum for each design case of the HPU can be determined individually with the customer and allows the optimal design of the hydraulic unit to the application with significantly less restriction from the above relationship between tank size and the desired oil condition. In the following the main focus areas of the defined **myCro** levels are described.

Optimized components • Standalone controlled degassing module • Sensors • Water separation module • Hydraulic components suitable for vacuum pressures	**Innovative methods and tools** • 3D-CFD Simulation • Initial assessment by **myCro**-Tools and experienced sales engineers
Effectiveness and efficiency combined By combining all the components and processes relevant to the degassing process, it is possible to optimize the hydraulic power unit in terms of tank size, oil volume and components in the shortest possible time	**Scientific knowledge and established experience** • Optimized internal tank design • Scientific investigation of air separation • Deriving customer-specific solutions • Simulation and evaluation criteria of tank design

*Table 2: Focus areas of the **myCro** levels*

For better comprehensibility and usability, **myCro** is subdivided into 3 different states of expression in which the possibilities of a reduction of the HPU are correspondingly exhausted by an increasing utilization of the individual elements of the modular engineering package.

The lowest state of expression is the package **myCro**, in which the oil tank is downsized with the least possible effort and only passive measures like described below.

myCro
• Initial evaluation of an application for oil tank downsizing by trained sales staff and supporting tool
• Passive measures (intelligent tank design) improve natural degassing to the desired level

The next or middle stage of expression is the package **myCro**$^{+}$, in which the options for reducing the size of the tank are further exploited with additional active measures like the degassing module.

myCro^{+}
• The degassing module further actively improves the oil conditioning and thereby enables even smaller power unit design
• Regulation and monitoring of the oxygen content in the operating medium

At the highest level of expression through package **myCro**$^{++}$, the additional use of the 3D-CFD-Simulation allows the possibilities of a tank reduction to be completely exhausted.

myCro^{++}
• 3D-CFD-Simulation of tank interior

4 Summary and Conclusion

Considering the technological change in industrial hydraulics towards electrification and electronification Bosch Rexroth offers with the modular engineering package **myCro** option a completely new approach for the efficient design of optimized system solutions using the latest technologies in terms of numerical methods, computational system assessment as well as newly developed fluid technologies and controls. Projects where **myCro** was implemented could achieve a reduction in tank size of up to 70% and the required floor space by up to 50% with an immediate return on investment (ROI), which underlines the efficiency of this approach.

References

/1/ The Hydraulic Trainer Volume 3, Planning and Design of Hydraulic Power Systems, Mannesmann Rexroth AG, 1988

/2/ Findeisen, D. , Ölhydraulik - Handbuch für die hydrostatische Leistungsübertragung in der Fluidtechnik, 5. Auflage, Springer-Verlag, 2006

REVIEWED

Computer-assisted modeling and automatic controller adjustment for hydraulic drives based on an innovative nonparametric identification method

Marcus Helmke *, Simon Ströbel **, Prof. Dr.-Ing. Peter Anders** and Tobias Schulze ***

TRsystems GmbH, Automation, Eglishalde 16, 78647 Trossingen, Germany *
Furtwangen University, Tuttlingen Campus, Faculty of Industrial Engineering, Kronenstraße 16, 78532 Tuttlingen, Germany **
TU Dresden, Institute for Fluid Power, Chair of Fluid-Mechatronic Systems (Fluidtronics), Helmholtzstraße 7a, 01069 Dresden, Germany***
E-mail: marcus.helmke@trsystems.de, simon.stroebel@hs-furtwangen.de, peter.anders@hs-furtwangen.de, tobias.schulze2@tu-dresden.de

Model-based control and regulation concepts will become increasingly important due to their specific advantages, for example in respect of performance, stability, consideration of nonlinearities etc., for hydraulic drives in particular. The fundamental prerequisite for their application is sufficiently precise knowledge of the system's response characteristic. The prerequisite for their acceptance, however, is the availability of computer-supported tools, methods and algorithms, which enable a case-specific identification and controller design. This article presents a concept for achieving these goals on the basis of an innovative nonparametric identification method, which has proved to be extremely efficient in initial applications.

Keywords: hydraulic presses, characteristic diagram, operating point, model based control, self-learning control
Target audience: stationary hydraulics, industrial applications

1 Introduction

1.1 State of the art

Demands in terms of drawing cushion pressure control increasingly require a highly dynamic control behavior, which cannot be satisfactorily achieved using a classic PI controller based on control error (feedback controller) alone. Model-based approaches on the one hand and progress in the field of digital technology on the other have enabled new concepts in the control of hydraulic drives in recent years. Rather than generating the actuating signal exclusively via a feedback controller, the basic idea of these concepts is to additionally generate the signal via a process model calculated in real time in a precontrol circuit (feedforward controller). This is known as a two degrees of freedom control concept (2DOF control concept, see Fig. 1) which was first introduced by Horowitz /1/. Generally speaking: The higher the quality of the basic model, i.e. the better the model represents reality, the better the ultimately achievable control quality. In this concept the feedback controller essentially only has the task of compensating for inaccuracies in the precontrol model, but the main contribution to the overall actuating signal should be generated via the precontrol circuit. There are several approaches to design such a linear or nonlinear feedforward control. In /2/ the feedforward control algorithm for an injection moulding machine was based on the linear transfer function for example. In the field of drawing cushion pressure control, use of the nonlinear stationary drive characteristic diagram in the form of a nonparametric look-up table has proven itself time and again as a precontrol model /3/4/. Nonparametric means that no model equations are present, which must be parameterized through corresponding quantitative system parameters (surface areas, orifice coefficients, overlaps …). Instead, the look-up table only contains numerical values which, although they describe the static response characteristic with sufficient accuracy, no longer have any explicit functional correlation /5/. A purely theoretically derived characteristic diagram (white box characteristic diagram), which are essentially based on the datasheet values for the components used, are generally too inaccurate for the increased demands on control quality, which is why the actually existing drive characteristic diagram must be determined metrologically (black box characteristic diagram). Previous experiences show a connection between the effort involved in creating or identifying the real characteristic diagram and the quality of the feedforward control, i.e. the ultimately achievable control quality. The determination of a sufficiently accurate characteristic diagram is therefore generally associated with considerable measurement and commissioning effort. In particular, the execution of operating points in the limit ranges of drive systems frequently leads to difficulties.

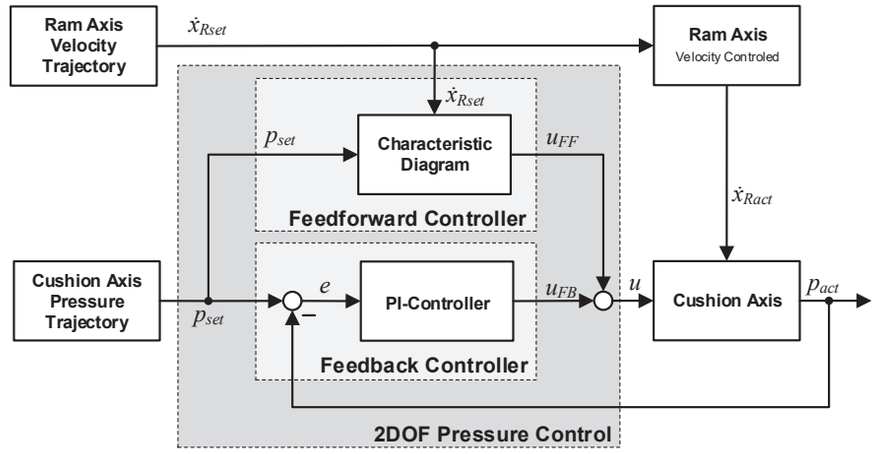


Figure 1: 2DOF structure for pressure control of cushion axis - state of the art

Use of the characteristic diagram-based feedforward control enables the actuating signal component of the PI controller in the sum actuating signal to be reduced to a fraction of 5%-10%, with a measuring scope of around 100 to 150 stationary points to be identified for determination of the characteristics. This not inconsiderable effort necessary for commissioning the feedforward control is also reflected on the maintenance side: Due to the wear on the flow edges of the valve, the system image generated during commissioning and the real flow behavior of the valve drift apart over time. At this point the maintenance engineer is forced to readjust the feedforward control with considerable measurement effort, which is why this adjustment is generally only performed after a valve replacement and poorer control characteristics are accepted in the meantime.

1.2 Motivation

The concept presented in this article presents an innovative method of identifying the drive characteristic diagram for the feedforward control, which uses both theoretical white box and metrologically obtained black box information. With even just a few stationary measuring points, however, this is able to deliver very good results during actuating signal generation, i.e. to represent the real characteristic diagram. As a result of the concept presented here, the commissioning and maintenance effort involved in hydraulic control should in principle be significantly reduced. The characteristics and results of the identification method are demonstrated using the example of the pressure control of a hydraulic try-out press of the type MW ZE2100 /6/. The identification method was performed offline, i.e. measuring data were recorded first of all and then the characteristic diagram identification was performed on the basis of the entire data material. When designing the identification method the fundamental requirement was set right from the beginning, however, that the process could in principle also be implemented in the form of online and real time-capable algorithms on a digital control computer, which can process the periodically occurring measuring data in the controller cycle, thus enabling an

adaptation/optimization of the precontrol model in virtually regular operation of the system. However, real-time implementation of the method has not been implemented yet.

A second concept for operating point-dependent adaptation of the feedback control parameters is also presented, which is again based on the (identified) drive characteristic diagram. Even if the feedback controller in the 2DOF concept no longer has the same fundamental importance as that of classic concepts for the reasons mentioned above, the feedback controller can now be parameterized to the precise operating point on the basis of the identified system model. Thus, in addition to the compensation of interference effects which cannot be acquired in the stationary characteristic diagram, corrections of the dynamic behavior can also be performed effectively and accurately. The entire 2DOF control design can therefore be considered as a coherent and logical overall concept. The design or parameterization of such a control no longer requires expert knowledge, but can also be algorithmized and automated. At present, however, this is still a theoretical concept, whose implementation and validation have not yet been performed on a real system.

2 Observed drive system

The concepts presented in the following for modeling the drive characteristic diagram for the feedforward control and the design of the feedback control parameters are derived and demonstrated using the specific example of a hydraulic 8-axis try-out press of the type MW ZE2100 /6/. This drive system will be described first of all and relevant model equations provided, which are necessary or helpful for the derivation and understanding of the methods described below. A single drawing cushion axis from the entire press is considered in the following.

2.1 System description

As shown in Figure 2, a drive axis essentially consists of a plunger and a highly dynamic (dual-flow) directional control valve of the type Moog D663 /7/, via which the discharged volume flow Q_V and consequently the relevant chamber pressure p can be regulated.

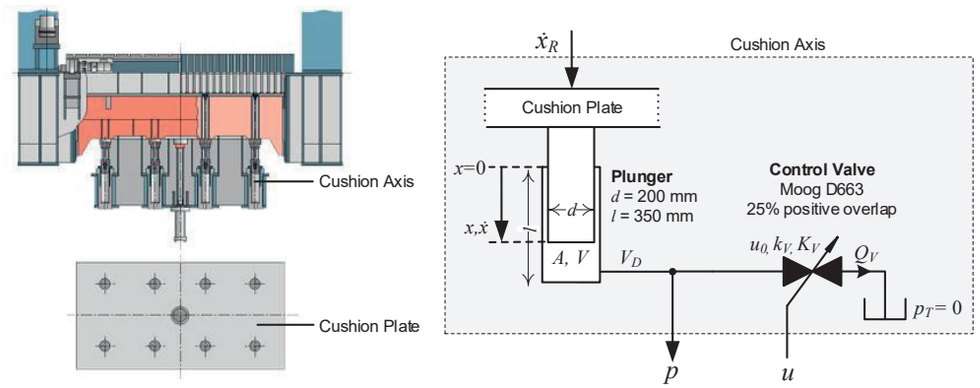


Figure 2: Drawing cushion drawing and technical diagram

The plunger with piston area A = 314cm² is externally impressed by the ram with speed $\dot{x}_R$ and it is always assumed in the following that $\dot{x}_R = \dot{x}$. The directional control valve is modeled as a simple discharge valve, whose degree of opening can be adjusted via the control voltage u = 0…+10V. The valve has a positive overlap of 25% (u_0 = +2.5V). Under the assumption of an ideal linear valve characteristic, the corresponding orifice coefficient follows from the datasheet values Q_{ref} = 350 l/min and p_{ref} = 5 bar, with k_V = 15.65 lpm/(V·bar$^{0.5}$). The movement impressed on the drawing cushion axis by the ram is an essential functional feature of drawing cushion drives. Only through the ram movement does a fluid compression and thus a pressure build-up in the chamber take place. From the point of view of the pressure control to be executed via the discharge valve, however, this impressed movement or the corresponding kinematic volume flow $Q_{kin} = \dot{x} \cdot A$ should be understood as the essential disturbance variable, which must be compensated almost constantly in order to maintain the required pressure p_{set}.

2.2 Model equations

The following four essential model equations can be specified for the volume flows Q_V (volume flow discharged via the valve → orifice equation) and Q_{kin} (kinematic volume flow), the chamber pressure p and the chamber volume V:

$$Q_V = \begin{cases} k_V \cdot u \cdot \sqrt{p} & for \quad u_0 \le u \le 1 \\ 0 & 0 \le u \le u_0 \end{cases} \qquad Q_{kin} = A \cdot \dot{x} = A \cdot \dot{x}_R \tag{1}$$

$$\dot{p} = \frac{1}{C_H(x)} \cdot Q_{comp} = \frac{E_{Fl}}{V(x)} \cdot (Q_{kin} - Q_V) \qquad V(x) = A \cdot (l - x) + V_{dead} \tag{2}$$

The valve dynamics is at first deliberately ignored at this point. The influence of the valve dynamics is discussed in section 4 in the design of the feedback control parameters.

3 Modeling, identification and optimization of the drive characteristic diagram

3.1 Definition of operating point and characteristic diagram

All stationary operating points accessible from a drive axis are ideally mapped in the drive characteristic diagram. An operating point **OP** is defined as the triple of a power flow variable (here speed $\dot{x}$), a power potential variable (here chamber pressure p) and the actuating variable (here valve voltage u). A specific operating point can be seen as an individual element of the characteristic diagram **CD**. The flow variable is usually applied in the characteristic diagram depending on the potential and actuating variable. Therefore $\dot{x}$ can here be formally regarded as on output variable dependent on the input variables p and u, where $\mathbf{x} = (p,u)^T$ describes the so-called input vector in the following. In summary, it can be stated that:

$$\mathbf{OP} = (p, u, \dot{x}) \qquad \mathbf{OP} \in \mathbf{CD} \qquad \dot{x} = f(\mathbf{x}) \tag{3}$$

Comment: It should be noted that $\dot{x} = f(\mathbf{x}) = f(p,u)$ is a purely formal and, for the following relationships, advantageous representation of the facts. From the viewpoint of the drawing cushion axis or the control task in accordance with Figure 1, the ram speed $\dot{x}_R = \dot{x}$ forms an input variable (disturbance variable) and the chamber pressure p forms the output variable (target variable) of interest in the controlled system.

3.2 White box characteristic diagram – Theoretical modeling

A theoretical white box characteristic diagram can be calculated for any drive system on the basis of corresponding model equations. As the characteristic diagram is a stationary model, dynamic effects (state changes) can and must be ignored in the model equations, therefore $\dot{p} = 0$ applies in the present case. In concrete terms this means that compression volume flows are ignored in the stationary observation. This is often a valid assumption, however, if the kinematic volume flows are dominant in relation to the compression volume flows in the relevant application. Under the assumption $Q_V = Q_{kin}$, the speed $\dot{x}$ depending on the pressure p and the actuating variable u results in the following, without further derivation:

$$\dot{x}_W(p,u) = \begin{cases} \frac{k_V}{A} \cdot u \cdot \sqrt{p} & for \quad u_0 \le u \le 1 \\ 0 & 0 \le u \le u_0 \end{cases} \tag{4}$$

The additional index W indicates that this is a theoretical *white box* description. This is a *parametric* (→ formula-based) representation of the characteristic diagram. If the p-u input space is suitably rasterized, for each of the possible p-u input variable combinations the relevant speed value can be explicitly calculated and stored in the form of a two-dimensional *nonparametric* look-up table with m rows and n columns.

CD	$u_1 = u_{\min}$	u_2	$\cdots$	$u_n = u_{\max}$
$p_1 = p_{\min}$	$\dot{x}_{11}$	$\dot{x}_{12}$	$\cdots$	$\dot{x}_{1n}$
p_2	$\dot{x}_{21}$	$\dot{x}_{22}$	$\cdots$	$\dot{x}_{2n}$
p_3	$\dot{x}_{31}$	$\dot{x}_{32}$	$\cdots$	$\dot{x}_{3n}$
$\vdots$	$\vdots$	$\vdots$	$\ddots$	$\vdots$
$p_m = p_{\max}$	$\dot{x}_{m1}$	$\dot{x}_{m2}$	$\cdots$	$\dot{x}_{mn}$

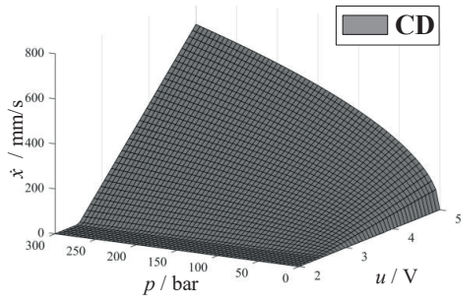


Figure 3: Look-Up Table and White Box Characteristic Diagram

From this look-up table, through specification of the set points p_{set} and $\dot{x}_{Rset}$ the actuating variable u_{FF} of the precontrol circuit can basically be calculated using suitable algorithms, e.g. bilinear interpolation, in accordance with Figure 1:

$$u_{FF} = f(p_{set}, \dot{x}_{Rset}) \tag{5}$$

Comment: The actuating signal component which is necessary in a defined load situation for compensation of the (expected) kinematic volume flow $Q_{kin} = \dot{x}_{Rset} \cdot A$, is therefore calculated de facto via the characteristic diagram. The characteristic diagram-based feedforward control can thus be seen quasi as a load-dependent disturbance variable compensation. Compression volume flows, which are required for a change in the pressure of the fluid (→ dynamic process), are ignored by this stationary model as a matter of principle. These model errors must therefore be compensated by the feedback controller in a 2DOF control concept.

3.3 Black box characteristic diagram – measurement-based identification

The theoretical white box characteristic diagram inevitably contains a multitude of inaccuracies or errors. Possible causes can, for example, be a non-ideal linear valve characteristic, effects not taken into account in the model (e.g. friction/leakage), non-ideal model assumptions (e.g. no ideal root-shaped relationship between volume flow and pressure) or deviations from the datasheet values due to manufacturing tolerances and wear. In the specific case of the MW ZE2100 deep drawing press, valves with a special piston were also used which, although they have a volume flow signal function that is advantageous for the application, differ considerably from the relevant datasheet value in terms of quantity. In this case the white box characteristic diagram is so flawed, that it is de facto unusable for the precontrol circuit.

Due to the resulting inadequate quality of the white box model, a measurement-based identification of the real characteristic diagram of each individual axis is generally performed instead. Previously this identification took the form of a classic point-for-point identification. That is, the largest possible number N of stationary operating points are approached and the identified operating points $\mathbf{OP}_B = (p_B, u_B, \dot{x}_B)$ are stored in a look-up table, similarly to the white box characteristic diagram. Index B stands here for observation/measurement = *black box* Information. The advantage of this approach is that the resulting characteristic diagram maps the real response characteristic of the drive system quasi optimally. The use of a nonparametric look-up table for mapping the static response characteristic has the fundamental advantage, in comparison to any parametric (equation-based) approach, that each data value in the table represents virtually any chosen degree of freedom. On the one hand no system parameters have to be determined from the measured data (no parameter fitting or similar identification methods necessary), and on the other hand it is irrelevant whether corresponding effects have been mapped incorrectly or not at all in the white box model equations: In the observed response characteristic in the form of an actually measured operating point $\mathbf{OP}_B$, all technical and physical effects which lead to the observed combination of power flow, power potential and actuating variable at this operating point are cumulatively mapped. For a control it is irrelevant why this particular combination is present at the observed operating point; a control only has to generate the correct actuating signal for the respective operating point. The disadvantage is, on the one hand, that this method is very time-consuming, as previously mentioned, since the largest possible number of operating points ($N \approx$ 100-150) should be approached, as part of the real characteristic diagram, for an accurate identification. On the other hand, however, many relevant operating points cannot even be approached, as due to the system dynamics in real operation and the limited cylinder stroke in limit ranges, no secured stationary state can be adopted and the measured data cannot, or rather may not, be interpreted as part of the real characteristic diagram.

3.4 Gray box characteristic diagram – measurement-based optimization

An innovative method for determining the real characteristic diagram is described in the following, which effectively combines the advantage of white box modeling (quickly accessible) and black box identification (highly precise) into a so-called gray box model. It is assumed that the white box characteristic diagram represents a qualitatively plausible description of the stationary response characteristic, even if this is not quantitatively correct on account of the modeling errors. This qualitatively approximately correct model will be corrected by a few ($N \approx$ 10-15 or even less) additional black box observations, as a result of which the measurement and commissioning effort can be reduced to around 10% of the original value. This is therefore not a classic measurement-based identification method, but can rather be seen as a measurement-based *optimization* method. This method basically comprises two steps: First, all transient system states must be reliably separated out from the accumulated measured data, so that reliable measured black box operating points, which can effectively be interpreted as unique "fingerprints" of the real characteristic diagram area, can be specified as a result. To this end a method based on time-discrete filter algorithms was developed, which will not be explained in more detail here, however. For all such operating points reliably identified as stationary, the error between the black box observation and the white box model must then be determined in a second step. If this error is related to the original white box data value, a corresponding relative/percentage error can be specified at the respective operating point defined through the input variable combination $\mathbf{x}_B = (p_B, u_B)$:

$$e_{rel}(\mathbf{x}_B) = \frac{\dot{x}_B(\mathbf{x}_B) - \dot{x}_W(\mathbf{x}_B)}{\dot{x}_W(\mathbf{x}_B)} \tag{6}$$

As only a few selected operating points $\mathbf{OP}_B = (p_B, u_B, \dot{x}_B)$ will be specifically identified in principle, the measurement-based information relating to the model errors must be suitably *generalized* for the entire characteristic diagram area, i.e. across the entire input space $\mathbf{x}$. Assuming this is possible, a gray box data value can be calculated at *each* point $\mathbf{x}$ of the input space (i.e. not only at the specifically observed points $\mathbf{x}_B$) in accordance with the following rule:

$$\underbrace{\dot{x}_G(\mathbf{x})}_{Gray\ Box} = \underbrace{\dot{x}_W(\mathbf{x})}_{White\ Box} \cdot \underbrace{\left(1 + e_{rel}(\mathbf{x})\right)}_{Black\ Box} \tag{7}$$

In short, this means that each original white box data value adapts on the basis of the relative model error determined at this point, i.e. the look-up table numerical value is increased or decreased accordingly. The question is therefore how the few relative model errors explicitly known at the points $\mathbf{x}_B$ can be generalized. It is plausible to assume here that in the local environment of a specifically identified operating point the relative model error is likely to be of a similar quantity to that at the identified operating point itself. However, as you move further away from this reliably identified point in the input space, this assumption becomes increasingly unreliable, or rather, more improbable. The model errors must therefore be meaningfully interpolated between the explicitly known points. A Normalized Radial Basis Function Network (NRBF), a special class of Artificial Neural Networks (ANN), is used for this purpose (see e.g. /8/ for further theoretical explanations and derivations). Each individual identified operating point $\mathbf{OP}_B$ effectively forms a neuron of this network, where $\mathbf{x}_B$ forms the basis of the respective neuron (= position in input space) and $e_{rel}(\mathbf{x}_B)$ the so-called neuron weight. The model errors at each point of the input space are calculated in accordance with the NRBF interpolation rule:

$$e_{rel}(\mathbf{x}) = \frac{\sum_{B=1}^{N} e_{rel}(\mathbf{x}_B) \cdot \psi_B(\mathbf{x})}{\sum_{B=1}^{N} \psi_B(\mathbf{x})} \tag{8}$$

With basic function ψ and distance d:

$$\psi_B(\mathbf{x}) = \exp\left(\frac{d(\mathbf{x})^2}{2\sigma_B^2}\right) \qquad d(\mathbf{x}) = \|\mathbf{x} - \mathbf{x}_B\| = \sqrt{(\mathbf{x} - \mathbf{x}_B)^T \cdot (\mathbf{x} - \mathbf{x}_B)} \tag{9}$$

The parameter σ_B is the so-called form or expansion parameter of a neuron, which expresses the expansion of an individual neuron and thus the degree of overlap of all neurons. This must be defined using suitable algorithms for each neuron, based on the number and distribution of all existing neurons. In the present case this parameter tells us, put simply, how far an identified operating point $\mathbf{OP}_B$ may disseminate the information relating to "its" model error $e_{rel}(\mathbf{x}_B)$ in the input space and thus influence/correct other points $\mathbf{x}$. Figure 4 illustrates the NRBF structure as a block diagram according to equation (8).

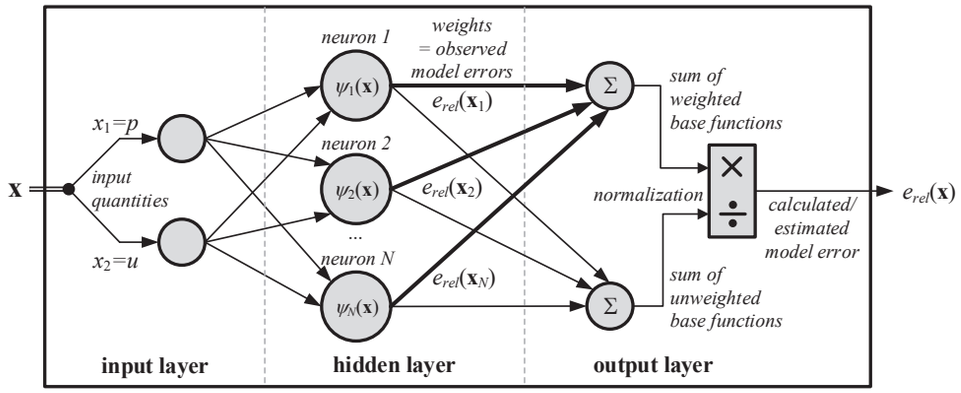


Figure 4: NRBF structure

On the observed deep drawing press, $N = 10$ example operating points were approached, identified as stationary black box operating points and used for the characteristic diagram optimization. The resulting NRBF network consequently has N =10 neurons. Figure 5 shows the original white box model $\mathbf{CD}_W$, the black box database $\mathbf{OP}_B$ and the resulting gray box characteristic diagram $\mathbf{CD}_G$. On the one hand the specifically identified operating points are clearly very well "matched" by the gray box characteristic diagram, and on the other hand the relevant information is meaningfully generalized for the entire input space.

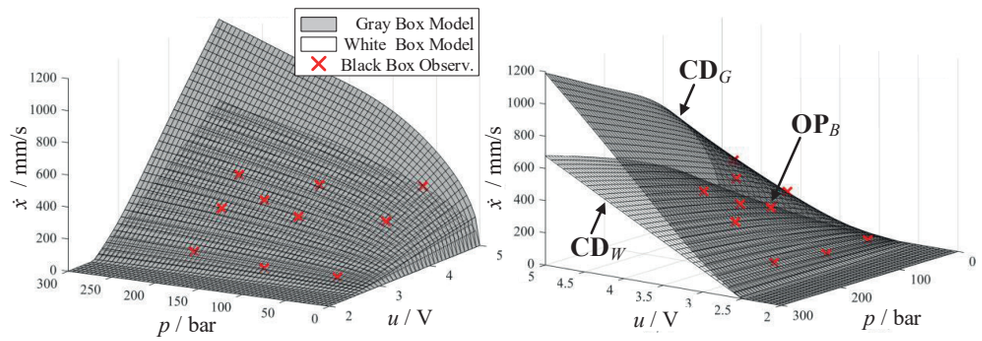


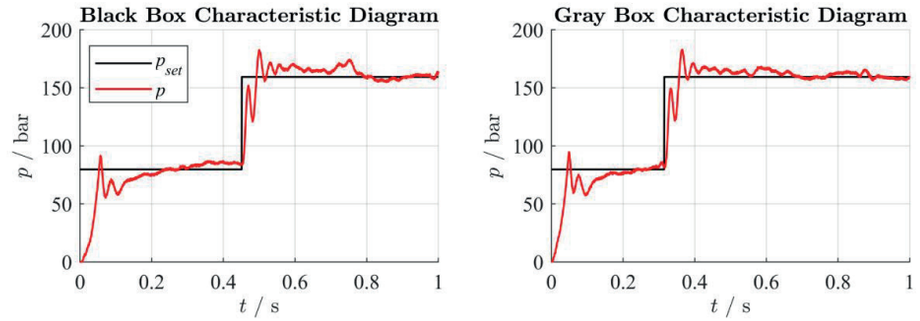
Figure 5: White Box and Black Box Characteristic Diagram

3.5 Control results with black box and gray box characteristic diagram

Comparison measurements were performed on the real deep drawing press, where on the one hand the originally implemented black box characteristic diagram and on the other hand the gray box characteristic diagram determined with the new NRBF optimization method were used as the precontrol model in the 2DOF control concept, and the PI feedback controller was also identically parameterized in all tests. The results of one of the eight axes of the deep drawing press are shown in Figure 6, where a) shows the results with reference variable step change and b) shows the results with disturbance variable step change.

It was expected that the control results would be virtually identical in the ideal case, with the advantage of the gray box characteristic diagram consisting almost exclusively in a reduced identification effort. It was observed, however, that with the gray box characteristic diagram even slightly better results could be achieved in the static and dynamic control behavior than previously. This could be due to the fact that the valve wear occurring since the original black box identification is reflected better in the more recent data used for the gray box characteristic diagram. In any case, however, it can be said that the gray box characteristic diagram generated through the NRBF interpolation can be achieved even with only a very approximately correct white box model as the starting point, and that a very good mapping of the real static response characteristic can be achieved based on a small number of measured data. Any nonlinearities implicitly present in the measured data, which were not included in the original white box model, are also recorded and mapped.

a) alternating pressure setpoint: p_{set} = 80 bar → 160 bar
constant ram velocity: $\dot{x}$ = 200 mm/s



b) constant pressure setpoint: p_{set} = 160 bar
alternating ram velocity: $\dot{x}$ = 150 → 75 mm/s

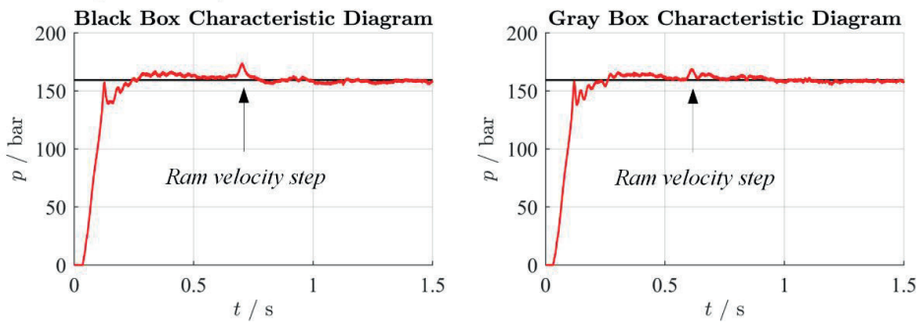


Figure 6: Control Quality with Black Box and White Box Characteristic Diagram

4 Operating point-dependent adaptation of the feedback control parameters

For the complete design of a control according to the 2-DOF concept, in addition to the feedforward control the classic feedback controller (PI controller) must also be parameterized, even if this no longer has the dominant role in the overall concept with a precisely tailored feedforward control. However, if one of the great advantages of the 2-DOF concept should be that the dominant nonlinearities of the system can also be taken into account via the precontrol circuit, then with distinctly nonlinear systems like hydraulic drives, the design of the feedback controller according to the classic methods of linear control theory (see /9/ for example) represents a certain

fracture within the overall concept, as the system must be linearized at a selected operating point. The consequence is that the feedback controller must either be designed based on the worst-case operating point and sub-optimal solutions must therefore be accepted at other operating points, or that the parameters of the controller must be adapted in real time operating point-dependently. In this last section we will show, using the example of the deep drawing press, that with in-depth knowledge of the response characteristic of the control system, which must in any case be available in model-based controls, the control parameters can also be adapted operating point-dependently in real time.

4.1 General observations

As explained above, the actuating signal component of the precontrol circuit ensures the provision of a volume flow component, which ideally largely compensates for the pressure-changing effect of the kinematic volume flow completely and in real terms. However, if this actuating signal component is generated without the involvement of the feedback controller, the following situation results:

1. From its perspective the piston is stationary, as the feedback controller obviously does not have to provide/compensate for any kinematic volume flow.
2. The pressure adapts to the set course "miraculously by itself", thanks to the feedforward control.
3. The hydraulic capacity nevertheless changes over the time $C_H = C_H(t)$

4.2 Nonlinear pressure build-up equation

For a further mathematical analysis the differential equation specified at the outset for the pressure build-up is considered:

$$\dot{p} = \frac{E_{Fl}}{V(x)} \cdot (Q_{kin} - Q_V) \quad \xrightarrow{yields} \quad \underbrace{\frac{V(x)}{E_{Fl}} \cdot \dot{p}}_{\textbf{Term 1}} = \underbrace{A \cdot \dot{x}}_{\textbf{Term 2}} - \underbrace{k_V \cdot u \cdot \sqrt{p}}_{\textbf{Term 3}} \tag{10}$$

This is a first order differential equation, where two of the three occurring terms, terms 1 and 3 are nonlinear. A linear model of the control system - i.e. of the pressure build-up in the chamber in this case - is required as the basis for the design of the feedback controller. This occurs in principle by linearizing the above pressure build-up equation. The following facts can be recorded first of all:

1. The prefactor $V(x)/E_{Fl}$ of the first term relates to the hydraulic capacity of the chamber. This should represent a constant for the respective linearization range. If we assume, as is customary and acceptable in a first approximation when designing a linear controller, that the effective bulk modulus E_{Fl} is constant, then on account of $V(x)$ the prefactor must normally be permanently adapted stroke-dependently.
2. The second term relates to the kinematic volume flow, which is ideally completely provided or compensated for via the feedforward control. As mentioned above, this can be interpreted from the perspective of the feedback controller as meaning that the piston is stationary and $\dot{x} = 0$ can therefore be assumed in the following, as a result of which the entire term can be omitted for further considerations.
3. The third term relates to the flow equation for the valve $Q_V(p,u)$ with a dual nonlinearity: The root function itself represents one and the product of the time-varying root function as a signal with another time-varying signal represents the other nonlinearity. The linearization of this relationship must occur at a suitable stationary operating point **OP**. The respective current operating point must be used as such for logical reasons. This is therefore defined by the current actuating variable u for the kinematic volume flow and the current chamber pressure p.

4.3 Linearized pressure build-up equation

The linearization of the flow relationship Q_V (Term 2) at an operating point **OP** = ($p_{\mathbf{OP}}$,$u_{\mathbf{OP}}$) (defined by the kinematic volume flow!) follows mathematically according to:

$$\hat{Q}_V = \underbrace{\left(\frac{\partial Q_V}{\partial p}\Big|_{\mathbf{OP}}\right)}_{K_p} \cdot \hat{p} + \underbrace{\left(\frac{\partial Q_V}{\partial u}\Big|_{\mathbf{OP}}\right)}_{K_u} \cdot \hat{u} \tag{11}$$

With the two resulting linearization factors

$$K_p = \frac{k_V \cdot u_{\mathbf{OP}}}{2 \cdot \sqrt{p_{\mathbf{OP}}}} \qquad K_u = k_V \cdot \sqrt{p_{\mathbf{OP}}} \tag{12}$$

The pressure build-up equation at the operating point is therefore, in deviation variables (indicated by the additional hat above variables)

$$\frac{V(x)}{E_{Fl}} \cdot \hat{\dot{p}} = -\left(K_p \cdot \hat{p} + K_u \cdot \hat{u}\right) \quad \xrightarrow{yields} \quad \frac{V(x)}{E_{Fl} \cdot K_u} \cdot \hat{\dot{p}} + \hat{p} = -\frac{K_p}{K_u} \cdot \hat{u} \tag{13}$$

Or with the substitutions

$$T_S = \frac{V(x)}{E_{Fl} \cdot K_p} \qquad K_S = -\frac{K_u}{K_p} \tag{14}$$

the differential equation follows:

$$T_S \cdot \hat{\dot{p}} + \hat{p} = K_S \cdot \hat{u} \tag{15}$$

This is the linear differential equation of the pressure build-up in the chamber for the speed-compensated case. The control must reduce the valve opening degree at a given kinematic volume flow in order to increase the pressure, and vice versa. This intuitively obvious fact is expressed in the differential equation in the sign reversal in the coefficient K_S of the excitation term on the right-hand side of the differential equation. With (15) a first order differential equation is now available, which describes the dynamic behavior of the control system, at least as long as the operating point is sufficiently close to the operating point defined by dead volume, kinematic volume flow and chamber pressure.

The following fact is important for the considerations below: Both parameters of the control system T_S and K_S are dependent on the linearization parameters K_p and K_u. These were determined by linearization of the parametric white box model equation at a *stationary operating point* **OP**. However, the linearization parameters are de facto nothing more than the gradients ($\mathrm{d}Q/\mathrm{d}p$ and $\mathrm{d}Q/\mathrm{d}u$) of the *stationary characteristic diagram* at that operating point. The numerical determination of the gradients from a numerical look-up table is almost trivial, however, and can easily be performed in real time. The current gradients or linearization parameters can thus also be determined from the gray box characteristic diagram, which reflects reality very well, in any controller cycle, and be assumed as known for further considerations.

4.4 Design of the feedback control parameters

The transfer function of the control system follows from (15):

$$G_S(s) = \frac{p(s)}{u(s)} = \frac{K_S}{T_S \cdot s + 1} \tag{16}$$

A PI controller can be used to control such a PT_1 system: This is permissible and sensible in system theory terms on the one hand, as the present case relates to a system with self-regulation and therefore in principle an integral controller component is necessary for the complete compensation of control errors that remain stationary. On the other hand it is dynamically sensible, as the respective operating point is mostly impressed by the feedforward

control in principle, and does not have to be assumed through large-scale integration of the integral controller branch. With the transfer function of a PI controller

$$G_R(s) = K_R \cdot \frac{T_{ZR} \cdot s + 1}{s} \tag{17}$$

it therefore follows for the open control loop

$$G_{OL}(s) = G_R(s) \cdot G_S(s) = \left(K_R \cdot \frac{T_{ZR} \cdot s + 1}{s}\right) \cdot \left(\frac{K_S}{T_S \cdot s + 1}\right) \tag{18}$$

The zero point (time constant) T_{ZR} of the controller is freely selectable in principle. If in accordance with

$$\boxed{T_{ZR} = T_S = \frac{V(x)}{E_{Fl} \cdot K_p}} \tag{19}$$

this is selected as being equal to the system time constant T_S, in order to compensate the latter, these formally cancel each other out in the open control loop:

$$G_{OL}(s) = \frac{K_R \cdot K_S}{s} \tag{20}$$

After closing the control loop, the controlled pressure chamber (again) has a PT_1 structure:

$$G_{CL}(s) = \frac{G_{OL}(s)}{1 + G_{OL}(s)} = \frac{\frac{K_R \cdot K_S}{s}}{1 + \frac{K_R \cdot K_S}{s}} = \frac{1}{\left(\frac{1}{K_R \cdot K_S}\right) \cdot s + 1} = \frac{1}{T_{CL} \cdot s + 1} \tag{21}$$

The time constant $T_{CL} = 1/(K_R \cdot K_S)$ can *theoretically* be arbitrarily small and the system can thus be made arbitrarily "sharp". This is possible in real terms but only provided that no significant limitations occur in the real system, which limit this dynamic behavior. This would be the case e.g. if a step response were required to a unit step of the control signal u via the time constant of the control loop, which the system cannot provide because the valve cannot supply the necessary volume flow quantity. Even if the value K_S (from the characteristic diagram) can be assumed as known, the question remains of how great a controller gain K_R can then be selected, through which the time constant T_{CL} is ultimately defined:

$$K_R = \frac{1}{T_{CL} \cdot K_S} = -\frac{K_p}{T_{CL} \cdot K_u} \tag{22}$$

Within the framework of the linear theory any PT_1 system can be made arbitrarily fast, and first-order systems cannot become unstable as long as no gradient reversal (→ change of sign of a parameter of the transfer function) occurs. The limit is therefore predefined by reality-based limitations alone. Such a limit should, however, always exist if the valve dynamics were not taken into account in the previous considerations, i.e. it has been assumed that the valve is infinitely fast and can therefore make the transition to a new operating point within an infinitely short time. This is of course not the case in reality. The dynamics of the pressure change are therefore, in the present case, predefined solely by the fastest possible volume flow change which the existing valve can provide. A dynamic limitation, as results in other systems, for example, due to the maximum possible pump rotation speed, is not present here. However, the build-up of the volume flow in the valve requires a certain time, which is for example described operating point-dependently via the valve time constant T_V (rate of rise $\dot{Q}_V = dQ_V/dt$ of the volume flow step response of the valve) and can generally be taken or estimated from the valve datasheet (Figure 7 a) /7/).

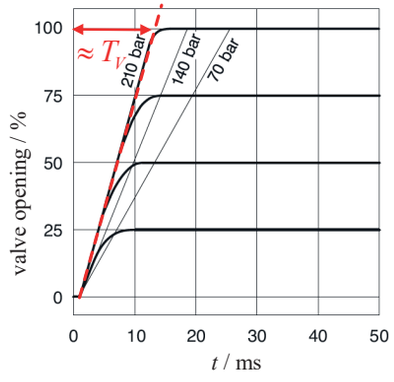
The time constant T_V of the actuator should be faster by a factor k (usually e.g. $k = 10$) than the time constant T_S of the controlled system. The time constant $T_{CL} = k \cdot T_V$ of the controlled system must therefore be selected depending on the valve dynamics. From this, the required controller gain follows:

$$\boxed{K_R = \frac{1}{T_{CL} \cdot K_S} = -\frac{K_p}{(k \cdot T_V) \cdot K_u}} \tag{23}$$

In summary it can be stated that both PI control parameters T_{ZR} and K_R can be designed/adapted meaningfully or optimally with the help of the (measured) piston position x (→ current hydraulic capacity) and the characteristic diagram gradients $K_p = dQ/dp$ and $K_u = dQ/du$ (linearization parameters). The dynamics of the closed control loop are ultimately only limited by the dynamics of the actuator, i.e. the valve (valve time constant T_V):

$$\boxed{T_{ZR}(K_p, x) = \frac{V(x)}{E_{Fl} \cdot K_p}} \qquad \boxed{K_R(K_p, K_u) = -\frac{K_p}{k \cdot T_V \cdot K_u}} \tag{24}$$

a) Estimation of valve timeconstant



b) Calculation of linearization parameters / gradients

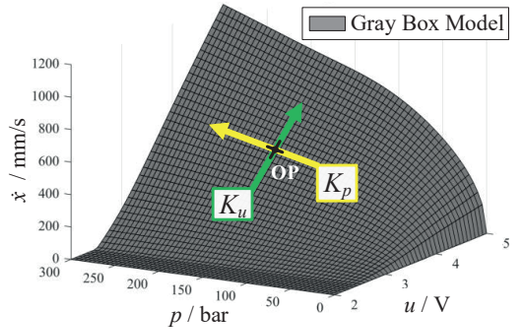


Figure 7: Determination of the feedback control parameters

4.5 Outlook: Model-based compensation of compression volume flows

The volume flows in a hydraulic system can in principle be divided into kinematic volume flows, i.e. the volume flows necessary for movement, and compression volume flows, for changing the pressure in the chamber. As mentioned above, the characteristic diagram-based feedforward control ideally applies exactly the actuating signal necessary for compensation of the kinematic volume flow. This is interpolated from the look-up table according to (5):

$$u_{FF}^{kin} = f(p_{set}, \dot{x}_{set}) \tag{25}$$

The feedback controller must consequently compensate for the (remaining) model error in the feedforward control on the one hand, and on the other hand generate the actuating signal necessary for the compression volume flows. If we think the entire model-based situation through logically to the end, however, the provision of an actuating signal component necessary for the compression volume flows is also possible in principle using a model-based approach, with a further parallel precontrol circuit. The linearized differential equation for the pressure build-up is considered again for this purpose:

$$T_S \cdot \dot{\hat{p}} + \hat{p} = K_S \cdot \hat{u} \tag{26}$$

If we assume that the current pressure $p_{\mathbf{OP}}$ corresponds to the current setpoint value p_{set} (current control goal reached, control error $e = 0$) and there is no pressure change at the current operating point $\dot{p}_{\mathbf{OP}} = 0$ (assumption of a stationary state), then this follows for the deviation variables resulting from the linearization:

$$\hat{p}_{set} = p_{set} - p_{\mathbf{OP}} = 0 \tag{27}$$

$$\dot{\hat{p}}_{set} = \dot{p}_{set} - \dot{p}_{\mathbf{OP}} = \dot{p}_{set} - 0 = \dot{p}_{set} \tag{28}$$

The differential equation is thus simplified as follows

$$T_S \cdot \dot{p}_{set} = K_S \cdot \hat{u} \tag{29}$$

By releasing the actuating variable we then get:

$$u_{FF}^{comp} = \frac{T_S}{K_S} \cdot \dot{p}_{set} \tag{30}$$

This actuating signal component is exactly the component that is necessary for a further pressure change, and which is therefore necessary to leave the operating point currently assumed as stationary (→ dynamic process). This is de facto nothing more, however, than the necessary compression volume flow to achieve the required pressure change according to the reference trajectory $\dot{p}_{set}$. In addition to the parameters to be determined operating point-dependently on the basis of the characteristic diagram K_S and T_S , only the setpoint value change $\dot{p}_{set}$ is necessary, which directly follows from the reference trajectory p_{set}, provided this is differentiable at least once, i.e. a pressure ramp is predefined as setpoint profile. The maximum achievable rate of rise of the pressure ramp is naturally once again dependent on the actuator dynamics. A further improved control behavior can be achieved through this additional operating point-dependent model-based precontrol term, as the actuating signal component necessary to realize the compression volume flows no longer has to be generated via the feedback controller and thus the control error.

5 Summary and conclusion

In principle, very good control results can be achieved using the stationary characteristic diagram in a 2DOF structure as model-based feedforward control. A method has been presented, which allows the drive characteristic diagram existing in reality to be reliably identified using just a few measured data. This method is essentially based on radial basis function networks, a special class of artificial neural networks. Using this method, the effort involved in characteristic diagram identification can be reduced to around 10% of the original value, and equivalent or even better control results can be expected than originally. In addition, a method also based on the drive characteristic diagram was demonstrated, which enables the feedback control parameters to be adapted operating point dependently. Both methods can in principle be implemented as real time-capable algorithms. The entire 2DOF control design can therefore be considered as a coherent and logical overall concept, which is based on the knowledge of a sufficiently accurate stationary model in the form of a nonparameteric look-up table. Both methods were described using the concrete example of an industrial deep drawing press. These are not limited to this specific drive system in principle, however, but can also be transferred to other drive systems. The characteristic diagram optimization in particular is a universally valid systematic concept which can be applied to any drive system, provided appropriate sensors are available for measuring stationary system states.

Nomenclature

Variable	*Description*	*Unit*
A	Area	[m²]
C_H	Hydraulic Capacity	[m³/Pa]
d	RBF Distance	-
e	Control/Model Error	-
E_{Fl}	Bulk Modulus Fluid	[Pa]
k_V	Valve Coefficient	[lpm/V·bar$^{0.5}$]
K	Gain Factor	-
l	Length	[m]
p	Pressure	[bar]
u	Control Signal/Voltage	[V]
T	Time Constant	[s]
V	Volume	[m³]
Q	Volume Flow	[m³/s]
x	Position	[m]
$\dot{x}$	Velocity	[m/s]
CD	Characteristic Diagram (Look-Up Table)	-
OP	Operating Point	-
x	Input Space	-
σ	RBF Form Parameter	-
ψ	Base Function	-

References

/1/ Horowitz I. M.; *Synthesis of Feedback Systems*, Academic Press, 1963

/2/ Räcklebe S., Radermacher T., Weber J., *Reduction of cycle time for injection moulding machines with electric hydrostatic drives*. In: 12th Scandinavian International Conference on Fluid Power, Tampere, Finland, May 18-20, 2011

/3/ Helmke M., Majer, H., Thanassakis, A., *Improvement of hydraulic control quality for deep drawing presses through retrofit*. In: 10th International Fluid Power Conference, 10. IFK, Dresden, Germany, pp 367–378, March 8-10, 2016

/4/ Heiss M., *Kennfelder in der Regelungstechnik*. In: at – Automatisierungstechnik, Volume 43, No. 8, pp 363-367, 1995, DOI: 10.1524/auto.1995.43.8.363

/5/ Isermann, R., Münchhof, M., *Identification of dynamic systems: An introduction with applications*, Springer, Heidelberg New York, 2011. ISBN: 3540788786

/6/ Müller Weingarten AG, *Produktportfolio*, Müller Weingarten AG, Weingarten, Germany, 2005

/7/ Moog GmbH, *Datenblatt Proportionalventile Baureihe D660*, Moog GmbH, Böblingen, 2005

/8/ Kroll, A., *Computational Intelligence: Eine Einführung in Probleme, Methoden und technischen Anwendungen,* München Oldenbourg, 2013, ISBN: 3486737422

/9/ Lunze, J., *Regelungstechnik 1: Systemtheoretische Grundlagen, Analyse und Entwurf einschleifiger Regelungen*, 10th edition, Springer, Berlin Heidelberg, 2014, ISBN: 978-364-25390-9-1

Dynamic High-Torque Test Stand with Hydrostatic Drive

Dr.-Ing. Wilhelm Hagemeister*, M.Sc. Nicolai Sümnik**

Ingenieurgemeinschaft IgH GmbH, Heinz-Bäcker-Straße 34, D-45356 Essen*
E-Mail: hm@igh.de
Voith Turbo GmbH & Co. KG, Centrumstr. 2, 45307 Essen**
E-Mail: Nicolai.Suemnik@voith.com

This paper presents a Dynamic High-Torque Test Stand with hydrostatic drive technology. The topics discussed within the scope of this paper are the mechanical design and the hydraulic characteristics as well as, detailed solutions implemented in this test rig using innovative technology. The evaluation methods used to determine the test specimen properties are also described in more detail.

Keywords: elastomer coupling, test rig, hydrostatic drive, torque sensor, correlation method, ellipse identification

Target audience: test rig building, measurement technics, mechanical design

1 Introduction

Couplings with elastomer components are widely used machine elements. Their dimensioning for a given drive train is usually carried out according to DIN 740, whereby the characterizing coupling properties, stiffness and damping, are used for the design.
Couplings with high natural rubber content are subject to production fluctuations, which requires continuous testing of these properties.

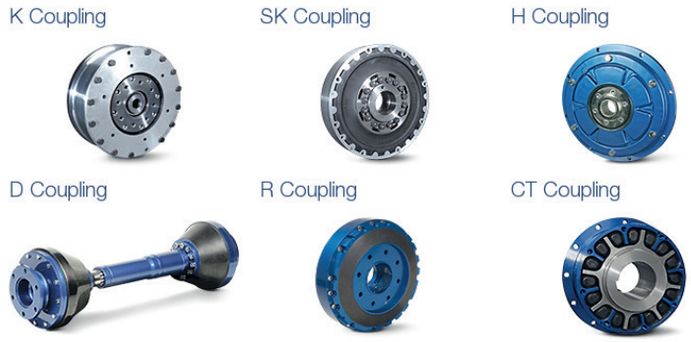


Figure 1: Coupling types

The measurement of stiffness and damping is performed dynamically by way of a harmonic angular motion and measuring of the moment at a frequency of 10 Hz.

For the acceptance test of coupling elements over three torque ranges of magnitude, IgH has developed, in close cooperation with Voith Turbo, a test rig, which provides dynamic testing from 25 Nm to 50.000 Nm.

Also within the scope of this paper, other topics discussed are, the characteristic properties of the test specimens and the design and interesting technical aspects of the test bench.

2 Test Specimen

As the compensation of alignment error is usually one of the main tasks of elastomer couplings, the couplings addressed here are mainly used for torque oscillation damping and for reducing high impulse loads. One of the main operation areas is the linking of combustion engines to drive trains of e.g. mobile machinery or in railway trains driven by diesel engines.

The high rotational speed variations of a diesel engine, if coupled more or less rigid to the drive train, results in high torque levels, which can be reduced efficiently with highly flexible couplings. These couplings reduce the natural frequency, requiring more damping effects. Within the design process the selection of the right coupling for a given drive train is an important task. It especially needs to be taken into account that the resonance region must be passed quickly and also that the drive train is to be operated over-critically, meaning the minimum excitation frequency has to be above the first natural frequency of the system. Figure 2 shows an example of the frequency response of a two-mass oscillator, which is the simplified model of a drive train with a highly elastic coupling.

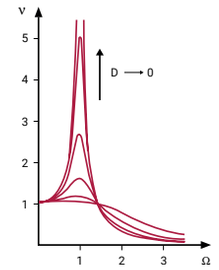


Figure 2: Frequency response of a two mass oscillator

The stiffness of the coupling - with the rotational inertia - is the dominant factor for the natural frequency of the drive train because it is usually the most flexible component. The damping is influencing the amplitude rise at the resonance frequency.

The elastomer element within the coupling is the determining factor of the entire coupling[1]. A good example would be a simple spring in parallel with a viscous damper. Stiffness and damping coefficients are of course dependent on temperature, excitation frequency and, with some materials, the amplitude of oscillation.

$$d\dot{\varphi} + C\varphi = M \tag{1}$$

W_d : dissipative work
W : reference work
M : torque
d : damping coefficient
C : dynamic stiffness
φ : angle
α, β: half axis of ellipse

[1]The coupling usually has, besides the elastomer element, also a friction damper,bearing, housing...

While deforming an elastomer element the deformation work can be split into:

- elastic energy: W, this can be reconverted into mechanical energy on the reverse movement
- viscose energy: W_d, this energy is converted into heat and then lost.

A typical torque angle characteristic curve of an elastomer element at sinusoidal torque excitation can be seen in figure: 3.

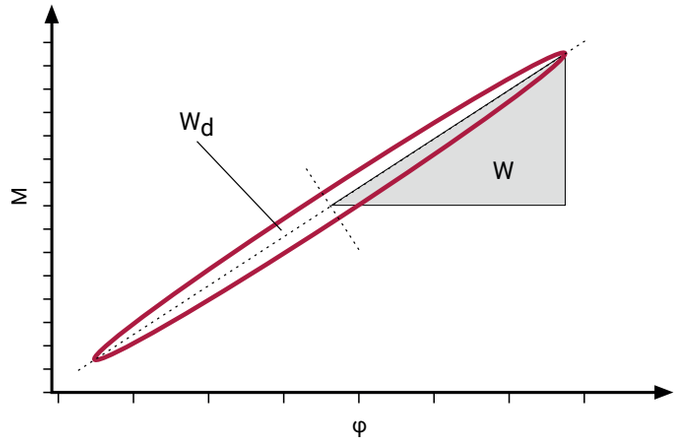


Figure 3: Torque angle characteristic of an elastomer element

W_D is the dissipative work, which can be calculated from the area of the hysteresis ellipse.

$$W_D = \pi \cdot \alpha \cdot \beta \tag{2}$$

W is the - so called - reference work, which is calculated from the surface area of the triangle which can be seen in figure 3[2].

$$W = \frac{1}{2} \cdot \varphi_{max} \cdot M\left(\varphi_{max}\right) \tag{3}$$

The characteristic material damping is defined as the quotient of the dissipative and reference work /2/.

$$\psi = \frac{W_D}{W} \tag{4}$$

The determination of the hysteresis ellipse and resulting parameters as stiffness and damping is the task of the test rig as part of the quality assurance process. Figure 4 shows a typical reading of torque and angle during a test.

During a test the coupling is loaded up to the permissible continuous alternating torque. Prior to the actual test a so called preconditioning takes place where the coupling is loaded up to the rated torque which is approximately three times the test torque. This prepares the coupling material for testing and allows its properties to stabilize. After the test the characteristic coupling parameters are calculated from the measured series of torque and angle (This is described in more detail in chapter 3.6).

[2] if the centre of the ellipse is moved in the coorinate origin

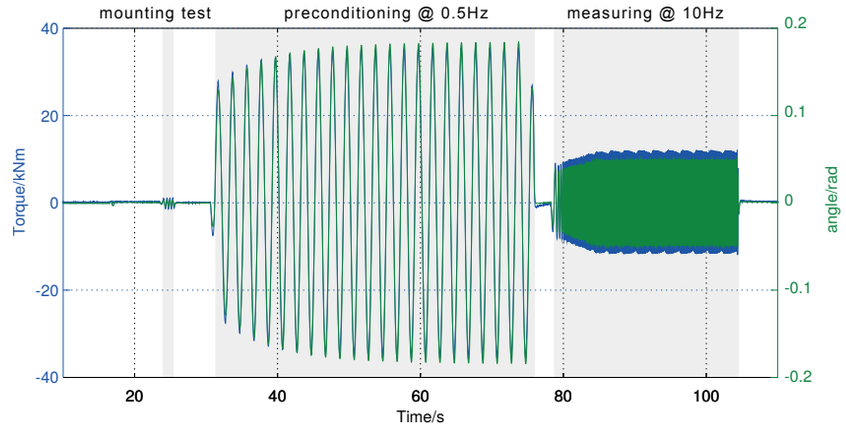


Figure 4: Time series of a acceptance test

3 Test Rig

Relevant for the design of the test rig are the parameters: torque range: 25 Nm - 50.000 Nm, a test frequency of 10 Hz with sinusoidal excitation and an angle range:[3] ±30° - ±60°. Moreover, it is required that the installation and deinstallation of the coupling should not take too much time. A low energy consumption is also desired. Besides the testing of coupling parameters, the test rig is designed to perform endurance tests, where couplings are tested at high torque rates until they fail.

3.1 Mechanical setup

As the main drive for the coupling, the principle of a hydraulic swivel motors is used.

The test specimen is mounted via the inner ring by means of an adapter without an intermediate support. This results in parasitic bending torque, axial and radial forces which act on the swivel motor bearing.

Torque is measured with a reactive sensor. The sensor is not rotating and measures the reaction torque at its support. Compared to a rotating sensor, this has the advantage that no flexible cabling needs to be guided to the sensor. Also, a compensation of rotary inertia is not necessary.

Mounting of the angle sensor is done in such a way that the deformation of the torque sensor is not relevant for the angle measurement.

Overall, this results in a compact design, which is best realized in a vertical direction. Vertically is ideal because the handling of large couplings is made easier and the customer was already equipped to handle the parts in this way.

[3] depending on coupling type

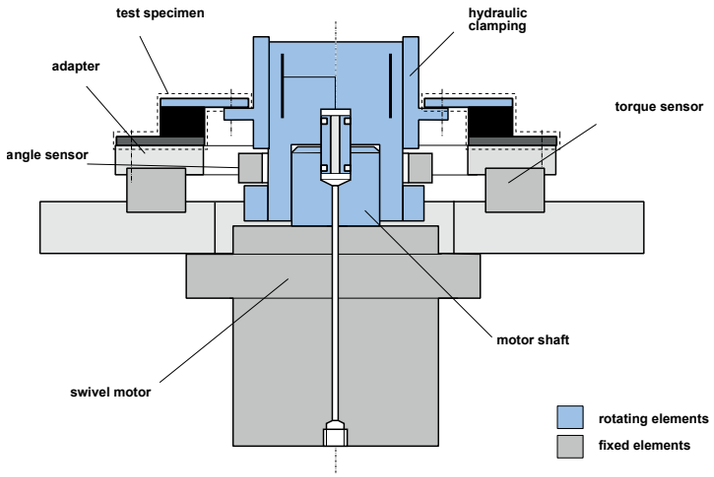


Figure 5: Concept drive train

3.2 Torque sensors

The requirement that the torque should be measured with an absolute accuracy of 1 % over the entire torque range resulted in the neccessity of having several test stations with torque sensors of different sizes. The angle range spread is a moderate ±30° up to ±60°.

The requirement that preconditioning and measuring must be done on the same station complicates the design of the torque sensors. To realize a sensor with high sensitivity, which withstands high torque, a design with mechanical end stops was chosen.

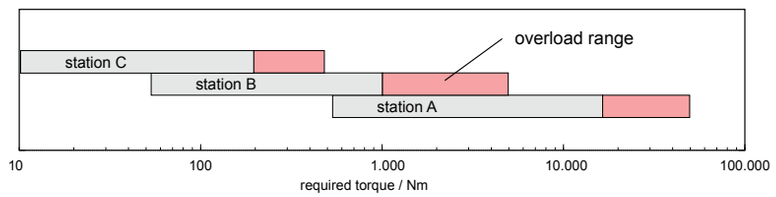


Figure 6: Torque sensor with overload range

The partitioning of the sensor ranges is shown in figure 6. The overload areas are marked in red. A torque reading in the overload range is carried out by means of calculating the torque from the hydraulic pressure difference at the swivel motor.

Figure 7 shows the design of the torque sensor with end stops for overload protection.

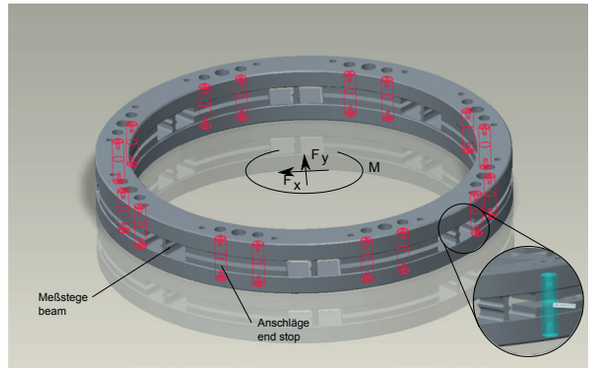


Figure 7: Torque sensor with end stops

The sensors are specially designed and are integrated optimally into the overall mechanical setup. Figure 8 shows the biggest sensor for the torque range, 500 Nm – 15.000 Nm, with an overload range up to 50.000 Nm. For torque sensing, the bending of the beams is used and the radial and axial force is measured by shear deformation. Using different deformation for torque and force allows there to be an individual influence on deformation and for an optimal design of the sensor.



Figure 8: Torque sensor for 50.000 Nm with endstops during application of the strain gauges

Figure 9 shows the functionality of the mechanical end stops. It can be seen that the end stops are reached at a torque of 24,5 kNm. For the transition between the torque signal from the sensor and the torque signal from the pressure difference of the swivel motor, a zone of 15 kNm to 16 kNm is defined.

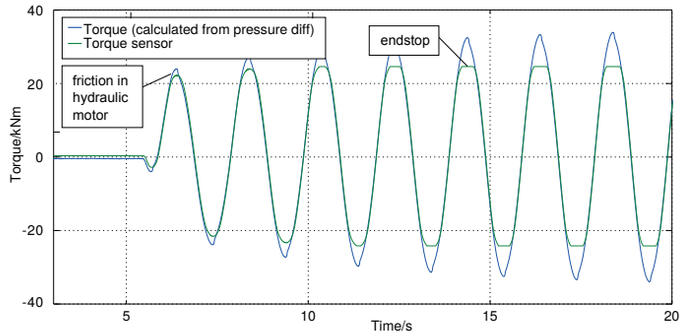


Figure 9: Functionality of the end stops

3.3 Hydraulic concept

Hydraulic swivel motors operating in the hydrostatic circuit are driven directly via a variable displacement pump[4]. A total of three different motors are used. In contrast to the otherwise usual resistance control, due to the hydrostatic transmission, in conjunction with the variable displacement volume of the hydraulic motor, the rated power usage of the test rig can be reduced to 1/4 while maintaining the same test capacity. In particular, the displacement control allows, as a matter of principle, the recovery of a portion of the work stored in the deflected clutch.

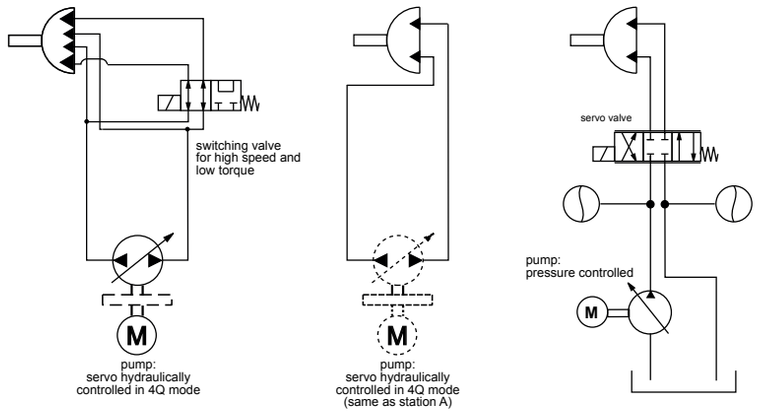
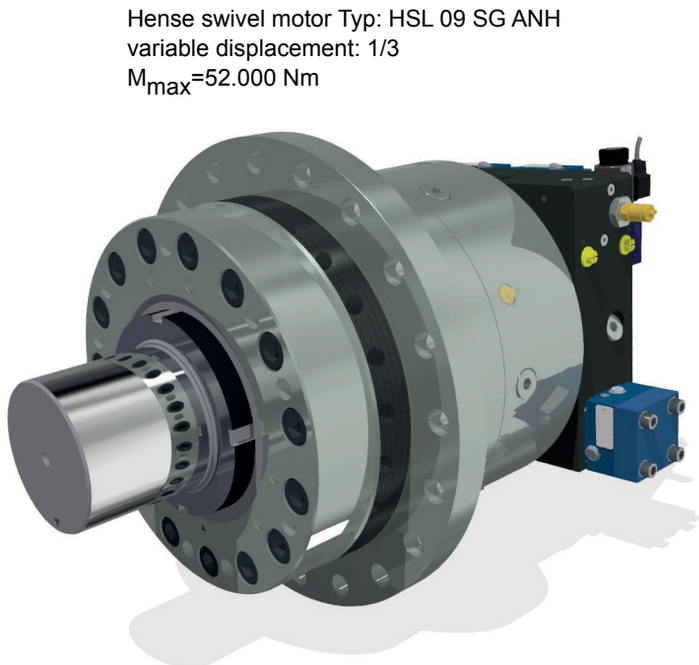


Figure 10: Hydraulic concept

As a special feature, the largest motor has a discrete variable displacement in order to be able to realize both the great moment for the preconditioning and a high adjustment speed for the measurement of the dynamic properties. The motor has three vanes, two of which can be switched off hydraulically via a switching valve. Due to the fact that the torque ratio from preconditioning to measuring is also approximately 1/3, this results in a dramatic reduction of peak supply power. The motor shaft support is realized with roller bearings to withstand high radial forces in high-speed mode. The motor was specially designed and built by the project partner Hense Systemtechnik GmbH & Co. KG who also delivered the two smaller motors.

[4]at two of the three stations



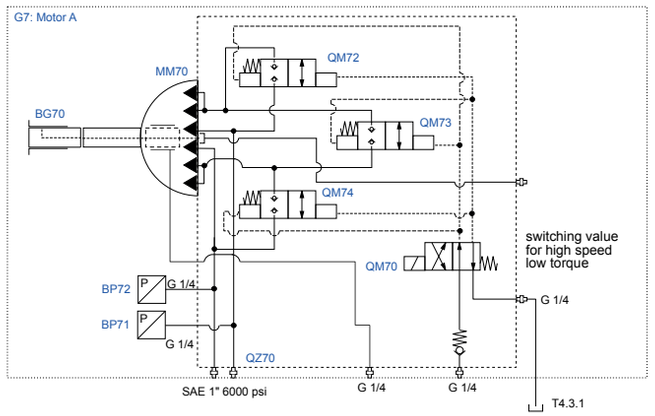


Figure 11: Swivel motor with adjustable displacement, Source: Hense

3.4 Clamping coupling

In comparison to the actual measuring time, the setup time is substantially longer. This means that for a quick coupling exchange the amount of screws needed to be reduced. For every test specimen a set of

adapters and hubs is delivered. The coupling is screwed, with help of the adapters, to the test bench and onto the hub. Torque transmission to the drive shaft is done over the hub which can be expanded hydraulically to transmit the torque via friction to the adapter. Pressure is supplied for this clamping system via a central hole in the motor shaft. Max clamping pressure is 700 bar. Figure 13 shows the setup for two different coupling types and a cross-sectional view of the clamping system.

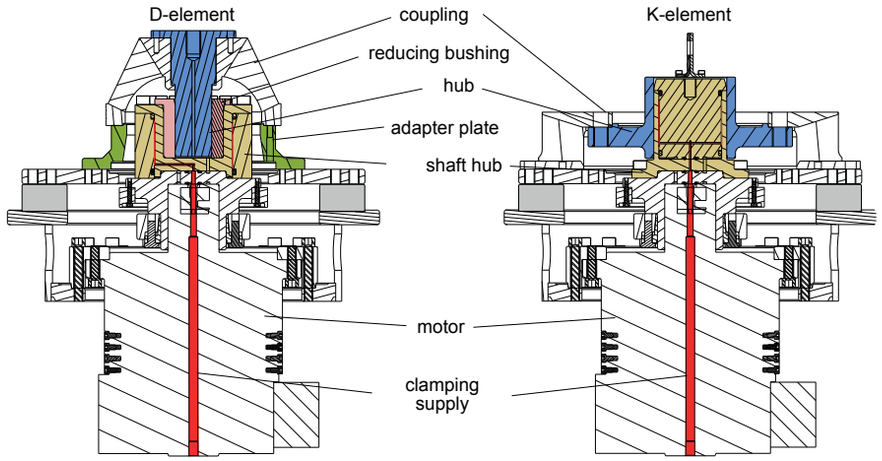


Figure 12: Cross-sectional view of the clamping system

The clamping system was designed according to Barlow's formula for thin-walled components with a comparative FEM calculation for two load cases to confirm the accuracy of the assumption. The design of the clamping system is an optimization problem with the parameters: wall thickness, clamping length, tolerances and required clamping pressure for a given torque and material parameters.

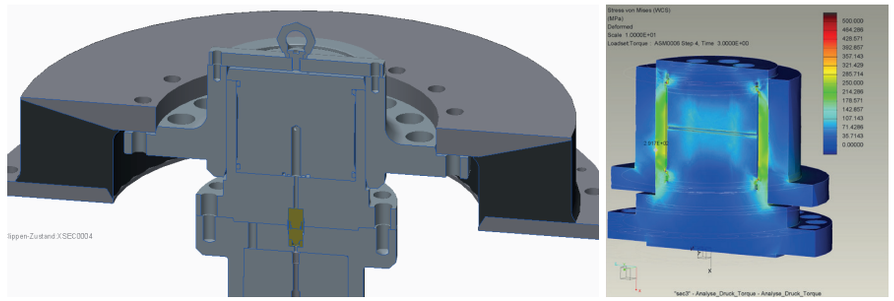


Figure 13: Clamping with FEM-Result

The following conditions have been used for the calculations:

- material: 42CrMo4
- max. allowable von Mises stress: 300 N/mm^2
- max. clamping pressure 700 bar
- tolerance between adapter and hub: H6-f6
- friction coefficient: 0.1

3.5 Test rig design

All three test stations are placed radially around a central column. This is also the housing for the hydraulic aggregate and the electrical cabinets. The test stations have transparent protection covers, which can be moved down and up for assembly and disassembly. Although the transparent covers are open at the top, they were designed to be at such a height that no one can access the test item during testing.

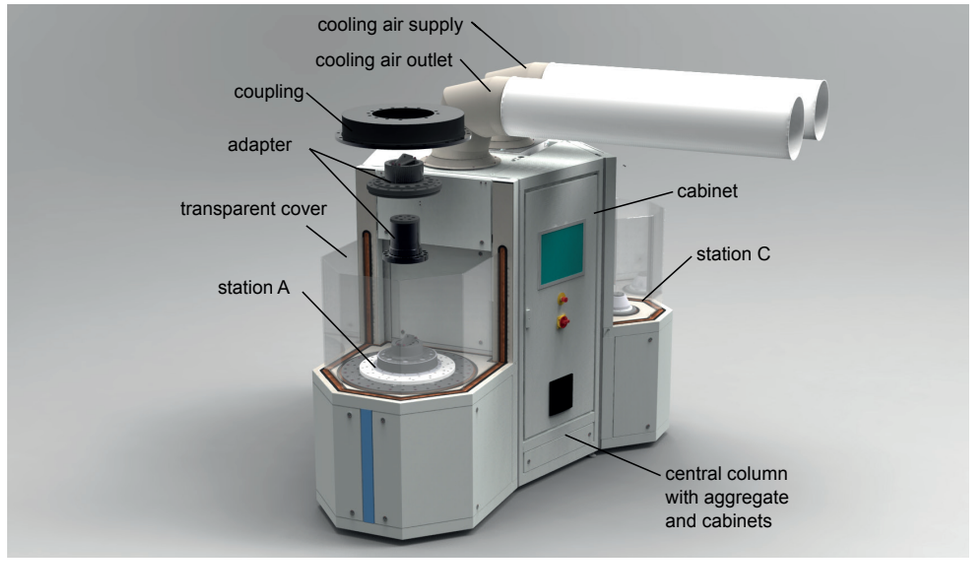


Figure 14: View of the test rig

The frame is made from welded steel profiles and all the doors and cover panels are equipped with sound insulation material to limit the noise emittance.

Figure 15 shows the steel contruction of the test rig.

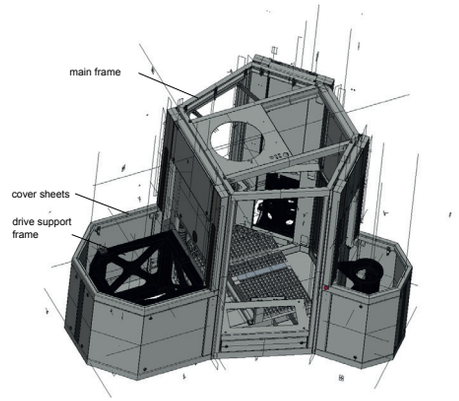


Figure 15: Steel frame

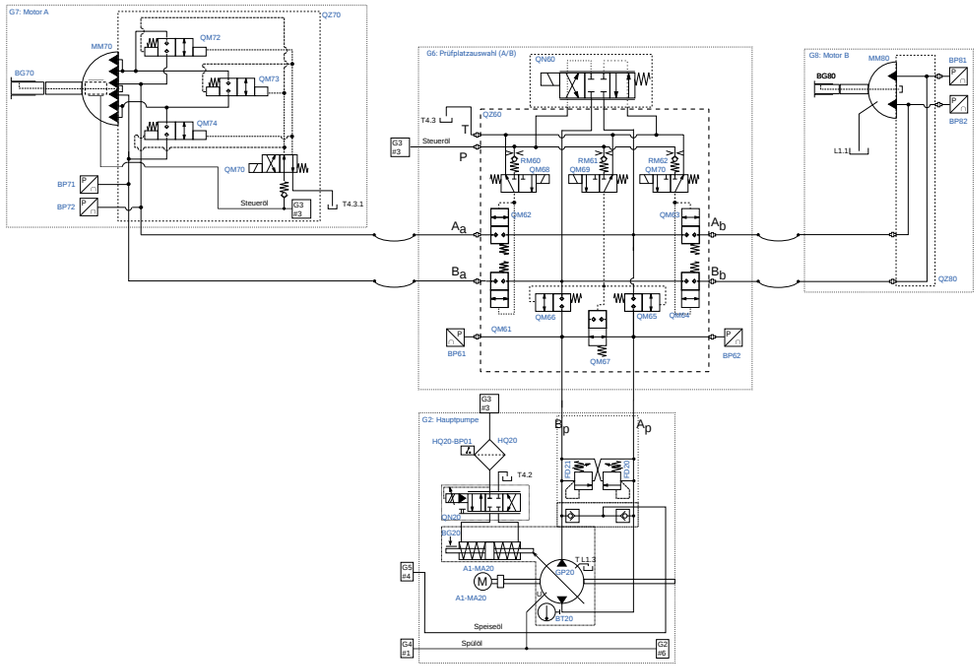


Figure 16: Main hydraulic circuit for station A/B

With the switching block (G6) the main pump can be connected to either motor A or B, which can only be operated alternately. This block also has a control valve for flushing the closed circuit. The variable displacement pump is controlled by a high flow servo valve which allows operation up to a frequency of 10 Hz.

Of course the hydraulic aggregate also has an additional feed oil supply circuit, a control oil circuit as well as a filter and cooling circuit. Details may not be addressed in the scope of this paper. Also, the hydraulic supply of the third motor for the small test station is not shown because this was realized conventionally as a servo-hydraulic axis.

3.6 Test evaluation

The base for the analysis is the time series of torque and angle as shown in figure 4. For evaluation the steady state at 10 Hz excitation is used.

Three different algorithms have been investigated for calculation of the coupling characteristics.

The **correlation method** is a quick and easy method to implement in order to calculate the frequency response for harmonically excited systems. This method is the best choice especially if only discrete frequencies are analyzed.

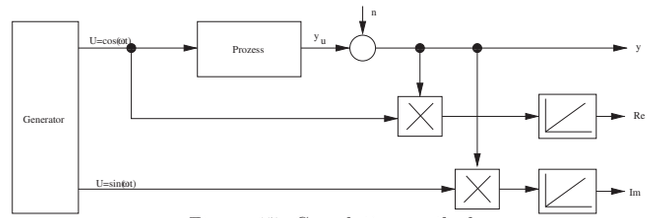


Figure 17: Correlation method

A stable, linear and time invariant system is excitated with a harmonic input signal.

$$u(t) = U \cdot cos(\omega \cdot t) \tag{5}$$

After a settling period the system output is also harmonic.

$$y_u(t) = Y_u \cdot cos(\omega \cdot t + \varphi) \tag{6}$$

Amplitude Y_u and phase shift φ can be picked directly from the frequency response

$$|G(j\omega)| = \frac{Y_u}{U} = \sqrt{Re^2 \cdot [G(j\omega)] + Im^2 \cdot [G(j\omega)]} \tag{7}$$

$$\varphi = arctan\left[\frac{Im[G(j\omega)]}{Re[G(j\omega)]}\right] \tag{8}$$

If the frequency response is calculated from torque to angle, the result for stiffness and damping are:

$$C = G(j\omega)\frac{1}{\sqrt{1+(\omega\varphi)^2}} \tag{9}$$

$$d = 2\pi\left[\frac{Im[G(j\omega)]}{Re[G(j\omega)]}\right] \tag{10}$$

To limit measurement errors it is necessary to integrate over a period of more than 10 cycles.

Another advantage of the correlation method is that it can be evaluated while the test is running. New results for stiffness and damping can be updated and displayed online.

With the **integration method** the area of the ellipse is geometrically integrated.

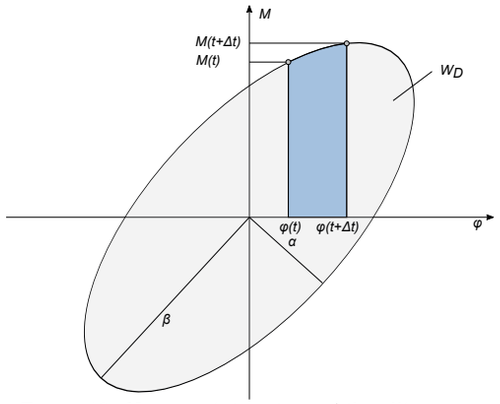


Figure 18: Numeric integration of the ellipse area

$$W_D = \oint M d\varphi \tag{11}$$

Elastic energy W (see figure: 3) can be calculated from the stiffness C, which can be evaluated via linear regression from the torque and angle reading.

In a third procedure a direct **approximation** of the ellipse is made via a regression method /4/. This procedure is well known and used in software-supported pattern recognition.

A comparison of all three methods can be seen in figure 19.

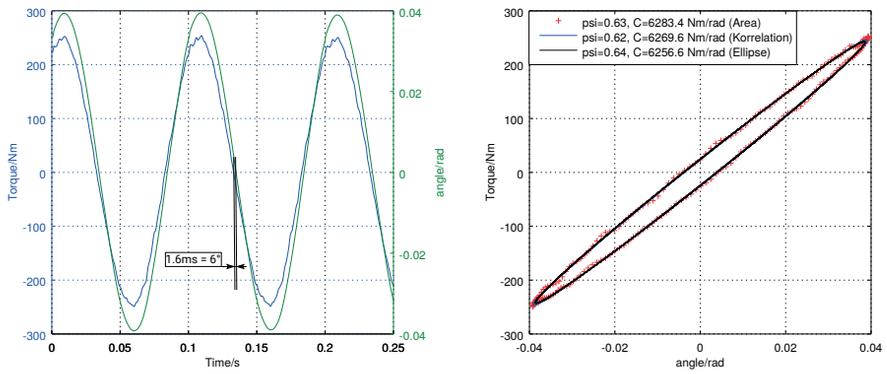


Figure 19: Comparison of three evaluation methods for stiffness and damping

All three methods evaluate the same results with linear material properties. This is as expected. There are differences if nonlinear material behaviour or real world influences of the test rig are present, resulting in degenerated ellipses. The maximum deviation from one another is about 10%. In accordance with the standard (DIN 740), the integration method is finally implemented into the test rig software.

3.6.1 Signal acquisition

Common coupling materials have damping properties in the range of d = 0.65 – 1.15. This results in a phase shift between torque and angle of about: 5.9° – 10.4° at a frequency of 10 Hz. Subsequently, this results in a time shift of 1.6 ms – 2.9 ms between torque and angle.

If the damping calculation is expected to be accurate within an error of 5%, the maximum allowed jitter or time shift between the signals must be smaller than 80 μs.

EtherLab /5/ is used as the automation system. The real time Ethernet: *EtherCAT* has the DC feature (distributed clocks), which can ensure that the jitter between individual samples of a channel, as well as between the channels themselves, is better than 1 μs. The angle signal is determined by a sin/cos encoder and the torque is measured via a signal amplifier with integrated A/D converter.

Both acquisition systems have unknown time shifts in the signal path, which is in the same dimensions than the allowed range. The actual time difference had to be determined by an experimental setup and is evaluated to 110 μs.

4 Summary

This paper presents a dynamic High-Torque Test Stand with hydrostatic drive technology used for production-related testing of elastomeric couplings. Aside from the properties of the test specimen, the hydraulic concept, detailed solutions, such as a torque sensor with end stops, a hydraulically operated clamping system, as well as the evaluation of the obtained measurement results are being addressed.

The test rig has been in operation, ensuring quality products, since April 2017.

References

[1] Murrenhoff, H. *Umdruck zur Vorlesung Servohydraulik*, RWTH Aachen, Germany 2012

[2] Betten Josef, *Zur Ermittlung der mechanischen Hysterese rheologischer Körper*, Zeitschrift für Naturforschung 27 a, Seite 718f., 1972

[3] Becker Markus, *Beanspruchungsgerechte Lebensdauerdimensionierung von dynamisch auf Drehschub belasteten Elastomerkupplungen*, 2006

[4] Radim Halíř, Jan Flusser, *Numerically stable direct Least Squares Fitting of Ellipses*, WSCG'98 Conf. Proc., Feb. 1998.

[5] Ingenieurgemeinschaft IgH, *EtherLab*, `www.etherlab.org`, 2006–2017

REVIEWED

Electro-Hydrostatic Drive Concept for the Ring Rolling Process

Ekhard Siemer*, Christoph Boes** and Ralf Bolik*

SMS group GmbH, Stockumer Str. 28, D-58453 Witten, Germany*
E-mail: ekhard.siemer@sms-group.com; ralf.bolik@sms-group.com
Moog GmbH, Hanns-Klemm-Str. 28, D-71034 Böblingen, Germany**
E-mail: cboes@moog.com

Rising electricity costs are forcing machine builders and plant operators to find solutions for how energy-intensive machines can be operated and produce more efficiently. Large potentials lie in the drive technology used. The example of the electro-hydrostatic drive concept for the ring rolling process demonstrates how a higher productivity with minimized power consumption and at the same time simplified and cost-effective installation brings competitive advantages. Together with Moog GmbH, SMS group GmbH has developed a new generation of ring rolling machine, the RAW ecompact, with a modern electro-hydrostatic drive concept.

Keywords: Power on demand, speed-controlled electro-hydrostatic drive, radial piston pump, ring rolling
Target audience: Industrial hydraulics, design process, metal forming industry

1 Motivation

“The most eco-friendly and cheapest kilowatt-hour is the one we don’t consume in the first place. And the more consciously and efficiently we use heat and electricity, the less we have to generate. That saves money, at the same time increasing the security of the supplies and contributing to us achieving our climate targets.” /1/

With this in mind, the German Federal government implemented the European Community’s ECO Design Directive 2009/32/EC with the act governing the ecodesign of energy-related products (Energy-related Products Act - EVPG). Whereas initially the primary goal was to reduce the energy consumption of hand-held tools such as circular saws, vacuum cleaners, lighting, etc., further product groups such as the ENTR5, machine tools, have now been added.

The SMS group’s answer to these demands from the market is EcoPlant Design. Criteria for an EcoPlant solution are the following four requirements:

- Significant reduction in the use of energy and process media
- Significant reduction in the use of raw materials
- Significant reduction in emissions
- Significant improvement in the recycling quota

As long ago as 1987, studies were conducted at the IFAS Aachen into reducing the energy losses of a conventional hydraulic system (throttle control) through the use of a direct pump drive (hydrostatic drive) (Figure 1). With the current pressure to save energy and the reduced costs of variable-speed drives, various suppliers have now come onto the market offering such components.

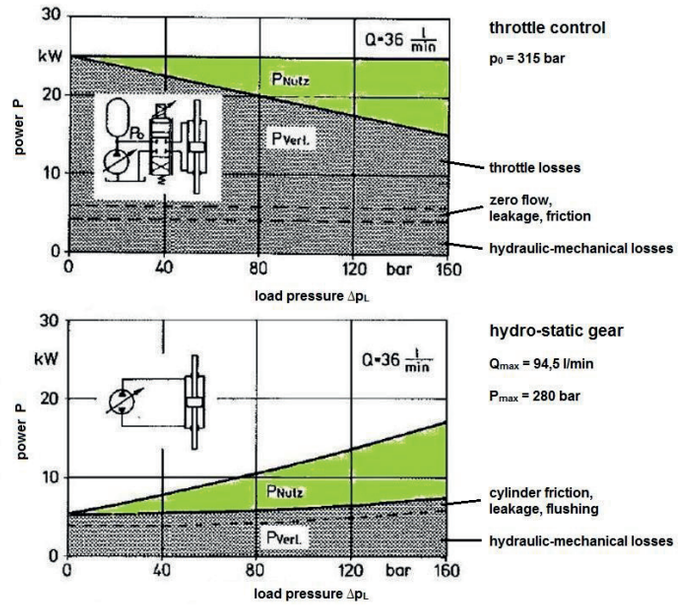


Figure 1: Performance of hydrostatic drives at constant volumetric flow /2/

2 R&D Goals

The goal was to develop a new series for a **RAW ecompact** radial-axial ring rolling machine that meets the SMS group criteria for an EcoPlant machine.

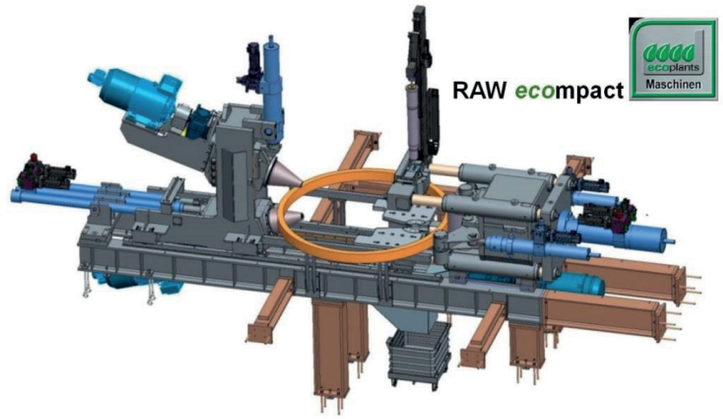


Figure 2: 3D View of the RAW ecompact machine series

The main objectives of this new development were

- Increased energy efficiency with process-related widely differing working points
- Drastically reduced central hydraulics and pipework in the field
- Cost optimisation through reduced erection and commissioning times
- Built-in condition monitoring

3 Ring Rolling Process

The ring rolling process (Figure 3) for the production of seamless rings is a very complex forming process with two roll gaps (radial and axial forming). By contrast with straight rolling, the infeeds change continuously. After a 360° ring rotation, the run-out geometry enters the roll gap again as the inlet geometry. The radial and axial roll gaps influence one another during rolling by changing the geometry of the rolled product. The very sensitive centering rollers ensure a stable rolling process. Due to the increase in the ring diameter, the axial stand has to be continuously repositioned.

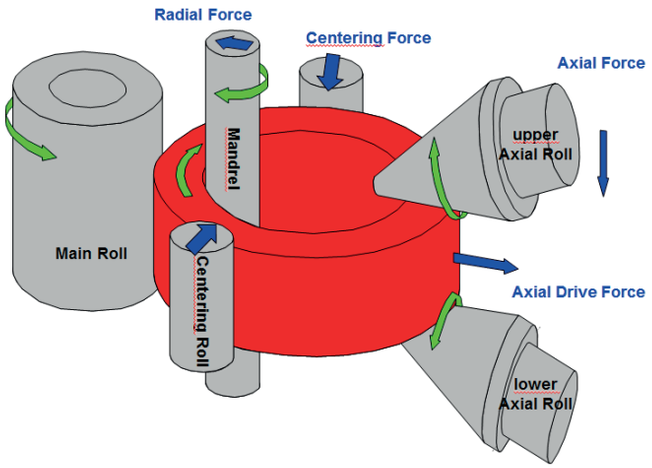


Figure 3: Principle of the ring rolling process

In addition to the main roll drives, there are up to 9 position or force-controlled axes that interact in parallel during the process. Traditionally these axes are designed as cylinder units with control valves that are supplied from a central hydraulic power pack.

4 Electro-Hydrostatic Drive Concept

Development of the new drive concept is based on the Moog electro-hydrostatic pump unit (EPU) product family. This unit consists of a dual-displacement radial piston pump with a maximum working pressure of 350 bar and a servo motor bolted to the pump by means of an adapter flange. These EPUs are available as a modular system, scalable from 19 ccm to 250 ccm (Figure 4).

Pump Vol. [cm³]	Q max [l/min]	p max [bar]
19	85	350
32	118	350
80	216	350
140	322	350
250	450	350



Figure 4: Moog EPU product family

The pump drive is optimised for variable-speed driving in 4-quadrant mode. There are no limitations in pressure-holding mode (high pressure with low volumetric flow). The pump is flanged directly to the servo motor without rubber or plastic coupling, resulting in both a reduction in costs and installation space and in an improvement in the dynamic behaviour. The drive concept selected here is based on a variable-speed pump drive with a douple rod cylinder (Figure 5).

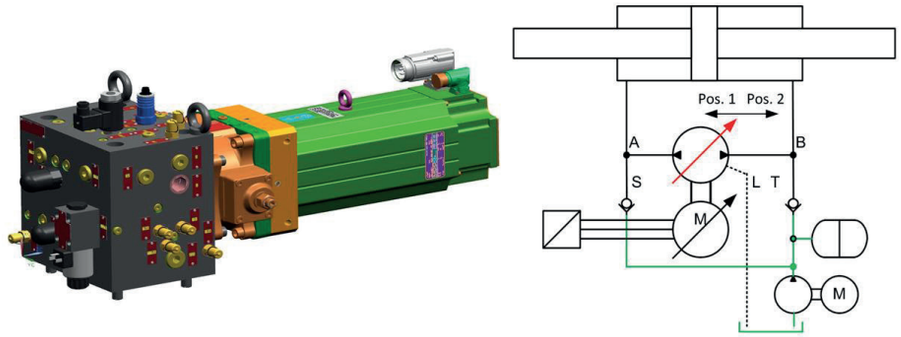


Figure 5: Electro-hydrostatic drive concept

All axes are centrally preloaded with approx. 10 bar (green lines) by a small, central hydraulic power pack. This unit serves at the same time to filter and cool the oil. The dual-displacement pump has two working positions: Position 1 with approx. 5 ccm displacement for rolling (max. 350 bar, 2000 rpm) and position 2 with 19 ccm displacement (max. pump delivery at max. 40 bar, 4400 rpm). The typical working points (torque over speed) are shown in Figure 6 for the “radial rolling force” axis.

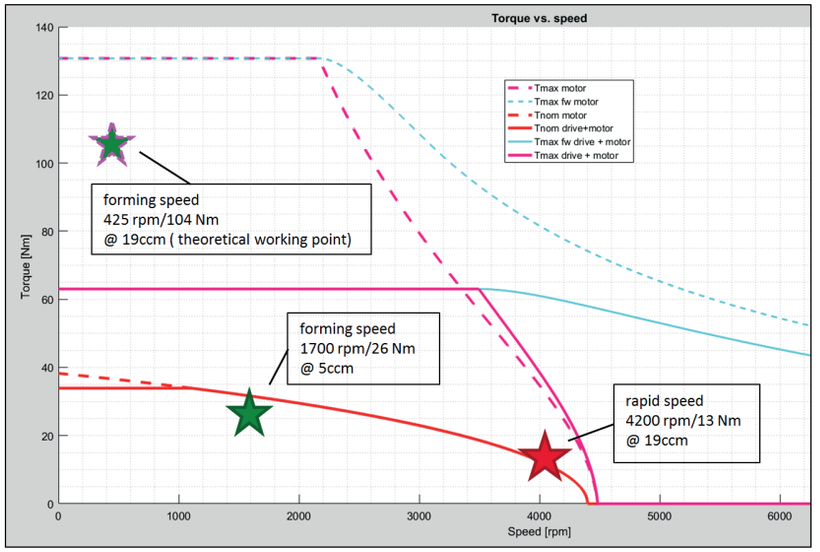


Figure 6: Typical working points of the drive unit

The term “rapid speed” corresponds to the opening and closing of the machine for loading and unloading, i.e. fast movements with low pressure. This point was set in the field weakening area of the motor above the S1 curve for continuous operation. The working point “forming speed” is below the curve for the rated torque (S1 mode for motor and converter), i.e. it can function under continuous load. If the displacement of the pump were not variable (e.g. a constant displacement pump with 19 ccm), this point would lie above the maximum torque curve (S3 intermittent duty, max. 10 sec overload) and would therefore be inadmissible for the rolling process. In this case a more powerful motor and converter would have to be used, leading to higher costs.

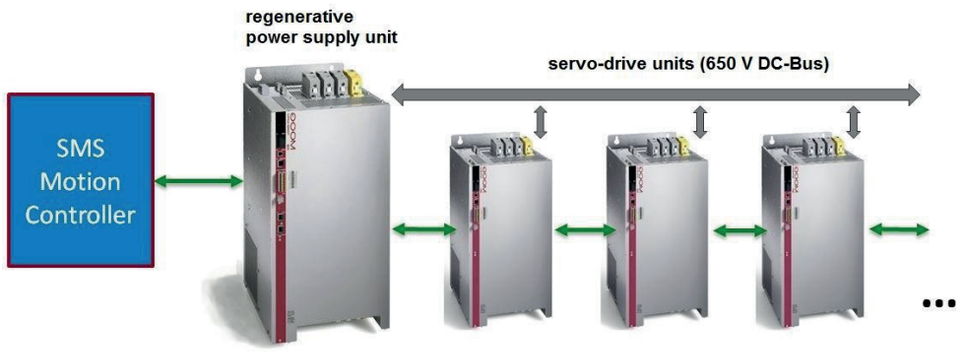


Figure 7: Communication structure of drive system

The servo drives of each EPU are powered by a regenerative power supply unit (PSU) via a 650 V DC bus (Figure 7). Communication is via an EtherCat field bus. The PSU and the drives operate as EtherCat slaves in closed loop. The motion controller as master performs the process control for the position and force control of the axes and transmits the speed settings digitally to the drives (Figure 8). The speed control for the servo motors is realized in the drives. The current process values, such as speed, current, power, temperature, etc. are feed back into the motion controller.

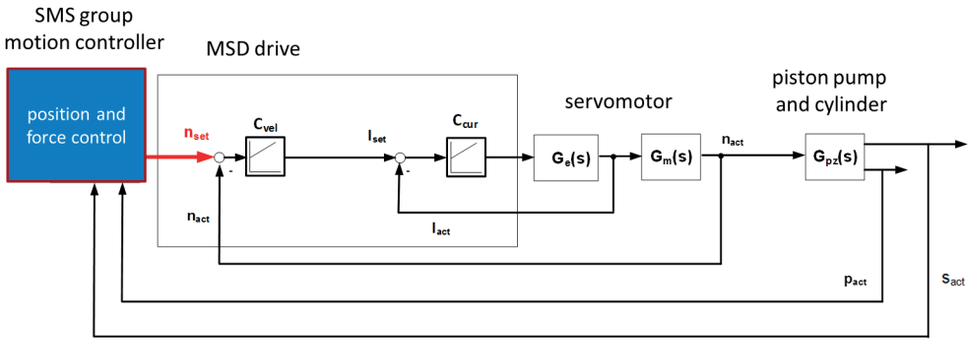


Figure 8: Structure of closed-loop control (simplified)

5 First Results and Feedback

Figure 9 shows a typical production cycle for the ring rolling process. After loading of the ring rolling machine with a pierced blank, the machine is closed to rolling position under no load at rapid traverse speed. The rolling process starts. The rolling forces are then set by the process according to the geometry and weight of the ring. If power or torque limits are reached, the roll feeds are reduced by the process controller so that rolling can be performed continuously in the limit range of the drives (S1 mode). The end of the rolling process is generally followed by a calibration phase in order to reliably achieve the ring dimensional tolerances, such as outside diameter or ovality. All the axes are then retracted to the unloading position at rapid traverse speed. Due to the extremely high pump speeds of up to 4500 rpm (”swirl effect”), the overall efficiency at rapid traverse speed is less than 20%. For the rolling process we achieve an overall efficiency of 40 to 50% even under partial load. This value corresponds to the expectations shown in Figure 1.

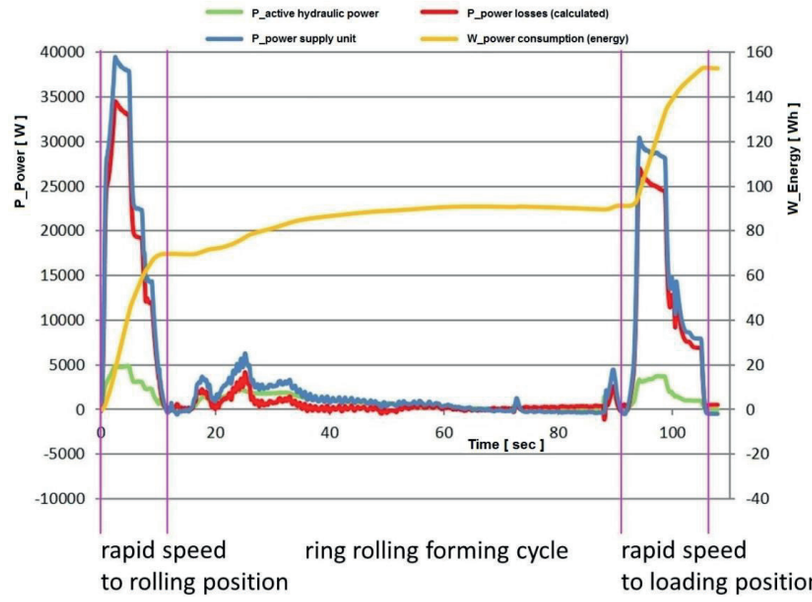


Figure 9: Typical production cycle for the ring rolling process /3/

A further critical point is the influence of pressure pulsation on the control quality of the axes. The pressure pulsation is caused by the physics of the radial piston pump and the speed of the drive (Figure 10).

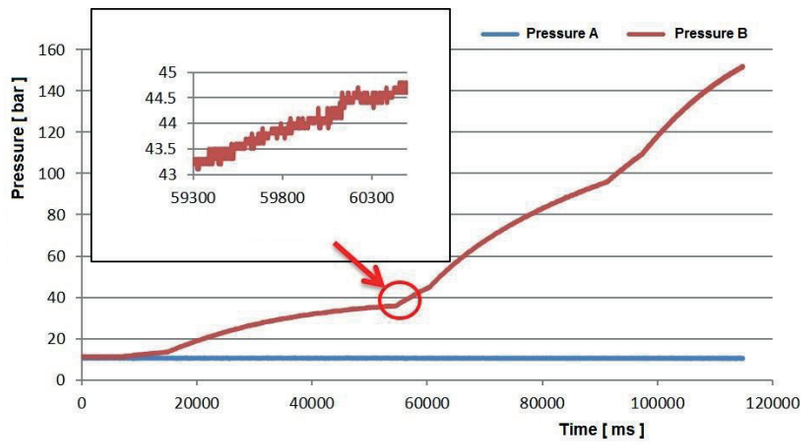


Figure 10: Measurement of the pressure pulsation /3/

Due to the friction in the cylinder and the relatively large oil volume of the cylinder in relation to the pump volume, the damping of the pressure pulsation is sufficient to allow the required positioning accuracy of +/- 0.1 mm at the end of rolling to be achieved (Figure 11). At rapid traverse speed, a positioning accuracy of approx. +/- 0.8 mm was achieved.

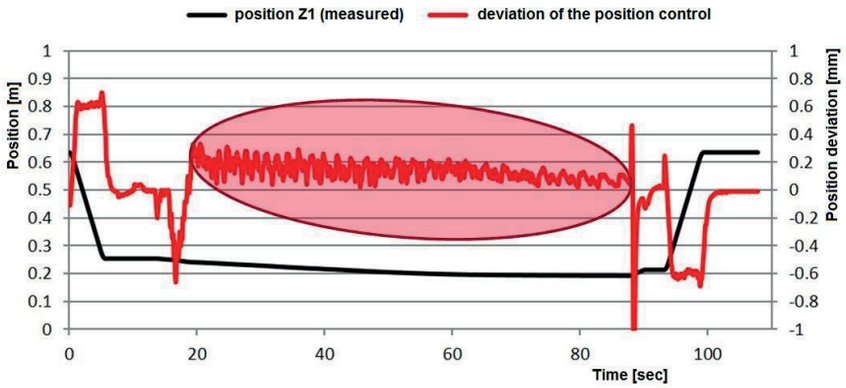


Figure 11: Measurement of the positioning accuracy /3/

The temperature behaviour plays an important role for the selection and dimensioning of the drive motor. The very compact design and the direct connection of the pump to the servo motor make a theoretical calculation of the temperature behaviour very difficult. Furthermore, the temperature of the motor is greatly influenced by the ambient temperature (hot forming) and the working cycle. In order to keep the drive concept as simple as possible, a purely convection-cooled motor was chosen for the design. Figure 12 shows the measured temperature behaviour of the servo motor in pressure holding mode (approx. 80 bar at 220 rpm, 7 Nm). For high-load applications with very short cycle times, water cooling can be used as an option for the motor.

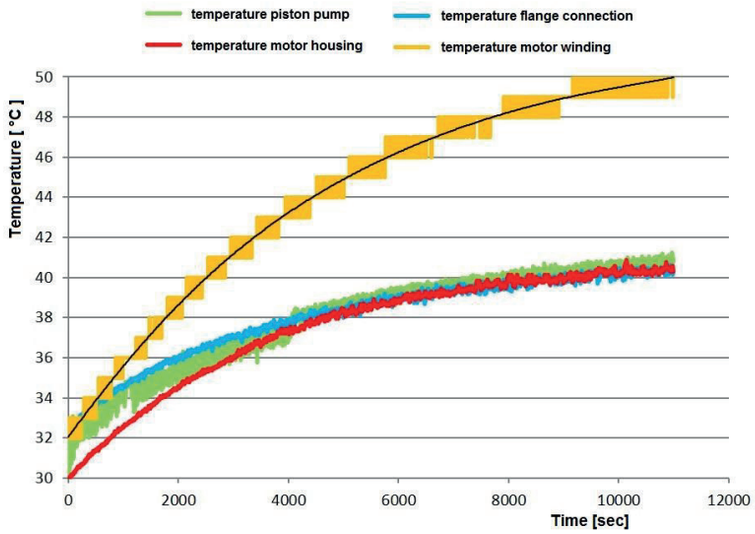


Figure 12: Temperature behaviour during pressure holding mode (80 bar, 220 rpm) /3/

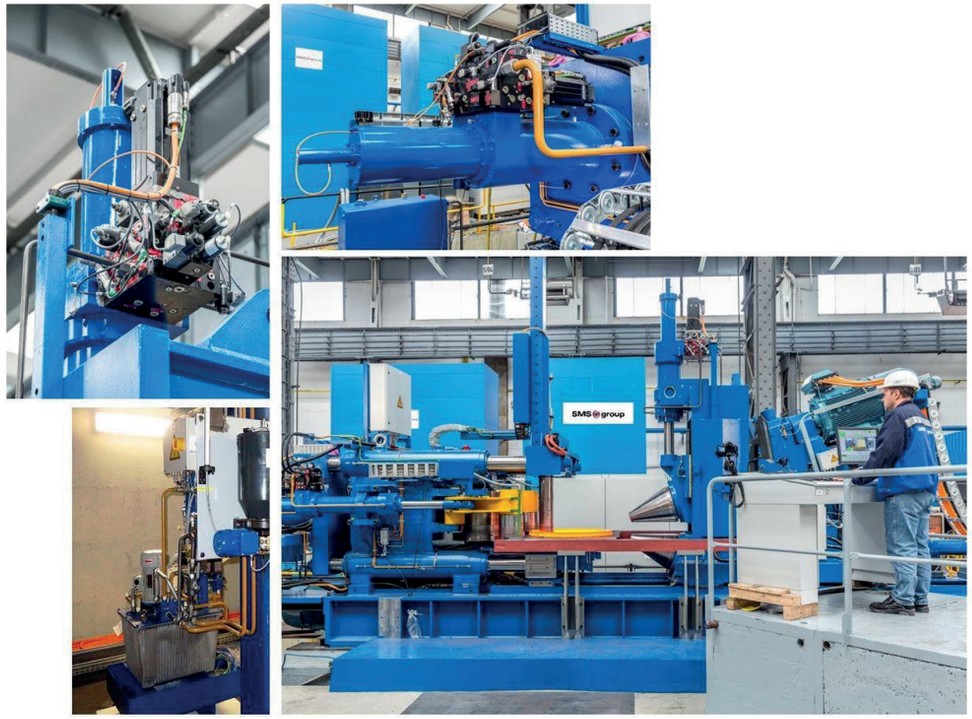


Figure 13: Ring Rolling Mill RAW ecompact, SMS group GmbH

The benefits of the electro-hydrostatic compact drives can therefore be summarised as follows:

- The basic design of the machines can remain unchanged
- Installed power is approx. 60% of the standard hydraulics (230 kW → 137.5 kW)
- Reduced oil volume in the machine (2000 litres → 200 litres)
- Reduced noise level thanks to “power on demand”
- Elimination of the hydraulics room → reduced demands on the foundation
- Significantly reduced piping work → simpler erection
- No flushing necessary at the erection site → commissioning times reduced by approx. 3 days
- Reduced number of components → reduced maintenance work
- Test operation before delivery possible
- Safety: Thanks to the modern converter technologies with SS1 (Safe Stop 1), STO (Safe Torque Off) and SLS (Safely Limited Speed), compliance with the Machinery Directive is easier than with conventional hydraulics.

The first experience with the electro-hydrostatic compact drives shows outstanding controllability (position and force) of the axes. The reduced number of components results in a very sturdy and fault-resistant system. The lowering of the energy consumption by up to 70% and the reduction in the noise emissions by approx. 30% make the machine an environment-friendly EcoPlant.

References

/1/ Federal Ministry for Economic Affairs and Energy, BMWi

/2/ Backé, W.; Berbuer, J., Neue Schaltungskonzepte für hydrostatische Getriebe (New circuit concepts for hydrostatic drives), o+p ölhydraulik und pneumatik 31, (1987), No. 6

/3/ Dany, S.; Masterarbeit “Untersuchung an einer elektrohydraulischen Achse für Ringwalzanlagen” (Study on an electro-hydraulic axis for ring rolling machines), IFAS RWTH Aachen, October 2016.

Systematic Data Analysis for Optimal System Design

Milos Vukovic*, Johannes Schmitz* and Jiayin Zhou*

Linde Hydraulics GmbH & Co. KG, Wailandstraße 13, D-63741 Aschaffenburg, Germany*
E-Mail: Milos.Vukovic@linde-hydraulics.com

As part of the trend towards greater digitalization the number of sensors installed in mobile machinery is increasing each year. OEMs are consequently now capable of collecting large amounts of component measurement data, which they unfortunately do not have time to analyze or are not capable of interpreting. This is quite a pity, because when used in the right way such information can be used to develop a much better understanding of the machine and to develop new systems with lower fuel consumption and improved performance. The following paper introduces an approach used at Linde Hydraulics to analyse and assess large amounts of data with the goal of systematically identifying potential and designing new and improved hydraulic systems.

Keywords: Mobile hydraulics, excavators, data analysis, system optimization
Target audience: Mobile machine manufacturers

1 Introduction

When an OEM decides to bring a new excavator to the market, the design of the machine is usually based on that of the previous generation. Rarely, is such a development started from scratch. In order to decide which changes should be made to the hydraulic system, OEMs need a fast and systematic approach to not only analyze but also optimize the hydraulics. Judging the effect of small changes on performance and fuel consumption is not simple, as the physical relations are all highly nonlinear /1,2/. Such effects are even more pronounced when the interfaces between the individual subsystems are changed, for example the diesel engine or the kinematics. Performing real-life tests with different machine setups is far too time and cost intensive. Only an approach based on data analysis coupled with system simulations is feasible. This paper presents an overview of the approach used at Linde Hydraulics to quickly and effectively help OEMs find and define a hydraulic system that meets their requirements.

The approach is shown in Figure 1 and can be summarized as follows. To begin with, measurements of the typical duty cycles are collected. The measurement data must include hydraulic actuator pressures, actuator displacements (cylinder translation and swing rotation), pump pressures and the joystick commands. Using this data, the flow of power through the machine and the location and extent of the individual loss mechanisms are determined and visualized in a series of histograms, allowing a more systematic and intuitive interpretation of the data. This analysis is followed by a simplified system simulation of the machine. A major advantage of the simulation is that it provides access to pressures and flow rates throughout the whole machine that are not included in the measurement data. With this additional information it is possible to systematically change individual components and test different system configurations.

The paper begins by introducing the reference machine as well as the dataset used for the analysis and then goes on to explain how the measurement data is post processed and interpreted. This is followed by a discussion of the simulation approach used to create a model of the reference system, which will serve as a benchmark for all further steps. The ability of this model is then demonstrated by using it to evaluate the fuel consumption of an optimized hydraulic system and compare it to the reference system.

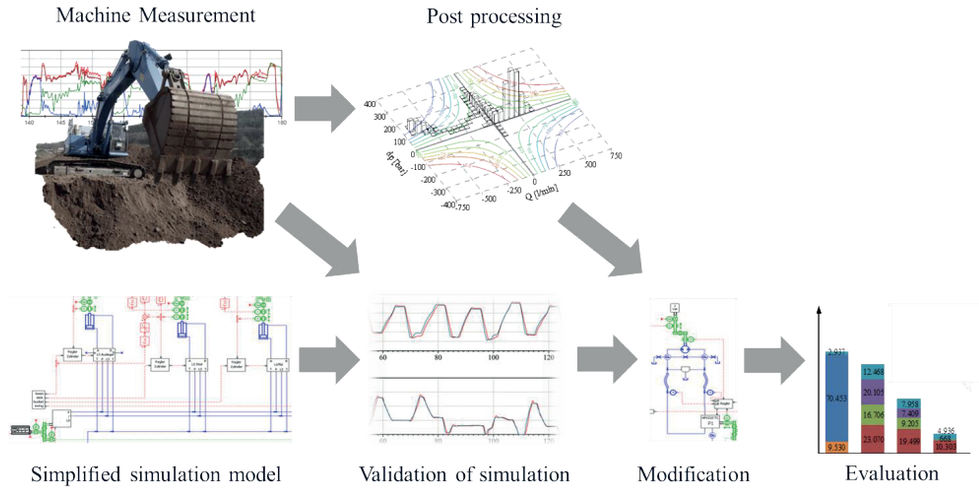


Figure 1: Approach based on data analysis and simplified system simulation

2 Example Dataset

To illustrate the approach, exemplary measurement data obtained from a 36 t crawler excavator with a single circuit Linde Load Sensing Control (LSC) hydraulic system are analyzed /4/. The hydraulic setup of the machine's implement system is shown in Figure 2. The cylinders (boom, arm and bucket) are controlled using valves with downstream pressure compensators. To ensure the swing is always supplied with oil an upstream compensator is used for this actuator. For clarity the figure does not show the compensators.

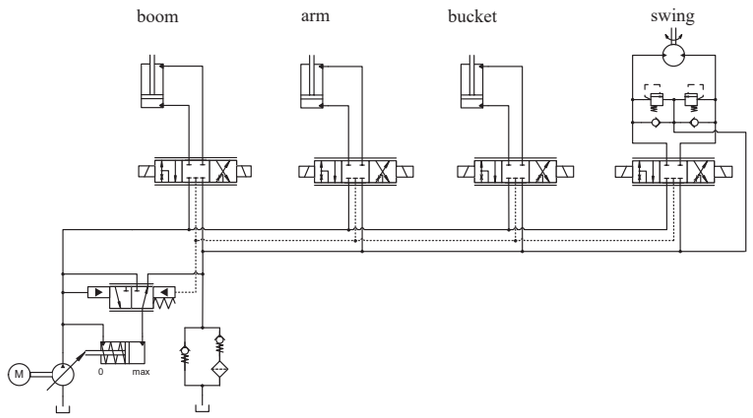


Figure 2: Hydraulic schematic

Although this machine is used for a variety of tasks, the paper will focus on data obtained from measurements of a 90° dig and dump cycle. An extract of the data is shown in Figure 3. The data includes measurements of the pump pressure, load sensing pressure, actuator chamber pressures as well as actuator displacements. Due to the large number of signals and their dynamic nature, evaluating system efficiency by just looking at the data as a function of time proves difficult /2,3/. In order to interpret the measurements and draw meaningful conclusions, the data must be postprocessed.

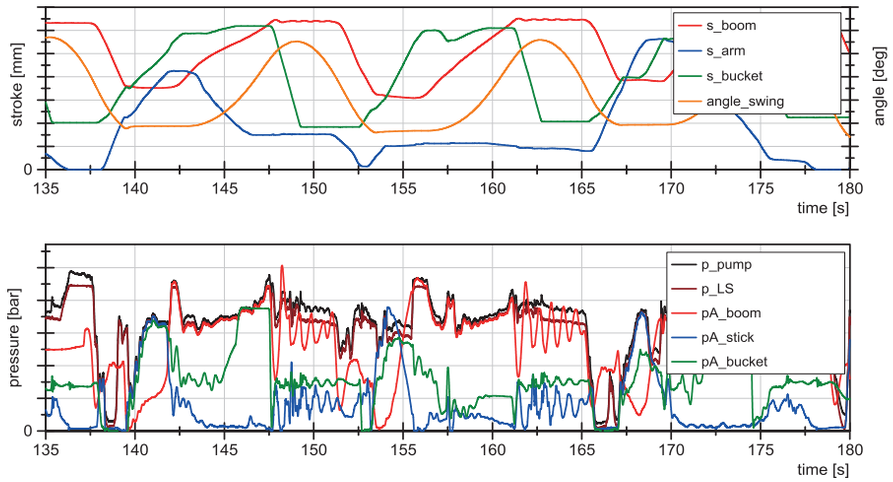


Figure 3: Extract of measurement data

3 Post Processing of Measurement Data

In a single circuit valve controlled hydraulic system, the major source of losses is the throttling across the metering edges due to differences between the supply pressure and load pressure of the individual actuators. By post-processing the measurement data the extent of these throttling losses can be visualized and quantified. The approach is explained in Figure 4. Instead of looking at the data as a function of time, the state of each actuator is described by showing the load pressure p_L as a function of load flow Q. The blue area enclosed by any point in the plane describes the amount of power, $P = p_L\, Q$, required to move an actuator or the amount of power that an actuator can release back into the hydraulic system. In quadrants one and three, the actuator has to be supplied with flow in order to overcome the load force, which opposes the direction of motion. In contrast, during operation in quadrants two and four the load force assists the motion and pressurized oil can be redirected back into the system.

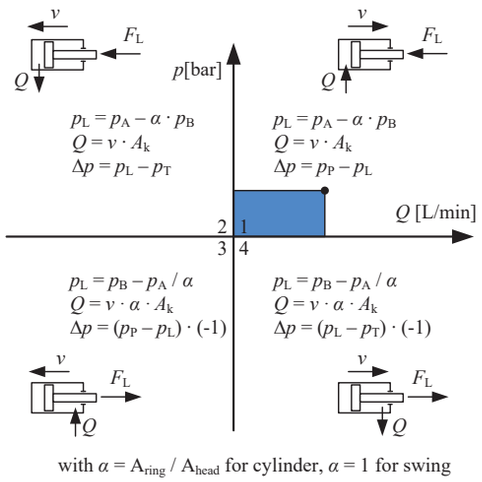


Figure 4: Definition of load pressure and load flow

To quantify the throttling losses Δp that occur when supplying an actuator with flow in quadrants 1 and 3, the difference between the pump pressure p_P and load pressure p_L has to be considered. The grey area shown in Figure 5 shows the power dissipated due to throttling. In quadrants 2 and 4, Δp is defined differently and describes the pressure drop between the actuator and tank, not between the pump and actuator. The grey area in these two quadrants is the recoverable energy that is throttled across the tank metering edge.

Due to their two dimensional nature, Figures (a) and (b) cannot be used to judge how often each operating point occurs. A third temporal dimension is, therefore, added to the diagram. The resulting columns in the histogram illustrate the frequency of occurrence of the individual points of operation, see Figure 5 (c).

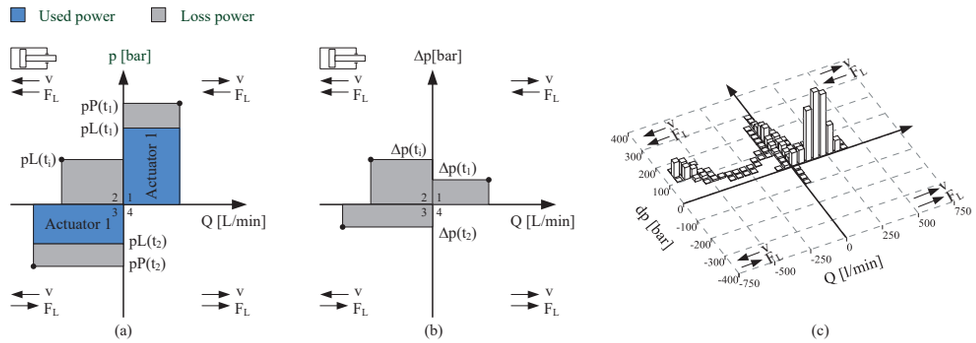


Figure 5: Analysis of load pressures and throttling losses

Using this procedure, measurement data from a dig and dump cycle is analyzed. Figure 6 shows the resulting histogram for the boom actuator. In order to judge the magnitude of the losses, constant power hyperbolas are added to the diagram. The losses occurring in quadrant 1 are all below 25 kW, indicating that the boom lifting motion is quite efficient. A look at quadrant 2 indicates that approximately 150 kW of power are dissipated across the tank metering edge during boom lowering. This recoverable energy comes in the form of a medium pressure, between 100 and 200 bar, and a high flow rate, more than 500 l/min, making it technically challenging to recover and reuse boom potential energy.

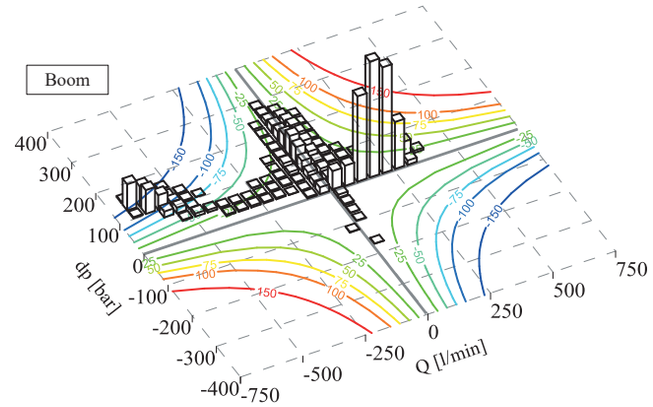


Figure 6: Throttling loss histogram of boom actuator

The histograms for all the actuators are shown in Figure 7. Regions with high losses are highlighted in red. These include swing braking in quadrants 2 and 4 and as already mentioned boom lowering in quadrant 2. The bottom

left diagram indicates that up to 150 kW of power are throttled during bucket dump motion. This is due to the large flow of approximately 500 L/min passing through the A-T metering edge.

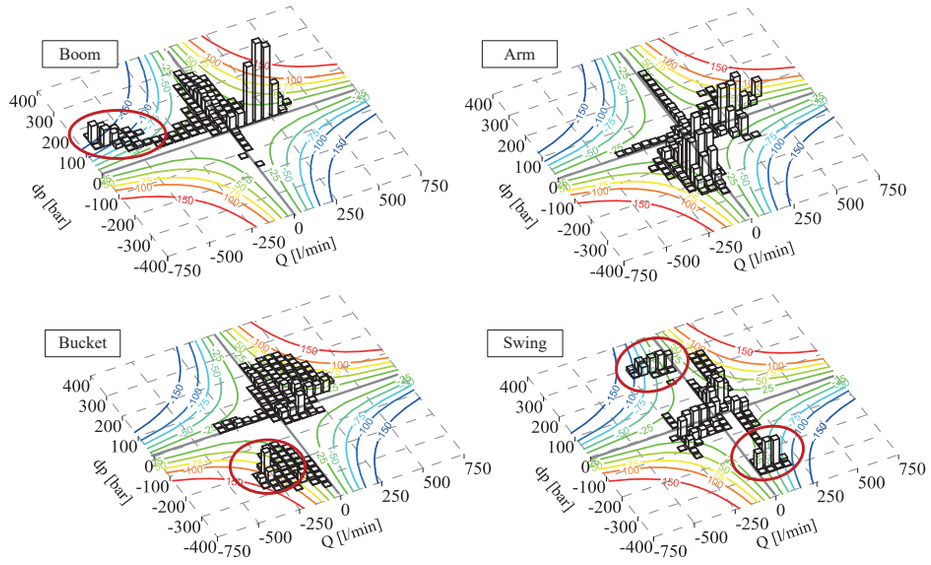


Figure 7: Delta p histograms of all actuators

4 Setup and Validation of Simplified Simulation Model

In the next step, a simulation model of the machine is created in AMESim. As shown in Figure 8, the model includes a diesel engine, hydraulic pump, main control valve and hydraulic actuators (bucket, arm, boom and swing).

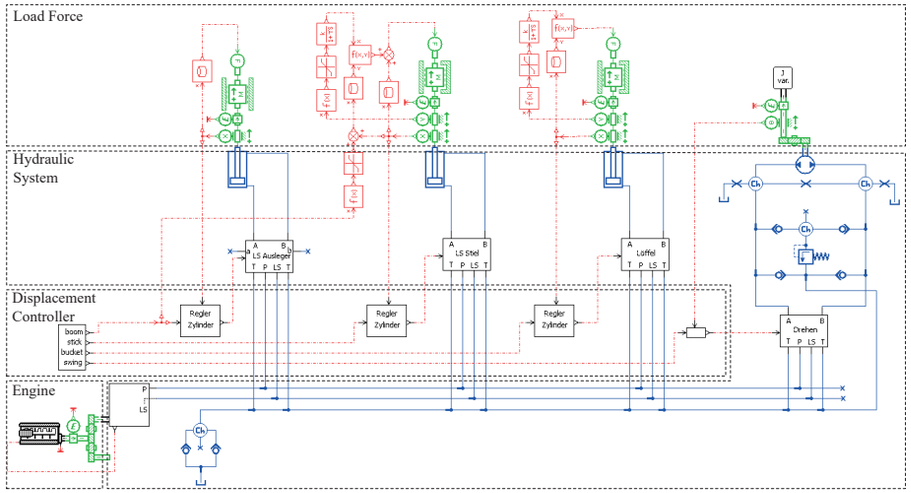


Figure 8: Simulation model of machine in AMESim

To replicate the actuator motion in the measurements usually only the measured pilot pressures are applied to the hydraulic valves in the model. This method unfortunately usually leads to large discrepancies between simulation and measurements, as it is difficult to capture the exact flow characteristics of each valve metering edge. To ensure the actuators closely follow the same trajectories as in the measurements, a closed loop displacement controller takes on the role of the "machine operator". Figure 9 illustrates the ability of such a controller to accurately follow the measured actuator displacements.

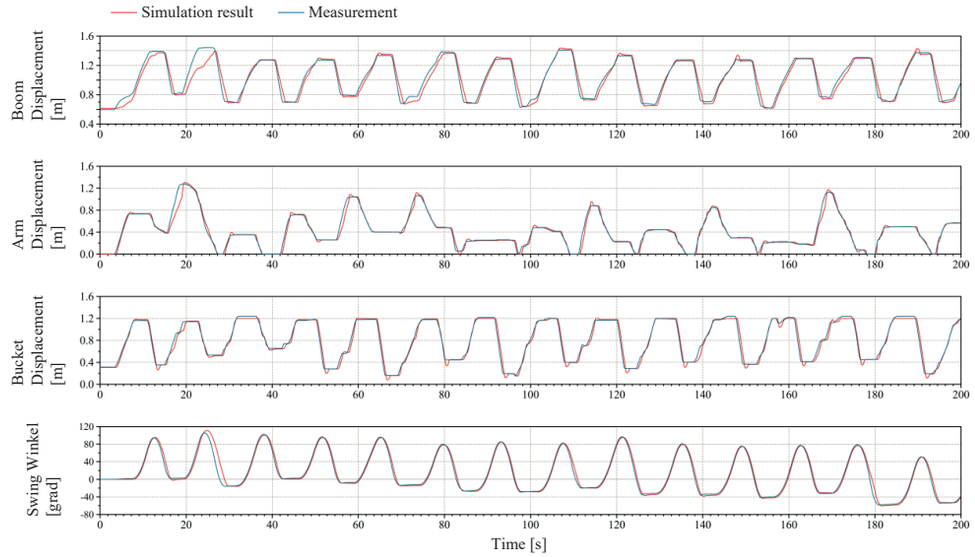


Figure 9: Validation of the closed loop displacement controller

A closer look at Figure 8 reveals that only the swing drive is connected to an inertial mass as in the real machine. To avoid long simulation times, no kinematic structure with inertia is used for the other actuators. The load is artificially created by applying the measured load forces to the individual actuators externally. Instead of applying the force only as a function of time, $F_L(t)$, the measurement data is used to create an averaged look-up table that applies the force as a function of actuator displacement, $F_L(x)$. This ensures that the correct force is applied even when the simulated and measured displacements do not match exactly. A closer analysis of the measurement data reveals that the arm load force is also a function of the boom actuator position, therefore a combination of two lookup tables is used for the arm $F_L(x_{Boom}, x_{Arm})$. A comparison of the measured and simulated load forces is shown in Figure 10.

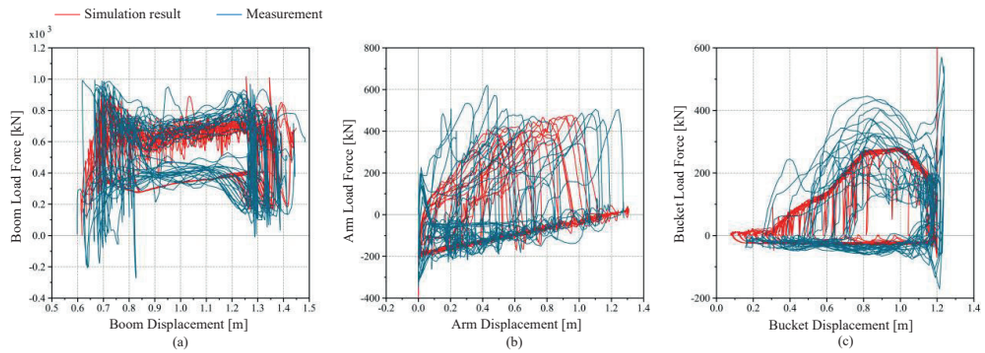


Figure 10: Comparison of the measured and simulated load forces

Figure 11 shows the histograms obtained from the simulation model. These show good agreement with the measurement results in Figure 7. The model is therefore validated and can be used to analyze and answer a whole range of questions. In contrast to the measurements, it is now possible to look at the pressures and flow rates throughout the whole system and not only at the locations where sensors are installed. The validated model is used as a reference to judge all further optimizations and system architectures.

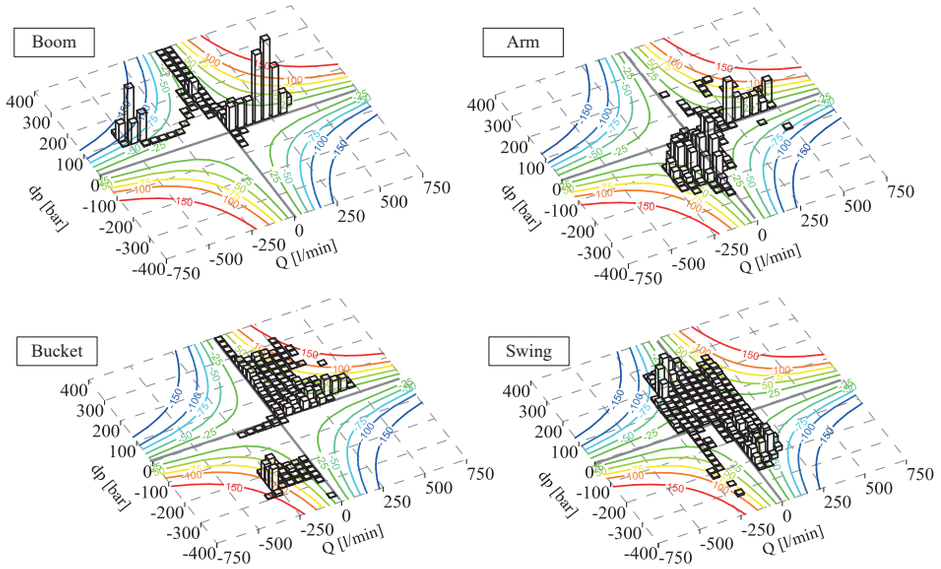


Figure 11: Simulated delta p histograms of all actuators

5 Optimized System Architecture

The simulation model can also be used to judge the energy saving potential and performance of new system configurations. The circuit shown in Figure 12 is used as an example.

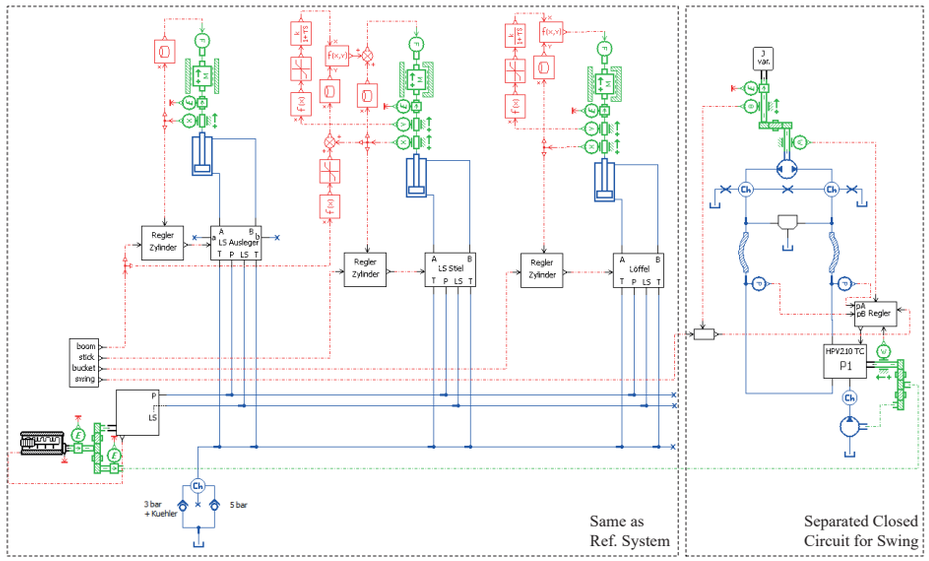


Figure 12: 1,5 circuit load sensing system

The setup is referred to as a 1,5 circuit LS system, which is basically a single circuit load sensing circuit with a closed loop swing. The advantages of the modified circuit are that a separate closed loop pump supplies the swing actuator with flow, thereby reducing throttling losses and enabling energy recovery across the engine shaft during swing braking.

Histograms of the optimized system are shown in Figure 13. Compared to Figure 11, the first major difference is the distribution of operating points for the swing. As is expected, no throttling occurs in swing quadrants two and four.

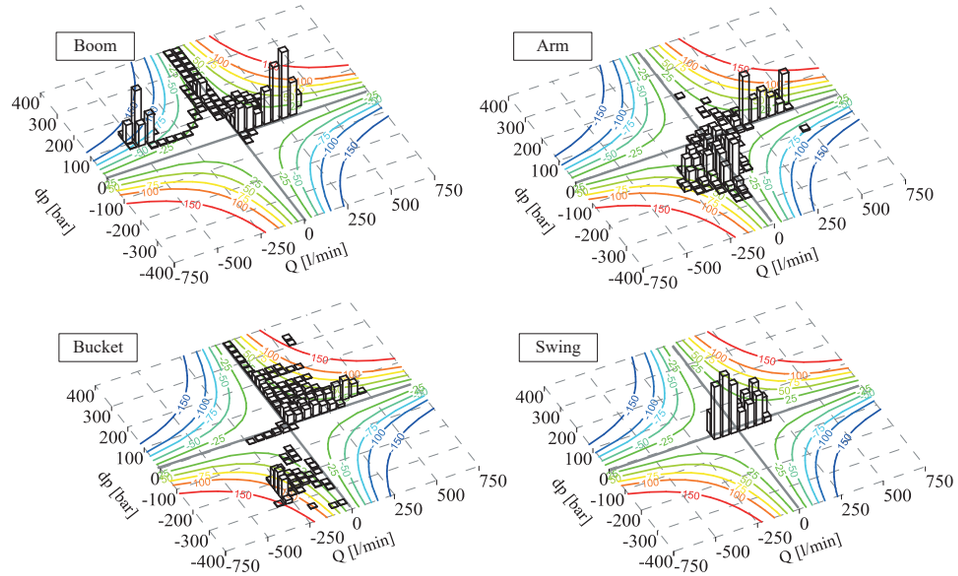


Figure 13: Simulated delta p histograms of optimized system

6 Simulation Results

An overview of the energy distribution of the reference system for a 90° dig and dump cycle is shown in Figure 14 (a). More than 260.000 kWs of energy in the form of diesel fuel enter the system. Due to the low efficiency of the internal combustion engine, only 33 % of this energy is converted into mechanical power (86.371 kWs). Another 4 % (11.967 kWs) is lost as the pump converts the incoming mechanical power across the shaft to hydraulic power, which is then sent to the main control valve. After throttling a further 12 % is dissipated, meaning that only 43.089 kWs actually reach the actuators. Approximately 36 % of this actuator energy never really leaves the machine because it is used to raise the boom and accelerate the swing, meaning that it can in fact be recovered during boom lowering and swing braking. In total, a mere 27.468 kWs or 11 % of the total incoming diesel energy is actually used to perform work on the surroundings and objects in contact with the machine.

Figure 14 (b) illustrates a more detailed distribution of the hydraulic power among the individual actuators. The main control valve delivers the most energy to the boom and bucket actuators, both approximately 21.000 kWs, followed by the swing and arm, both around 15.000 kWs. Very little energy is lost across the boom valve, as its load pressure is usually the highest in the system. Due to their lower pressure levels, only half the energy passing through the swing and arm valves actually reaches the actuator. Worst of all, only about a third of energy passing

through the bucket spool actually reaches the bucket cylinder. This is one of the major disadvantages of a single circuit system, in which only one supply pressure is available.

A look at the negative actuator energy column in the figure reveals that approximately half of the energy used to raise the boom and more than 60 % of the energy used to accelerate the swing can be recovered during lowering and braking. Because the reference system is not capable of recovery or recuperation, this energy is dissipated as heat across the valves.

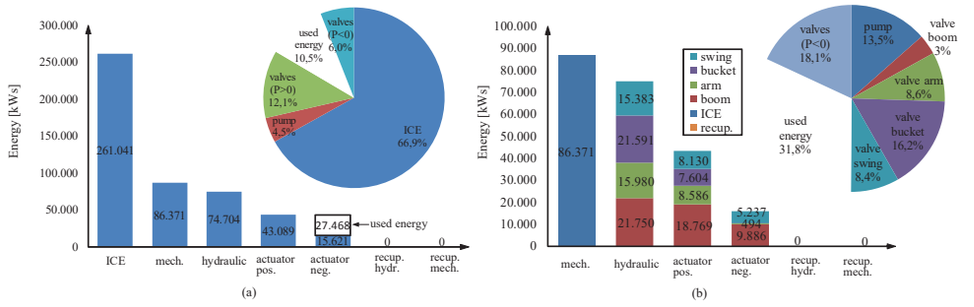


Figure 14: (a) Energy flow through reference system; (b) Energy consumption of individual actuators

Figure 15 shows the analysis for the optimized system with a closed loop swing architecture. A first look confirms that for the same cycle the optimized system consumes less fuel than the reference system, 247.575 kWs compared to 261.041 kWs. The total system efficiency increases from 10,5 % to 11,2 %. Using the closed loop swing 3.854 kWs of the available 4.936 kWs are recuperated during braking. Due to the efficiency losses in the displacement unit, only 2.937 kWs of mechanical energy actually reach the shaft. Because the other three actuators (boom, arm and bucket) are still connected to one pump, the throttling losses are comparable to those of the reference system.

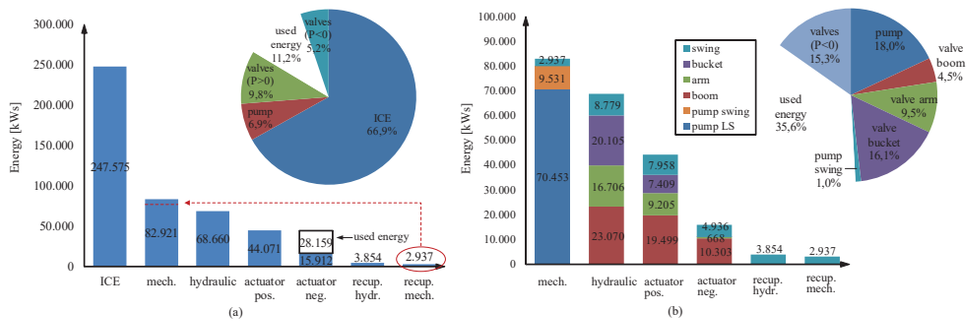


Figure 15: (a) Energy flow through optimized system; (b) Energy consumption of individual actuators

As the performed work for two the configurations is not identical, it makes sense to compare the relative fuel consumption [mL/kWs] and not only the absolute fuel consumption. These values are summarized in Table 1. The optimized circuit lowers the relative fuel consumption from 0,254 mL/kWs down to 0,235 mL/kWs, which is an improvement of 7,5 %.

	Reference system	Separated closed circuit for swing
Performed work [kWs]	27.468	28.159
Consumed fuel [L]	6,986	6,626
Rel. consumption [mL/kWs]	0,254	0,235

Table 1: Efficiency Comparison

7 Summary and Conclusion

The amount of machine and measurement data available to OEMs and their suppliers is increasing at a rapid rate. Knowing how to use and manipulate this data will prove valuable as it gives engineers the opportunity to develop a whole new level of understanding for the systems they design. The following paper has focused on the data analysis approach developed at Linde Hydraulics aimed at serving the needs of their customers more efficiently. Although a 36 t excavator was used to illustrate the methodology, the same tools can be used to optimize the hydraulic systems in a wide range of mobile machinery.

Nomenclature

Variable	*Description*	*Unit*
p_A	Actuator Chamber A pressure	[bar]
p_B	Actuator Chamber B pressure	[bar]
p_L	Actuator Load Pressure	[bar]
p_{LS}	Load Sensing Pressure	[bar]
p_P	Pump Pressure	[bar]
v	Actuator Speed	[m/s]
α	Actuator Area Ratio	[-]
Δp	Throttling Losses	[bar]

References

/1/ Vukovic, M.; Leifeld, R.; Murrenhoff, H., Reducing Fuel Consumption in Hydraulic Excavators—A Comprehensive Analysis, Energies 2017, 10, 687.

/2/ Holländer, C., Untersuchungen zur Beurteilung und Optimierung von Baggerhydrauliksystemen, Ph.D. Thesis TU Braunschweig, 1988..

/3/ Sturm, C., Bewertung der Energieeffizienz von Antriebssystemen mobiler Arbeitsmaschinen am Beispiel Bagger, Ph.D. Thesis Karlsruhe Institute of Technology, 2015.

/4/ N.N., Linde Synchron Control System, http://www.linde-hydraulics.de/de-de/catalogue/detail.aspx?pid=56833&gid=43841&pg=OD9T%2bXx7XsWDi%2baaXF3t2g%3d%3d

Experimental Evaluation of the New Meter Out Sensing Architecture

REVIEWED

Marani Pietro*, Massimo Milani**, Davide Mesturini*** and Ulderico Busani***

C.N.R.-IMAMOTER, Via Canalbianco 28, 44124 Cassana, (FE), Italy*
Department of Sciences and Methods for Engineering, University of Modena and Reggio Emilia,
Via Amendola 2 - Pad. Morselli42122 Reggio Emilia, Italy**
Walvoil S.p.A, Interpump Group, Via Adige 13/D - 42124 Reggio Emilia – Italy
E-Mail: p.marani@imamoter.cnr.it

This paper presents the experimental assessment of the very first prototype of Meter Out Sensing System architecture. The system, based on the proportional control of meter out valves, is a novel hydraulic architecture in the field of Mobile Machines. The objective of the hydraulic control is obtained firstly by a negative control of the supply system, adjusting the pressure drop on the meter out to a given value, secondly by a three way compensator able to regenerate the flow. The energy saving is then obtained because of lower throttle losses on meter in connection and the regeneration feature that is enabled hydraulically under specific operating condition.

Keywords: Regeneration, Meter Out Control, Energy Saving, Proportional Hydraulic Controls,
Target audience: Mobile Hydraulics, Proportional Valves, Hydraulic Architecture Design

1 Introduction

Looking at the Mobile Machines Currently in production, two hydraulic control architectures dominate the market: Open Centre and Load Sensing. In the field of open circuits the Independent Metering architecture is as well available but with low market share, until now.

The Open Centre architectures are less user friendly than LS because they are not locally compensated, thus the flow rate depends on the load, especially in case of multiple actuations, even if nowadays their energy management is enhanced through variable displacement pumps use (Negative, Positive Control /1/),.

In spite of a big share of the Off Road Machines Market, Load Sensing (LS) systems /2/ are often criticized for their energy efficiency, in particular pointing out at the compensation mechanism that equalizes the difference in pressure loads (interference) through throttling losses, then it clearly follows that high energy waste and heat generation occur in case of high pressure unbalance between simultaneous actuators /3, 4/. Moreover, LS systems don't allow energy recuperation nor regeneration, since they are based on a meter-in control. High overrunning loads, in fact, can only be controlled by means of additional throttling elements such as overcenter valves.

On the other hand the Independent Metering (IM) Systems /5/ represent a step forward in the state of the art: first of all IM are able to manage regeneration functions basing on electronic sensors feedback and secondly they optimize the throttle losses to minimize parasitic losses. Going more into detail, in case of multiple actuation, the flow area of proportional valves is adjusted to compensate the interference with a real time control of the position of the spool according to measured pressure drops and spool area map. Then, one can conclude that if the parasitic losses are neglected, IM systems introduce the same theoretic throttle loss of the conventional closed centre systems, including LS systems.

However the Independent Metering System are limited to quite few applications on the market with respect to competitor architectures /5/. One reason for this fact is the complex control requirements, in fact accurate spool position control is required and, moreover, complex electronic strategies command the shifting between different operating modes. Furthermore, additional expenses regarding components such as high performance valves and transducers have to be taken into account.

MOS system aims at overcoming the drawbacks of open circuit systems at state of the art. The system in fact offers a control in which the flow rate is proportional to Meter Out Area, without additional motion control valves to manage overrunning load. The MOS system can manage positive and negative loads and implement regeneration with fully hydraulic controls, this means that sensors and complex electronic controls are not required, moreover costly high precision / high dynamic valves are not mandatory.

In /6/ the system was simulated showing the capability to provide proportional flow control to actuators according to the metering area of the inherent spool valve, for single or multiple actuation such as in Load Sensing systems. The Flow Rate obtained for given control area is approximately the same in both overrunning and resisting loads (even in regeneration), with a big energy saving potential demonstrated with proper energy figures of merit.

In /7/ the system was described more into detail from the mathematical point of view and additional results of the multiple actuation were displayed, showing the feature of compensation and of flow regeneration that can be achieved even from one section to another.

2 The Meter Out Sensing Architecture and Operating Principles

The Architecture and Operating Principles are explained into detail in /6,7/ but for the sake of comprehension the architecture and the operating principle will be briefly summarized

2.1 Architecture

The architecture can be explained referring to figure 1. In first place it is important to understand the supply system consisting of a variable displacement pump controlled by a pump compensator according to the pressure on the pilot system connected to the actuators.

The Meter Out Sensing signal line 3, is supplied by a two way flow control valve 7 and it is sensing the lower among all working ports signal through the check valves connected to actuators ports

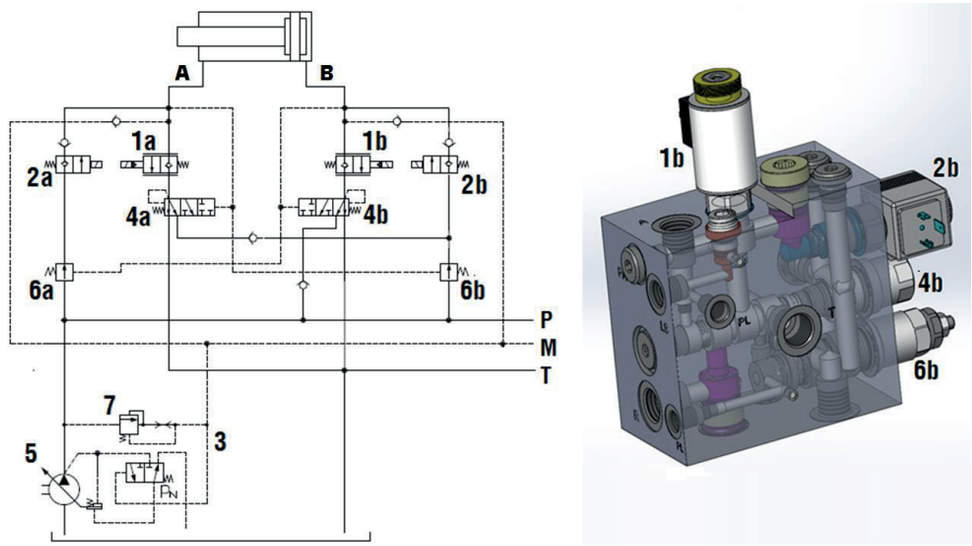


Figure 1: Meter Out Sensing System.

In case of resisting loads, by convention positive, the Metering Out Sensing line pressure is related to the flow rate through meter out edge of the higher load section through turbulent flow equation, if it the signal higher than a given Pressure Margin the pump will decrease the displacement, if it is lower it will swash out according to the compensator setting "p_N". In case of overrunning loads the Meter Out Sensing line will adjust to pressure of inlet of actuator at least at the compensator setting "p_N", avoiding cavitation.

Each section includes two proportional valves (1a, 1b), commanded one at a time, simultaneously activating the opposite side ON–OFF inlet valve (2b, 2a). The speed of actuator is proportional to metering area of metering out valve according to turbulent efflux equation in both positive negative/ regenerative load condition thanks to 3 way compensator.

The 3 way compensator (4a, 4b), in case of multiple actuation, is able to set the correct pressure margin to all active sections, but it also provides important additional features. In fact the system controls overrunning loads without additional motion control valve, moreover the architecture automatically enables the regeneration if the load is overrunning, reducing the flow supplied by the pump thus reducing energy consumption.

The Indirect Pressure Reducer (6a, 6b) is a normally open valve placed on inlet line of actuators and indirectly controlling the pressure at opposite side. The valve is useful to avoid the pressure multiplication effect in regeneration or in presence of simultaneous opposite loads.

The distributor architecture was implemented into two prototype hydraulic blocks including the control valves listed before. Looking at the supply system, the prototype of the pump is still not available then an alternative supply system was implemented with the same control logic for the test bench.

2.2 Operating Principles

In the following paragraphs the Operating Principles of a Single Section in Power Extension, of a Section in Power Extension Compensating and of a Single Section in Overrunning Extension are considered.

The first case is those of the Power Extension Mode, in case we have a single section actuation (or the section is controlling the maximum among the loads). The pump regulates the flow rate according to the pressure on rod side p_B to the pump compensator setting. The 3 way compensator 4a is near to saturated open position and the proportional valve 1a is subjected to the pressure drop p_N, then the flow rate across valve 1a depends only from the flow area obtained for a particular spool position.

The second case is those of Power Extension Mode, in case we have another section controlling an higher load, then considering the compensation. In this case the supply pressure sets according to the maximum load in the system and supplies directly the actuators. The interference on the compensated section is controlled by the 3 way compensator 4a to keep a constant pressure drop across valve 1a (achieving a compensated proportional control), then the pressure on port B will increase accordingly.

In Overrunning Retraction Mode the Load is controlled by the three way compensator 4b, controlling the pressure drop across 1b by regenerating from base side to rod side and discharging the excess to tank. The pressure on both sides of actuator will be more than the setting p_N, thus the pump will decrease the displacement towards zero. Also in the third case a compensated flow control is achieved.

The energy saving is then obtained because of lower throttle losses on meter in connection and the regeneration feature that is enabled hydraulically if the load is overrunning or under specific operating condition including high load pressure difference between different actuators (interference).

It is important to recall that in each work condition (resisting load, overrunning load,) or operating mode (compensation, regeneration) the flow rate is kept proportional to the area proportionally controlled by meter out valve.

3 Testing of the MOS System

In this paragraph the Test Rig will be discussed. The Test Rig is powered by a 37 kW Electric Motor moving a variable displacement pump coupled to a Load Sensing proportional valve, then the system is capable to work at constant flow rate. The Coupling of LS pump and distributor basically works like an ideal fixed displacement pump at constant speed. For the sake of simplicity the Supply Group (Pump + Distributor) is represented as a fixed displacement pump in the following scheme. The test bench has a Lift Arm to simulate a cycle in a real mobile machine and to create a proper load on the hydraulic blocks mounted on the bench. The Lift Arm can be loaded with variable ballast until 2 ton. The MOS hydraulic system is supplied at constant flow rate by the test rig supply group and feeds the lifting boom of the bench.

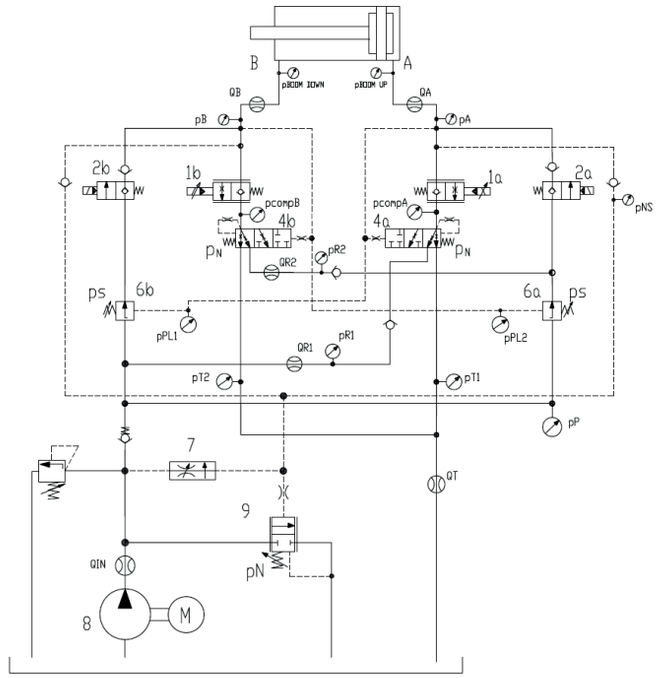


Figure 2: Test Bench Layout

Since the prototype of variable displacement pump with proper control (see figure 1, part 5) is still not available, the tests were carried out with a Constant Flow Supply (Fixed Pump 8 and Flow Compensator 9). In next lines it will be made more clear that this alternative system is equivalent to a variable displacement pump from the point of view of functionality of hydraulic block, even if it is clearly worse from the energy point of view. The hydraulic block can then be tested in all its functionalities while the complete system will be tested when the MOS pump prototype will be available.

Comparing the operating principles of the Test Rig Supply System (element 8 and 9 fig 2) to the variable displacement pump (7 in figure 1) it can be seen that the pump adjusts its displacement according to the pilot pressure signal, thanks to a pump compensator. The metering out sensing pressure is compared to a fixed setting "p_N" (Pressure Margin) just as flow compensator 9 adjusts its position according to the balance between the metering out sensing line and the valve spring set to p_N value.

If the pilot pressure is greater than the setting, the displacement of the variable pump 7 is decreased, conversely valve 9 discharges excess flow. On the other hand , if the signal is lower than "p_N", the pump swashes out, increasing the displacement and the valve 9 closes increasing the flow to MOS hydraulic blocks. The result of

the working principles is the adjustment of a constant pressure margin on the meter-out edge, like an LS systems controls the pressure drop on the a meter-in edges.

Physical variable	Designation	Sensor type	Measurement Range	Overall precision
Volumetric flow rate	QT	Gear flow meter	0,1 ÷ 120 lpm	±0,3% reading
Volumetric flow rate	QA	Gear flow meter	1 ÷ 250 lpm	±0,3% reading
Volumetric flow rate	QB	Gear flow meter	1 ÷ 250 lpm	±0,3% reading
Volumetric flow rate	QR1	Gear flow meter	0,1 ÷ 120 lpm	±0,3% reading
Volumetric flow rate	QR2	Gear flow meter	0,1 ÷ 120 lpm	±0,3% reading
Volumetric flow rate	Qin	Gear flow meter	0,1 ÷ 120 lpm	±0,3% reading
Gauge pressure	pP	Thin film press. transd.	0 ÷ 600 bar	±0,3% Full Scale
Gauge pressure	PNS	Thin film press. transd.	0 ÷ 600 bar	±0,3% Full Scale
Gauge pressure	pA	Thin film press. transd.	0 ÷ 600 bar	±0,3% Full Scale
Gauge pressure	pBoomdown	Thin film press. transd.	0 ÷ 600 bar	±0,3% Full Scale
Gauge pressure	pR1	Thin film press. transd.	0 ÷ 600 bar	±0,3% Full Scale
Gauge pressure	pC1	Thin film press. transd.	0 ÷ 600 bar	±0,3% Full Scale
Gauge pressure	pCompA	Thin film press. transd.	0 ÷ 600 bar	±0,3% Full Scale
Gauge pressure	pT1	Thin film press. transd.	0 ÷ 600 bar	±0,3% Full Scale
Gauge pressure	pB	Thin film press. transd.	0 ÷ 600 bar	±0,3% Full Scale
Gauge pressure	pPL1	Thin film press. transd.	0 ÷ 600 bar	±0,3% Full Scale
Gauge pressure	pCompB	Thin film press. transd.	0 ÷ 600 bar	±0,3% Full Scale
Gauge pressure	pBoomup	Thin film press. transd.	0 ÷ 600 bar	±0,3% Full Scale
Gauge pressure	pT2	Thin film press. transd.	0 ÷ 60 bar	±0,3% Full Scale
Cylinder stroke	Boom_str	Magnetostrictive	0 ÷ 605 mm	±0,4% Full Scale
Cylinder stroke	Bucket_str	Magnetostrictive	0 ÷ 595 mm	±0,4% Full Scale
Current	Iprop	High curr. analog input	0 ÷ 3 A	±0,1% Full Scale
Current	IEC	High curr. analog input	0 ÷ 3 A	±0,1% Full Scale

Table 1: List of Sensors Acquired

The operation of lifting and lowering in this first test is done manually by an human operator, controlling an electronic joystick piloting the electronic valves. The currents controlling the valves are measured to acquire the operator's command. After this early stage an automatic electronic command will be implemented to ensure better repeatability of the tests.

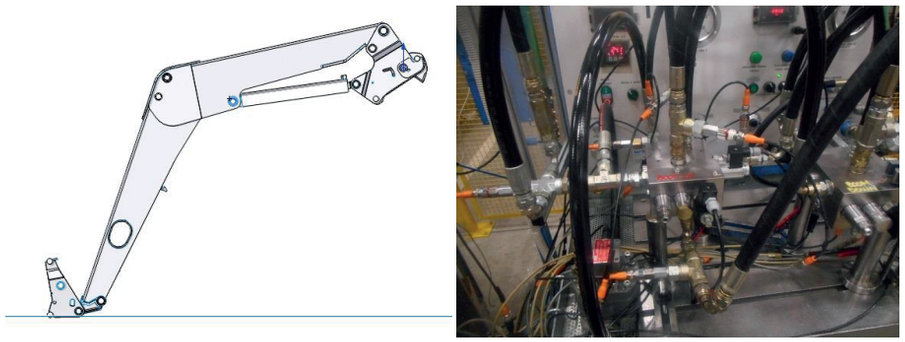


Figure 3: Left Lifting Arm CAD model, Right MOS hydraulic block on Bench,

From figure 2, representing the hydraulic test rig with sensors, it can be noted that a great number of measurement points are available in order to obtain a complete characterization of the system. Table 1 reports a complete list of the sensors mounted on the test rig and simultaneously acquired at 1kHz frequency.

4 Experimental Testing Results

Some samples of the testing results are displayed and commented in this section. Even though the activity of testing and optimization is still ongoing, some interesting evaluations can be done from this first results.

4.1 Power Extension Compensation Test

The Power Extension Compensation Test was carried out at constant supply pressure, this condition simulates the operation of an additional section at constant pressure. This condition assesses the flow control through the proportional meter out valve through the proper operation of the 3 way compensator in compensation mode.

The test is carried out with the load at the minimum height, then the proportional valve 1a is gradually opened causing the lifting of the ballast. The supply pressure is connected directly to A port of Actuator (via ON-OFF valve 2b) and since the supply pressure is higher than the load pressure, the pressure must be increased on B port of the actuator to compensate any load difference (interference of loads). The purpose of the compensation is to have a constant pressure drop between B port and the measurement point PCompB (fig. 2) in order to have a proper control of the flow through proportional valve 1a.

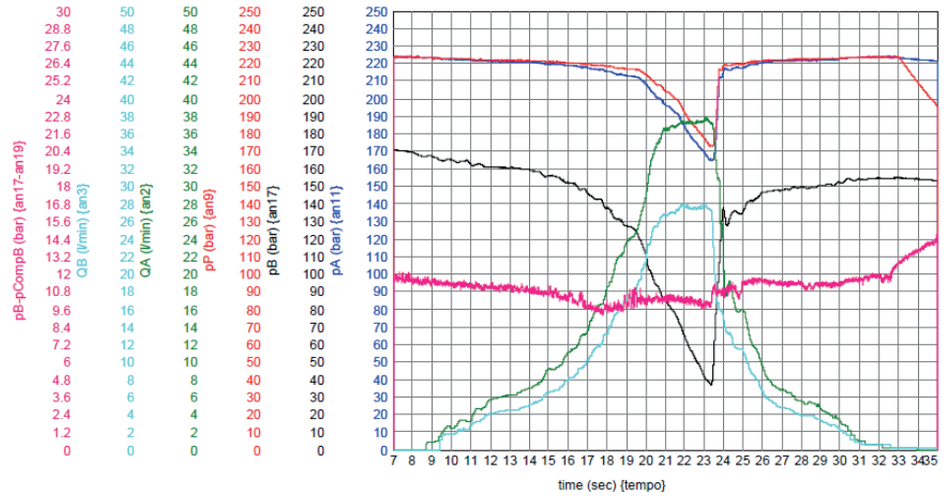


Figure 4: Power Extension- High Load (1000 kg Ballast).

Figure 4 Shows the results of a Power Extension Test with Compensation and high load, more specifically, the boom lifts a ballast of 1000 kg. The pressure is kept at about 225 bar at the beginning of the test via pressure relief valve. This test represents the condition of a load on another section of an hydraulic sectional distributor.

In the starting phase (11-21s) the proportional valve on B side (1a on figure 2) is gradually opened, the flow increases on A side (Green Line) and conversely on B side (Light Blue Line), the compensator on B line keeps the pressure drop on B side at almost constant value (Purple Line) at 10-12 bar of pressure margin.

Then, increasing the opening of the valve the flow saturation is reached and the supply pressure decreases sharply (21-23.5s). In the phase from 23.5s to 34s the opening of the valve is decreased and at second 24 the system exits from flow saturation condition and the supply system is able to keep the nominal pressure, in this phase QA and QB decreases until complete closing position of the valve.

With this test the feature of compensation is confirmed, it is possible to note a slight variation of the pressure drop across the proportional valve that can be in general found in the most common load sensing locally compensated systems as well.

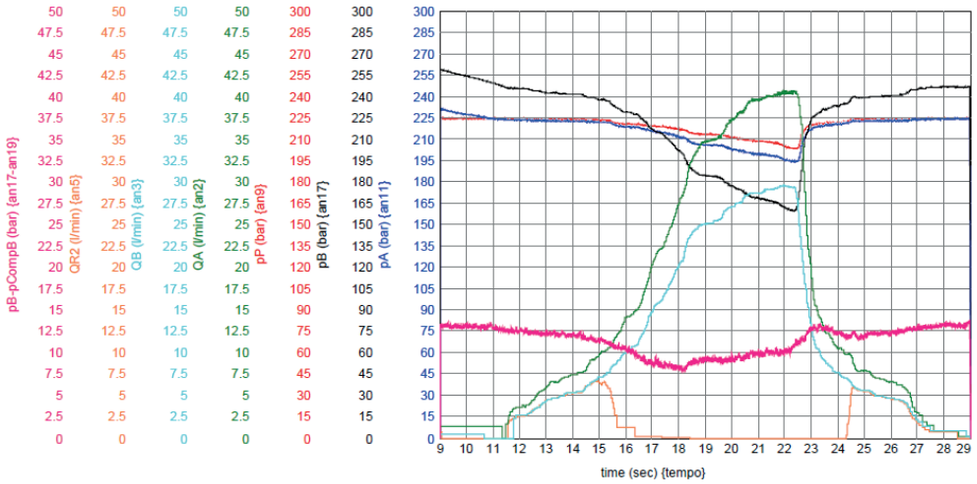


Figure 5: Power Extension- Low Load (0 kg Ballast).

Figure 5 Shows the results of a Power Extension Test with Compensation and low load. The Boom Lifts an empty ballast container, then the load is represented by the mass of the lifting machine itself. The pressure is kept at about 225 bar, as in previous case, representing the condition of a high load on another section.

It can be noted that, similarly to the previous case, the compensator on B side increase the pressure on port B to compensate the load difference between sections (the section under test and a second virtual section at 225 bar load). Because of area differential of cylinder the pressure on B side could be higher than those on A side, this condition is favourable to regeneration, even if the load is of the resisting type.

From 11s to 21s the proportional valve on rod side is gradually opened, the compensator 4a keeps the pressure drop across the valve almost constant increasing the pressure on B.

It can be noted that from 11s to 16.5s the pressure on B (pB, black line) is higher than in A (pA, blue line) then regeneration is obtained, to confirm that one can note that QB, light blue line equal to QR2, orange line. Then the flow rate from B port is discharged through regeneration line to A side (connected to supply), the difference flow rate (QA-QB) is integrated by the pump.

In subsequent phase (16.5-21s) all the flow rate to base side (QA, green line) is supplied by the pump with no regeneration because the rod side pressure (black line) drops under the base side pressure (blue line).

In the phase from 21 to 22.5 we can hypothesize flow saturation recognisably by the drop of supply pressure (pP, red line). Then we have a decrease of the flow rate according to proportional valve position (22.5-29s), at second 24.5 until the closure of the proportional valve regeneration is activated again in reason of the pressure difference between B and A, as in the beginning phase QB flows through regeneration line to A port, adding to the supply flow .

One can note that the flow rate supplied to the Base side in lifting operation is less than a conventional system, in particular the supply flow is decreased in the regeneration phase. The amount of energy saving obtained thanks to regeneration depends on the duration of regeneration phase.

4.2 Overrunning Retraction Test

The Overrunning retraction test is carried out with the load at the maximum height, then the proportional valve 1b is gradually opened causing the lowering of the ballast. In this test the system automatically sets to zero the flow rate from supply group and the fluid from A port divides in two flow rates: one to tank and the other supplying B port.

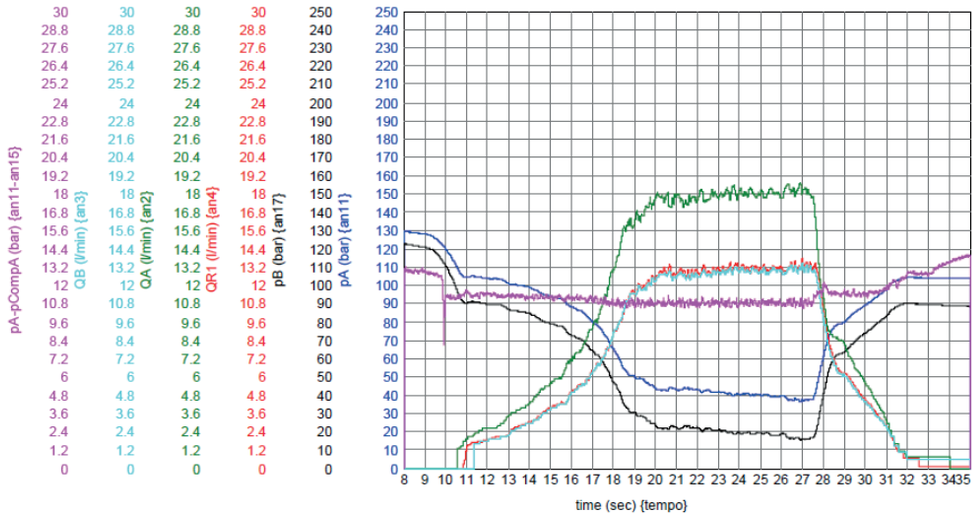


Figure 6: Overrunning Retraction Test - Low Load (0 kg Ballast).

Figure 6 Shows the results of an Overrunning Extension Test with low load. The Boom lowers an empty ballast container, then we have only the load of the lifting equipment.

The pressure generated in base side (pA) is able to feed rod side of the Boom (pB). Proportional valve 1b is gradually opened (and conversely the ON-OFF valve 2a on rod side) the flow rate is regenerated via compensator 4b, then the system reaches maximum opening and finally it gradually closes.

It can be noted that all of the flow to port B is regenerated then the flow rate at port B QB (green line) is equal to flow rate regenerated (QR1, red line), the rest of the flow outgoing from A port is discharged to tank. Another interesting point is that the pressure drop across the proportional valve 1b (purple line) is kept constant by the compensator.

From the flow rate balance it can be deduced that the flow rate introduced to the system by the supply group is zero, then in case of a system variable displacement pump the operation would be at zero energy expense. Finally it is important to recall that the movement of the cylinder is proportionally controlled by a compensated system, independently from the load.

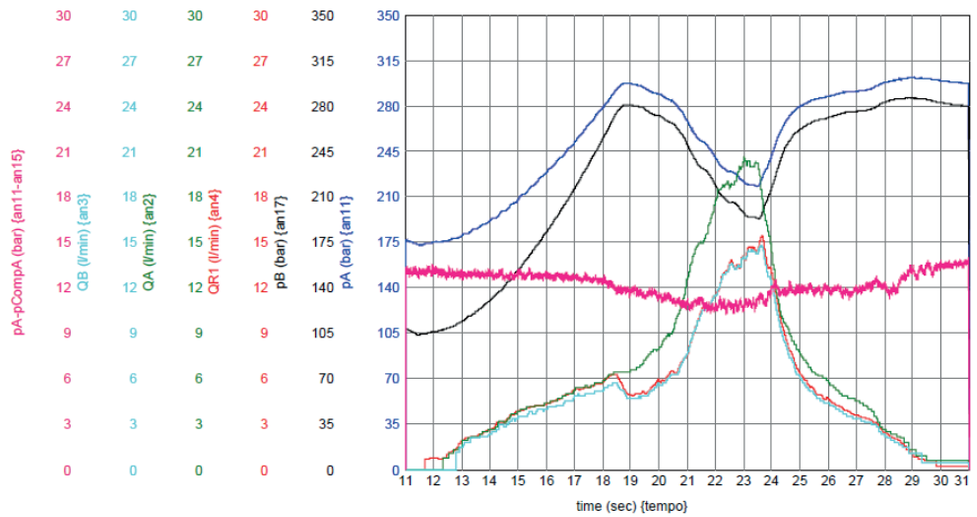


Figure 7: Overrunning Retraction Test - High Load (1000 kg Ballast).

Figure 7 Shows the results of an Overrunning Extension Test with high load. The Boom lowers a 1000 kg ballast container.

As in previous case the Proportional valve 1b is gradually opened and the valve 4b modulates both to Regeneration Line and Tank discharging the excess. Looking at pB black line and pA blue line from12-18s, it is possible to note that the connection of A side of Boom to B side cause an increase of pressure of the system.

Then the increasing opening causes a decrease of pressure on B side caused by the increase of pressure drops in the system for increasing flow rate (18-23.5s). Finally, the pressure increase (23.5-31) with the decreasing of flow rate from A to B for the above mentioned reason.

The first thing to note is that the pressure drop across the proportional valve 1b (purple line) is almost constant because of the compensator, moreover as mentioned before the flow rate introduced by the supply line is zero because the flow rate to B port is equal to Regenerated Flow (QR1). In this case we would have zero energy expense in case of system with variable displacement pump, but it can be further hypothesized that if we have an additional section activated the excess flow discharged at high pressure from base side side of actuator will be able to feed the second actuator with consequent energy saving.

Another aspect to note is that the pressure could rise above safe levels in regeneration , for this reason the valve 6a is implemented, reducing the pressure in B side to keep A side below the maximum permissible pressure. In the test shown above (fig. 7) the valve 6a is kept mechanically opened so the pressure could theoretically rise indefinitely.

In next test shown (fig. 8) it can be seen that properly setting the valve 6b, the system is able to reduce the pressure on rod side indirectly regulating the pressure on base side. In this test, similar to the previous one with regard to load and operator's command, it can be seen the effect of indirect reducer 6a. Without going into detail of all the plots, since the results are similar to previous, it is possible to note the limitation of pressure on A side (blue line) caused by the effect of the reducer 6a on line B (black line).

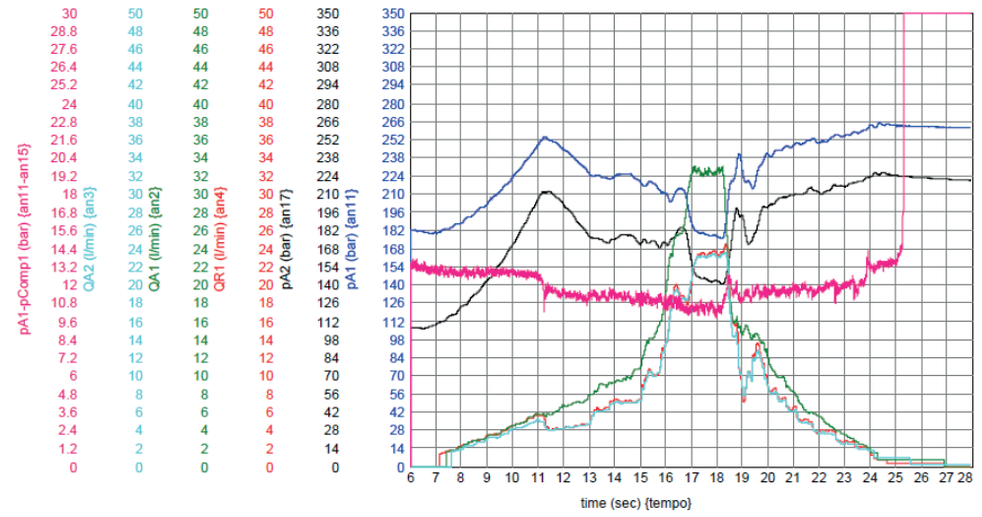


Figure 8: Overrunning Retraction Test - High Load (1000 kg Ballast), with indirect pressure reducer activated

The Flow Rate Plots indicate the equivalence of Flow rate to Rod Side (QB, light blue line) to Regeneration Flow (QR1, red line) and a proper control of the pressure drop on the meter out proportional valve (purple line). So it is verified that even in this case the proper control (correct pressure drop) is achieved and the energy saving can be obtained (regeneration is activated).

5 Summary and Conclusion

The paper has presented the results of the first tests on Meter Out Sensing System. In the introductory part the characteristics of the architecture were briefly summarized.

The operating principle of Meter Out System is based on the meter-out edge control instead of the meter-in edge control of conventional systems; the supply group is able to set the flow rate in the system according to the minimum pressure among all the operating actuators, a 3 way compensator valve is able to control the interference between loads and to activate the regeneration according to the operating conditions.

The MOS System aims at improving the energy management with respect to Load Sensing Systems for the low throttle losses on the supply line of actuators and for the absence of motion control valves. Moreover the regeneration feature reduces the power demand from the pump.

Comparing to Independent Metering Systems, the MOS system can manage positive and negative loads and implement regeneration as well, but in more cost effective implementation, because sensors, electronic controls and high precision / high dynamic valves are not mandatory.

The results of the test carried out at Walvoil Testing Department has assessed some important features of the system.

Power Extension Compensation Tests have shown that the prototype hydraulic block is able to control resisting loads and to perform compensation, the pressure drop across the proportional valve is therefore constant, thus the system can work properly in Multiple Actuator Operation. For high load interference it is possible to obtaining regeneration through the compensation.

Overrunning Retraction Test highlight the feature of regeneration, a gravity load is controlled through the compensator, regenerating the flow from the rod side of the cylinder to the Base Side, in this case the necessary flow is regenerated without any contribution from the supply group. The overrunning operations shows potential

for energy savings because in the conventional systems these operations are often performed with the aid of overcenter valves working at the expense of the supply group.

The paper has shown are the first available results, however the development of the system is still ongoing, additional test are necessary to further assess and optimize the MOS system.

The Lumped Parameters Models /6,7/, not shown in this paper but still in progress, will be compared to the test results and improved as well. These Models will be further used in the subsequent phase of optimization of the system. Finally an important task towards implementation on a Mobile Machine will be that of designing, testing and optimizing a variable displacement pump with proper hydraulic control to be coupled with the MOS hydraulic blocks.

6 Acknowledgements

The Authors wish to thank Guido Denti at Walvoil R&D department, Cesare Dolcin, Matteo Rubiani and Mirco Teneggi at Walvoil Test Department for the great support to this research programme.

References

/1/ S. Gessi, M. Martelli, and E. Tonini, *A Survey on Negative Control Architectures for Hydraulic Excavators*, ASME/BATH Symposium on Fluid Power and Motion Control, 2015.

/2/ Aoki, Y., Uehara, K., Hirose, K., Karakama, T., Morita, K., Akiyama, T., Load Sensing Fluid Power Systems, SAE Technical Paper 941714, 1994.

/3/ Marani, P., Ansaloni, G., Paoluzzi, R., Load Sensing with Active Regeneration System, Proc.s Of The 7th Japan International Fluid Power Symposium, Toyama, Japan, 2008.

/4/ Murrenhoff, H., Sgro, S., Vukovic, M., An Overview of Energy Saving Architectures for Mobile Applications, 9th International Fluid Power Conference, Aachen, Germany 2014.

/5/ Shenouda, A., Quasi-Static Hydraulic Control Systems and Energy Savings Potential Using Independent Metering Four-Valve Assembly Configuration, Ph.D. Thesis of Woodruff School of Mechanical Engineering Georgia Institute of Technology, 2006.

/6/ P. Marani, M. Martelli, *Energy and Control Characteristics of a Novel Meter Out Hydraulic System for Mobile Applications*, ASME/BATH Symposium on Fluid Power and Motion Control, 2017

/7/ P. Marani, M. Milani, *Operating Principles And Simulation Of A Novel Meter Out Control System For Mobile Machines*, Proc.s Of The 10th Japan International Fluid Power Symposium, Fukuoka, Japan,2017

Adaptive Park Brake Technology to Improve Stability of Wheeled Excavators

Davide Moser, Lorenzo Serrao and Giulio Ornella

Dana Mechatronics Technology Center, Via Zeni 8, 38068 Rovereto (TN), Italy

E-Mail: davide.moser@dana.com, lorenzo.serrao@dana.com, giulio.ornella@dana.com

Rocking is often observed in wheeled excavators while digging, which impacts driver comfort and precision. To minimize rocking, wheeled excavators need special axles with brakes at the wheel-end. The paper presents a new solution to use low cost in-board brakes achieving the same or better stability compared to wheel brakes. This is achieved by disconnecting one axle and braking it, while torque is actively applied on the other axle with a hydrostatic traction motor, to preload the driveline and keep the vehicle more stable. The system hydraulic circuit and the corresponding control algorithms are presented, as well as experimental results that prove the concept feasibility.

Keywords: Fluid power systems, mechatronics, excavator, driveline, control
Target audience: Mobile Hydraulics, Construction Machinery, Mechatronics

1 Introduction

This paper presents a new concept to reduce the rocking phenomenon observed in wheeled excavators while digging. This phenomenon significantly impacts the operator comfort perceived and the driver precision during digging phase, reducing the vehicle stability.

Field tests highlighted that the vehicle oscillations are caused by: mechanical backlashes between tire and brake; tire slipping and deformation; and shaft torsional deformation. These effects induce a dynamic load transfer that amplifies the oscillation perceived from the driver seat. This is depicted in Figure 1, while an example of oscillation measurements is shown in Figure 2.

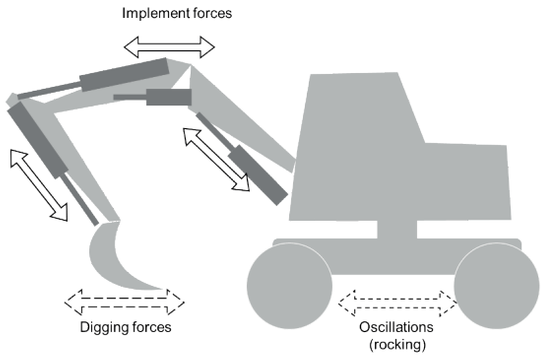


Figure 1: Vehicle rocking (oscillations) during digging

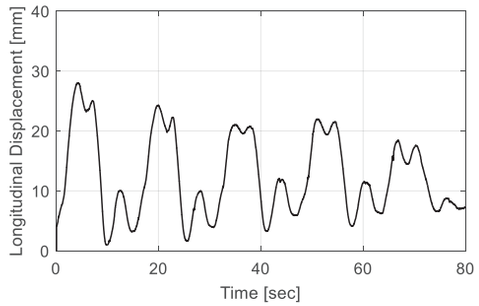


Figure 2: Experimental characterization of vehicle oscillation (longitudinal frame displacement) during digging

The brake system installed in the axles is very important for the overall stability characteristics. A typical off-highway axle provides several functions: structural support; drive torque transmission with speed reduction at the bevel set (differential) and at the wheel hub; service brakes; and park brakes. Service brakes are often based on multiple wet disc solutions, which can be installed at one of the following locations, shown in Figure 3:

- At wheel: the friction components act on the wheel hub (i.e. after the hub-drive reduction);
- Outboard: the friction components act on the axle half shaft, and are located close to the hub;
- Inboard: the friction components act on the axle half shaft, and are located close to the differential.

The solution with brakes at wheel is more expensive due to the larger amount of torque to be generated by the brakes, and more complex in terms of integration in the axle design. However, it is the only solution that provides an acceptable level of vehicle frame oscillation during digging, since the only deformable element between the brakes and the external environment is the tire. On the other hand, inboard brakes hold the inner side of the half shaft, but the vehicle/terrain forces can generate oscillation due to tire deformation and half shaft torsion.

The goal of the concept described here is to avoid this solution and instead use inboard or outboard brakes, while achieving equal or better stability performance compared to the wheel brakes. The concept and the testing results provided here are based on a vehicle equipped with axles using inboard brakes, and a hydrostatic transmission, based on centrally-mounted two-speed gearbox, with disconnection device for the front axle.

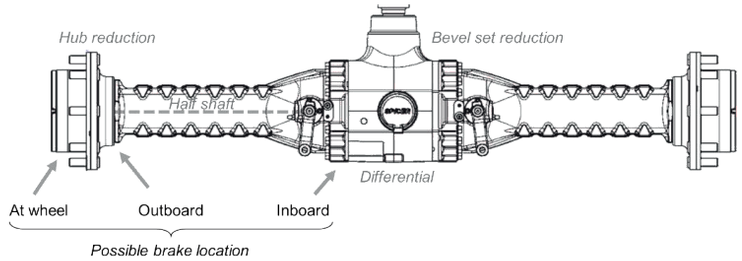


Figure 3: Off-highway axle and brake locations

2 Concept and system architecture

The Adaptive Park Brake (APB) is a mechatronic device that can be used to improve the stability of a wheeled excavator. It applies to a vehicle where one axle is driven, or equipped with a disconnect device if both axles are driven (as in most construction vehicles), so that one axle is disengaged from the traction during system operation. The APB function can be summarized as follows: while the vehicle is stationary and is performing a digging

operation, one axle is disengaged, and brakes are applied on it; at the same time, the traction motor generates torque on the other axle. The motor torque opposes the brakes and thus overcomes the mechanical backlashes and shafts torsion by “preloading” the entire driveline and the tires. The result is a reduction of vehicle oscillations thanks to the elimination of backlash and deformation.

In the examples shown in this paper, the system engages the front brakes and actuates the hydraulic motor which is connected to the rear axle. The motor torque can be applied in either direction: pushing the powered axle towards the braked axle (compression preloading of the driveline, shown in Figure 4), or pulling it away (extension preloading of the driveline).

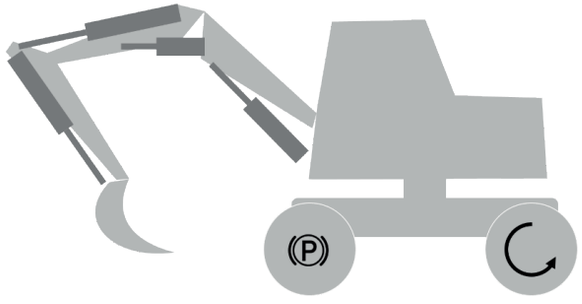


Figure 4: Basic idea of driveline pre-loading for stability

The motor torque generating the preload is not constant, but rather it is computed in real-time to stabilize the vehicle without reaching the limit of wheel slip on the terrain. The system is developed for a hydrostatic transmission, so the torque generated can be controlled by using the motor displacement or the pressure. Pressure control is preferred, for two main reasons:

- the variation of pressure can be faster than the actuation of displacement;
- controlling the torque via the pressure allows to implement the system even in drivelines where the motor is of the fixed-displacement type, or is equipped with a non-electronic displacement control (e.g. purely hydraulic automotive displacement control, or electronic control with hydraulic override).

A schematic representation of the system as implemented in a Dana prototype vehicle is shown in Figure 5. Through the use of sensors, the system state is identified, and an electronic control unit generates an appropriate set-point of torque to be applied at the motor.

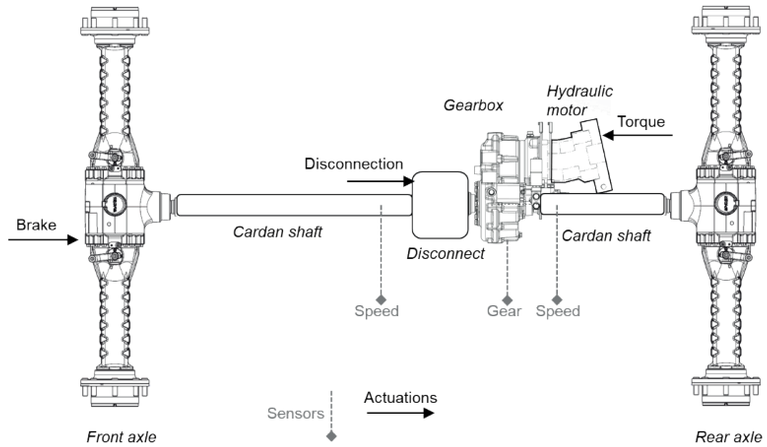


Figure 5: System architecture

3 Hydraulic circuit

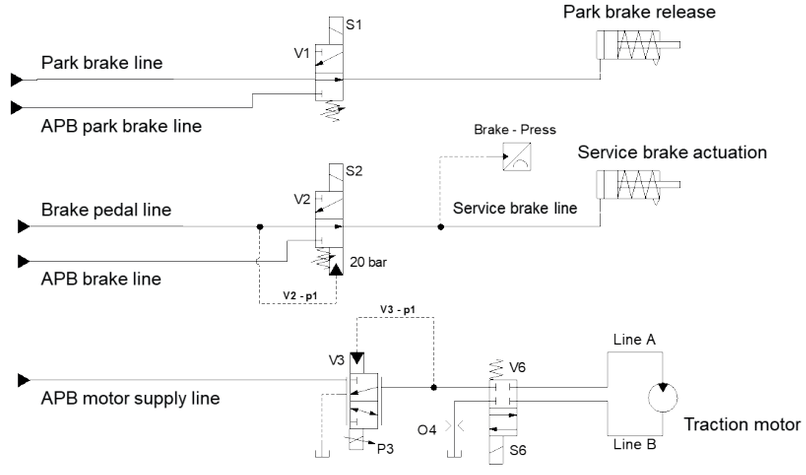


Figure 6: Hydraulic circuit for APB

The APB function can be realized using different circuits. The solution shown in Figure 6 implements the basic functionality of APB: release the standard park brake, apply the service brakes on front axle, apply pressure on the motor acting on rear axle, and ensure safe operation of the system (i.e. ensure that torque is not applied on rear axle without braking the front axle first).

Valve V1 is used to release the park brake: this operation is necessary because the system needs to apply torque at the rear wheels with the traction motor, and the front wheels are already subject to the service brake.

The system applies braking torque by generating pressure on the service brake line using valve V2. The brake pressure corresponds to either the APB brake line supply, or to the standard brake-pedal pressure. The switch between these two values is determined by valve V2: when actuated (by the APB controller), it applies the APB supply brake line to the service brakes; when disabled, instead, it ensures the brake pressure is at the value set by the brake pedal. If the brake pedal is actuated during APB operation, the pedal pressure acts on V2 via the pilot line V2-p1, and pushes V2 back to its rest position. Thus, the brake line receives the pressure from the brake-pedal line, overriding the APB brake pressure setpoint. This means that the driver always has the ability to stop the vehicle using the service brake pedal, independently of the APB status.

To apply the correct amount of pressure to the hydraulic motor, V3 is a continuous electrically-actuated pressure reducing/relieving valve, which sets the pressure value between zero and the power supply value, according to the control signal to solenoid P3.

To guarantee safe operation, pressure on Motor 1 can be applied by APB only when the brake line is pressurized with a pressure level sufficient to hold the vehicle still. This is achieved by measuring the brake pressure level with a sensor, and using the information in the controller to enable the actuation of solenoids S6 (for on/off valve V6) and P3 (for continuous pressure-reducing valve V3). Note that V6, instead of a simple on/off, could be a 3-position directional valve to determine the direction of traction motor actuation.

The time sequence of the APB operation is as follows:

i. Generation of pressure in brake line
ii. Release of park brake
iii. Generation of motor pressure

The supply circuit for the APB signals is shown in Figure 7. The circuit uses the standard pump that generates the power supply for the main hydraulic line, and a set of pressure reducing/relieving valves to generate adequate pressure levels at the different lines. The accumulator A1 is present to ensure an approximately constant pressure and flow to the APB brake line even in case of pump failure. The dynamic response of the pump and the accumulator system is such that the pressure in the APB motor supply line slows down the generation of pressure at the motor, creating a smooth torque actuation.

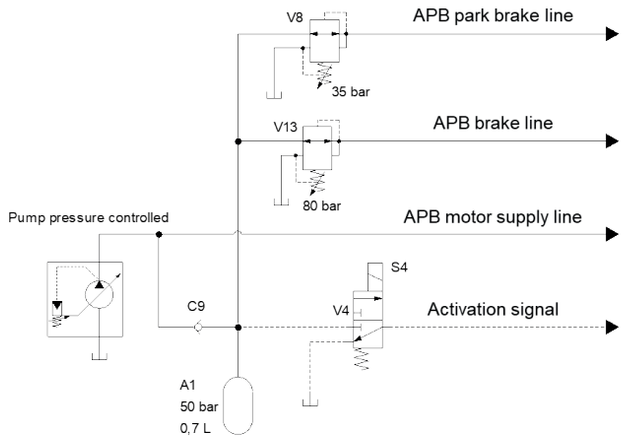


Figure 7: Supply circuit

4 Control strategy

The control system is composed of the following main functions:

F1) Safety supervisor: this is a supervisor layer that constantly monitors the APB operating conditions. In case of anomalous conditions, the supervisor disables the APB system in a controlled manner ("soft dump")

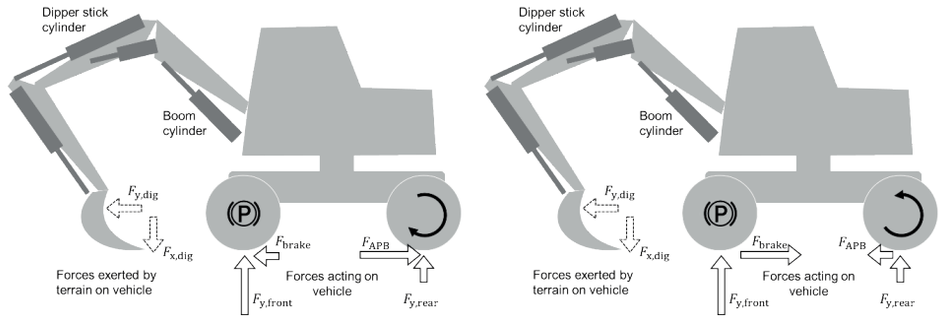
F2) Slip limit detection: this part of the algorithms detects the amount of friction at the ground/wheel interface and therefore the conditions of impending wheel slip. This condition depends on many factors, mainly: ground type; weather condition; presence of a limited-slip or lockable differential; pneumatic tire type, wear, and pressure; vehicle weight. This control is executed at APB activation, and it is corrected during operation by the function F3 (next point). From a practical point of view, the output of this function is the max torque $T_{\max}$ that can be applied by the motor without creating wheel slip, and is determined by continuously monitoring the available speed measurements.

F3) Motor torque setpoint: this value, T_{sp}, is generated as a value smaller than $T_{\max}$. The difference depends on the type of ground (which is identified in F2, as it is strictly related to the value of $T_{\max}$).

F4) Anti-slip: This function controls the tire slip, trying to maintain the tires in the condition of zero slip, by generating the torque T_{sp} with the motor. This is achieved by acting on the pressure of the motor line. The amount of torque to be realized depends on instantaneous operating conditions, for instance on the amount of load acting on the motor axle (which is variable during the digging operation). Thus, if slip is detected while applying the torque T_{sp} determined in F3, a new (reduced) setpoint is immediately applied in order to reduce the tire slip. The system learns the values of torque that produce more or less slip during operation and periodically updates F2.

The forces acting on the vehicle during digging operation are shown in Figure 8. The largest forces are those generated by the main actuation cylinders:

- Dipper stick cylinder, which generates a mostly longitudinal force that tends to move the vehicle frame forward (when the driver is digging, i.e. moving the bucket towards the cabin, as shown)
- Boom cylinder, which generates a force with a longitudinal component (same effect as above), and a vertical component that tends to move the front axle downward (increasing its vertical load) and the rear axle upward (decreasing its vertical load).



a) Reverse mode *b) Forward mode*

Figure 8: Operating modes

At the vehicle level, the longitudinal equilibrium is always:

$$F_{\mathrm{APB}} + F_{\mathrm{brake}} = F_{\mathrm{x,dig}}$$

where F_{APB} is the force generated, via the hydraulic motor, by the APB system; $F_{\mathrm{x,dig}}$ is the digging force acting on the bucket and due to the digging operation (it is time-varying and unknown); and F_{brake} is the force generated by the brake acting on the front axle. F_{brake} can be likened to a static friction force, which is not known because it can take any value between zero and the maximum brake force corresponding to the brake actuation pressure.

The system can be controlled using one of two control modes, which differ for the direction of the torque generated by the hydraulic motor.

In the *reverse* mode (Figure 8.a), the hydraulic motor pushes the vehicle backward, against the direction in which the boom would tend to move it. The force generated by the motor torque balances the sum of the digging forces and deforms the driveline recovering all backlash and elastic deformation; thus, $F_{\mathrm{APB}} > F_{\mathrm{x,dig}}$, which means that F_{brake} is negative (in fact, as shown, it is acting opposite to F_{APB}): the brake is balancing the driveline preload torque. When the rear axle is lifted (or the load on it decreases to a point that the tire starts to slip), the motor torque cannot be transferred to ground, which means the force becomes zero and the driveline preload disappears, so that backlashes appear again. However, the overall performance is still better than the standard vehicle without APB (i.e., rocking decreases). The advantage of the reverse mode is that the overall force opposing digging is high, being the sum of the APB and parking brake effects.

In the *forward* mode, the hydraulic motor pushes the vehicle forward, towards the boom, i.e. in the same direction as the vehicle would tend to move if not held by the brakes. Referring to Figure 8.b, the motor tends to rotate the rear tires in CCW direction, and to generate a force on the vehicle frame that is concordant with the digging force. This means the brake on the front axle must be able to keep the vehicle stopped acting against both F_{APB} and $F_{\mathrm{x,dig}}$, which may require a higher brake pressure. Compared to the reverse case, the APB system must generate a much smaller force F_{APB}, i.e. only the amount needed to overcome the backlashes, because anything more would effectively reduce the total amount of braking. Despite the higher braking pressure required, this strategy generates the best APB results, in terms of oscillation reduction, because the slip of the rear axle in instants of low vertical load does not nullify the driveline preload as in the previous case. For this reason, it was implemented on the vehicle prototype realized for experimental validation of the concept.

5 Experimental results

The preliminary tests and the implementation of control algorithm were realized using an internal proto vehicle, based on a Komatsu PW110 wheeled excavator. The front and rear axle were replaced by a Dana Spicer 212 steering axle. The hydrostatic driveline is composed by a 90-cc load sensing pump, a 110-cc bent-axis motor with electro-proportional control, and a Dana Spicer 367 shift-on-fly gearbox, which is a 2-speed mechanical transmission equipped with disconnect device. The hydraulic transmission is of the open-circuit type. Several sensors were installed to characterize the system behaviour: cable position sensor on rear blade to measure the longitudinal movements (with respect to the ground), engagement switch on gearbox and disconnect device, pressure sensors on hydraulic power and pilot lines, speed sensors on gearbox, motor and cardan shaft. A picture of the vehicle prototype is shown in Figure 9.



Figure 9: Experimental vehicle (driven by the first author)

Tests were performed in different conditions and using both the control modes described before as *reverse* and *forward*; as mentioned, the best results were observed with the *forward* mode. An example is shown in Figure 10, which demonstrates how the use of the system allows to reduce the longitudinal oscillations considerably. The amplitude decreases by roughly 50%, and the high-frequency oscillations disappear in the case with APB. For this reason, the comfort perceived by the driver is sensibly improved. The vehicle is much more stable during the digging operation, and this is clearly observed from the outside.

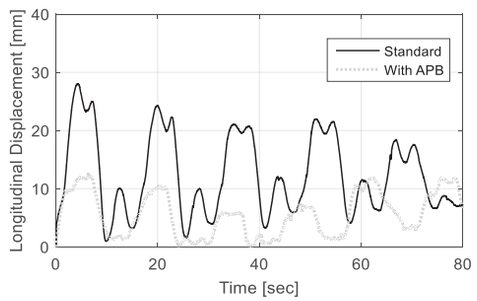


Figure 10: Experimental results (longitudinal frame displacement during digging)

6 Conclusion

The adaptive park brake system constitutes an effective solution for the rocking problem, based on innovative use of existing components via system integration and control. The experimental proof-of-concept demonstrate a visible and perceivable reduction of the oscillation while digging, which improves the operator comfort and precision. The system is currently under testing and future work includes further development towards production-intent design.

Quantification of Energy Saving Influencers in a 21t Excavator Hydraulic System – A Holistic Investigation?

Dr.-Ing. Martin Inderelst, Dipl.-Ing. Fabian Weidner,
Dongdong Niu, B.Eng., Prof. Dr.-Ing. Christian Stammen

Xuzhou Construction Machinery Group (XCMG), European Research Center (ERC) GmbH,
Europark Fichtenhain B4, D-47807 Krefeld, Germany
E-Mail: inderelst@xcmg-erc.com

The paper is about to show a comprehensive evaluation of energy efficiency in the field of excavating machinery. The results detected with 21t excavator platforms over years deal as a basis to determine the major energy efficiency influencers in and outside the machine. Cycles are given for a state of the art hydraulic system in Asian markets. The measurement data collected and results provided finally lead into an ABC-analysis to show the urgent need for new approaches to really save energy in future construction processes.

Keywords: Hydraulic systems, energy efficiency, loss analysis, ABC-analysis, excavators
Target audience: Mobile Hydraulics, Mining Industry, Machine and process design

1 Introduction

The XCMG European Research Center GmbH was founded in Krefeld/Germany in 2013. XCMG ERC is responsible for all research and development activities in Europe and owns test rigs and test grounds for detailed investigations with XCMG's mobile machines. The goal is to optimize and develop innovative technologies for our construction machinery in the fields of hydraulic, drive and control systems that finally result in especially efficient, environmentally friendly, multifunctional and ergonomic construction equipment products for the global market.

Through the last five years our team in excavator–related development projects investigated and optimized various systems, components and test conditions. All investigations covered different hydraulic system approaches like negative flow control and load-sensing systems. We optimized these systems with regard to costs, higher dynamics and controllability as well as to fuel consumption and digging performance. The optimizations realized were implemented by adaptions of own hydraulic components like valve spools and main control valve manifolds, new control principles in the sub-circuits for pilot oil supply and joystick actuation or through the selection of new pumps and drives of new suppliers.

The following chapters deal with the energy efficiency influencers in excavating machinery. For this purpose, test machines and conditions will be specified before discussing the results. All data provided and dealing as the basis has been conducted on 21t excavators using fully hydraulic drive systems and controls.

2 Demonstrator and hydraulic systems

Along with the projects on excavator machinery in XCMG ERC in Krefeld several tests have been realized to finally improve controllability and digging performance but also fuel consumption. For this purpose, series machines from China were sent to Krefeld for detailed testing, analysis and several optimizations in the hydraulic system of the machines. The two test machines are equal 21t crawler excavator platforms with same diesel engines, cooling systems, electrics, steel structure parts and hydraulic drives like the differential cylinders for boom, arm, bucket and the hydraulic motors for the swing and the track drives.

Corresponding data that deals as the basis for all tests discussed later can be taken from *Figure 1*. The differences within the hydraulic system layout and pumps (NFC vs. LS) are described later in more detail.



	Total weight			21t
	Diesel Engine	Stage II		128 kW
	Cooling Power			10kW
		Boom	Arm	Bucket
Cylinders	Piston-Ø [mm]	120	135	115
	Rod-Ø [mm]	85	95	80
	Stroke [mm]	1221	1475	1060
Steel	Mass [t]	1.65	0.83	0.8
	Length [m]	5.8	2.9	1.2
	Capacity [m³]			0.9
Pump Swing	Displacement [ccm]		129.2	
	Gear box ratio [-]		121.6	
	LS-Pump [ccm]		210	
	NFC-Pump [ccm]		2x106	

Figure 1: Variety of digging results for excavator efficiency and performance testing

Both machines have been equipped with powerful measurement systems of the same structure. Each measurement system consists of a local PLC with EtherCAT connection to a large number of data acquisition components and more than 100 sensors to detect all state variables within time steps of 5 ms. The most important signals collected by the data acquisition system are listed as follows and refer to the setup used in the investigations by /1/:

- Diesel engine: set and actual speed values, fuel consumption
- Hydraulic system: Oil temperature, position and speeds of all cylinders and rotary drives, pressure sensors (joystick outputs and valve spool actuation, pump pressures and pump control signals, internal piloting signals for special functions, load ports at MCV and at the drives, local pressures close to valves, tank line backpressure etc.)
- Electrics: Boost function, travel mode, pilot oil switch and pump power solenoid current

The test machines vary in the hydraulic system like mentioned above. One machine is still equipped with a series level Negative Flow-Control system. The other test excavator is based on a single-pump circuit load-sensing system. As both system principles vary significantly, they are schematically introduced by *Figure 2*. The diagrams only feature connections and components to distribute power in the hydraulic systems. All valve piloting and logic circuits to activate any special functions are neglected.

The load-sensing system of the first test machine is based on a single-pump circuit. All valves to control the consumers are connected to a common pump. Pilot oil is provided by an additional gear pump. All closed-centre valves regulate the flow by primary pressure compensators, if pump pressure is higher than the individual load pressure resulting from higher loads operated in another sections. The load-sensing signal limited through a pressure relief valve in a way that the pump pressure cannot exceed the opening pressure for the main pressure relief valve, so that this component has mainly a safety function. For the arm and boom sections locking valves

are integrated to avoid undesired movements of the cylinder function in the non-actuated direction. Regeneration features to regenerate flow from the rod to the piston side (arm section) and in the other direction (boom section) are used to share more flow in the arm section for the levelling task or to save energy for lowering the boom during digging. Parallel function speed ratios are to be set by various parameters like the valve curve setups, the compensator spring, the ratio of saturation and the effective pressure to actuate the valve spools. For power control, the pump is equipped with an electric pressure control valve to manipulate the offset of the LS-pressure. In this way the pump's displacement can be reduced to finally limit the torque on the engine shaft and therefore, engine droop together with an electric controller.

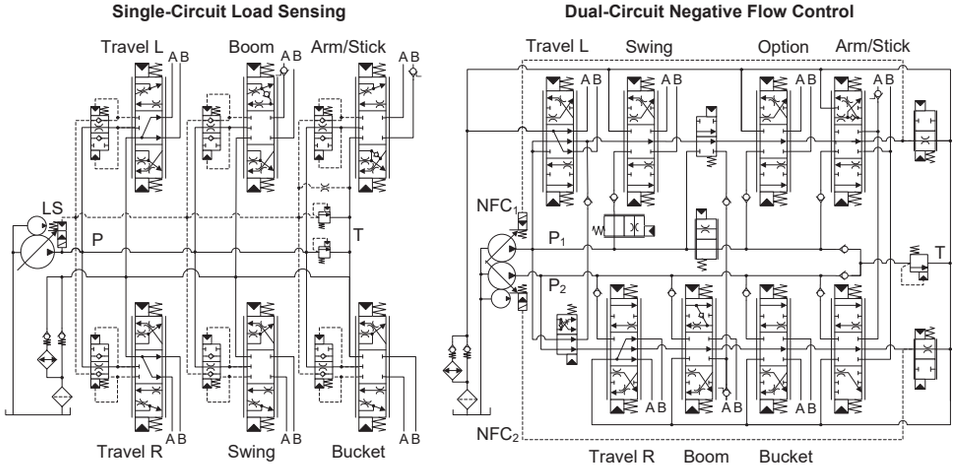


Figure 2: LS and NFC system architecture for 21t excavators (only power circuits; logics and signals neglected)

The negative flow system is a dual-pump circuit system using two rows of open-centre valves. They relieve idle pump flow through NFC orifices to tank or, when activated, distribute the pump flow among parallel functions while manipulating the pump-controlling NFC signal by reducing the open-centre flow. Critical over-pressure is relieved through a common pressure relief valve whenever flow provided by the pumps cannot be totally consumed by the hydraulic drives activated. The sections are arranged to one of each pump pressure lines and in special order along the open centre line to set their priority. Whenever these measures are not enough to distribute flow in the desired ratio, priority valves will be activated to limit or block flows. Only arm and boom function have valves arranged on both pumps as these consumers require total flow of both pumps for some tasks. A confluence valve is integrated between both pump circuits to manage straight travelling while additional functions located in the upper frame or of the attachment are activated. In this situation, this valve distributes the flow in a way that travel track drives are supplied together out of one pump while the other pump supplies all the working functions of the upper frame. Like in the load-sensing system, regeneration features and locking valves are available for both arm and boom. The double pump is equipped with an internal power limitation and can vary hydraulic power set value through a solenoid valve.

In contradiction to the excavator test machines known from other investigations on hydraulic systems /1/, /2/, /3/, /4/, XCMG reference and test machines already feature state of technology solutions in terms of boom and arm regeneration that have been used over years in excavator machinery. In consequence, many later publications in the hydraulic community may lack accuracy when talking about efficiency improvements achieved by new system approaches, as those have been referenced to outdated or simplified valve system technology without these standard regeneration circuits.

However, both hydraulic systems presented are based on the throttle principle which is conventionally used in today's 21t excavator machinery. In addition, both machines share the principle of full hydraulic joystick actuation. A comparison about the major difference between both systems is roughly given by *Table 1*. The evaluation is based on the experience gained through all projects executed with excavators and other construction machinery inside XCMG in the last years.

The comparison shows, that the LS-system features higher load-forces and load-compensation by its principle. The driver feedback is that LS-system cannot feature a so-called pseudo-coupling of joysticks and the attachment drives that he can feel in the flow-controlled systems. A possible explanation can be given by the fact, that the LS-pump regulates the pressure that must be adapted to the right pressure drops through the metering edges by pressure compensators to finally provide the demanded speed along. It is obvious that load-sensing systems prior the force and not the speed. In addition it benefits better part-load energy conditions whenever the drives cannot consume the pump flow available.

Criteria	Full Hydraulic LS-System			Full Hydraulic Flow-Control-System (NFC)
Main PRV Opening	Only for safety reasons to protect hydraulic components from over-pressure	+	-	Safety reasons, bypass function when pump flow higher than consumed by active drives
Force/Power	Controlled by pump in 1st priority	+	-	Result of power available and flow distributed
Load compensation	Precisely realized through primary pressure compensators	+	o	Roughly implemented using priority valves
Speed handling	Depends on compensator and pump dynamics	o	+	Set by the pump in 1st priority
Oscillation potential	By pump controller, pressure compensator setup and load pressure changes	-	+	Generally stable, some effects from pump controller or oscillating main PRV
Controllability	Force always available, missing pseudo-coupling of joystick to the attachment	o	+	Drivers experience an intuitive or pseudo connection from joystick to the attachment
Energy Consumption	Low: flow only provided when consumed in closed-centre (CC) systems	+	o	Medium, as flow is bypassed through main relief valve during acceleration of the functions

Table 1: Differences between full hydraulically operated LS and NFC systems

In contradiction, flow-controlled systems feature a much better connection between the joysticks and the attachment drives that can be explained by the direct use of the pump flow. But, as the pump flow is not limited to the real flow consumption of the drives and the pressure-relief valve will open under this conditions, especially during acceleration of the rotary drives and when the cylinders reached the end stop positions, full hydraulic flow-control system have worse part-load energy condition than the LS-systems.

To sum up, hydraulic systems in excavators vary in terms of controllability, comfort, available forces and the energy consumption. The operating comfort is to be realized by avoiding harsh impacts of the functions under each condition which can occur by pressure peaks in the system. Controllability varies with characteristics like dynamics, response, resolution, hysteresis and the speed ratios for multi-operations. Digging forces and energy consumption are finally the result of the system principle, the special circuits implemented and the setup of all hydraulic components. When also taking regulations for exhaust gas emissions and the CE declaration into account it becomes obvious, that hydraulic system development for 21 t excavators is a challenging tasks.

3 Tests and boundary conditions

Over years of pump load-sensing system investigations and development various test data has been recorded. Digging tests have been realized under same conditions, so that today comparison and analysis of the data is possible. Because of the long-time passing, boundary conditions and changes of the machine have been noted carefully. However, data is maybe not documented perfectly, but was selected in a way to determine the key performance indicators of energy efficiency in mobile hydraulic systems, especially for 21 t crawler excavators. General influencers on the fuel consumption and digging performance are expected in various sub-systems. Some of them are known from different publications. These influencers are roughly described as follows.

1. Machine structure and design with regard to the kinematics, sizes and weights of the steel parts (boom, arm, bucket/tools and counterweight), etc.
2. Engine-related influencers covered by the combustion principle, engine type and sizes, speed settings, load conditions, cooling system, etc.
3. Hydraulic system configurations defined by the circuit type (open / closed), number and sizes of pumps, valves and drives, settings of different backpressure levels for tank line, load-sensing offset pressure, spring and orifices settings, leakage values, oil cooling power, filtering, pipe/hose diameters, etc.
4. Task description: type (digging, levelling, travelling, etc.), precision, truck and obstacle positions, etc.
5. Material: density, compaction, humidity, homogeneity, ice, corn size, etc.
6. Driver: experience level, job strategy (digging direction, filling level) /5/, daily feeling, talent, motivation, concentration, fitness, simultaneous functions, etc.
7. Weather conditions: day/night, wind, temperature, rain, snow, fog, etc.
8. Service state: lubrication, wear, filtering, etc.
9. Air condition: temperature, humidity, density, oxygen, pollution, etc.

It is obvious that some of those parameters cannot be set as constant values but will vary with the testing. The boundary conditions changed along with the investigations will be discussed by the chapters below.

3.1 Standard duty cycle and task description / definition

Regarding duty cycles and energy consumption detection, there is no clear standard available. Some standards like the JCMAS H020 /6/ already regulate how to test excavators, but test description only contains part load conditions for air digging tests with empty buckets. For detecting full load digging fuel consumption test conditions have still not been fixed and agreed upon by the construction machinery companies. In consequence, fuel consumption data cannot be found in the data sheets for excavators like it is familiar for passenger cars that are regulated via NECD and NFCD cycles. For excavators, the most typical test to evaluate the digging and fuel consumption performance is the 90° digging cycle for a fixed time period while the truck is standing next to and in the same altitude than the excavator. Data detected on both machines for such boundary conditions is shown in Figure 3. This data is similar to the data provided by other studies on similar excavators /1/, /2/.

The diagram shows all movements of cylinders and the swing drive as well as corresponding forces or torque in the same time frame. In addition to this load cycle data for an average load cycle in 1 m depth and an unloading height of roughly 3 m, pressures are given for the pump outputs, the system-related signals for LS or NFC and the joystick signals. Such the cycles were detected for both systems with a number of different drivers, so that the different operating habits can be also derived from these diagrams.

As mentioned before, the working task is not furthermore specified and it is not clear that the driver will always perform same cycle conditions. For reasons to more specify and to finally better analysis and compare the test data, the working task has been defined in another way. Old and new task descriptions are given as follows:

- Old task: "*Dig as fast as possible until fuel tank (10 litres) is empty"* – time and cycles to be recorded
- New task: "*Dig a hole with the dimensions of 5x4x3 buckets"* – time, cycles and fuel to be recorded

In contradiction to the old cycle that only aims for digging and fuel performance values, the new task now allows also covering controllability aspects being remarkable whenever engine power is not consumed totally caused by higher positioning efforts. The task is defined by the hole dimensions that finally lead to a total volume of approximated 70 m³ and a mass to be moved of about 126 t. It is the basis for all investigations being discussed in the following sections.

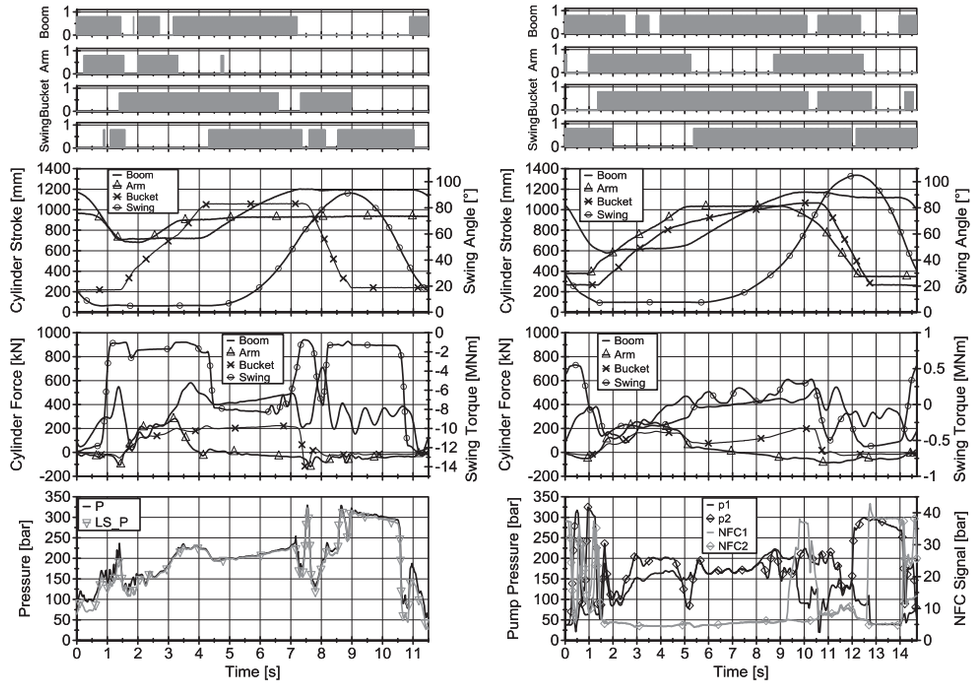


Figure 3: LS and NFC 90°-digging cycle data

3.2 Test setup / matrix

The idea of the investigation is to not only focus on the hydraulic system or drive train and the primary energy source, e.g. the diesel engine, like it has been done in several other studies /3/, /4/, /7/, /8/. These studies provide so-called holistic investigations that are limited to a hydraulic system boundary that is fixed between the engine and the mechanical power take-offs of the hydraulic drives. For hydraulic component and system suppliers this system boundary can be accepted.

As a developer and producer of the entire excavator application, measures to benefit fuel consumption and the performance of the machine need to be balanced with other criteria like controllability, additional costs and so on. For more detailed understanding and a more comprehensive investigation, the system boundary needs to cover the full machine design, the environment, the driver and the process as well. For this purpose, the investigation was extended to consider more influences on the performance and fuel consumption of the machine. *Figure 4* shows the parameters changed over all tests being executed with both test machines in Krefeld in the last years.

	Alternatives	Engine Emission Class	Engine Power [kW]	Engine Speed [rpm]	System	Regenerations	Flow Management	dp Valve Spool [bar]	Impact Setting	Parameter Setup	Swing Drive Motor	Track Drive Motor	Operator	Obstacle Height [m]	Unloading Angle [°]	Ground Condition	Air Temperature [°C]
		A	B	C	D	E	F	G	H	I	J	K	L	M	N	O	P
1		Stage 1	125	2050	NFC2	Both	On	15	Low	1	0	0	1	3	90	Dry Sand	25
2		Stage 2	100	1850	NFC1	Arm	Off	20	High	2	1	1	2	0	180	Wet Sand	15
3		Stage 3		1700	LS1	Boom		25		3	2		3	1	0	No Load	15
4		Stage 4		1550	LS2	None		30		4	3		4	2		Frozen Sand	35
5		Stage 5			LS3			35		5			5			Stones	
6					PFC					6			6			Test Weights	

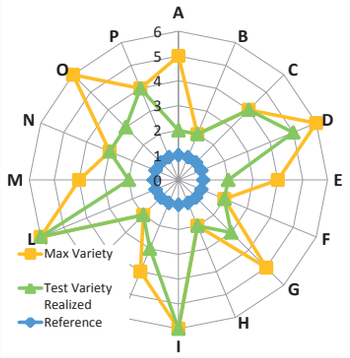


Figure 4: Modifications in test conditions among the investigation range

The table shows the different criteria varied from test to test in columns, the lines represent the options available in each criterion. The first blue line shows the definition of the reference machine which was the series product configuration of 2014. The green coloured fields have been covered with the test being executed whereas the orange fields are intended to be tested soon, but are not taken into consideration for the results being presented in this article. For easier demonstration of all changes in the test setup or the machines, modifications to the reference will be given in the spider grid diagram. In here, reference is always set to option "1" and illustrated by a blue line whereas the green line shows the variety realized by the tests.

For sure, data collected by this procedure is not standardized and gives no statistically evidence to exactly quantify the real influences on efficiency of the different influencers. However, it will provide new more comprehensive impressions.

4 Results

4.1 Overall Results

For a better overview all tests executed are summarized in the diagrams provided in *Figure 5*. The digging performance diagram on the left-hand side shows the fuel consumption per hour on the y-axis versus the digging performance in tons per hour on the x-axis. It deals as a diagram to illustrate overall digging performance for excavating machinery by the ratio of output work which is represented by the material moved to fuel energy, see eq. (1). The ratio can be also understood as an efficiency value.

$$\eta_{tot} = \frac{W_{out}}{E_{in}} \sim \frac{m_L}{V_{Fuel}} \tag{1}$$

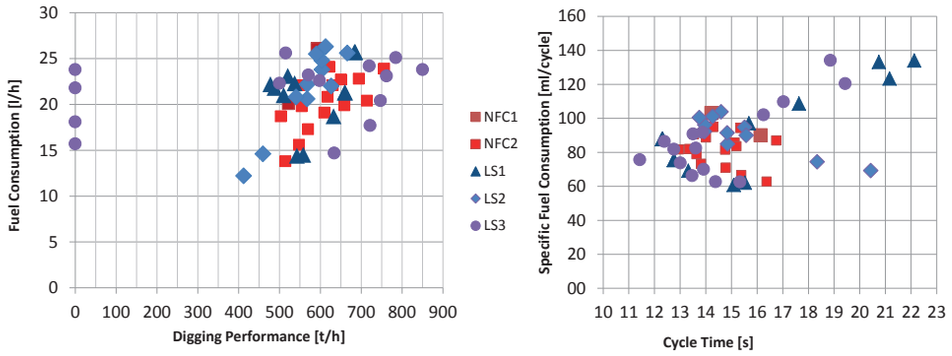


Figure 5: Variety of digging results for excavator efficiency and performance testing

Data is marked for five different hydraulic systems. It becomes obvious that even with same machine platforms and a same task, fuel consumption and digging performance values can vary significantly. This is the root cause that makes the determination of precise fuel consumption or digging performance values so difficult and therefore has not lead to data provided in data sheets until today. Furthermore, data discussed in many research projects all over the globe must be rated carefully if based on a low number of tests.

The second diagram on the right-hand side shows the specific fuel consumption per cycle versus the cycle time. The results look different compared to the first diagram, because the amount of soil moved varies with the tests and therefore the load in the bucket changes. The question to be answered is how to reduce confusion about the results and give a more clear understanding. For this purpose, data in the diagrams will be deeper analysed in the following subchapters.

4.2 Changing Conditions

In the following subsections, results we be provided to figure out the influences of all modifications covered by the different tests executed. The results will be finally used to determine most significant influencers of energy efficiency in the crawler excavator machinery by an ABC-analysis, see more in section 4.3.

4.2.1 Engine

During the investigations with both test machines, different engine speeds have been set and tested, see *Figure 6*. Specific fuel consumption was detected for different engine speeds and operators on the same machine. The data strongly varies with Diesel engine speed as for all drivers the ratio between fuel consumption and digging performance decreases. In general, efficiency is better for lower engine speeds.

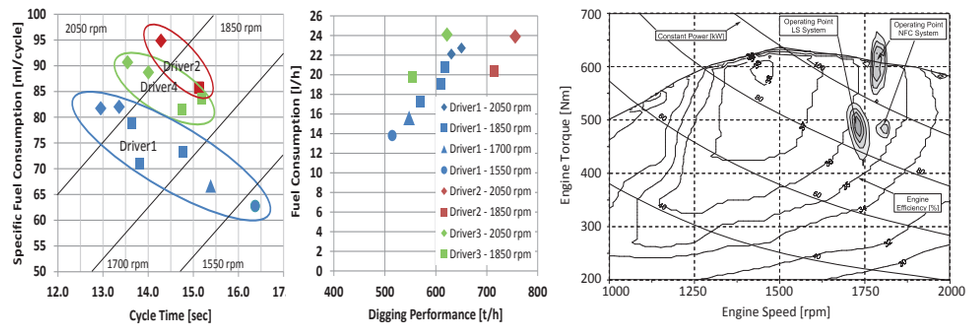


Figure 6: Diesel engine operation points and digging values versus engine speed

The right diagram shows an engine efficiency map that considers the shaft torque on the y-axis and the engine speed on the x-axis. In addition, lines of equal power are provided. Both of the systems, the load-sensing and the negative flow control, are plotted to the map whereas engine operation points are high-lighted for 90 % energy performed for the digging tasks. Both systems are exemplarily compared by considering the best digging performance values in the economic mode with an engine set speed value of 1850 rpm. Average engine efficiency varies for both of the system between 35 – 36 %. Best engine operation points provide energy by roughly 40 % efficiency whereas minimum efficiency in idle mode can perform close to 25 % /1/, /3/.

It turned out that the fuel efficiency is better for lower diesel engine speed along with lower digging performance values. This means, a compromise has to be found in the balance of fuel consumption and digging performance. Assuming the diesel fuel price won't increase significantly, fuel saving costs by lower diesel engine speed cannot compensate higher costs for operator capacities needed to move the same amount of material. In the future, fully autonomous excavators could move more slowly but not being time-limited and therefore can work in better operation points. As the machine can work more than 8 - 10 hours a day, digging performance can also be increased when productivity is rated per day.

4.2.2 Hydraulic Components

To quantify losses in the hydraulic components, the bubble plot diagrams in *Figure 7* show pump operation points for the load-sensing and the NFC system for different speed settings. Other parameters were not changed during the tests. As engine speed varies with the bubble groups, pump pressure is drawn against the relative pump displacement.

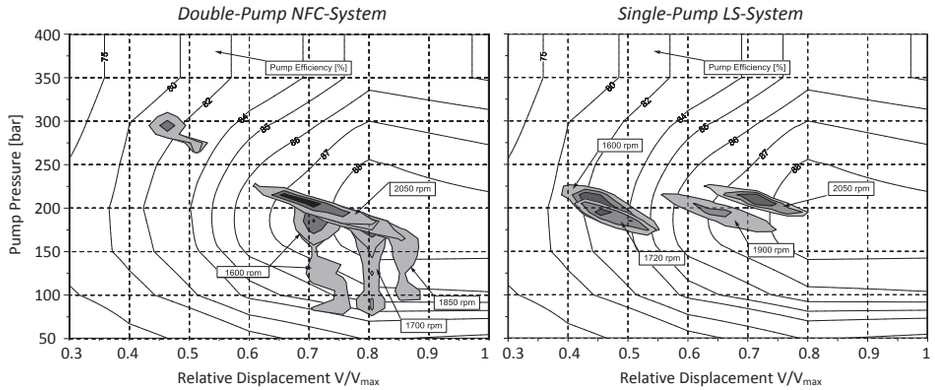


Figure 7: Pump operating points of both test machines

The diagram shows, that the operation points shift to lower pump displacements with the reduction of the engine speed set value. This is caused by the fact that lower engine power available at lower speeds limits the pump power and hence the pump displacements when load pressure conditions are nearly the same. The operation points of the both the systems LS and NFC vary in an overall pump efficiency range between 80 % and 89 %. In consequence, this strong relationship between pump efficiency and engine speed settings needs to be considered during the development process and the selection of suitable pump hardware when designing for energy efficiency. The pump size selection is a compromise between efficiency under full load conditions of the diesel engine whereas pump displacement will be limited due to the maximum speed available for the tasks operated in part load conditions of the diesel engine.

Regarding the other components like cylinders, motors and valves, *Figure 8* illustrates corresponding diagrams by drawing the load pressure on the y-axis versus other state variables on the x-axis like the velocity (cylinders, left-hand side), and the relative rotational speed (swing drive, right-hand side). The bubbles plotted in the diagrams consider all drives for arm, boom, bucket and swing.

The efficiency values of the cylinder operating map already show that these components indicate less losses compared to components like valves and motors. The efficiency values of the cylinders vary between 96 % and 98 %. For boom and arm cylinders operational points consider the regeneration function during fast feed operations and whenever potential energy drives these functions.

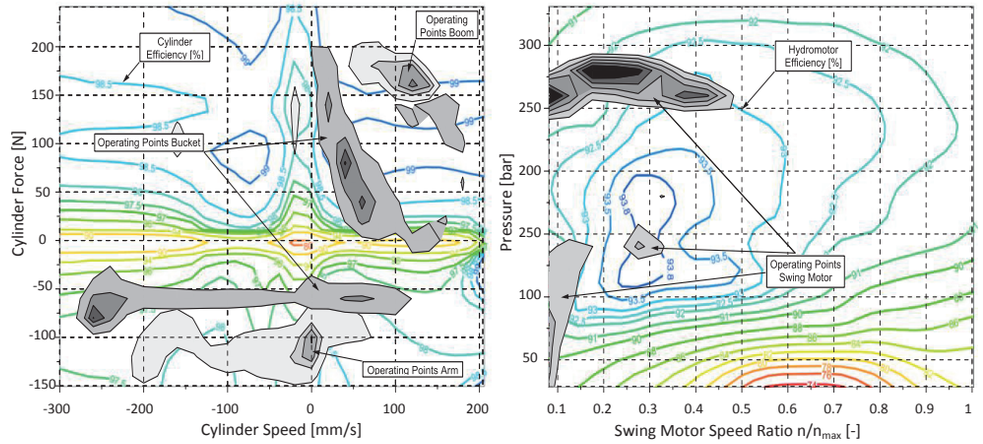


Figure 8: Operational points of the cylinders, valves and the swing drive motor

For the exemplary digging cycle plotted, major swing drive energy is consumed in ranges of 90% efficiency and higher. It can be seen that maximum swing speed cannot be achieved over the 90°-digging cycle. In general, swing drive motor efficiency is quite high for the operating points covered through digging.

As a conclusion it can be pointed out that hydraulic components already feature quite good efficiency values in wide ranges of the digging cycle for the 21t excavator applications. It can be advisable to check if further efficiency improvements are necessary or if the development focus of such components should be adjusted on finding reasonable balance between efficiency, endurance and costs by maybe also decreasing efficiency again. If costs can be reduced this way, the cost savings can maybe compensate additional costs necessary for improvements in non-hydraulic excavator sub-systems with higher influences on energy efficiency of excavating machinery. In general, customers will accept higher costs for the machine for a better product, but those additional costs should be compensated by the fuel savings within the first year.

4.2.3 Systems

To roughly rate influences of the hydraulic system configuration and parameter setups for LS and NFC, both machines were tested with varying configurations, see *Figure 9*. The LS setups therefore feature different valve spool geometries as well as diverse parameter sets balancing driving comfort versus fuel efficiency. The two NFC system states tested represent two generations of development, mostly valve spool sizing differs. In addition on the right-hand side, results from /7/ are illustrated in a way the energy consumption and losses of different new hydraulic system approaches applied to excavator machinery can be estimated.

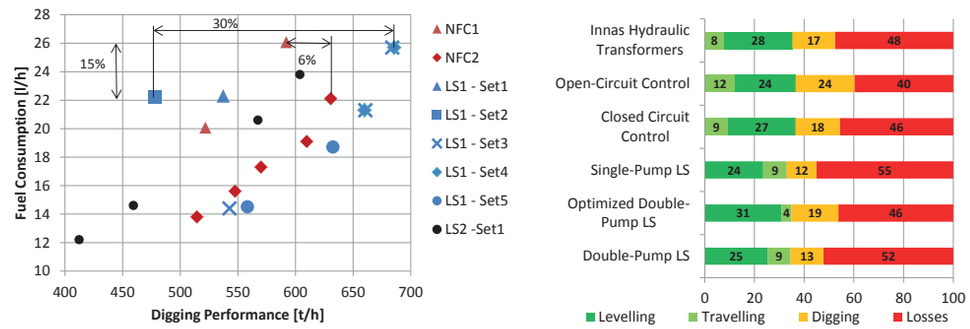


Figure 9: Variety of digging results for excavator efficiency and performance testing

The results show that the system efficiency for valve systems varies very much with the parameter setups that are a compromise between driving comfort, energy savings and controllability in other tasks. In the LS-system the digging performance varies in a range of 30% along with fuel differences of 15%. Fuel savings of 15% can be achieved by the second generation NFC-system machine. For the single-pump LS-system with a series level parameter setup, fuel and digging performance is located between the first and second generation NFC systems.

The second diagram shows the overall hydraulic system efficiency for the different tasks digging (full load conditions, orange), travelling and levelling (part load conditions, green). The red colour represents permanent losses of each the systems that cannot be avoided. Net efficiency of all systems including pump and drives is between 45-60%. The results show the known fact that full load conditions in the digging cycle have much higher effective energy share than part load conditions for levelling or travelling. Valve-based or throttle type system architectures in excavators have quite low efficiencies for the levelling tasks that can be significantly reduced by any displacement control-based approach. But, for the displacement control-based system principles, travelling becomes less energy efficient by the drag torques of all inactive pumps.

The results collected by the investigations are compared with the results known from public research in the field of excavator hydraulic system improvements /1/, /3/, /4/, /7/, /9/. To better understand the results of the digging process analysis, total efficiency is in the following defined as the ratio between the work performed at the output and the total Diesel fuel energy invested at the input, see eq. (1).

$$\eta_{tot} = \frac{W_{out}}{E_{in}} = \frac{n \cdot (m_L \cdot g \cdot h_{av} + 0.5 \cdot m_L \cdot (\omega \cdot r_L)^2)}{E_{Fuel}} \quad (1)$$

The work at the output of the excavator is in here understood as the mass of ground material moved. Work is separated into potential energy and kinetic energy. The average height is defined as the sum of average digging depth and unloading height. The speed of the load is considered by the rotational speed of the upper structure during the turn-lifting phase times the bucket distance to the vertical axis. The corresponding data can be seen in *Figure 10*. The results show that the new system approaches that control the hydraulic drives directly by the pump improve the efficiency but also feature a higher digging performance. The single-pump LS-system seems to be competitive to replace a double-pump NFC system without influencing digging performance and fuel consumption. Furthermore, the results obviously point out, that overall machine efficiency is rising with the machine size from less than 1% up to 13% for excavators between 4 t and 30 tons.

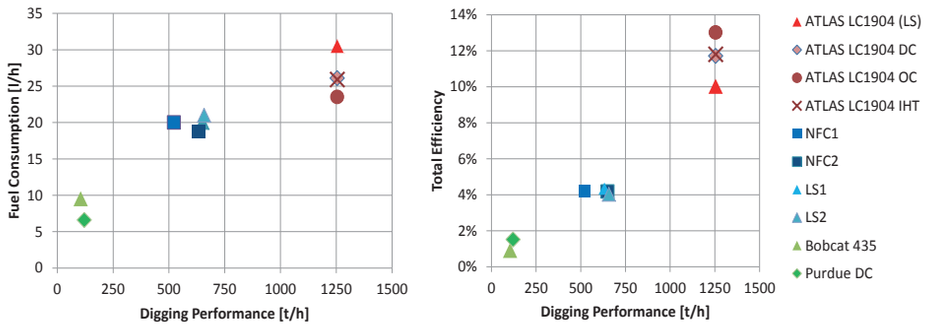


Figure 10: Variety of digging results for excavator efficiency and performance testing

The right diagram shows also that the excavator machine is generally not suitable for energy efficient digging, if digging is understood as the pure movement of material. The energy consumed to cut through the ground and to crush or mix the material is considered as a loss here. Which parts of these losses may be useful work or not is to be considered when thinking of future machine concepts.

4.2.4 Structure and Machine Design

In this section, results have been selected to determine losses impacted by the machine design. For this purpose, *Figure 11* provides data and diagrams for the digging performance, the specific fuel consumption per cycle vs. the cycle time as well as an energy distribution for the attachment during the 90°-digging cycle.

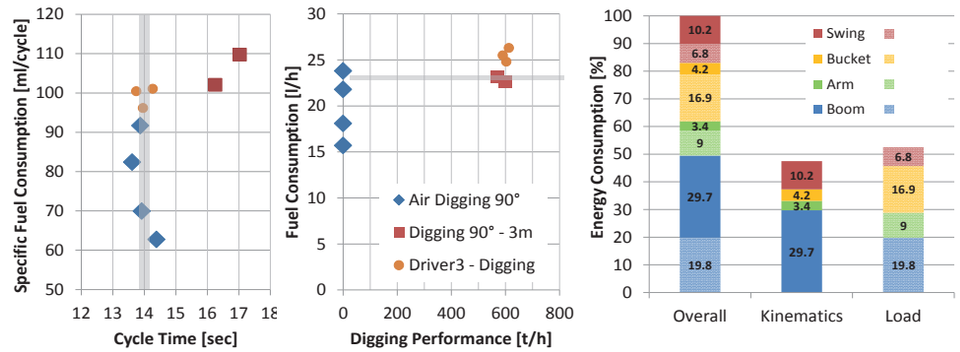


Figure 11: Energy consumption of the attachment

The energy consumption for the unloaded bucket situation which is in following called *air-digging* is quite high compared to the loads operated. As the cycle time varies too much, it is hard to precisely determine the real impact of the structure with the results available. For a better understanding results of another driver are used too directly compare in the same time frame. Along with Diesel engine speed reduction, the fuel consumption varies between 10% and 38% along with the investigations. The big fuel consumption differences during the air-digging test can be explained by the part load operations of the diesel engine, but also of the pump especially when pump flow is not totally demanded by the driver for the higher engine speed settings.

Multi-body simulations allow a more detailed determination of the energy consumed by only the steel structure parts along the digging cycle. It turned out that the energy consumption strongly depends to the load in the bucket. With higher loads in the bucket, relative energy share of the attachment becomes less. During conventional digging tests providing the data illustrated in *Figure 11* the load in the bucket only consumes 54% of total energy invested in the movement of the attachment and the swing drive, so that the machine's steel structure or kinematic maximum efficiency is roughly rated to 46%. When watching the results provided in terms of digging performance, it becomes obvious that air digging efficiency of the machine must be set to zero as air digging has no effective work realized at the output.

4.2.5 Operators

The investigations with different hydraulic system configurations installed in the same crawler excavator platform have been executed by different drivers from EU and Asian countries on both systems. The results can be seen in *Figure 12*. All results for specific fuel consumption, the moved material per hour or the cycle time are drawn against the average amount of simultaneous functions, like presented by /10/. For the values determined in the diagrams, the driver was the only change among the test conditions that means that the points selected share same engine speed settings. The diagrams demonstrate that operators generally keep their individual simultaneously level for the 90°-digging cycle when operating machines with difference hydraulic systems like here the LS and the NFC. The results also show that all drivers nearly achieve the same cycle time on the NFC system along with comparable specific fuel consumptions for this system. For the LS system the results of all operators are more varying in which driver 1 had the highest experience level on the load-sensing system.

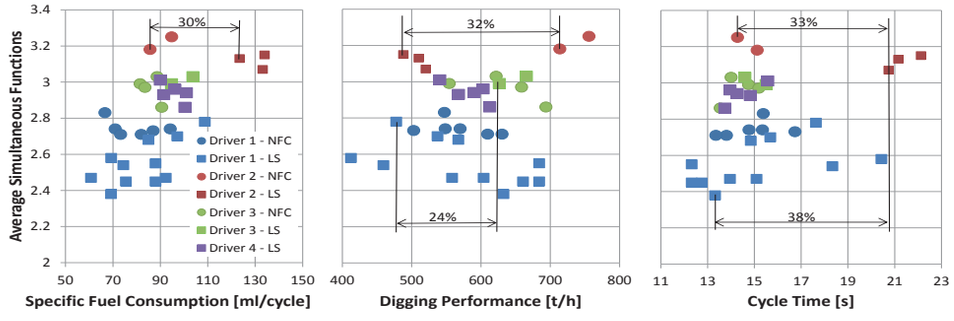


Figure 12: Digging results influenced by the operator

In terms of the specific fuel consumptions, the highest deviation between the LS and NFC system are about 30% for the same operator. The deviation between different drivers on the same system is up to 44%. Regarding digging performance results vary 24% for different drivers on the same machine whereas the same operator on different systems deviates up to 32%. The cycle varies under the same conditions between 32% and 38%.

4.2.6 Cycle and Ground Conditions

Regarding the energy influences of the cycle conditions, tests have been executed with the same driver and same machine, but cycle conditions were changed. Changes were realized by changing the truck position for unloading while the unloading height was about 3 m. This is normal boundary conditions when the truck and the machine are standing in the same height level. Results can be taken from the diagrams in *Figure 13*.

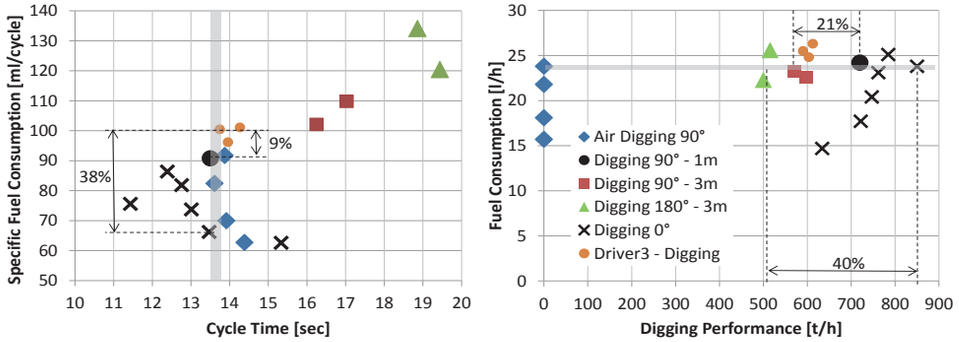


Figure 13: Digging energy consumption varying with the cycle conditions

The difference in digging performance realized by a 180°-digging cycle are about 14 %. For digging and unloading in the same angle range results vary about 30 % to the reference 90°-digging cycle. In addition, the machine was standing higher that the truck, so that effective digging height was only 1 m. The results show that just with the digging height reduction the excavator performs roughly 25 % more material movement with the same fuel investment. Air-digging results discussed above but referenced also in the diagrams indicate that load changed by the ground conditions like stones, gravel, etc. might also change digging performance with comparable fuel consumptions.

When looking at values for specific fuel consumption per cycle versus the cycle time, energy savings can be easier derived from results operated in the same time periods. To rate against the 90°-digging cycle with loaded bucket, results of another driver with a comparable cycle time are added to the diagram. Load changes can be quantified in a range of higher fuel investment between 9 and 30% depending to the engine speed set points. Regarding the digging angle influencing the results as swing drive was not operated for the 0°-digging cycle, fuel savings of about 38% seem to be possible. To sum up task efficiency it becomes obvious that the digging task itself has high potential to reduce fuel efficiency by 38% or to increase the digging performance by 40%.

4.3 ABC-Analysis

All efficiency values determined and discussed in the chapters above are fed into an ABC-analysis that contains the whole digging process from fuel energy input through all parts and sections of the excavator machine and process influencers like the driver, the tasks and so on, see *Figure 14*. The upper red bars show permanent losses of each the influencers which are always given and cannot be avoided. The variable range in orange colour depends on different boundary conditions whereas energy that is always consumed effectively is coloured in green.

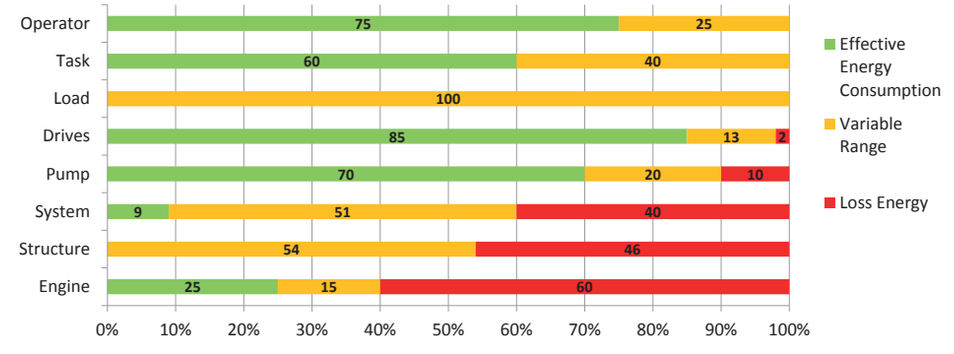


Figure 14: ABC-Analysis over full digging process

It turned out that not only the diesel engine efficiency impacts the fuel consumption dramatically, also the steel structure parts or in general kinematics of the excavator that build the basic machine principle as well as the hydraulic system are major energy dissipaters and therefore of class A. These energy dissipaters should be reduced by new principles which means, a new machine to realize the digging task both with high digging productivity but also efficient fuel consumption. But, to define new digging processes and machines along with changing laws cannot be realized by the construction machinery companies only, so that there is a need for public research.

Comparably low losses occur in the hydraulic components like cylinders, motors and pumps which are categorized into class B. Pumps and motors have higher potential for further efficiency improvements than cylinders, but the question is if corresponding efforts in costs will be finally accepted by the producers or the customer, like it was discussed in 4.2.2.

The influencers like the task, the load in the bucket and the operator are of class C and can influence the energy consumption during digging, but is hard to rate with regard to permanent losses. In consequence, this class does not share any permanent losses, but a huge range exists that impacts the fuel consumption of an excavator machine. Measures to manage the digging task will become more and more important in the future and training of the operators for more efficient digging using machine data seems to be reasonable /11/.

5 Summary and Conclusions

Along with several development and research projects at XCMG European Research Center GmbH various digging performance test data has been collected for 21t excavators. The analysis of the data enables a comprehensive view on the influencers of energy efficiency of such machines. An ABC-analysis of the influencing factors on energy consumption covering the full digging process discovered the diesel engine, the steel structure as well as the hydraulic system as the major energy dissipating factors. It turned out that excavator machinery has been designed for ergonomic benefits and the digging performance but not for efficient operation of the digging tasks itself. Also the task and the truck position impacts the digging results significantly. As there are very high losses in the total machine significant improvements could be only achieved by new digging principles and machine designs in the future.

The results also show that bad machine efficiency is not caused by the hydraulic components. Here, cost savings through allowing less efficiency realized by higher volumetric losses in hydraulic pump and motor units can provide the investment cost for bigger changes in the hydraulic system but also can improve the cooling and wear behaviour of these components. Valve-controlled systems have in general higher losses especially in part load conditions than displacement-controlled system approaches presented by /4/, /7/. Lower engine speeds result in lower digging performance along with higher fuel savings. As less comfortable system setups can also save fuel it becomes obvious, that an automatization of excavators will end-up in huge efficiency improvements. As these machines will be able to work the entire day in contradiction to human operators, also higher digging performance can be expected by the customers for tasks and conditions that allow automated work.

It becomes obvious by the data presented that the energy efficiency for excavators is hard to evaluate and to understand as there are so many different factors that can significantly influence the tests and final results. The excavator machine efficiency finally rises with the bucket and hence the excavator size.



Figure 15: Will excavating change in the future?

The final question is how excavating will develop in the future and how to develop new competitive hydraulic systems in future. The need for higher productivity and more energy savings along with higher intelligent systems justify starting machine development on blank papers again. For this purpose, public research at universities and other institution could play an important role for future excavating system and processes.

Nomenclature

Variable	*Description*	*Unit*
E_{Fuel}	Diesel fuel energy amount	[kJ]
E_{In}	Input energy	[kJ]
g	Gravitational constant	[m/s²]
h_{av}	Average digging height	[m]
m_L	Mass of the load or material in the bucket	[kg]
n	Number of cycles	[-]
r_L	Distance of bucket to the rotating axis during turn-lifting	[m/s]
V_{Fuel}	Diesel fuel amount	[l]
W_{out}	Total work performed	[kJ]
η_{tot}	Discharge Coefficient	[-]
ω	Angle	[°]

References

/1/ Holländer, C., *Untersuchungen zur Beurteilung und Optimierung von Baggerhydraulik-systemen,* Fort.-Ber. VDI Reihe 1 Nr. 307, VDI Verlag, Düsseldorf, Germany, 1998.

/2/ Melchinger, U., *Simulation der Arbeitsbewegungen und Antriebssysteme von Hydraulikbaggern*, Fort.-Ber. VDI Reihe 1 Nr. 212, VDI Verlag, Düsseldorf, Germany, 1992.

/3/ Vukovic, M. Hydraulic Hybrid Systems for Excavators, Dissertation, RWTH Aachen University, Aachen, 2017.

/4/ Zimmermann, J., et al., *40% Fuel Savings by Displacement Control Leads to Lower Working Temperatures – A Simulation Study and Measurements*, 52nd NCFP, Las Vegas, USA, 2011

/5/ N.N. *FUEL SAVING OPERATION GUIDE*. Product Information, Komatsu, Germany, 2010.
Link: http://www.komatsu.com.au/AboutKomatsu/NewsAndPublications/Brochures/Service%20Brochures/Fuel%20Saving%20Guide/FINAL_Fuel%20Saving%20Operations%20Guide_June10_completesample_LR.pdf, visited on 20.12.2017

/6/ JCMAS H020, *Earth-moving machinery – Fuel consumption on hydraulic excavator – Test procedure*, Japan Construction Machinery and Construction Association for Hydraulic Excavators, 2007.

/7/ Inderelst, M. *Efficiency Improvements in Mobile Hydraulic Systems* – Dissertation, RWTH Aachen University, Shaker, Aachen, Germany, 2013.

/8/ Heybroek, K., *Saving Energy in Construction Machinery Using Displacement Control Hydraulics*, Thesis, Linköping University, Sweden, 2008.

/9/ Inderelst, M., Stammen, C., Wu, X., *Rating of Efficiency Improvements in Mobile Hydraulic Systems*, In: 9th IFK, Aachen, Germany 2014

/10/ Mieth, S., *Typical performance cycles of mobile machinery taking into account the operator influence*, In: 8th IFK, Dresden, Germany 2012

/11/ Pfab, H., et al., „“*Flottenauswertung zur Optimierung des Maschineneinsatzes*“, In: Hybride und Energieeffiziente Antriebe für mobile Arbeitsmaschinen 2017, Karlsruhe, Germany, 2017

Control design and validation for the hydraulic DOT500 wind turbine

REVIEWED

ir. Sebastiaan Mulders*, dr.ir. Niels Diepeveen** and dr.ir. Jan-Willem van Wingerden*

Delft Center for Systems and Control, Faculty of Mechanical Engineering, Delft University of Technology,
Mekelweg 2, 2628 CD Delft, The Netherlands*
DOT B.V., Raam 180, 2611 WP Delft, The Netherlands**
E-Mail: s.p.mulders@tudelft.nl

Offshore wind turbines are getting larger in terms of size and power output, resulting in lower rotation speed and higher torque at the rotor. As hydraulic transmissions are generally employed in high load systems, the case for compact hydraulic drive trains is becoming ever stronger. The hydraulic Delft Offshore Turbine (DOT) concept replaces drive train components with a single sea water pump, and pressurizes sea water to a central multi-megawatt electricity generation platform. This paper presents the first steps in realizing the DOT concept, and prototype tests are conducted with a single full-scale wind turbine with a hydraulic configuration. A hydraulic torque control strategy is developed and in-field test results are presented.

Keywords: Control Strategies, Fluid power networks, Control Design, New Approaches and Methods, Feasibility
Target audience: Control system design, novel concepts

1 Introduction

The drive train of horizontal-axis wind turbines (HAWTs) generally consists of a rotor-gearbox-generator configuration in the nacelle, which enables each wind turbine to produce and deliver electrical energy independent of other wind turbines. While the HAWT is a proven concept, the turbine rotation speed decreases asymptotically and torque increases exponentially with increasing blade length and power ratings /1/. As offshore wind turbines are getting ever larger, this results in lower rotation speed and higher torque at the rotor axis. The increased loads primarily affect the gearbox, which makes it a maintenance critical and high mass component in the turbine /2//3/. Furthermore, due to the contribution of all components to the total nacelle mass, the complete wind turbine support structure is designed to carry this weight for the entire expected lifetime, which in turn leads to extra material, weight and thus total cost of the wind turbine /4/.

In an effort to reduce turbine weight, maintenance requirements, complexity, and thus the Levelized Cost of Energy (LCOE) for offshore wind, a novel and patented /5/ hydraulic concept by the Delft Offshore Turbine (DOT). The DOT only requires a single water pump directly connected to the turbine rotor and replaces high-maintenance components in the nacelle, which in effect reduces the weight, support structure requirements and turbine maintenance frequency. In contrast to conventional wind farms, Delft Offshore Turbines are designed to operate in clusters of multiple turbines, collectively pressurizing sea water to a central multi-megawatt generator platform, where the hydrodynamic energy is converted to electrical energy. The DOT approach has great potential in reducing the number of components, and thus simplifying maintenance and reducing costs. The concept also enables multiple wind turbines to be controlled collectively. A feasibility study of the concept is performed in /6/.

Conventional Variable-Speed Variable-Pitch (VSVP) wind turbines aim to maximize the rotor power coefficient in the below-rated operating region by directly influencing the generator torque demand to the rotor /7/. In the hydraulic DOT configuration, the centralized generator is decoupled from the wind turbine drive train, making generator torque control inconsequential for the rotor speed. A spear valve is used to control the nozzle outlet area, which in effect influences the fluid pressure in the discharge line of the water pump. This forms an alternative way of controlling the reaction torque to the rotor.

This paper presents the first steps in realizing the integrated hydraulic wind turbine concept, by full-scale prototype tests with a retrofitted 600 kW wind turbine, of which the conventional drive train is replaced by a 500kW hydraulic configuration. In contrast to previous work /8//9/, the rotor is coupled to a fixed-displacement pump, making constant line pressure control infeasible. The main contribution of this paper is to elaborate on the control design process for a hydraulic drive train with a fixed-displacement pump, subject to efficiency and controllability maximization of the system.

The paper is organized as follows. In Section 2, the DOT concept is explained, and drive train components used during the actual field tests are specified. Subsequently, in Section 3 hydraulic wind turbine operational and control strategies are elaborated, and a drive train component efficiency analysis is presented. In Section 4, the hydraulic torque control implementation is described and evaluated on the actual full-scale turbine, of which test results are presented. Finally, a conclusion and summary is given in Section 5 and acknowledgements are made in Section 6.

2 The DOT concept test set-up description

The Delft Offshore Turbine (DOT) aims to make offshore wind farms a cost-effective source of energy, by redesigning the way wind energy is converted to electrical energy using a hydraulic drive train. The main objective of the hydraulic concept is to radically reduce the weight, complexity and costs of offshore wind turbines by removing multiple heavy components from the nacelle and replacing them with robust hydraulic components /10/. In doing so, individual wind turbines collaborate in clusters collectively pressurizing sea water to a central multi-megawatt generator platform, where hydrodynamic energy is converted to electrical energy.

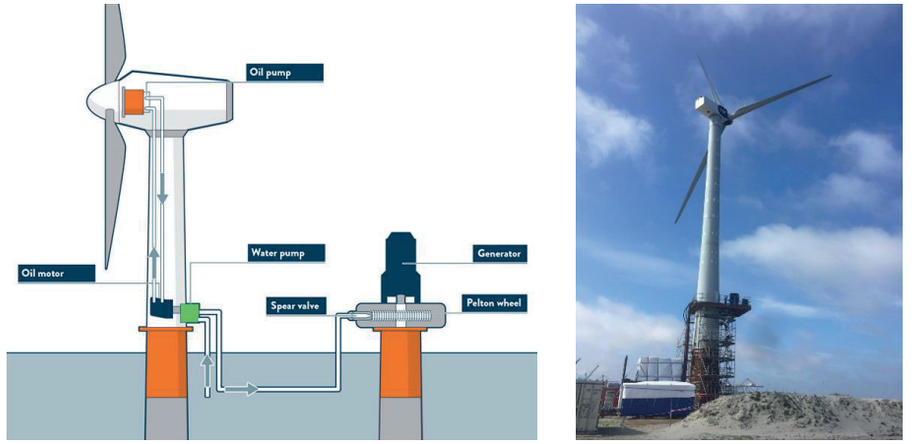


Figure 1: DOT concept with single turbine (left), photograph of the actual DOT500 wind turbine set-up (right)

At the time of writing the required low-speed, high-torque water pump required for the ideal DOT concept is not commercially available. For this reason, an intermediate concept, as schematically shown in Figure 1, using of-the-shelf components is proposed to speed up development and test the practical feasibility. In this concept, a low-speed oil pump is coupled to the rotor and its flow is directed towards a high-speed oil motor, which is directly coupled to a commercially available high-speed water pump. The oil loop acts as a hydraulic gearbox between the rotor and the water pump. It is known and taken into account that the additional components and energy conversions result in a reduced overall efficiency compared to the ideal concept described in /6/. However, as previously stated, the intermediate concept allows for prototyping and faster development towards the ideal concept. In parallel to the intermediate prototype tests, a sea water pump is being developed by DOT, enabling the ideal concept in later stages of the project /11/. From this point onward, all discussions will refer to the intermediate set-up, including the oil loop.

To make prototype tests possible, a 600kW turbine is used and its drive train is retrofitted into a 500 kW hydraulic configuration. A photograph of the actual set-up is shown in Figure 1 and will be referred to as the DOT500 turbine. A prototype was erected in June 2016 at Rotterdam Maasvlakte II, the Netherlands.

3 Operational strategy

3.1 Operational strategies

The drive train of conventional wind turbines consists of the rotor, generator and a gearbox. As the efficiencies of the latter two mentioned components are generally assumed to be high, the largest contributor to the drive train efficiency is the turbine rotor. The power coefficient C_p represents the rotor power extraction capabilities from the wind, and is thus a measure of the rotor efficiency. Conventionally, in below-rated operating conditions, the power coefficient is maximized by regulating the tip-speed ratio at λ using generator torque control. The operating point $C_\mathrm{p,max}$ is indicated in Figure 2 (left), and represents a theoretical estimation of the power coefficient curve for the turbine rotor as function of tip-speed ratio λ and blade pitch angle β. Generally, the maximum power coefficient tracking objective is attained by implementing the feedforward torque control law

$$\tau_\mathrm{sys} = \frac{\rho_\mathrm{air}\pi R^5 C_\mathrm{p,max}}{2\lambda^3}\omega_\mathrm{r}^2 = K_\mathrm{r}\omega_\mathrm{r}^2, \tag{1}$$

where R is the rotor radius, ω_r the rotor speed, and ρ_air is the density of air taken as a constant value of 1.225 kg m^{-3}. K_r is the optimal mode gain in [Nm (rad/s)$^{-2}$] for tracking the rotor $C_\mathrm{p,max}$ trajectory.

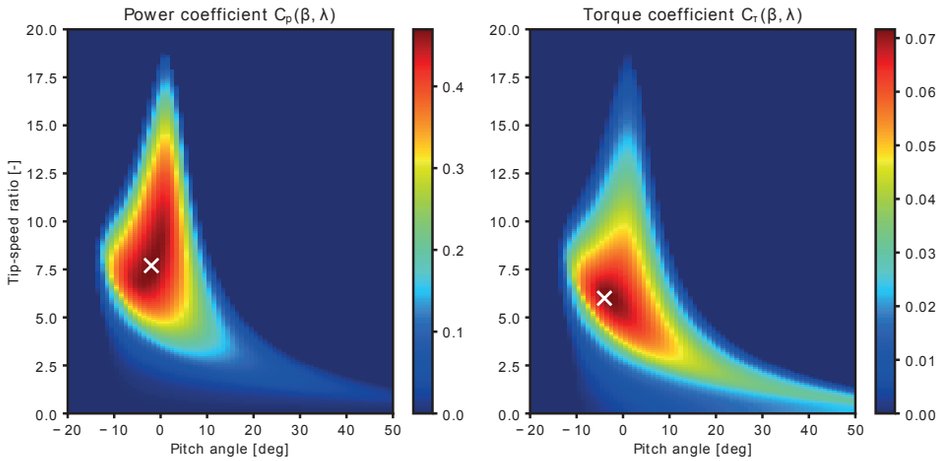


Figure 2: Rotor power and torque coefficient curve obtained from a BEM analysis performed on measured blade-geometry data. The maximum power coefficient $C_{p,max}$ of 0.48 is attained at a tip-speed ratio of 7.8. The maximum torque coefficient of $C_{\tau,max}$ is given by 0.072 at a lower tip-speed ratio of 5.9.

As the DOT500 drive train lacks the option to directly influence the system torque, hydraulic torque control is employed using spear valves. An equation for the system torque for the hydraulic drive train configuration presented in Figure 1 is derived as a function of component characteristics and spear valve position.

$$\tau_\mathrm{sys} = \frac{\rho_\mathrm{w}}{2C_\mathrm{d}^2 A_\mathrm{nz}^2(s_s)}\left(\frac{V_\mathrm{p,OP}V_\mathrm{p,WP}}{V_\mathrm{p,OM}}\right)^3 \frac{\eta_\mathrm{v,OP}^2\eta_\mathrm{v,OM}^2\eta_\mathrm{v,WP}^2}{\eta_\mathrm{m,OP}(\omega_\mathrm{r},\Delta p_\mathrm{OP})\eta_\mathrm{m,OM}(\omega_\mathrm{OM},\tau_\mathrm{OM})\eta_\mathrm{m,WP}(\omega_\mathrm{OM},\Delta p_\mathrm{WP})} = K_\mathrm{s}\omega_\mathrm{r}^2, \tag{2}$$

where ρ_w is the water density, C_d the nozzle discharge coefficient, s_s the spear position, V_p the volumetric displacement, and η_v and η_m the volumetric and mechanical efficiencies. The oil pump, oil motor and water pump are indicated by the subscripts $(\cdot)_\mathrm{OP}$, $(\cdot)_\mathrm{OM}$ and $(\cdot)_\mathrm{WP}$ in respective order. Equation (2) shows that when K_s is constant, the tip-speed ratio can be regulated in the below-rated region by a fixed nozzle area A_nz. Under ideal circumstances, it is shown in /12/ that the nozzle area can be chosen constant to let the rotor follow the optimal power coefficient trajectory. This means that no active control is needed up to the near-rated operating region, and only blade pitch control is needed in near- and above-rated wind speed conditions. For this purpose, the optimal mode gain K_s of the system side needs to equal that of the rotor K_r in the below-rated region.

Because hydraulic components are known to be more efficient in high-load operating conditions /13/, it might be advantageous for a hydraulic drive train to operate the rotor at a lower tip-speed ratio for maximization of the total drive train efficiency. Operating at a lower tip-speed ratio results in a lower rotational rotor speed and a higher system torque. A consequence of operating the turbine at a lower tip-speed ratio is the decreased rotor power coefficient C_p. An analysis of this trade-off will be presented and is divided into two cases:

- **Case 1:** operating the rotor at its maximum power coefficient $C_{p,max}$;
- **Case 2:** operation at the maximum torque coefficient $C_{\tau,max}$.

A stability concern for operation at the maximum torque coefficient needs to be highlighted. Referring to Figure 2, it is noted that the torque coefficient gradient with respect to the tip-speed ratio $\partial C_\tau/\partial\lambda(\lambda)$ is positive on the left side of its maximum value, and negative on the right side. For stable operation of the wind turbine, the gradient needs to be smaller than zero /14/ - i.e., $\partial C_\tau/\partial\lambda(\lambda) < 0$. Operation at a lower tip-speed ratio decreases the rotor torque, resulting in unstable turbine operation and deceleration of the rotor speed to standstill. The torque control strategy for case 2 will be designed for a calculated minimum tip-speed ratio, and in-field test results need to confirm the practical feasibility of the implementation.

Referring to the rotor power/torque curve in Figure 2, and substituting the values for operation at $C_\mathrm{p,max}$ and $C_\mathrm{\tau,max}$ in Equation (1), optimal mode gain values of $K_\mathrm{p} = 1.00 \cdot 10^4$ and $K_\tau = 2.05 \cdot 10^4$ Nm (rad/s)$^{-2}$ are found for cases 1 and 2, respectively. The result of evaluating the rotor torque in the below-rated region for the two cases is presented in Figure 3. Due to the lower tip-speed ratio, the rotor speed is lower for equal wind speeds; or a higher wind speed is required for operation at the same rotor speed resulting in a higher torque.

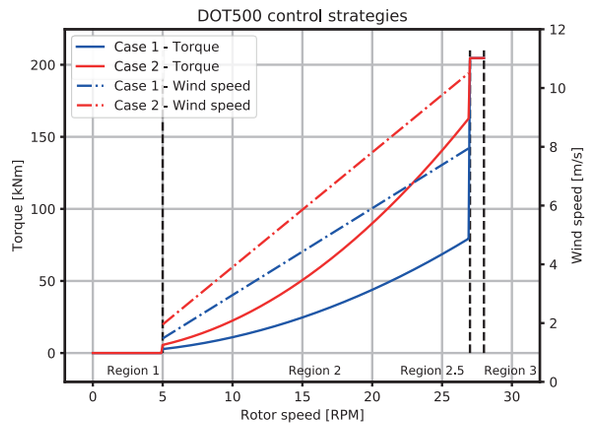


Figure 3: Torque control strategies for maintaining a fixed tip-speed ratio λ, tracking the optimal power coefficient $C_{p,max}$ (case 1) and the maximum torque coefficient $C_{\tau,max}$ (case 2). The dash-dotted lines show the corresponding wind speed to the distinct strategies, and the vertical dashed lines indicate boundaries between operating regions.

3.2 Drive train efficiency analysis

This section presents the available component efficiency data, and evaluates steady-state drive train performance and operation characteristics for the two previously introduced operating cases. The components in the hydraulic drive train have varying static and dynamic characteristics which influence the response of the system throughout its entire operating region. The efficiency characteristics of the components primarily influence the steady-state response of the wind turbine, as shown in Equation (2). The considered drive train system is defined as the mechanical power at the rotor low-speed shaft, to the hydraulic power at the water pump discharge side. To perform a fair comparison between case 1 and 2, the rotor efficiency is normalized with respect to $C_{\mathrm{p,max}}$, resulting in a constant factor of 0.85 for operation case 2. Detailed efficiency data is available for the oil pump and motor. As no data for the efficiency characteristics of the water pump is available, a constant mechanical efficiency of $\eta_{\mathrm{m,WP}} = 0.83$ assumed.

As the oil pump is only supplied with total efficiency data, this data is manipulated into a mechanical efficiency mapping $\eta_{\mathrm{m,OP}}$ as a function of speed ω_{r} and the supplied system torque τ_{sys} by assuming a constant volumetric efficiency of 98%, and is presented in Figure 4 (left). The plotted data points (dots) are interpolated on a mesh grid using a regular grid linear interpolation method from the Python SciPy interpolation toolbox /15/. Operating cases 1 and 2 are indicated by the dashed lines. The mechanical efficiency data for the oil motor $\eta_{\mathrm{m,OM}}$ is also given, and the result is presented in Figure 4 (right).

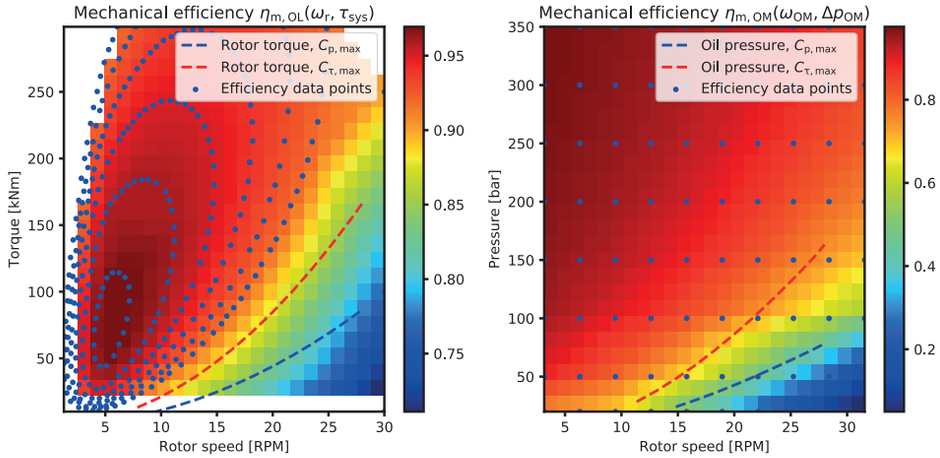


Figure 4: Mechanical efficiency mapping of the oil pump and motor. Manufacturer supplied data (blue dots) is evaluated using an interpolation function. Operating cases 1 and 2 are indicated by the blue and red dashed lines, respectively.

As observed in the efficiency curves, hydraulic components are generally more efficient in the low-speed high-torque/pressure region. It is immediately clear that for both the oil pump as well as the motor, operating the rotor at a lower tip-speed ratio (case 2) is beneficial from a component efficiency point-of-view. However, operating at higher component efficiencies might lead to a lower lifetime expectation of the components. This should and will be taken into account during the LCOE trade-off.

An operational drive train efficiency evaluation for operating cases 1 and 2 is given in Figure 5. The lack of efficiency data at lower rotor speeds in the left plot of Figure 5 (case 1) is due to unavailability of data at lower pressures. From the right plot of Figure 5 it is concluded that the overall drive train efficiency for case 2 is higher and more consistent compared to case 1. The consistency of the total drive train efficiency is advantageous for control, as this will enable passive torque control to maintain a constant tip-speed ratio as seen in Equation (2). As

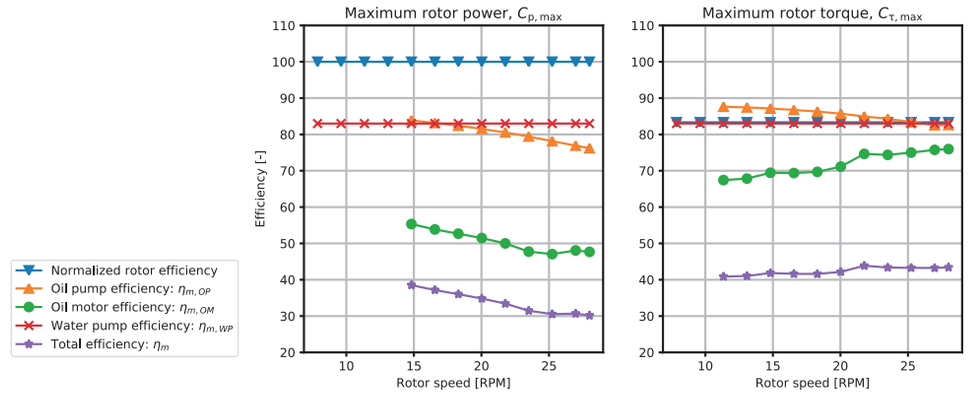


Figure 5: Comparison of the total drive train efficiency for operating cases 1 and 2. It is observed that the total efficiency is higher in the complete below-rated region for case 2. Also, the efficiency over all rotor speeds is more consistent, enabling passive torque control using a constant nozzle area A_{nz}.

a result of this observation, the focus is henceforth shifted to the implementation of a torque control strategy, tracking the maximum torque coefficient.

4 Control implementation and in-field results

In this section, the operational control strategy derived in this paper is implemented and evaluated on the actual in-field DOT500 turbine. A grid search for a range of valve positions and wind speeds is performed to gather mappings of actual turbine properties, such as the output power curve and tip-speed ratio mapping. The goal of the power curve is to gather a better insight in the actual drive train behavior, which is particularly interesting as actual drive train component characteristics are unknown. Moreover, a stability analysis of the rotor can be obtained from the real-world turbine.

First, a grid search is performed to obtain an output power curve of the actual wind turbine. For this purpose, a range of fixed spear positions (nozzle areas) is defined. This is done on a normalized scale, where 0 % is the minimum spear position (larger nozzle area), and 100 % the maximum spear position (smaller nozzle area, rated conditions). The spear position is the only control input in the below-rated region, and is independent from other system variables. By fixing the valve position and making sure that at each operating point sufficient data is collected (throughout all wind speeds), a steady-state mapping of the drive train performance is derived. During data collection, the pitch system regulates the rotor speed up to its nominal value of 28 RPM.

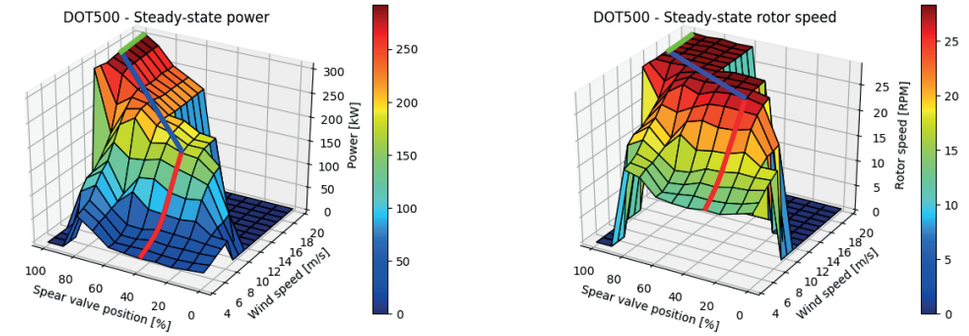


Figure 6: Steady-state power output (left) and rotor speed curve (right) obtained for predefined spear valve positions (nozzle area) and wind speed conditions. The red lines indicate the operation strategy at fixed spear

valve position in the below-rated region, whereas the blue trajectories indicate active spear valve position control towards rated conditions. The effect of blade pitching is indicated in green.

Figure 6 presents the output power and rotor speed curve, binned in the predefined spear valve positions and wind speeds. The figure includes a visualization of the implemented control strategy (see also Figure 3) for below-rated (red) and near-rated (blue) operating conditions. Below-rated, the spear valve position is kept constant: flow fluctuations influence the water discharge pressure and thus the system torque. In near-rated conditions, the spear position is actively controlled by a PI-controller, which continuously adjusts the effective nozzle area and thus water discharge pressure to regulate the rotor speed to 27 RPM. Once the turbine reaches its nominal power output, the rotor limits wind energy power capture using gain-scheduled PI pitch control (green), controlling the rotor speed to 28 RPM.

A schematic diagram of the two controllers is given in Figure 7. As the controllers have a common control objective of regulating the rotor speed and are implemented in a decentralized way, it is ensured that they are not active simultaneously. This is also ensured by the reference speed difference between the spear valve and pitch controller. In-field test results of the above described strategy is given in Figure 8. It is shown that active spear valve control combined with pitch control regulates the wind turbine in (near-)rated conditions, and the strategy has sufficient bandwidth to act as a substitute to conventional torque control. The dynamics of the oil and water lines are not taken into account during the analysis and control design. Dynamics of the water line are assumed to be negligible due to the limiting effect of the high mass moment of inertia of the wind turbine rotor on the fluid inertia. However, as characteristic properties of an oil column are highly dependent on external conditions like pressure and temperature, including them in the analysis presumably leads to higher control performance in terms of speed and stability and mitigation of fluid resonances.

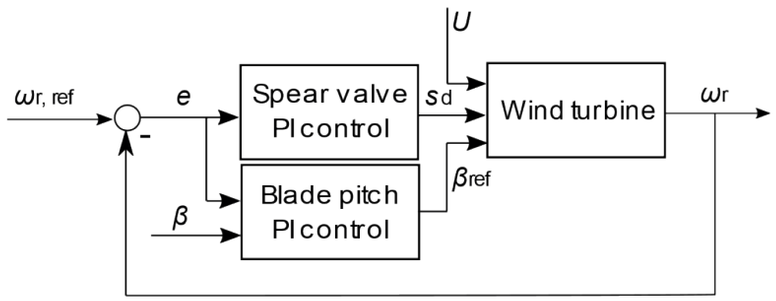


Figure 7: Schematic diagram of the DOT500 control system. Near the above-rated operating region, the rotor speed ω_r is actively regulated by adjusting the spear valve position s_s to influence the fluid pressure and the system torque. When the spear valve is at its rated minimum position, gain-scheduled pitch controller generates a pitch angle set point β_{ref} to regulate the rotor speed at its nominal value.

A mapping of the attained tip-speed ratios as function of the spear valve position and rotor speed, is given in Figure 9. The wind speed is obtained from a downwind anemometer, i.e., behind the rotor. The attained tip-speed ratio averages are presented in the left plot, and the right plot shows a two-dimensional visualization of the data indicated by the red dashed line, including one standard deviation. The red line indicates the fixed spear position of 70 %, chosen as the position for passive torque control in the below-rated region.

It is shown that the calculated tip-speed ratio is regulated around a mean 5.5 for below-rated conditions. The attained value is slightly lower than the theoretical calculated minimum tip-speed ratio of 5.9, but stable turbine operation is attained during in-field tests, which could be a result of the damping characteristics of hydraulic components compensating for the instability as shown in /16/. It has stressed again that for calculation of the tip-speed ratio, the wind speed measurement is obtained from a downwind anemometer at hub-height, and the influence of rotor induction on this measurement is not included in this analysis. The tip-speed ratio tends to

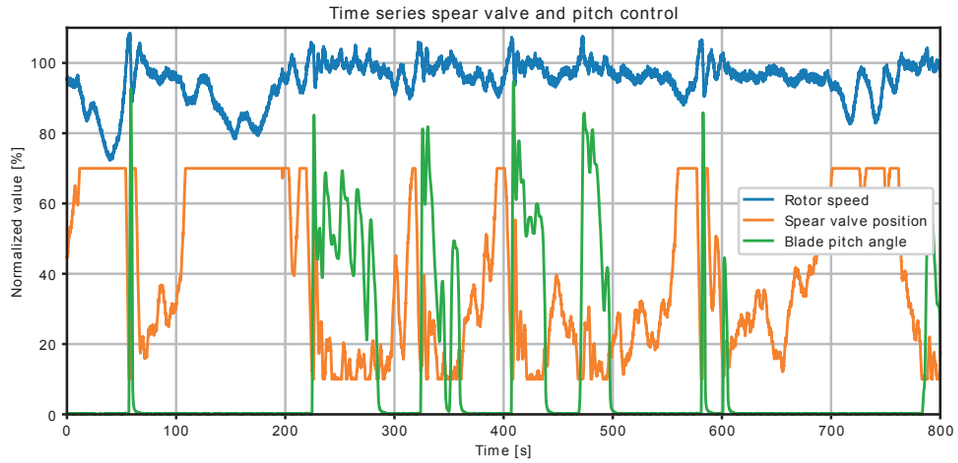


Figure 8: A time-series showing the hydraulic control strategy for the DOT500 turbine. The spear valve position (orange) actively regulates the rotor speed (blue) as a substitute to conventional turbine torque control. In the above-rated region, pitch control (green) is employed to keep the rotor at it nominal speed (100 %). All signals in this plot are normalized.

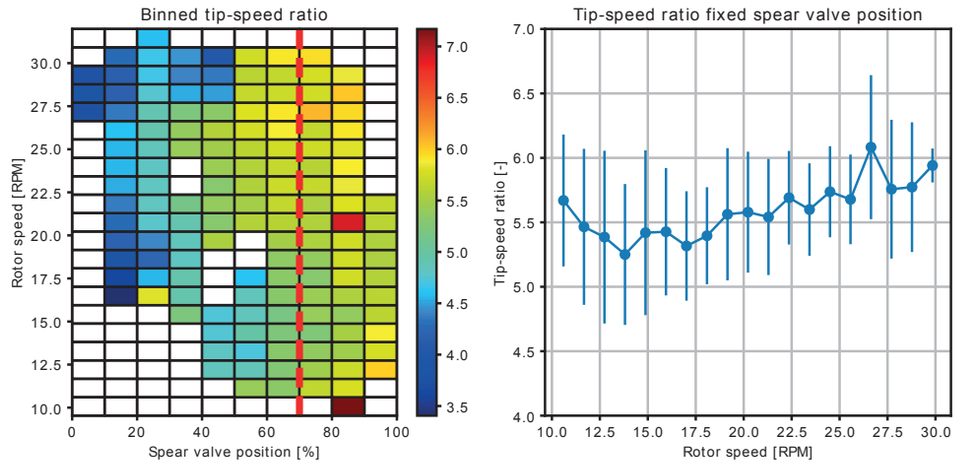


Figure 9: Binned tip-speed ratio to the spear valve position and wind speed. The left plot shows the binned means, and the right plot the corresponding standard deviations.

increase to larger values for higher rotor speeds. This is most probably caused by non-constant mechanical efficiency characteristics of the water pump.

5 Summary and conclusions

This paper presents the control design for the DOT500 wind turbine with hydraulic drive train. The discussed drive train is an intermediate configuration of the final set-up, including more components. All used components are commercially available, and therefore the overall turbine efficiency was known to be low beforehand. The aim of retrofitting an actual wind turbine with a hydraulic drive train and performing in-field tests, is to show the practical feasibility of the hydraulic DOT concept.

Conventional generator torque control has been substituted by a hydraulic torque control implementation. The hydraulic control strategy is twofold: it is passive in the below-rated region (i.e., a self-regulating control

implementation), and active during the transition between below- and above-rated operating conditions. It is shown that by properly choosing the effective nozzle area, while considering the efficiency characteristics of all drive train components, below-rated tracking of a predefined tip-speed ratio is possible, without the need for active control. For the transition region it is verified that spear valve torque control implementation has sufficient bandwidth to regulate the rotor speed to its reference value.

6 Acknowledgements

The research presented in this paper was part of the DOT500 ONT project, which was conducted by DOT in collaboration with the TU Delft and executed with funding received from the *Ministerie van Economische zaken via TKI Wind op Zee, Topsector Energie*.

References

/1/ T. Burton, N. Jenkins, D. Sharpe, E. Bossanyi, *Wind energy handbook*, John Wiley & Sons, 2011.

/2/ F. Spinato, P. Tavner, G. Van Bussel, E. Koutoulakos, *Reliability of wind turbine subassemblies*, IET Renewable Power Generation 3 (4) (2009) 387–401.

/3/ A. Ragheb, M. Ragheb, *Wind turbine gearbox technologies*, in: Nuclear & Renewable Energy Conference (INREC), 2010 1st International, IEEE, 2010, pp. 1–8

/4/ P.-E. Morthorst, S. Awerbuch, *The economics of wind energy*, EWEA, 2009.

/5/ J. van der Tempel, *Energy extraction system, has water pump attached to rotor, windmill for pumping water from sea, water system connected to water pump, for passing water pumped from sea, and generator connected to water system*, (2009).

/6/ N. Diepeveen, *On the application of fluid power transmission in offshore wind turbines*, Ph.D. thesis (2013).

/7/ E. Bossanyi, *The design of closed loop controllers for wind turbines*, Wind Energy 3 (3) (2000) 149–163.

/8/ D. Buhagiar, T. Sant, M. Bugeja, *A comparison of two pressure control concepts for hydraulic offshore wind turbines, Journal of Dynamic Systems*, Measurement, and Control 138 (8) (2016) 081007.

/9/ P. Silva, A. Giuffrida, N. Fergnani, E. Macchi, M. Cantu, R. Suffredini, M. Schiavetti, G. Gigliucci, *Performance prediction of a multi-MW wind turbine adopting an advanced hydrostatic transmission*, Energy 64 (2014), 450–461.

/10/ E. Innes-Wimsatt, C. Qin, E. Loth, *Economic benefits of hydraulic-electric hybrid wind turbines*, International Journal of Environmental Studies 71 (6) (2014) 812–827.

/11/ J. Nijssen, A. Kempenaar, N. Diepeveen: *Development of an interface between a plunger and an eccentric running track for a low-speed seawater pump*, Proceedings of the 11th International Fluid Power Conference. RWTH Aachen, 2018.

/12/ N. Diepeveen, A. Jarquin-Laguna, *Wind tunnel experiments to prove a hydraulic passive torque control concept for variable speed wind turbines*, Journal of Physics: Conference Series, Vol. 555, IOP Publishing, 2014, p. 012028

/13/ E. Trostmann, *Water hydraulics control technology*, CRC Press, 1995.

/14/ F. Bianchi, H. De Battista, R. Mantz, *Wind turbine control systems: principles, modelling and gain scheduling design*, Springer Science & Business Media, 2006

/15/ Scipy.org, *Interpolation (scipy.interpolate.RegularGridInterpolator)*, (last access: 2017-07-01) (2017). URL: https://docs.scipy.org/doc/scipy-0.19.1/reference/interpolate.html

/16/ J. Schmitz, N. Diepeveen, N. Vatheuer, H. Murrenhoff, *Dynamic transmission response of a hydrostatic transmission measured on a test bench*, EWEA, 2012

REVIEWED

Characterization and Calibration of a Power Regenerative Hydrostatic Wind Turbine Test Bed using an Advanced Control Valve

Biswaranjan Mohanty and Kim A. Stelson

University of Minnesota
Department of Mechanical Engineering, 111 Church Street SE, Minneapolis, MN, USA
E-Mail: mohan035@umn.edu, kstelson@umn.edu

A hydrostatic transmission is commonly used in off road construction equipment for its high power density. It can also be used in wind turbines for more reliable and cost effective transmission than a conventional gearbox. A power regenerative test platform has been built at the University of Minnesota to understand the performance of a hydrostatic transmission in a wind turbine. In this paper the use of an advanced control valve to characterize the components of the test bed has been demonstrated. The electrohydraulic valve has precise control on pressure and flow and gives more flexibility to the testbed.

Keywords: hydrostatic transmission, wind turbine, efficiency, calibration
Target audience: Mobile Hydraulics, Mining Industry, Renewable Energy

1 Introduction

The global demand for wind energy is increasing rapidly. The worldwide wind capacity has reached 456 MW at the end of June 2016, which is 4.7% of the world's electricity [1]. The US Department of Energy (DOE) has a target of generating 20% of the nation's electricity by 2030 [2]. Most large wind turbine farms are far away from the point of use, increasing transmission cost. In contrast, distributed wind relies on small and mid-size turbines installed at or near the point of use. This reduces the transmission loss and makes the distributed grid more reliable and stable.

A multi stage fixed ratio gearbox is used in a conventional turbine to transmit power from the low speed rotor to the high speed generator. Studies conducted by the National Renewable Energy Laboratory show that electrical systems fail frequently but with shorter downtimes, but gearboxes and generators fail less frequently but with longer downtimes [3][4]. The failure of gearboxes and generators is due to fatigue loading caused by unsteady wind, which reduces the life of the components. This failure increases the maintenance cost and decreases the annual energy production of the turbine.

The reliability of a wind turbine can be improved by replacing the gearbox with a hydrostatic transmission (HST). An HST is one type of high power density continuous variable transmission. HSTs are simple, light and cost effective. They are commonly used in off road construction equipment. The slight compressibility of the hydraulic fluid in an HST reduces the shock loading on mechanical components increasing their life. Because it is continuously variable, an HST decouples the generator speed from the rotor speed, allowing the generator to run at synchronous speed with time varying wind speeds. This eliminates expensive power converters [5] [6].

The University of Minnesota test bed is focused on using a hydrostatic transmission on smaller wind turbines typically used in community wind. It is capable of generating 100 kW with a maximum pressure of 350 bar with 55 kW of electrical input. The test bed has a single pump and motor and is equipped with multiple sensors to accommodate and test a variety of hydraulic fluids, components and controls. The novelty of the paper is use of an advanced control valve to characterize the hydraulic components of the test bed.

This research compliments the HST wind turbine research at RWTH Aachen University. The RWTH test bed has a power level of 1 MW and uses multiple pumps and motors. The RWTH control approach emphasized the switching of pumps and motors to maximize the efficiency at different power levels [7] [8].

2 Power Regenerative Hydrostatic Test Platform

2.1 Hydrostatic Transmission

In its simplest form, a hydrostatic transmission consists of a hydraulic pump driving a hydraulic motor. The proposed HST for a wind turbine is shown in Figure 1 consisting of a fixed displacement pump and a variable displacement motor. This choice takes advantage of commercially available hydraulic components, control simplicity, transmission efficiency and cost, and is therefore the most practical solution. A closed circuit HST is chosen, eliminating the need for a bulky reservoir. To measure the efficiency and performance of an HST wind turbine, a power regenerative wind turbine test bed has been built at the University of Minnesota.

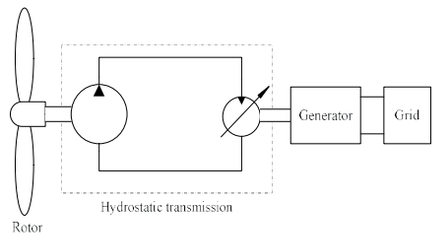


Figure 1: Schematic of HST wind turbine

2.2 Hydrostatic Wind Turbine Test Bed

The power regenerative research platform consists of two closed loop hydrostatic circuits as shown in Figure 2. The block in dark gray is the hydrostatic transmission under investigation. The block in light gray is the hydrostatic drive (HSD), to simulate the rotor driven by time varying wind.

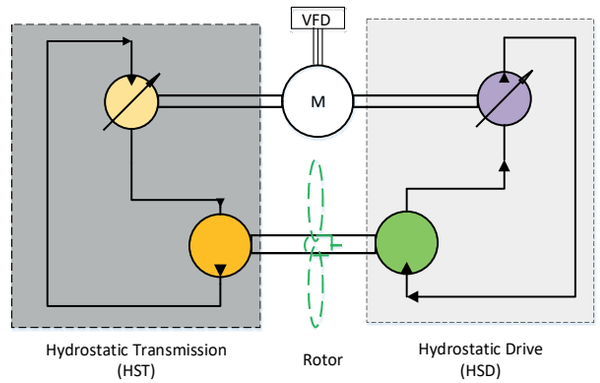


Figure 2: Schematic of power regenerative test bed

In the power regenerative test bed, the output power from the HST is fed back into the input of the HSD. A variable frequency drive (VFD) electric motor is coupled to the turbine output shaft to compensate for the losses of the HST and HSD. The VFD regulates the speed of turbine output shaft speed to simulate grid conditions. The power regenerative test platform is shown in Figure 3.

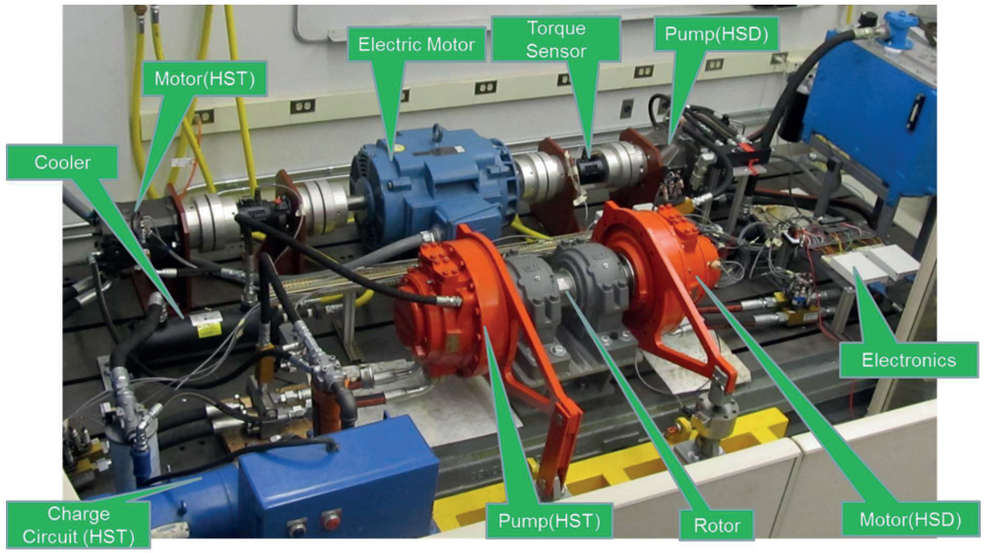


Figure 3: Power regenerative test bed

The HSD of the test platform consists of a variable displacement axial piston pump and a fixed displacement radial piston motor. The HST consists of fixed displacement radial piston motor used as a pump and a variable displacement axial piston. Torque and speed sensors have been installed in the high speed (1800 rpm) and low speed (rotor) shaft to measure shaft torque and speed. Pressure, flow and temperature sensors have been installed in all hydraulic lines. An advanced electro hydraulic valve with independent metering is used to calibrate the hydraulic sensors and to characterize the performance of the pump and motors.

3 Advanced Control valve

The Advanced Control Valve (ACV) is a CAN enabled electrohydraulic sectional valve with independent metering spool valves. It is capable of controlling either flow or pressure using pressure and spool position sensors, on-board electronics and an advanced control algorithm that delivers high precision and fast response. For pressure and position control the precision is determined by the accuracy of the sensor. Since the flow is not directly measured, the precision for flow control is determined by a calibrated lookup table. For 15 cSt hydraulic oil, the valve has a bandwidth of 17.5 Hz and a rise time of 24 ms. The ACV is shown in Figure 4.

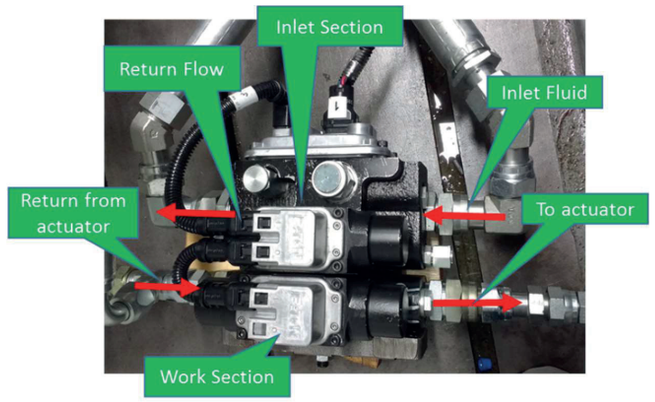


Figure 4: Advance Control Valve

This commercial ACV (Eaton CMA200) is integrated in to the power regenerative circuit to calibrate flow sensors and characterize each hydraulic pump and motor. The schematic of the ACV is shown in Figure 5 with inlet section on the left and work section on the right.

The inlet section is connected to the HST pump. The inlet section has a pilot valve that gets its commands from the controller and controls a main stage valve to maintain the inlet pressure. It also has a pressure relief valve that is set at the maximum operating pressure to keep the system safe. The inlet section is connected to a work section valve.

The work section is comprised of two independent spools. The independent pilot spools control the each main stage valve that has its own position sensor for precise operation as shown in Figure 5. The two spools can be controlled as a pair or separately. This allows us to control the inlet A and return B ports of the work section independently. Pressure sensors are located in the A, B, pressure and tank lines. The pilot spool of the work section gets its command from the controller. With the upstream and downstream pressure information and the pilot command, the mainstage spools are moved to create the appropriate orifice area for the desired flow rate. Although the ACV can be used in a wide range of applications, in the wind power test bed it is used to control the pressure of the inlet section to load the pump and control the output flow of the work section.

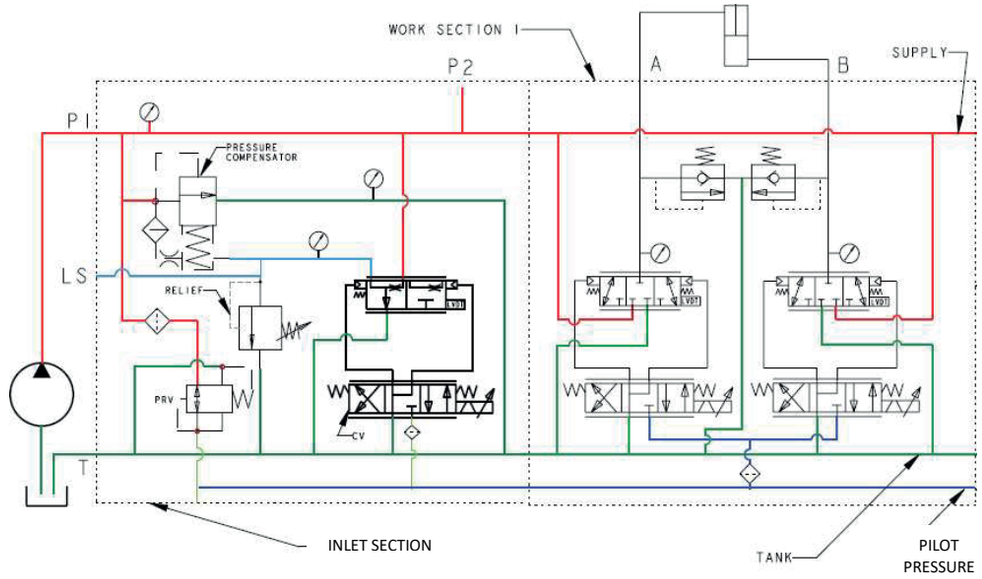


Figure 5: Schematic of Advanced Control Valve with inlet section (left) and outlet section (right)

4 Calibration of sensor

The hydraulic line of the power regenerative test bed is connected to pressure, temperature and flow sensor modules. The main lines of the HSD and HST are measured with a 15-300 lpm flow sensor, while case drain lines of HST are measured with 8-150 lpm flow sensors. The ACV is used to calibrate all flow sensors on the test bed. The schematic of flow sensor calibration is shown in Figure 6(a). The inlet section of the ACV is connected to the HST pump and the work section is connected to the calibrated flow sensor and test flow sensor in series. While one of the spools in the working section is commanded to control the flow, the other one is commanded to the fully open position to minimize any pressure drop in the returning fluid from the flow sensor. As fluid passes through the orifices, frictional dissipation produces heat. A small volume of fluid is bled out from the circuit and passed through a heat exchanger to reduce the temperature. A charge pump is used to make up for the losses of the fluid on the testing side.

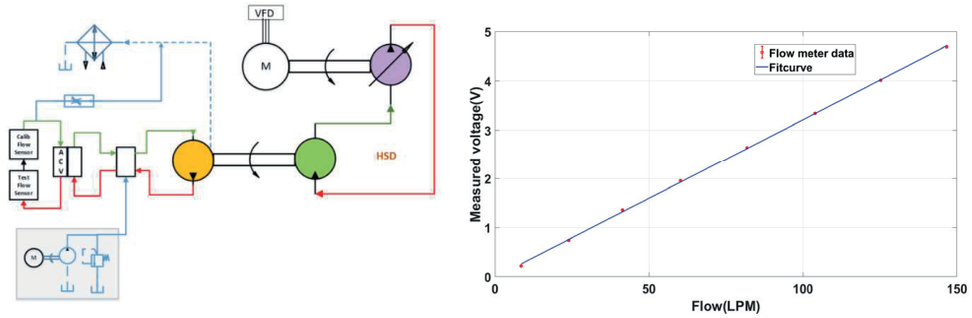


Figure 6: (a) Schematic flow calibration. (b) Flow sensor data

The HST pump is driven by the HSD of the power regenerative platform. The pressure of the inlet section of the ACV is set to 60 bar. The ACV does not measure the flow but rather it controls the flow by controlling the position of the spool. A calibrated flow sensor is used to measure the flow of the work section. The output voltage of the test flow meter is collected in the data acquisition system of the wind turbine test platform. The flow sensor data of a 8-151 LPM flow sensor is shown in Figure 6(b) with the calibrated flow measurement in x-axis and the output voltage of the test flow meter in y-axis. A straight line is fit through the data points to compute the gain and bias of the sensor.

The pressure sensor of the module is calibrated with a dead weight tester. The temperature sensors are calibrated using a water bath and calibrated temperature sensors.

5 Characterization of components

The testbed has two pumps and two motors. Each pump and motor unit has been characterized on the testbed using the ACV. The inlet section of the ACV is connected to the HST pump to load the HSD motor. The schematic of the test bed for characterization of the hydraulic unit is shown in Figure 7(a). The work section of the ACV is connected to the HST motor. The HST motor is coupled to the high speed shaft. Both electric motor and HST motor drive the HSD pump. The torque and speed sensors are mounted in between the electric motor and the HSD pump to measure the mechanical input power to the HSD pump. Pressure sensors have been installed at each port to measure port pressure of the pump and motor as shown in Figure 7(b). A flow sensor module consisting of flow, pressure and temperature sensors has been mounted in each hydraulic line.

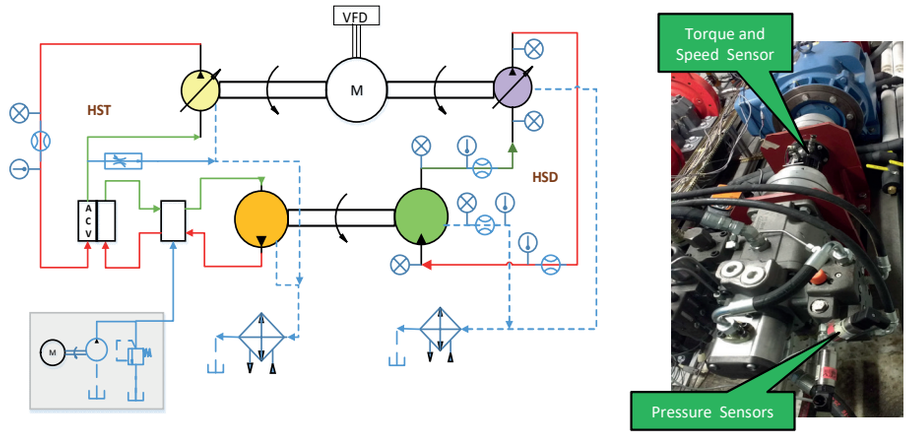


Figure 7: (a) Schematic of the test bed for characterization of the pump and motors. (b) Speed, torque and pressure sensors on HSD pump.

A certain volume of fluid is directed from the low-pressure line of the HST motor to a heat exchanger to compensate for the heat generated by the metering of the ACV. The temperatures of the hydraulic oil (ISO 68) in both the HSD and HST are maintained at 40 degrees C. The performance of the HSD pump and motor of the power regenerative test bed is discussed in this paper.

5.1 HSD pump

A variable displacement axial piston pump with maximum pump displacement (D_p) of 160 cc/rev is used in the HSD circuit. For wind turbine applications, the HSD pump rotates at a constant speed (ω_p). The pump output flow (Q_p) is varied by changing the swashplate angle. The position of the swashplate angle is changed by a servo valve. x is the displacement fraction of the pump. The volumetric efficiency (η_{p_vol}) of the pump is given by Equation (1). .

$$\eta_{p_vol} = \frac{Q_p}{xD_p\omega_p} \tag{1}$$

The volumetric efficiency of the HSD pump at 1000 RPM is shown in Figure 8(a). The pump shows nearly constant efficiency at higher displacement fractions. However, there is a sharp decrease in volumetric efficiency below 30% displacement fraction. As pressure increases the leakage flow through the orifice increases and hence volumetric efficiency decreases.

The mechanical performance of the pump is computed by measuring the pressure at the high pressure port ($P_{p_{hp}}$) and the low pressure port ($P_{p_{lp}}$). The torque (T_p) applied to the pump is measured by a rotary torque sensor. The pressure difference across the port has been created by loading the pump by ACV. The mechanical efficiency of the pump is given by Equation (2).

$$\eta_{p_mech} = \frac{xD_p(P_{p_{hp}} - P_{p_{lp}})}{T_p} \tag{2}$$

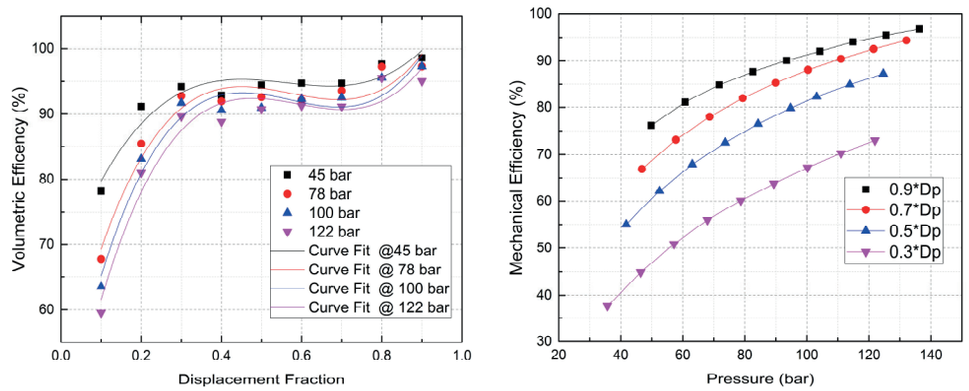


Figure 8: (a) Volumetric efficiency of the HSD pump at different pressures. (b) Mechanical efficiency of the HSD pump at different displacement fractions.

The mechanical efficiency of the pump with respect to the pressure difference ($P_{p_{hp}} - P_{p_{lp}}$) and displacement fraction is shown in Figure 8(b). The mechanical efficiency is proportional to the pressure difference. However, the efficiency of the variable displacement pump decreases with decreases in displacement fraction.

5.2 HSD Motor

In the power regenerative test bed, the HSD motor is used to emulate a low speed and high torque wind turbine rotor. A fixed displacement radial-piston type motor with a motor displacement (D_m) of 2512 cc/rev has been used in the testbed. The input flow (Q_p) to the motor is measured at its inlet port. The motor is connected to the rotor shaft through the hollow shaft of the cylinder block. The rotor speed (ω_r) is measured by a speed encoder mounted at the shaft end. The volumetric efficiency (η_{m_vol}) of the motor is given by Equation (3).

$$\eta_{m_vol} = \frac{D_m \omega_r}{Q_p} \tag{3}$$

The volumetric efficiency of the motor with respect to pressure and speed is shown in Figure 9(a). As the port pressure increases, the leakage through the orifice increases, thereby decreasing the efficiency. The efficiency also increases with increase in rotor speed.

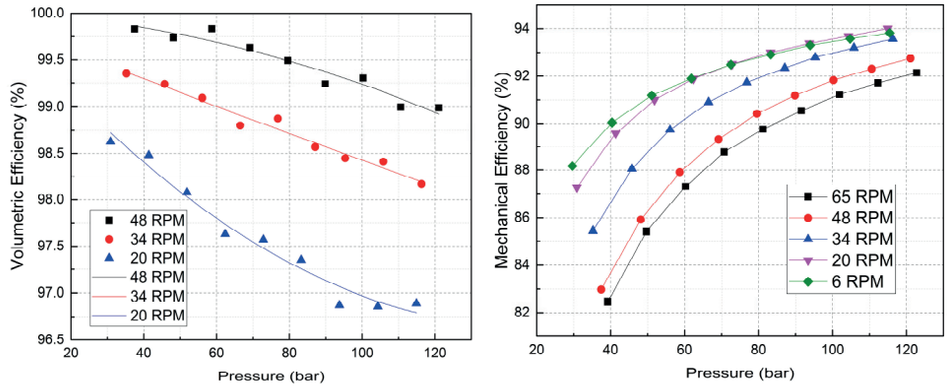


Figure 9: (a) Volumetric efficiency of the HSD motor at different pressure and speed (b) Mechanical efficiency of the HSD motor at different pressure and speed.

The mechanical torque (T_r) is transmitted to the rotor shaft through the splines. The torque is computed from the load cell measurement of the motor torque arm. The port pressure at the inlet ($P_{m_{hp}}$) and outlet ($P_{m_{lp}}$) of the motor has been measured. The mechanical efficiency (η_{m_mech}) of the motor is computed by Equation (4).

$$\eta_{m_mech} = \frac{T_r}{D_m(P_{m_{hp}} - P_{m_{lp}})} \tag{4}$$

The mechanical efficiency of the HSD motor is shown in Figure 9(b). The efficiency of the motor decreases with decreasing port pressure. With increasing rotor speed, the velocity of the piston increases and hence frictional loss between cylinder and piston increases. Due to increases in frictional loss, the mechanical efficiency decreases.

6 Summary and Conclusion

The electrohydraulic advanced control valve is equipped with multiple sensors, on-board electronics and an advanced control algorithm that delivers high precision and fast response. The ACV is integrated with in to the power regenerative test platform to calibrate flow sensors and measure the performance of each hydraulic component. The ACV provides a flexible architecture to characterize hydraulic pumps and motors by using the existing power of the testbed. In both the pump and motor, mechanical efficiency increases with increasing pressure but volumetric efficiency decreases. The volumetric efficiency of the motor is around 99% during high-speed operation. The pump and motor performance at higher pressure and higher speed will be evaluated in the future.

7 Acknowledgements

This project is funded by the National Science Foundation under grant #1634396. We also thank Eaton, Linde, Danfoss, Bosch Rexroth, Flo-tech and ExxonMobil for donating the components for the test bed. We are thankful to our summer undergraduate researchers Christina Geiser, Diana Luc and Yida Niu for working on calibration of sensors, data acquisition and temperature control of the test platform. We are also grateful to graduate students in our lab, Daniel Escobar and Yuhao Feng for helping us in setting up the experiments.

Nomenclature

Variable	*Description*	*Unit*
T	Torque	[Nm]
P	Pressure	[bar]
η	Efficiency	[-]
D_p	Pump Displacement	[m3/rev]
D_m	Motor Displacement	[m3/rev]
Q	Flow	[m3/sec]
ω	Angular Speed	[rad/sec]
χ	Displacement Fraction	[-]

References

/1/ World wind energy association report, www.wwindea.org

/2/ Wind vision report by Department of Energy, www.energy.gov

/3/ Sheng, S., Report on wind turbine subsystem reliability- a survey of various databases. National Renewable Energy Laboratory, Golden, CO, Tech. Rep. NREL/PR-5000-59111, 2013.

/4/ Lange, M., Wilkinson, M., and Thomas van Delft, T. V., Wind turbine reliability analysis. DEWEC, Bremen, 2011.

/5/ Thul, B., Dutta, R., Stelson, K. A., Hydrostatic transmission for mid-sized wind turbines, 52nd National Conference on Fluid Power, Las Vegas, USA, 2011.

/6/ Dutta R., Wang F., Bohlmann B.F., Stelson K.A. Analysis of short-term energy storage for midsize hydrostatic wind turbine. Journal of Dynamic Systems, Measurement, and Control. 2014 Jan 1; 136(1):011007.

/7/ Schmitz, J., Vatheuer, N., & Murrenhoff, H. (2011). Hydrostatic drive train in wind energy plants. RWTH Aachen University, IFAS Aachen, Germany.

/8/ Schmitz, J., Diepeveen, N., Vatheuer, N., & Murrenhoff, H. (2012). Dynamic transmission response of a hydrostatic transmission measured on a test bench. EWEA.

Electrification of Hydraulics Opens New Ways for Intelligent Energy-Optimized Systems

Dr.-Ing. Mirjana Ristic*, Dipl.-Ing. MatthiasWahler**

Bosch Rexroth AG, Business Unit Automation and Electrification,
Development Mechatronics Solutions and Systems
Bgm.-Dr.-Nebel-Str. 2, 97816 Lohr am Main, GERMANY
E-mail: Mirjana.Ristic@boschrexroth.de *, Matthias.Wahler@boschrexroth.de **

Based on different motivations and driving forces for the electrification of hydraulics, this paper introduces and explains the solutions and basic principles used for increasing the energy efficiency by electrification. The following chapters explore these solutions and principles in depth. The key success factors for the electrification of hydraulics are intelligent energy management and appropriate energy storage type and size. Particular attention is paid to the energy storage systems giving an overview of their optimal application fields. The „Smart Energy Mode“ energy management solution for industrial applications is then introduced. Afterwards, the Smart Energy System Design is explained by way of an industrial and a mobile example. The paper concludes with a remark concerning the current needs of automatic linking of different model-based tools. This ensures the holistic approach required in this context.

Keywords: Energy management, electrification, variable-speed pump drives, simulation, sizing, energy buffer
Target audience: Mobile Hydraulics, Mobile Applications, Mobile Working Machines, Industrial Hydraulics, Industrial Applications, Marine-Offshore, System and Machine Design Process

1 Introduction

The electrification of industrial hydraulics was initiated in the context of specific product developments in the past decade /11/. Electro-hydraulics combines the advantages of both technologies, that is to say the energy density of hydraulics plus the energy efficiency, noise behavior and easy commissioning of electro-mechanics. Today /10/, the electrification of industrial hydraulics is furthermore advanced by the following technological trends:

- Energy management and efficiency
- Industry 4.0 and
- Condition Monitoring (CM).

On the other hand, the trend of electrifying mobile machines comes from the electro-mobility in the automotive industry. However, the first steps were already taken more than 20 years ago /9/. As regards this industry, an increasing public awareness can be observed in the market, in the politics and in the media. This awareness has caused more and more manufacturers of mobile working machines to engage in electric drive concepts. In this case, the focus is on the complete or partial electrification of the traction drive. Depending on the requirements, different performance classes accepted in the market become apparent. Today, they define the operating limits of the technology, but at the same time drive the developments of drive technology components toward increasingly higher performances.

The motivations and reasons for electrifying mobile machines are more diverse than in the case of the electrification of industrial hydraulics. Although the tighter emissions legislation is generally considered to be the main driver of electrification of mobile applications, the important driving forces in the energetic context are:

- **Increasing the energy efficiency** and consequently **reducing the energy consumption, energy and fuel costs** are the main driving forces of electrification in most of the mobile applications.
- The electrification provides several options for intelligently exchanging energy and for integrating the energy storage media to buffer energy and cover the temporary power peaks. This allows the **diesel engine to be downsized** and thus allows the **costs for fuel to be reduced**. According to the performance class, the downsizing can be of higher relevance for compliance with the emission standards and the allowed emission values. In many regions, extensive exhaust aftertreatment is mandatory for a motor power of 19 kW and above. Due to downsizing, in some cases this aftertreatment will not be necessary anymore. The weight reduction of the diesel engine caused by downsizing is mostly or partly compensated by the additional electrical components, such as energy buffers.

In addition, one has to mention the requirements of **eliminating local emissions** for applications underground or in enclosed buildings, **reducing noise** of municipal vehicles for night-time work, **spacial machine design flexibility** for machines with foldaway attachments and a high **control quality**, as well as the requirement of **oil-free** machines /15/.

Electrification usually leads to hybrid machines. In the majority of applications, the axes of high power density, i.e. the working axes, are implemented as electrohydraulic axes, and those of lower power density are implemented as electric axes, e.g. secondary functions or the traction drive in mobile applications. The technological advantage with regard to energy efficiency primarily lies in the coupling of multiple axes in the DC bus group (DC grid). This increases the flexibility for engineering of energy-optimized system solutions. Electric main power split opens up new paths for transferring existing low-loss electric drive technology solutions that the chapter below will deal with.

1.1 Solutions and basic principles for increasing the energy efficiency by electrification

The primary measures for increasing the energy efficiency by electrification can be divided into four groups:

1. **Efficient components and systems, i.e. minimizing the losses** on the component or axis level; the following measures are used in accordance with the application:
    a. Replacing the loss-dominated valve controls by variable-speed pump controls which in turn allows „power on demand“ solutions to be used
    b. Generally using low-loss components
    c. Energy-oriented operational optimization by displacing the operating points to the ranges of optimal, higher efficiencies, or by optimizing the working cycles with regard to energy consumption, e.g. by optional deceleration of cycle parts
    d. Controlling the reactive current eliminates the losses caused by it in the mains connection phase within the drive system. The mains supply is utilized in the best possible way and only the active power is transmitted. /1/
    e. Controlled regeneration: Maintains the power factor on a very high level, causing the reactive power to be reduced on the mains side and thus the feeding back processes to the mains to be optimized. /1/.
2. **Energy recovery and storage** implies intelligent management of energy amounts obtained from generator operating mode phases and it is a key issue for electrification. Decisive is application defined recuperation potential during the work cycle (e.g. down-stroking presses, tele handler) and choice of the proper energy storage unit corresponding to the energy amounts to be stored. Energy optimization in this case takes place on the higher system or machine level, or within a DC bus group (a DC grid). This generally includes

a. demand-based electric energy distribution within a DC bus group incl.

b. energy buffering in an appropriate energy buffer, and

c. optimized supply and energy regeneration from the, and to the mains[1].

3. **Smart Energy System Design:** The potentials for energy saving on component level are very limited. Therefore, an intelligent and application-oriented selection and combination of different measures for increasing the energy efficiency is the deciding factor for energy-optimized measures contribution. A holistic approach is required at least on the system level and mostly on the machine level to achieve the relevant energy-optimizing steps. In most cases they result from the accumulation of multiple optimization measures. In view of today's highly complex drive technology and machines, these measures can rarely be taken without the help of professional model-based sizing tools /2/, /6/ and appropriate commercial simulation tools. These tools are used during the entire, often iterative engineering process /10/ that involves the following steps:

   a. system concept design including the energy management concept, use case definition for energy storage and quantification of energy amounts to be stored

   b. deriving the requirements on the components

   c. energy-efficient components selection and sizing incl. the energy storage unit

   d. functional development or selection of control and energy management functions

   e. functional verification by simulation

   f. determination and quantification of improvements with respect to the referred conventional drive solution[2]

   g. optimization, if necessary

   h. price-performance ratio comparison with respect to the referred drive solutions; solution decision and technical implementation

4. **Energy on Demand**, i.e. energy usage according to consumer needs, stand-by mode in inactive cycle phases (see item 1a) and control routines ensuring need-based energy consumption.

The hybrid drive technology is today in transition. The trend toward electrification cannot be stopped and increasingly picks up speed. For many applications, however, there is a drive-related technology performance limit. This performance limit has to be constantly determined, especially because it keeps being expended in the direction of higher performances due to ongoing developments in the electric drive technology. It is therefore immensely important to apply the engineering process described above also to conventional reference systems or machines. In this way the value contribution of the selected system solution is quantified and ensured for each application.

2 Energy management solutions for the electric drive technology

The existing energy management solutions for the electric drive technology emerged from the following industrial requirements:

- Minimizing the power peaks of supply from the mains
- Minimizing the power dissipation
  - in all components, particularly the power to be dissipated in the braking resistors; ideally braking resistors should not be required
  - in mains connection and supply unit
- Storing energy amounts obtained from generator operating mode
- Ensuring the power supply in the case of mains failure or unstable line conditions
- High power density
- Utilizing high motor speeds that require high DC bus voltage
- Independence of mains voltage that requires controlled DC bus voltage
- Reducing the mains load - requires using energy buffers to avoid frequent switch between in feeding and regenerative mode

Figure 1 contains an overview of the basic energy recovery solutions. These solutions are: the energy distribution, energy buffering and energy regeneration on demand. That is to say the recovered energy can be exchanged between multiple axes within the DC bus group, depending on the demands, buffered in a suitable energy buffer or regenerated to the mains. The latter, however, should be avoided if possible.

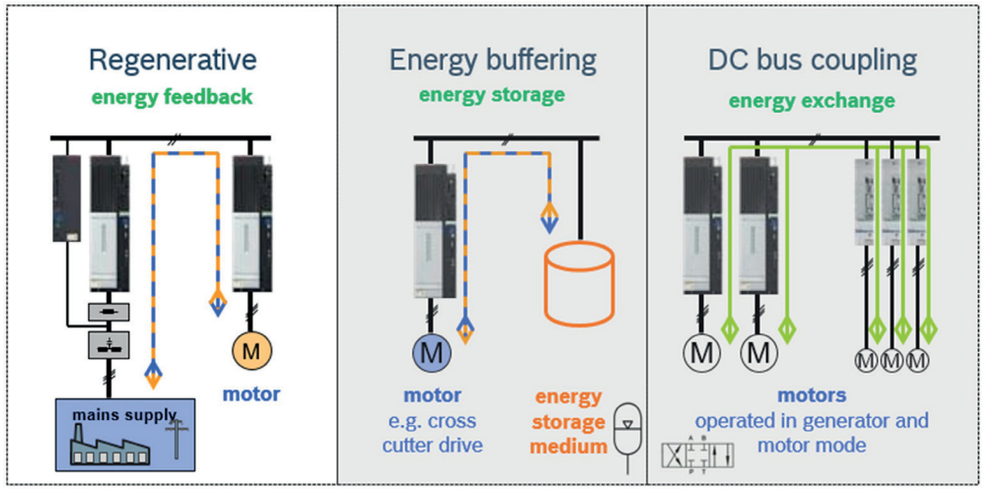


Figure 1: Energy Recovery Solutions Overview

In most of the applications, the energy flow control is physically implemented as a power management. Additionally, the energy distribution on demand in some solutions results from active or passive DC bus voltage control or energy control /4/. The active DC bus voltage control is implemented according to IEC 61131 on a drive-internal PLC platform (MLD) of the IndraDrive controllers. The passive DC bus voltage control is implemented in the firmware of the IndraDrive supply units and will be explained in detail in the following chapter.

2.1.1 Smart Energy Mode /4/

Regenerative supply units /4/ with Smart Energy Mode reduce current and power peaks on the mains side. The Smart Energy Mode limits the maximum device current to the 1.1-fold value of the nominal current. Furthermore, according to the machine-specific process, the recuperative energy amounts obtained are basically stored in a suitable energy buffer in the DC bus and returned to the corresponding consumers according to their energy needs

[1] In the case of industrial applications, and should be avoided if possible.
[2] for this solution is in most cases the same engineering process necessary, unless it is based on a known conventional system for which the first 2 steps are not required

(Figure 2). Primarily, capacitive and kinetic energy buffers were used (for details see chapter 3). From the technical point of view, however, it is possible to use other energy storage types.

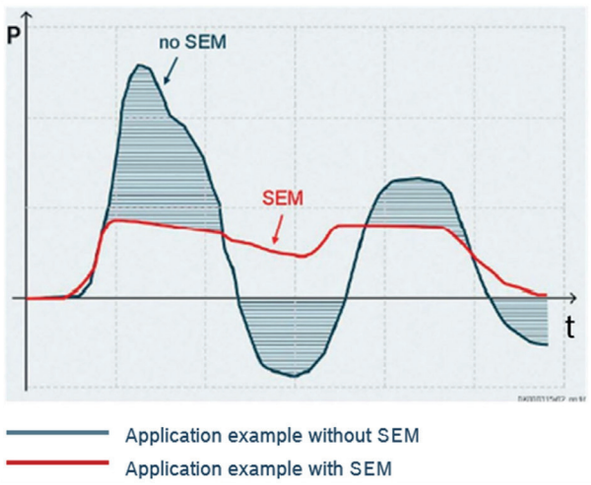


Figure 2: Mains power with or without Smart Energy Mode (SEM)[3]

Depending on actual DC power and DC voltage the Smart Energy Mode distinguishes 4 operation cases that are illustrated in Figure 3 below: motor and generator operation mode, each of them in feeding and regenerative.

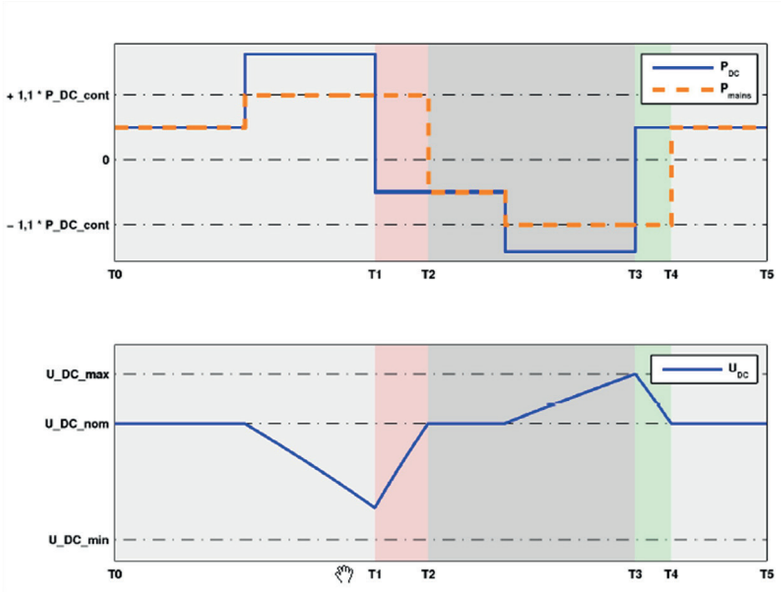


Figure 3: DC power and DC voltage progression curves for different operation cases

Only the in feeding motor operation mode is briefly explained below. The correlations for the other operation cases can be easily derived corresponding to Figure 3.

[3] Hachured areas mark the buffered/boosted energy.

If the conditions (1) and (2) have been fulfilled, the installation or machine is in the in feeding motor operation mode:

$$P_DC(t) \geq 0 \tag{1}$$

$$U_DC(t) \leq U_DC_nom \tag{2}$$

The maximum DC bus voltage correspond to the nominal DC bus voltage. If P_DC(t) > 1.1 × P_DC_cont, the DC bus the used energy buffer (e.g. capacitance) has to supply the additional energy. The DC bus voltage may not fall to the mains peak. This means that the DC bus energy buffer has to have at least the energy E_DC_min. For details see Figure 3.

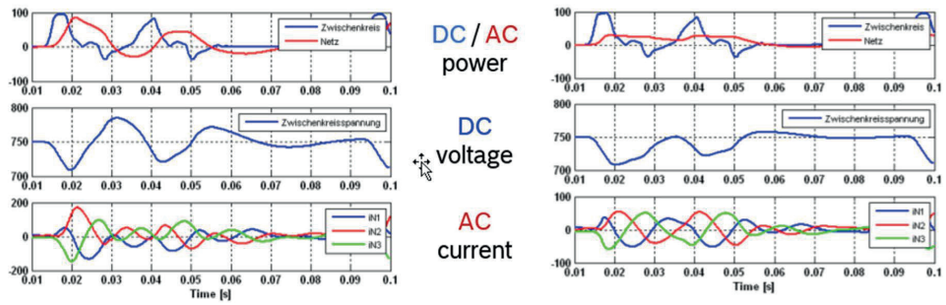
Conventional solution	Solution with the **Smart Energy Mode**
High pulse load on the mains side by cyclically punching head acceleration and deceleration Performance: 1060 strokes/min	Clearly reduced mains load Regeneration is avoided by use of energy buffers Performance: 1060 strokes/min unchanged
Average connected load	
7.3 kW	5.1 kW, i.e. -30%
Maximum power	
53 kW	22 kW, i.e. -58%
	
Simulation results	
	

Table 1: Exemplary implementation in an fully electric Trumpf TruPunch 3000 punching machine

Table 1 shows the exemplary implementation in an industrial all-electric machine.

The characteristic aspects of this energy management are:

- The DC bus voltage is not constant, but fluctuates on a high level within a certain tolerance band.

- The DC bus voltage remains independent of the mains voltage within an extended voltage range.
- Energy buffers in the DC bus are utilized in the best possible way.
- The energy can be recovered at a high power factor ($\cos(\varphi) \approx 1$); this minimizes mains disturbances and reactive power on the mains side

Mains supply units with Smart Energy Mode have the following effects:

- Reduction of the power consumption from the mains by up to 30%
- Reduction of the pulse load in the mains by up to 50%
- Reduction of power losses in the control cabinet

This provides the following benefits:

- Reduction of the energy consumption and energy costs
- Usage of smaller components in the mains connection and for cabinet cooling
- control cabinet space saving

3 Energy storage systems

Energy storage systems are very diverse with regard to the product portfolio available in the market, the basic principle and the performance. Many citations provide a good overview, e.g. /14/. The energy storage systems that are suitable for the electric and electro-hydraulic drive technology target applications due to their properties are shown schematically in Figure 4. This overview shows that as compared to the hydraulic ones, the number of energy buffers within electric power split is much higher, which allows a wider combinational matrix. This illustrates the new energy storage possibilities for hydraulics which are opened up by their electrification. Apart from that, the possible solutions of hydraulic power and energy distribution basically entail higher losses.

Figure 4 contains rough recommendations and notes for the use of different energy storage systems in the drive technology. Apart from that, it has to be mentioned that the electro-chemical energy storages also cover a large variance with different technical features, particularly if you include hybrid energy storage in the consideration. In this connection, different Ragone plots may provide manageable support. The terms and definitions for rechargeable batteries are specified in DIN 40729.

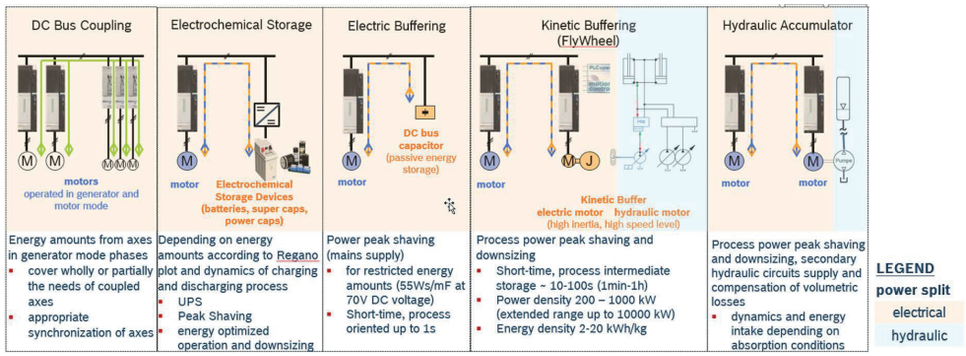


Figure 4: Overview of the energy storage solutions suitable for electric and electro-hydraulic drive technology

For the electric power split the lithium-ion and lithium-ion capacitors (LIC batteries) as well as super capacitors (UltraCaps) and batteries are the most interesting ones of electro-chemical and hybrid batteries. The further differentiation between them can be done according to the application based on their performance.

3.1.1 Application areas, comparison and sizing criteria for the energy storage

The most important selection criteria for a suitable energy storage are:

Use case	Technical performance
• Uninterrupted power supply (UPS), • Coverage of power peaks (peak shaving), • Ensuring an optimized, i.e. minimized energy consumption or component downsizing by including recuperative energy amounts obtained • Emission-free supply of electric or electro-hydraulic working axes	• Amounts of energy to be absorbed • Storage duration and self-discharge • Cyclic or needs-based energy absorption and supply • Required service life • Dynamics of the charging and discharging processes • Environmental conditions • Maximum weight allowed • Inflammability

Table 2: Selection criteria for energy storage

The common energy storage comparison or design characteristics are:

- **Energy density [kWh/kg] or [kWh/l]:** Energy amount that can be stored per weight or per volume. This characteristic is decisive for the solution dead weight, i.e. for its degree of compactness and thus a very relevant technical characteristic for mobile machines.
- **Power density [W/kg] or [W/l]:** describes how much power per volume or mass can be taken from the energy storage medium. This characteristic specifies the dynamic behavior (acceleration ability).
- The **service life** of most energy storages[4], particularly of electro-chemical ones, is limited by degradation processes and specifies the number of charging-discharging cycles after which an energy storage only has a certain rest charging capacity (generally 80% of the nominal capacity).
    - Service life in operating hours[5] is used in the case of systemic sizing and has to be converted according to the underlying cycles. In the ideal case, the service life of the energy storage used should approximately correspond to the service life of the drive systems used (~30,000 h) or to that of the weakest component in the residual system.
- **Efficiency** as characteristic describes the ratio of the achievable energy to the energy used for charging. Like all components, every storage system has physically inherent losses, as well; consequently, their efficiency is a relevant characteristic within energetic optimization considerations.

4 Exemplary implementations of Smart Energy System Design

The Smart Energy System Design is explained in more detail using two exemplary implementations that illustrate today's necessity of holistic approaches and the integrated, closed linking of model based sizing and simulation tools.

[4] Except for kinetic buffers
[5] With most battery types, 1,000 to 2,000 cycles are now guaranteed. Ultracap up to approx. 1,000,000 cycles. For capacities, the market assumes or expects a service life of approx. 8 years.

4.1 Sizing and simulation of a forging press

The first example focuses on an engineering process and the project planning of an industrial installation.

The initial information comprises the load profiles of the working axes and the requirements in the form of concrete technical performance characteristics. The first process step is the system conception and system design based on this information, followed by the first components selection and sizing. Due to the restricted initial information and missing tools for an automatic selection of the components, this process step is often carried out by using very simple calculation tools e.g. self-written Excel, MATLAB or Simster /3/ calculations.

After a concept[6] (see Figure 5) has been fixed and the related components have been designed, simulation models of included axes can be created. In this way, the concept of overall system or overall installation is simulated with application-specific cycles, checked for feasibility and optimized according to the concrete requirements.

In the ideal case, a positive result is immediately achieved. However, often several alternative solutions are checked or the process iterates some loops at this point. From the positively evaluated final result, the load profiles are then derived for electrical components and based on this, the final drive component selection is made using commercial sizing tools based on wide product database /2/, /6/.

In this concrete case, several energetic optimization solutions have been created and implemented for hydraulic main axes /8/, /12/, /13/. For process-inherent reasons, down-stroking presses offer large recovery potential regarding the potential and/or braking energy from the lowering movements of the upper ram. The recovered energy is supplied into the DC bus by electro-hydraulic energy conversion and fed back into the mains. The energy recovery from the decompression and the suspension of the press frame happens in the same way. Due to the three-chamber cylinder construction /8/, re-suction from the tank via the filling valves is omitted in rapid movement; this prevents a power loss of up to 10kW. Apart from that, the press standstill is held by safety valves. The servo motors of these axes are then also in standstill and only the secondary axes for the work piece handling are active (power on demand).

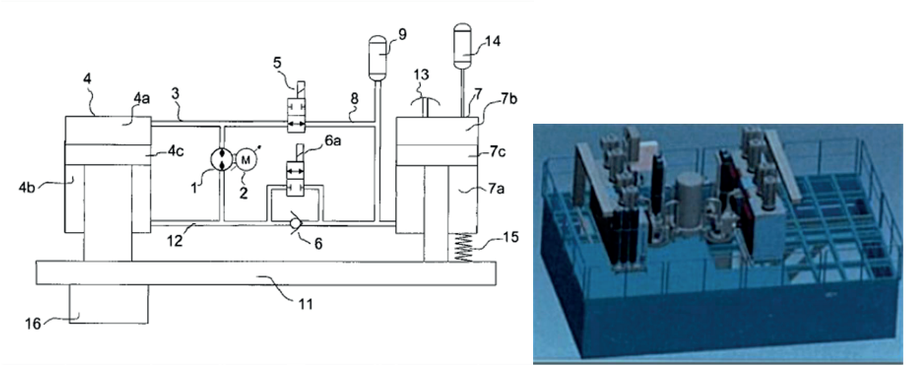


Figure 5: New hydraulic concept for 20 MN forging press (ring blank press) /8/, /13/

The sizing tools referred above actually does not support the sizing of supply units; the latter are currently sized either by use of simple, common sizing tools or using simulation models[7] in an iterative and half-manual manner. That is to say in the next sizing step, the entire DC bus group (Figure 6) incl. available simulation models of the Smart Energy Mode, energy and kinetic buffering module, which are often modeled separately, but in the same simulation environment. The inputs for these partial models are the load profiles in the form of power or torque and speed progression curves over the time. They are either available as result of individual axis simulations or as customer specification. This process step results in

- the selection and/or dimensioning of energy buffer and supply unit
- the DC bus power[8] on the basis of which it is then possible to calculate the required maximum and effective mains current for the given mains conditions.

Based on the determined load profiles, the cooling of the control cabinet and the motors is also designed and sized. The cooling concept is a fundamental part of the system concept. The cooling is on the one hand an important boundary condition to ensure perfect thermal operating conditions and thus the service life of the components concerned. On the other hand, the cooling design is also part of energetic and supply-related considerations for the overall system and also an energy efficiency indicator for concerned components in the relevant application case.

The control cabinet cooling consists of air cooling and water cooling. The required cooling power for water cooling for this installation is about 20 kW and that for the air cooling about 7 kW, which will dissipate a control cabinet power loss of about 27 kW.

The motor power loss to be cooled can be calculated in different forms and here amounts to 3.62 kW per motor. It can, for example, be calculated from efficiency maps on the basis of the effective power (and/or the effective torque and the average speed). Another possibility is the calculation using the calculation formula for the main losses, i.e. the speed-dependent iron and the current-dependent copper losses that can also be included in the simulation models. In detailed considerations, extensive loss models are moreover implemented in the simulation models.

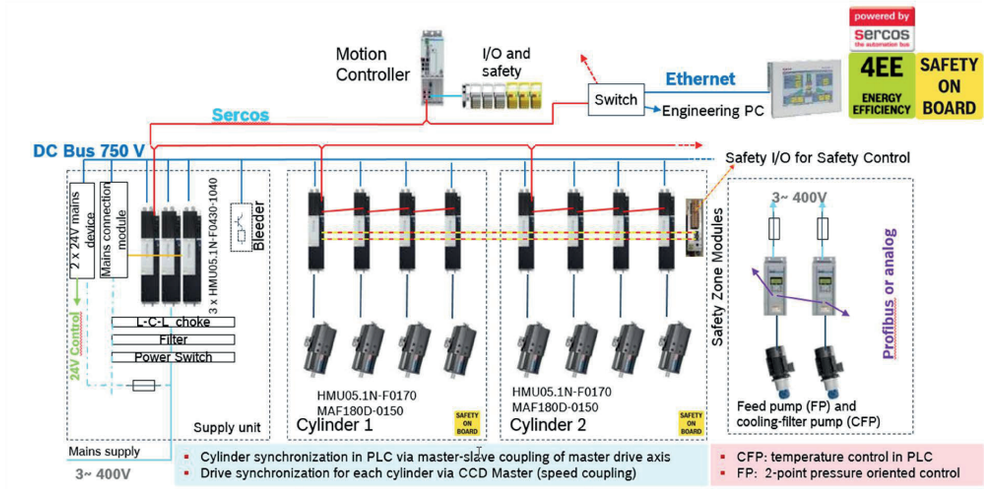


Figure 6: DC grid drive solution for a 20 MN EcoPlant forging press (ring blank press)

Today, the engineering process described here is carried out in an open linking of model-based tools by different technology experts.

4.2 Development of an electrical traction drive for mobile working machines

The Figure 7 shows the principle electrification system solutions for mobile applications, more precisely for their traction drive. The second example refers the hybrid diesel – electric solution and is shortly explained below (Figure 8).

[6] or several alternative concepts
[7] decoupled but in the same simulation environment

[8] Total power in the DC bus (8 motors) is 1,252 kW as peak for 11.2 s and effectively 330 kW with a cycle time of 64 s

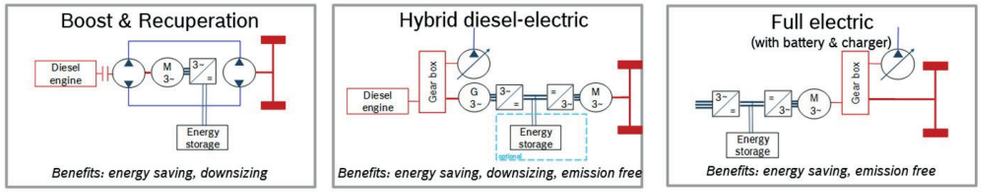


Figure 7: Electrification steps – traction drive system structures

4.2.1 Characteristics of electrified drive train for mobile working machines

This development is characterized by a mixture of new developments and transfer of the available know-how from the existing solutions for industrial applications. This also comprises an adjustment development of the existing industrial product portfolio of electric drives /15/ due to specific requirements for mobile applications (e.g. environmental conditions).

Energy recovery and storage are the key issues leading to the main energetic benefits of electrification, i.e. downsizing and reduction of energy/fuel consumption. The target applications are identified according to simulation based estimation of these benefits for a reference working cycle. The latter is deciding in terms of quantifying of energy amounts which can be recuperated from breaking operations and boosted in accelerating operations. Based on these energy amounts the energy storage units and all drive components are chosen and sized. Furthermore, the system weight and price can be calculated. Opposing the energetic benefits together with technical performance at one side and calculated price and weight at the other side leads to decision, if the electrification of drive train is worthwhile for the application of interest. At this point is to be mentioned that beside intelligent energy management the critical technology breakthrough factors are sizing and prizing of energy storages. From this point of view commercial sizing tools for different energy storage systems are missing and required.

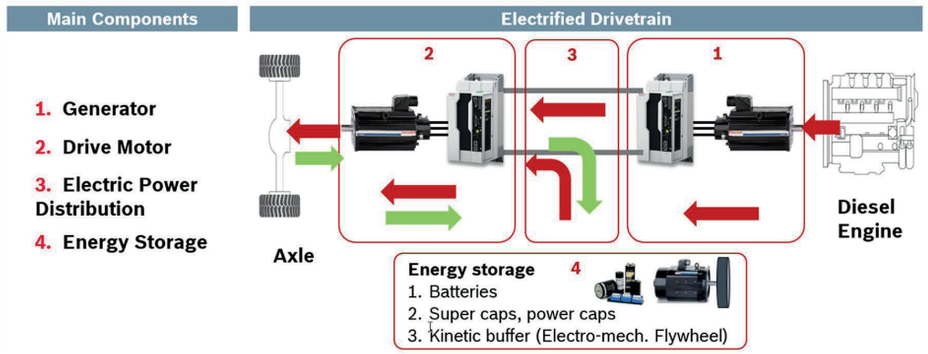


Figure 8: Basic system design of an electric traction drive

4.2.2 Development process and tool chain for electrification of drive train for mobile working machines

This example focuses on the simulative-methodical approach with different development phases in the electrification of traction drives for mobile machines.

As opposed to the presented example from industrial hydraulics, the underlying process here comprises a deciding, complex and extensive step regarding the development of the control and energy management functions. In the concept phase, these control functions are perfectly simulated with a “desired behavior” in order to enable the simulation of an overall system concept. In this way, the requirements on the control and energy management functions are defined automatically within the scope of the concept phase and at the highest level.

Another difference to the previous example is a more distinct integration of the simulation tools stretching across the process up to the final point of the implementation, i.e. to the automatic code generation and the test. The tool chain is shown in Figure 9.

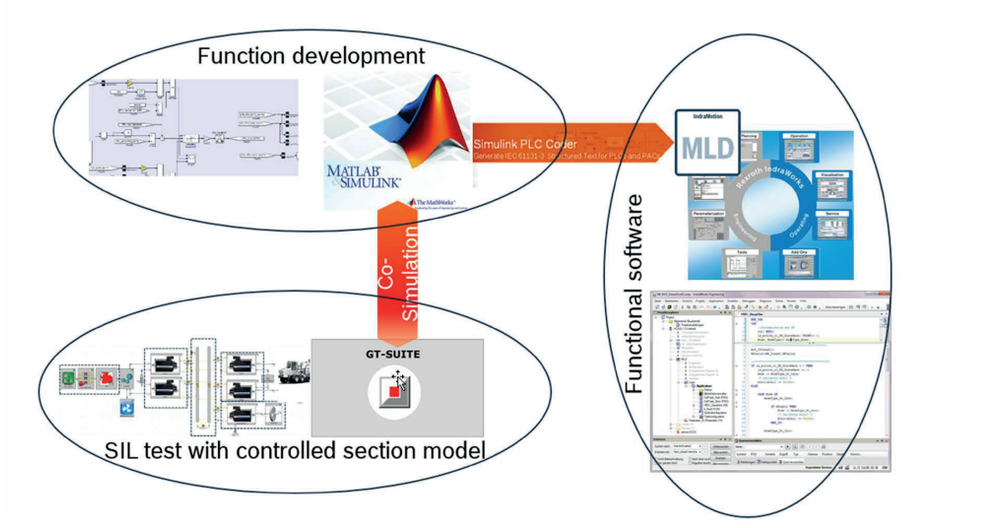


Figure 9: Tool chain for sample development of an electric traction drive

One exemplary result from the concept phase is shown in Figure 10 and illustrates a certain granularity of energetic optimization steps that are carried out and necessary.

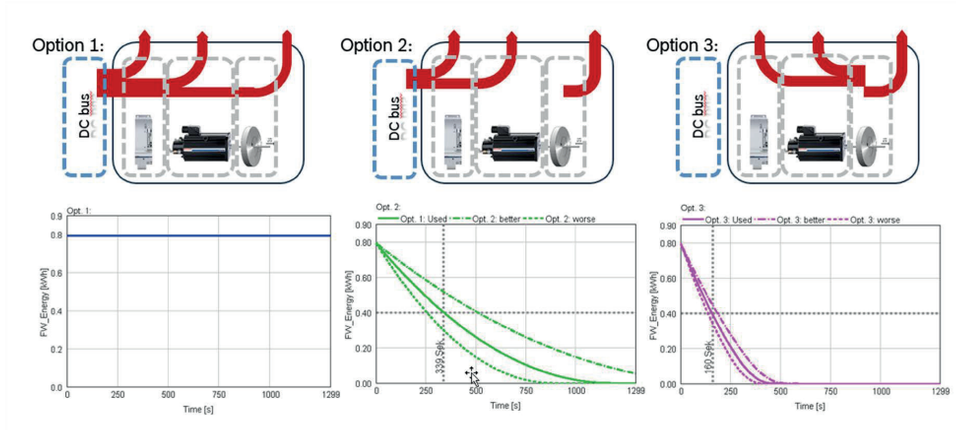


Figure 10: Kinetic Buffer operating modes analysis for one typical driving cycle[9]

Figure 10 shows the simulation results from the examination of different idle operating modes of the selected kinetic energy buffer (FlyWheel). In this simulation three operating methods have been examined and evaluated:

- **Option 1: Constant speed:** with this option, all losses are covered by the DC bus and thus, charge retention is ensured. One related disadvantage is that it may be necessary to generate the DC bus power with bad efficiency. This option is necessary for mid-/long-term storage.

[9] Curves „better“ and „worse“ are defining the tolerance band for self-discharging process curve due to possible unknown design parameters variance.

- **Option 2: no mechanical power at the shaft** (or torque is 0 Nm) results in reduced DC bus power which may possibly have to be generated with bad efficiency. This option is the appropriate one for mid- or short-time cyclical (dis)charging.
- **Option 3: DC bus power is zero:** with this option, all losses are dissipated within the Flywheel. This option is characterized with the lowest "half-life" time and hence appropriate for short-time cyclic (dis)charging.

The energetic value contribution of the electrification determined in the concept phase using simulation model with detailed loss models of all relevant components within the system for electrified drive train and this sample vehicle is: Reduction in fuel costs by up to 40% and downsizing of the diesel engine by up to 20%.

5 Summary and outlook

Due to its connection to a central electric power split, the electrification of hydraulics results in a high level of flexibility for optimal energy distributions and a considerable extension of the energy storing possibilities. The latter are the critical technology breakthrough factors, especially their sizing and prizing. An intelligent combination of different optimization solutions from a holistic system or machine point of view for hybrid machines and systems of today and tomorrow makes the remarkable energy efficiency increasing possible. In order for this to be successful, well-geared, cross-technology expert teams and an integrated platform or workbench for the closed coupling and linking of different sizing and simulation tools are necessary.

6 Acknowledgments

The product development, marketing and sales of the drive technology of "today and tomorrow" is faced with the challenges of increasing technical-informative complexity. Thus, cross-technology expert teams together with integrators constitute an indispensable creative and motive force /7/. At this point, we would like to thank to all our partners in such multi-technological projects and in this publication for very good collaboration and support.

Nomenclature

Variable	*Description*	*Unit*
E_DC	DC bus energy	[kJ]
P_DC	DC bus power	[kW]
$Pmains$	Mains power	[kW]
U_DC	DC bus voltage	[V]
	Subscripted Characters	
cont	the continuous value	
max	Maximum value	
min	Minimum value	
nom	the nominal value	
	Shortcuts	
SIL	Simulation In the Loop	

References

/1/ Bosch Rexroth AG, Drive & Control Academy, *Handbuch Energieeffizienz*, 1. Auflage (1. März 2017)

/2/ Bosch Rexroth AG, IndraSize, www.boschrexroth.com/IndraSize

/3/ Bosch Rexroth AG, *Simster*, www.boschrexroth.com/Simster

/4/ Bosch Rexroth AG, *HMV0x.1R Supply Units, Smart Energy Mode*, Project Planing Manual, R911343308 (EN), R911343261 (DE), © Bosch Rexroth AG 2013

/5/ Bosch Rexroth AG, *Rexroth for Energy Efficiency*, RD08503/09.V

/6/ Bosch Rexroth AG, *Sytronix Size*, www.boschrexroth.com/SytronixSize

/7/ Ehrlenspiel, K., Meerkamm, H., *Integration versus Spezialisierung – Von der Notwendigkeit einer ganzheitlicher Konstruktionsforschung und –lehre an Universitäten und Hochschulen,* Konstruktion März, 3-2016, Seiten 70-73., Springer VDI Verlag, Düsseldorf, 2016, www.konstruktion-online.de

/8/ Hendrix, G., *Hydraulische Achse*, Patentschrift Bosch Rexroth DE2011 116 964 A1, 2011.

/9/ Indramat Report Unsere: *Produkte im Einsatz, Elektroauto kommt*, Ausgabe 1, Oktober 1994

/10/ Ristic, M., Wahler, M., *Elektrifizierung hydraulischer Antriebe: Mit integrativen Entwicklungsmethoden zum optimalen Produkt:(Electrification of hydraulic drives: integrative development methods for the optimal product)*, In: 17th Drive Train Technology Conference, 17. ATK, March 7-8, 2017

/11/ Ristic, M., *Conversant Technology – New Key Aspects: Development of Variable-speed Drives,* In: 6th international Fluid Power Conference, Dresdener Verein zur Förderung der Fluidtechnik e.V. Dresden, Dresden, 31.03.-02.04.2008

/12/ Siemer, E., Kluger A., *EcoPlant Design – Moderne Antriebskonzepte für Schmiedepressen*, https://www.oup-fluidtechnik.de/ecoplant-schmiedepressen/

/13/ Siemer, E., Kluger, A. , *Moderne Antriebskonzepte für Schmiedepressen (EcoPlant Design)*, 31. Aachener Stahl Kolloquium 10.03.2016 - 11.03.2016, Aachen, Germany, 2012.

/14/ VDI Statusreport Oktober 2017, *Energiespeicher*, www.vdi.de , 2017.

/15/ Wahler, M., Gassmann, M.: *Electric Drivetrains – The right solution for every power level*, MOBILE 2017 Perspectives and Dialogue: Next Level of Safety, Efficiency and Automation, Technical Papaers, RE 00207/06.2017

Design study of a high speed power unit for electro hydraulic actuators (EHA) in mobile applications

Tobias Pietrzyk*, David Roth**, Katharina Schmitz*, Georg Jacobs**

RWTH Aachen University, Institute for Fluid Power Drives and Systems (IFAS), Campus Boulevard 30, D-52074 Aachen, Germany*
RWTH Aachen University, Institute for Machine Elements and Machine Design (IME), Schinkelstraße 10, D-52062 Aachen, Germany**
E-Mail: tobias.pietrzyk@ifas.rwth-aachen.de

One way to increase the compactness and power density of electro hydraulic power units is to increase the rotational speed level. Hence, a high-speed electrical drive and a high-speed gear pump are connected. Particularly, high-speed internal gear pumps are not state of the art and increasing rotational speed entails a lot of challenges for the hydraulic system. This paper analyses the influence of different pump parameters for the speed limit of internal gear pumps. Furthermore, a preliminary dimensioning of drive concepts is used to identify the best concept in terms of power density.

Keywords: High-speed power unit, EHA, high-speed pump, internal gear pump
Target audience: Mobile Hydraulics, pumps, energy management

1 Introduction

One of the most commonly used hydraulic mobile machines are excavators. In recent years, many concepts with potential to improve the efficiency have been investigated. As a matter of principle, pump controlled systems avoid throttling losses through valves. In /1/ four displacement controlled pumps are used to control the hydraulic actuators of a mini-excavator, showing the potential of pump controlled concepts for mobile applications. For a typical dig and dump cycle, experiments show an increased fuel energy efficiency of up to 40% compared to a state of the art load sensing system (LS-system) /2/. However, because of the centrally located pumps, the hydraulic energy has to be transferred to the actuators via hoses, pipes and elbows, which causes line losses. Decentralized driving concepts, such as electro hydraulic actuators (EHA) minimize these losses due to short pipe lengths. In EHA, variable speed motors and pumps are often used. The movement of the actuator is controlled by the rotational speed of the electrical motor. In recent years, many hydraulic manufacturers have designed different products of an EHA, characterized by high energy efficiency, good dynamic behaviour and low installation complexity /3/. However, existing solutions do not conform to the request of mobile machines for high power density and compactness. Therefore, the Institute for Machine Elements and Machine Design (IME) and the Institute for Fluid Power Drives and Controls (IFAS) at RWTH Aachen University are developing an EHA for the high requirements of mobile applications for compactness and power density. The purpose of this project is to replace the conventional cylinder with a decentralized EHA, which is shown in figure 1.

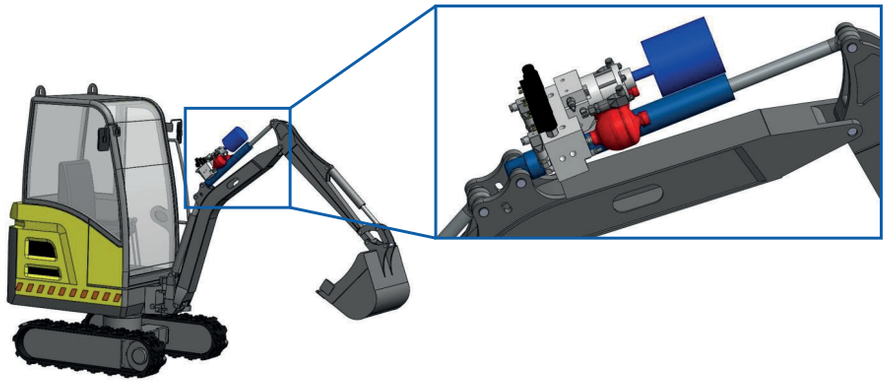


Figure 1: Replacement example for the conventional cylinder of an excavator with a decentralized EHA

One possibility to achieve a higher power density is to increase the rotational speed of the power unit. Schröter et al. illustrate the potential of high-speed drives and compare a standard motor (n_{max} = 3 000 rpm and P = 15 kW) with a high-speed drive with two shiftable gear stages (n_{max} = 22 500 rpm, P = 22 kW) and a directly coupled high-speed motor (n_{max} = 35 000 rpm, P = 15 kW, without housing) /4/. They also showed that the power to weight ratio is increased by factor 5 for the high-speed drive and by factor 34 for the high-speed motor, compared to the standard motor /4/. Furthermore, the power density of the hydraulic pump can be increased by raising the rotational speed. The aim of the study is to increase the rotational speed limit of the pump up to 10 000 rpm. For this purpose, an internal gear pump is chosen. As part of the project, an electro-mechanical high-speed drive will be developed. The high peripheral speed poses challenges for the design of a gear stage, such as an increased risk of scuffing damages, a more complex lubrication, as well as high requirements for the machine elements, such as bearing and sealing. Furthermore, increasing the rotational speed of the internal gear pump entails addressing topics, such as cavitation, overheating and filling problems of the tooth spaces. In this paper, the authors compare different pump geometries. The aim of this work is to evaluate the influence of the gear dimensions for the rotational speed limit of internal gear pumps. A Computational Fluid Dynamics (CFD) simulation model is built up. Thereby, four different pump variants are analysed qualitatively concerning their tendency for cavitation. The simulation results affect the future concept for the high-speed pump.

2 Concepts of High-Speed Drives for an Electro-Hydraulic Actuator

In this chapter, two different drive concepts for the electro-hydraulic power unit are presented – an electrical high-speed direct drive and an electro-mechanical high-speed drive. Since the speed of the pump is increased to raise the power density of the pump, a direct drive concept already provides a higher power density than conventional direct drives for electro-hydraulic actuators. To achieve a further increase of the power density the electro-mechanical high-speed drive uses a mechanical gear stage to operate the electrical machine at an even higher rotational speed than the internal gear pump.

2.1 Selection of Electrical Machines

In a first step, an appropriate type of electrical machine is chosen to enable a comparison independent of the motor technology. Finken et al. evaluated several motor types for an application in electric hybrid vehicles. In order to identify the optimum machine type, a direct current machine (DC), an induction machine (IM), a permanent magnet excited synchronous machine (PMSM) and a switched reluctance machine (SRM) are pre-dimensioned and compared in terms of power density, efficiency, costs, reliability, technical maturity and controllability (costs). The comparison shows that the PMSM achieves the best results in terms of power density and efficiency. A disadvantage, however, is the high costs incurred by using rare earths /5/. Comparable

applications – for example the high-speed traction drive developed by Schröter et al. /4/ – show that the power density and efficiency are the main evaluation criteria for use on mobile machines. Therefore, a PMSM is selected for the further design of the direct and the electro-mechanical high-speed drive. To compare the power density of both concepts, a closer analysis of the correlation between motor size and rotational speed is necessary. For the same thermal and magnetic load on the active material of an electrical motor, the desired torque determines the volume of the active part and thus the size of the motor /6/. This correlation can be described by equation 1.

$$T = \sigma \cdot \pi \cdot D_{\text{rotor}} \cdot l_{\text{rotor}} \cdot \frac{D_{\text{rotor}}}{2} \tag{1}$$

The rotary thrust σ is characterized by the mentioned thermal and magnetic utilization of the active material and describes the tangential force on the surface of the rotor. Multiplying the rotary thrust and the surface of the rotor, the resulting tangential force is calculated. In combination with the lever arm of the rotor $\left(\frac{D_{\text{rotor}}}{2}\right)$, the resulting tangential force leads to the torque T acting on the rotor /6/. The required volume of the active part (V_{active}) can be calculated by equation 2, using the diameter D_{rotor} and the length l_{rotor} of the active part.

$$V_{\text{active}} = \frac{\pi}{4} \cdot D_{\text{rotor}}^2 \cdot l_{\text{rotor}} \tag{2}$$

A correlation between the volume of the active part and the rotational speed (n), shown in equation 3 and 4 can be derived from equations 1 and 2. The output power of the electrical machine is described by P.

$$V_{\text{active}} = \frac{P}{2 \cdot \sigma} \cdot \frac{1}{n} \tag{3}$$

$$V_{\text{active}} \sim \frac{1}{n} \tag{4}$$

An exemplary evaluation of the inversely proportional correlation is shown in Figure 2 for a power output of 60 kW. To validate the shown dependency between rotational speed and stator volume, motors of several manufacturers are entered in the diagraph.

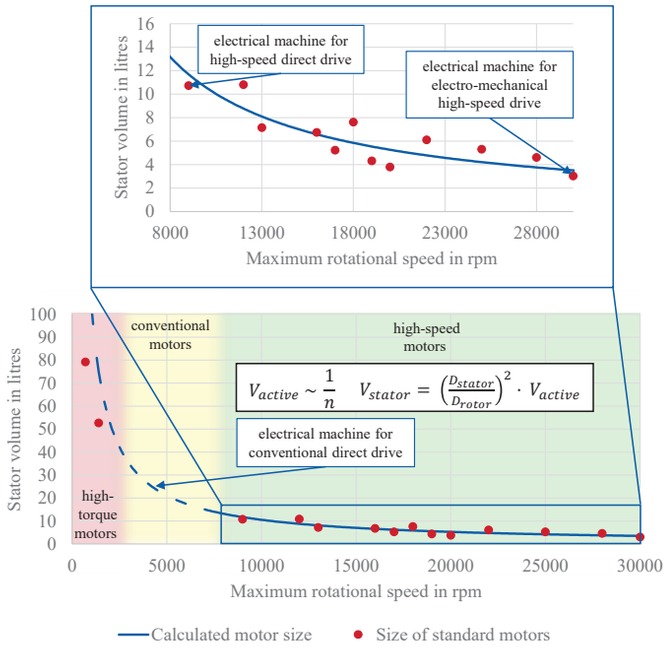


Figure 2: Correlation between the volume of the active part and the rotational speed of electrical motors

For the calculation of the stator volume, the average ratio of stator and rotor diameter is determined for the consulted series motors and multiplied in square with the volume of the active part.

As shown in Figure 2, the volume of the stator can be reduced from approximately 25 litres for a conventional electro-hydraulic power unit with a maximum rotational speed of 4 000 rpm to a volume of approximately 11 litres for a high-speed direct drive on a speed level of 10 000 rpm. For the electro-mechanical high-speed drive, an electrical motor with a maximum rotational speed of 30 000 rpm is chosen. On one hand, it is difficult to find available electrical motors on the market with a power of 60 kW and a maximum rotational speed above 30 000 rpm, and on the other hand, as Figure 2 shows, the gradient of the graph decreases with an increasing rotational speed. That said, a further increase of the rotational speed would not lead to a significant reduction of the motor volume but increase the requirements for the electrical machine as well as the machine elements of the required gear box. Hence a motor with a rotational speed of 30 000 rpm provides a compromise between power density and stress of the used components. For this rotational speed, a volume of the stator of approximately 3.5 litres can be achieved.

2.2 Preliminary Design of a High-Speed Gear Box

After the specification of motor type and speed level of the electrical machine for the electro-mechanical high-speed drive, a preliminary design of a high-speed gear box is necessary to estimate the gear box volume and thereby the volume of the drive. For adapting the rotational speed of the electrical motor (30 000 rpm) to the lower rotational speed of the gear pump (10 000 rpm), two different gear box variants are possible – a spur gear and a planetary gear. The main advantage of planetary gears compared to spur gears is the allocation of the power flow over several planetary wheels and the coaxiality of the input and output shafts. By the reduced load on every tooth mesh, a reduction of the assembly space of approximately 60 % and a weight reduction of approximately 50 % is possible /7/. A further advantage is the high efficiency. In addition to increased manufacturing costs, disadvantages arise from the rotation of the carrier shaft. Those disadvantages are high loads on the planetary bearings caused by centrifugal forces, splashing losses and lubrication problems /7/. Since the design of the drive train is focused on the achievable power density, a planetary gear is used. Under the previously defined boundary conditions of a maximum gear input speed of $n_{in,max} = 30\,000\,rpm$ and a maximum gear output speed of $n_{out,max} = 10\,000\,rpm$, a transmission ratio of $i = 3$ is required and can be achieved by only one planetary gear stage. Using a single-stage planetary gear with one input and one output shaft, three different transmission architectures can be used to reduce the input speed. The possible transmission architectures are shown in Table 1.

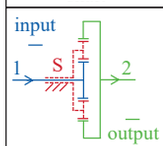
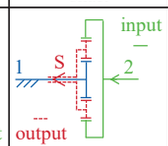
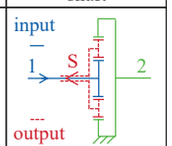
fixed carrier shaft	fixed sun shaft	fixed ring shaft
		
$i_{12} = \frac{z_2}{z_1}$	$i_{2S} = 1 - \frac{z_1}{z_2}$	$i_{1S} = 1 - \frac{z_2}{z_1}$

Table 1: Transmission architectures for a high-speed planetary gear stage

Schröter et al. developed a high-speed gear stage for an electro-mechanical wheel hub drive /4/. The required transmission ratio of $i = 95$ was distributed over three gear stages, one high-speed gear stage and two low speed gear stages. Based on the comparable input speed of $n_{in,max} = 20\,000\,rpm$, the conclusions can be used as a reference for the selection of the optimum transmission architecture in this paper.

Using a fixed carrier shaft, Schröter et al. solved the mentioned problems of planetary gears of centrifugal forces, splashing losses and lubrication problems caused by the rotating carrier shaft. For the same assembly space,

however, the concept with a fixed carrier shaft provides a lower transmission ratio than both other concepts. Thereby, this concept achieves the lowest power density. Due to the fact that the impact of the problems caused by the rotating carrier shaft increases for high rotational speeds, the transmission architecture with a fixed carrier shaft is chosen for the further design of a high-speed gear stage. To estimate the assembly space of the gear box, the gear wheels are sized according to DIN 3990 for the transmission of the occurring torques. At this phase of conception, the smallest possible size is intended to reduce the assembly space on one hand and to limit the peripheral velocities on the other hand. A specific optimization of the tooth geometry for high peripheral speeds is pursued in the following design process. Figure 3 shows the result of the preliminary dimensioning of the planetary high-speed gear stage.

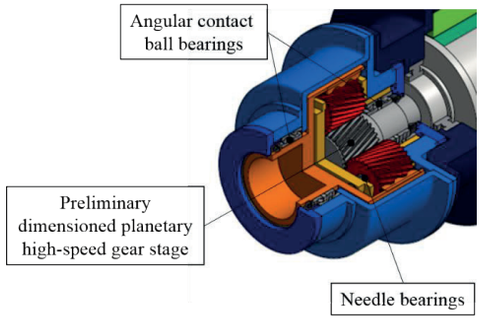


Figure 3: Preliminary dimensioning of a high-speed gear box

Angular contact ball bearings are used in an adjusted bearing arrangement to support the ring and the sun shaft. The planet gears are supported by needle bearings. An optimization of the bearing construction will be pursued in the subsequent design process as well. For example, an adjustment of the maximum thermal speed limit can be achieved by an appropriate oil perfusion.

2.3 Comparison of Drive Concepts

The result of the pre-dimensioned high-speed gear stage, in particular the estimated assembly space, is compared to the high-speed direct drive as well as the conventional direct drive in Table 2. Compared to the high-speed direct drive, a reduction of the assembly space of approximately 65 % and compared to the conventional direct drive, a reduction of approximately 83 % can be achieved by the electro-mechanical high-speed drive.

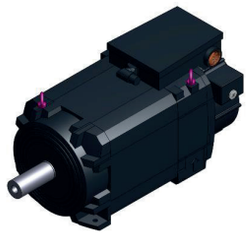
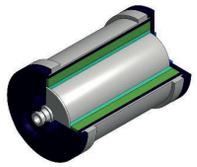
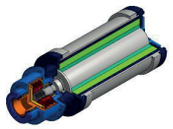
conventional servo synchronous motor	electrical high speed direct drive	electro-mechanical high speed drive
		
• 61 kW • $n_{motor,max}$ = 4 000 rpm • $n_{motor,rated}$ = 1 500 rpm • V ≈ 39 litres	• 66 kW • $n_{motor,max}$ = 9 000 rpm • $n_{motor,rated}$ = 2 000 rpm • V ≈ 19 litres	• 64 kW • $n_{motor,max}$ = 30 000 rpm • $n_{motor,rated}$ = 12 000 rpm • V ≈ 6.5 litres

Table 2: Comparison of drive concepts /8/

The preliminary dimensioning proved the potential of high-speed drives for high power densities. In the following design of the high-speed gear stage, an optimization of the tooth geometry for high peripheral velocities is necessary. After the final design of the electro-mechanical high-speed drive, the power density, efficiency, acceleration capacity and costs will be evaluated against the electrical high-speed direct drive as a reference system.

3 CFD simulation model

The aim of this study is to evaluate, which gear design is the best to achieve high rotational speeds. Therefore, four different gear geometries are simulated using the commercial tool Ansys CFX. Table 3 shows the parameters of the used gear combinations. The geometrical displacement of the pump should be nearly constant at 16 cm³. The gear transmission ratio between internal and external gear is identical for gear geometries V1 to V3. Due to the lower normal module, the face width of the gears increases. The profile shift coefficients x_1 and x_2 are adapted for every single gear to avoid undercut at the gears. Geometry V4 has the same face width as V3, but a reduced gear ratio. Therefore, the angle where the tooth volumes are filled increases by nearly 10 %.

Name	z_{R2}/z_{R1}	m	α	x_1	x_2	b	b/d_{a1}
V1	19/13	3.5 mm	20°	0.4939	-0.5549	16 mm	0.286
V2	19/13	2.75 mm		0.5078	-0.5658	24 mm	0.545
V3	19/13	2.5 mm		0.4976	-0.5850	32 mm	0.8
V4	19/14	2.5 mm		0.4488	-0.5622	32 mm	1.077

Table 3: Gear geometries for design study

The fluid volume of the pump can be splitted into a stator domain and a time dependent rotor domain. The stator domain has no dependency on time or rotational angle.

3.1 Stator fluid domain

For the design study, a simple stator geometry, axially connected to the suction and the high-pressure port, is chosen. The dimensions of the stator are basically dependent on the gear dimensions. Table 4 shows the root circle and external diameter for the internal and external gear. For a better suction behaviour, an additional fluid pocket is arranged in face of the suction port. Due to the high rotational speed, the inlet as well as the outlet port is designed for a high volume flow. The port diameter at the inlet and outlet is 28 mm. This matches the inner diameter of a 38S pipe. The separation between the low suction port and the high-pressure port can be calculated by the working pressure angle and the forehead base pitch /9/. For the design study, a symmetrical separation is chosen.

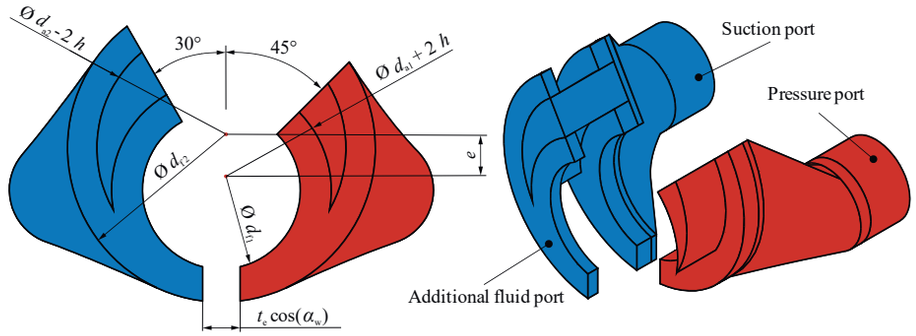


Figure 4: Stator dimensions for design study

Name	d_{f1}	d_{a1}	d_{f2}	d_{a2}	h
V1	40.207 mm	55.985 mm	78.434 mm	63.384 mm	5 µm
V2	31.668 mm	44.063 mm	61.687 mm	49.862 mm	
V3	28.738 mm	40.024 mm	56.025 mm	45.425 mm	
V4	30.994 mm	42.310 mm	56.061 mm	45.311 mm	

Table 4: Stator geometries for design study

The stator mesh is generated by Ansys Meshing. Prism layers are used to mesh the wall surfaces of the stator volume with the exception of the end face of the separate fluid pocket at the suction port. The first element height of the prism layers is set to 0.1 mm.

3.2 Rotor fluid domain

Due to the functional principle of positive displacement pumps, such as internal gear pumps, there are areas where the fluid domains inside the rotors undergo a change in volume. Therefore, the commercial tool TwinMesh was used. TwinMesh generates the moving meshes for each rotor position before the simulation. For the internal gear pump, two separate hexahedral meshes, one for the internal gear, as well as one for the external gear, are generated and connected by an interface contour. During the simulation, a Fortran routine imports the pre-generated meshes for each solver time step /10/. The angle of one tooth engagement can be calculated by the quotient of 360° and the number of external gear teeth. For the presented simulations, the angle of one tooth engagement is divided into 30 time steps. Between two time steps, the rotor fluid domain is rotated by an increment angle. For the pump geometries with 13 teeth of the external gear, this results in an angle increment of 0.923° between two time steps, related to the external gear.

3.3 CFD simulation setup

Table 5 shows the number of nodes and elements of the simulated internal pump geometries. For a higher solution quality and efficiency, the meshes mainly consist of hexahedral elements /10/. The total number of elements is nearly constant for the different pump variants. The stator and the rotor meshes are connected by general grid interface (ggi) connections. Figure 5 shows the different meshed stator and rotational fluid volumes and gives a good impression of the differences between the geometries. Figure 5 does not show the mesh of geometry V4, because of its similarity to V3.

Name	Nodes	Elements	Tetrahedra	Pyramids	Wedges	Hexahedra	Volume
V1	1 109 553	1 198 975	215 403	3 004	58 000	922 568	112 175 mm³
V2	1 028 216	1 135 565	220 634	1 219	68 347	845 365	92 218 mm³
V3	1 196 184	1 240 700	178 333	2 101	56 720	1 003 546	89 116 mm³
V4	1 180 519	1 223 109	174 472	2 029	56 350	990 258	86 446 mm³

Table 5: Number of nodes and elements

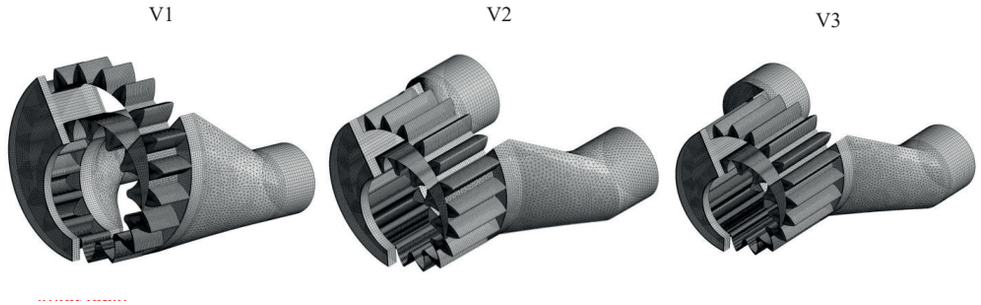


Figure 5: Fluid volume for the different pump geometries

The chosen material properties for the liquid fluid match the properties of a standard mineral hydraulic oil. The compressibility of the liquid fluid is considered by the density, see equation 5. The saturation pressure of the liquid is assumed to be 4 Pa /11/. In the CFD simulation, no thermal changes are included. The fluid temperature is set to 313.15 K. The pressure at the suction port and at the pressure port is set as boundary condition.

- $\nu = 46$ mm²/s
- $\rho_0 = 860$ kg/m³ at ambient pressure
- $E = 15\,000$ bar

$$\rho = \rho_0 \left(1 + \frac{p_{abs} - 1}{E}\right) \tag{5}$$

As cavitation model, the Rayleigh Plesset model is used. This cavitation model describes the vapour generation as well as the condensation. For the Rayleigh Plesset model, the Ansys CFX 18.1 default values are used /12/. The coefficients for evaporation f_{vap} and condensation f_{con} are set to zero for the first 150 time steps and increased linearly to the given values in 15 time steps. Therefore, no cavitation effects are calculated in the first 150 time steps. As turbulence model, the shear-stress-transport model (SST) is chosen.

- $f_{vap} = 50$
- $f_{cond} = 0.01$
- $R_{nuc} = 1$ µm
- $r_{nuc} = 5$ 10-4

4 Results CFD simulation

For the design study, the operation point at $n = 10\,000$ rpm and pressure difference $\Delta p = 250$ bar is analysed using CFD simulations. The pressure at the inlet and at the outlet is set as boundary condition. Figure 6 shows the development of the volume flow over the run time. Each simulation takes about 10 days for two rotations of the external gear R1. In the first phase of the simulation, the amplitude of the volume flow changes for each tooth engagement. Between time steps 500 and 600, the volume flow adjusts itself and is nearly periodic. For the presented work, the last four tooth engagements are used for evaluation. These correspond to 120 time steps in the CFD simulation. In Figure 6 the volume flow is illustrated over the rotation angle of the external gear R1.

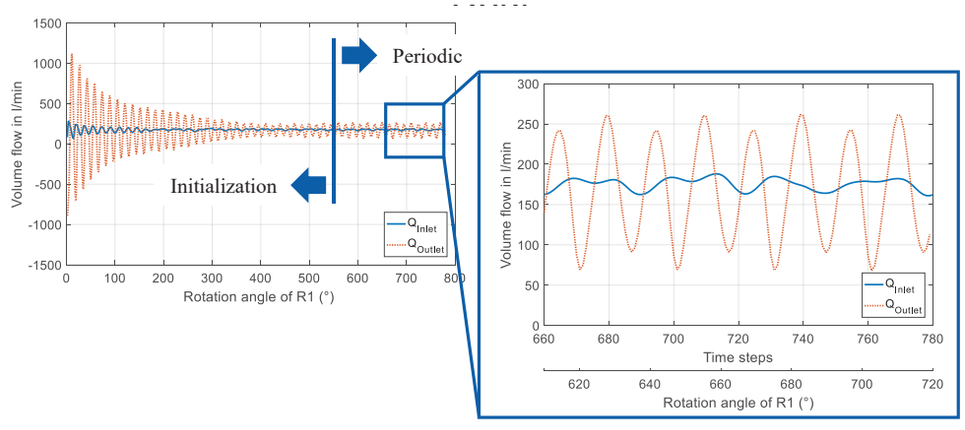


Figure 6: Example for the development of the volume flow over the run time

In addition to comparing four different pump variants, two different boost pressures at the inlet are analysed. The aim is to evaluate the influence on the cavitation tendency. Because of the high rotational speed of the pump, high flow velocities are expected. Due to local high flow velocities, the local pressure decreases and may cause cavitation. In hydraulic components, cavitation causes noise and reduces the efficiency, as well as the life-time expectancy/13/. Therefore, the vapour volume inside the fluid domain is used to compare the different pump geometries, see Figure 7 and Figure 9.

Table 6 shows the average volume flow at the inlet and the outlet for different boost pressures. The boost pressure is noted relative to the ambient pressure. The volume flow is calculated by the local density and the mass flow. On one hand, the difference between inlet and outlet volume flow results from the compressibility of the fluid. On the other hand, leakage flow reduces the volume flow at the outlet. The values of the volume flow are in the expected range and comparable to each other. Pump geometry V4 is only analysed at 10 bar boost pressure. The pressure difference is constant at Δp = 250 bar.

Name	$Q_{Inlet,\ averg.}$		$Q_{Outlet,\ averg.}$	
Pressure at suction port	5 bar	10 bar	5 bar	10 bar
V1	185.3 l/min	175.3 l/min	165. 7 l/min	167.5 l/min
V2	175.4 l/min	173.3 l/min	153.6 l/min	155.9 l/min
V3	200.7 l/min	191.2 l/min	169 l/min	170.9 l/min
V4	-	197.2 l/min	-	182.7 l/min

Table 6: Average volume flow at inlet and outlet of the pump

Figure 7 shows the absolute vapour volume inside the pump's total fluid domain at 5 bar rel. boost pressure. The diagram shows that the gear dimensions have a big impact on the cavitation tendency. Pump geometry V1 has a face width of 16 mm and V3 a face width of 32 mm. The value of the vapour volume of V3 is about three times the value for V1. The geometry V2 confirms the tendencies that gears with a slim face width are better for high-speed operation points.

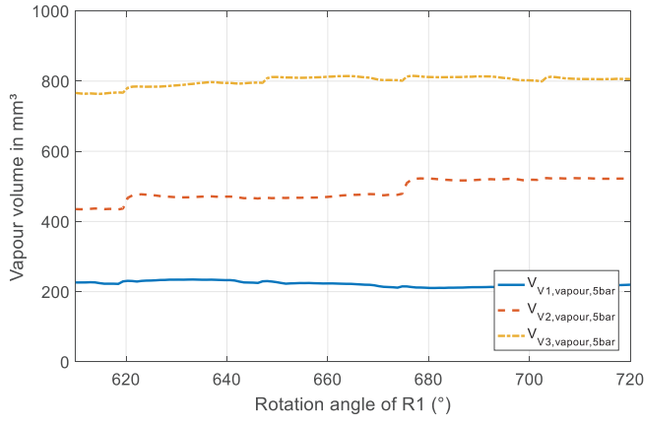


Figure 7: Vapour volume for the different gear geometries at 5 bar boosts pressure

Figure 8 compares the vapour fraction for 5 bar boost pressure and shows the position of potential cavitation zones. The whole fluid domain of the pump is shown transparently. The coloured volumes are mesh elements with a vapour fraction above 0.1%. Elements with a volume fraction under 0.1% are not shown. The main cavitation zone is always located inside the low pressure domain, where the tooth volumes are filled with fluid. In this area, the circumferential velocity of the gears and the flow velocity for filling the tooth volumes are superposed. Figure 8 confirms the tendency shown in Figure 7. To analyse the influence of the pressure, the same simulations are done with 10 bar boost pressure.

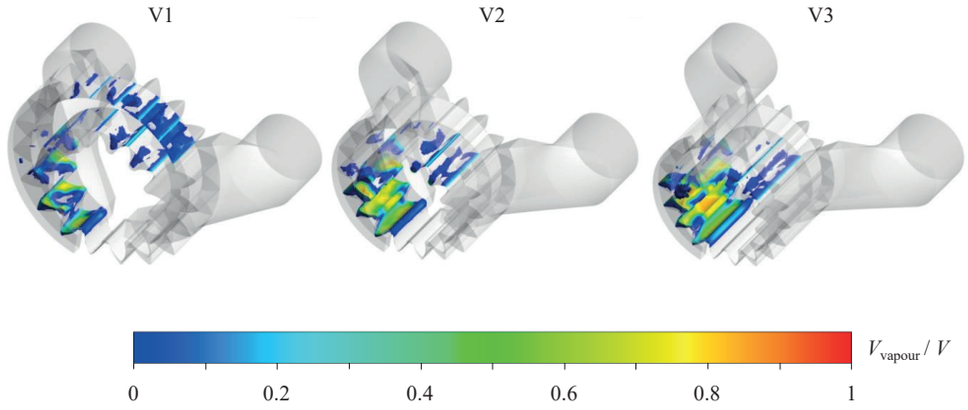


Figure 8: Vapour fraction at 5 bar boost pressure

Figure 9 shows the absolute vapour volume inside the fluid domain at 10 bar rel. boost pressure. The diagram depicts the same tendency as Figure 7. The value of the vapour volume of V3 is nearly six times larger than the value of V1. The comparison between Figure 7 and Figure 9 also shows that the boost pressure has a massive influence on the cavitation effects. For example, the vapour volume of V1 is reduced by a factor of four by increasing the boost pressure by a factor of two. For the other pump geometries, the vapour volumes are reduced by a factor of 2.5 to 3. In Figure 9, the simulation results for geometry V4 are also shown. Geometry V4 has the same face width as V3, but the external gear has one more tooth. Due to the reduced gear ratio, the angle where the tooth volumes are filled is nearly 10% bigger. This results in more time for filling the tooth volumes and a reduced flow velocity. The result of the CFD simulation shows that over a wide range of operating points, the vapour volume for V4 is smaller than for geometry V3.

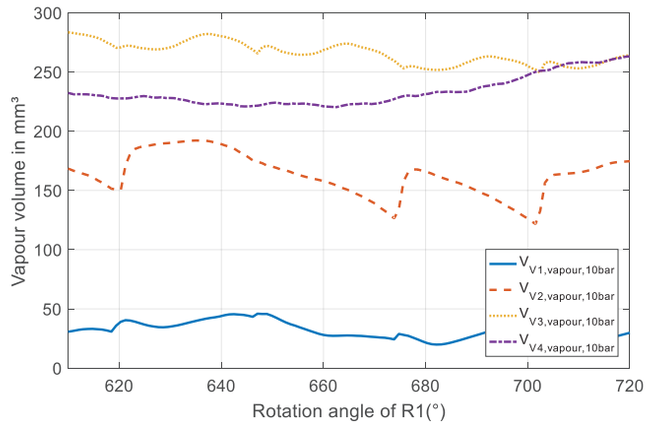


Figure 9: Vapour volume for the different gear geometries at 10 bar boost pressure

Figure 10 compares the vapour fraction for 10 bar boost pressure. As in Figure 8, the fluid domain of the pump is shown transparently and the coloured volumes are mesh elements with a vapour fraction above 0.1%. Compared to Figure 8, the cavitation zones in Figure 10 are drastically decreased. For the pump geometries V2 and V3, the cavitation areas at the crescent disappear completely. For the geometry V1, the cavitation zone decreases as well as the value of vapour fraction. The cavitation zones for geometry V3 and V4 are very similar.

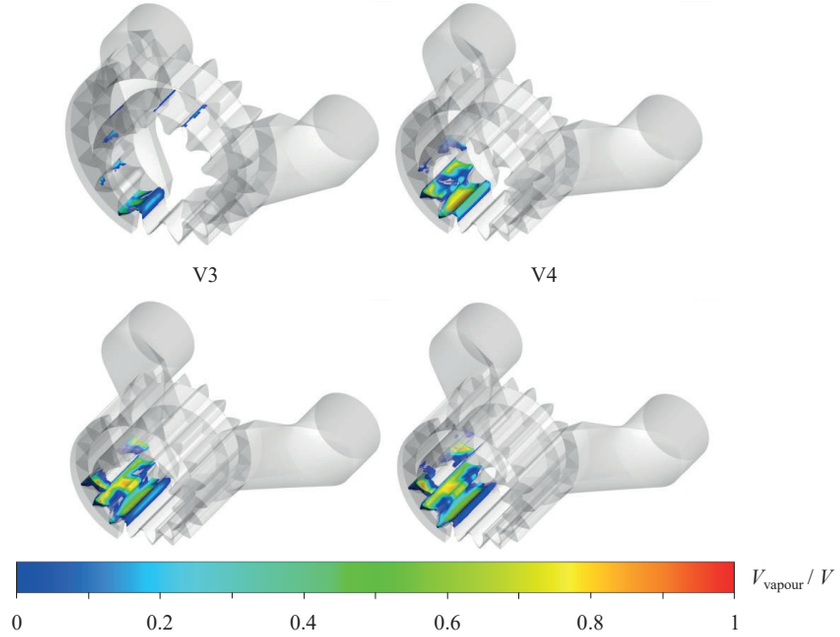


Figure 10: Vapour fraction at 10 bar boost pressure

5 Summary and Conclusion

In recent years, a lot of new concepts with the potential to improve the efficiency of mobile applications have been investigated. Decentralized driving concepts, such as EHAs minimize throttling losses through valves, as well as line losses by very short pipe lengths. But existing EHA solutions do not conform to the request of mobile machines for high compactness and power density. Therefore, high-speed components are used for the power unit. Increasing the rotational speed of the hydraulic pump entails addressing topics, such as cavitation and filling problems of the tooth spaces. For the high-speed power unit, an internal gear pump is chosen. The analysis of different drive concepts showed that an increase of the power density of a direct drive of 51 % can be achieved by raising the maximum rotational speed from 4 000 rpm to 9 000 rpm. A roughly designed gear box was used to operate the electrical machine on an even higher rotational speed (30 000 rpm). Thereby, a further increase of the power density by 66 % was reached. In the next step, a closer design of the high-speed gearbox, focusing on the high-speed capability, is necessary for a comparison of the electro-mechanical and the electrical direct high-speed drive in terms of efficiency, acceleration capacity and costs. In this paper, four different pump geometries and two different boost pressures are compared. The used stator geometries, as well as the gear dimensions are presented, followed by a description of the used boundary conditions and models. The simulation results show a massive impact of the boost pressure. For the geometry V1 with a slim face width, the vapour volume inside the fluid domain decreases by factor of about four by increasing the boost pressure from 5 to 10 bar. The simulation results also show that the gear dimensions have a big impact on the cavitation tendency of the pump. Thus, for high-speed applications, the face width of the gears in internal gear pumps should be minimised.

In the future, a high-speed power unit as well as an EHA will be built up by the authors. Therefore, the results of the design study are used to develop an internal gear pump with a geometrical displacement of about 4 cm³ and a 10 kW high-speed drive.

6 Acknowledgements

The IGF research projects 19224 N / 1 and 19224 N / 2 of the research association Forschungskuratorium Maschinenbau e. V. – FKM, Lyoner Straße 18, 60528 Frankfurt am Main was supported from the budget of the Federal Ministry of Economic Affairs through the AiF within the scope of a program to support industrial community research and development (IGF) based on a decision of the German Bundestag.

Nomenclature

Variable	*Description*	*Unit*
b	Face width	[mm]
d_{a1}	Tip diameter for external gear R1	[mm]
d_{a2}	Tip diameter for internal gear R2	[mm]
d_{f1}	Root diameter for external gear R1	[mm]
d_{f2}	Root diameter for internal gear R2	[mm]
D_{rotor}	Diameter of the active part	[mm]
E	Bulk modulus of the liquid fluid	[bar]
f_{cond}	Constant of the mass transfer rate for condensation	[-]
f_{vap}	Constant of the mass transfer rate for vapour generation	[-]
h	Radial gap between internal/external gear and crescent	[µm]

i	Transmission ratio	[-]
i_{12}	Transmission ratio between sun and ring wheel	[-]
i_{1S}	Transmission ratio between sun wheel and carrier shaft	[-]
i_{2S}	Transmission ratio between ring wheel and carrier shaft	[-]
l_{rotor}	Length of the active part	[mm]
m	Normal module	[mm]
n	Rotational speed	[rpm]
n_{max}	Maximal rotational speed	[rpm]
$n_{\mathrm{motor,max}}$	Maximum rotational speed of the electrical motor	[rpm]
$n_{\mathrm{motor,rated}}$	Rated rotational speed of the electrical motor	[rpm]
P	Power	[W]
p_{abs}	Absolute pressure	[bar]
Δp	Pressure difference	[bar]
$Q_{\mathrm{Inlet,average}}$	Average volume flow at the inlet	[l/min]
$Q_{\mathrm{Outlet,average}}$	Average volume flow at the inlet	[l/min]
R_{nuc}	Nucleation site radius	[µm]
r_{nuc}	Volume fraction of the nucleation site	[-]
T	Torque of the electrical motor	[Nm]
t_e	Forehead base pitch	[mm]
V	Volume	[l]
V_{active}	Volume of the active part	[l]
V_{stator}	Volume of the stator	[l]
V_{vapour}	Vapour volume	[mm³]
x_1	Profile shift coefficient for external gear R1	[-]
x_2	Profile shift coefficient for internal gear R2	[-]
z_1	Number of teeth of the sun wheel	[-]
z_2	Number of teeth of the ring wheel	[-]
z_{R1}	Number of teeth for external gear R1	[-]
z_{R2}	Number of teeth for internal gear R2	[-]
α	Pressure angle at normal section	[°]
α_{w}	Working pressure angle	[°]
ν	Kinematic viscosity	[mm²/s]
ρ	Density	[kg/m³]
ρ_0	Density at ambient pressure	[kg/m³]
σ	Rotary Thrust	[N/mm²]

References

/1/ Williamson C., Zimmerman J., Ivantysynova M., Efficiency Study of an Excavator Hydraulic System Based on Displacement-Controlled Actuators, Fluid Power and Motion Control FPMC 2008, pp. 291-307

/2/ Zimmerman, J., Busquets, E.,Ivantysynova, M., 40% Fuel Savings by Displacement Control Leads to Lower Working Temperatures - A Simulation Study and Measurements, Proceedings of the 52nd National Conference on Fluid Power 2011, pp. 693-701

/3/ Voith Turbo H + L Hydraulic GmbH & Co. KG, Servoantrieb CLDP - Technisches Datenblatt, Firmenschrift, 2013

/4/ Schröter J. et al., Development of High Speed Electrical Drives for Mobile Machinery – Challenges and Potential Solutions, 9th International Fluid Power Conference, Aachen, 24-26 March, 2014, pp. 416-427

/5/ Finken, T. et al., Comparison and design of different electrical machine types regarding their applicability in hybrid electrical vehicles, Proceedings of the 2008 International Conference on Electrical Machines, Marseille, France, 2008.

/6/ Fischer, R., Elektrische Maschinen, 17. Auflage, Hanser, 2017

/7/ Jacobs, G. Maschinengestaltung – Band II. Lecture Notes, RWTH Aachen University, Druck & Verlaghaus Mainz, Aachen, Germany, 04/2013.

/8/ Siemens AG, 1PH8165-2FF00-0GA1 – Technisches Datenblatt, 2017

/9/ Schwarzer S., Optimierung der Auslegung und des Betriebsverhaltens von hohlradgetriebenen Innenzahnradpumpen, Dissertation, TU Ilmenau, 2013

/10/ Spille-Kohoff A., CFD Simulation of Cavitation in an Internal Gear Pump, International Rotating Equipment Conference, Düsseldorf, 2016

/11/ Murrenhoff H., Grundlagen der Fluidtechnik Teil 1: Hydraulik, Shaker Verlag , Aachen, 2012

/12/ ANSYS Documentation, CFX 18.1, 5.13.5.1. The Rayleigh Plesset Model, visited on November 28, 2017.

/13/ Siebert C., Longhitano M., Murrenhoff H., Einsatz von Kavitationsmodellen in ölhydraulischen Systemen, In: O+P Ölhydraulik und Pneumatik, No. 4, 2014

High-dynamic Proportional Solenoid on basis of Established Production Technologies

Dr. Peter Tappe, Robert Müller and Sebastian Probsthain

Magnet-Schultz GmbH & Co KG, Memmingen, Germany
E-Mail: peter.tappe@magnet-schultz.de

Proportional solenoids generate a proportional force effect from an electrical input signal. The force is created between the movable armature and the magnetizable counter-piece. Due to this known physical effect and inherent to the functional principle, the magnetic force can actuate in one direction only. The return movement is made by a spring. Based on this principle the realization of well controllable hydraulic and pneumatic valves is possible. The novel solenoid design developed at MSM enables a bi-directional force effect. For this, particularly the armature is considerably modified and fitted with permanent magnets. In addition to the influence of the force direction, the pre-magnetisation of materials causes a considerable improvement of dynamics.

Keywords: solenoid, high dynamic, proportional valve, hydraulic
Target audience: Actuators and Sensors

1 Introduction

It is known that proportional solenoids serve to transform an electrical control signal into a proportional force effect. The high-pressure resistant tube is an important element of the constructive design for hydraulic valve applications. In turn, this tube is enclosed by a coil and the appropriate iron parts so that a suitable iron circuit is created. By energizing the coil a magnetic flow is generated in the iron part now. The tube is equipped with a non-magnetic separation in order to have a suitable effect on this flow. Thus, the magnetic field lines are conducted into the armature. They act via the head surface of the armature and the surrounding geometry in such a way that a proportional force effect is generated.

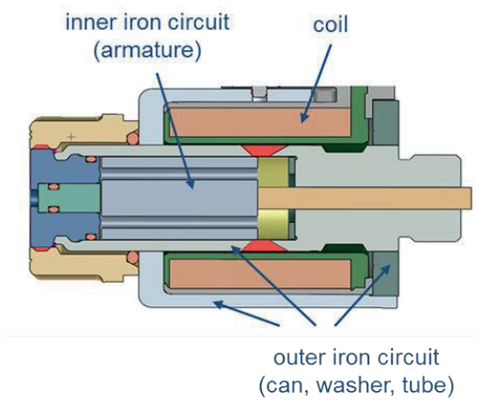


Fig. 1: Constructional design of a conventional proportional solenoid

In order to achieve a bi-directional force effect, the armature of the proportional solenoid is conside modified. It consists of permanent solenoids as well as discs made of conventional ferromagnetic material also modified pole tube has been only slightly adapted in the area of the magnetic separation. The armature with permanent solenoids is arranged at a suitable position in the slightly modified pole tube. Due t symmetric arrangement the permanent magnetic forces neutralise each other in neutral position. A standar is used for the generation of the magnetic flow. During the energization of this coil, a nearly proportio acting bi-directional magnetic force is created.

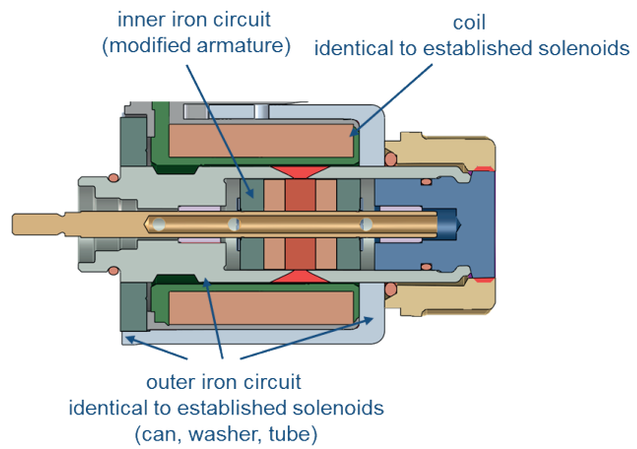


Fig. 2: Constructive design of the bi-directional proportional solenoid

In the presented iron circuit a magnetic flow is generated by the electric coil in combination with the perma magnet. By energization of the coil in two directions the corresponding magnetic flow changes direction. S overlap generates a bi-directional force. The following figure shows the overlap of the magnetic field lines simplified way.

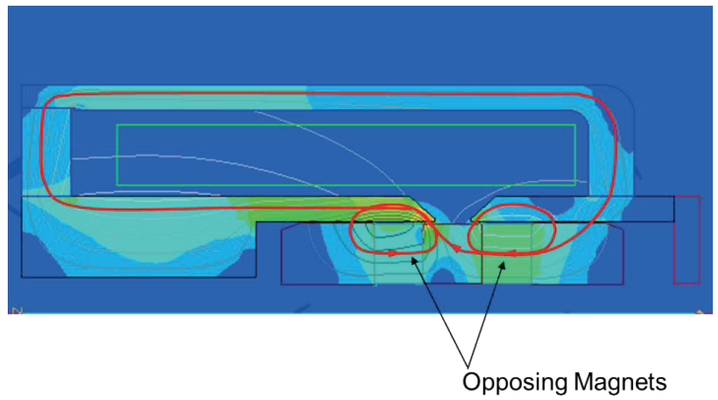


Fig. 3: Bi-directional force effect (FEM), both directions

The generated force is shown in figure 4. For clarification of the applicability in hydraulic valves the wo areas are highlighted in colour, the bi-directional effective direction of the forces can be identified b positive and negative scaling.

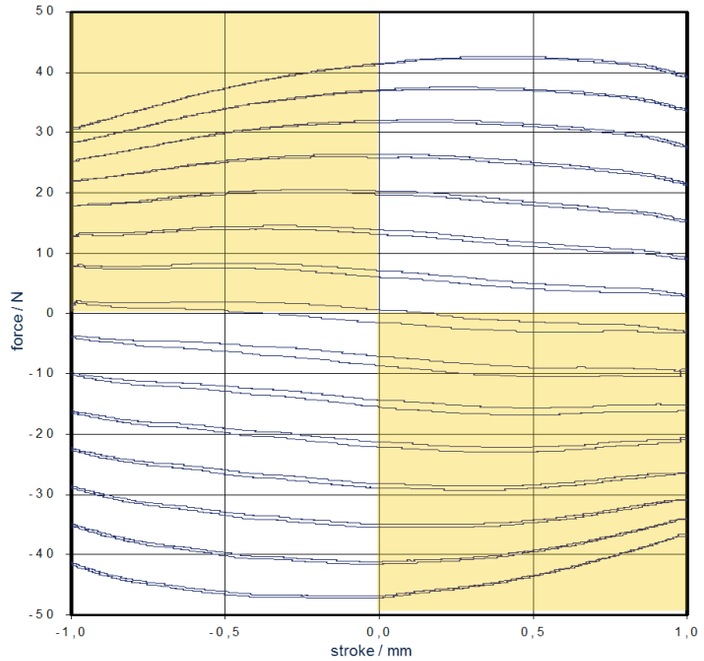


Fig. 4: Force vs. stroke characteristic diagram

The armature design as combination of permanentmagnetic and ferromagnetic sections is responsible for the fundamental bi-directional effect. Additionally the geometric design of the so-called cone geometry is a further possibility to influence the force characteristic diagram. Similar to conventional proportional solenoids, the working stroke and the increase of the characteristic curve is adjusted to the application. In figure 5 two characteristic diagrams are exemplarily overlapped as an example with considerably different characteristic so that the variation possibilities are clearly visible.

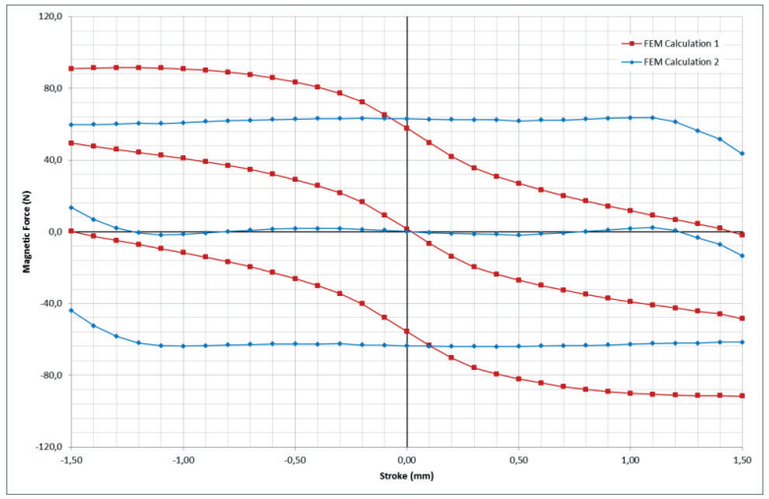


Fig. 5: Comparison of different characteristic diagrams

The here presented solenoid drive is perfectly suitable for appropriately adapted control valves. Such control valves can use the advantage of the bi-directional force effect because they can be well designed with the considerably reduced construction space and the assembly on only one side of the valve block. The next figure no. 6 optically illustrates the advantages of the construction space.

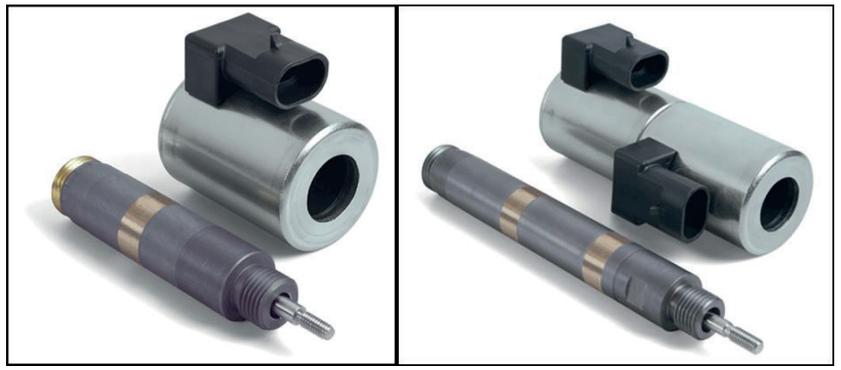


Fig. 6: Comparison of the construction space: conventional / bi-directional solenoid

In order to be able to use the advantages of the reduced construction space, constructive adaption works are necessary. The stroke movement must be transferred bi-directionally to the valve slide. Whereas the force transfer in push direction is uncomplicated, a positive connection must be provided for the opposite direction (e.g. via thread). In addition, the performance of the bi-directional solenoid must be compared to the conventional variant. In figure 7, the characteristic curves of the new solenoid have been compared to the force vs. stroke characteristic field of a conventional solenoid under the same current feed. The bi-directional solenoid shows a similar force behaviour as a conventional solenoid. This comparison also shows that in the direct comparison with a double actuated valve, adaption works at the valve will be necessary regarding the spring force and the hydraulic design.

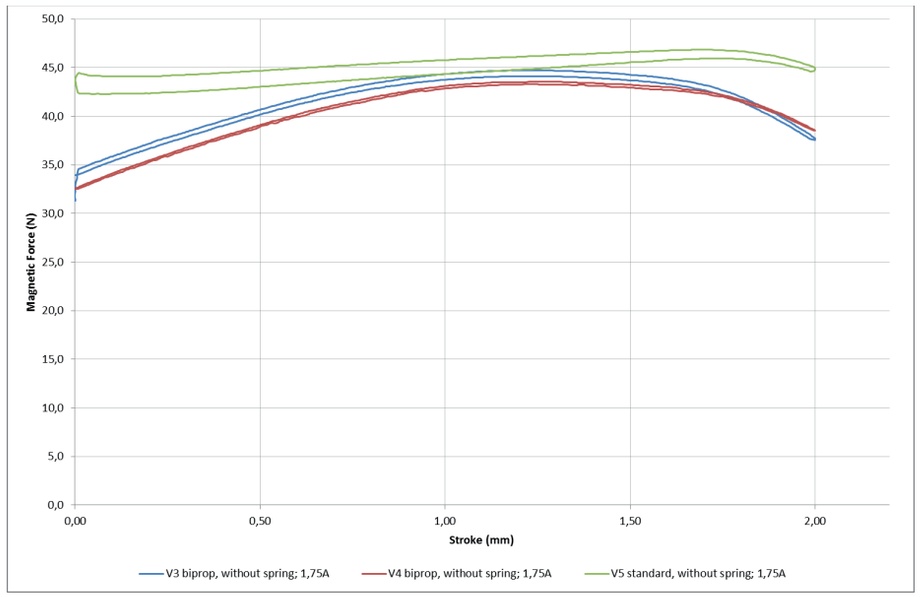


Fig. 7: Force comparison: conventional / bi-directional solenoid

The replacement of 2 conventional solenoids by a novel bi-directional solenoid is a challenging task requiring constructive adaption works. For new developments, the constructive boundary conditions can be well adapted to the solenoid properties. A common requirement for the solenoid size 35 mm is a force of around 20 N with a

stroke of +/- 0,75 mm. Against this background, the maximum achievable force can be positively assessed also in direct comparison to conventional solenoids.

Besides the static forces, the dynamic features are important for the use in control valves. With conventional proportional solenoids, the iron material is more and more magnetized for force generation on the basis of the non-magnetised condition by the coil energization so that the actuation force is generated depending on the magnetisation properties of the materials. For dynamic applications, this correlation has the property that the non-linear effect of the complete magnetisation of the materials must be processed (see figure 8). This causes a fundamental dynamic disadvantage in build-up of force and finally a limited valve dynamics. This dynamics is sufficient for a huge part of hydraulic valves.

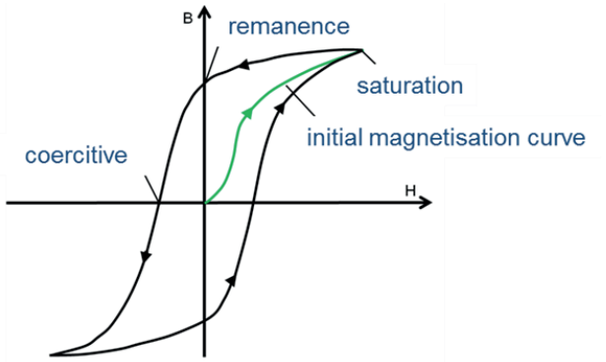


Fig. 8: Typical magnetisation characteristic curve (B-H-characteristic)

A considerable increase of dynamics can be principally effected by a pre-magnetisation of the material. It can be effected e.g. with a basic energisaton or the installation of permanent solenoids. This is, however, not useful in a conventionally designed solenoid system because an unwanted force effect is directly generated.

The new design of a proportional solenoid developed at MSM avoids this negative effect and generates a high dynamics with sufficient force density at the same time. As already described, the armature of the proportional solenoid is considerably modified for this purpose and fitted with permanent magnets as well as discs of conventional material. Due to the symmetrical arrangement, the permanent-magnetically generated forces neutralise each other. So, there is no unwanted force effect but the materials take a considerable pre-magnetisation.

The considerably higher dynamics compared to the conventional proportional solenoids could be proved by measurings (see figure 9). The time constant of the new solenoids is lower by the factor 2 to 3. Another advantage is that the considerably lower inductance is nearly independent of the armature postion.

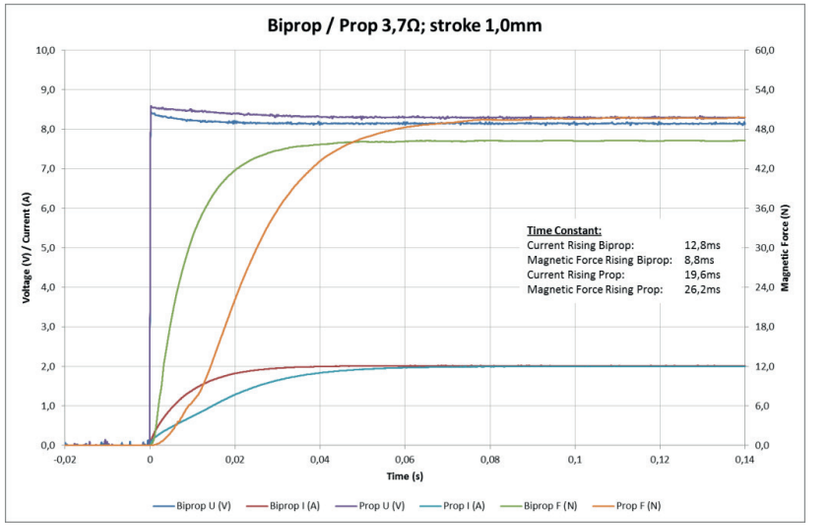


Fig. 9: Step response behaviour

Another effect of pre-magnetisation concerns the force vs. current characteristic curve. Due to the positive effect of pre-magnetisation, a characteristic curve is generated which shows a directly increasing force effect in the lower current range (see figure 10).

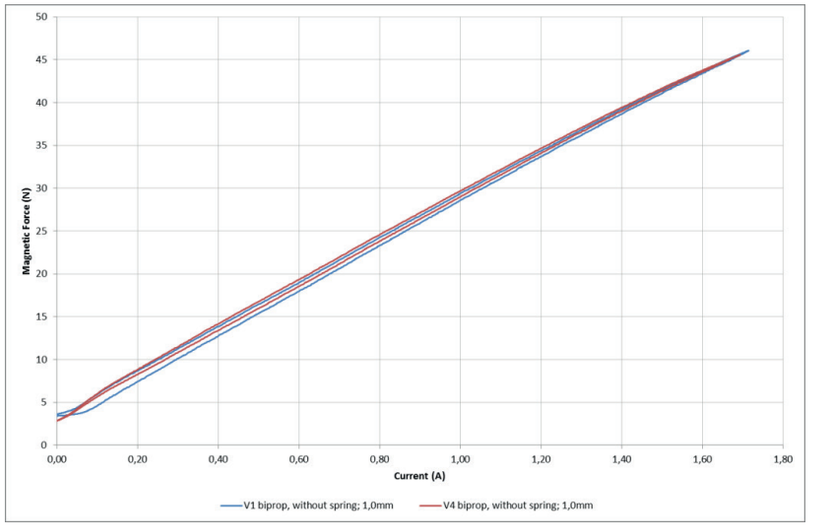


Fig. 10: Force vs. current characteristic curve

The shown measurement data and presented notes on the function illustrate the good applicability of such solenoids in hydraulic valves. The bi-directional solenoid has further advantages in the application. It can be designed with only slightly modified pole tubes and the appropriate standard coils. So the user has the possibility to design a highly dynamic valve function by the change of the proportional solenoid without modification of the geometric and electrical interfaces. A system change of the actuator function is not necessary. Only the current control must be modified. Figure 11 illustrates in a simplified way the constructive design of a conventional pole tube and of the armature.

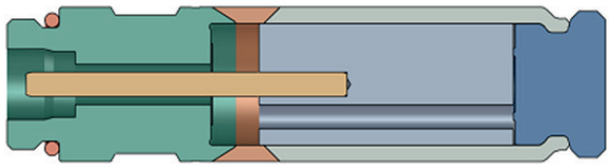


Fig. 11: Constructive design of conventional pole tubes and armatures

For the sector of the high-pressure resistant proportional solenoids, Magnet-Schultz has developed a structured modular system. Within this system, a large variety of functions can be illustrated with production processes for large series by the use of similar components. At the same time, individual customer requirements can be realised. Within this modular system, also ON/OFF solenoids with reduced functional quality can be produced besides challenging proportional solenoids. A survey of this modular system is shown in figure 12.

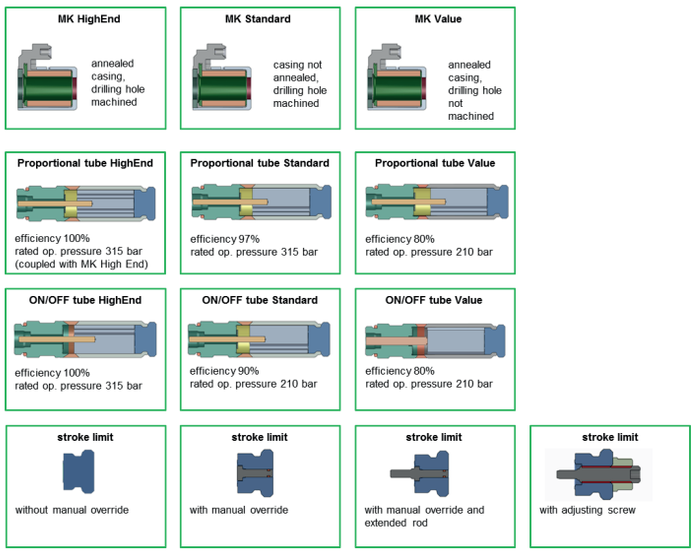


Fig. 12: Modular system for hydraulic solenoids

Due to the constructive design of the here presented high-dynamic proportional solenoid, the manufacturing advantages of the modular system can be used. The production technology for the pole tube and the solenoid coil correspond completely to the currently used principles. The single parts of the armature are also conventionally producible. Only the assembly poses higher demands due to the permanent magnets

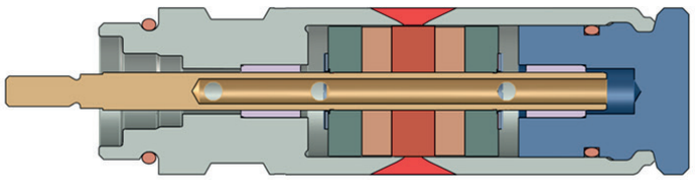


Fig. 13: Constructive design of pole tube and armature at the bi-directional solenoid

In this contribution, a high-dynamic and bi-directionally effecting solenoid has been presented. The illustration of functioning and the constructive design explain the advantages of the solenoid for the realisation of a high-dynamic valve function. At the same time, the used construction principles and the appropriate production procedures are established in large series. So, this is a combination of technical advantages while using conventional production procedures. Under these conditions, a successful use can be also expected in small series with comparably moderate development effort.

References

/1/ Gamble, Johnathan / Tappe, Peter: Kraftentfaltung in zwei Richtungen, ölhydraulik und pneumatik, Germany, 2008

Proportional Pressure Reducing Valves with Intrinsic Fail Safe Function

Dr. Jörg Schneider, Daniel Ferres, Dr. Jens Krallmann

Thomas Magnete GmbH, Mobile Hydraulics, Innomotion Park 3, D-57562 Herdorf, Germany
E-Mail: joerg.schneider@thomas-magnete.com

During the last two decades the aspect of functional safety has constantly gained more importance for all manufactures of mobile hydraulic machines or manufactures of subsystems used therein. Initiated by the IEC 61508 /1/ first issued in 1998 many divisions have deduced their own standards concerning functional safety with the goal to build control structures that are leading to fewer occurrence of dangerous situations during normal machine operation as well as in the case of a failing subsystem.

Looking into the failure modes assigned to a Proportional Pressure Reducing Valve (PPRV) within the ISO standard 13849 /2/ it was possible to integrate an intrinsic safety function into various types of pressure reducing valves. In the case of a stuck valve spool this fail safe function opens a second flow path from the control port to tank (Figure 1) resulting in a limited output pressure (Figure 2). For applications where this limited control pressure is in accordance with a safe situation this fail safe function is lowering the number of failure modes that are contributing to a dangerous situation and therefore is able to increase the diagnostic coverage of a subsystem build with such a fail safe valve. Depending on the working principle of the pressure reducing valve different types of fail safe designs are needed in order to realize this functionality.

Keywords: functional safety, pilot valve, PPRV, fail safe function, pressure control valves

1 Introduction

Proportional pressure reducing valves are very often used for ‘forced actions’ as called by the ISO standard 13849 in its ‘fault and fault exclusion Table’ in Annex C. An energized valve is meant to activate a hydraulic function, which is generally accompanied by movements of large heavy objects. A malfunction of the pilot valve can result in a dangerous or even life-threatening situation. This article describes special design features of such pressure reducing valves that are able to compensate the outcome of some common malfunctions keeping the machine function still in a safe state.

2 Functional principle of a PPRV

Direct operating pressure reducing valves are working as force balancing regulators. The magnetic force FM is always counterbalanced by the sum of the spring force FS and the hydraulic force acting on the valve spool PA (see Figure 1). Under normal operation conditions the spool is dithering at its metering edge resulting in a constant metering flow of hydraulic fluid from the pump port into the control port and back from the control port into the tank. As long as the force balance is maintained the pressure at the control port (PC) is proportional to the magnetic force FM and thus proportional to the electrical current through the solenoid.

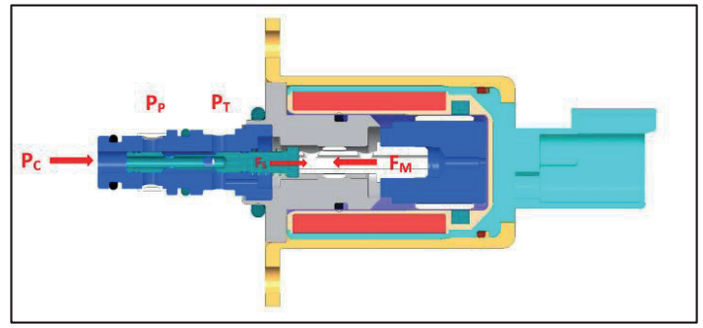


Figure 1: Force balance of a direct operating pressure reducing valve

Due to contamination or other mechanical influences it is possible that the spool gets stuck in its open position where the pump port is connected with the control port. In such a situation the control port pressure is rising within a short time to the level of the pump pressure and in standard application, where the PPRV is used as pilot valve, this is resulting in a fully actuated main stage (see figure 2). In mobile hydraulic applications such a scenario is mostly accompanied by a possible dangerous situation and has to be avoided by certain measures.

Depending on the strategy of the OEM there are different ways to avoid such uncontrolled movements. It is possible to use pilot valves that are extreme robust against a definite level of contamination and during normal operation the contamination level of the hydraulic fluid is always monitored and kept below a critical value. Other machine manufactures are implementing position sensors at the main spool of their sectional valves in order to detect actively an unmotivated actuation. In case of such an unwanted actuation the movement is stop by an on-off valve that shuts off the hydraulic supply to the sectional valve.

The following chapter will describe special design features that are able to keep the machine function still in a safe state although the pilot valves spool is stuck. This will be shown for two different valve types.

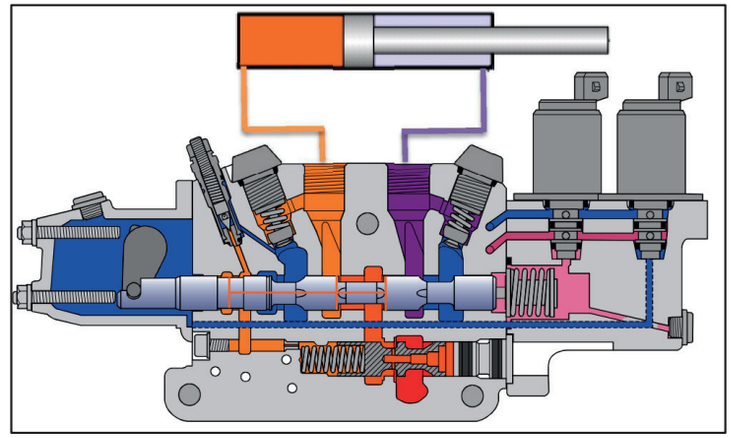


Figure 2: Sectional valve with two pilot valves. One energized and acting on a hydraulic cylinder.

3 Functional principle of the fail safe versions

In standard sectional valves the main spool always needs to travel a certain idle stroke until its metering edge comes into action. This is related to a certain minimum pressure at the control port of the pilot valve. Therefore not only a control port pressure of 0 bar is ensuring a not activated hydraulic function but also a pressure level significantly below that threshold pressure.

Figure 3 is describing how an additional flow path through the spool of a 25 bar valve is able to keep the control pressure below the critical value of – for example - 5 bar although the spool sticks at the metering edge. Under normal operation conditions the armature bar is closing the additional path with a sealing element. In the case of a stuck spool the armature bar retracts and opens the additional path to tank.

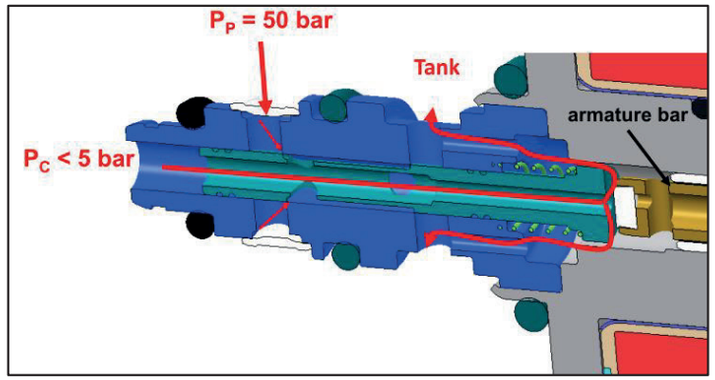


Figure 3: Functional principle of a fail safe valve. Basic type PPCD04 with nominal flow 4 l/min.

The residual pressure level in the control port depends on the flow restrictions of the different flow paths as well as on the supply pressure. The biggest influence has definitely the opening area that is created by the sticking spool at its P-metering edge. To be sure that the fail safe function is correctly and sufficiently working this opening area has to be limited.

Hence, a possible argumentation for the correct use of such a design feature as safety function must contain the exclusion of silting processes that are able to let the spool fully stuck open and additionally the particles that are causing the sticking spool have to be limited in size. The second condition is easy to ensure by the usage of filters meshes. A standard filter screen of a THOMAS PPRV has a mesh width of 125 µm. It is normally applied only to the pump port but if possible contamination with large particles through other ports cannot be excluded, additional filter elements at control and tank port are necessary. Figure 4 shows the pressure trace for a spool that got blocked during its retraction movement by a 125 µm thick wire and is therefore representative for the pressure situation of a particle of maximum size has entered the valve through from the pump port and blocked the spool.

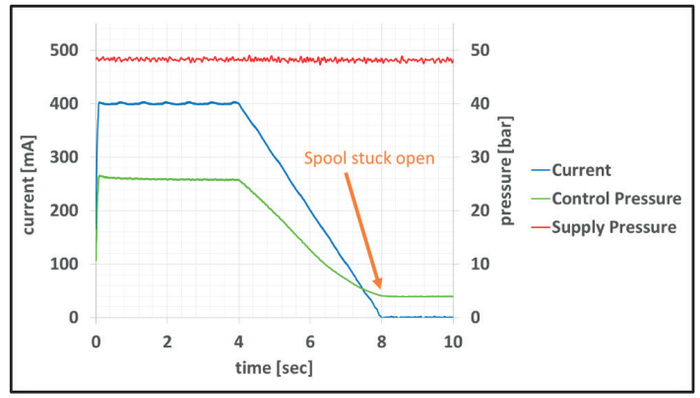


Figure 4: Pressure trace of an unenganged pilot valve with stuck open spool. 125µm thick wire opends the P-port.

The fail safe valve shown in figure 3 is a valve with a direct acting solenoid. The armature bar is applying the solenoid force directly to the spool. Due to the working principle of the balancing forces the spool diameter is limited and just as well is the flow capacity of such a valve restricted. Different valve types that are working with a pressure pin can compensate for this limitation – providing a higher flow capacity together with a normal reducing pressure range.

Figure 5 shows a cross section of such a PPCD06 valve. For this kind of pressure reducing valve it is also possible to open an additional flow path in the case that the spool is sticking right at the metering edge. The solution is realized by a spool, which is built out of two parts with two independent moving metering edges. During normal operation both parts are pressed together by the solenoid force on the one side and the hydraulic pressure in the control port on the other side. If the spool get stuck and the armature is retracted, the pressure pin opens an additional tank path and depressurizes the area behind the 'right' (see figure 5) part of the spool. Then the T-metering edge is opened and the flow from the pump port can be bypassed around the spool directly into tank resulting in a relatively low control pressure.

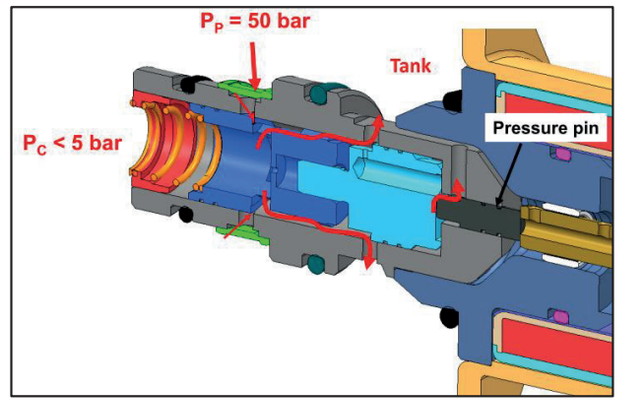


Figure 5: Functional principle of a fail safe valve. Basis type PPCD06 with nominal flow 16 l/min.

The biggest difference between the two fail safe features is their influence on the stability of the complete system. While the modified PPCD04 valve does not show any additional trend for instabilities the PPCD06 valve is more sensitive to instabilities due to the separately working metering edges. If such a valve is working against a closed control port and does not have to deliver any significant flow into the control port, no instabilities are visible (see figure 6a). As soon as the valve has to deliver some flow accompanied with a tendency for the spool to overshoot (see figure 6b) measures have to be taken in order to keep such instabilities under control. It is possible (see figure 7a) but the optimization between the overlap of the three metering edges (including the one at the pressure pin) and all possible dampening mechanisms inside the valve have to be precisely adapted to the valves load and overall stability over a large temperature range is extremely difficult to achieve. Especially fast commands (see figure 7b) have to be avoided or - to put it in other words – as long as the hydraulic system is not demanding a high dynamic behavior the fail safe valves can be used without large restrictions.

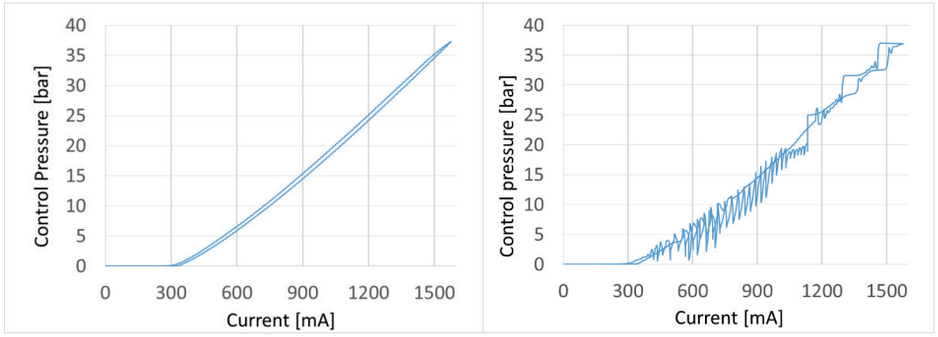


Figure 6: Left) PPCD06 fail safe working against a blocked port. Right) same valve working against a sectional valve.

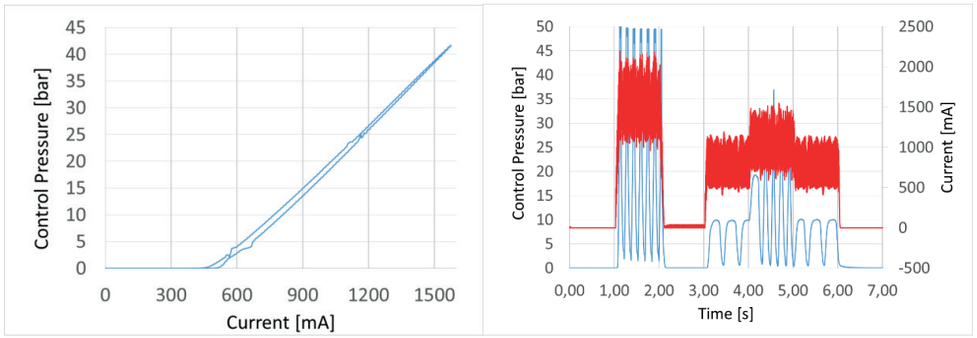


Figure 7: Left) Optimized PPCD06 valve working against a sectional valve. Right) Step response test with the same setup.

4 Limitations and restrictions

In the previous chapter it was discussed that the residual pressure of a valve with sticking spool is depending on the used pump pressure as well as the p-port opening given by the stuck spool. The graph in figure 8 shows the residual control pressure of a 25 bar fail safe PPRV where the metering edge is kept open by a metal wire simulating a large hard particle out of the initial contamination that are usually present in hydraulic systems. These measurements clearly reveal that the maximum size of the particle that can possibly cause the blockade has to be limited to 300 µm in order to use not more than 50% of the pilot valves pressure range for the idle stroke of the main section. In system where this cannot be assured and where silting effects as source for a sticking spool cannot be excluded the maximum residual pressure has to be limited by a general flow restriction from the pump port into the pilot valve.

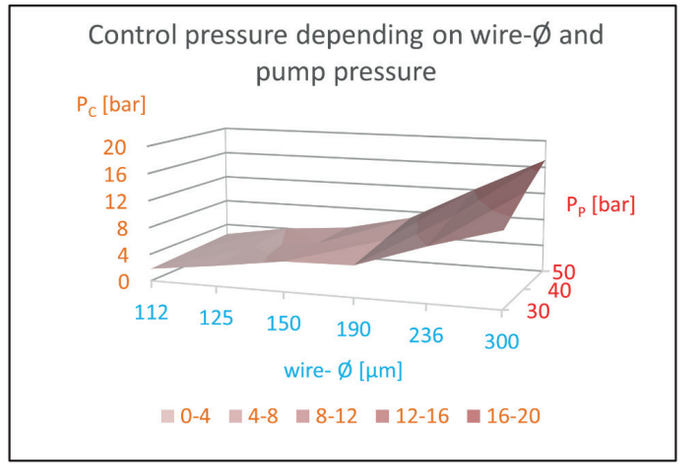


Figure 8: Residual control pressure of a PPCD04 Fail Safe valve with respect to the pump pressure and the opening area at the p-metering edge.

Figure 9 displays the residual control pressure of a 25 bar Fail Safe PPCD04 with a fully opened sticking spool and with different orifices implemented in the pump line. With such a general flow restriction it is possible to ensure a safe system situation independent from the actual clamping position but at the same time this goes along with a significant loss in dynamic behavior.

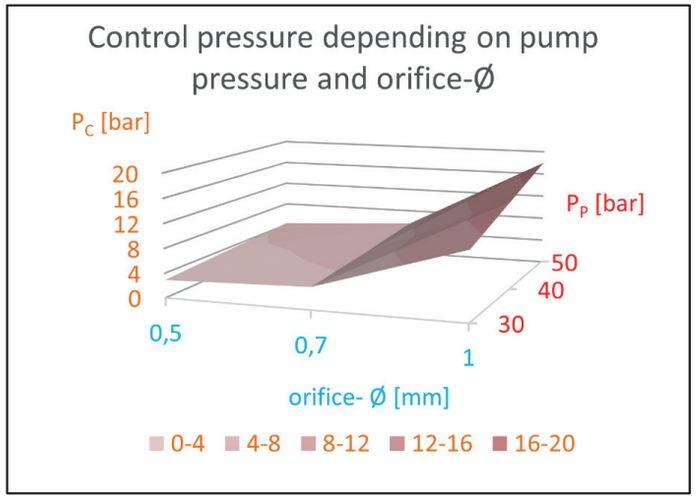


Figure 9: Residual control pressure of a PPCD04 Fail Safe valve with respect to the pump pressure and an additional orifice.

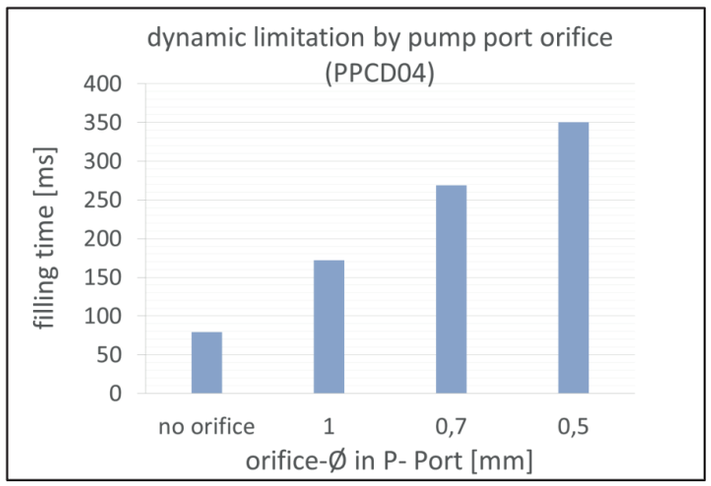


Figure 10: Dynamic limitation by an additional orifice.

In figure 10 the filling time of a spring loaded piston (complete suppressed volume = 6 ml) with a p-restricted Fail Safe valve is shown.

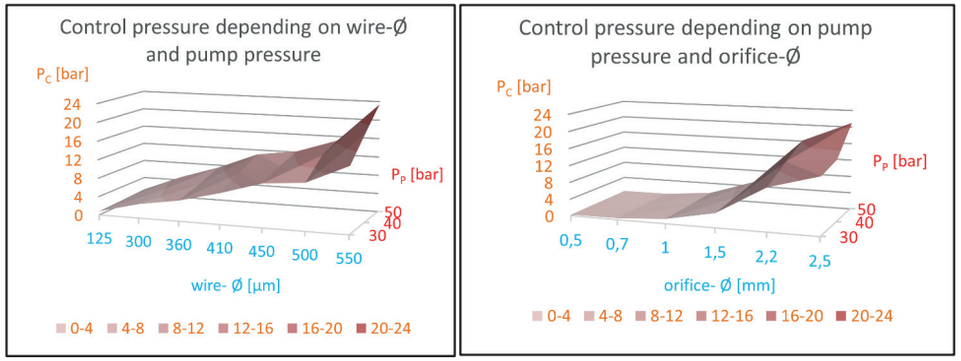


Figure 11: Residual pressure with and without additional orifice for a PPCD06 Fail Safe valve.

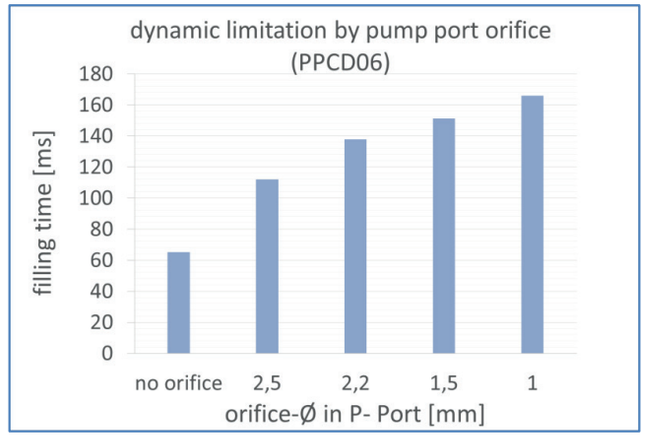


Figure 12: Dynamic performance of a PPCD06 Fail Safe valve with an additional flow restriction.

Figure 11 and 12 are displaying the results of identical measurements done with a 32 bar Fail Safe PPCD06.

For each individual system a compromise has to be found between the dynamic requirements and the allowed residual control pressure. Once such a compromise is found the rating of the complete system concerning its functional safety level can be improved significantly.

5 Influence on the functional safety rating

In general the rating of mechatronic systems with respect to the regulations of ISO 13489 are mainly determined by the influence of their hydraulic or pneumatic components. Electronic components normally do have reasonable large MTTFd values and it is relatively easy to implement diagnostic functions in order to accomplish a high diagnostic coverage (DC) value. Hydraulic and pneumatic components with their standard performance are generally those parts of a mechatronic system that are responsible for a low safety rating. The usage of Fail Safe PPRVs can significantly enlarge the DC value of a linear (not redundant) signal chain.

Taking as an example an electrohydraulic that is used as pilot system for a sectional valve actuator (see figure 13). Its main signal chain consisting of a CAN input signal, a microcontroller as CPU and field effect transistors to modulate PWM signals that are controlling the currents through the coils of the pilot valves. For such an electrohydraulic actuator a reasonable Safety Function in terms of ISO 13489 can be defined as 'Ensure a low enough pressure output at both working ports of the pilot valves if the input signal is indicating neutral position for the sectional valve'.

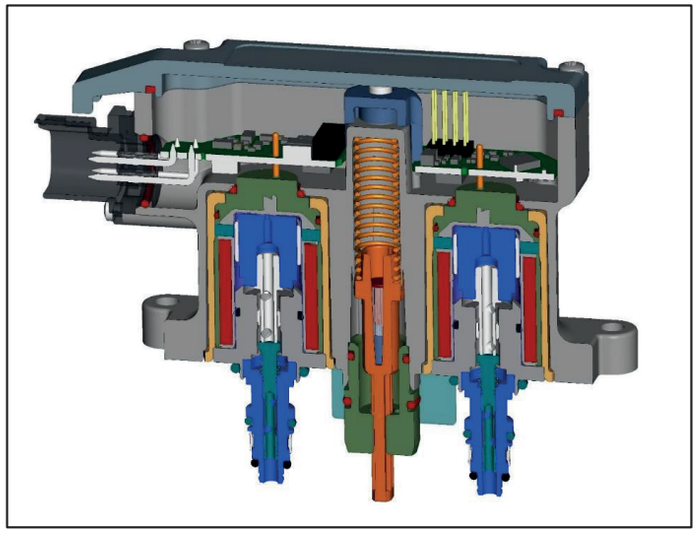


Figure 13: Cross section of the electrohydraulic actuator.

The single components of the active signal chain for that Safety Functions together with their assigned MTTFd and DC values are displayed in figure 14 and figure 15. The first figure shows the reliability model of a system with standard PPRVs as pilot valves while the second contains Fail Safe valves. In both cases the pilot valves are the components with the lowest MTTFd and DC values. The MTTFd value of 150 years is justified by the design rules for pressure valves given in table C1 and C2 of ISO 13849 and this value has to stay constant independent on the number of possible failure modes that are resulting in dangerous system situations. This argumentation is the reason for a constant MTTFd value of 29.1 years for both reliability models. The usage of Fail Safe PPRVs is not decreasing the probability for a safety relevant incident to happen but out of the three dangerous failure modes (Table C6 in ISO 13849) the number of detected and compensated failures is increased from one to two. This results in a significant larger diagnostic coverage value - for the signal component (33% -> 66%) as well as for the complete signal chain (71% -> 84%).

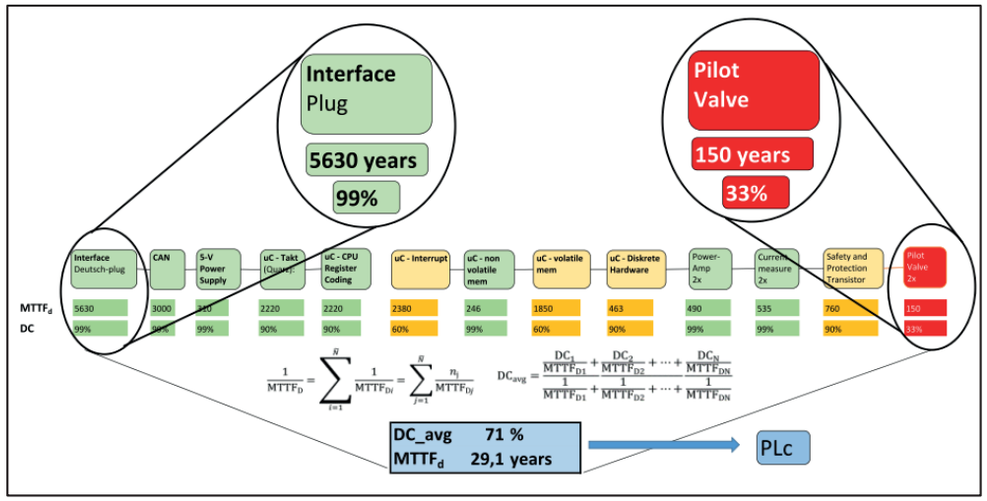


Figure 14: Reliability model of main signal chain for an electrohydraulic actuator with standard PPRVs.

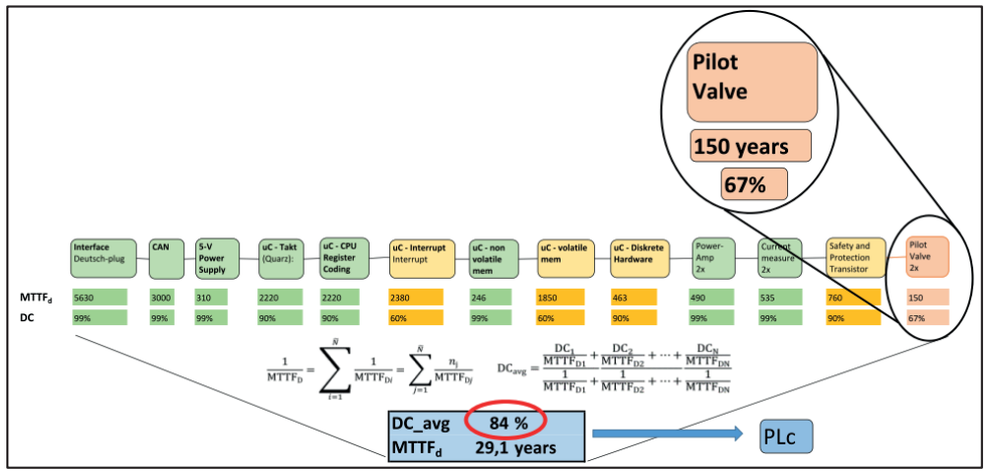


Figure 15: Reliability model of main signal chain for an electrohydraulic actuator with standard PPRVs.

In the given example the increased DC value does not lead to a change in the overall performance level of the product but this can be different depending on the systems structure and safety related characteristics of the other components of the signal chain.

In any case the usage of a Fail Safe PPRV is able to enlarge the safety level of a system that uses proportional pressure reducing valves as long as the safe situation is accompanied with an unengaged pilot valve.

References

/1/ IEC 61805: Functional safety of electrical/electronic/programmable electronic safety-related

/2/ ISO 13849: Safety of machinery - Safety-related parts of control systems

Proportional Leak-Free Pressure Control Valve

Christian Stauch, Frank Schulz, and Dr.-Ing. Michael Reik

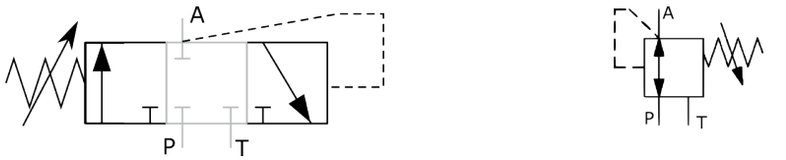
HYDAC Fluidtechnik GmbH, Justus-von-Liebig-Straße, D-66280 Sulzbach/Saar, Germany
E-Mail: christian.stauch@hydac.com

Pressure control valves combine both a reducing and a relieving function. Such valves typically are spool type valves which principally suffer from leakage flow. Additionally, in case of an electrical failure, usual proportional pressure reducing and relieving valves fully open either the supply port connection or the tank port connection. In some applications like clamping functions in machine tools, this is a clear disadvantage. For fail safe operation in machine tools, it is desired to hold the set pressure in case of failure. The article introduces a new kind of proportional pressure reducing and relieving valve, which is leak-free due to seat valve technology. Furthermore, the valve is able to keep the set pressure in case of power-off and is therefore well-qualified for clamping applications.
Keywords: control valve, independent metering, leak-free pressure control
Target audience: machine tool, industry hydraulics, test stand

1 Introduction

Pressure control valves, also referred to as pressure reducing/relieving valves, are commonly used in fluid power systems in order to regulate a pressure at a certain point in the system(e.g. such as an actuator). Such valves exist in wide range of varieties. In order to illustrate the generic function of a pressure control valve, the simplest type is used in the following subsection (cf. Figure 1).

1.1 Function of a pressure control valve



(a) Functional symbol *(b) Simplified symbol*

Figure 1: Symbols for a pressure control with manually adjustable set pressure.

A pressure control valve, typically having 3 ports, combines both a pressure reducing function and a pressure relieving function. When either increasing the load pressure or maintaining a constant set pressure with a flow rate consumption at the working port A, then the valve is in reducing mode. In this case it causes a pressure drop from the supply port P to the working port A such that the pressure at the working port A reaches the desired value. If the flow direction is reverse or the working port pressure is to be decreased, then the valve changes to pressure relieving mode. In this case, the flow path from the working port A to the relief port T is used. The valve causes a pressure drop between these two ports such that again the desired pressure value in the working port A is achieved. The quality of the regulation in terms of precision and dynamics heavily depends on the construction type of the valve. Obviously, there is a great variety in the requirements for pressure control valves as there are plenty of different applications for such valves.

1.2 Types of pressure control valves

A common way to classify pressure control valves is to differentiate by looking not at the control properties but at the underlying construction principles of the valve. Some relevant distinguishing properties are listed and discussed in the following:

- Set point adjustment
  The set pressure of a control valve can be adjusted either **manually** (e.g. by manipulating the preload force of a spring) or **electro-proportionally** (e.g. by using electromagnetic actuation). Whereas the electro-proportional set point adjustment offers clear advantages in terms of flexibility and adaptability, the classical manual adjustment still has its raison d'être in applications that are either very cost-sensitive or have special safety requirements.
- Pressure feedback
  In valves with **direct feedback**, the control pressure at the working port A causes a feedback force acting on the control element, typically being a spool. By contrast, some types of valves rely on an **indirect or electronic feedback** using a pressure signal from a sensor in order to control the spool. Typically, a direct hydraulic-mechanical feedback is much more dynamic than an electronical feedback which also depends on the dynamics of both the sensor and the actuator. However, an exception to this is given by high-response and servo valves that also can be used for pressure control with an underlying highly dynamical position control for the main spool. An intermediate type of feedback is the combination of a direct force feedback for high dynamic control with an additional low-dynamic outer electronic control loop for steady-state precision.
- Main control element
  Most pressure control valves are **spool-type** valves having a main spool whose position defines the flow areas of the flow paths in the valve. However, there are a few **poppet-type** pressure control valves in the market which have the advantage of leak-freeness in the closed position.
- Mounting type
  As nearly all kinds of valves, pressure control valves exist both as **cartridge** (slip-in or screw-in) valves and as flange- or **plate mounted** valves. Cartridge valves are used mainly, but not exclusively, in mobile applications, e.g. for clutch controls whereas sub-plate mounted pressure control valves are to be found in industrial applications almost exclusively.

The resulting variety of valve types including some examples is illustrated in Figure 2. This classification is by no means claimed to be complete or canonical in any sense. Further categories such as pilot operated/direct operated could be added easily.

Having a closer look to the proportional valve branch in Figure 2, a gap becomes obvious: so far, there is no proportional seat-type pressure control valve in the market, at least to the best of the authors' knowledge. The focus of this article therefore is the presentation of a novel market-ready leak-free proportional pressure control valve.

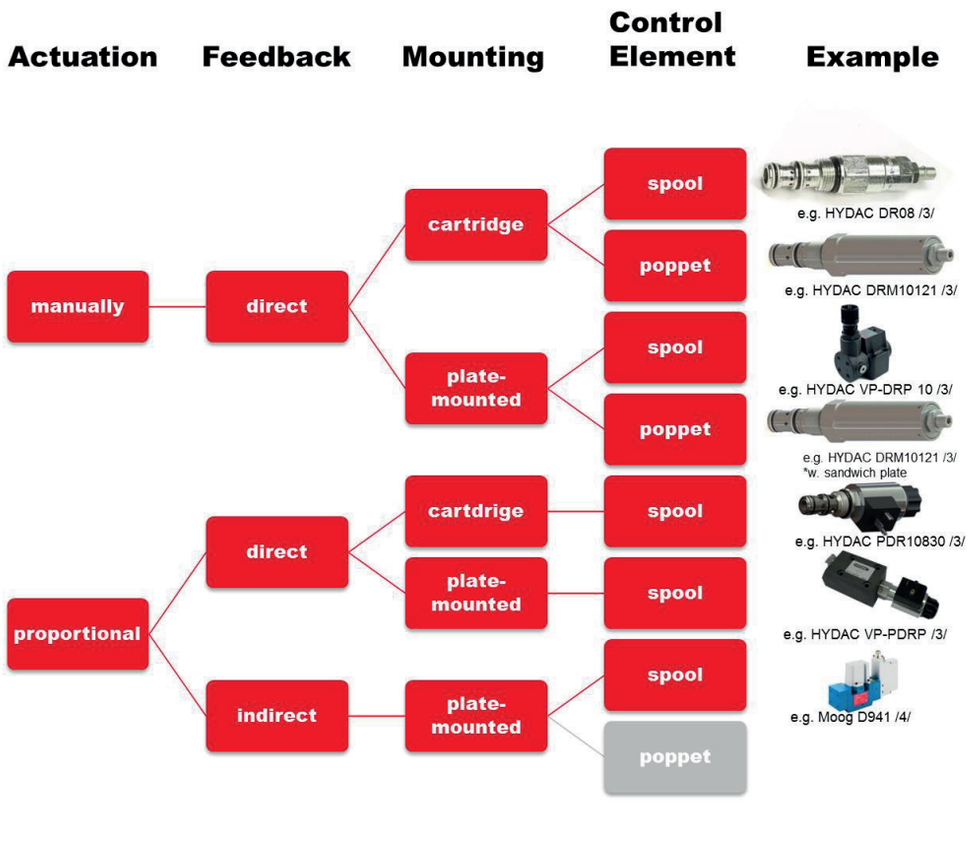


Figure 2: Different types of pressure control valves.

2 The leak-free proportional pressure control valve P3RSEE 6

The main motivation for designing the P3RSEE 6 was to close the gap shown in Figure 2, i.e. to have a poppet-type proportional pressure control valve. The origin of this principle lies in the research area of digital hydraulics /1/, where two 2/2 poppet-type on/off valves are used in combination with a pressure sensor and PWM valve control in order to regulate the pressure between the two valves. However, the PWM principle requires very fast switching valves which are not available at marketable costs. A principle using poppet valves similar to the pressure control valve presented here was successfully implemented by Plöckinger et al. for the position control of a hydraulic membrane actuator /2/.

The novel pressure control valve P3RSEE6 (cf. Figure 1 Figure 4) combines the advantages of closed loop pressure control, independent metering, and poppet-type valve elements in one highly integrated subplate-mounted size 6 valve with on-board electronics (OBE).

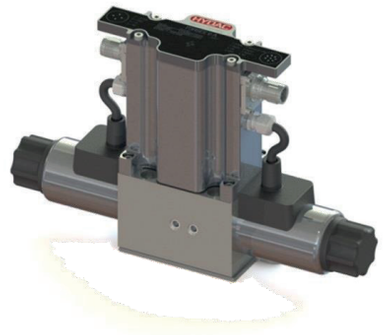


Figure 3: Pressure Control Valve P3R.

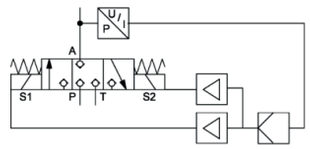


Figure 4: Functional circuit symbol.

2.1 Functional principle

The valve involves a housing with a standard mounting interface, an integrated on-board digital electronics (OBE) and two poppet valve elements which can be activated independently from each other. One valve element connects the supply port P to the working port A, the other element connects the working Port A to the relief port T. The use of seat-type valve technology avoids undesired leakage cross flow from both supply port P and working port A to the tank port T. A pressure transducer detecting the working port pressure is integrated in the valve housing. The pressure signal is fed to the digital OBE, where a pressure control algorithm determines the opening of the poppet elements. The desired set pressure is also fed to the OBE via an analogue input signal. Additionally, the OBE involves the underlying current control for the valve coils.

2.2 Features

First of all, the availability of an integrated pressure transducer and an OBE allows for closed loop pressure control which brings about several advantages: Most obviously, with closed loop control, the hysteresis can be reduced to the limits given by the pressure transducer which is below 1% of the measurement scale. In Figure 5, the pressure-current-curve shows the quasi-static characteristic of the valve. Another benefit of closed loop control is the linearity of this characteristic curve. The major advantage however is the flow compensation due to the closed loop control. Figure 6 shows the pressure-flow characteristic of the valve in relieving mode. The influence of the flow rate on the set pressure is reduced significantly as compared to open loop pressure control valves.

The combination of poppet-type elements and independent metering principles allows realising zero overlap control behaviour while at the same time having zero leakage in the “neutral position”. This brings about another advantageous load-holding feature of the valve: in case of an electrical failure, e.g. an undesired power-off or an emergency stop, both flow paths from supply port P to working port A and from port A to the relief port T are closed by the poppet elements. Besides, in another case of known failure where the hydraulic power is lost (i.e. the supply pressure breaks down) the valve allows to relief the pressure from the working port A to T in a fully controlled manner.

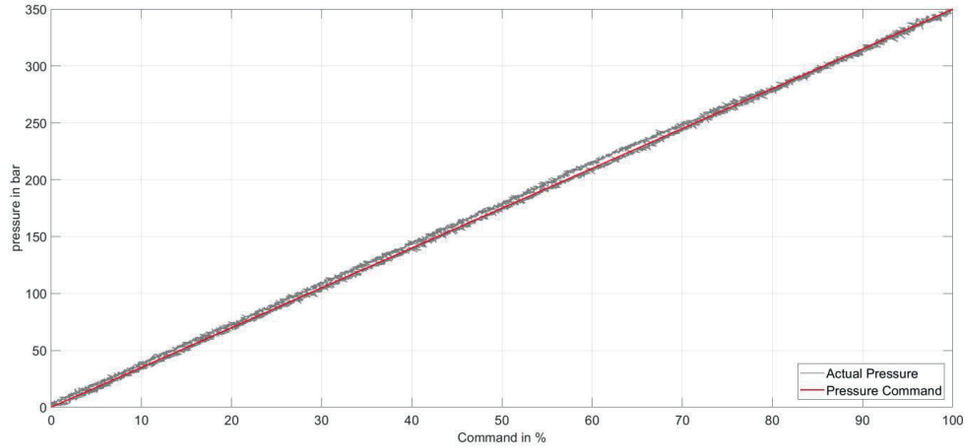


Figure 5: Pressure control characteristic.

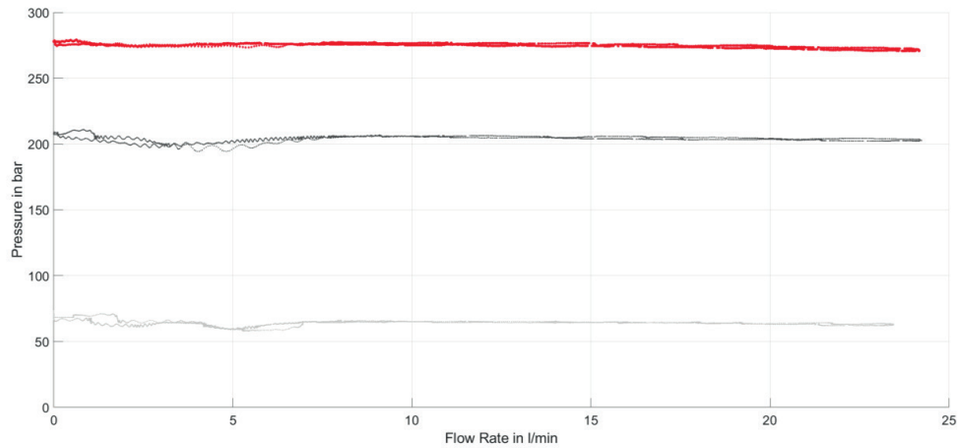


Figure 6: Pressure-flow-characteristic.

The sales-ready version of the valve has an analogue monitoring output, where the actual pressure determined by the pressure transducer can be forwarded to any higher level control system which allows for a more sophisticated process control and monitoring; a fact from which predictive maintenance systems also might benefit. Further development of the valve involves the complementation of digital communication interfaces (cf. Section 4).

2.3 Technical Specification

The pressure control valve P3RSEE 6 has a CETOP 03 standard interface in accordance to ISO4401. The nominal flow is 25 l/min and the maximum pressure range is 350 bar. The dynamics of the valve depends on the operating conditions, the load dynamics attached and the controller parameters. Typical step response times are in the range of 50-300 ms. The pressure drop per metering edge is in the range of 5 bar at 8 l/min flow rate.

2.4 Case study

A technology demonstrator is used to illustrate the main features of the pressure control valve (cf. Figure 7). This demonstrator includes an accumulator charging circuit with a compact power unit being connected to the supply port P of the valve. The relief port is connected to the tank of the power unit. A pressure gauge and a pressure transducer are mounted at the working port A with an overall trapped oil volume of 25 ml. The set pressure is repeatedly ramped up and down between 0 and 100 bar using ramp times of 1 s and holding times of 1 s, i.e. the overall cycle time is 4 s. The hysteresis set points of the charging logics are chosen such that the power unit starts charging at a supply pressure of 101 bar and stops when the pressure has reached 115 bar. Within one accumulator charging cycle, the valve is able to perform 225 load pressure cycles. Taking into account the accumulator dimensioning, the overall amount of oil consumed within these 225 cycles can be estimated to 50 ml. Approximately 80% of this amount are used for repeatedly compressing the trapped oil at the working port A. This experiment emphasises the valve's ability for pressure control at almost zero leakage level and load holding at zero leakage.

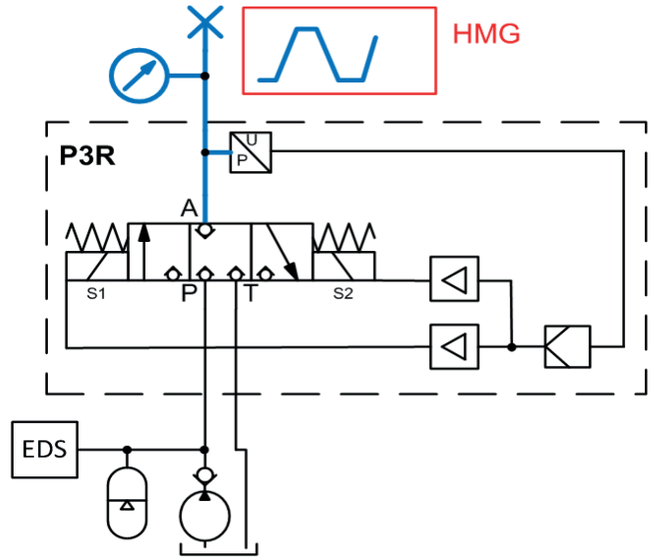


Figure 7: Circuit sketch of the technology demonstrator.

3 Application areas

The most obvious target application area is clamping in machine tools. Here, most of the features of the presented valve bring about added value for the application. The possibility to precisely control the clamping force dependent on machining processes and workpieces becomes more important in machining of lightweight workpieces and materials. The integrated pressure feedback enables a process monitoring and fine-tuning without the need to install additional sensors. The integrated load holding feature allows for increased functional safety. Modern clamping hydraulics often relies on accumulator charging circuits with variable speed drives. The avoidance of leakage in the clamping not only yields a significant benefit regarding the energy efficiency of the system but also reduces the fluid heating due to energy loss in the hydraulic system. This in turn might reduce the necessary expenses for cooling in the hydraulic system. Additionally, the decrease in leakage losses in an accumulator-based clamping hydraulics either allows for downsizing of the accumulator or the pump drive or requires less recharging cycles. Summing up, the pressure control valve P3RSEE 6 enables a change in the design of the clamping hydraulics that might bring significant benefits in efficiency, cost and service life.

Other target application areas can be found both inside and outside the field of machine tools. Presses with high numbers of working cycles will benefit from the increased energy efficiency due to the reduced leakage and leak-free load holding. The same holds true for variable counterbalancing functions in machine tools. Requirements that are very similar to those of clamping circuits can also be found in the field of hydraulic brakes.

In general, any pressure or force control application that is both sensitive to leakage or energy loss and requires precise control with intermediate dynamics is a possible target area for the presented pressure control valve. Other applications that might benefit are such where both proportional pressure control and leak-free load holding in case of power-off is needed.

4 Outlook: Further development and additional features

The pressure control valve P3RSEE 6 as presented in the Sections 1-3 is available for sales. Nonetheless, the valve is under constant development. The next development step will be the complementation of digital communication facilities.

In addition to new state-of-the-art communication interfaces, the control software itself is subject to further development. The implementation of adaptive control algorithms and auto-tuning capabilities is the main focus of current development in this area. Recent experiments have shown that the valve is qualified for online identification of plant parameters. A recursive identification algorithm that is fed with test signals and measurements that are available within the OBE yields a parameter α that gives a measure for the load capacity attached to the working port A (cf. Figure 8). In most of the relevant applications, this load capacity determines the plant dynamics. Therefore, future control algorithms can be tuned automatically in dependence of this parameter α which then will be identified on-line.

Further activities in development aim at increasing the physical dynamics of the valve in order to be applicable to systems that have higher requirements regarding the closed-loop dynamics as those mentioned in section 3.

5 Summary

The present article introduces a novel kind of proportional pressure control valve with on-board digital electronics relying on independent metering principles and poppet-type valve elements. This allows pressure control at very low leakages and low hysteresis as compared to conventional pressure control valves and load holding at zero leakage. The integrated pressure sensor may also be used for monitoring purposes at higher levels in the control hierarchy. These features may bring about significant advantages regarding energy efficiency, cost and service life in applications like clamping hydraulics and similar areas. The valve as presented is project ready. Further development efforts aim at including additional features like auto-tuning and increasing the valve dynamics.

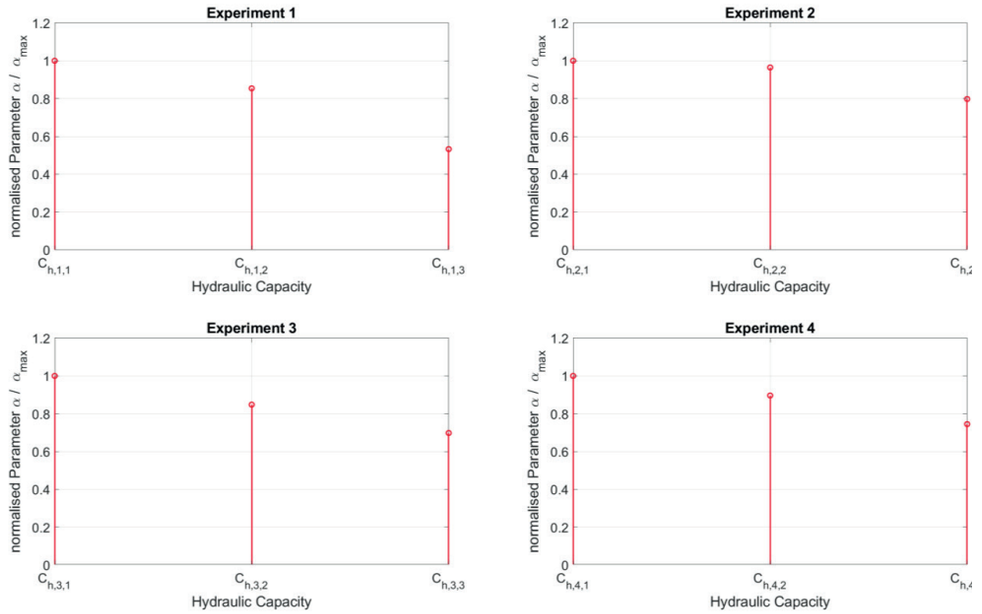


Figure 8: Relation between the identified parameter α and the load capacity C_L.

References

/1/ Linjama, M. *Digital fluid power: State of the art*. In 12th Scandinavian International Conference on Fluid Power, Tampere, Finland, May 2011.

/2/ Plöckinger A., Winkler B., Foschum P., Scheidl R.: *Digital Hydraulics for an Industrial Micro-Positioning System*, in: Hubertus Murrenhoff (Eds.): Proceedings of the 9th International Fluid Power Conference (9th IFK), 24th - 26th March 2014, Aachen, Germany, Volume 1, Page(s) 478-489, 2014

/3/ HYDAC International GmbH, *Compact Hydraulic. Product Catalogue*, https://www.hydac.com/fileadmin/pdb/pdf/PRO00000000000000000000053000010011.pdf, visited on December 11, 2017.

/4/ Moog Inc., *Proportionalventile Baureihe D941*, http://www.moog.de/content/dam/moog/literature/ICD/d941seriesvalvesD.pdf, visited on December 11, 2017

Smart hydraulic cylinder with force measurement system

Roman Weidemann, Mehdi Javdanitehran, Torsten Winkler and Torsten Boldt

WEBER-HYDRAULIK GMBH, Heilbronner Str. 30, D-74363 Güglingen, Germany
E-Mail: roman.weidemann@weber-hydraulik.com

The trend of intelligent components can be observed in various fields. Intelligent component means components with highly integrated sensors and control technology. This enables the system manufacturer to design more complex equipment, and nevertheless decrease in the required integration effort. As a customer-oriented supplier and development partner WEBER-HYDRAULIK concern itself with the development of highly integrated, reliable and reasonably priced sensors for hydraulic cylinders. While an optical position transducer is developed for mass production, this article focuses on the development activities of an in-cylinder integrated force measurement. Parallel to the further development of the application-specific force measurement system for supporting cylinders, a universally applicable concept for contactless force measurement was investigated.

Keywords: smart components, contactless force measurement, integrated sensors, hydraulic cylinders
Target audience: Mobile Hydraulics, Stationary Hydraulics, Hydraulic System Designers

1 Smart hydraulic cylinders from WEBER-HYDRAULIK

WEBER-HYDRAULIK is following the path of evolving from component supplier to system solution provider over the past years. We have observed that application areas of the customer are becoming more complex where the performance, energy efficiency or ease of use of drive systems must be maximized mainly through the application of electronic control systems. The control systems require acquisition of information from various process parameters. Integration of measurement systems is often challenging. On the one side, the application effort must be kept to the minimum. On the other side, the sensor components must be protected in the best way against harsh environmental condition e.g. on the construction sites or in the agricultural environment. Against this background, WEBER-HYDRAULIK develops smart hydraulic components with fully integrated sensor technology. An optical position measurement sensor which can be integrated into a cylinder and a customer-specific solution for force measurement in supporting cylinder are already in mass production. /1/

1.1 Integrated optical position transducer

There are various technical solutions for measuring the current position of hydraulic cylinders. The developed integrated measuring sensor detects the cylinder position by optical recognition of a binary barcode applied on the piston rod, which has a unique code structure in every position. The sensor is available as a redundant version to meet more strict safety requirements. Its compact design makes the sensor particularly suitable for mobile applications in agricultural and construction machinery.



Figure 1: WEBER-HYDRAULIK optical position transducer

The sensor is made up of an exposure unit, a sensor unit to capture the image and an electronic module for image processing and communication. A section of the code is illuminated by the exposure unit for a short period of time which is detected by the sensor unit then. This takes place at specific intervals which adapted to suit the maximum traversing speed of the rod. The images are analysed individually, and the position is determined respectively.

The code is unambiguous over its entire length. This means that every change of position results in a unique piece of code over the entire measured length.

The sensor is mounted on the cylinder guiding piece outside of the pressure chamber and directly behind the wiper. It is thus an external sensor, which is, however, highly integrated into the cylinder design. Nevertheless, its installation can be optimally adapted to suit the customer's system. In many cases this allows the sensor to be implemented without increasing the retracted length of the cylinder. At the same time, the sensor is protected against manipulation, as it cannot be influenced from the outside, for example by being mechanically separated from the system.

Due to its design, component reliability and the safety measures implemented, the sensor is suitable for requirements corresponding to PLe (EN ISO 13849 [1]). The maximum feasible measuring length for the planned system is approx. 6,000 mm.

1.2 Integrated force measurement

WEBER-HDRAULIK was previously involved in the development of an application-specific solution for integrated cylinder force measurement and currently pursues the further development of integrated supporting force measurement.

To monitor the stability of supported mobile vehicle e.g. cranes, aerial ladders or concrete mixer pumps it would be advantageous to have information about supporting condition. In daily practice, the loading capacity of the supporting base is often unknown since the surrounding condition doesn’t allow for a complete outrigging of supporting plates or the load carrying capacity of the ground is limited. The safety can be increased using electronic monitoring system for loading condition. This means the acquisition of outrigger positions as well as the supporting load of each supporting cylinder.

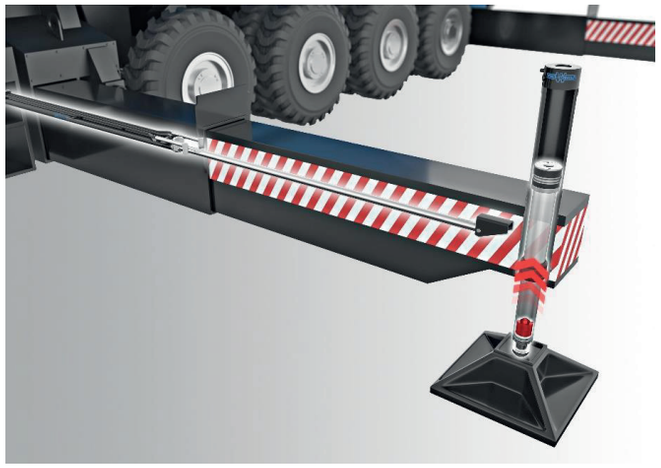


Figure 2: Supporting cylinder with integrated force measurement

The force of supporting cylinder is commonly measured indirectly through the pressure of piston chamber. Although this method is not precise especially that measurement deviation over 20% can occur under transversal loading condition, due to the friction of the sealing system. To assure a safe operation at any given moment, safety factors are required which consequently reduces the available loading capacity of the system.

Using a supporting cylinder with integrated force measurement system, the force will be measured directly on the ball head. Hence, a force gauge was developed that is fully integrated into the piston rod. The measurement signal is transmitted directly through the cylinder and end cap to the crane control system using a standard interface. Consequently, a sensitive and disturbing cable connection outside of piston rod of the supporting cylinder is not required anymore.

The goal of further development of this system is mainly reduction of sensitivity of the system to transversal load as well as enhancement of robustness of the system in the field. An exemplary goal is increasing the allowable transversal load from 10% to 20% of the axial supporting load.

2 Contactless force measurement

Hydraulic cylinder with integrated force measurement is not solely interesting for the supporting application. There are several applications such as force controlled manufacturing processes where the force measurement is required or the performance and finish quality can be enhanced with.

As a reason, WEBER-HYDRAULIK is not only following the development of a new generation of supporting force measurement system but also the development of a universal integrated solution of force measurement for cylinder applications

2.1 Measurement concept

The loading condition of a component can be mainly categorized to tensile, compressional, bending, shear and torsional loading, which are illustrated schematically in the following *Figure 3*.

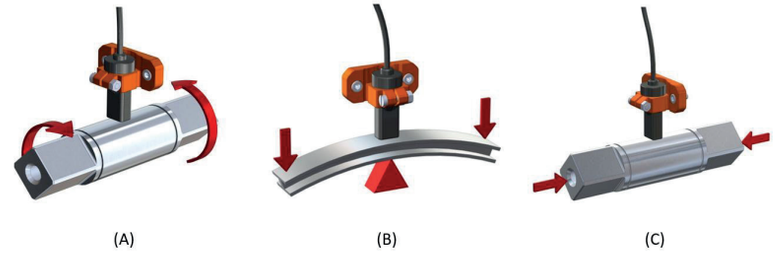


Figure 3: Torsional (A), bending (B), Tensile/Compressional loading conditions

Various methods are developed to measure the loading ranging from strain gauges to piezoelectric crystal. Among them, strain gauges with various executions are widely used in industrial and mobile applications. The requirement of contacting point in this technique is a major disadvantage which makes it liable especially as the component is overloaded. The contactless measurement system developed by TRAFAG GmbH based on the magnetic induction principle is beneficial as the measuring cell is not touching the component. Since the sensor is not directly subjected to forces, the possibility of occurrence of mechanical damage due to the loading (especially by shock and vibration) decreases drastically. Consequently, the degradation of performance due to fatigue can be prevented. The components of the inductive sensor are illustrated schematically in *Figure 4*.

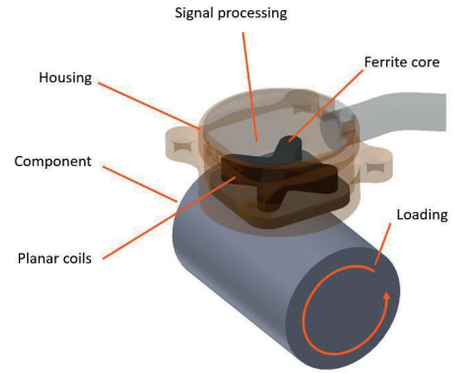


Figure 4: Components of the measurement system

The planar coils generate a magnetic field which penetrates in the component and receives the resulting magnetic field as measurement signal. A ferrite core acts as a magnetic flow conductor to guide direction dependent measurement signals during the loading of the component. The measurement signals are processed directly in the signal processing.

The exciter planar coil generates an alternating magnetic field with a frequency within kHz range. The alternating field is emitted through the ferrite core in the component. The resulting magnetic field of the component induces a current in four signal coils S1 to S4 which are referred as measurement signals which are depicted in the *Figure 5*. Ferromagnetic materials are principally suitable for contactless inductive measurement. The magnetic properties of the material change under a loading as it deforms. This changes the magnetic flux in the signal coils consequently which affects the induced current. These changes show a linear dependency on the applied loads /2/. The sensor calculates the force by measuring these changes. The component shall be dimensioned properly to achieve the desired safety by overloading and to enhance the precision of measurement.

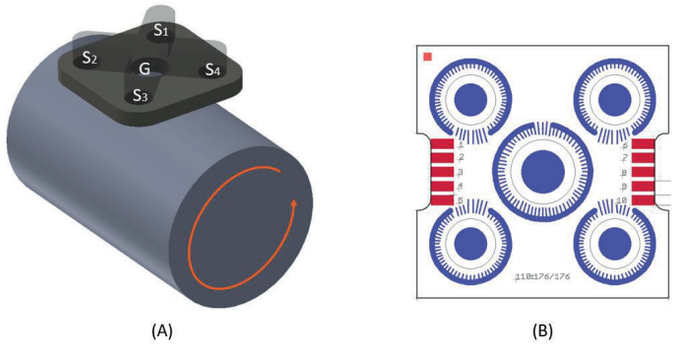


Figure 5: Arrangement of the planar coils to the component (A), top view of the arrangement of coils (B)

2.2 Hydraulic cylinder integration

Through the application of multiple sensor and proper arrangement, one can measure a multiaxial loading condition (e.g. compression and bending). In a preliminary investigation, the sensor was adapted to measure the forces of a hydraulic cylinder with a piston diameter of 110 mm and rod diameter of 90 mm. The rod of the cylinder is made of case hardened 30CrNiMo8 which makes it suitable for inductive contactless measurement. Two different executions are considered in this investigation to find an appropriate assembly for further development. In the first execution form which is depicted in *Figure 6* (B), the sensor housing is attached to the piston rod next to the rod head. Up to four sensor modules are placed circumferentially orthogonal in the housing to consider the effects of the lateral forces. There's a gap of up to 1 mm between the rod surface and the sensor modules. In the second execution form, the sensor housing is mounted at the cylinder gland while the piston rod can slide freely in the housing (Figure 1*Figure 6* (A)). This assembly is beneficial in many applications as the signal/power transmission line doesn't have to compensate the length changes during cylinder's extraction and retraction.

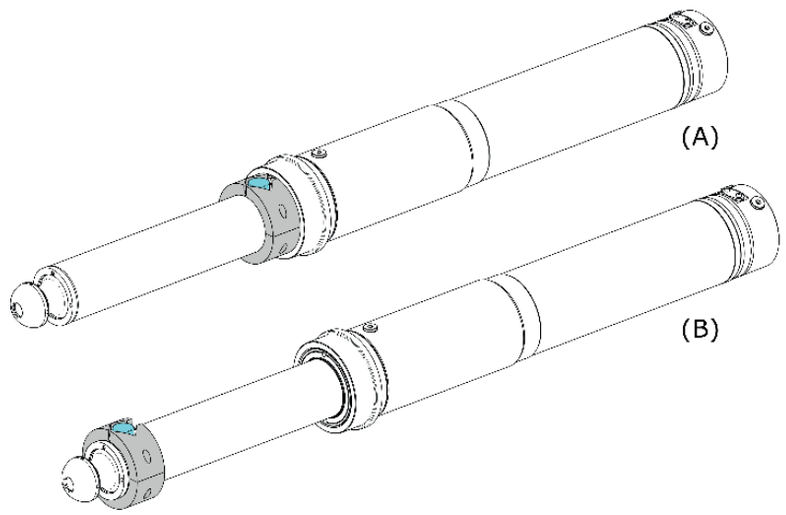


Figure 6: The sensor housing attached to cylinder's gland (A) and to the cylinder's rod (B)

2.3 Concept verification

A series of tests are performed to study the linearity of measurement signal as well as reproducibility of the results. Meanwhile the precision of the measurement results using a contactless sensor can be estimated against the calibrated reference force measurement system. A detailed description of the reference system can be found in section 3.

2.3.1 Rod mount design

First step was to investigate the rod mount design. Performing basic functionality tests, the unfiltered signals of sensors are evaluated using a USB oscilloscope with a downstream amplifier since the prototype modules are not equipped with integrated processing units. A multi-cycle loading program with load steps of 50 kN was applied to the cylinder. The step wise increase of the load in each cycle facilitates the comparison of sensor values and the measurement of a reference system.

1. Loading from 0 to 300 kN and unloading back to 0 kN
   (Reference loading to prevent measurement deviations due to setting effects)
2. Loading from 0 to 300 kN and unloading back to 0 kN
3. Loading from 0 to 300 kN and unloading back to 0 kN
4. Preload of 50 kN with five load cycles between 200 kN and 50 kN

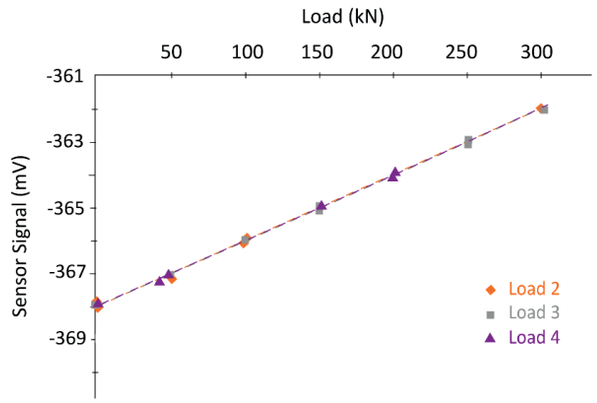


Figure 7: Characteristic curve of the sensor under a multi-cycle loading

The measured characteristic curve of the sensors shows a good linearity as depicted in *Figure 7*. The linear balance lines are used to evaluate each measurement to determine the sensitivity and zero point. The standard deviation of sensitivity is 0.4 %. Not considering the zero offset between the first and second load step, the deviation of offset is ±0.85 kN which correspond to ±0.28 % of the nominal force of 300 kN.

The test results of this study promise applicability of this technique. Combined with design modification such as flat surfaces on the rod the performance of this method may be further improved which makes it a convenient and robust method for direct force measurement.

2.3.2 Gland mounted design

In the preliminary test investigating the gland mount design, the piston rod extracts and retracts without load while the sensor measures continuously. As the piston rod moves, a zero-point offset of up to 800 kN appears which is more than 200 % of maximum loading (*Figure 8*).

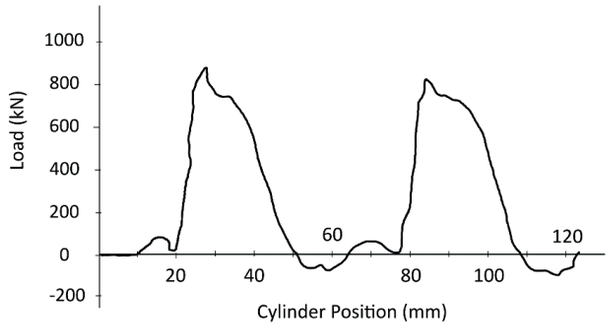


Figure 8: Zero-point offset of the gland mount design

This phenomenon can be caused due to residual magnetism or inhomogeneities of the piston rod. The result suggests an impossible short-term implementation of the gland mount design. But different mid-term approaches are considered. For example, an active rod position based compensation of the zero-point or a compensation facilitated by the application of more sensor elements.

3 New cylinder force test bench

A modern test bench for development and validation was developed as the foundation for an effective implementation of the long-term strategy of WEBER-HYDRAULIK through to intelligent components. The hydraulically driven test bench with reference force measurement has been developed study the repeatability, precision, reproducibly and hysteresis of the new integrated force measurement systems (Figure 9). Equipped with a calibrated reference force measurement system in axial and transversal directions which are capable of measuring axial forces up to 3.000 kN and realizes overall deviations under 0,5 % of the maximum load.

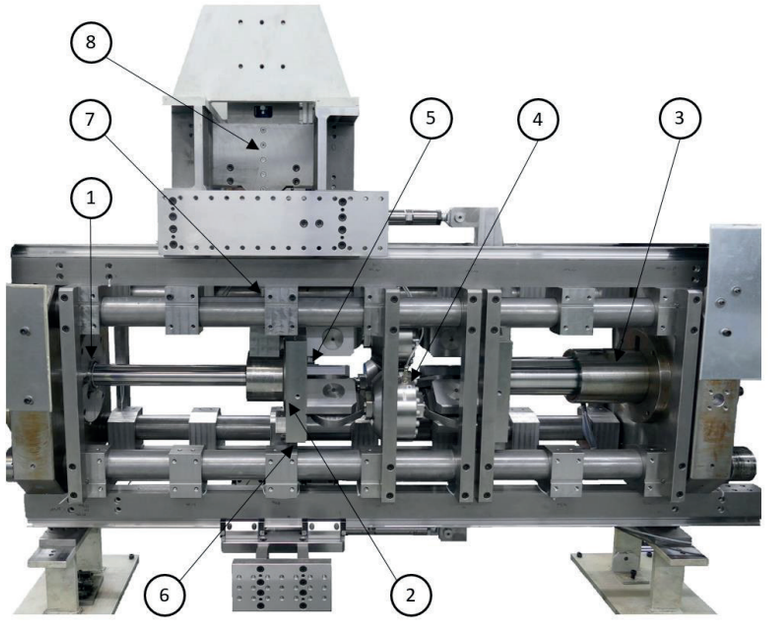


Figure 9: Picture of the new test bench, capable up to 3.000 kN axial force.

The test bench consists of a specimen holder (1) and a force measuring platform (2). The test cylinder is installed in-between where the platform is pivoted to be able to move horizontally. The axial load is exerted using the axial load cylinder (3) which is transmitted over three flexibly connected reference force cells (4) to the force measurement platform. The platform is held in its position by the push rod (5) and loss force cell (6). If the specimen should be loaded transversally a non-positive connection between specimen and force measurement platform is required. When this requirement is met, the transversal force can be transmitted over a transverse force unit (7) and an intermediary force cell (8) where the force cell (6) the loss of transverse force due to friction can be measured.

4 Summary and Conclusion

With the aim of development of intelligent hydraulic components, WEBER-HYDRAULIK has developed an optical position measurement system for mass production. Moreover, the current integrated force measurement for supporting cylinder is developed further to enhance the robustness of the system in field applications. Another development project, which is the focus of this article, is a universal system for integrated force measurement in a hydraulic cylinder. A contactless magnetic induction-based force measurement technique is investigated and different integration concepts are elaborated. Preliminary functional test with sensors attached to the piston rod has shown promising results in term of linear deviation and repeatability. Rest magnetism and irregularities in the piston rod hampers the short-term implementation of the cylinder gland execution which is beneficial from various aspects. Despite the disturbing factors the concept will be follow up and the chances of different compensation method will be investigated.

References

/1/ Javdanitehran M., Brecht T., *Intelligent systems in mobile hydraulics*, 9. Kolloquium Mobilhydraulik, Karlsruher Schriftenreihe Fahrzeugsystemtechnik Band 49, 2016, P. 2-10

/2/ Sukegawa T., Uesaka M., *Magnetic nondestructive evaluation of ferromagnetic steels due to mechanical loading*, Electromagnetic Nondestructive Evaluation (VI), ISO Press, 2002, P, 135-142

Sealing Systems for Hydraulic Cylinders

Gonzalo A. Barillas, Steven Cowell, Martin Goerres, Wolfgang Lipphardt, Uwe Siegrist, Sascha Möller

Freudenberg Sealing Technologies GmbH, Lead Center Fluidpower Industry, Ascheröder Str. 57, 34613 Schwalmstadt, Germany*
E-Mail: Gonzalo.barillas@fst.com

While designing an hydraulic cylinder, you may spend a long time choosing the right seals, guide rings and wipers that will fit into the application. In the case of a standard cylinder with a wide application range, the plentiful options offered in the market will make the search difficult and validating the different combinations will be costly. Based on standard applications in mobile hydraulics, Freudenberg Sealing Technologies has developed sealing systems for rod and piston taking into consideration the cylinder application and the right combination of sealing elements and guide rings. The designer can rely on expert knowledge to quickl pick up a sealing system for the cylinder instead of spending time searching for every single seal in the cylinder.

Keywords: Fluid power cylinder, hydraulic cylinder design, standardization, sealing
Target audience: Mobile Hydraulics, Design Process.

1 Introduction

The reliability of an hydraulic cylinder strongly depends on its components. In addition to the right materials, dimensions for the tube, caps, rod and defining its surface finishing (bore, rod, painting) and the assembly process (welded, threaded) among others, also the sealing system chosen will have a significant impact in the cylinder costs, performance and lifetime. Experience and time are required to search out of the vast amount of seal designs the right one for a specific application range. As the seal itself will have interaction with oil, counter surface surrounding sealing elements, guide rings, wiper etc., the search for each optimum sealing component will usually consume time and arise lots of questions. Over the decades the sealing manufacturers have been developing new seal profiles, new materials and due to this, the quantity of seals in seal manufacturers' and distributors' catalogues is big and confusing. However, even if a single seal performs best in a test, that seal as a part of a sealing system will show a different behaviour. So changing one sealing element in a sealing system may cause a significant change in the cylinders behaviour leading to premature failures. Using a sealing element in a sealing system should improve not only its own functionality but also enhance the performance level of other parts and so allow higher loads, performance and/or service intervals. For cylinder designers not only a seal, but the whole sealing system including static seals and guide elements for a specific application range is of importance, and having a quick guide to set the right components into a reliable system is of big value in the cylinder design and validation process.

2 Sealing Systems Approach

In the 1980's the concept of using a primary seal –mostly called buffer seal- assembled towards the pressurized chamber of the cylinder together with an additional seal -or secondary seal- assembled after the primary seal and a wiper building a sealing system became popular as it improved the performance of cylinders in heavy duty applications.

Today, the right combination of different sealing elements in a sealing system will strongly influence the cylinder's performance depending on its application. A deep understanding of each sealing element's behaviour as well as the application requirements for a sealing system is needed to choose seals for a specific sealing system.

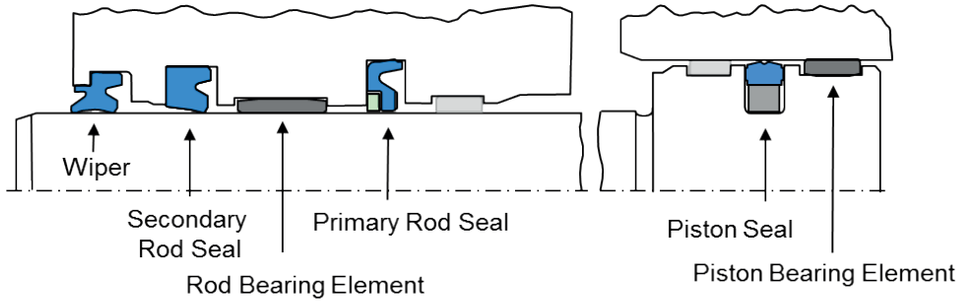


Figure 1: Sealing System in an hydraulic cylinder

2.1 Primary rod seal

The primary seal absorbs the pressure peaks and does not really need a zero leakage function. The pressure peaks may be generated by the cylinder operation conditions as well as through the hydraulic system and the way valves are shifted, among others. This primary seal needs to work with a minimum leakage amount to guarantee sufficient lubrication of itself, the secondary seal, bearing elements and the wiper assembled after the primary seal. Otherwise lack of lubrication may cause premature wear and therefore cylinder failure. As this seal needs a lubricant film for long life, it will let pass a small oil film on the rod during the outstroke. This small amount of leakage will be retained by the secondary seal inside the cylinder. After several in- and out-stokes, the space between both seals can be filled with oil and a drag flow pressure will be built up. To avoid this, the primary seal needs to be designed with pressure release notches and/or bores, allowing an oil conveyance into the pressure chamber and high pressure load on the secondary seal.

Profile	Product line (Gland)	Material	Pressure	Temperature	Comments
	SM (ISO 7425-2)	95 AU V 142 94 AU 30000	40 MPa	- 30 to 110 °C - 35 to 120 °C	Standard primary seal
	OMS-MR (ISO 7425-2)	PTFE B602 70 NBR B 276	40 MPa	- 30 to 100 °C	Primary seal, lowest friction, available with and without pressure release function
	OMS-MR (ISO 7425-2)	PTFE B602 70 FKM	40 MPa	- 10 to 200°C	Primary seal, lowest friction, available with and without pressure release function with high temp. FKM O-Ring

Table 1: Typical primary seals.

As the primary seals will be exposed to high pressures, their main function requirements are extrusion resistance, good conveyance behaviour and keeping friction low, with short axial dimensions. A thermoplastic Back Ring for the TPU U-Cup with pressure release channels and a filled PTFE glide ring with axial bores will reduce the extrusion risk for these seals.

2.2 Secondary rod seal

The secondary seal works in a sealing system under lower pressure conditions as the primary seal throttles the main system pressure and is responsible for reducing the leakage to a minimum level. This means a small oil film on the rod to achieve the lifetime of the cylinder. The secondary seal is not to be understood as a redundant seal to the primary seal; it is more a complementary seal in the system. It has to be out of a material and design with high dynamic response to rod displacements. It is important that this seal has an excellent oil conveyance behaviour to return the oil film on the rod into the pressure chamber. This is why the best option for this seal is a U-cup.

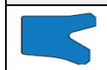
Profile	Product line (Gland)	Material	Pressure	Temperature	Comments
	T 20 (ISO 5597)	95 AU V 142 94 AU 30000	40 MPa	- 30 to 110 °C - 35 to 120 °C	Standard U Cup seal
	LF 300 (ISO 5597)	94 AU 925 94 AU 30000	32 MPa	- 30 to 110 °C - 35 to 120 °C	Standard U Cup seal with lower friction
	KI 310	94 AU 925	40 MPa	- 30 to 110 °C	Compact seal
	HDR 2 C (ISO 5597)	92 AU 21100 / 98 AU 928	50 MPa	-50 to 110 °C	U- cup with hard/soft combination for broad application range

Table 2: Typical secondary seals.

2.3 Wiper

The pressure trapping effect described between the primary seal and the secondary seal (see 2.1) will also happen in the room between the secondary seal and the wiper. The pressure release function is therefore necessary in both elements, mostly achieved with bores and beads in the wipers' design. Depending on the application and or the cylinder design, the wiper may have, besides its wiper lip to the atmosphere, an additional sealing lip; such wipers are commonly known as double acting wipers. Wipers have two additional design categories: The ones with a metal insert to provide enough stiffness to keep the wiper in an axially open gland and the ones without a metal insert, which will need a gland with an axial intersection to keep the element in the cylinder cap. Wipers used in a sealing system must allow a pressure release to prevent a pressure build up. Without this feature, the pressure could press the wiper out of its gland, after which, the cylinder is open to damage from outside debris.

Profile	Product line (Gland)	Material	Dirt load	Temperature	Comments
	PRW1 (ISO 6195 A)	95 AU V 142	Medium	- 30 to 110 °C	Standard double lip wiper with pressure release function
	PU 5 (ISO 6195 A)	95 AU V 142	Medium	- 30 to 110 °C	Standard wiper
	DMRW2 (ISO 6495 B)	94 AU 30000	High	- 35 to 110 °C	Standard double lip wiper with metal insert and pressure release function
	AU AS R (ISO 6495 B)	94 AU 925	High	-30 to 110°C	Standard lip wiper with metal insert

Table 3: Typical wipers.

2.4 Piston seals

The hydraulic power can only be transduced into motion and force through the cylinder's piston. Two main cylinder designs are the most common: the plunger cylinder, where the rod's diameter itself will bear hydraulic pressure and no piston is needed, and the differential cylinder where an additional piston is needed. Plunger cylinders will need external forces to move the rod into the cylinder. Differential cylinders use the piston area for the in- and out-stroke of the rod. Under pressure, the cylinder tubes will expand, increasing the clearance between the piston and the tube bore diameter and so exposing the piston seals to higher extrusion risk. Seals must be able to follow the tube displacement immediately to avoid leakage and so a drift of position. Pressure from both axial faces can lead to blow by (uncontrolled and extremely high leakage) if the seal design does not allow the correct activation of its profile. Different from the hard chrome plated rods, cylinder tubes may show different surfaces finishes, varying from welded tubes with honed surfaces to cold drawn tubes without further treatment. Piston seals must primarily provide a high extrusion resistance, high wear resistance, high reliability against blow by and avoid cylinder drift. These requirement are covered by a two component solution, having an extrusion and wear resistant sealing ring (TPU, Thermoplastic or PTFE) gliding in the tube supported by an elastomeric energizer.

Profile	Product line (Gland)	Material	Pressure	Temperature	Comments
	Simko 300 (ISO 7425-1)	98 AU 928 / 80 NBR	40 MPa	- 30 to 100 °C	Standard piston seal for multiple purposes
	HDP 330 (ISO 7425-1)	PA 4112 / 80 NBR	50 MPa	- 30 to 100 °C	Standard piston seal for heavy duty
	OMK-PU (ISO 7425-1)	95 AU V 142 / 80 NBR	25 MPa	- 30 to 100 °C	Piston seal for medium pressure ranges
	OMK-MR (ISO 7425-1)	PTFE B602 70 NBR B 276 70 FKM K655	40 MPa	-30 to 100°C - 10 to 200°C	Piston seal for low friction / high temperature

Table 4: Typical piston seals.

2.5 Guide rings / Bearing rings

The motion of rod and piston in the cylinder cap and tube requires a good alignment of the components to each other. Here is where the guide rings define the quality of a cylinder through covering manufacturing tolerances and keeping extrusion gaps in an acceptable level and avoiding metal to metal contact which could lead to rod and/or tube surface damage causing premature seal failures. Side load on the rod together with a deviation of cylinder and rod axis lead to high local stresses on the bearing rings. So high dimensional accuracy, stiffness, wear resistance, low friction and easy installation are the main requirements for these crucial elements in a sealing system.

Profile	Product line (Gland)	Material	Load	Temperature	Comments
	FRI / FRA (ISO 10766)	PA 4112	Medium 30 MPa	- 40 to 100 °C	Standard thermoplastic bearing ring
	SB / KB (ISO 10766)	HG 517 (HG 650)	High 50 MPa	- 40 to 120 °C	Standard phenolic bearing ring
	SBK / KBK (ISO 10766)	HG 517 (HG 650)	Very high 80 MPa	- 40 to 120 °C	Heavy duty, avoids stress concentration and brittle failure
	SF / KF (ISO 10766)	PTFE B 500	low 7,5 MPa	-40 to 200°C	High temperature

Table 5: Typical bearing rings.

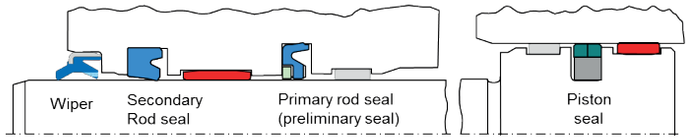
3 Cylinder Application Field

Hydraulic cylinders are built to fulfil a broad application field. Aerospace, mining, offshore, construction and agriculture are just a few of the application fields. Based on the requirements regarding load parameters, some sealing system developments will be presented.

3.1 High pressure and temperature range with long operation time

In this category we can find the heavy construction machinery cylinders. They have to work all over the world and 24 hours, 7 days a week. This equipment is mostly leased, so the maintenance will often not be done as required. As a result, the oil quality will be reduced, moisture and dirt will be part of the hydraulic system. Sealing systems must be absolutely reliable and allow a global application, even under very harsh conditions.

In such applications the sealing system must be able to bear 40 MPa constantly with peaks that can go as high as 60 and more MPa. Due to high operation time, temperatures are high. Global usage of cylinders requires a sealing system which will perform well in regions with high humidity, which can deteriorate oils and cause seal material aging and damage (hydrolysis). Seals must show extreme high extrusion and high hydrolysis resistance. To face these requirements, besides the right seal geometry, its materials will play a significant role. Extreme high extrusion and hydrolysis resistant polyurethane is the best choice for the wiper and rod seal materials. The sealing system on the rod with the chosen elements will provide a good seal element lubrication. Bearing rings designed to follow rod deviations without stress concentration will also provide a long lasting operation. The piston seal with a glass fibre reinforced PA glide ring with an NBR energizer will bear the pressures without extrusion and wear. The sealing system for this application is summarized in Fig. 2.



Designs and Materials				
Wiper	Secondary rod seal	Primary rod seal	Guide	Piston seal
DMRW2 94 AU 30000	**T20** 94 AU 30000	**SM** 94 AU 30000 / POM	**SB (K) / KBK (K)** HG 650	**HDP 330** PA 4112 / 70 NBR

Typical application parameters		
Pressure	40 (60) MPa 5800 (8700) psi	
Temperature (mineral oil)	100°C (110°C) 212°F (230°F)	
Duration of use (running track)	high	
Dirt contamination high		DMRW2
Dirt contamination medium / light		PRW1

Guidance:

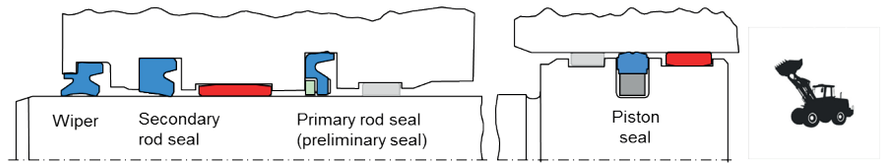
- Very good leak tightness (rod)
- Piston seal with stepped cut, permissible tube stretching < 0.15mm/0.006in
- Materials with especially high temperature-/ media resistance (AU 30000, PA4112)
- Easy installation
- Application example
  Cylinders for heavy-duty construction machinery, mining

Figure 2: Sealing System for high pressure and temperature range with long operation time

3.2 Middle pressure and temperature range with long operation time

A large percentage of hydraulic systems in mobile machines work with pressures of around 32 MPa. The operation time may be high but generally with interruptions. The temperature of the application is normally 80°C and can rise up to 100°C.

For such applications the sealing system will be very similar to the one presented above. The lower pressures and temperatures allow the use of other standard materials. This is especially of interest for the piston seal. The gliding ring of the piston seal can be done out of one closed ring made of an 98 Sh A polyurethane with an NBR energizer that can be snapped on into the piston groove. The sealing system with a primary (buffer) seal, secondary seal in U cup shape and a double acting wiper will provide an excellent leakage behaviour and lifetime. Details can be seen in Fig. 3.



Designs and Materials				
Wiper	Secondary rod seal	Primary rod seal	Guide	Piston seal
PRW1 94 AU 925	**T20** 95 AU V142	**SM** 95 AU V142 / POM	**SB (K) / KBK (K)** HG 650	**SIMKO 300** 98 AU 928 / 80 NBR

Typical application parameters		
Pressure	32 (40) MPa 4640 (5800) psi	
Temperature (mineral oil)	80°C (100°C) 176°F (212°F)	
Duration of use (running track)	high	
Dirt contamination high		DMRW2
Dirt contamination medium / light		PRW1

Guidance:

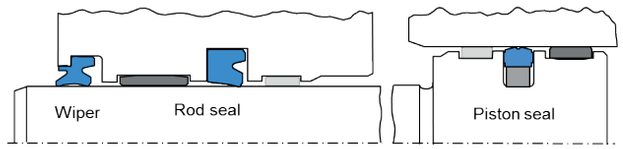
- Very good leak tightness (rod)
- Piston seal with very good drift behavior
- Easy installation
- Application example
  Cylinders for medium-heavy construction machinery

Figure 3: Sealing System for high pressure and temperature range with long operation time

3.3 Low / medium pressure and temperature range

Machines without the need of high pressure hydraulic systems show advantages as valves and all hydraulic components can be designed for lower loads. Not only material cost can be reduces, lower loads also increase the reliability and lifetime of products. Often such systems do not need a 24/7 operation time.

The sealing of such cylinders can be covered by sealing systems without a primary or buffer seal. This increases the requirements for the only rod seal, as it will bear the pressure during operation. A double lip wiper with pressure release function is the best choice in these cylinders. Standard materials for standard (ISO) glands allow standardization in the production. Fig. 4 shows such a sealing system.



Designs and Materials				
Wiper	Secondary rod seal	Primary rod seal	Guide	Piston seal
PRW1 94 AU 925	**without**	**T 20** 95 AU V 142	**FRI / FRA** PA 4112	**SIMKO 300** 98 AU 928 / 80 NBR

Typical application parameters		
Pressure	26 (40) MPa 3760 (5800) psi	
Temperature (mineral oil)	80°C (100°C) 176°F (212°F)	
Duration of use (running track)	medium	
Dirt contamination high		DMRW2
Dirt contamination medium / light		PRW1

Guidance:

- Cost-effective since no preliminary seal or guides are produced in the tool in IM process
- Very good leak tightness (rod)
- Piston seal with very good drift behavior
- Easy mounting
- Application example
  Cylinders for agricultural machinery, mini-excavators



Figure 4: Sealing System for high pressure and temperature range with long operation time

In this way, different cylinder types for standard applications can be assembled using a reduced amount and well-chosen standard sealing elements.

4 Test Results

Up to this point, the selection of the sealing elements to build up a sealing system for each application has been done based on the expectance on the product behaviour. Field experience in many applications has confirmed these and other sealing systems based on few standard sealing elements.

For end-users, a sealing system fails, when leakage appears. To be able to compare the effects of sealing systems on leakage, here some comparative test results are summarized.

4.1 Test procedure

As leakage will be the most important criteria for end-users, the test rig was build up to measure the leakage of rod sealing systems. The leakage volume is built by the rod diameter d, stroke s and the oilfilm h on the rod after each load cycle /2/:

$$V = \pi \times d \times s \times (h_{outstroke} - h_{instroke}) \quad (1)$$

The main factors influencing the oilfilm h are the oil's viscosity, the stroke velocity and the contact pressure distribution $\left(\frac{dp}{dx}\right)_{max}$ between seal and rod.

$$h_{outstroke} = \sqrt{\frac{2\times\eta\times v_{outstroke}}{9\times\left(\frac{dp}{dx}\right)_{max}}} \quad ; \quad h_{instroke} = \sqrt{\frac{2\times\eta\times v_{instroke}}{9\times\left(\frac{dp}{dx}\right)_{max}}} \quad (2)$$

The predominant pressure gradient $\left(\frac{dp}{dx}\right)_{max}$ in a sealing system will depend on the different seals in it, the pressure of the system, as it deforms the seal shape and on the direction of the stroke. The relevant gradient can be on a different seal for each stroke direction.

The pressure was limited up to 20 MPa with a HLP 46 hydraulic oil. At this pressure, the seals' cross section is deformed by the fluid and has a complete contact to the rod, the contact pressure distribution reaches its highest deviation from the non-pressurized state. The stroke velocity was variable to reach a factor of 4 between 0.4 m/s and 0.1 m/s. The rod was driven by an electric drive with a constant velocity of 0.4 m/s in one (right) direction and with different velocities in the opposite (left) direction. The oil viscosity depends on the temperature, the tests were done at a constant temperature of 60°C, with temperature controlled hollow rod and oil test cell.

In a test cell in which a rod was externally driven back and forth, the sealing systems were placed at both openings, see Fig. 5. Every test was done using same sealing systems on both sides.

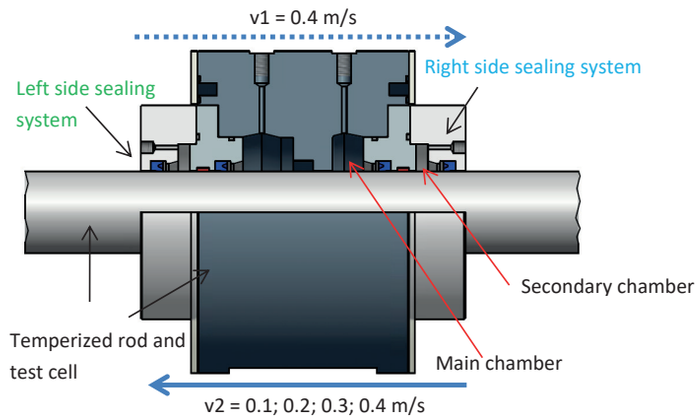


Figure 5: Test rig pressure cell (principle)

The leakage was measured as the oil on the rod, which was wiped with a tissue and weighed after 100 double cycles. The rod chosen was a 60 mm diameter hard-chrome plated rod, the stroke was 400 mm.

4.2 Test results

4.2.1 Sealing systems with a wiper and a U-cup rod seal

These systems are used in cylinders with moderate performance requirements (pressure, operation time, temperature), see 3.3.

The leakage building fluid film on the rod will depend on the stroke direction and velocity: During the outstroke, the predominant pressure gradient will be found at the seal's sealing edge, a high velocity will increase the oil film. During the instroke the highest pressure gradient may be found at the heel of the seal or at the wiper's lip, depending on the seal and wiper design. A typical leakage behaviour can be seen in Fig. 6, where the leakage is influenced by the outstroke/instroke velocity ratio and the oil pressure.

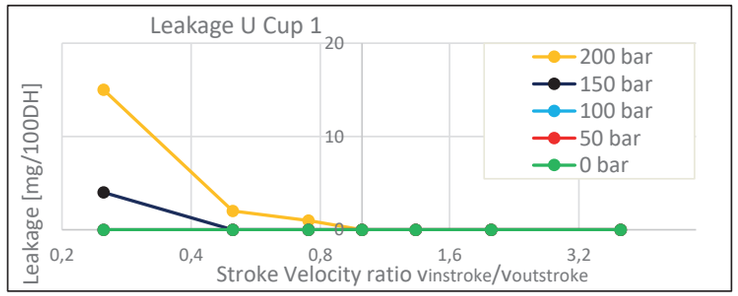


Figure 6: Leakage dependency on pressure and stroke velocity ratio (exemplary)

Test results show for the tested systems a leakage that mainly depends on the wiper. This means, that for applications with the need of a hard wiping function, the system may not only keep the contaminations particles out of the hydraulic system, they may also create leakage. This will always be a contradictory requirement for a sealing system and the user will need to find the best compromise. A double lip wiper will always reduce the leakage as its sealing lip reduces the fluid film on the rod during the outstroke. Figure 7 shows the leakage for sealing systems with different wipers and the same seal when the outstroke velocity is 0.4 m/s and the instroke velocity is 0.1 m/s at 20 MPa and 60°C. Double lip wipers with the standard polyurethane U cup did not show any leakage at all, this means an excellent lubrication for the sealing system during operation is provided. In the group of the heavy duty application wipers the leakage performance decays in favour of a good dust wiping function. These heavy duty application wipers have a strong wiping lip and a metal insert, this resulting in a high pressure gradient $\left(\frac{dp}{dx}\right)_{max}$ for the instorke and an oil film retention outside the cylinder. In this group of wipers, the dual lip polyurethane wiper with metal insert and pressure release bores in the sealing lip performs best, while other wipers for heavy duty applications show up to 160% higher oil film.

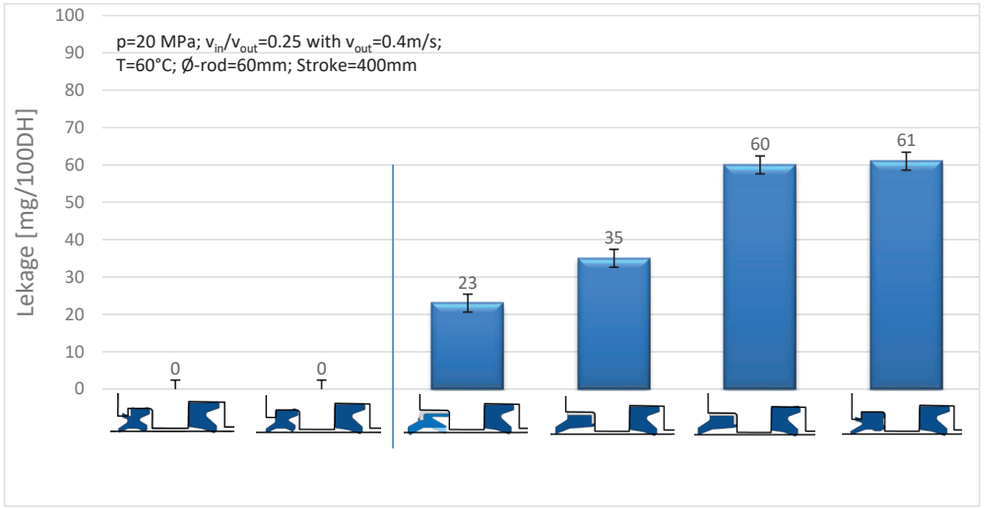


Figure 7: Leakage for sealing systems with one seal and wiper

4.2.2 Test results for sealing systems with primary and secondary seal

Sealing systems for higher requirements (pressure, temperature, operating time, environment, etc.) have an additional seal that bears main pressure and pressure peaks –the primary seal- and a strong wiper lip to keep mud, water, dust and other contamination out of the hydraulic system (see Chapter 3). The primary seal bears the whole system pressure leaving the secondary seal with little or no pressure. As a result, the primary seal will be deformed completely against the rod and the secondary seal will have little deformation and so a minimum contact to the rod. The oil film during the outstroke will be minimized by each of the sealing elements, during the instroke the seals and wiper must show a very good conveyance behaviour to avoid leakage through an external oil retention.

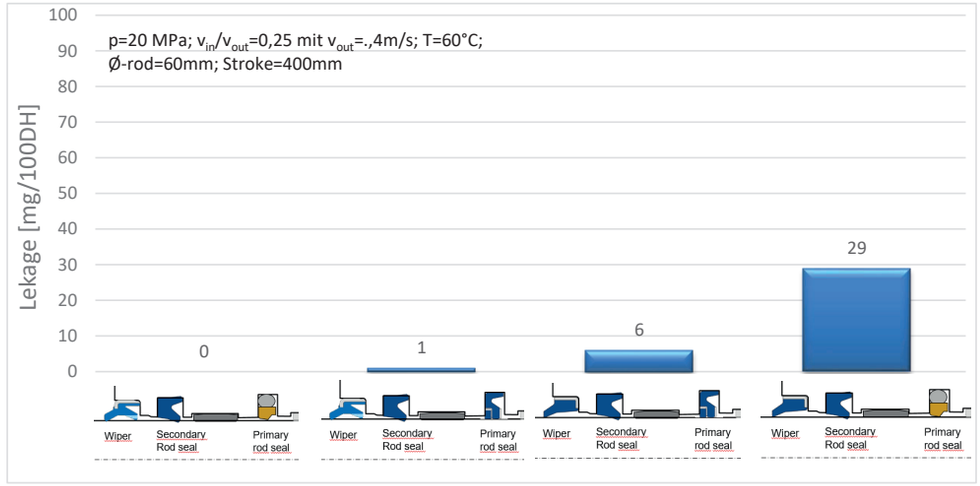


Figure 8: Leakage for sealing systems with primary and secondary seal and wiper

Figure 8 shows how the leakage from sealing systems perform. Here the main influence on the sealing effect comes again from the wiper. The wiper with a single wiper lip and with a sharp wiping function will not allow the oil film on the rod to be conveyed back into the cylinder. Without a secondary sealing lip, the oil film transported out of the cylinder will be higher than the double lip wiper would let out. The wiper with the secondary sealing lip with pressure release function is also able to convey more oil inside the cylinder reducing the leakage. The primary seal strongly affects the leakage, but only in combination with a strong wiping wiper. Generally, it can be noticed that the leakage level of sealing systems with primary and secondary seals are significantly lower compared to sealing systems without a primary seal. These results show the very critical situation of an outstroke under pressure at high velocity with a slow rod velocity during instroke under pressure. At speed ratios with lower outstroke velocities, the leakage performance of the sealing systems will always be better and even sometimes neglectable (see Fig. 6).

5 Summary and Conclusions

The performance of sealing elements cannot only be assessed based on single product testing. In the reality seals are assembled with wipers and other elements building sealing systems. It has been shown that the recommendation of sealing systems needs a deeper understanding of each product's performance and its interaction in a sealing system and the load applied to it. And that the use of a sealing system will have a strong influence on the sealing performance of an hydraulic drive.

Tests show that the leakage performance of a sealing system can be strongly influenced with variation of system pressure, stroke velocity ratio (instroke vs. outstroke) and wipers, independently from the seals in the cylinder. Results also show the positive impact in sealing performance of a sealing system with a primary and secondary seal. The usage of sealing systems can be underlined based on test data.

Nomenclature

Variable	*Description*	*Unit*
V	Leakage volume	[mm³]
d	Rod diameter	[mm]
s	Rod stroke	[mm]
h	Oil film thickness	[mm]
v	Velocity	[m/s]
η	Viscosity	[Pa s]
$\frac{dp}{dx}$	Pressure gradient	[MPa/m
T	Temperature	[°C]

References

/1/ Freudenberg Sealing Technologies e-catalog, https://ecatalog.fst.com/dichtungen/

/2/ Müller, H., *Adichtung bewegter Maschinenteile*, Medienverlag, Waiblingen, Germany 1990.

/3/ Barillas, G.; Richter, S; Weber, J.: Dirt Ingress Behavior of Wipers for Hydraulic Cylinders, 10th. International Fluid Power Conference (10th. IFK), Dresden, March 8th-10th. 2016, vol. 1 pp 585-596.

/4/ Kaiser, F.; Bock, E.; Sauer, B.: Anwendung der dynamischen Dichtspaltsimulation auf Stoßdämpfer und Ventilschaftdichtungen. ISC Internationale Dichtungstagung 2012, 13.- 14.09.2012, Stuttgart

/5/ Stoll, M.; Hörl, L.;Haas, W.:Influence of Different Rod Surfaces on PU-U-Cups and PTFE-Step Sea 19th. International Sealing Conference, A09, Stuttgart Oct. 12th.-13th. 2016

The improvement of the total efficiency of the gerotor orbital hydraulic motor

Ervin Strmčnik and Franc Majdič

Faculty of Mechanical Engineering, Laboratory for Fluid Power and Controls, Aškerčeva 6, 1000 Ljubljana, Slovenia
E-Mail: ervin.strmcnik@fs.uni-lj.si

In this study, the efficiency of the low speed high torque gerotor hydraulic motor for mobile hydraulic was investigated. A gerotor with the floating outer ring is rarely described in literature. The purpose of this paper was to analyse the influence of the size of the holes in the valve plate on the total efficiency of the gerotor. A very high total efficiency was obtained with the hole size of Φ6,3 mm. In that case, the total efficiency was on average 5 % higher in comparison to the initial hole size of Φ5,5 mm. Some tribological tests have been performed. We investigated relationship between surface roughness, contact force and friction. The minimum friction was 0,077.

Keywords: Mobile Hydraulics, Hydraulic Motor, Efficiency
Target audience: Mobile Hydraulics

1 Introduction

In this paper, the results of the measurement of low speed high torque orbital hydraulic motor are presented. The rapid development of the hydraulic components in the last few years has contributed many novelties, innovations and improvements in hydraulics. One of the groups of hydraulic component is hydraulic motor group. Hydraulic motors convert hydraulic energy into the mechanical energy. The most crucial measure of performance of the hydraulic motor is the total efficiency. There are many factors, which influence the hydraulic motor performance. They are related to hydraulic, tribological, material and other challenges. The performance of the hydraulic motor depends on the construction parameters as well. A gear pair has the largest influence on performance, whereas other parameters are also very important. We investigated the influence of the size of the holes in the valve plate. The holes are important for inlet and outlet flow of the fluid. Fluid takes care of the relative movement of the gear pair and lubrication of the main parts of the hydraulic motor. Within research, we found out that the diameter of the holes in the valve plate influences hydraulic motor performance significantly. With the right choice of hole diameter, we can raise the total efficiency on average around 5 %. The paper is structured as follows. In the introduction is described an objective and the purpose of the research. Section 2 presents the theoretical framework of the conducted research. Hydraulic gerotor motor was described as well as procedure for the determination of the volumetric, mechanical-hydraulic and total efficiency. Furthermore, the calculation of the gerotor's derived displacement volume is proposed according to the international standard ISO 8426. Methodology is described in section 3. A test rig of the experiment is shown in section 4. The Results are presented in section 5 and conclusions are summarized in section 6. In the last two sections, there is a list of references and a nomenclature explanation.

1.1 Literature review

There are many factors, which influence the performance of the gerotor. The viscosity, viscosity index, high-shear viscosity, piezo viscosity and shear stability of prototype fluids have been characterized in the research of fluid properties influence on the total efficiency of low speed high torque hydraulic motors [1]. In literature, there exists very little scientific papers, which deal with hydraulic gerotor motor with the floating outer ring. Usually the classical orbital hydraulic motor with inner rotor and gerotor's housing are analysed. In the past few decades, many designs have been disclosed in relative patents, but many of them were not feasible for actual motor production. A kind of deep analysis of multiple performance attributes and structural design of the gerotor motor has been extensively investigated through multi-objective optimization design of the gerotor motor [2]. Pressure distribution within gerotor and some other physical quantities were analysed through a CFD model for orbital gerotor motor [3]. A CFD analysis helps us to understand the physics of gerotor's operation and enable us a rapid development of new hydraulic motors [4]. The total efficiency is very much related to losses. Experimental and torque losses in gerotor were investigated in case of hydrostatic machines which represent complex fluid dynamic systems due to intricate and partially unknown dynamics [5]. Some losses are related to tribological behaviour. The most important are friction [6] and wear [7, 8]. Regarding rotational speed, there are two types of hydraulic motors. A low speed hydraulic motor does not exceed the rotational speed of 250 min^{-1}. On the other hand, a high speed hydraulic motor reaches rotational speed higher than 250 min^{-1}. A difference between the above mentioned group is shown in Figure 1 [9]. The low speed hydraulic motors achieve a higher total efficiency when they rotate relatively slowly (Figure 1, line 1). The total efficiency of the high speed hydraulic motor increases in case of the rising rotational speed (Figure 1, line 2).

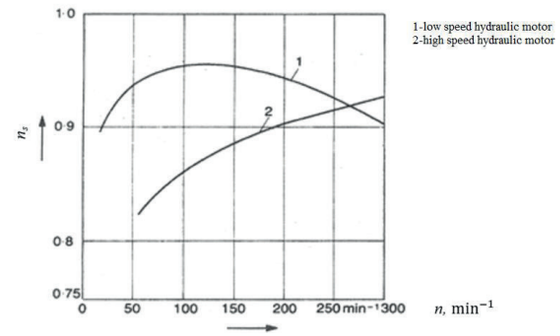


Figure 1: The total efficiency of low and high speed hydraulic motor.

Nowadays, there are many different types of hydraulic motors. Gear, vane, axial piston and radial piston hydraulic motor. Geroller and gerotor are two special types of gear hydraulic motors. Our scientific paper deals with the gerotor, which has two special characteristics. It is a low speed hydraulic motor with high torque capability. In literature, it is often abbreviated as LSHT ("low speed high torque"). Other precendences and limitations are listed in Table 1.

Precendences:	• relatively simple construction compared to other types of hydraulic motors
	• high torque
	• low speed
	• self-braking ability
	• relatively small and light
	• relatively cheap
Limitations	• friction
	• wear
	• low sealing ability of lobes between the inner rotor and outer ring
	• low total efficiency

Table 1: Precendence and limitations of the hydraulic gerotor motor.

2 Hydraulic gerotor motor with the floating outer ring

The hydraulic gerotor motor with the floating outer ring, its design, and principle of operation are presented in this section. At the end of the section we will introduce the procedure of displacement volume and efficiency determination for such a type of hydraulic motor.

2.1 Design and principle of operation of the gerotor

Gerotor has a mass of around 20 kg. Its working pressure is up to 35 MPa. The hydraulic gerotor motor consists of thirty different parts. The maximum diameter is Φ174 mm, whereas the maximum dimension represents the length of the gerotor – it is 250 mm (Figure 2).

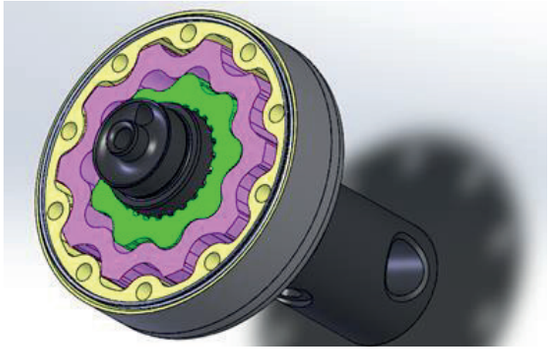


Figure 2: The hydraulic gerotor motor design (Φ174 mm × 250 mm).

There are four very important parts according to the functionality of the gerotor. The most influential elements of the hydraulic motor regarding principle of operation are: 1-the inner rotor, 2-the outer ring, 3-the gerotor housing and 4-the valve plate (Figure 3).

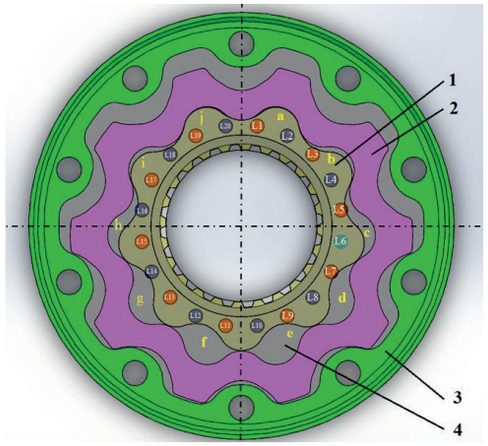


Figure 3: Four basic parts of the hydraulic motor (Φ 174 mm).

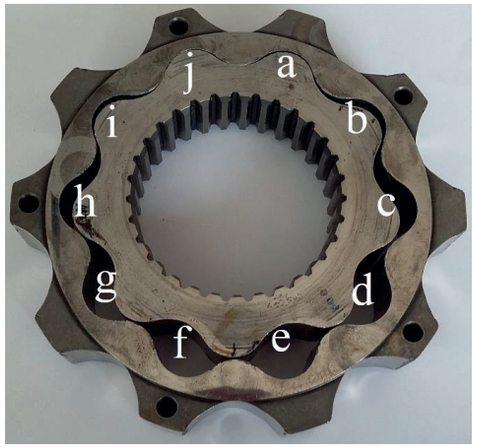


Figure 4: Lobes.

The outer ring has 10 teeth, whereas the inner rotor has 9 teeth and. They together constitute 10 lobes, which are designated with the small letters on Figure 3 and Figure 4. On Figure 3 we can recognize twenty holes, which are part of valve plate. The first hole has the mark L1, and the last one L20. Odd numbers represent holes which are connected with the high pressure zone, and even numbers represent holes which are linked to the low pressure zone. As operators, we can change low and high pressure zone with the control valve. A main function of the gerotor housing is the limitation of motion of the outer ring.

2.2 Gerotor displacement volume (ISO 8426)

In theory, there are two kinds of displacement volumes. The first one is the theoretical VG and the second one is the derived displacement volume VI. The difference between them is that the derived displacement volume considers the real production tolerances. The estimated deviation between VG and VI was 2-3 % [10]. Gerotor displacement volume is very important information that helps us to determine the volumetric and hydraulic-mechanical efficiency of the hydraulic motor. There exist three methods of determination of derived displacement volume [9]: a) Measurement of displacement volume with the two reservoirs; b) Toet-method; c) Method regarding ISO 8426. Due to international accepted standard, we decided to use the third method. The above mentioned standard ISO 8426 [11] proposes the measurement of volume flow rate with different pressure differences, whereas the speed of shaft of the hydraulic motor is the constant value. We have to determine the volume flow rate for $\Delta p = 0$. We can do this graphically either with the help of the method of least squares as it is shown in equation 1.

$$V_i = \left\{ \left(\frac{1}{k} \sum_{i=1}^{k} Q_i \right) - \left[\frac{\frac{1}{k} \sum_{i=1}^{k} (\Delta p_i Q_i) - \frac{1}{k^2} \left(\sum_{i=1}^{k} \Delta p_i \right) \left(\sum_{i=1}^{k} Q_i \right)}{\left(\frac{1}{k} \sum_{i=1}^{k} \Delta {p_i}^2 \right) - \left(\frac{1}{k} \sum_{i=1}^{k} \Delta p_i \right)^2} \right] \left(\frac{1}{k} \sum_{i=1}^{k} \Delta p_i \right) \right\} \frac{1}{n} \tag{1}$$

2.3 Gerotor efficiency

In reality, there are many kind of losses. Volumetric losses include external volumetric losses, internal volumetric losses, losses due to compressibility, losses due to incomplete filing. Hydraulic-mechanical losses represent viscosity friction, friction losses due to turbulent flows, due to pressure differences. The most important fact related to energy consumption of the hydraulic component is efficiency. It represents the ratio between the useful output to the total input, in energy terms. According to hydraulic gerotor motor there are three different types of efficiency:

- total efficiency,
- volumetric efficiency,
- hydraulic-mechanical efficiency.

It's not possible that any of these efficiencies would be greater than 100 % in real applications.

A conversion of hydraulic energy into mechanical energy is the main purpose of the hydraulic motor. Hydraulic energy (equation 2) is a function of volume flow rate and pressure difference, whereas mechanical energy (equation 3) depends on rotational speed and torque.

$$E_h = Q_1 \cdot (p_1 - p_2) \tag{2}$$

$$E_m = 2 \cdot \pi \cdot n \cdot M \tag{3}$$

The total efficiency of the hydraulic motor is ratio between input hydraulic energy and output mechanical energy as it is shown in equation 4.

$$\eta_t = \frac{2 \cdot \pi \cdot n \cdot M}{Q_1 \cdot (p_1 - p_2)} \tag{4}$$

If we would like to determine volumetric and hydraulic-mechanical efficiency, we have to have information about the derivate displacement volume of hydraulic motor. Volumetric efficiency of the hydraulic motor is a function of rotational speed, derivate displacement volume, and volumetric input flow rate into the hydraulic motor (equation 5).

$$\eta_v = \frac{n \cdot V_i}{Q_1} \tag{5}$$

Hydraulic-mechanical efficiency of the hydraulic motor depends on effective torque, pressure difference and derivate displacement volume of the hydraulic motor (equation 6).

$$\eta_{hm} = \frac{M \cdot 2\pi}{(p_1 - p_2) \cdot V_i} \tag{6}$$

3 Methodology

According to the previous research activities, we decided to observe hydraulic motor operation in eighteenth different measured points, which are stated in the Table 2. We chose two different rotational speeds: 15 min^{-1}, 17 min^{-1} and nine different pressure differences: 16 MPa, 17 MPa, 18 MPa, 19 MPa, 20 MPa, 21 MPa, 22 MPa, 23 MPa, and 24 MPa. Within the wide set of the measurement activities we took into account recommendations and guidelines from different international standards, whereas we would like to emphasise the importance of the international standard ISO 8426 [11] as well as other standards which are related to different types of hydraulic motor efficiency. Our main purpose was to determine hydraulic motor displacement volume and total, volumetric, and hydraulic-mechanical efficiency of the investigated hydraulic motor.

#	**1**	**2**	**3**	**4**	**5**	**6**	**7**	**8**	**9**
Rotational speed *n*,	15	15	15	15	15	15	15	15	15
Pressure difference *Δp*, MPa	16	17	18	19	20	21	22	23	24
#	**10**	**11**	**12**	**13**	**14**	**15**	**16**	**17**	**18**
Rotational speed *n*,	17	17	17	17	17	17	17	17	17
Pressure difference *Δp*, MPa	16	17	18	19	20	21	22	23	24

Table 2: List of eighteen selected measured points.

The ambient temperature was 25 °C, whereas the fluid's temperature was 60 °C. One set of the measurements represents 18 measurements points with the one specific hole diameter in valve plate – for example, Φ5,9 mm. For the testing of one set of the measurements we spent around four hours. Two hours for the preparation and measuring installation, and additional two hours for determination of physical quantities, which are represented in equations for hydraulic motor efficiency. All measurements were accomplished in the laboratory for fluid power and controls at the Faculty of Mechanical Engineering, University of Ljubljana. The uncertainty analysis was done according to the international standard JCGM 100:2008-BIMP [12]. International standard ISO 8426 addresses three classes of measurement accuracy: A, B and C. In the Table 3 are permissible systematic measuring instruments errors for each class.

Parameter	**Permissible systematic measuring instrument errors for each class of measurement accuracy**		
	A	**B**	**C**
Rotational frequency (%)	± 0,5	± 1	± 2
Flow rate (%)	± 0,5	± 1,5	± 2,5
Pressure, MPa gauge where $p < 0,15$	± 0,001	±0,003	± 0,005
Pressure, MPa gauge where $p \geq 0,15$	± 0,05	± 0,15	± 0,25
Test fluid temperature (°C)	± 0,5	± 1	± 2

Table 3: Permissible systematic measuring instrument errors [11].

Within measurement, we were able to ensure the following errors for desired physical quantities: Pressure difference: ± 0,05 MPa, Rotational speed: ± 0,1 min^{-1}, Fluid Temperature: ± 1 °C. The original diameter of holes in the valve plate was Φ5,5 mm (Figure 5). It was the first set of the measurements. Every additional set had 0,2 mm incremental increase in hole diameter. The maximal hole diameter was Φ7,1 mm (Figure 6).



Figure 5: The minimal hole size (Φ5,5 mm) in the valve plate (Φ174 mm × 15 mm).



Figure 6: The desired maximal hole size (Φ7,1 mm) in the valve plate (Φ174 mm × 15 mm).

To conclude, hole diameter in the valve plate was the only parameter which was being changed. As an objective function we selected the total efficiency of hydraulic gerotor motor. As it was mentioned in the first part of paper, hydraulic motor consists of some very important elements. Friction in contacts (Figure 7) represents losses which lead to lower hydraulic-mechanical efficiency and consequently lower total efficiency. In the second part of research we did some basic tribological tests. Relationship between contact force *F* (14 N, 40 N, 114 N), surface roughness *Ra* (0,05 µm and 0,2 µm) and friction was investigated.

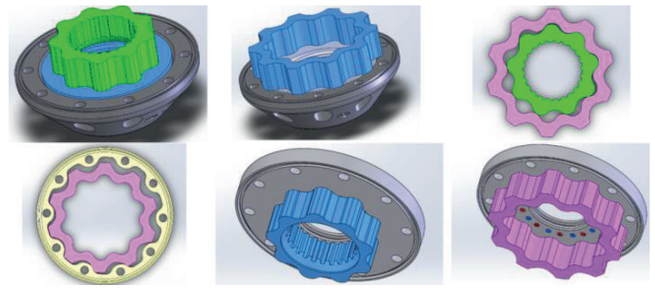


Figure 7: Tribological pairs of the main gerotor's parts.

4 Test rig

The test rig of the experiment consisted of sixteen different hydraulic components (Figure 8), whereas we would like to describe just the most important parts. The experiment was carried out by (1)-the electromotor and (2)-variable displacement pump. The tested hydraulic motor is denoted with the number (3). We used (7)-pressure reduction valve and (8)-pressure relief valve. Five different physical quantities have been measured. We applied (12)-volume flow rate meter, (13)-torque sensor, (14)-rotational speed sensor, (15)-pressure sensor and (16)-temperature sensor. If we would like to determine different kind of efficiencies of the hydraulic motor, we have to measure the physical units properly in sense of location of sensors. We would like to emphasize that on the inlet

flow side we have to measure flow rate (Q_1) and pressure (p_1). On the other hand, outlet pressure (p_2) is absolutely essential, because the pressure difference of the inlet and outlet flow of the hydraulic motor is very important.

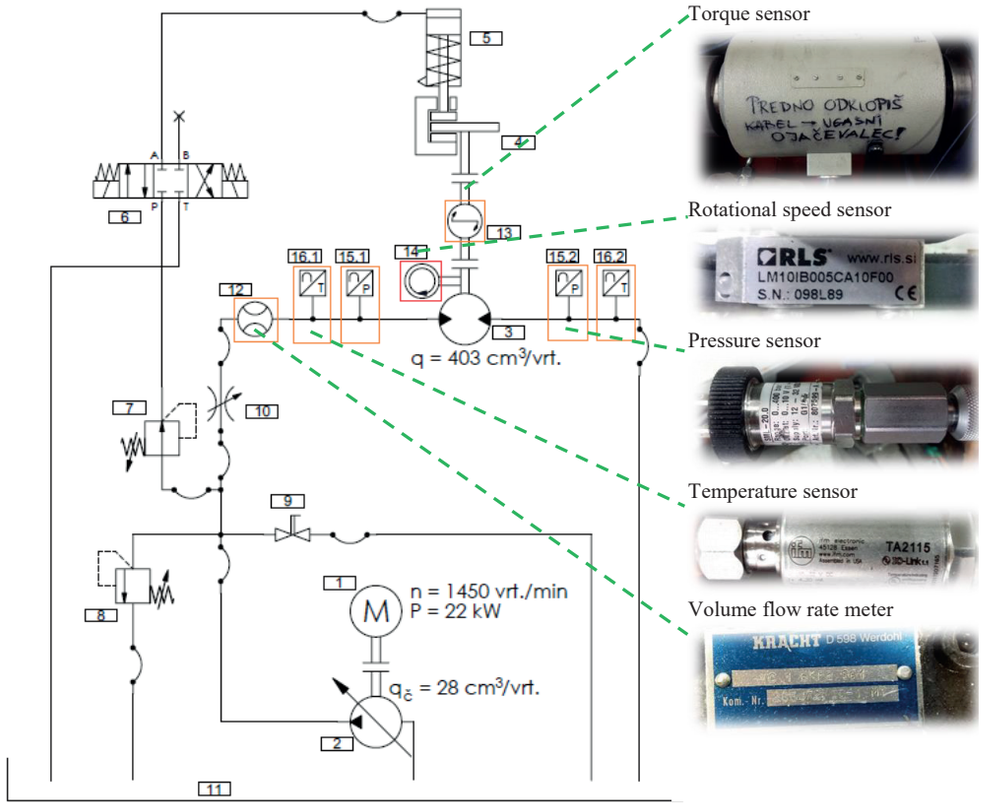


Figure 8: Test rig of the experiment.

5 Results and discussion

The result of research is presented in three sections. In the first section is presented the influence of the size of the holes in the valve plate on efficiency. In the second section is the result of tribological investigation. In the third part is introduced the uncertainty analysis.

5.1 Influence of the size of the holes in the valve plate on efficiency

The results of the research are presented in Figure 9, which show a relationship between pressure difference, size of the holes in the valve plate and total efficiency. Different colours represent different holes' size. There is pressure difference (range: from 160 bar to 240 bar) on the y-axis and total efficiency (range: 0 % – 45 %) on the x-axis. The length of a row represents a value of the total efficiency in a specific measured point. The longer the length of the row, the greater the total efficiency of the hydraulic gerotor motor. In the case of rotational speed 15 min^{-1}, the initial total efficiency of gerotor with the valve plate with the diameter Φ5,5 mm was 30,7 %. The highest total efficiency was 36,2 %, returning an 18 % higher total efficiency compared to the initial state. The highest total efficiency was obtained with the hole diameter of Φ6,3 mm. The additional increase of the hole diameter had a negative influence on the gerotor characteristics - total efficiency dropped down dramatically. For example, the total efficiency of the gerotor with the valve plate with hole diameter Φ7,1 mm was just 11,4 %. There exists almost the same trend for every set of pressure differences. In general, we found out that the total efficiency increases with the increase of pressure differences if we observe the total efficiency of one specific hole diameter. For example, the total efficiency values for hole diameter of Φ6,7 mm were increasing in the following way: 20,5 %, 24,3 %, 26,5 %, 29,5 %, 32,0 %, 33,3 %, 35,1 %, 35,5 %, 36,2 %. When we accomplished the measurement of the gerotor with rotational speed 17 min^{-1} (Figure 9), we found out that there exist similarities with the results of gerotor with rotational speed 15 min^{-1}. If we look at the results in the second case, we can find out that gerotor has a slightly lower total efficiency. There exists the increasing and the decreasing trend of total efficiency within every set of measurements. If we focus on the total efficiency in both cases (n = 15 min^{-1}, n = 17 min^{-1}), we can see that the total efficiency was higher in case of slightly larger holes. In the initial state, total efficiency was relatively low. When we enlarged hole diameter from Φ5,5 mm to Φ6,3 mm, the hydraulic motor reached the maximum total efficiency in a few sets of meausurements. Additional escalation of the hole diameter led to lower total efficiency. In some cases, the holes are so big that the hydraulic motor couldn't operate.

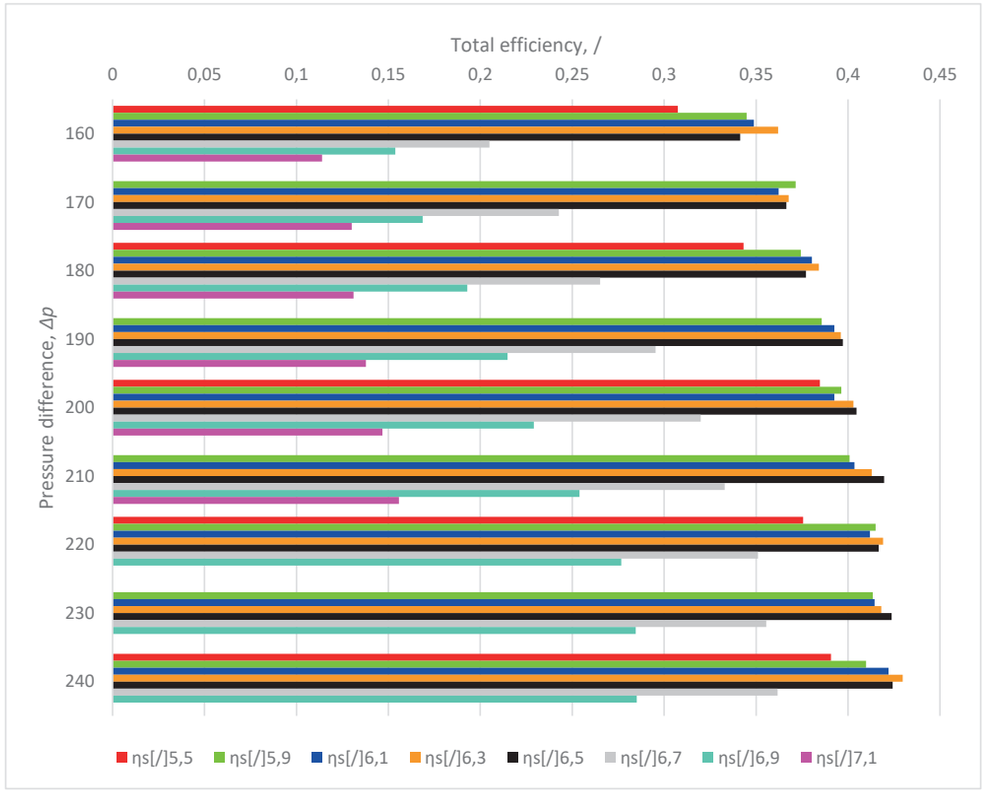


Figure 9: Total efficiency of the gerotor (operating point: n = 17 min^{-1}).

To summarize, we found out that a hole diameter of Φ6,3 mm is the most appropriate size of holes in the valve plate regarding total efficiency of the hydraulic gerotor motor. In this case, the total efficiency is around 5 % higher on average.

5.2 Tribological investigation

Tribological tests have been done with the tribometer TE77. We used a stainless steel AISI 440C. The result (Figure 10) shows that the surface roughness has very important influence on friction. The minimum friction was obtained by surface roughness Ra = 0,05 µm and maximum contact force F = 112 N. It was 0,077. It has been proven that the surface with higher roughness causes higher friction. Red bars are on average 16 % higher than blue bars. We found out that friction is dependent on contacts force. Higher contact force means lower friction.

Friction by contact force 112 N was always lower than friction by contact force 40 N or 14 N for the same surface roughness. Future investigation are going to be dedicated to friction and wear analysis of different lubricants such as water and ionic liquid.

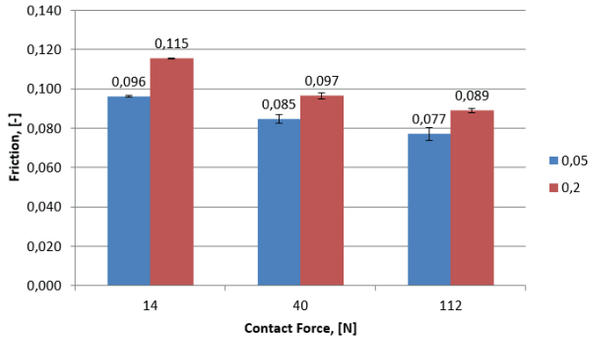


Figure 10: Coefficient of friction of stainless steel AISI 440C.

5.3 Uncertainty analysis

The uncertainty analysis gave us information about the confidence in the results. Within the study, we measured 5 physical quantities: pressure, flow rate, torque, rotational speed, and temperature. Briefly, we would like to present the uncertainty analysis for the first four physical units. The expanded uncertainty analysis was done by assuming triangular and rectangular distribution and a coverage factor = 2 (Table 4).

	Rectangular distribution [%]	Triangular distribution [%]
Pressure	1,50	1,06
Flow rate	1,73	1,22
Torque	2,02	1,43
Rotational speed	1,73	1,22

Table 4: Expanded uncertanty analysis.

6 Conclusion

A research of the hydraulic gerotor motor efficiency with the floating outer ring is presented in this paper. The findings of this study can be summarized as follows: The diameter of holes in the valve plate influences the total efficiency of the hydraulic gerotor motor. For each set of the measurements exists an optimal diameter of holes. Very high total efficiencies were reached with holes' diameter being Φ6,3 mm in most cases. The highest total efficiency was on average 5 % higher than the total efficiency of the original hole size. It means that a hydraulic motor with the hole diameter Φ6,3 mm in the valve plate has on average 5 % better operation characteristic in every measured point than a hydraulic motor with the hole size Φ5,5 mm in the valve plate. We can conclude that we would be able to optimize the gerotor's operation with some simple mechanical operation. With drilling we can make hole diameter larger to raise the total efficiency of the gerotor around 5 % on average. This happens if the diameter of holes in the valve plate is Φ6,3 mm. According to the tribological prospective we found out that surface roughness and contact force play very important role regarding friction. The lowest friction was 0,077, it occourred when surface roughness was $Ra = 0{,}05$ µm and contact force was 112 N. The results and research findings present a very important contribution to science. Hydraulic gerotor motors with the floating outer ring were very rarely discussed in scientific papers. There is a lack of such analysis in literature. An influence of hole diameter in the valve plate on the total efficiency of hydraulic gerotor motors represents novelty and original insight in the gerotor's group of hydraulic motors.

Acknowledgement

The authors greatly acknowledge the company KGL d.o.o. Slovenia.

7 References

/1/ Michael, P., Burgess, K., Kimball, A., Wanke, T.: Hydraulic Fluid Efficiency Studies in Low-Speed High-Torque Motors; SAE Technical Paper 2009-01-2848 (2009), Nr.7; doi:10.4271/2009-01-2848

/2/ Dong, X.: Multi-Objective Optimization Design of Gerotor Orbit Motors; SAE Technical Paper 2002-01-1350 (2002); doi:10.4271/2002-01-1350

/3/ Ding, H., Lu, X. J., Jiang, B.: A CFD model for orbital gerotor motor; IOP Conference Series: Earth and Environmental Science (2012), Nr.6 (15)

/4/ Mishev, A., Stehle, T.: CFD-Analyse zur Leistungssteigerung eines Orbit-Motors, Untersuchung des Einflusses von Rotorzähnezahl und Exzentrizität auf die Performance des Motors (2015)

/5/ Conrad, F., Trostmann, E., Zhang, M.: Experimental identification and modelling of flow and torque losses in gerotor hydraulic motors; Proceedings of the JFPS International Symposium on Fluid Power (1993), Nr.2; page 677-682

/6/ Garcia, J. M.: Surface effects on start-up friction and their application to compact gerotor motor design (2011); http://search.proquest.com/docview/900865878?accountid=16468. (29.11.2016)

/7/ Furustig, J., Almqvist, A., Pelcastre, L., Bates, C. A., Ennemark, P., Larsson, R.: A strategy for wear analysis using numerical and experimental tools, applied to orbital type hydraulic motors; http://pic.sagepub.com/content/early/2015/06ogled/10/0954406215590168. (29.11.2016)

/8/ Ranganathan, G., Hillson Samuel Raj, T., Mohan Ram, P.V.: Wear characterisation of small PM rotors and oil pump bearings; Tribology International (2004), Nr.1(37); page 1-9

/9/ Ivantysyn, J., Ivantysynova M.: Hydrostatic Pumps and Motors, First English Edition, Akademia Books International, 2000

/10/ Schlösser, W. M. J., Hildbrands, J.W.: Das theoretische Hubvolumen von Verdrängermaschinen; Ölhydraulik und Pneumatik (1963), Nr.4 (7)

/11/ Standard ISO 8426; Hydraulic fluid power – Positive displacement pumps and motors, Determination of derived capacity, 2008

/12/ Evaluation of measurement data – Guide to the expression of uncertainty in measurement, JCGM 100:2008, GUM 1995 with minor correction, 2008

8 Nomenclature

Variable	*Description*	*Unit*
i	Index	[-]
k	Number of samples	[-]
n	Rotational speed	[min^{-1}]
p_1	Pressure at the inlet port of hydraulic motor	[bar]
p_2	Pressure at the outlet port of hydraulic motor	[bar]
E_h	Hydraulic energy	[-]
E_m	Mechanical energy	[-]
M	Torque	[Nm]
Q_1	Volume flow rate at the inlet port of hydraulic motor	[m^3s^{-1}]
V_g	Geometric displacement volume	[m^3]
V_i	Derived displacement volume	[m^3]
Δp	Pressure difference	[bar]
η_{hm}	Hydraulic-mechanical efficiency	[-]
η_v	Volumetric-efficiency	[-]
η_t	Total efficiency	[-]

An Active-control digital hydraulic damper: Design, modeling and simulation

Cheng-long WANG*, Zhi-Wei QIU, Qing-Liang ZENG, Yan-xi Liu, Gen-yuan Miao

Shandong University of Science and Technology, College of Mechanical and Electronic Engineering, 266590, Qingdao, China

E-Mail: wcllym@163.com

In the paper, an active-control digital hydraulic damper is designed and modelled, which is comprised of multiple digital throttle units. The digital throttle units consist of a throttle valve and high speed on/off solenoid valve which are connected in series. A mathematical model of the digital throttle unit is provided. A control algorithm based on PID is given which is used for the active control of the variable throttle area. The working process of the active damper is simulated and analyzed in AMESim with a comparison of the working process of a passive Porous Hydraulic Damper. Pressure-Time curves, Displacement-Time curves and Velocity-Time curves are given which show thet performance differences between the active-control digital hydraulic damper and the passive Porous Hydraulic Damper. According to the simulation comparison, it is clear that the buffering stroke of the active-control digital hydraulic damper is increased by 8.9% but the peak pressure of the active-control digital hydraulic damper is reduced by 20% compared with the passive Porous Hydraulic Damper. It indicates better performance of the Digital hydraulic damper which can complete the damping process more smoothly and effectively.

Keywords: High speed on/off solenoid valve, digital throttle unit, digital hydraulic damper, active-control
Target audience: Mobile Hydraulics

1 state of art

The hydraulic damper is often used as a shock absorber to alleviate violent impacts. The basic principle of a Hydraulic damper is absorbing energy through the orifice as liquid flows, this is called flowing resistance. It is used increasingly because of its large energy density and stable damping performance. According to the control way, the hydraulic damper can be divided into these three types: passive hydraulic damper, semi-active hydraulic damper and active hydraulic damper. The damping process for a passive hydraulic damper is achieved by means of the constant throttle area. The damping process for a semi-active hydraulic damper is achieved by means of controlling the constant throttle area semi-active. The damping process for an active damper is achieved by means of controlling adjustable throttle area damper.

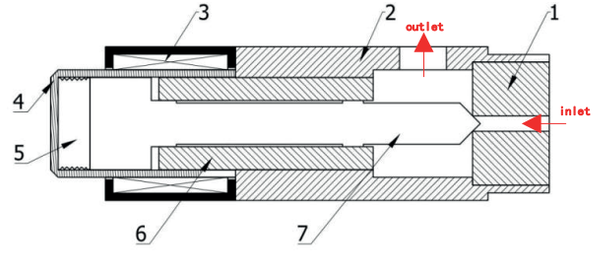
Feng Shuai analyses the influence of parameters on the performance of passive hydraulic damper used for the artillery[1].Based on the Bernoulli equation, a mathematical model of a passive hydraulic damper is given by Huang Jingfeng[2] and simulated in Simulink. Geometric modelling, numerical analysis and visualization of passive damper are done by Zheng Biao[3] by means of CFD technology. Based on Runge-Kutta method, the effect of nonlinear damping on the response of a hydraulic shock absorber is studied by Chandra, Shekhar and Hatwal [4]. As a new concept, semi-active damping control is proposed by Lord M.J.Cosby and D.C.Karnopp Davis[5], which is different from full active damping control. Liu Hui designed a semi-active damping device for landing gear by means of a parallel high-speed on-off valve, a mathematical model is set up and related experiments are carried out to verify the simulation result[6]. Based on the high-speed on-off valve, YangJianwei[7] developed a semi-active shock absorber for a high-speed vehicle. Liu Shaojun etc.[8] have given a simulation model of semi-active shock absorber based on the high-speed on-off valve and simulated its control method. An active damper for landing gear based on the hydraulic servo valve is developed by NASA[9-10].

Under uncertain conditions, satisfying the requirements of damping for a heavy impacting force, ensuring the stability and response speed of the damper with decreasing working pressure in the chamber, are big challenges for the researchers. In this paper, an Active-control digital hydraulic damper is introduced which has the features of the low cost, good stability and high response speed.

2 The working principle of the digital hydraulic damper

using high-speed on-off valve as the digital unit, active variable-throttle-control of the damper can be accomplished by means of a computer. The throttle valve and the high-speed on-off valve are connected in series so as to form the digital throttling unit shown in Figure 1, which consists of the throttle valve body, coil, valve core, gas spring, keeper and pole shoe. A number of digital throttle units are combined together in parallel to form a digital throttle valve-group. The working principle of the digital throttling unit is as follows:

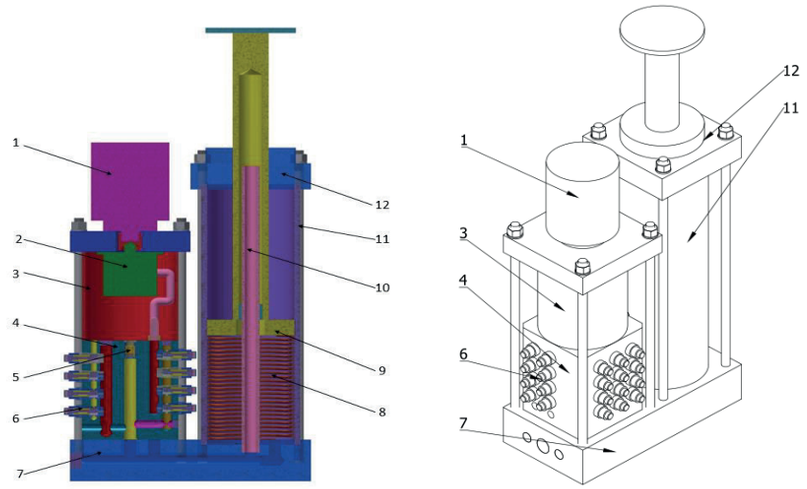
When the coil is energized, a magnetic force will be generated that drives the valve core to move, the throttle valve will be opened and the gas spring will be compressed so as to let the oil pass through. When the power of the coil is lost, the valve core will be reset by the gas spring and the throttle valve will be closed.



1.throttle valve2.valve body3.coil4. keeper 5.gas spring 6. pole shoe 7. valve core

Figure1.digital throttle unit diagram

The digital hydraulic damper, which is shown in figure 2, is mainly composed of a cushion cylinder, digital throttling unit, valve block,gear-pump, motor and tank.



1.motor2.gear pump3.tank4.valve block 5.rod cavity charging valve6.digital throttle unit 7.connection unit 8.rest spring 9.piston 10.internal guide rod 11.cylinder 12.cylinder head

Figure2.digital hydraulic damper diagram

The general configuration of the digital hydraulic damper is given in figure 3. For the digital hydraulic damper, with the help of an accelerometer and pressure sensor, real-time adjustment of the throttle area can be obtained according to the impacting force, and real-time adjustment of capacity can be obtained according to the information given by the sensors.

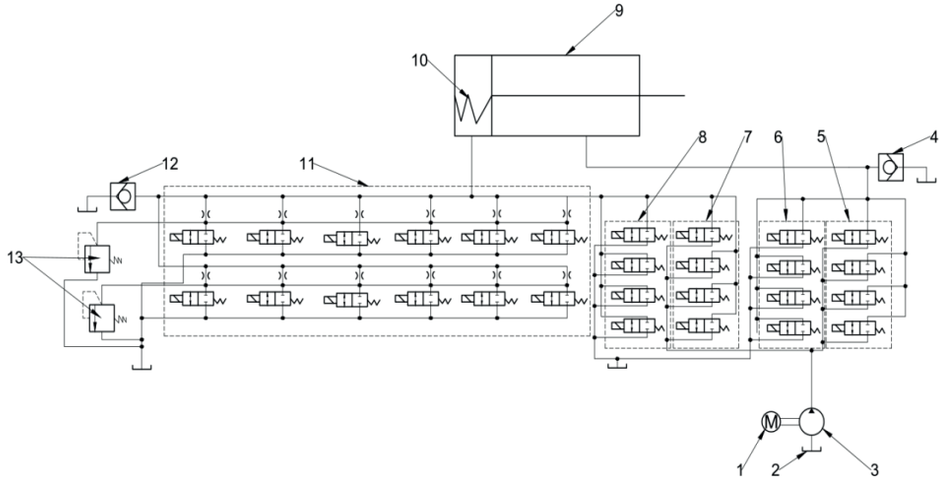
The basic working process is as follows:

In the first stage, before the head of digital hydraulic damper is shocked by impacting workpiece, the acceleration of the impacting workpiece is detected by the accelerometer. According to the acceleration value of the impacting workpiece, the predefined stroke and the initial pressure of digital hydraulic damper are given. Through the gear pump, a group of control valves for the non-rod chamber and a group of control valves for the rod chamber, the stroke and the initial pressure can be adjusted in real-time.

In the second stage, after the head of digital hydraulic damper is shocked by the impacting workpiece, the acceleration of the impacting workpiece will be detected in real-time by the accelerometer and the pressure in buffering chamber will be detected in real-time by the pressure sensor. By means of the average value processing, the processed value will be inputted to the digital throttling unit which is mounted on the valve block as shown in Figure 2, so that the optimal throttling area can be given with real-time control.

With the control valve for the non-rod chamber, the oil can be supplied from the tank quickly during the buffering process, avoiding suction or the effect of negative pressure. With the control valve for the rod chamber, the rapid reset of the digital hydraulic damper can be realized in the resetting process.

Using a non-rod cavity control valve, oil can be provided quickly from the tank during the buffering process, avoiding the suction or influence of negative pressure. With the rod cavity control valve, the digital hydraulic damper can be reset quickly during the reset process.



1.motor 2.tank3.gear pump 4.check valve for rod chamber 5. group of oil inlet control valves for rod chamber 6. group of oil outlet control valves for the rod chamber 7. group of oil inlet control valves for the rodless chamber

8. group of oil outlet control valves for the rodless chamber 9.cylinder10.Reset spring11.digital throttle unit 12. check valve for the rodless chamber 13 safety valve

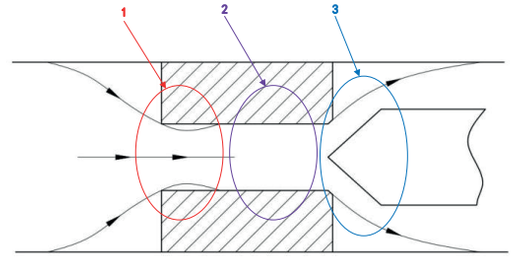
Figure3.digital hydraulic damper Hydraulic system schematic diagram

There are two safety valves in the damper. These two safety valves can help to prevent accidents if the buffering process cannot be achieved in the case of an electrical system failure. In addition, these two safety valves can provide a security guarantee for effectively buffering in unexpected circumstances.

3 Calculation model of the digital throttle unit

A digital hydraulic damper consists of several digital throttle units which are made up of the high-speed on-off valve and the throttle valve. When the oil passes through the unit, there is a local pressure loss and frictional pressure loss, a damping force is created so as to buffer the impacting object until it stops. For the fluid in the damper, the following assumptions are made:

- The fluid is incompressible
- Quality of the fluid is negligible
- The fluid is Newtonian fluid



1. local pressure loss abrupt contraction in cross-section 2. friction pressure loss through the orifice 3. local pressure loss through cone valve port Figure4.energy loss in digital throttle unit

As shown in Figure 4, when the fluid flows through the digital throttling unit, there are three kinds of energy losses which are local pressure loss for an abrupt contraction in cross-section, frictional pressure loss through the orifice and local pressure loss through the cone valve port. A mathematical model for the energy loss of the unit is analyzed according to the above three factors.

3.1 local pressure loss for an abrupt contraction in cross section

In Figure5, local pressure loss for an abrupt contraction in cross section is illustrated when fluid flows into the orifice of the digital throttle unit. Local pressure loss $_m$es for an abrupt contraction in a cross-section can be described as follows. C_c is obtained from the experiment by J.Weishach[11], which is shown in Table 1.

$$h_m = \left(1 + \frac{1}{C_v^2 C_c^2} - \frac{2}{C_c}\right)\frac{v_2^2}{2g} = \zeta \frac{v_2^2}{2g} \qquad (1)$$

3.2 frictional pressure loss through the orifice

According to the Navier-Stokes equation, the pressure lossΔp[12]flow through the distance of L is as follows:

$$\Delta p = \frac{32 \mu l v_2}{d^2} \qquad (2)$$

3.3 local pressure loss through the Cone valve port

Flow through the orifice can be expressed as follows：

$$Q = C_q A_2 \sqrt{\frac{2\Delta p}{\rho}} \qquad (3)$$

The theoretical formula of flow coefficient C_q[13] is as follows:

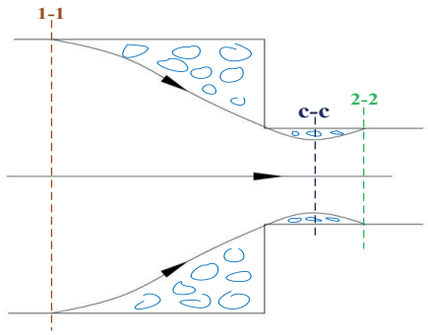
$$C_q = \left\{ \frac{24}{\sin\theta}\left(\ln\frac{d_1}{d_2}\right)\frac{1}{Re\left(\frac{2h}{d_m}\right)} + 0.18\left(\frac{d_m}{d_2}\right)^2 + \frac{54}{35}\left(\frac{d_m}{d_1}\right)^2 \right\} \quad (4)$$

In figure 6, if the number of opened digital throttle units is n at the moment, then the flow Q which is flowing through the port of the cone spool is as follows:

$$Q = \frac{Av}{n} \quad (5)$$

The pressure loss caused by the cone spool of the digital throttle unit is as follows:

$$\Delta p = \frac{\rho}{2}\left(\frac{Av}{nC_qA_2}\right)^2 \quad (6)$$



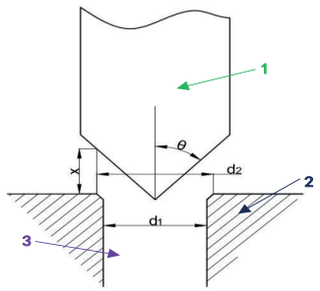


Figure5. local pressure loss for an abrupt contraction in cross-section *Figure6. spool Schematic of the digital throttle unit*

A_2/A_1	0.01	0.10	0.20	0.30	0.40	0.50	0.60	0.70	0.80
C_c	0.618	0.624	0.632	0.643	0.659	0.681	0.712	0.755	0.813
C_v	0.98	0.982	0.984	0.986	0.988	0.990	0.992	0.994	0.996
ζ	0.49	0.458	0.396	0.364	0.317	0.264	0.197	0.126	0.197

Table1.C_c、$C_v$and ζ of abrupt contraction in cross section

4 Control algorithm

As mentioned in part 2, there are two working stages for the damper. During the first stage, the value of buffering stroke is calculated according to the measured acceleration value. In this case, the safety coefficient is set as 1.3 to prevent accidents.The initial pressure is determined according to the stiffness of the reset spring and 10% of the total buffering energy.

During the second stage, a PID control algorithm is adopted, in which the control goal is to get a minimum peak buffering force during the shocking process. In the ideal case, the force-displacement curve of the damper is shown in Figure7. When the force-displacement is approximately trapezoid, the maximum buffering force of the damper is a constant value, the buffering efficiency is the highest, and the impact energy absorbed by the damper is the largest. It can be described in equation 7.

$$F = F_N \quad (7)$$

When the mass and the velocity of the moving object impacting the damper is known, the energy absorbed by the damper in each stroke is described in equation 8.

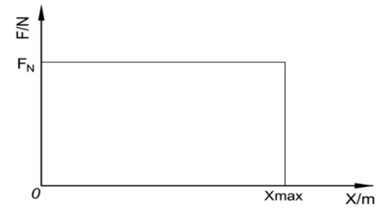


Figure7. force- displacement in ideal state

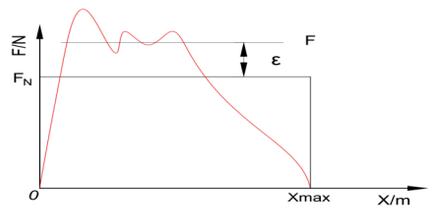


Figure8.Control target diagram

$$W = \frac{1}{2}mv_1^2 \quad (8)$$

Therefore, in the ideal case, the ideal maximum buffering force of the damper is described as follows:

$$F_N = \frac{W}{X_{max}} \quad (9)$$

When the real working condition shown in red in Figure 8 is taken into consideration, the control objective function proposed in this paper is as follows:

$$\varepsilon = F - F_N \quad (10)$$

PID control flow chart of the damper is shown in Figure 9.

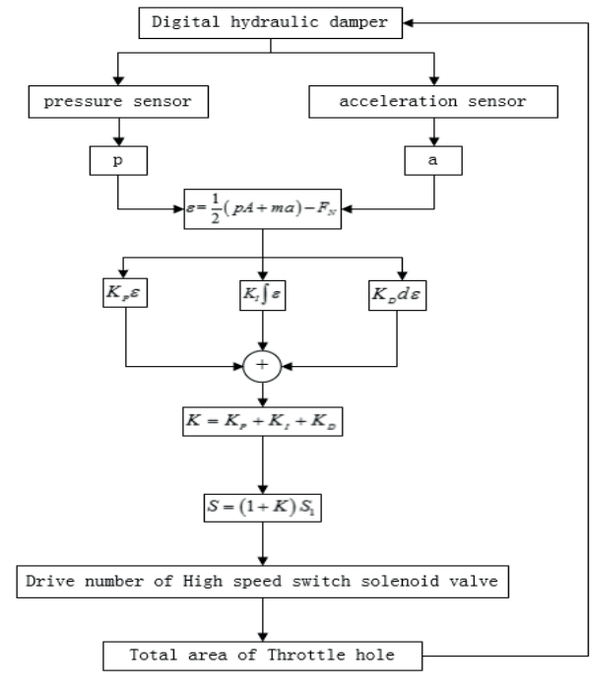
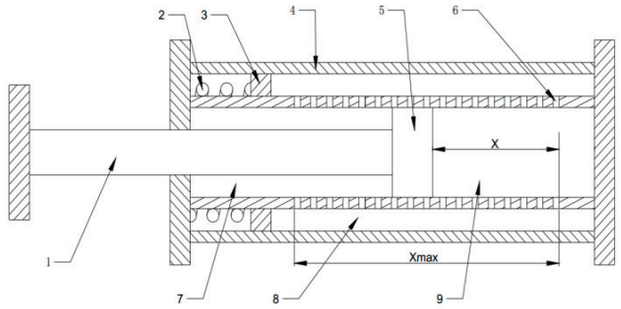


Figure 9. PID control flow chart

5 Simulation analysis with a comparison of the active-control digital hydraulic damper and the passive Porous Hydraulic Damper.

At the same time, a passive Porous Hydraulic Damper is also designed, the 2D assembly drawing of the passive Porous Hydraulic Damper is shown in Figure 10. The passive Porous Hydraulic Damper has the same maximum orifice area as the Digital hydraulic damper. During the working process, the buffering capacity and buffering force cannot be changed in the passive Porous Hydraulic Damper.

The same simulation parameter is applied to the passive Porous Hydraulic Damper and the Digital hydraulic damper.The pre-defined simulation parameter is given in table 2. A simulation model of a passive Porous Hydraulic Damper is given in Figure 11. A simulation model of the Digital hydraulic damper is given in Figure 12. According to the simulation results shown in Figure 13 to Figure 15, different performance characters are shown, which illustrates the advantages of the Digital hydraulic damper.



1. rod 2.resetting spring 3.resetting piston 4.outer cylinder 5.piston 6. orifice 7. chamber with a rod 8. resetting chamber 9. non-rod chamber

Figure 10. 2D assembly drawing of the passive Porous Hydraulic Damper

Parameter	value
the weight of impact object, M	200Kg
Velocity of impact object, V	4.427m/s
Working pressure of Hydraulic Damper, Pw	80Bar
Maximum Working pressure of Hydraulic Damper, Pmax	100Bar
Diameter of piston, D	63 mm
the wall thickness of the outer cylinder, Toc	7.5 mm
piston stroke, ps	150 mm
Diameter of rod, Dr	30mm
Diameter of inner cylinder, Dic	63mm
Spring constant	23.4 N/mm

Table 2. simulation parameter

In Figure 13 it shows that the maximum pressure in the non-rod chamber of the passive damper is 84 bar and the maximum pressure in the non-rod chamber of the active damper is 63 bar, the peak pressure is reduced approximately by 20%. In Figure 14 it shows that the damping displacement of the passive damper is 120mm and the damping displacement of the active damper is 130mm, it also shows that the damping displacement is increased by 8.3% and the change of rate of displacement is relatively stable in the initial stage.

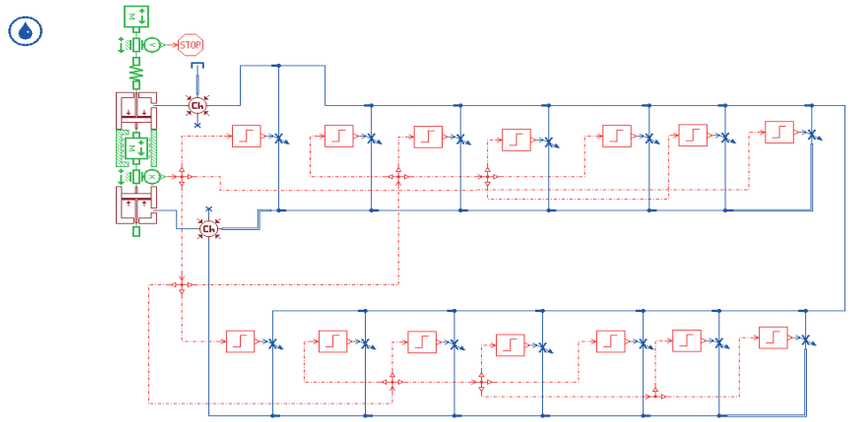


Figure 11. Simulation model of a passive Porous Hydraulic Damper

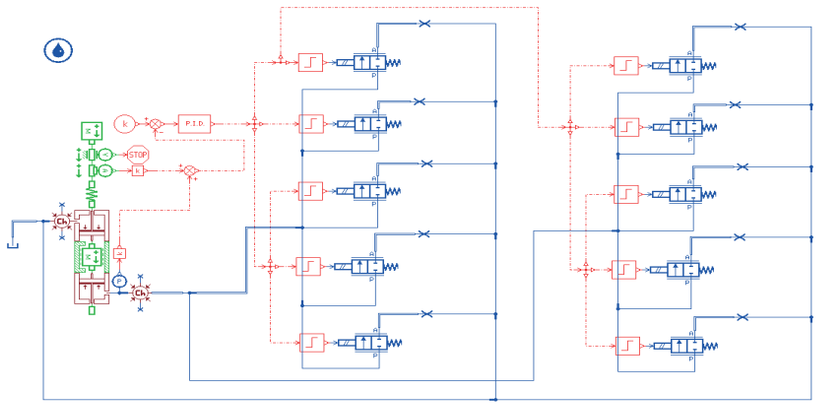


Figure 12. Simulation model of the Digital hydraulic damper.

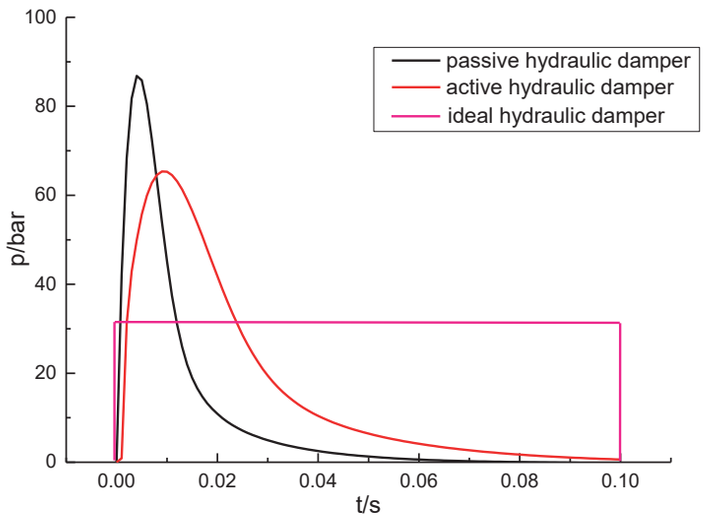


Figure13. Pressure-Time curves of non-rod cavity

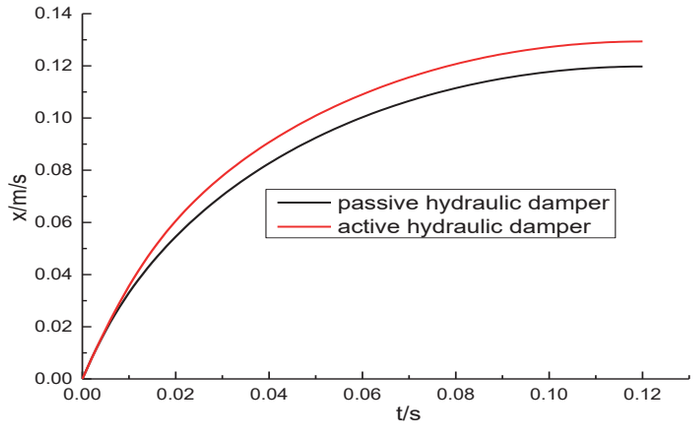


Figure14. Displacement-Time curves

In Figure 15 it shows that the speed of the active damper is decreased, which is slower than the speed of the passive damper so that severe shock pressure and higher pressure in the non-rod chamber can be avoided when the speed of the impact object is relatively high. The working pressure in the non-rod chamber is decreased obviously and the performance of the active damper is stable.

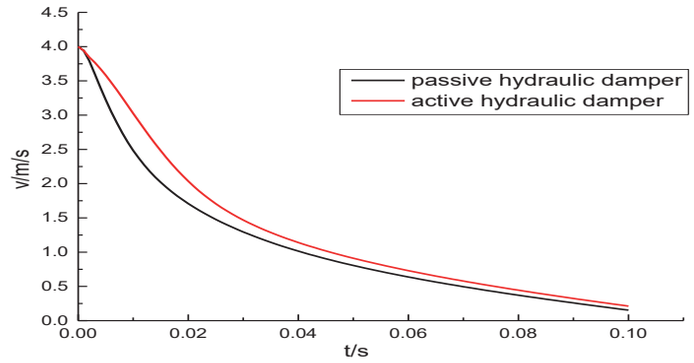


Figure15. Velocity -Time curves

6 Conclusion and future works

In the paper an active-control digital hydraulic damper is designed and modelled, a mathematical model of the digital throttle unit model is provided. Control algorithm based on PID is given to achieve active control of variable throttle area. According to the simulation, it is clear that the damping stroke of the active-control digital hydraulic damper is increased by 8.9% but the peak pressure of the active-control digital hydraulic damper is reduced by 20% compared with the passive Porous Hydraulic Damper. It demonstrates that the Digital hydraulic damper can complete the damping process more smoothly and effectively.

In the future, the physical prototype will be tested in the performance testing system so as to test the relevant parameters that affect the performance of the hydraulic damper. The model will be verified and validated according to the testing data.

7 Acknowledgements

This work was supported by the Natural Science Foundation of Shandong Province(ZR2016EEM02), the National Natural Science Foundation of China (51375282), State Key Laboratory of Mining Disaster Prevention and Control Cofounded by Shandong Province and the Ministry of Science and Technology (51010305029).

Nomenclature

Variable	*Description*	*Unit*
p_F	Surface Pressure	[bar]
T	Temperature	[K]
v	Velocity	[m/s]
α_D	Discharge Coefficient	[-]
ε	Angled	[rad]
C_c	Contraction coefficient of stream	[-]
A_c	Area of stream in cross-section c-c	[m^2]
A_2	Area of throttle orifice in cross-section 2-2	[m^2]
C_c	Contraction coefficient of stream	[-]
A_c	Area of stream in cross-section c-c	[m^2]
A_2	Area of throttle orifice in cross-section 2-2	[m^2]
C_v	Coefficient of flow rate, $C_v = \frac{v_c}{v_0}$	[-]
V_c	Average flow rate in cross-section c-c	[m/s]
V_0	Average flow rate in cross-section 1-1	[m/s]
V_2	average flow rate in cross-section 2-2	[m/s]
Z	Coefficient of local pressure loss in cross section	[-]
G	Gravitational acceleration	[m/s^2]
M	Kinematic viscosity of fluid	[m^2/s]
D	The diameter of orifice	[m]
P	Fluid density	[kg/m^3]
C_q	Flow coefficient	[-]
Δp	Pressure loss between inlet port and outlet port	[bar]
X	Rising height of the cone spool	[m]
Θ	The half angle of the cone spool	[rad]
H	xsinθ	[m]
Re	$\frac{v_m d_m \rho}{2\mu}$	[-]
v_m	Average flow rate in section d_m	[m/s]

d_1	Chamfering diameter in the outlet port	[m]
A	Area of piston in cross section	[m^2]
v	Piston velocity at the moment	[m/s]
F	Buffering force at any time of the damper	[N]
F_N	Ideal maximum buffering force	[N]
v_1	Initial velocity of the moving object before contacting with the damper	[m/s]
W	Energy absorbed by damper in one stroke	[N*m]
X_{max}	Maximum buffering stroke	[m]
E	Difference between F and F_N	[N]

References

/1/ FENG Shuai.Design and Research of 60mm Automatic Light Mortar Recoil Buffer and Direction [D]. Shenyang:Dongbei University,2013.

/2/ HUANG Jing-Feng, DONGNan, LIU Sheng-Jie.Dynamic Characteristic Analysis of Hydraulic Buffer Based on Simulink[J]. Machine Tool and Hydraulics,2015, 43(13):145-148.

/3/ ZHENG Biao.Computational Analysis and Experimental Study of a New Type of Liquid gas Buffer Based on CFD Technology[D].Dalian: Dalian University of Technology,2014.

/4/ Liu Hui.Research on Property and Semi-active control of Landing Gear Shock Absorption System[D].Nanjing: Nanjing University of space and Aeronautics and Astronautics,2007.

/5/ M.J. Cosby, D.C vibration control, Karnopp, The active damper-a new concept for shock and Shock and Vibrations Bulletin, 1973, 43(4): 119-133.

/6/ YANG Jian-Wei.Study on Semi-Active Control System for Lateral Vibration of High-Speed Vehicle[D].Beijing: Academy of Railway Sciences.

/7/ LIU Shao-jun.Simulation of the Lateral Semi-Active Damper of High-Speed Train with Sky-hook Control[J]. Machine tools and hydraulics,2006(10),70-72.

/8/ CHANDRA SHEKHAR N, H.HATWAL.The response of Non-linear Dissipative Shock Isolators[J].Journal of Sound and Vibration,1998,20(04):15-30.

/9/ CBrecher , A Schulz ,M Week.Electrohydraulic Active Damping System[J].Manufacturing Technology , 2005 , 54 (1) :389-392.

/10/ J.N. Daniels, A method for landing gear modeling and simulation with experimental validation[J].NASA Contractor Report201601,1996.

/11/ SHENG Jing-Chao.Hydraulic fluid mechanics，Beijing：Machinery Industry Press，1980.

/12/ WeisbachJ.,Die Experimental-Hydraulik, Engelhardt, Freiburg,1855.

/13/ 市川常雄,清水孝.ポペット弁の流量係数について,机论 31 卷 222 号，1965.

A control approach for fast voice coil actuators for servo valve applications in mobile and industrial hydraulics

Lucian Năsțuțiu*, Olivier Reinertz** and Hubertus Murrenhoff**

Technical University of Cluj-Napoca, Faculty of Mechanics, Mechanical Engineering Department,
Muncii str. 103-105, 400641 Cluj-Napoca, Romania*
RWTH Aachen University, Institute for Fluid Power Drives and Systems (IFAS),
Campus Boulevard 30, D-52074 Aachen, Germany**
E-Mail: Lucian.Nascutiu@termo.utcluj.ro

The resonant behaviour of voice coil actuators driven by fast changing signals limits their application in hydraulic servo valves. A very good damping, precision and the ability to dynamically overcome the effects of flow forces are some special requirements. The paper attempts to propose some control strategies and solutions to reduce the effects of raising impedance near the resonant frequency, thus improving the damping, which allows further enhancements in bandwidth. Theoretical models and simulation results are presented and discussed and some recommendations are proposed. The parameters used in simulation correspond to those of an already developed and tested voice coil prototype.

Keywords: voice coil actuators, direct operated servo valves, fast switching valves, impedance, robust control
Target audience: Industrial and Mobile Hydraulics, Hydraulic Components, Process Control

1 Introduction

The nowadays research focuses on the issues that arise in specific servo hydraulic applications in power generation, building safety (smart buildings, smart structures, mobile bridges), materials testing, automotive and aerospace engineering, and astronomy (intelligent telescope mirror control) as well as in manufacturing technology. New technological advances require an increase in speed and accuracy, while at the same time augmenting demands for safety, energy saving, efficiency and for environmental compatibility arise. This applies especially for applications in the field of industrial and mobile hydraulics. The requirements for precision and high dynamics in hydraulic drive systems can be accomplished by introducing intelligent fluid devices that operate at low power levels and can handle very high power with high efficiency. A special category of such fluid devices is represented by proportional valves and servo valves /1/, /2/. They are nowadays, mostly microprocessor based mechatronic devices. To further increase their performances, some researchers have proposed original solutions, by improving also the internal valve's mechanical structure. An example is the roto-translating valve, which presents a secondary rotary type actuator connected to a sleeve interposed between the spool and the valve body, thus composing a roto-translating valve. Due to its structure, the metering control precision and valve speed are virtually quadratic in respect to the traditional spool position control /3/, /4/.Another technological advance in the field refers to high performance valve actuators /1/, /5/, /6/, /7/, /8/, /9/. The voice coil motors are here representative. They show a high level of accuracy and high acceleration, making them a very good candidate in the valve technology field. Nowadays, a special application of the voice coil motors lies in the field of digital hydraulics /5/. This area is particularly of high interest to increase the efficiency in wind power plants, where the mechanical transmissions are to be replaced with hydraulic transmissions /5/, /10/. In this case the electrical generator is directly driven at rated speed, which corresponds to a 50 Hz frequency of the grid. The digital hydraulic machines are discretely-adjustable variable displacement units (pumps or motors) having a number of independent controllable cylinder-piston pairs. The total flow rate sink or sourced of those machines varies stepwise, like the binary representation of the numbers in digital systems. A number of cylinder-piston pairs (usually 5,7 or 9), driven simultaneously by a slow rotating camshaft, can be dynamically enabled, disabled or idled by using fast switching valves (for example for 7 pairs the flow rate can take 2^7=128 discrete values). They are driven by voice coil motors, in PWM mode or continuous mode, to adjust the flow rate at the required level. For a pump or a motor operating at 50 Hz (20 ms period), in order to achieve a 10% pulse width, the valves must be switched in 2 ms! A very well damping behaviour is required for these valves, in order to prevent very high pressure peaks and high amount of heat losses. The switching technology in fluid power systems leads to very small throttling losses and therefore to high efficiency.

A voice coil motor, designed for direct operated hydraulic servo valves must fulfil some special requirements. A very good damping behaviour, very high developed force, the ability to quickly overcome the effects of the flow forces and a very precise positioning capability of the valve's spool are some conditions to achieve a very good stationary and transient behaviour as well as a good efficiency of the driven system. An earlier work of the authors proposes to investigate new alternatives of electro-mechanical drives to replace the still expensive special (piezo and magnetostrictive) materials /1/, or sensitive structures (torque motors) while at the same time improving the stationary and transient behaviour according to the new technological advances. The authors have developed a highly dynamic and very precise valve actuator prototype /8/, based on the voice coil principle. Its properties and performances are shortly presented in the following.

2 Properties and performance of the first prototype

A novel geometry of the magnetic circuit and the arrangement of the coil windings inside the voice coil actuator allows to reduce the electrical time constant, thus supporting a high dynamics. The coil geometry consists of three groups of windings (series connected). Each two adjacent groups are wounded in opposite direction; therefore the mutual inductance is negative. Moreover, double of this mutual inductance is subtracted from the sum of self-inductances. This arrangement yields therefore an overall lower inductance for the same wire resistance, compared to a coil with the same number of turns wounded in the same direction.

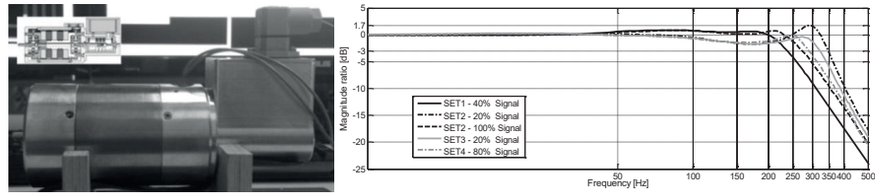


Figure 1: The IFAS prototype (left) and the experimental Bode plot (right)/8/

The properties of the test assembly and the prototype are summarised in the following tables:

Supply voltage	36 V
Maximal supply current	3.6 A
Coil excursion	±1.2 mm
DC coil resistance at 20 °C	7.2 Ω
Mechanical natural frequency	176 Hz
Movable mass	70 g

Force factor k_F	29 N/A
Back-emf constant	28.8 V s/m
Electrical time constant	0.388 ms
Maximal force	104 N
LVDT gain	4.45 V/mm
Current sensor gain	1.6 V/A

Table 1: The prototype parameters /8/.

The actuator was tested without a real load (i.e. a servo valve). To simulate a real damping, the gaps of the magnetic circuit were filled with a small amount of mineral oil based ferro fluid, thus increasing the viscous friction on both sides of the coil /11/. The curves of the Bode plot corresponds to the actuator with ferro fluid inserted in the gaps, except the SET1.The -3dB frequency of the responses lies between 270 Hz and 350 Hz, depending on the controllers' parameters.

3 The mathematical model of the voice coil motor

3.1 The linear model

The mathematical model of the actuator /8/, /9/, /12/, /13/ is mainly composed of two linear differential equations corresponding to both the electric and the mechanical part:

$$\begin{cases} u = R_\mathrm{e} \cdot i + L_\mathrm{e} \cdot \dfrac{di}{dt} + k_\mathrm{emf} \cdot \dot{x} \\ k_\mathrm{F} \cdot i = m \cdot \ddot{x} + c_\mathrm{D} \cdot \dot{x} + k_E \cdot x + F_\mathrm{D} \end{cases} \tag{1}$$

The coefficientk_F, represents the motor force sensitivity or force factor, k_emf the back-emf constant ($k_\mathrm{emf} \approx k_\mathrm{F}$), R_e the DC resistance of the coil, L_e the inductance of the coil, u the effective voltage applied to the coil, m the total moving mass, c_D the damping coefficient, k_E the total suspension stiffness, i the current through the coil and$x$ the coil position. The force F_D takes into account all disturbances seen from the load side.

3.2 The impedance model of the voice coil motor

The impedance model of the voice coil motor can be derived from the equation system 1, by dividing the second equation by the force sensitivity k_F and considering the variable i (the coil current), the output variable /8/. With the variable u (the coil voltage supply) as input, the complex impedance is then calculated as $Z_0(j\omega) = U(j\omega)/I(j\omega)$, which is actually the inverse of the transfer function.The following notations are adopted:

$$C_\mathrm{m} = \frac{m}{k_\mathrm{F} \cdot k_\mathrm{emf}}, R_\mathrm{m} = \frac{k_\mathrm{F} \cdot k_\mathrm{emf}}{c_\mathrm{D}}, L_\mathrm{m} = \frac{k_\mathrm{F} \cdot k_\mathrm{emf}}{k_\mathrm{E}} \tag{2}$$

whereC_m, R_m and L_m are virtually electric quantities, which represent the influence of the mechanical system on the overall actuator behaviour. They are called the "mechanical" capacity, resistance and inductivity respectively. With the above notations the total impedance can be written in frequency domain, as follows:

$$Z_0(j\omega) = R_\mathrm{e} + L_\mathrm{e} \cdot j\omega + \frac{j\omega}{C_\mathrm{m} \cdot (j\omega)^2 + R_\mathrm{m}^{-1} \cdot j\omega + L_\mathrm{m}^{-1}} = Z_{0\mathrm{e}}(j\omega) + Z_{0\mathrm{m}}(j\omega) \tag{3}$$

Equation3 represents the total impedance of the actuator itself. It has two components. $Z_{0\mathrm{e}}(j\omega)$is the so called blocked impedance, which depends only on the electrical parts, R_e and L_e. It can be measured directly with a RLC bridge by blocking the movement of the coil from outside. $Z_{0\mathrm{m}}(j\omega)$is represents the so called motional impedance that is related mostly to mechanical parts. Nevertheless, it includes also the influence of the electrical part by means of the induced voltage in the coil due to its speed. Moreover, if the load impedanceZ_L,is also taken into account, the new impedance becomes:

$$Z_0 = Z_{0\mathrm{e}}(j\omega) + \frac{Z_{0\mathrm{m}}(j\omega) \cdot Z_\mathrm{L}(j\omega)}{Z_{0\mathrm{m}}(j\omega) + Z_\mathrm{L}(j\omega)} \tag{4}$$

which is calculated by means of parallel connection of motional impedance with the load impedance. There is a lack of knowledge to develop a proper model of the load impedance and therefore, the load influence on the overall behaviour can be considered as disturbance. Therewith, a control scheme with good ability to overcome the effects of disturbances is required.

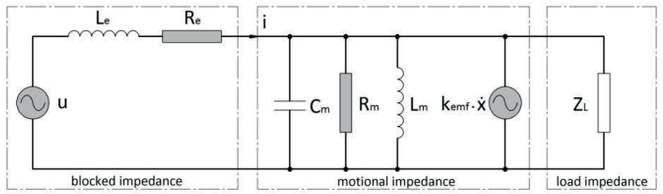


Figure 2: Actuator impedance model

In case of a voice coil driven servo valve, some parameters, which would describe the load impedance, can be included in motional impedance. One of these is the spool's mass, which can be added to the coil assembly mass, increasing therefore the mechanical capacity. The damping behaviour is related to the friction between the spool and the sleeve due to the fluid viscosity. This behaviour can also be taken into account by means of the overall damping coefficient,c_D.Some parameters can be estimated with sufficient accuracy by measurements, like coil DC resistance at a given temperature, coil inductance, the total movable mass and the spring stiffness. The estimation of other parameters, like the damping coefficients, can be more difficult and requires ,e.g, to perform flow simulations (CFD) of the valve's behaviour under certain conditions. A simple way to estimate the damping of a given servo valve will be presented later in this paper.

4 The control strategies

The developed force of the voice coil motor is directly related to the current that flows troughs the coil windings. Therefore, a very good transient behaviour of the current control system is required, especially when high transient flow forces are developed, e.g., as a result of a fast transition at small openings of a servo valve's spool.

4.1 The speed feedback

One of the most significant issues of voice coil motors is the relatively small damping /8/. Near the resonant frequency of the coil assembly, the total impedance, seen by the voltage supply, raises quickly and reaches a maximum value, which is sometimes an order higher, relative to the impedance at low frequencies. The increasing impedance effectively blocks the current to flow through the coil windings and the motion of the coil assembly gets out of control.

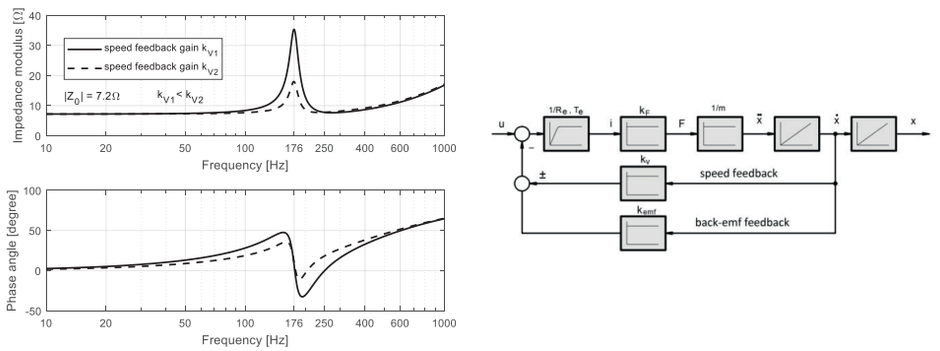


Figure 3: The influence of the speed feedback on the equivalent electrical impedance

The well-known speed feedback is used to improve the damping behaviour, but there are some limitations. In order to be effective, this feedback strategy must fulfil some conditions and namely the bandwidth of the electrical part must be much higher than the bandwidth of the mechanical part /9/. With the given parameters of the developed prototype $\tau_e = 0.388$ ms, the -3dB corner frequency of the electrical part (blocked impedance) lies at a frequency higher than 2000 Hz, which is much higher than the mechanical natural frequency$\omega_m =$ 176 Hz. There are also limits to increase the k_v gain, by means that the feedback voltage cannot be higher than the voltage supply.Mathematically, the speed feedback will be done by adding or subtracting the speed gain,k_V, to or from the back-emf constant, as shown in figure 3, right. By this, the virtual electric parameters become:

$$C_\mathrm{m} = \frac{m}{k_\mathrm{F} \cdot (k_\mathrm{emf} \pm k_\mathrm{v})}, R_\mathrm{m} = \frac{k_\mathrm{F} \cdot (k_\mathrm{emf} \pm k_\mathrm{v})}{c_\mathrm{D}}, L_\mathrm{m} = \frac{k_\mathrm{F} \cdot (k_\mathrm{emf} \pm k_\mathrm{v})}{k_\mathrm{E}} \tag{5}$$

As it is shown in figure 3, the speed feedback operates just on the impedance at the resonant frequency, thus reducing the impedance peak and doesn't affect the impedance at low frequencies. According to equation 3, the total impedance at $\omega = 0$ is:

$$|Z_0(j\omega)|_{\omega=0} = R_e \tag{6}$$

At the resonant frequency$\omega = \omega_{0m}$the total impedance becomes:

$$|Z_0(j\omega)|_{\omega=\omega_{0m}} = |R_e + L_e \cdot j\omega_{0m} + R_m| = \left|R_e + L_e \cdot j\omega_{0m} + \frac{k_F \cdot (k_{emf} \pm k_v)}{c_D}\right| \tag{7}$$

which can be adjusted by changing the speed gain.

4.2 PID control

Due to its simple design and performance characteristics a PID controller has been used first in the closed loop control of the actuator prototype. One of the main drawbacks of the PID controller arises from the fact that the control action takes place without a comprehensive knowledge of the process dynamics. Although some good performances were achieved, the overall stationary and transient behaviour was a compromise between a higher dynamics and a well damped system.

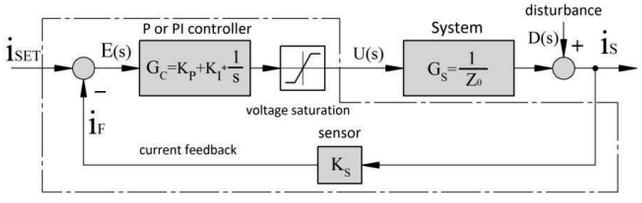


Figure 4: PI control of the current system

The PID control of the prototype was implemented according to the scheme in figure 4. Additional information on PID control and its properties can be found in /16/, /17/. However, to have a comparative basis, the step responses in current and position, determined during the experimental phase of the prototype development are presented in figure 5 /8/.

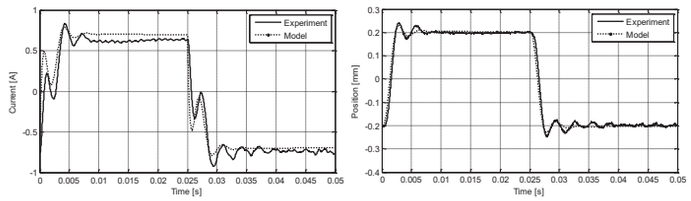


Figure5: Step responses in current and position /8/

The current behaviour (figure 5,left) shows a relatively large oscillation during the transient phase, as well a relatively large overshoot as the current approaches the steady-state value. However, a good agreement between the experimental and simulation results can be observed. This similarity will be useful in the design of the following control strategy, based on the internal model control.

4.3 Internal model control (IMC)

The internal model control principle /16/, /17/, /18/, /19/ is based, first of all, on a comprehensive knowledge of the system model. To achieve certain robustness the controller must include a low pass filter. Its order has to be adjusted to the model order. The filter must be selected in such way that the controller is physically realisable. This implies that the transfer function $G_C^* = G_C(s) \cdot G_F(s)$ must be proper, otherwise excessive derivative action occurs. Here G_C is the transfer function of the controller and $G_F$the transfer function of the filter.

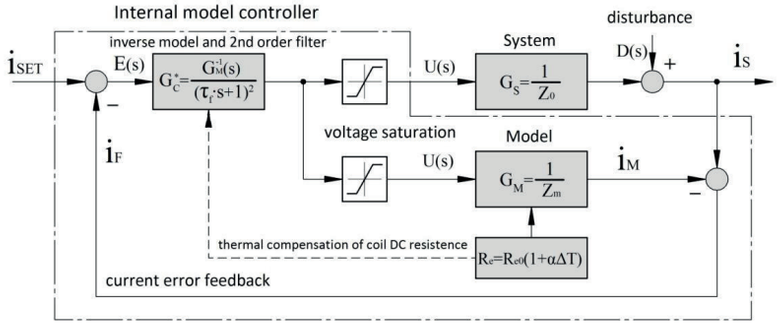


Figure 6: The implementation of the internal model control IMC.

Some properties of the IMC control are /16/, /17/, /19/:

- Dual stability - if the model perfectly matches the system and if the system and controller are both stable, the IMC structure guarantees the closed loop stability;
- Supposing that the controller transfer function is exactly the inverse of the model transfer function, than there is no steady-state error at the output for both inputs, set point and disturbance.

The structure of the internal model control (IMC), figure 6, uses a feedback signal, i_F, built as the difference between the system output,i_S and the model output, i_M. If the model $G_M(s)$ perfectly matches the system $G_S(s)$ then the feedback signal $i_F(s)$ represents the disturbance $D(s)$. Also, if the disturbance $D(s) = 0$, then the signal $i_F$is a measure of the discrepancies between the system and the model. The signal i_F is then subtracted from the set point i_{SET} resulting in the input signal of the controller, E. The voltage at the controller's output is feed into both, the real system and its model. This voltage forces the system to behave like the model. One of the most important properties of the IMC is the ability to efficiently reject the effects of disturbances. This behaviour takes place even if there are some discrepancies between the system and the model.

In the following the transfer function of the closed loop system is calculated according to the IMC control structure, shown in figure 6. To simplify the notations the complex variable s is omitted. So, for example $G_C$means $G_C(s)$. Referring to figure 6, the signal $I_S$equals:

$$I_S = G_C \cdot G_S \cdot E + D \tag{8}$$

and the output of the model is:

$$I_M = G_C \cdot G_M \cdot E \tag{9}$$

The controller's input is defined by:

$$E = I_{SET} - I_F = I_{SET} - (I_S - I_M) = I_{SET} - E \cdot G_C \cdot (G_S - G_M) - D \tag{10}$$

or

$$E = \frac{I_{SET} - D}{1 + G_C \cdot (G_S - G_M)} \tag{11}$$

The output of the system is:

$$I_S = \frac{I_{SET} \cdot G_C \cdot G_S + (1 - G_C \cdot G_M) \cdot D}{1 + G_C \cdot (G_S - G_M)} \tag{12}$$

Now, if the transfer function of the controller,G_C, is exactly the inverse of the model transfer function G_M, that is:

$$G_C = G_M^{-1} \tag{13}$$

the disturbance D is completely rejected, even if there are some differences between the real system $G_S(s)$ and his model$G_M(s)$. The output of the real system is then:

$$I_S = \frac{I_{SET} \cdot G_C \cdot G_S}{1 + G_C \cdot (G_S - G_M)} \tag{14}$$

Moreover if the model $G_M(s)$ exactly matches the real system $G_S(s)$, then:

$$I_S = \frac{I_{SET} \cdot G_C \cdot G_S}{1 + G_C \cdot (G_S - G_M)} = \frac{I_{SET} \cdot G_M^{-1} \cdot G_M}{1 + G_M^{-1} \cdot (G_M - G_M)} = I_{SET} \tag{15}$$

and therefore the output current of the real system perfectly follows the input.

The transfer function of the system is calculated by taking the inverse of the total impedance $Z_0(j\omega)$ and replacing the variable $j\omega$ with the complex variable s:

$$G_S(s) = \frac{1}{Z_0(s)} = \frac{C_\mathrm{m} \cdot s^2 + \frac{1}{R_\mathrm{m}} \cdot s + \frac{1}{L_\mathrm{m}}}{L_\mathrm{e} C_\mathrm{m} \cdot s^3 + \left(R_\mathrm{e} C_\mathrm{m} + \frac{L_\mathrm{e}}{R_\mathrm{m}}\right) \cdot s^2 + \left(\frac{R_e}{R_\mathrm{m}} + \frac{L_e}{L_\mathrm{m}} + 1\right) \cdot s + \frac{R_\mathrm{e}}{L_\mathrm{m}}} \tag{16}$$

The transfer function of the model takes the same form, but the coefficients are in this case estimates of the system coefficients:

$$G_M(s) = \frac{1}{Z_M(s)} = \frac{C_\mathrm{m}^* \cdot s^2 + \frac{1}{R_\mathrm{m}^*} \cdot s + \frac{1}{L_\mathrm{m}^*}}{L_\mathrm{e}^* C_\mathrm{m}^* \cdot s^3 + \left(R_\mathrm{e}^* C_\mathrm{m}^* + \frac{L_\mathrm{e}^*}{R_\mathrm{m}^*}\right) \cdot s^2 + \left(\frac{R_\mathrm{e}^*}{R_\mathrm{m}^*} + \frac{L_\mathrm{e}^*}{L_\mathrm{m}^*} + 1\right) \cdot s + \frac{R_\mathrm{e}^*}{L_\mathrm{m}^*}} \tag{17}$$

The transfer function of the controller results of a series connection of the model impedance with a low pass filter:

$$G_C^*(s) = \frac{G_M^{-1}(s)}{(\tau_\mathrm{f} \cdot s + 1)^2} = \frac{Z_M(s)}{(\tau_\mathrm{f} \cdot s + 1)^2} \tag{18}$$

The filter time constant is the only tuning parameter of the controller, making the tuning process much easier. A low value of the time constant leads to a smoother response but also a lower bandwidth. A high value, however, leads to a noisy system, especially in case there are some significantly discrepancies between system and model or in case of model uncertainties.

5 The simulation models and simulation results

5.1 Estimating the damping coefficient of a real servo valve

In order to estimate the damping coefficient of a real valve, some parameters must be taken into account. The damping coefficient depends on a number of factors like viscosity, temperature, the clearance between the spool and the sleeve, the number and the length of the spool's shoulders. Some authors have proposed the following formula to calculate the damping coefficient /14/, /15/:

$$c_\mathrm{D} = \eta \cdot n \cdot l_\mathrm{s} \cdot R_0 = \nu \cdot \rho \cdot n \cdot l_\mathrm{s} \cdot R_0 \tag{19}$$

where the equivalent radius is:

$$R_0 = \frac{8\pi \cdot (R_2^2 - R_1^2)}{R_2^2 + R_1^2 - \frac{R_2^2 - R_1^2}{ln(R_2/R_1)}} \tag{20}$$

withR_1 the spool radius and $R_2$the sleeve radius respectively.

Property	Density	Viscosity at $+40^oC$	Viscosity at $+100^oC$
Value	0.880	46	6.7
Units	$[g/cm^3]$	$[mm^2/s]$	$[mm^2/s]$

Table 2: Some properties of hydraulic oil HLP46 according to DIN51524 specifications (LIQUIMOLY)

For a nominal size NG10 of a given servo valve, the spool diameter is $D_1 = 2 \cdot R_1 = 9.992\ mm$and the sleeve diameter is $D_2 = 2 \cdot R_2 = 10.000\ mm$. The spool has four shoulders, each having a length of $l_s = 6\ mm$. With the values of the parameters given in table 2, the calculated damping coefficients for 40°C and 100 °C are $c_{D40} = 91.5\ N \cdot s/m$ and $c_{D100} = 13.3\ N \cdot s/m$. respectively.

5.2 The impedance of the system under control

The total system impedance can be calculated by taking the inverse of the transfer function given by equations16 (system) and 17 (model). A Matlab code was written to calculate the overall impedance as a function of the frequency and to represent the corresponding curves.

The impedance curve of the system under IMC control, shown in figure 7 with dashed line, corresponds to the ideal case, as the transfer function of the model perfectly matches the transfer function of the system. A smooth change in phase can be observed and a 90^o phase shift, between the current and applied voltage, occurs at a frequency above 1000 Hz. The IMC control theoretically allows the overall system to behave like a pure resistive impedance of 1Ω, at the frequencies lower than the low pass filter corner frequency $f = 1/\tau_\mathrm{f}$.The PI control (dotted line), allows to reduce the overall impedance to a value of about 4Ω,for frequencies lower than resonant frequency, as well as the peak resonance to a value lower than 10Ω.

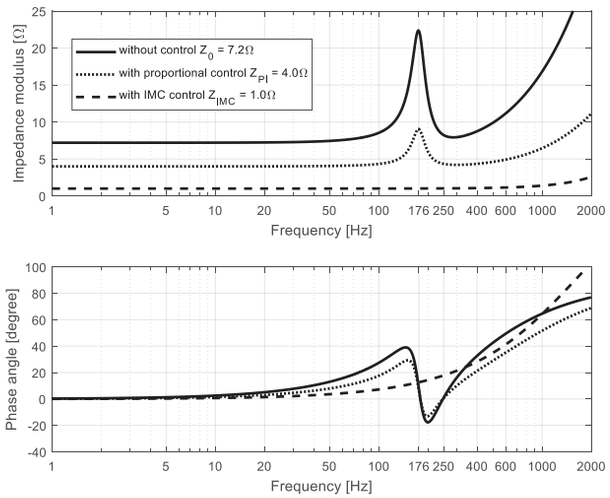


Figure 7: Comparison between impedance curves using different control strategies

The Bode plot in figure 8 shows the frequency behaviour of the system for three cases. The represented curves correspond to the open loop behaviour (dotted line), closed loop with PI control (dashed line) and closed loop with IMC control (continuous line) respectively. In all three cases the speed feedback was switched on.

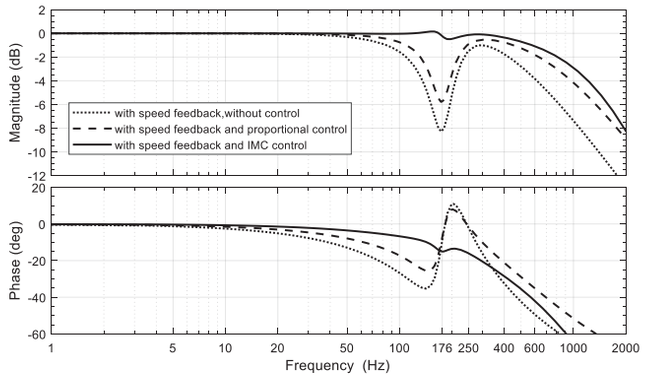


Figure 8: Current dynamics - Bode plot

To highlight the effect of a system-model mismatch, an overestimated damping coefficient was taken into account for the model ($c_D = 20$and $c_D^* = 35$). The corresponding behaviour can be observed around the resonant frequency (176 Hz). The -3dB frequency lies at a frequency of about 1000 Hz in case of IMC control with a smooth behaviour along the frequency.

5.3 Stability of the system under IMC control

To verify the stability of the controlled system both the transfer function of the system $G_S(s)$, as well as the transfer function of the controller $G_C^*(s)$, were converted in a state-space representation /16/.

$$\begin{cases} \dot{x} = A \cdot x + B \cdot u \\ y = C \cdot x + D \cdot u \end{cases} \quad (21)$$

with x, the vector of state variables, A, the state matrix, B, the input matrix, u, the vector of the input signals, y, the vector of the output signals, C, the output matrix, and$D$, the feed forward matrix. Next,the eigenvalues of the state matrix A for both the system and the controller is calculated. Using dedicated Matlab code /20/, with dedicated function and using the numerical values given in table 1 and $\tau_f = 0.1$ms, the eigenvalues are:

$$eig(A_S) = 10^3 \cdot [-2.39 \quad -0.39 + 1.15 \cdot i \quad -0.39 - 1.15 \cdot i] \quad (22)$$

with A_S being the system state matrix and

$$eig(A_{C^*}) = 10^3 \cdot [-10 + 6.02 \cdot 10^{-8} \cdot i \quad -10 - 6.02 \cdot 10^{-8} \cdot i - 0.25 + 1.8 \cdot i \quad -0.25 - 1.8 \cdot i] \quad (23)$$

with A_{C^*} being the controller state matrix. All real part of the state matrix eigenvalues are negative, thus both the system and the controller are stable. Based on the property of the IMC structure, if both the system and the controller are stable and the model matches the system, the closed loop is stable as well.

5.4 The Simulink simulation model

The Matlab-Simulink model /20/, includes both types of control (PI and IMC) to allow the comparison of step responses for the same set point, as well as for the same disturbances. Both models include also the speed feedback already described. The simulation model was driven first by an input signal of 2A (figure 10), at the simulation time $t = 5ms$ and the system was loaded with a disturbance signal of -1.5 A (at time $t = 20ms$), which represents 75% of the input signal (heavy load).

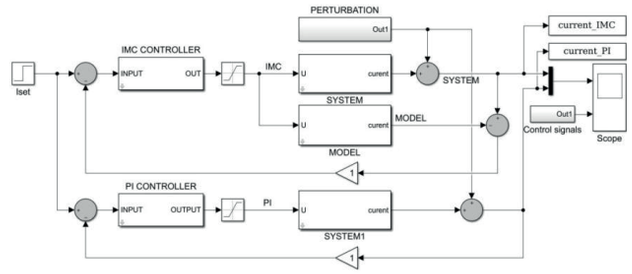


Figure 9: The simulation model - Simulink

A fast, smooth and also overshoot free response can be observed in case of IMC control, thus proving its robustness. The disturbance is also fast and smooth rejected.

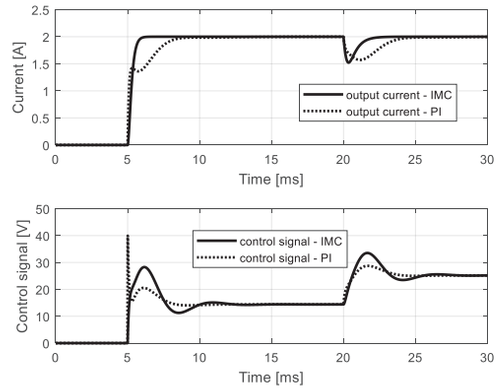


Figure 10: Comparison between step responses with two controller types

In contrast, the system response under PI control takes more as double the time to approach the steady state value, for both the input as well as the disturbance signal. Moreover, the response shows a slight undershoot.

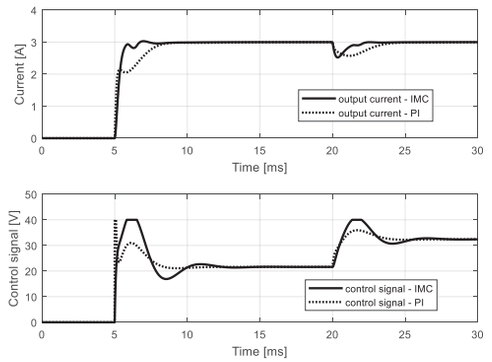


Figure 11: The effect of the voltage limitation at higher set point currents (3A)

Appropriate saturation blocks were introduced in the simulation model to simulate the voltage limitation of the controller. The limits were set to ±40V. As it has been shown in figure 10, a higher voltage reserve from the power supply can be observed in case of IMC control (about 10V for 2A current set point). In comparison, the control signal in case of PI control goes already in saturation. In the next test case, the model was driven by a higher input signal of 3A, as shown in figure 11, and the disturbance signal was maintained at the same level as

above. The control signal goes in saturation for both models. The IMC response takes longer time to approach the steady state, but is obviously faster than PI response and shows a slight undershoot. As a recommendation, a higher voltage supply than nominal voltage of the voice coil motor is required (usually 50% higher) in order to ensure a faster transient phase, a smoother response and a good ability to overcome the effect of disturbances, especially in case of higher input signals, as well as in case of high level of disturbances.

6 Summary and Conclusion

The paper deals with a comparative study of different control strategy types, applied to overcome the increase in impedance of voice coil motors at resonance frequency and its effects on the overall transient behaviour. The speed feedback, proportional-integral control (PI) and internal model control (IMC) strategies are presented and discussed. The proposed models were investigated and interpreted using the electrical analogy. Several improvements are shown and implemented in simulation models in order to stabilise and to lower the impedance over a wide range of frequencies, thus increasing the bandwidth. The numerical values of the parameters used in simulation, correspond to a prototype already developed by the authors. Finally, simulation results are presented and discussed. The future work will be focused on experimental research to verify and test the model validity and to make appropriate adjustments, in order to achieve better performances. The development of an accurate load impedance model, corresponding to a real valve and the investigation of its influence on the actuator-valve assembly are also future objectives.

7 Acknowledgements

Part of this work was supported by the German Academic Exchange Service (DAAD) and the Institute for Fluid Power Drives and Systems at RWTH Aachen University (IFAS).

Nomenclature

Variable	*Description*	*Unit*	*Variable*	*Description*	*Unit*
u	Coil supply voltage	[V]	i	Coil current	[A]
R_e	Coil DC resistance	[Ω]	L_e	Coil total inductance	[H]
m	mass of coil assembly	[Kg]	x	Coil position	[m]
k_{emf}	Back-emf constant	[V s/m]	k_F	Motor force factor	[N/A]
k_E	Suspension stiffness	[N/m]	c_D	Damping coefficient	[N s/m]

References

/1/ Reichert, M., *Development of High-Response Piezo-Servovalves for Improved Performances of Electrohydraulic Cylinder Drives,* Thesis RWTH Aachen University, Shaker, Aachen, Germany, 2010.

/2/ *Direct Operated Proportional DC Valve Series D1FP*, www.parker.com, 2017.

/3/ Ruggeri, M., Marani, P., *A New High Performance Roto-Translating Valve for Fault Tolerant Applications*, SAE Technical Paper 2014-01-2403, 2014.

/4/ Ruggeri, M., Marani, P., *New Roto-Translating Valve Functional and Safety Feature Analysis*, 9th JFPS International Symposium on Fluid Power, Matsue, Japan, 2017.

/5/ Roemer, D.B., Bech, M.M., Johansen, P., Pedersen, H.C., *Optimum Design of a Moving Coil Actuator for Fast-Switching Valves in Digital Hydraulic Pumps and Motors*, IEEE/ASME Transactions on Mechatronics Volume 20, Issue 6, December 2015, Article number 7084166, Pages 2761-2770.

/6/ Guo, H., Wang, D., Xu, J., *Research on a high-frequency response direct drive valve system based on voice coil motor*, IEEE Transactions on Power Electronics, Volume 28, Issue 5, Article number 6313926, Pages 2483-2492, 2013.

/7/ Wu, S., Jiao, Z., Yan, L., Zhang, R., Yu, J., Chen, C.-Y., *Development of a direct-drive servo valve with high-frequency voice coil motor and advanced digital controller*, IEEE/ASME Transactions on Mechatronics Volume 19, Issue 3, Article number 6523134, Pages 932-942, 2014.

/8/ Nascutiu, L., Reinertz, O., Siebert, C., Murrenhoff, H., High Performance Actuators for Fluid Power Drives, The 9th International Fluid Power Conference, vol. 3., Aachen, Germany; 03/2014.

/9/ Nascutiu, L., *Voice Coil Actuator for Hydraulic Servo Valves with High Transient Performances*, Automation, Quality and Testing, Robotics, 2006 IEEE International Conference, Cluj-Napoca, Romania, pp. 185 – 190, May 25-28, 2006.

/10/ Schmitz, J.,Vatheuer, N., Murrenhoff, H., *Hydrostatic Transmissions: A Power Play in Wind Turbine Design*, Hydraulics & Pneumatics, 2013.

/11/ Anton, I., Vekas, L., *Brochure Magnetic Fluids – a special category of nanomaterials, proprieties and applications*, Romanian Academy –Timisoara Branch and "Politehnica" University Timisoara, 2002.

/12/ Schurer, H., *Linearization of Electroacoustic Transducers*, Thesis University of Twente Enschede, ISBN 90-365-1032-5, Print Partners Ipskamp, Enschede, Netherlands, 1997.

/13/ Thorborg, K., Unruh, A., Struck, C., *An Improved Electrical Equivalent Circuit Model for Dynamic Moving Coil Transducers*, Audio Engineering Society, Convention Paper presented at the 122th Convention, Vienna, Austria, May 5-8, 2007.

/14/ Deacu, L., Banabic, D., Radulescu, M., Ratiu, C., *Tehnica Hidraulicii Proportionale,* Dacia, Cluj-Napoca, 1989.

/15/ Lescenko, V.A., *Ghidravliceskie slediascie privodî stankov s programnîm upravleniem,* Mașinostroenie, Moskva, 1975.

/16/ Levine, W. S., *The Control Handbook, Second Edition: Control System Fundamentals*, CRC Press, 2010.

/17/ Levine, W. S., *The Control Systems Handbook, Second Edition: Control System Advanced Methods*, CRC Press, 2010.

/18/ Tham, M. T., *Internal Model Control*, Chemical and Process Engineering, University of Newcastle upon Tyne, 2002.

/19/ Muhammad, D., Ahmad, Z., Aziz, N., *Implementation Of Internal Model Control (IMC) In Continuous Distillation Column*, The 5th International Symposium on Design, Operation and Control of Chemical Processes, PSE ASIA 2010, Singapore, July 25-28, 2010.

/20/ *** www.mathworks.com, *Control system toolbox*

The optimization design algorithm of hydraulic components under multiple operating conditions

Jiaming Wang *, Pengfei Wang**, Jun Zou*, Xiaodong Ruan*, Xin Fu*

Zhejiang University, State Key Laboratory of Fluid Power and Mechatronic Systems, Zheda Rd. 38, D-310027 Hangzhou, China*
Zhejiang University City College, School of Engineering, Huzhou St. 51, D-310035 Hangzhou, China**
E-Mail: wjm0@zju.edu.cn

With the rapid development of industry, the dynamic performance of hydraulic components has drawn more and more attention /1/. In many hydraulic systems, it is difficult to optimize the designs of the flow components because of many complex parameters and dynamic flow field/2/. At the same time, it is necessary to find out the key structure areas that affect the relevant hydraulic performance and ensure that multi-parameters are optimized synchronously. In this study, the multi-conditions optimization design algorithm is proposed to achieve the optimization of hydraulic components (for example, the throttle valve) by combining the adjoint method and the mesh deformation technique.

Keywords: Optimization, adjoint method, mesh morphing, multiple conditions
Target audience: Design Process

1 Introduction

Many fluid machines have a variety of working conditions, such as the valve at different openings. And control valve characteristic curves and pump dynamic characteristics are both the main performance indicators. Therefore, we need to focus on these performance in the design of these fluid machines. The core of the optimization problem is how to establish the relationship between structural parameters and performance requirements of hydraulic valves /3/. Most of traditional methods are based on stochastic optimization algorithm, and the optimal model is selected by filtering the throttle characteristic data of different parameter models /4/. These traditional methods are mainly based on experience or stochastic optimization. The disadvantage of these methods is blindness, which takes a lot of computing time. Gradient-based algorithms guide the direction of optimization, which is widely applied in aerodynamics. The adjoint method, which was proposed by Pionneau /10/, offers an efficient alternative for computing gradient. With the method of adjoint method, the gradient between performance targets and structural parameters is obtained in only two steps, the primal solver and the adjoint solver. The performance index of this study is dynamic performance, which is manifested in different working conditions. Dynamic performance is the multi-objective performance under various working conditions. In fluid calculations, this problem requires the dynamic grid technology because of the changing of fluid boundary. By adjoint method, the gradient of the fluid boundary mesh for each working state is calculated. In order to achieve optimal deformation of the fluid machine, it is necessary to ensure that the mesh topology on the boundary under different states keep in accordance. Radial Basis Function(RBF) mesh deformation method has been widely used in CFD simulations with moving boundaries due to its high robustness and accuracy/9/. RBF morphing can transform the surfaces of the original model into a new position or shape. In this study, RBF morphing is used not only for rigid dynamic motion but also for optimizing deformation.

The purpose of the study is the establishment of the gradient relationship between throttle valve structure parameters and the flow characteristic curve/5/. The amount of changes in the optimization parameters is quantified by means of computational fluid dynamics. According to the working characteristics of the throttle valve, this study presents the multi-conditions optimization design algorithm combing adjoint solver and Radial Basis Function(RBF) mesh deformation technology. Compared to the generalized optimization design, the optimization strategy in this paper not only reduces the time and cost, but also directly finds out how key parts affect the performance under multiple operating conditions, and it can be also applied to the design of other fluid mechanical components.

2 Methodology

2.1 Adjoint method

An adjoint method can be applied to elegantly compute the sensitivities of the cost function wrt. each mesh cell, which can be fed into a gradient-based optimization algorithm/8/. The constraint of the flow domain in a optimization problem is steady state Navier-Stokes equation. And the purpose of adjont method is to obtain the gradient relationship between the cost function and the design parameters. The flow variables are expressed as velocity $\mathbf{v}$, pressure p, and design variable α and the optimization target is expressed as the minimum value of J, then the problem can be written as

$$\text{minimize } J = J(\mathbf{v}, p, \alpha) \tag{1}$$

$$\text{such as } R = \begin{Bmatrix} (\mathbf{v}\cdot\nabla)\mathbf{v} + \nabla p - \nabla\cdot(2\nu D(\mathbf{v})) = 0 \\ \nabla\cdot\mathbf{v} = 0 \end{Bmatrix} \tag{2}$$

with kinematic viscosity ν and the strain-rate tensor $D(\mathbf{v}) = \frac{1}{2}(\nabla\mathbf{v} + \nabla\mathbf{v}^T)$.

It is difficult to calculate the $\frac{dJ}{d\alpha}$, but it can be tackled by reformulation the cost function with Lagrange multipliers $(\mathbf{u}, q)$ as follows:

$$L = J + \int_\Omega (\mathbf{u}, q)R\mathrm{d}\Omega \tag{3}$$

where R is the flow equation Eq. 3, Ω is the flow domain.

The partial derivative of L is as follows:

$$\delta L = \delta_\alpha L + \delta_{\mathbf{v}} L + \delta_p L \tag{4}$$

In order to get a direct relationship between L and α, the last two terms of Eq. 4 are set to zero.

$$\delta_{\mathbf{v}} L + \delta_p L = 0 \tag{5}$$

The integrands for $\delta\mathbf{v}$ and δp must be zero individually. After deduction, the adjoint equations are expressed as follows:

$$-2D(\mathbf{u})\mathbf{v} = -\nabla q + \nabla\cdot(2\upsilon D(\mathbf{u})) - \frac{\partial J_\Omega}{\partial\mathbf{v}} \tag{6}$$

$$\nabla\cdot\mathbf{u} = \frac{\partial J_\Omega}{\partial p}$$

The specific expressions of adjoint equations depend on the chosen cost function. As the adjoint equations are like the primal flow equation, they can use the same discrete solver. But adjoint boundary conditions need to be specified, these are

$$\mathbf{u}_t = 0 \tag{7}$$

$$u_n = -\frac{\partial J_\Omega}{\partial p}$$

$$\mathbf{n} \cdot \nabla q = 0 \quad \text{at wall and inlet}$$

$$q = \mathbf{u} \cdot \mathbf{v} + u_n \cdot v_n + \upsilon(n \cdot \nabla)u_n + \frac{\partial J_\Gamma}{\partial v_n} \tag{8}$$

$$0 = v_n \mathbf{u}_t + \upsilon(n \cdot \nabla)\mathbf{u}_t + \frac{\partial J_\Gamma}{\partial \mathbf{v}_t} \quad \text{at outlet}$$

After solving the adjoint equations for **u** and q, the sensitivities can be computed according Eq. 4

$$\frac{\partial L}{\partial \alpha_i} = \mathbf{u}_i \cdot \mathbf{v}_i V_i \tag{9}$$

2.2 RBF morphing

RBF provide a very general and flexible way of interpolation in multi-dimensional spaces, even for unstructured data where it is often impossible to apply polynomial or spline interpolation/9/. In the RBF morphing, mesh is updated by a function of motion of control points. The interpolation function s(x) representing the displacement of mesh points, consists of a series of functions:

$$s(x) = \sum_{j=1}^{N_b} \gamma_j \phi(x - x_{b,j}) + q(x) \tag{10}$$

Where x is the interpolation location, x_b is the set of N_b locations carrying the data, $\emptyset(x)$ is the basis function, dependent on point distance and q(x) is the polynomial function, depending on choice of basis function and γ_j.

It is needed for the consistency of interpolation that all polynomials of the order lower than q(x) disappear at data points, equation is as follows:

$$\sum_{j=1}^{N_b} \gamma_j p(x_{b,j}) = 0 \tag{11}$$

The coefficients of the basis function are determined by a function,

$$\begin{bmatrix} s(x_{b,j}) \\ 0 \end{bmatrix} = \begin{bmatrix} \phi_{bb} & Q_b \\ Q_b^T & 0 \end{bmatrix} \begin{bmatrix} \gamma \\ \beta \end{bmatrix} \tag{12}$$

Where $s(xs_{b,j})$ is the function valve at interpolant locations, γ carries all γ_j coefficient and β carries all β_j coefficient, $\emptyset_{bb}$ carries the evaluation of the basis function for pairs of interpolation points, and Q_b is the rectangular matrix with $[1\ x_b]$ in each row. The Eq. 12 is difficult to solve using standard iterative techniques. A QR decomposition (direct solver) is very helpful for the computing of the dense matrix.

So, in the procedure of RBF morphing, we first establish locations of data-carrying x_b and their values, and then assemble and solve the equation set for γ and β using direct solver, finally we calculate values at desired locations by evaluating s(x).

3 Valve application

In the paper, the optimization design algorithm of hydraulic components under multiple operating conditions is described by taking the optimization of valve quick-opening characteristic as an example. The valve shown in Fig.1 represents the fluid field and inlet/outlet boundaries for a typical dynamic system component. To simplify the model calculation, we created a rotational symmetry model with 5-degree angle. The resulting mesh consist of approximately 62.056 thousand primarily grid points. The flow is assumed to be incompressible and steady state with physical properties derived from water at 20 °C.

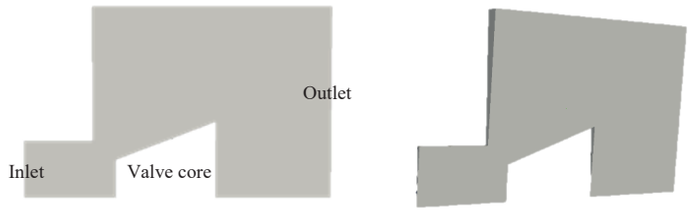


Figure 1: the model of the target valve fluid domain.

A hybrid formulation of the k-ε turbulence model is used, and constant inlet properties are set a static pressure of 1000 Pa and outlet properties are set an out pressure with 0 Pa. Velocity boundary conditions are zero-gradient everywhere except on the walls, where a fixed velocity of 0 is enforced. The solver is run initially to obtain a steady solution for the primal fluid field (1000 iterations).

4 Approach

4.1 Adjoint solver settings

We choose six different valve positions. After the mesh deformation, we get six fluid domains and perform flow field simulation for each flow field. Because the target of the study is the optimization of the control valve characteristic curve, the objective function of the adjoint solution is outlet flow rate.

$$J = \int_{\text{outlet}} v_n \mathrm{d}A \tag{13}$$

Substituting the objective function into the adjoint boundary equation gives a specific boundary condition setting.

$$\mathbf{u}_t = 0 \tag{14}$$

$$u_n = 0 \quad \text{at wall and inlet}$$

$$\mathbf{n} \cdot \nabla q = 0$$

$$q = \mathbf{u} \cdot \mathbf{v} + u_n \cdot v_n + \upsilon(n \cdot \nabla)u_n + 1 \quad \text{at outlet} \tag{15}$$

$$0 = v_n \mathbf{u}_t + \upsilon(n \cdot \nabla)\mathbf{u}_t$$

Since the sensitivity in Eq. 9 can't be calculated on the boundary due to the zero velocity on the boundary. So, we set the sensitivity on the boundary mesh cell as the data on the boundary.

4.2 Mesh morphing settings

In order to reduce the impact of mesh deformation on the calculation results, the boundary parallel to the valve core moves with the valve core. So, in the RBF morphing, motion control points are located on the valve core and parallel boundaries of it, static control points are located around the inlet and outlet and other boundaries move with deformation. The movement speed of valve is 0.02 m/s, and the valve is changed from full close to full open in 1s time. Six intermediate states are selected in the study.

In the shape optimization process, increasing the sampling rate of the control points can improve the deformation accuracy. The steepest descent method is used to transform the gradient data into control point deformation. The deformation coefficient is 1.2e-4.

5 Results

Fig 2 shows the meshes of six positions of valve. The mesh topology in the fluid domain between them does not change during motion. This reduces the effect of warping grids on the fluid calculations. In the meantime, the grid on the left side of valve core is stretched and the grid on the right is compressed.

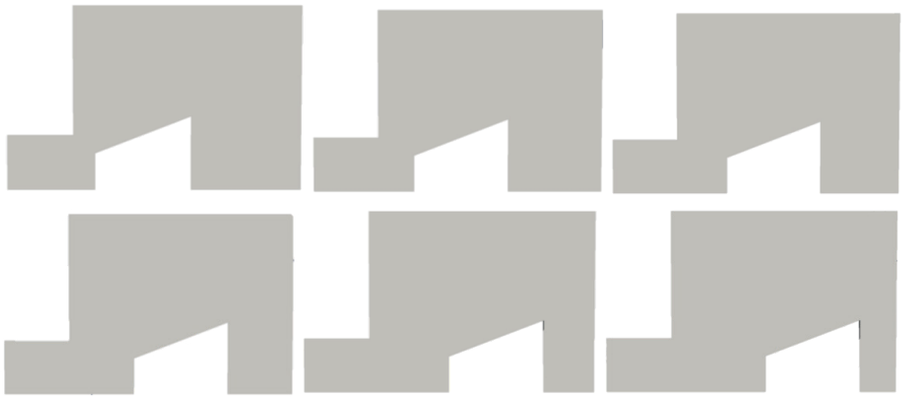


Figure 2: the models of valve core in different positions.

In the Fig 3, the sensitivity results of valve core boundary to the flow rate are shown. Positive(negative) values represent that the objective function can be reduced by displacing to the outside(inside) of the fluid field. Under each location, the influence of the boundary structure on the flow rate is different. In order to improve the quick opening characteristics of the valve, the flow rate in the middle position needs to be enlarged. From the sensitivity results, we can obtain regions that is helpful for increasing the flow rate in the opening state without affecting the flow rate in the fully open state. The sensitivity data in the opening states is screened with the sensitivity data in the fully open state (state 6). Then the sensitivity data for each state is linearly combined as the source of the overall optimization. The coefficient data can be chosen according to the different requirements of the valve. In the study, all coefficients are set 1 by default.

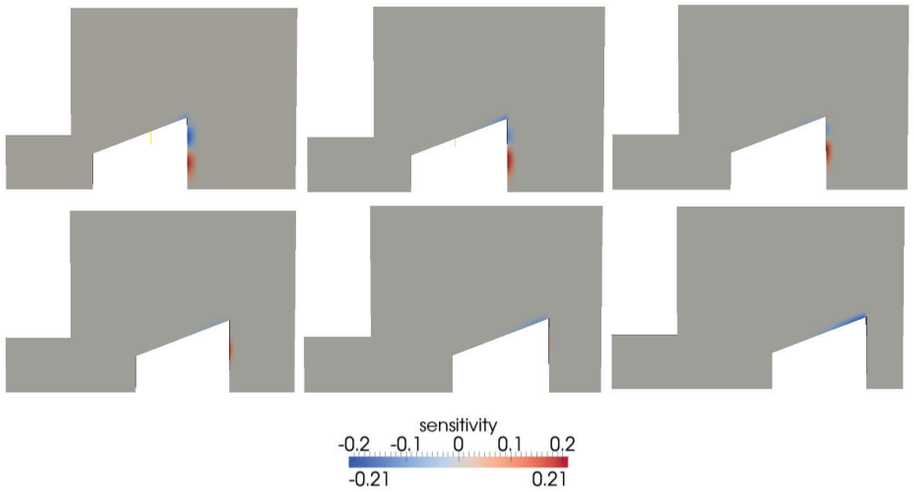


Figure 3: the sensitivity distribution of valve cores in different positions.

In the Fig 4, the deformation results of the valve core are shown.



Figure 4: the shape of optimized valve core.

In the Fig 5, the comparison chart of the flow characteristic before and after optimization are shown. The calculation results show that the optimization process helps to improve the quick opening characteristics of the valve.

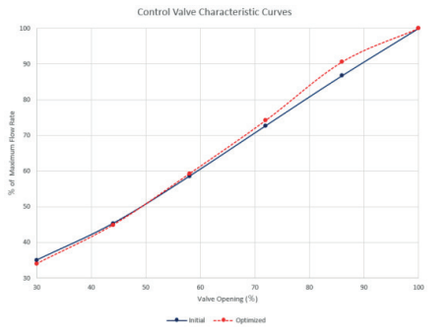


Figure 5: comparison char of valve characteristic curves.

Creating more state models can improve the accuracy of the calculation. The method is also suitable for optimizing other valve performance, such as cavitation performance.

6 Summary and Conclusion

The adjoint method is one of the fastest growing areas in CFD research and has great application prospects in the design of automated products. The calculation of the sensitivity derivatives is equivalent to the cost of the solution of the primal problem, which gives adjoint methods a huge advantage compared stochastic optimization. However, there are still many problems that need to be addressed in the practical application process. The hydraulic components not only need to meet the design requirements in the rated operating conditions, but also need to have good robustness and stability in the dynamic process /6/. The optimization under multiple operation conditions is the focus of this paper. The research presented here is based on the application of continuous adjoint of the incompressible Naiver-Stokes. In the first stage, the specific objective function is derived. After the solution of the primal and the adjoint equations, the sensitivity derivatives are calculated /7/. And then the geometric structure and mesh distribution are changed with sensitivity derivatives. Finally, after a series of iterations, the optimization model can be successfully obtained /8/. In the whole process, the most critical part is how to get relations between the design parameters and the objective function. It is very important for a comprehensive analysis of the entire optimization process that sensitivity information for each grid point can be calculated. For the multiple conditions optimization, how to build an optimal relationship under various conditions is the key issue. A simple solution is as follows, models under different operation conditions are created and calculated separately, and then the structure is improved by comparing the sensitivity of different calculation results. We have presented the theory underlying the computation of adjoint surface sensitivity and RBF morphing into the dynamic performance optimization. The application of the developed code to optimization of valve port flow characteristics demonstrated the potential of this methodology. During the optimization process, all grids are updated synchronously, and sensitivity derivatives contains the optimization information of all models. The presented method is developed in the open-source optimization tool based on OPENFOAM 2.2.

However, this method still has many problems in practical application: the adjoint solutions of some optimization objectives have very poor convergence and it is necessary to improve the calculation accuracy. After many iterative calculations, the mesh deformation causes the quality to drop, which will affect the fluid calculation. Further work is needed in excellent mesh deformation technology without affecting the calculation of flow field. In addition, for complex transient conditions optimization, selecting a reasonable multi-objective to ensure the accuracy of the calculation is of great help to the practical application of the method.

7 Acknowledgements

This work was supported by the National Basic Research Program of China [Grant No. 2015CB057301]; and the Science Fund for Creative Research Groups of the National Natural Science Foundation of China [GrantNo.51521064].

Nomenclature

Variable	*Description*	*Unit*
p	Static Pressure	[Pa]
v	Velocity	[m/s]
$\boldsymbol{v}_t$	Tangential speed	[m/s]
v_n	Legal speed	[m/s]
V	Grid volume	[m^3]

References

/1/ Liang J, Yuan X, Yuan Y, et al. Nonlinear dynamic analysis and robust controller design for Francis hydraulic turbine regulating system with a straight-tube surge tank[J]. Mechanical Systems & Signal Processing, 2017, 85:927-946.

/2/ Shi L, Tang F, Xie R, et al. Design Optimization of Axial-Flow Pump Blades Based on iSIGHT[C]// ASME/JSME/KSME 2015 Joint Fluids Engineering Conference. American Society of Mechanical Engineers, 2015.

/3/ Yamaguchi K, Kondo H, Kawamori K. Studies on the Characteristics of the Flow and the Flow Rate in Throttle valve with a Divergent Sectional Groove [J]. Journal of Applied Polymer Science, 2002, 84(84):256-260.

/4/ Zhu B H, Liu Y S, Zhuang yun L I, et al. Experimental Investigation of the Flow Characteristics of Throttle Valves in Water Hydraulics and Development of a New-type Water Throttle valve[J]. Machine Tool & Hydraulics, 2004.

/5/ Kondo M, Kim S J, Fujiwara Y, et al. Sensitivity analysis and design optimization of three-dimensional non-linear aeroelastic systems by the adjoint method[J]. International Journal for Numerical Methods in Engineering, 2003, 56(56):911-933.

/6/ Liang J, Yuan X, Yuan Y, et al. Nonlinear dynamic analysis and robust controller design for Francis hydraulic turbine regulating system with a straight-tube surge tank[J]. Mechanical Systems & Signal Processing, 2017, 85:927-946.

/7/ Karpouzas GK, De Villiers E, Schumacher T. Industrial application of an adjoint level-set based optimization method. 9th OpenFOAM Workshop. Zagreb, Croatia, 23-26 June 2014.

/8/ Othmer, Carsten, Eugene de Villiers, and Henry G. Weller. "Implementation of a continuous adjoint for topology optimization of ducted flows." In 18th AIAA Computational Fluid Dynamics Conference, June. 2007.

/9/ Bos, Frank M., Bas W. van Oudheusden, and Hester Bijl. "Radial basis function based mesh deformation applied to simulation of flow around flapping wings." Computers & Fluids79 (2013): 167-177.

/10/ O. Pironneau, On optimum design in fluid mechanics, Journal of Fluid Mechanics 64 (01) (1974) 97–110.

The Development of an integrated monitoring and filtration system for performance assurance of hydraulic mould oscillation systems used in continuous casting machines at flat steel plants

Taher Salah El-Din, Karim El-Gewily, and Mohamed El-Shafie

EZDK-EZZ-Dekhila Steel Company/Utilities, Repair and Construction division, Central Repair Department,
Alexandria-Matrouh highway – Dekhila – Alexandria, Egypt
E-Mail: melshafie@EZZSteel.com.eg

Abstract

In flat steel industry, a hydraulic mould oscillator (HMO) sophisticated mechanism is frequently used to provide oscillatory motion to the steel casting mould. The HMO system is highly sensitive to oil contamination, accordingly for the sustainability of operation, oil contamination level must be monitored and controlled to ensure that it meets system requirements. While continuous oil filtration had been practiced in EZDK Co. factory in past years, now a novel approach is being adopted that incorporates online monitoring of oil contamination level and its control via an external filtration unit. This approach lowers filtration unit electric power consumption and increases its service life-time.

Keywords: HMO, mould, oil cleanliness, oil filtration unit, servo, cylinder
Target audience: Mobile Hydraulics, metallurgical industries.

1 Introduction

In flat steel industry, a sophisticated hydraulic mould oscillator (HMO) mechanism is frequently used to provide an oscillatory motion to the steel casting mould (3) via two hydraulic servo cylinders (1) and (2) , as shown in Figure 1 /1/. The two electro-hydraulic servo cylinders (1) and (2) are driven by two hydraulic servo valves, one valve for each cylinder. The performance of the HMO system can be influenced by many parameters including oil contamination level of cylinders and valves.

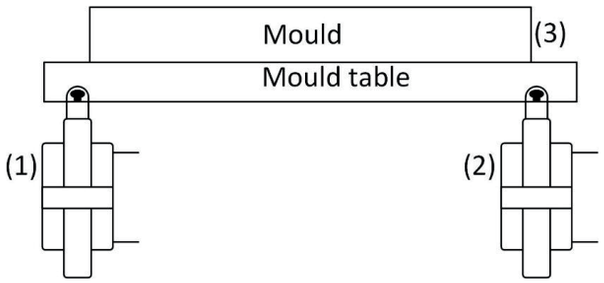


Figure 1: Hydraulic mould oscillator mechanism.

Thus oil contamination level has to be continuously monitored and controlled via a proper oil filtration unit /2/. Formerly continuous filtration was adopted in EZDK Co. factory, however in recent years with the significantly increasing costs of electric energy supply for domestic and industrial facilitates, it became necessary to seek a new approach. Accordingly a modern integrated solution has been introduced to maintain the required oil cleanliness level for the HMO system and decrease the running hours of the filtration unit, to lower its depreciation rate and increase service life time. The system consists of an on-line particle counter with electronic interface signal, an intermediate control system and a mobile oil filtration unit. The on-line particle counter sensor is connected in parallel with the pump delivery line that supplies oil to the servo valves, as shown in Figure 2. It samples and analyzes the delivery flow contamination and if the recorded contamination exceeds the permissible levels stated in the ISO 4406 standards, it automatically triggers a signal to the intermediate control circuit that starts the filtration unit till the triggering signal from the online particle counter is disabled. Figure 3 and Figure 4 show the layout of the system and the automatic control block diagram respectively.

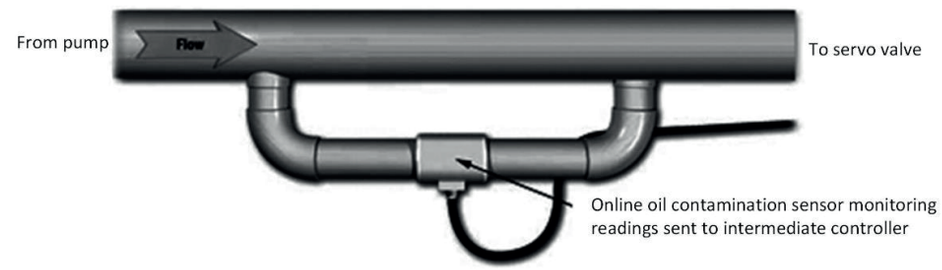


Figure 2:On-line continuous monitoring sensor connected to the pump delivery line.

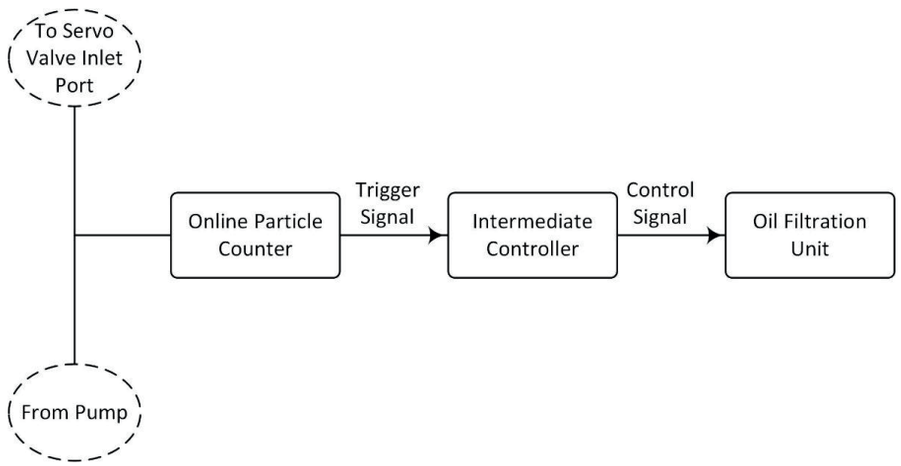


Figure 3: Layout of the system.

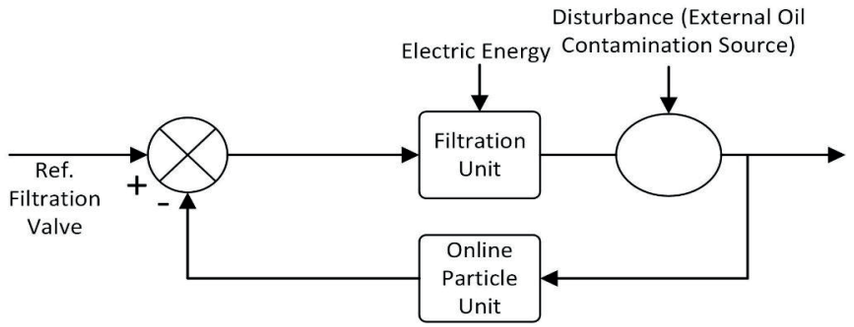


Figure 4: Block diagram of the monitoring and filtration system.

2 SYSTEM DESCRIPTION

2.1 The hydraulic circuit diagram of the HMO system

Figure 5 shows part of the hydraulic circuit diagram of the HMO system, which has an oil tank of capacity 3 m^3. Hydraulic power supply is provided via three axial piston pumps, each of geometric volume 125 cm^3 /rev., running at 1450 rpm, as well as one circulating screw pump of geometric volume = 132 cm^3 /rev, running at 1500 rpm for filtration and cooling purposes.

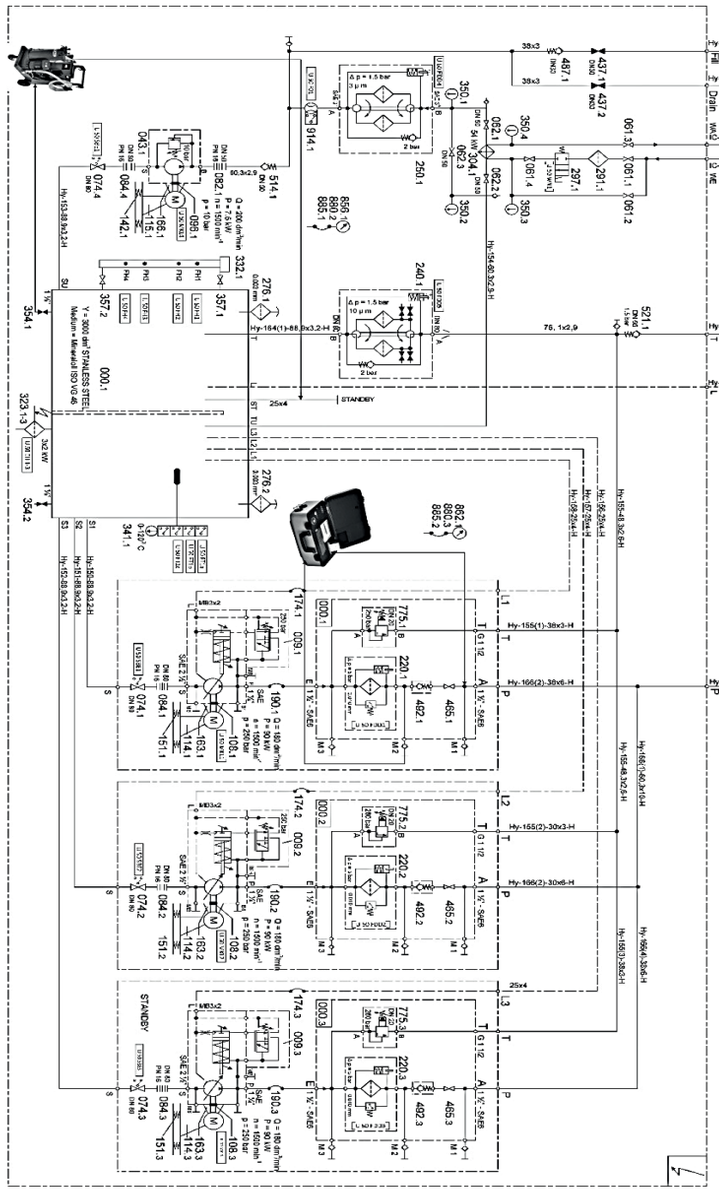


Figure 5: hydraulic circuit diagram of the HMO hydraulic system.

The pumps delivery line is equipped with one accumulator of 32 liter volume, and two manifold blocks mounted on the two servo cylinders that oscillate the mould mechanism, as shown in Figure 6. Each servo cylinder is driven separately via a hydraulic 3-stage servo valve.

The maximum pressure of the main hydraulic system is limited via the relief valve (No.775) to a pressure of 31.5 MPa. A high pressure filter (No.220) of filtrations 10 µm, filters the oil supplied by the pump. The pump delivery line includes a check valve (No.492), a shut off valve (No.465), an unloading valve (No.531) beside the accumulator (No.366).

The main filtration system of the HMO hydraulic system is composed of the twin inline filter unit for the main circulation system (No.250), pressure line filter (No.220) directly mounted at each pump delivery line, and the return line twin filter unit (No.240), in addition to a 3 µm fine filter allocated before servo valves (4) and (5).

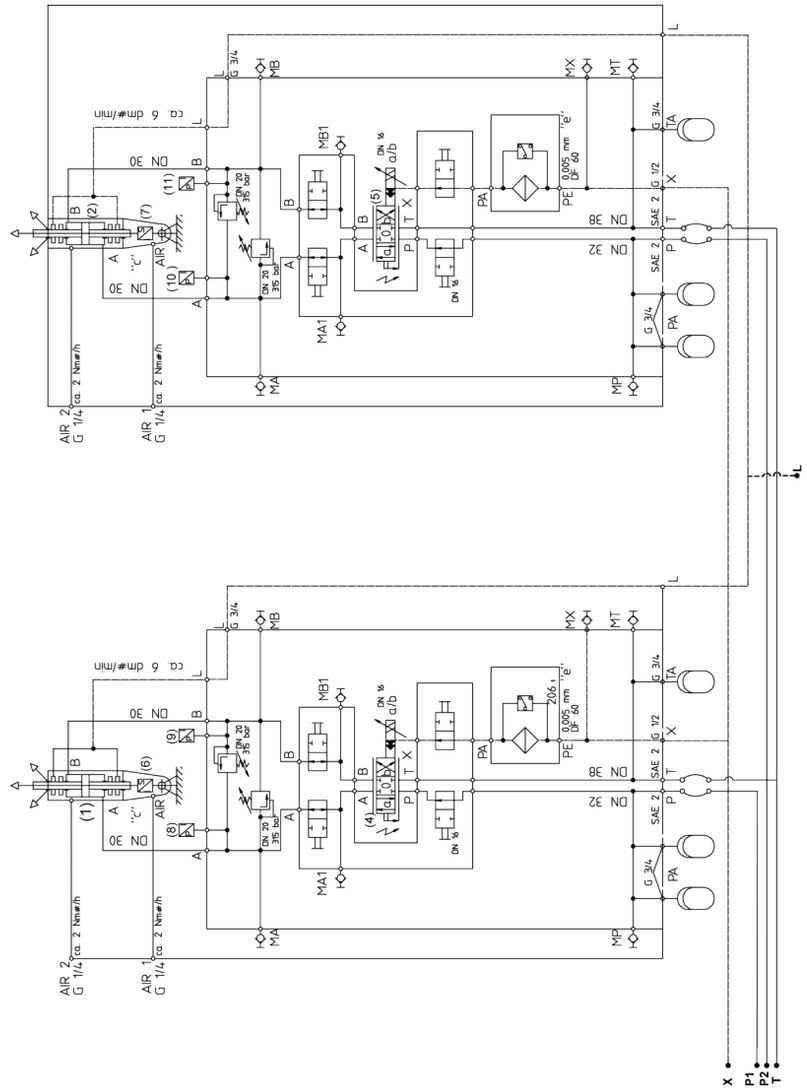


Figure 6: HMO mechanism.

In order to maintain HMO hydraulic system cleanliness below the critical value of permissible degree of contamination of pressure fluid which is 18/16/13 contamination class according to ISO 4406 /3/, an external filtration unit of type OFU10 was connected for years to the hydraulic tank and was run on a continuous basis for several weeks. An oil sample was taken every 4 weeks and tested to indicate the oil cleanliness level, and accordingly a decision was made to either keep the external filtration unit working or to disconnect it. Naturally this approach results in excessive power loss and rapid depreciation of the filtration unit. The continuous operation of the external filtration unit was found to consume about 2160kWhr per month.

2.2 Contamination sources in HMO

Contamination sources found in the HMO system are classified as external and internal sources of contamination. External sources of contamination come from exchanged parts such as hoses and valves as a result of routine maintenance activities .After parts exchange some dust and fibres enter in the system, while internal sources of oil contamination result of component wear during the normal operation of moving components such as axial piston pumps and servo cylinders.
Main wear metal elements found in this system are copper, chromium, iron and silicon, with an average concentration of 35, 24, 29 and 22 ppm respectively.

2.3 On-line particle counter type HIAC [PM4000]

This device is designed to measure and quantify the number of solid contaminants in hydraulic oils. The HIAC - PM4000 is a laboratory accurate instrument suitable for "on-site'' applications utilizing mineral oil as the operating fluid in the HMO /4/. The operation principle is based on light extinction, whereby a laser light beam passes through the fluid and hits on photodiodes. When a particle cut the beam it reduces the amount of light received by the diode, and from this change in the amount of received light, the size of the particle can be detected. Figure 7 shows the particle counter unit.
The particle counter has an alarm limit setting according to ISO codes for each particle size, and the alarm LED is activated (flickers) when this limit is exceeded.

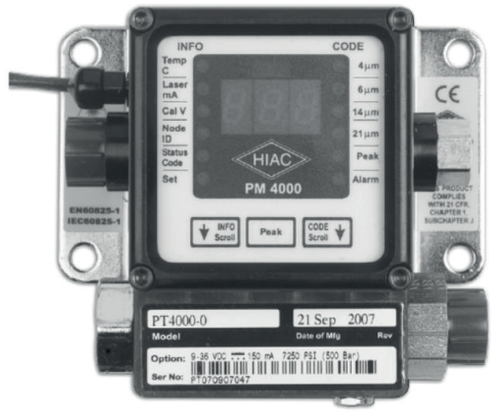


Figure 7: HIAC on-line particle counter type PM4000

2.4 Mobile filtration unit type HYDAC [OFU10]

The mobile filtration unit shown in figure 8 is used as an external filtration unit. It has a constant displacement pump of a flow rate of 100 l/ min that runs at a speed of 1500 rpm. It can filter all the oil in the HMO oil tank, of volume 3 m^3 that contains about 2000 lit of oil, in about 20 minutes for one filtration cycle. The filteration pump delivers the oil consequently to a 5 µm filter as shown in figure 9 , before returning to the HMO tank /5/.

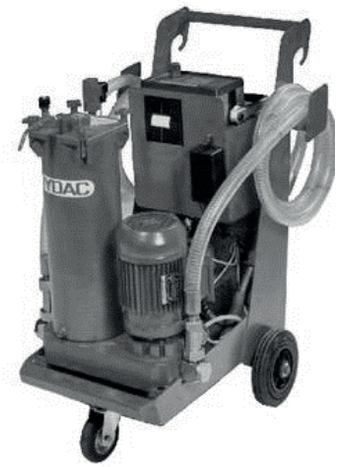


Figure 8: Hydac mobile filtration unit.

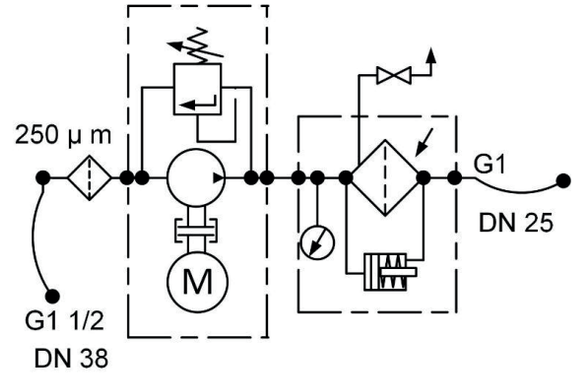


Figure 9: Hydac Mobile Filtration Circuit.

2.5 The Concept of the Detection/ Trigger System

The detection/ trigger system depends on the results recorded by the HIAC-PM4000 online particle counter, which flickers the alarm LED when the contamination level exceeds the ISO coded programmed limits. At the start of HIAC PM4000 the alarm LED flickers 4 times as an indication of system start up. To employ the alarm for contamination detection, a controller with dedicated logic must be interfaced with the particle counter. The detection is done by connecting the pins of the alarm LED from the particle counter to an ARDUINO UNO controller board and then the number of pulses(flickers) received from the LED pins are recorded. If the number of pulses exceeds 4 which is the start-up normal check up number, the controller will give a trigger signal to external relay to activate the filtration unit for a period of 20 minutes and then a reset signal is sent by the controller to stop the filtration unit and reset the particle counter alarm.

2.6 Control System

The control system is based on ARDUINO UNO controller board, set of relays, and a 3-phase contactor for powering the filtration unit as shown in Figure 9.

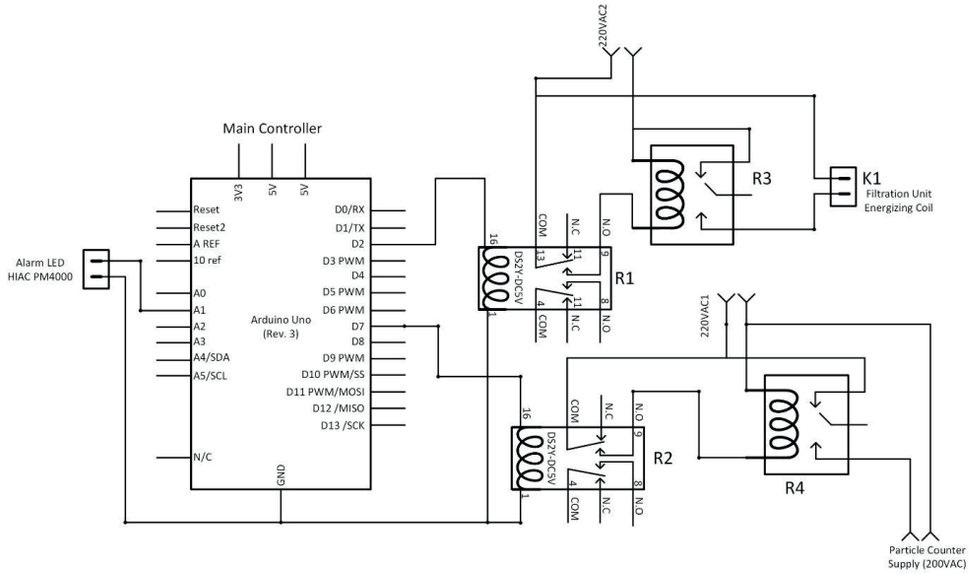


Figure 9: Schematic of control system.

3 Experimental work and results

The concept of contamination detection/ trigger of filtration unit depends on the number of flickers received from the particle counter alarm LED. The alarm in the particle counter device has been set to respond to the contamination level per millilitre for particles with a size larger than 4 µm, with target 18/16/13contamination class according to ISO 4406-1999. The alarm setting is shown in Figure 10. The controller is designed to wait for 15 incoming pulses “1”after the 4 pulses resulting at the start of work. After these 15 pulses have been counted “2”, a trigger signal “3” is initiated to start the filtration unit as shown in Figure 11.The filtration unit would run for 20 minutes after receiving the starting signal from the controller then, it will be shut down due to triggering signal being reset by the controller as shown in Figure 12.

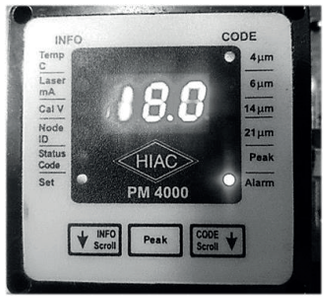


Figure 10: Alarm setting for 4µm particles with target ISO code 18/16/13 according to ISO 4406.

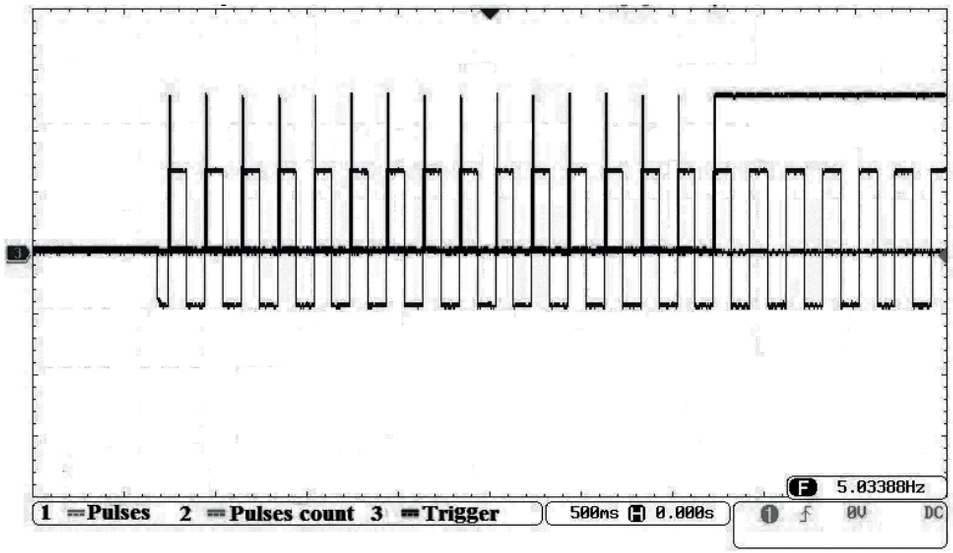


Figure 11: Trigger signal “3” goes up after set of pulses.

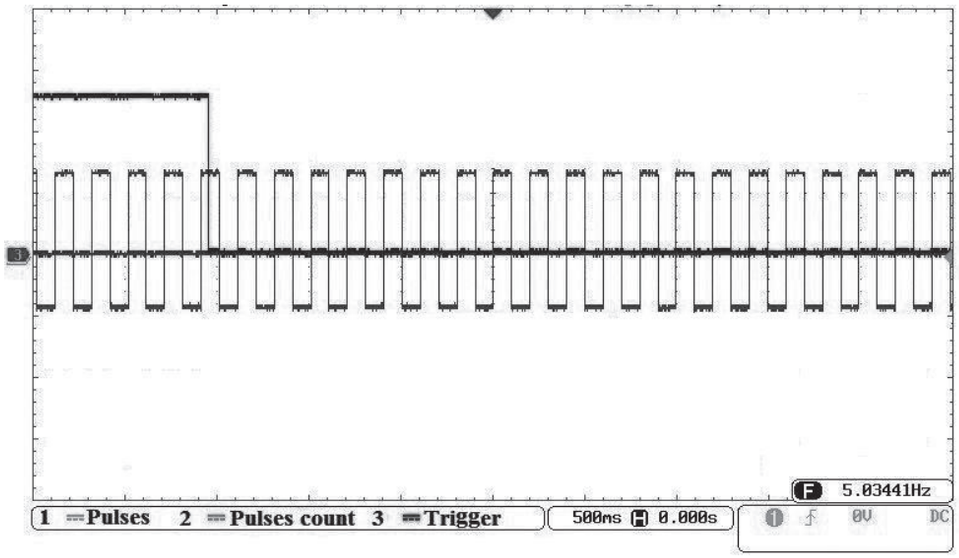


Figure 12: Trigger signal goes down after a period of time.

4 Summary and Conclusion

In any running hydraulic system, there are several sources of oil contamination. The usage of an on-line particle counter can be more effective compared with off-line monitoring, maintenance procedures based on periodical physical sampling and analysis either in an onsite or off-site laboratory. Equipped laboratories can run complete diagnostic checks on the lubricant, but in some cases it can take up to several days or even weeks to obtain the

oil analysis results. In the meantime, an unreliable system component may by then have completely failed, resulting in productivity downtime and major repair expenses. On the other hand, the continuous operation of the filtration system consumes power (when the contamination is eliminated), moreover this will decrease the life expectancy of the filtration unit. A control system is implemented to achieve filtration unit operation based the on-line particle counter when the contamination level reaches the set limit value, this allows good utilization for the filtration unit, saving power consumption by approximately 96 % and monthly reduction of the unit service hours by 680 hours.

Tests have been carried out on the HMO hydraulic system and results have confirmed the high reliability of the filtration/on-line monitoring device.

With such a system, considerable positive development on operation and maintenance costs of hydraulic servo systems can be realized.

5 Acknowledgements

The authors wish to expresses their sincere gratitude to EZDK Co. management for their support that enabled the implementation of this project. Thanks are also due to Professor Saad Kasem for his keen review of the present paper.

References

/1/ SMS DEMAG GmbH. 2002. Hydraulic mould oscillation functional description.

/2/ Salah El-din, T. 2010. Enhancement of Performance of an Electrohydraulic Servo System for Mould Oscillation Control in Continues Casting Machines. Ph.D. thesis, Faculty of Engineering, Cairo University, Egypt.

/3/ Bosch Rexroth,datasheetRE29595/10.02, Servo valve, 4-way version - Type 4WSE3EE.

/4/ HIAC,6 December 2007 - Edition 5,particle Counter PM4000, operator manual, RPS.

/5/ Hydac, OFU10, datasheet EN7936-4-09-17, filter pump transfer unit.

Experimental Investigation of a Directly Driven Hydraulic Unit in an Industrial Application

REVIEWED

Teemu Koitto*, Heikki Kauranne*, Olof Calonius*, Tatiana Minav*, and Matti Pietola*

Aalto University, Department of Mechanical Engineering, P.O. Box 14400, Espoo, Finland*
E-Mail: teemu.koitto@aalto.fi

Government-enforced regulations have led to increasing demands for energy efficient solutions in the industry. To diminish the losses of hydraulic systems and to increase their energy efficiency, several pump control methods have been developed. In this work, a new experimental direct drive actuator solution, powered directly by a servo motor controlled hydraulic pump-motor, is evaluated. As an additional innovative feature, a load compensating hydraulic circuit has been introduced in order to reduce power consumption even further. The study presents results of performance measurements of this new concept.

Keywords: direct driven hydraulics, electro-hydraulic actuator, displacement-controlled hydraulics, load compensation, industrial, experimental
Target audience: industrial applications, electro-hydraulic actuators

1 Introduction

Rapid rise of government-enforced regulations leads to increasing demands for energy efficient systems in every sector of industry and society. Traditionally, many hydraulically operated stationary industrial applications have been based on valve control principle, which in actual fact means controlling the system by controlling the system's losses. To diminish the losses and to increase the system's energy efficiency, several pump control methods have been developed. One typical variant of such system is a constant pressure circuit, which is based on a constant speed variable displacement pump equipped with a pressure controller. In this case, the pump strives to maintain a constant pressure level at its outlet port regardless of the required flow rate. In some cases, where the level of required flow rate varies significantly and is, however, on average on some intermediate level, this leads to oversizing the pump in relation to the average flow need just for ensuring the maximum required flow rate. In these cases, it is reasonable to use a smaller pump together with pressure accumulator, which acts as an energy reserve and a parallel flow source whenever high flow rates are required. Besides this, the accumulator also stabilizes the source pressure.

This kind of system, with its valve-controlled actuator, is able to produce high output powers with very low response times, mainly determined by the valve's response time. However, from the point of view of energy efficiency it suffers from the need to throttle the flow that goes to the actuator, which is due to the difference between the pump maintained pressure and the actual pressure need of the actuator. Especially in mass lowering and velocity decelerating cases in general the throttling need is typically very high and causes significant power losses.

A solution for overcoming these throttling problems is valve-less closed-circuit pump control where the flow rate to the actuator is directly controlled either by controlling the rotational velocity, the displacement of the pump or both. In these solutions the flow rate of the pump and the system's pressure level are always matched to the need of the actuator and the power loss generated in the system is minimized. These pump-controlled systems have been common in mobile hydraulics for a long time, but in stationary applications interest in them has in greater extent only awakened during the last decade. The main problems hindering their wide use in these applications have been the longer response times of the controlled quantity and the higher implementation costs compared to the valve-controlled systems. The development of electric drives and the decline of their prices has, however, enabled implementing pump-controlled systems that are competitive with valve-controlled systems in these respects. This has resulted in systems that combine high energy efficiency, high dynamics and relatively low prices.

During the last decade several studies have been published comparing closed circuit pump-controlled systems with valve-controlled systems, and in some studies also with pure electro-mechanical drives /1, 2, 3/. In these studies, the properties of the speed-controlled or in addition displacement-controlled pump-control systems were found to be fully competitive or even superior in comparison in terms of dynamics and energy efficiency. Most of the studies have been mainly theoretical studies, e.g. /4, 5/, but also some applied studies have been published, e.g. /6, 7/, albeit the number of these has been low in the recent past. In addition to the above-mentioned benefits of pump-controlled closed-circuit systems, several studies also demonstrate that the noise level and warming of the system is lower than with the other system types. Since the temperature raise is low and mostly due to the long fluid transferring lines, large fluid volume isn't required for cooling purposes, a solution for further reducing of the losses is packing the drive motor – pump – actuator to a compact actuator-specific entity, which means transition from central hydraulics to decentralized hydraulics.

With pump-controlled system the high variations in required actuator power do not cause any significant changes in the system's efficiency providing that the components are sized correctly. Furthermore, by equipping the actuator with a load compensating device, the energy consumption of the system can be further reduced.

Most of the problematics concerning pump-controlled systems are related to the stability of the actuator velocity when an asymmetric (differential) cylinder is used as an actuator, or when the work cycle of the actuator includes plenty of transitions between several operation points. The latter may lead to drastically reduced energy efficiency if the pump's speed-displacement-controller is optimized for merely static operation. These problems are addressed with different controllers and control strategies /8, 9, 10/, or with an asymmetric pump, whose inlet and outlet flows are matched to the piston areas of the actuator /11/.

2 Methods

In this section, an industrial case is introduced as an example application for a novel method to achieve a more energy efficient stationary industrial application. Chapter 2.1 presents the studied industrial case implemented with traditional valve-controlled system and also the proposed novel electro-hydraulic actuator, which is realized with a direct driven hydraulic (DDH) approach and a load compensating hydraulic circuit.

2.1 Studied industrial case

The studied case is an industrial application where an actuator is required to shift a large mass continuously between two vertical positions. The distance between the positions is 260 mm and each of the movements, either lifting or lowering, should be achieved in less than one second. 700 kg mass was used during the experiments.

In this paper two different hydraulic circuits for realizing the required function are investigated and their characteristics and performance compared. At this stage of research no requirements for cooling have been considered in either of the systems.

2.1.1 Traditional valve controlled system

Currently the industrial application is operated using a traditional valve controlled system illustrated in Figure 1.

A proportional 4-way valve controls the movement of the cylinder whose position is fed back to the electronics controlling the opening of the valve, no other feedback is used in this case. Instead of a simple supply pressure control with a fixed displacement pump and a pressure relief valve the system is for energy saving purposes realized with a pressure accumulator and a pressure controlled variable displacement pump.

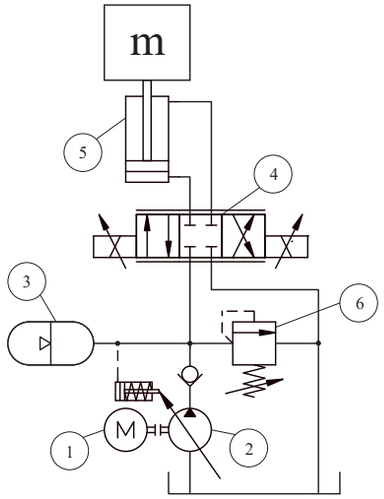


Figure 1: Traditional valve controlled implementation of studied industrial application, open circuit.

The flow needed to move the cylinder is taken from the accumulator and the displacement of the pump turns to a positive value whenever the accumulator requires a fill-up, otherwise the pump stays at zero displacement. The major components of the simulated system with their relevant data are listed in Table 1.

Number	Type	Description
1	Motor	1500 r/min
2	Pump	28 cm^3/rev
3	Accumulator	2.4 l, preload pressure 26 bar
4	Proportional valve	85 l/min, 5 bar/control edge
5	Differential cylinder	50/36 mm
6	Pressure relief valve	Opening pressure 150 bar

Table 1: Fluid power components of the simulated traditional system.

2.1.2 Electro-hydraulic actuator test setup

The second studied system is an electro-hydraulic actuator, Figure 2, where the cylinder position is controlled solely by pump rotation speed and direction. Design process for this circuit and further details on the industrial case is described in reference /12/. Pump and valves are mounted to a manifold that is directly attached to the main cylinder. Detailed component descriptions are listed in Table 2.

In the load compensating circuit, the pre-charge pressure of the 10 l accumulator (13) is converted into a vertical force, opposing the gravitational force of the load (m), with the differential cylinder. The pre-charge pressure is varied between the experiments in order to establish the circuit's energy saving potential. Three different magnitudes of load compensation were tested; a) Full in which the gravitational force of the load mass was fully compensated with opposing force of the compensator cylinder, b) Half in which half of the force of the load mass was compensated, and c) None in which the pressure in the compensating circuit was zero.

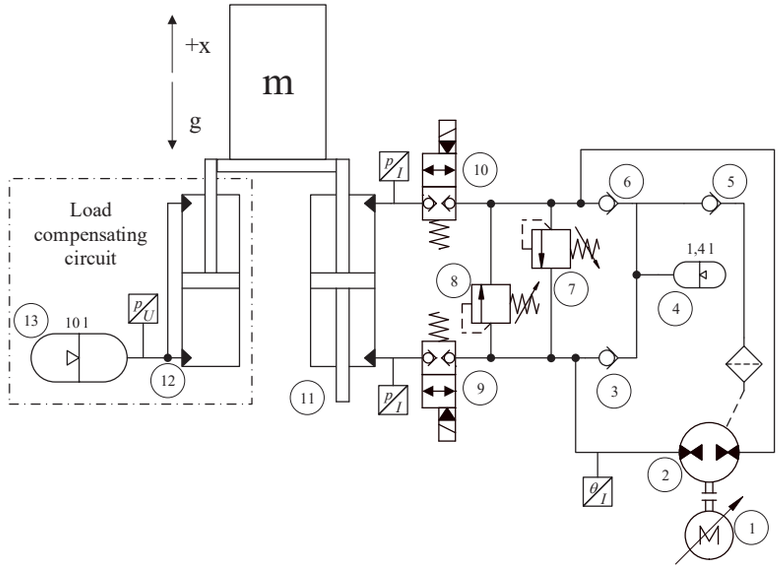


Figure 2: Novel pump controlled DDH implementation of studied industrial application, closed circuit.

Internal leakage of the pump-motor is fed back to the low-pressure side of the circuit via a filter and check valves. This section of the system also contains a small volume pressure accumulator which acts as a buffer and keeps the closed circuit filled with fluid in case of small external leaks.

Control and instrumentation of the test setup is done with a PLC as depicted in Figure 3. The PLC is running a central Sytronix controller /13, Fig. 6–12/, which is basically a PD controller, commanding the electric drive's (IndraDrive) control system that has a cascaded PI controller /14, Fig. 7–3/. Measured data from the system is acquired and the solenoids of safety valves (9, 10) are controlled through IndraControl S20 modules.

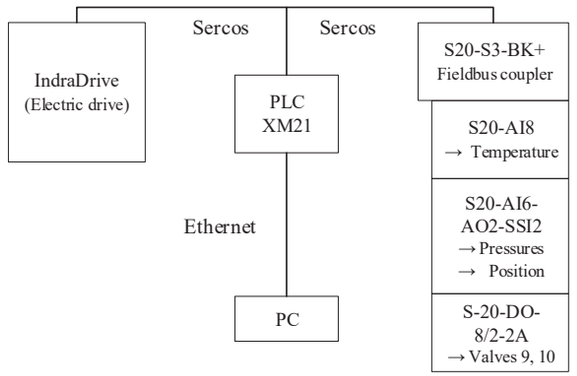


Figure 3: Control and instrumentation of the test setup.

Sytronix loop is operating with 4 ms cycle time, electric drive's velocity loop is running at 125 µs and current loop at 62.5 µs cycle time.

2.2 Simulations

The purpose of the traditional valve controlled system (Figure 1) was to be a benchmark for the novel pump controlled DDH system (Figure 2). Since measurements of an actual traditional system were not possible, the system was only simulated. Specifications for components used in the simulated system are presented in Table 1.

Performance of the simulated traditional system in terms of work cycle, cylinder transition and rise time was tuned to match the performance of the novel system in order to be able to compare the system's energy consumption characteristics in similar operational conditions. The results of the Matlab/Simulink/Simscape simulations are presented in Chapter 3.

2.3 Experiments

The experiments were made with a full scale test rig. The hydraulic circuits of the test rig are presented in Figure 2 and the components of the circuits are listed in Table 2.

	MAIN CIRCUIT		
Number	Type	Description	Details
1	Motor	Permanent magnet synchronous motor	Bosch MSK101E-0300-NN
2	Pump	Inline axial piston pump, 45 cm^3/rev	Bosch A10VZG045EZ400
11	Main cylinder	Symmetrical cylinder 50 mm piston 36 mm piston rod 300 mm stroke length	Bosch CGM1F3/50/36/300A20 /F11CKUTS42580
4	Accumulator	1,4 l bladder accumulator @ 2 bar	Bosch HAD1,4-250-1X
3,5,6	Check valve	Cracking pressure 0,3 bar	Sun hydraulics CXEE-XAN
7,8	Pressure relief valve	Opening pressure 160 bar	Bosch DBDS 10 K1X/200
9,10	Load holding valve		Bosch VEI8A2T12
	LOAD COMPENSATING CIRCUIT		
12	Cylinder	Differential cylinder 50 mm piston 36 mm piston rod 300 mm stroke length	Bosch CDM1MP5/50/36/300A20 /B11CFUMWW
13	Accumulator	10 l bladder accumulator	Bosch HAB10-330-6X

Table 2: Fluid power components of the test rig.

In addition to the fluid power components, the test rig has a significant number of electric and electronic components used for power supply and for measurement instrumentation, Table 3.

Sensors		
Pressure transducer	4-20 mA	Bosch HM 20-2X/250-C-K35
Pressure transducer	0-10 V	Bosch HM18-1X/210-V-S
Temperature sensor	4-20 mA	Ifm TA2405
Position sensor	Magnetostrictive, Analog output	Santest GYSE-A-650-N-CN-CD10
Electronics		
Motor	Permanent magnet synchronous motor	Bosch MSK101E-0300-NN
IndraDrive power section	Continuous current 95 A, Maximum current 150 A	Bosch HCS03.1E-W0150
Servo drive	Firmware version: MPB-20VRS	Bosch CSB02.1B-ET
PLC	Firmware version: MLC14VRS	Bosch XM21
Data acquisition		
I/O system	IndraControl S20	Bosch S20-S3-BK+

Table 3: Electric and electronic components of the test rig.

The motion sequence used in this study comprised a rapid lift followed by 1.5 s standstill before the load was returned to its starting positon for another standstill period, after which the next cycle began. The sequence consisted of five cycles and the same sequence was used regardless of the magnitude of load compensation (full, half, or none) used in the test. The starting position of the motion was 20 mm and the end position was 280 mm corresponding to a stroke of 260 mm. Since the maximum stroke of the cylinder was 300 mm, the actual motion left 20 mm piston travel unused in both ends. Figure 4 presents part of a motion sequence recorded with full load compensation. The position command from the PC to the Sytronix controller was of a rectangular shape (Master command), but the controller forwarded the command to the electric drive in a trapezoidal shape (Actual command). The (proprietary) controller is performing either setpoint rate limiting or motion profile planning. Throughout the study, a target velocity of 700 mm/s was specified for the actuator together with 8000 mm/s^2 acceleration in the control software.

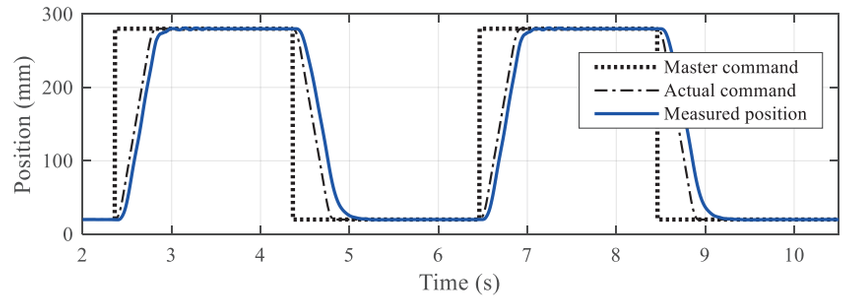


Figure 4: Part of the five cycle motion sequence.

Three test cases were run with the motion sequence, utilizing three different magnitudes of load compensation as described in Chapter 2.1.2.

The power consumption of the test setup was monitored in several locations (cf. Figures 2 and 5) in the system as the power was transferred from electric motor input power to mechanical shaft output power and onward to

hydraulic power utilized by the cylinder actuator, and finally to mechanical power delivered by the actuator to the load carriage.

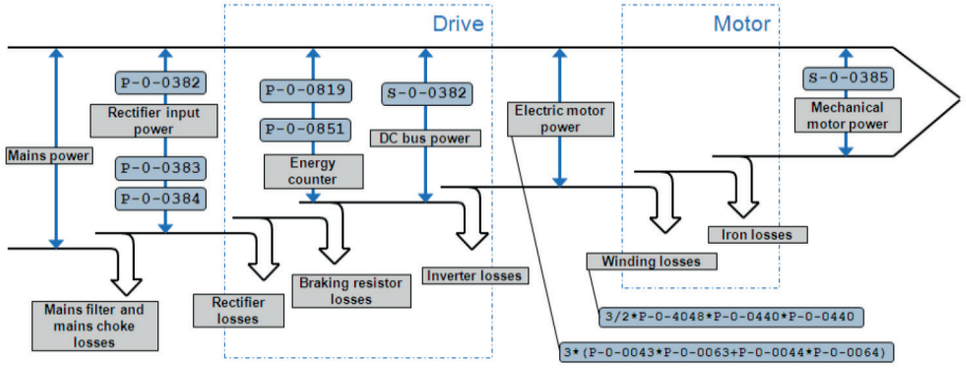


Figure 5: Energy and power parameters of the IndraDrive electric drive system. /14/

The energy counter of IndraDrive was selected to be monitored representing the energy consumption of the drive system. Electric motor power (effective electric power) transferred from the drive to the servomotor (motor input power) was calculated according to Equation (1) /14, Fig. 11–65/.

$$P_{\mathrm{e,m}} = 3 \times (I_{\mathrm{q}}U_{\mathrm{q}} + I_{\mathrm{d}}U_{\mathrm{d}}) \tag{1}$$

Mechanical output power of the servo motor was directly recorded by one of the axis parameters (S-0-0385) of the IndraDrive system.

The hydraulic power of the pump was computed using the port pressure of the pump and the actuator's flow rate, Equation (2)

$$P_{\mathrm{h,p}} = p_{\mathrm{p}}q_{\mathrm{V,p}} = p_{\mathrm{p}}v_{\mathrm{a}}A_{\mathrm{a}} \tag{2}$$

Hydraulic power of the cylinder was computed using the actuator's flow rates and port pressures, Equation (3). Actuator leakage was assumed to be zero, thus the inlet and outlet flow rates are equal.

$$P_{\mathrm{h,a}} = p_{\mathrm{a,in}}q_{\mathrm{V,a}} - p_{\mathrm{a,out}}q_{\mathrm{V,a}} = (p_{\mathrm{a,in}} - p_{\mathrm{a,out}})v_{\mathrm{a}}A_{\mathrm{a}} \tag{3}$$

The mechanical power delivered by the actuator was computed as a product of the cylinder output force times the linear speed of the load carriage, Equation (4).

$$P_{\mathrm{m,a}} = F_{\mathrm{m,a}}v_{\mathrm{a}} \tag{4}$$

The actuator output force was calculated as the sum of the compensated load (gravitational force minus force produced by the load compensation cylinder) and the force needed to overcome the inertia. The energy inputs and outputs of the different power transformers in the system were calculated by integrating the calculated powers.

3 Results

Simulation results of the valve controlled traditional system and the measurement results of the pump controlled DDH system are presented below. The legends used in the figures are as follows:

Master command	= Original position command	PressureA	= Pressure in lower cylinder chamber
Actual command	= Controller modified command	PressureB	= Pressure in upper cylinder chamber
Measured position	= Position of cylinder, measured	Pelec	= Electric power of electric motor
Simulated position	= Position of cylinder, simulated	Pmotor	= Mechanical power of electric motor
Lin velocity	= Linear velocity of cylinder	Ppump	= Hydraulic power of pump
Rot speed	= Rotational speed of electric motor	Pactuator	= Mechanical power of cylinder

Curves for one lifting-lowering cycle are presented; Figures 6–8 present results for the traditional valve controlled system and Figures 9–11 for the pump controlled DDH system.

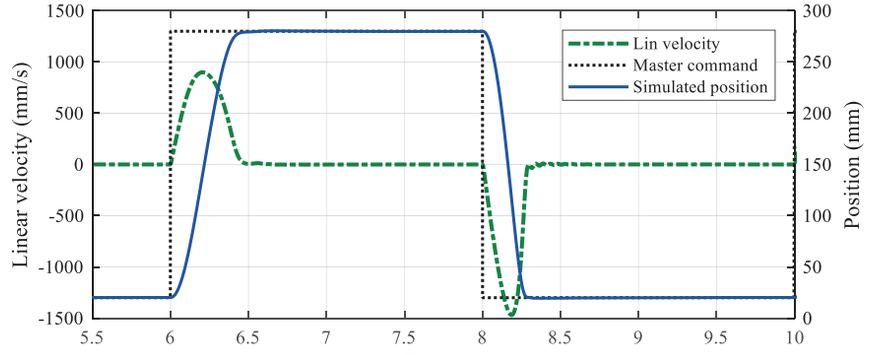


Figure 6: Simulation results; Traditional valve controlled system. Example curves for one lifting-lowering cycle, showing position reference and actual value, as well as measured linear actuation velocity.

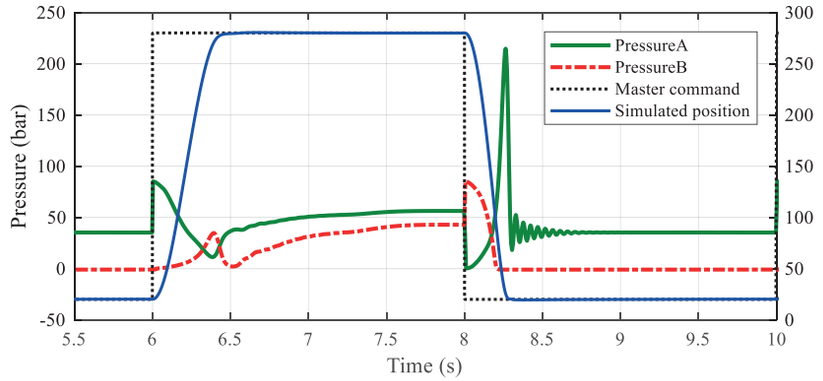


Figure 7: Simulation results; Traditional valve controlled system. Example of recorded chamber pressures together with the position curves for reference.

In Figure 8, at the beginning of the lifting phase the actuator is fed with the sum of pump and accumulator powers, and at the beginning of lowering phase in addition with the mass power, therefore during the transition phases there's a period when the actuator power is greater than the system's electric input power.

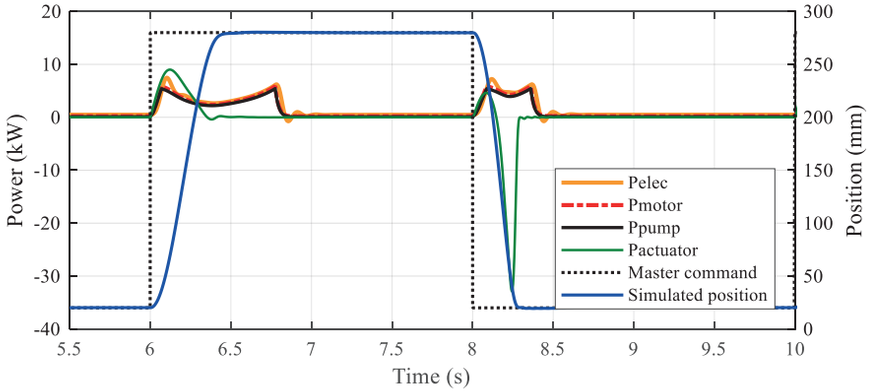


Figure 8: Simulation results; Traditional valve controlled system. Power curves corresponding to one lifting lowering cycle together with the position curves for reference.

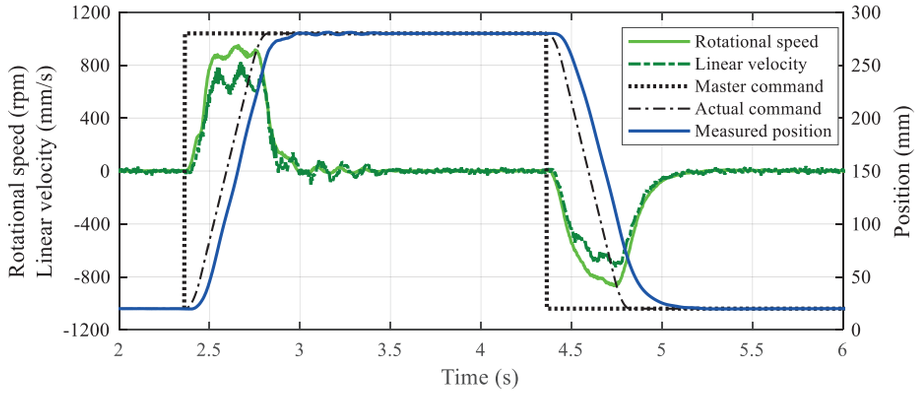


Figure 9: Experimental results; Pump controlled DDH-system. Example of one lifting-lowering cycle, showin rotational speed of motor and measured linear actuation speed as well as position reference and actual valu (test run without load compensation).

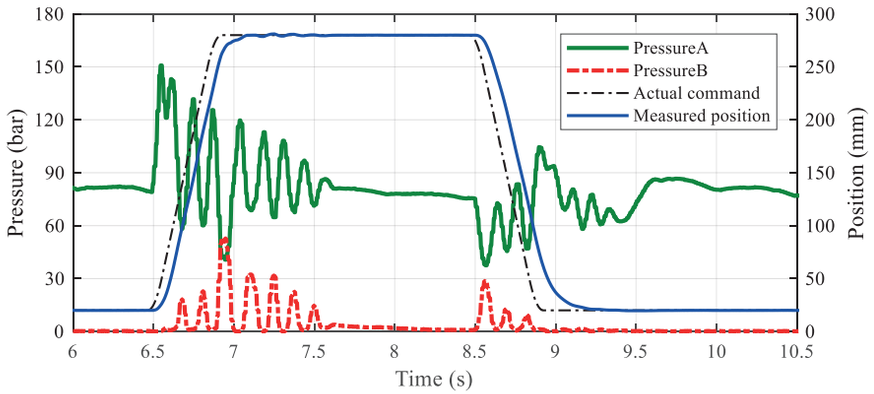


Figure 10: Experimental results; Pump controlled DDH-system. Example of chamber pressures for one lifting lowering cycle together with the position curves for reference (test without load compensation).

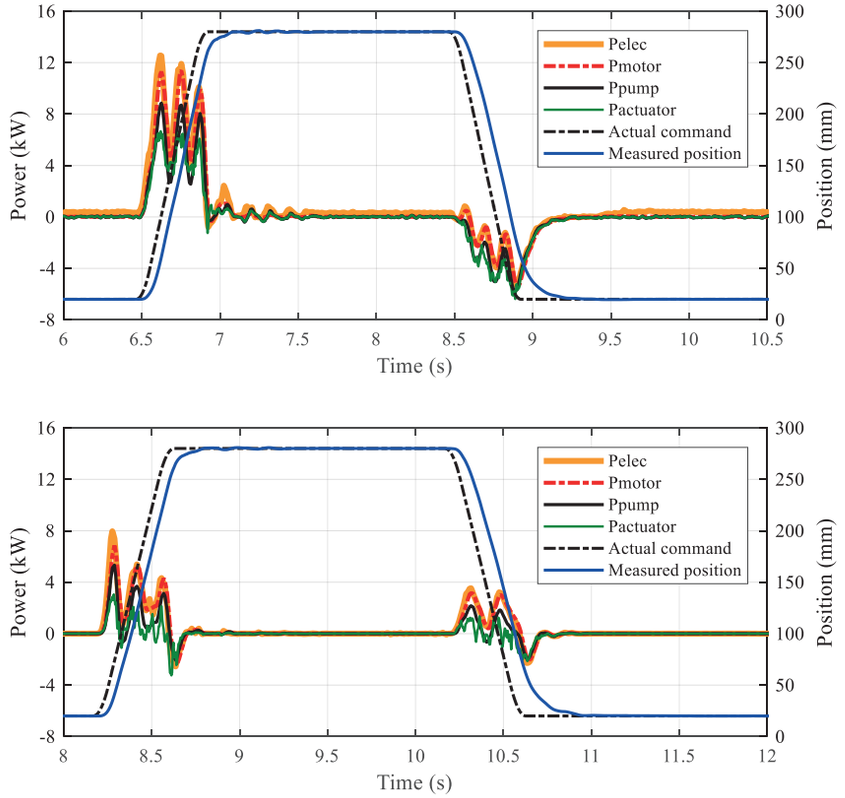


Figure 11: Experimental results; Pump controlled DDH-system. Power curves for one lifting-lowering cycle and position curves for reference. Above: test without load compensation, below: test with full load compensation.

The average energy consumption and possible recovery is shown in Table 4 as averages computed for five lifting-lowering cycles. In addition to the values per lifting-lowering cycle, separate values for lifting and lowering phases are shown for the hydraulic and mechanical energy of the actuator.

Load comp.	Energy counter $E_{e,c,c}$ [kJ]	Electric motor $E_{e,m,c}$ [kJ]	Electric motor $E_{m,m,c}$ [kJ]	Pump $E_{h,p,c}$ [kJ]	Actuator $E_{h,a,c}$ [kJ]	Actuator (lifting) $E_{h,a,lift}$ [kJ]	Actuator (lowering) $E_{h,a,lower}$ [kJ]	Actuator (lifting) $E_{m,a,lift}$ [kJ]	Actuator (lowering) $E_{m,a,lower}$ [kJ]
Full	1.80	1.67	1.59	0.75	0.75	0.99	0.42	0.15	0.10*
Half	2.27	2.03	1.69	0.73	0.73	1.65	0.20	0.99	0.93*
None	3.83	3.24	1.79	0.59	0.59	2.34	0.12	1.75	1.74*
Trad.sys.	N/A	6.37	5.13	4.45	3.03	2.11	0.91	2.63**	

N/A : Value is not available from simulation * : Recovery ** : Combined value for lifting and lowering

Table 4: Average energy inputs/outputs. During lowering phase, mechanical energy is recovered by actuator.

During the lifting phase the actuators of both systems require a certain hydraulic input energy to overcome the loading of the mass and friction forces. This energy is presented as parameter $E_{h,a,lift}$ in Table 4. During the lowering phase the mass's potential energy acts as the actuator's driving force which together with the hydraulic driving force generated by the pressure in the motoring (upper) chamber of the actuator pushes the piston downwards thus generating mechanical power (Figures 8, 11). This power is transmitted to the pumping (lower) chamber of the actuator via the piston and transformed into hydraulic power/energy, which can be recovered. The variable $E_{h,a,lower}$ expresses the hydraulic input energy that is required in the upper chamber to drive the actuator to the lower position from its upper position. The recoverable energy generated during the lowering phase is presented in Table 5. In the traditional system, energy is not recovered, but converted into heat in the system's control valve.

Load comp.	Energy counter $E_{e,c,rec}$ [kJ]	Electric motor $E_{e,m,rec}$ [kJ]	Electric motor $E_{m,m,rec}$ [kJ]	Pump $E_{h,p,rec}$ [kJ]	Actuator $E_{h,a,rec}$ [kJ]	Actuator $E_{m,a,rec}$ [kJ]
Full	-0.56*	-0.54*	-0.51*	-0.15*	-0.15*	0.10
Half	0.26	0.28	0.31	0.66	0.66	0.93
None	1.09	1.13	1.18	1.55	1.55	1.74
Trad.sys.	N/A	N/A	N/A	N/A	N/A	N/A

N/A : Energy recovery not available in simulated system * : energy is not recoverable

Table 5: Average energy inputs/outputs during the lowering phase in the different test runs.

4 Discussion

In this research, a typical working cycle of a stationary industrial lifting application was studied. The energy inputs and outputs of the main components in both a traditional fluid power implementation (Figure 1), and a novel pump controlled implementation (Figure 2) were compared. The traditional valve controlled implementation was modelled and simulated with Matlab/Simulink/Simscape for reference purposes against the pump controlled DDH implementation. The model was tuned to match the measurement results of the DDH system to enable straight comparison between these two systems. Although actual dimensioned component data was used in the models available in Simscape, the somewhat simplified formulation of these models may affect the simulation results. In practice, the losses of the simulated system, characterized by the difference in energy consumptions between the electric input energy of the drive motor and the mechanical output energy of the cylinder actuator (Table 4), may be somewhat underestimated because of the simplifications.

The DDH implementation was studied experimentally. In all three test cases (with different load compensation), the actuator tracked the position reference of the Sytronics controller reasonably well. There were only small oscillations after the target position had been reached, Figures 10–11. Also, the target stroke time set for this study (260 mm in less than one second), was reached. For example the rise time for reaching 98 % of the stroke for the different load compensation cases were: no compensation 0.55 s, half 0.53 s, and full compensation 0.54 s.

The results manifest strong pressure fluctuations (Figure 10) during both lifting and lowering phases. These were concluded to arise because of the mechanical imperfections in the test rig, which had excessive clearances between the vertical guide rails and the rollers of the load carriage. During its motion, the carriage hit both the sides and bottom of the rails several times in an oscillatory way and thus the rollers were not carrying the carriage throughout the movement like they were expected to. This caused changing friction forces, which in turn caused some variation in the actuator's load. Because the relation between cylinder velocity and the rotational speed of the pump depends on the cylinder load, e.g. /11/, both the cylinder's velocity and pump's rotational speed varied during the movement which was observed in the measurements (e.g., Figure 9). The phase shift between these variations caused pulsation in the inflow of the actuator's working chamber. This in turn resulted in high pulsation in the working chamber's pressure because of the relatively low chamber volume and the low compressibility of the fluid. The pulsation continued for a while after the actuator had reached its target position, this was concluded to result from the spring-mass nature of the system and also from the fact that the pump also kept on pulsating at very low speeds until the actuator settled to its target position causing similar inflow pulsation of the working chamber as during the fast movement. The measured pressure pulsations are naturally reflected in the calculated powers of Figure 11. In order to reach smoother operation, the rail-roller system should be modified.

The results show that the energy consumption of the DDH system is considerably lower than that of the traditional valve-controlled system. This is perhaps best reflected in the $E_{e,m,c}$ values (electric energy input to the motor) in Table 4. The differences in energy consumptions were due to two major factors; firstly, the hydraulic losses of DDH system were lower because of the absence of the actuator controlling valve, and secondly, because the closed circuit DDH was able to recover energy, which was not possible in the simulated open circuit valve-controlled system. Furthermore, the utilization of load compensation reduced energy consumption quite significantly. If using a DDH system without load compensation reduced the electric energy input by 49 % (3.24 kJ vs. 6.37 kJ), applying full load compensation further reduced the electric energy consumption by 48 % (1.67 kJ vs. 3.24 kJ). Thus the combined effect of using a DDH system with load compensation resulted in a reduction of 74 %.

The ability of DDH to recover energy due to regenerative braking depends on the level of load compensation (Table 5). Without load compensation the quantity of recovered energy is higher than with lower compensation levels, but also the consumption of energy is simultaneously higher. Actually, with full load compensation there is no energy to be recovered. This can also be deduced by comparing the power curves in Figure 11.

Load compensation decreases the load and pressure in the main circuit, which enables the use of a smaller diameter hydraulic cylinder. This can be used to increase actuator velocity or to decrease pump size, of which the latter is extremely valuable as it would decrease the rotational inertia of the pump enhancing its dynamics and make the system cost-wise more competitive compared to a traditional valve-controlled system.

5 Conclusion

This research has shown that pump controlled fluid power significantly reduces energy consumption in an industrial application for rapid-stroke handling of high loads, compared to a simulated valve controlled system based on traditional fluid power components. The energy consumption of the pump controlled DDH system was measured in experiments in a full scale test rig equipped with a hydraulic load compensation circuit and utilizing a motion sequence of five consecutive lifting-lowering actions. By using the DDH system, it was found that the electric energy input could be reduced by 49 % compared to the simulated traditional system. Moreover, a reduction of 74 % could be achieved when full hydraulic load compensation was used together with the DDH system. Indeed, utilizing a load compensation circuit appears to be an economical and simple solution for bringing down energy costs in this type of application. In summary, energy consumption values of the DDH system were in all tests substantially lower than the energy consumption values of the traditional system, indicating a large potential for energy savings in industrial fluid power systems.

The presented findings were based on short test runs. Therefore further studies should involve investigating the long term characteristics of the DDH system including, e.g., how the thermal conditions evolve during continuous usage and the possible need for cooling.

6 Acknowledgements

This research was enabled by the financial support of Tekes (the Finnish Funding Agency for Innovation, project EL-Zon), and internal funding from the Department of Mechanical Engineering at Aalto University, Finland.

The contributions of D.Sc. (Tech) Henri Hänninen, M.Sc. (Tech) Antti Sinkkonen, Mr. Ville Vidqvist, and Mr. Rainio Kuisma in making the test rig operational are greatly appreciated.

Nomenclature

Variable	*Description*	*Unit*
A_a	Piston area of actuator	[m^2]
$E_{e,c,c}$	Electric energy input value of energy counter for one lifting-lowering cycle	[kJ]
$E_{e,c,rec}$	Electric energy recoverable from frequency converter during the lowering phase	[kJ]
$E_{e,m,c}$	Electric energy input to electric motor for one lifting-lowering cycle	[kJ]
$E_{e,m,rec}$	Electric energy recoverable from servo motor during the lowering phase	[kJ]
$E_{h,a,c}$	Hydraulic energy input of actuator for one lifting-lowering cycle	[kJ]
$E_{h,a,lift}$	Hydraulic energy input of actuator for one lifting phase	[kJ]
$E_{h,a,lower}$	Hydraulic energy input of actuator for one lowering phase	[kJ]
$E_{h,a,rec}$	Hydraulic energy recoverable from actuator during the lowering phase	[kJ]
$E_{h,p,c}$	Hydraulic energy output of pump for one lifting-lowering cycle	[kJ]
$E_{h,p,rec}$	Hydraulic energy recoverable from pump during the lowering phase	[kJ]
$E_{m,a,lift}$	Mechanical energy output of actuator for one lift phase	[kJ]
$E_{m,a,lower}$	Mechanical energy recovered by actuator during one lowering phase (= $E_{m,a,rec}$)	[kJ]
$E_{m,m,c}$	Mechanical energy output from electric motor for one lifting-lowering cycle	[kJ]
$E_{m,m,rec}$	Mechanical energy recoverable from servo motor shaft during the lowering phase	[kJ]
$F_{m,a}$	Actuator force	[N]
I_d	Flux generating current	[A]
I_q	Torque generating current	[A]
$p_{a,in}$	Pressure in the working chamber of actuator	[Pa]
$p_{a,out}$	Pressure in the counter acting chamber of actuator	[Pa]
p_p	Pressure at pump outlet port	[Pa]
$P_{e,m}$	Electric input power of servo motor	[W]
$P_{h,a}$	Hydraulic input power of actuator	[W]
$P_{h,p}$	Hydraulic power of pump	[W]
$P_{m,a}$	Mechanical output power of actuator	[W]
$q_{V,a}$	Inlet and outlet flow rates of actuator	[m^3/s]
$q_{V,p}$	Pump outlet flow rate	[m^3/s]
U_d	Flux generating voltage	[V]
U_q	Torque generating voltage	[V]
v_a	Actuator velocity	[m/s]

References

/1/ Michel, S., Weber, J., *Energy-efficient electrohydraulic compact drives for low power applications*, Fluid Power and Motion Control FPMC 2012, September 12–14, 2012, Bath, Great Britain. ISBN 978-0-86197-187-9.

/2/ Boes, C., Helbig, A., *Electro hydrostatic actuators for industrial applications*, 9th International Fluid Power Conference, 9. IFK, March 24–26, 2014, Aachen, Germany. ISBN 978-3-9816480-1-0.

/3/ Helbig, A., Boes, C., *Electric hydrostatic actuation - modular building blocks for industrial applications*, 10th International Fluid Power Conference, 10. IFK, March 8–10, 2016, Dresden, Germany.

/4/ Räcklebe, S., Helduser, S., *Electric hydrostatic drive – a concept for the clamping unit of a high-speed 245 injection moulding machine*, Power Transmission and Motion Control PTMC 2007, September 12–14, 2007, Bath, Great Britain. ISBN 978-0-86197-140-4.

/5/ Tašner, T., Les, K., Tič, V., Lovrec, D., *Energy efficiency of different electrohydraulic drives*, 9th International Fluid Power Conference, 9. IFK, March 24–26, 2014, Aachen, Germany. ISBN 978-3-9816480-2-7.

/6/ Müller, K., Dorn, U., *Variable Speed Drives - Customer Benefits in Injection Molding Machines and Presses*, 7th International Fluid Power Conference, 7. IFK, March 22–24, 2010, Aachen, Germany.

/7/ Brahmer, B., *CLDP – Hybrid drive using servo pump in closed loop*, 8th International Fluid Power Conference, 8. IFK, March 26–28, 2012, Dresden, Germany.

/8/ Willkomm, J., Wahler, M., Weber, J., *Model Predictive Control of Speed-Variable Variable-Displacement Pumps to Optimize Energy Efficiency*, 9th International Fluid Power Conference, 9. IFK, March 24–26, 2014, Aachen, Germany. ISBN 978-3-9816480-0-3.

/9/ Willkomm, J., Wahler, M., Weber, J., *Potentials of Speed and Displacement Variable Pumps in Hydraulic Applications*, 10th International Fluid Power Conference, 10. IFK, March 8–10, 2016, Dresden, Germany.

/10/ Sun, Y., Imam, A., Wu, C., Sepehri, N., *Stability study of a pump-controlled circuit for single rod cylinders via the concept of Lyapunov exponents*, ASME/BATH 2017 Symposium on Fluid Power and Motion Control FPMC 2017, October 16–19, 2017, Sarasota, Florida, USA. ISBN 978-0-86197-187-9.

/11/ Quan, L., Ge, L., Wang, B. C., Li, B., Zhao, B., Lu, Z., *Performance of speed variable asymmetric pump controlled asymmetric hydraulic cylinder*, The 10th JFPS International Symposium on Fluid Power 2017, October 24–27, 2017, Fukuoka, Japan.

/12/ Hänninen, H., Minav T., Pietola M., *Replacing a constant pressure valve controlled system with a pump controlled system*, Proc. BATH/AASME 2016 Symposium on Fluid Power and Motion Control FPMC 2016, September 7-9, 2016, Bath, UK.

/13/ Rexroth HydraulicDrive 13VRS Central Controller Functional Description, Edition 2, R911336586, Bosch Rexroth AG, Germany, 2013

/14/ *IndraDrive MPx-20 Functions,* Application Manual, Edition 1, R911345608, Bosch Rexroth AG, Germany, 2017.

Reliability Evaluation of Hydraulic Pump Based on Performance Degradation

Xiaoping Liu*, Dejun Cui*, Lihang Wang* and Lijie Zhang*

Key Laboratory of Advanced Forging & Stamping Technology and Science, Ministry of Education of China, Yanshan University, Qinhuangdao Hebei 066004, China *
Hebei Key Laboratory of Heavy Machinery Fluid Power Transmission and Control, Yanshan University, Qinhuangdao Hebei 066004, China *
E-Mail: ljzhang@ysu.edu.cn

Aiming at the disadvantage of long time and high cost in the reliability evaluation of the hydraulic pump based on the life test or accelerated life test, a reliability evaluation method for hydraulic pump based on performance degradation is proposed. The stochastic volatility, individual differences and measurement errors have been considered in the creation of the degradation model. Compared with the method based on degradation path model and Wiener process model, it is necessary to consider the stochastic volatility with time, individual differences and measurement errors of performance degradation in the reliability evaluation of hydraulic pump based on degradation.

Keywords: Hydraulic pump, reliability evaluation, performance degradation, Wiener process
Target audience: Hydraulic Pump Manufacturer, Hydraulic Pump Customer, Aircraft Industry

1 Introduction

The hydraulic pump is the core component in the hydraulic system, and its reliability and remaining useful life have a vital influence on the reliability and health of the equipment. Therefore, the accurate evaluation of the reliability and the remaining useful life of the hydraulic pump has great significance to the failure prediction and health management (PHM) of the equipment [1-3]. At present, the reliability evaluation method based on life test or accelerated life test is common. In America, the standard of life test for military hydraulic pump has undergone a series of development such as MIL-P-19692C, MIL-P-19692D, MILP-19692E, SAE-AS19692A and so on. Russia has issued a series of guidelines for accelerated life test: OCT 100228-77, OCT 100389-80, OCT 100149-82, M4-73 and M35-84[4]. In the literature [5], the sensitive stress of hydraulic pump was analysed and the multiple stress accelerated model was given. In the literature [6], double – constant - stress sequential test was carried out by increasing the load, and the method of determining the sequential accelerated life test of the aviation gear pump was obtained. However, the reliability evaluation method based on life test or accelerated life test needs to observe the failure time of the product, which takes long time. The hydraulic pump has large power and long life. Carrying out the long life test not only consumes a lot of manpower and material resources, but also is not consistent with the rapid development demand of the hydraulic pump. Therefore, short time, high efficiency and accurate reliability estimation method is urgently needed.

The technology of reliability evaluation and life prediction based on performance degradation can obtain reliability information without failure, it has gradually become the development trend of reliability evaluation and remaining useful life prediction of highly reliable products with long lifetime[7-8], and has been widely unitilized in the models of degradation and reliability evaluation, such as LED[9], bridge beam [10], crack length [11] and lithium-ion battery[12], etc.It also provided a method of reliability evaluation and remaining useful life predicting of hydraulic pump. The hydraulic pump is a typical product with performance degradation. Affected by wear, temperature, load and other environmental factors, the characteristic parameters of its components will degrade and this phenomenon will result in the degradation of output flow the main performance index of piston pump. And soft failure will occur when performance degradation exceeds the specified threshold [13]. Based on this characteristic, literature [13] took piston pump flow signal as performance degradation parameter, based on considering randomness of degradation, combined with path tracing method and graphic method, reliability evaluation of piston pump is realized. In literature [14]，the signal of high temperature and low flow were taken as performance degradation parameter，and the change rule of reliability was obtained by using degradation path fitting method to analyse reliability of an aviation piston pump under constant stress accelerated degradation test (CSADT). Literature [15] took the signal of high temperature and low flow of piston pump as the degradation characteristic parameter. Under the CSADT, the least square method is used to fit the degradation path and multiple regression method is used to get the degradation model, and the life of the piston pump is successfully predicted. In literature [16], volumetric efficiency was taken as the signal of performance degradation and obtained the characteristic life of the axial piston pump by applying nonlinear least squares method and optimization theory to study the degradation path of performance parameters of hydraulic pump under accelerated stress.

It can be seen that the reliability evaluation of hydraulic pump based on performance degradation is relatively few, and smooth curves is used to fit the degradation path frequently. Because of the factors such as wear, environment, load and other uncertainties, the performance degradation path of the hydraulic pump has randomness. The impact of environment, instruments and manufacturing errors in manufacturing process result in the inconsistency of product degradation, that is, individual differences. The interference of the external environment or the inaccuracy of measuring instruments will result in the measurement errors. These factors have a certain influence on the reliability evaluation of the hydraulic pump. Therefore, in this article, the volumetric efficiency was taken as the characteristic parameter of performance degradation. Under the consideration of the individual differences and the measurement errors, we established the performance degradation process with stochastic characteristics of hydraulic pump based on linear Wiener process. The effectiveness and accuracy of the hydraulic pump reliability evaluation method proposed are demonstrated through case studies.

2 Degradation Model of Hydraulic Pump Based on Linear Wiener Process

2.1 Degradation model Based on Linear Wiener Process

Because of the uncertainty of the factors such as wear, environment, load and so on, the performance degradation path of the hydraulic pump has randomness. The Wiener process driven by Brown motion can characterize the dynamic characteristics of the degradation. So it can build the model of the hydraulic pump performance degradation path effectively. Suppose the real degradation process of the hydraulic pump can be interpreted by linear Wiener process

$$x(t) = x(0) + \lambda t + \sigma_B B(t) \tag{1}$$

Where, $x(t)$ denotes the real value of degradation of product's performance at time t, $x(0)$ denotes the initial value of degradation, λ is the drift parameter representing the degradation rate and σ_B is the volatility parameter, $B(t)$ denotes a standard Wiener process representing the degradation dynamic characteristics.

2.2 Degradation Model Considering Individual Differences and Measurement errors

However, the real degradation data is difficult to be measured precisely because of the random errors caused by the instrument or environment. Similar to the degradation model proposed in literature [17], based on wiener process with measurement errors under constant stress, measurement value of performance degradation of hydraulic pumps can be described as follow

$$y(t)=x(t)+\varepsilon \tag{2}$$

Where, $y(t)$ represents the value of degradation of product's performance characteristic at time t and the measurement errors term ε follows a normal distribution as $\varepsilon\sim N(0,\sigma_\varepsilon^2)$.

The degradation rate of hydraulic pumps is different affected by the random effects such as environment, instrument, manufacturing errors in manufacturing process. So it cannot be neglected in the reliability evaluation and the remaining useful life test. Therefore, refer to the literature Peng and Tseng[17] and Tang[18], drift parameter λ is set as a random parameter to represent the individual differences, which follows a normal distribution as $\lambda\sim N(\mu_\lambda,\sigma_\lambda^2)$. λ and $B(t)$ are mutually independent.

The hydraulic pump is deemed to be soft-failed when its degradation first exceeds a predefined failure threshold ω. Therefore, the hydraulic pump's lifetime T at first hitting time can be defined as follow

$$T=\inf\{t: y(t)\ge\omega \mid y(0)<\omega\} \tag{3}$$

The probability density function and the reliability function of the life distribution can be expressed as [19]

$$f(t)=\left[\frac{\omega\sigma_B^2+\mu_\lambda\sigma_\varepsilon^2}{(\sigma_\varepsilon^2+\sigma_B^2 t)\sqrt{\sigma_\varepsilon^2+\sigma_B^2 t+\sigma_\lambda^2 t^2}}-\frac{\sigma_\lambda^2\sigma_\varepsilon^2 t(\omega-\mu_\lambda t)}{(\sigma_\varepsilon^2+\sigma_B^2 t)(\sigma_\varepsilon^2+\sigma_B^2 t+\sigma_\lambda^2 t^2)^{3/2}}\right]\phi\left(\frac{\omega-\mu_\lambda t}{\sqrt{\sigma_\varepsilon^2+\sigma_B^2 t+\sigma_\lambda^2 t^2}}\right) \tag{4}$$

$$R(t)=\Phi\left(\frac{\omega-\mu_\lambda t}{\sqrt{\sigma_\varepsilon^2+\sigma_B^2 t+\sigma_\lambda^2 t^2}}\right)-\frac{\sigma_B^2}{\sqrt{\sigma_B^4-4\sigma_\lambda^2\sigma_\varepsilon^2}}\exp\left(\frac{2\mu_\lambda\omega}{\sigma_B^2}+\frac{2\mu_\lambda^2\sigma_\varepsilon^2}{\sigma_B^4}+\frac{2\sigma_\lambda^2(\omega\sigma_B^2+2\mu_\lambda\sigma_\varepsilon^2)^2}{\sigma_B^4(\sigma_B^4-4\sigma_\lambda^2\sigma_\varepsilon^2)}\right)\times \tag{5}$$

$$\Phi\left(-\frac{\omega(\sigma_B^2+2\sigma_\lambda^2 t)+\mu_\lambda(\sigma_B^2 t+2\sigma_\varepsilon^2)}{\sqrt{(\sigma_\varepsilon^2+\sigma_B^2 t+\sigma_\lambda^2 t^2)(\sigma_B^4-4\sigma_\lambda^2\sigma_\varepsilon^2)}}\right)$$

Where, ϕ and Φ are the probability density function and the distribution function of the standard normal distribution.

Similarly, the remaining useful life at first hitting time can be defined as $L_t=\inf\{l_t: T-t\mid T>t\}$, and the probability density function and the expectation value of the remaining useful life can be respectively written as

$$f_{L_t}(l_t)=f(t+l_t)/R(t) \tag{6}$$

$$E_{L_t}(l_t)=\int_0^\infty l_t f_{L_t}(l_t)\mathrm{d}l_t=\int_t^\infty (s-t)f(s)\mathrm{d}s/R(t) \tag{7}$$

3 Parameter Assessment

Assume that n units are to be tested. Each unit is measured once every Δt hours and is measured m times totally. For 2.1 section, the degradation process without consideration of individual differences and measurement errors, the increment of the degradation of the i-th unit under the j-th measurement $\Delta x_{ij}=\lambda\Delta t+\sigma_B\Delta B(t_j)$, $\Delta x_{ij}=x_i(t_j)-x_i(t_{j-1})$, $\Delta B(t_j)=B(t_j)-B(t_{j-1})$, $\Delta t=t_j-t_{j-1}$, t_j is the time of measurement, $t_0=0$, $i=1,2,\cdots,n$, $j=1,2,\cdots,m$. Known from the stationary independent increment of Wiener process, $\Delta x_{ij}\sim N(\lambda\Delta t,\sigma_B^2\Delta t)$. According to the maximum likelihood estimation (MLE) method, we can obtaine

$$\hat{\lambda}=\frac{\sum_{j=1}^{m}\sum_{i=1}^{n}\Delta x_{ij}}{mn\Delta t} \tag{8}$$

$$\hat{\sigma}_B^2=\frac{\sum_{j=1}^{m}\sum_{i=1}^{n}\left(\Delta x_{ij}-\lambda\Delta t\right)^2}{mn\Delta t} \tag{9}$$

For the 2.2 section, the hydraulic pump performance degradation process considering the individual differences and measurement errors, the increment of performance degradation is not independent. In this section, the two-step MLE method [12] is used to estimate the unknown parameters of the degradation model. According to the Equation (2), the performance degradation of the i-th unit under the j-th measurement can be expressed as

$$y_i(t_j)=\lambda_i t_j+\sigma_B B(t_j)+\varepsilon \tag{10}$$

Let $\boldsymbol{Y}_i=(y_i(t_1),\cdots,y_i(t_m))^{\mathrm{T}}$ represent the vector of the performance degradation of the i-th unit, $\boldsymbol{Y}=(\boldsymbol{Y}_1',\cdots,\boldsymbol{Y}_n')$ represent the performance degradation matrix of the sample, $\boldsymbol{t}=(t_1,\cdots,t_m)^{\mathrm{T}}$, from the Equation (10), it can be seen that $\boldsymbol{Y}_i$ obeys a multivariate normal distribution whose mean value is $\bar{\mu}_i=\lambda_i\boldsymbol{t}$ and the covariance is $\boldsymbol{\Sigma}$

$$\boldsymbol{\Sigma}=\sigma_B^2\boldsymbol{Q}+\sigma_\varepsilon^2\boldsymbol{I}_m \tag{11}$$

Where, $\boldsymbol{I}_m$ is a unit matrix with order m, and $\boldsymbol{Q}=\begin{bmatrix} t_1 & \cdots & t_1 \\ & t_2 & \cdots & t_2 \\ \vdots & \vdots & \ddots & \vdots \\ t_1 & t_2 & \cdots & t_m \end{bmatrix}$.

The degradation inspections in different units are mutually independent, and then the log-likelihood function (Log-LF) can be expressed as

$$L(\boldsymbol{\theta}\mid\boldsymbol{Y})=-\frac{mn}{2}\ln(2\pi)-\frac{n}{2}\ln|\boldsymbol{\Sigma}|-\frac{1}{2}\sum_{i=1}^{n}(\boldsymbol{Y}_i-\lambda_i\boldsymbol{t})^{\mathrm{T}}\boldsymbol{\Sigma}^{-1}(\boldsymbol{Y}_i-\lambda_i\boldsymbol{t}) \tag{12}$$

Where, $\boldsymbol{\theta}=(\lambda_1,\cdots\lambda_n,\sigma_B,\sigma_\varepsilon)$ denotes the vector of unknown parameters.

Equation (13) can be derived from the first derivation of λ_i in Equation (12), which can be written as

$$\frac{\partial L(\boldsymbol{\theta}|\boldsymbol{Y})}{\partial\lambda_i}=\boldsymbol{t}^{\mathrm{T}}\boldsymbol{\Sigma}^{-1}\boldsymbol{Y}_i-\lambda_i\boldsymbol{t}^{\mathrm{T}}\boldsymbol{\Sigma}^{-1}\boldsymbol{t} \tag{13}$$

Let Equation (13) equal to zero, the restricted MLE of λ_i can be obtained by the following equation

$$\hat{\lambda}_i(\sigma_B,\sigma_\varepsilon)=\frac{\boldsymbol{t}^{\mathrm{T}}\boldsymbol{\Sigma}^{-1}\boldsymbol{Y}_i}{\boldsymbol{t}^{\mathrm{T}}\boldsymbol{\Sigma}^{-1}\boldsymbol{t}} \tag{14}$$

Substitute Equation (14) into Equation (12), the profile Log-LF of the unknown parameter can be expressed as the following equation

$$L(\sigma_B,\sigma_\varepsilon\mid\boldsymbol{Y})=-\frac{mn}{2}\ln(2\pi)-\frac{n}{2}\ln|\boldsymbol{\Sigma}|-\frac{1}{2}\sum_{i=1}^{n}(\boldsymbol{Y}_i-\hat{\lambda}_i\boldsymbol{t})^{\mathrm{T}}\boldsymbol{\Sigma}^{-1}(\boldsymbol{Y}_i-\hat{\lambda}_i\boldsymbol{t}) \tag{15}$$

The MLE of the model parameters, σ_B and σ_ε can be obtained by maximizing the profile Log-LF (15). The MLE of λ_i can be obtained by substituting $\hat{\sigma}_B$ and $\hat{\sigma}_\varepsilon$ into Equation (14).Finally, the estimated values of μ_λ and σ_λ^2 can be obtained by Equations (16) and (17)

$$\hat{\mu}_\lambda=\frac{1}{n}\sum_{j=1}^{n}\hat{\lambda}_j \tag{16}$$

$$\hat{\sigma}_{\lambda}^{2}=\frac{1}{n}\sum_{j=1}^{n}(\hat{\lambda}_{j}-\hat{\mu}_{\lambda})^{2} \tag{17}$$

4 Application Example

The A4VS series axial piston pumps produced by a company were used as the test object to demonstrate the validity and accuracy of the reliability evaluation and the remaining useful life prediction method. The rated pressure of this series of pumps is 350 bar, and the peak pressure is 400 bar. Four hydraulic pumps were randomly selected for the test, and the measurement interval was set as Δt=12h , test pressure was set as rated pressure. The volumetric efficiency ($z_i(t_j)$, $j=1,2,\cdots,85$) was calculated. The performance degradation value $d_i(t_j)$ of hydraulic pump's volumetric efficiency can be expressed as $d_i(t_j)=z(0)-z_i(t_j)$, $z(0)$=0.955 is the mean of initial volumetric efficiency of the axial piston pump under the rated pressure, and the performance degradation trend of the tested pumps are shown in Figure 1.

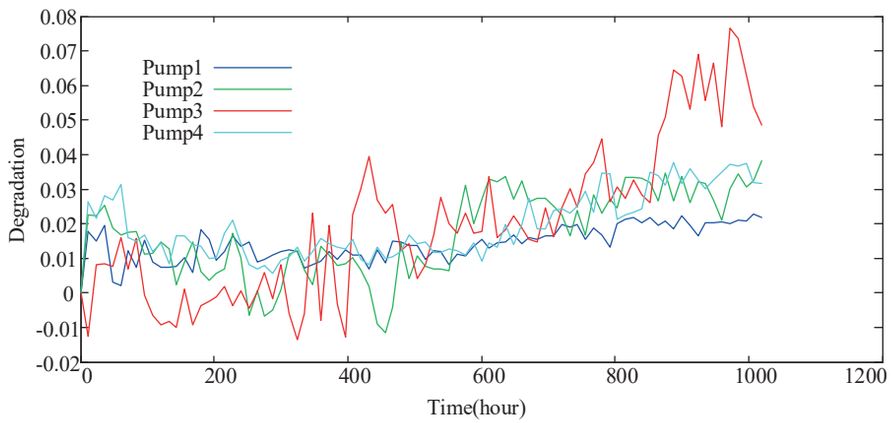


Figure 1: A trend Diagram of the Performance Degradation of the Hydraulic Pump.

In order to facilitate subsequent calculation and analysis, the degradation data shown in Figure 1 is standardized by Equation (18)

$$y_i(t_j)=d_i(t_j)/d_{\max} \tag{18}$$

Where, $i=1,2,\cdots,n$, $j=1,2,\cdots,m$, $d_{\max}$ is the maximum value of the performance degradation $d_i(t_j)$.

In order to demonstrate the validity and accuracy of the proposed method, the model defined in 2.1 section is denoted as M1， the model in Section 2.2 is denoted as M2 and the method of curve fitting based on [16] is defined as M3.

For the method M1, using the autocorrelation function to inspect the independence of the increment of standardized performance degradation firstly. Figure 2 is an autocorrelation function chart of the standardized performance degradation increment of 4 hydraulic pumps. From Figure 2, it can be observed that the first order autocorrelation coefficients are close to or exceed the two horizontal lines, that is, approximate or exceed the positive and negative two times of the sample autocorrelation coefficient approximate standard deviation($\pm 2/\sqrt{m}$). It means if standardized degradation obeys Wiener process model, the standardized incremental sequence of degradation did not pass the inspection of independence. We should not choose M1 method but M2 to model the hydraulic pump performance degradation process.

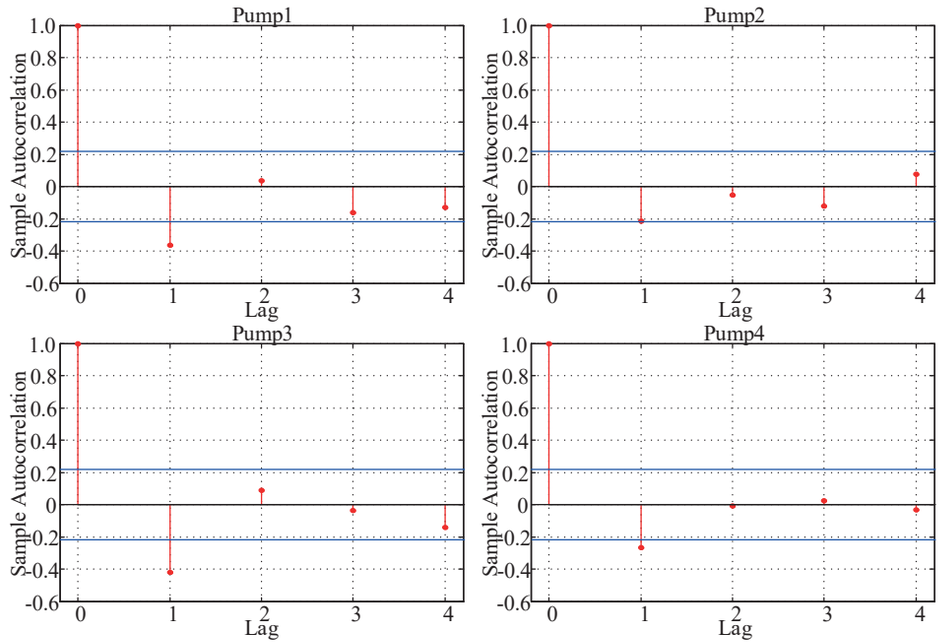


Figure 2: Independence Test of Performance Increment.

Similar to literature [16], we think that the soft failure occurred on the hydraulic pump when the volumetric efficiency of the hydraulic pump drops to 87%. The initial volumetric efficiency of the series axial piston pump is 95.5%, so we think that the hydraulic pump failed when the performance degradation (Figure 1) reaches the failure threshold of 0.085. Aimed at the standardized data, failure threshold ω is $0.085/y_{\max}$. According to Equations. (8) and (9), the parameter estimation of M1 can be obtained, $\hat{\lambda}=4.4798\times10^{-4}$, $\hat{\sigma}_B^2=8.1470\times10^{-4}$. Let $\hat{\sigma}_{\lambda}^2=0$ and $\hat{\sigma}_{\varepsilon}^2=0$, it can be calculated that the average life of the hydraulic pump is 2.4771×10^3 h by substituting the parameters into the Equation (7).

For the method M2, according to the parameter estimation method proposed in the section 3, we can obtain $\hat{\lambda}_1=2.8078\times10^{-4}$, $\hat{\lambda}_2=4.6211\times10^{-4}$, $\hat{\lambda}_3=6.7492\times10^{-4}$, $\hat{\lambda}_4=4.1791\times10^{-4}$, $\hat{\mu}_{\lambda}=4.5893\times10^{-4}$, $\hat{\sigma}_{\lambda}^2=2.0021\times10^{-8}$, $\hat{\sigma}_B^2=2.7833\times10^{-4}$ and $\hat{\sigma}_{\varepsilon}^2=3.3039\times10^{-3}$. It can be calculated that the average life of the hydraulic pump is 3.7706 $\times10^3$h by substituting the parameters into the Equation (7).

Comparing the parameter estimation results of M1 and M2, it can be seen that the estimated value of drift coefficient $\hat{\lambda}$ is close to $\hat{\mu}_{\lambda}$, which demonstrated the correctness of the two models fitting for degradation trend. The result of diffusion coefficient estimation $\hat{\sigma}_B^2$ is quite different. This is because M1 does not consider the measurement errors. The fluctuation of measurement errors is reflected by diffusion coefficient. Meanwhile, it demonstrated that the measurement errors cannot be ignored.

The results of method M3 are given by literature [16]. The life distribution of the hydraulic pump obeys the two-parameter Weibull distribution, its characteristic value is $m=2.5$, $\eta=4482.4$, and the average value of life is 4.1275×10^3 h.

Comparing the average value of life obtained by the three methods, it can be seen, the average values of M1 and M2 are less than M3. Because of failure was defined by the first hitting time (Equation (3)), the result tends to be conservative, which has positive significance for the preventive maintenance and health management of hydraulic

pump. Meanwhile, the average life of M2 is close to M3, and the correctness of the method proposed in this paper is also demonstrated. For a more direct comparison to illustrate the characteristics of the three methods, Figure 3 and Figure 4 give the probability density function curves and reliability function curves respectively.

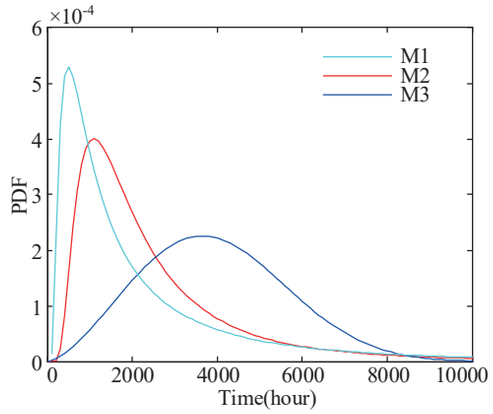


Figure 3: Probability density function graph.

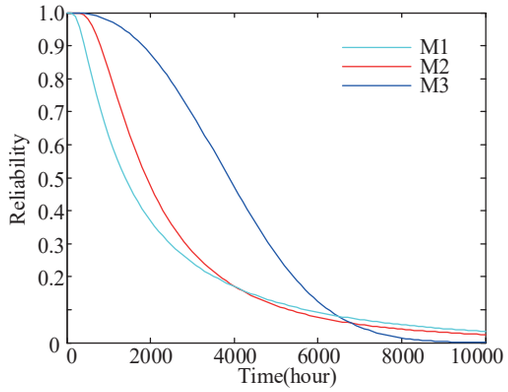


Figure 4: Reliability function graph.

As can be seen from figure 3, the life distribution of M1 is very concentrated, and it is mainly concentrated within 2000h, which is not in conformity with the reality. The life distribution of M3 is very dispersive, which is not very reasonable in the life distribution of marginal. It can be seen from figure 4, the reliability estimation results of M1 and M2 are more conservative than that of M3, which is consistent with the above conclusions. The pump 3 almost failed at the end of the test, indicating that the reliability of these hydraulic pump at time 1000h was lower than that of the M3. Therefore, we think the reliability estimation method proposed in this paper, M2, can be used to estimate the life distribution of the batch hydraulic pump well.

5 Conclusion

Taking volumetric efficiency as the characteristic parameter of performance degradation, a reliability evaluation method for hydraulic pump based on performance degradation is proposed. And the stochastic volatility, individual differences and measurement errors have been considered in the creation of the degradation model. Aiming at the performance degradation data of the 4 hydraulic pumps, the two-step MLE method is used to estimate the unknown parameters, and the average life and the life probability density function of the batch of pump are obtained. Compared with the reliability evaluation method of degradation path model and Wiener process model, it is necessary to consider the stochastic volatility, individual differences and measurement errors in the reliability evaluation of the hydraulic pump based on degradation. Using the first hitting time to define the degradation failure of the hydraulic pump will lead to the results tend to be conservative. The reliability estimation method based on performance degradation does not need to observe the failure of hydraulic pump, compared with the method based on lifetime, it can reduce the test time and the cost.

6 Acknowledgements

This work was supported in part by the Innovation Funding for Postgraduates in Hebei Province under Grant no. CXZZBS2017040.

Nomenclature

Variable	*Description*	*Unit*
$x(t)$	The real value of product performance degradation at time t	[-]
λ	Drift coefficient	[-]
σ_B	Diffusion coefficient	[-]
$B(t)$	Standard Brownian motion	[-]
$y(t)$	Degradation path of product	[-]
ε	Measurement errors	[-]
T	First-hitting-time of product	[hour]
$f(t)$	The probability density function of the product life	[-]
$R(t)$	Reliability function	[-]
$\phi(\cdot)$	The probability density function obeying the standard normal distribution	[-]
$\Phi(\cdot)$	Standard normal distribution function	[-]
L_t	Remaining useful life of hydraulic pump	[hour]
$f_{L_t}(l_t)$	Probability density function of remaining useful life	[-]
$E_{L_t}(l_t)$	Remaining useful life expectation	[hour]
n	Total sample number	[-]
m	The measurement number of each sample during the test	[-]
Δt	The interval of test time	[hour]
Δx_{ij}	The increment of the degradation of the i-th unit under the j-th measurement	[-]
$\boldsymbol{Y}_i$	The vector of the performance degradation of the i-th unit	[-]
$\boldsymbol{Y}$	The performance degradation matrix of the sample	[-]
$\boldsymbol{I}_m$	Unit matrix with order m	[-]
$\boldsymbol{\Sigma}$	Covariance matrix	[-]

$\boldsymbol{t}$	Vector of measurement time	[hour]
$\boldsymbol{\theta}$	Vector of unknown parameters	[-]
$z_i(t_j)$	The volumetric efficiency of the *i*-th unit under the *j*-th measurement	[-]
$d_i(t_j)$	The performance degradation of the *i*-th unit under the *j*-th measurement	[-]
$y_i(t_j)$	The normalized performance degradation of the *i*-th pattern under the *j*-th measurement	[-]

References

/1/ Wang, X., Lin, S., Wang, S., *Remaining Useful Life Prediction Based on the Wiener Process for an Aviation Axial Piston Pump*, In: Chinese Journal of Aeronautics, Vol. 29, No. 3, pp. 779-788, 2016.

/2/ Han, L., Wang, S., Zhang, C., *A Partial Lubrication Model between Valve Plate and Cylinder Block in Axial Piston Pumps*, In: Proceedings of the Institution of Mechanical Engineers, Part C: Journal of Mechanical Engineering Science, Vol. 229, No. 178, pp. 3201-3217, 2015.

/3/ Du, J., Wang, S., Zhang, H., *Layered Clustering Multi-Fault Diagnosis for Hydraulic Piston Pump*, In: Mechanical Systems and Signal Processing, Vol. 36, No. 2, pp. 487-504, 2013.

/4/ Ma, J., Ruan, L., Fu, Y., *A Review on Method of Accelerated Lifetime Test for Aircraft Hydraulic Pump*, In: Chinese Hydraulics & Pneumatics, No. 6, pp. 6-12, 2015.

/5/ Yuan, Z., Wang, S., *One Method Solving Parameter Estimation of Varying Stress Accelerated Life Test*, In: Journal of Beijing University of Aeronautics and Astronautics, No. 11, pp. 1172-1176, 2005.

/6/ Zhang, J., Li, H., Fu, J., *Research of Sequential Accelerated Life Test Method for Aviation Gear Pump*, In: Chinese Hydraulics & Pneumatics, No. 05, pp. 101-104, 2012.

/7/ Ye, Z., Chen, N., Shen, Y., *A New Class of Wiener Process Models for Degradation Analysis*, In: Reliability Engineering & System Safety, No. 139, pp. 58-67, 2015.

/8/ Hu, C., Lee, M., Tang, J., *Optimum Step-Stress Accelerated Degradation Test for Wiener Degradation Process under Constraints*, In: European Journal of Operational Research, Vol. 241, No. 2, pp. 412-421, 2015.

/9/ Huang, J., Golubović, D., Koh, S., *Lumen Degradation Modeling of White-Light Leds in Step Stress Accelerated Degradation Test*, In: Reliability Engineering & System Safety, No. 154, pp. 152-159, 2016.

/10/ Wang, X., *Wiener Processes with Random Effects for Degradation Data*, In: Journal of Multivariate Analysis, Vol. 101, No. 2, pp. 340-351, 2010.

/11/ Pan, Z., Balakrishnan, N., Sun, Q., *Bivariate Constant-Stress Accelerated Degradation Model and Inference*, In: Communications in Statistics—Simulation and Computation®, Vol. 40, No. 2, pp. 247-257, 2011.

/12/ Tang, S., Yu, C., Wang, X., *Remaining Useful Life Prediction of Lithium-Ion Batteries Based on the Wiener Process with Measurement Errors*, In: Energies, Vol. 7, No. 2, pp. 520-547, 2014.

/13/ Ma, J., Zhan, X., *Performance Reliability Analysis of a Piston Pump Affected by Random degradation*, In: Journal of Mechanical Engineering, Vol. 53, No. 14, pp. 189-193, 2010.

/14/ Fang, J., Wei, X., Fan, L., *Reliability Analysis of Aircraft Hydraulic Pump Based on Performance Degradation Data*, In: Mechanical Research & Application, No. 06, pp. 30-33, 2008.

15/ Huang, A., Guo, Y., Yu, J., *Research on Residual Life Prediction Technique of Hydraulic Pump Based on Accelerated Degradation Data*, In: Machinery Design & Manufacture, No. 01, pp. 154-155, 2011.

16/ Guo, R., Shi, Y., Zhao, J., *Short-time Test Method of Reliability for Hydraulic Pumps*, In: Transactions of the Chinese Society of Agricultural Machinery, No. 03, pp. 405-412, 2016.

17/ Peng, C., Tseng, S., *Mis-Specification Analysis of Linear Degradation Models*, In: IEEE Transactions on Reliability, Vol. 58, No. 3, pp. 444-455, 2009.

18/ Tang, S., Guo, X., Yu, C., *Accelerated Degradation Tests Modeling Based on the Nonlinear Wiener Process with Random Effects*, In: Mathematical Problems in Engineering, No. 2, pp. 1-11, 2014.

19/ Pan, D., Wei, Y., Fang, H., *A Reliability Estimation Approach via Wiener Degradation Model with Measurement Errors*, In: Applied Mathematics and Computation, No. 320, pp. 131-141, 2018.

Efficiency Study of an Electro-Hydraulic Excavator

REVIEWED

Ville Salomaa*/**, Tatiana Minav*, Jouni Mattila** and Matti Pietola*

Aalto University School of Engineering, Department of Mechanical Engineering, Otakaari 4, FI-02150 Espoo, Finland*
Tampere University of Technology, Department of Automation and Hydraulic Engineering, Korkeakoulunkatu 6, FI-33101 Tampere, Finland**
E-Mail: ville.k.salomaa@student.tut.fi

A Matlab/Simulation model is utilized to study the total energy consumption and power distribution of the micro excavator. The model consists of the hydraulic and mechanical systems related to actuation of front hoe, i.e. boom, arm, and bucket. The excavator is equipped with pressure and position sensors, from which the measurement data is collected for parameterization and verification of the simulation model. Two different duty cycles, named *digging and loading cycle* and *leveling cycle*, based on the JCMAS standard, are utilized in this study. The results indicate a formidable room for improvement, concerning the hydraulic system, since a power loss of as much as 60% is localized in the directional valve group.

Keywords: Excavator, efficiency, hydraulics, losses
Target audience: Mobile Hydraulics

1 Introduction

Off-highway working machines cover a wide range of applications, including agriculture, earth-moving, and mining machinery. These machines are often utilized in challenging conditions, and their duty cycles consist of quick and high power peaks. This makes off-highway working machines a demanding target for research and development. Their requirement for high maximum power, along with full mobility is a reason why these machines are predominantly powered by a diesel engine. Due to the fluctuating fuel price and tightening regulation for emissions, there is a constant need to improve the efficiency and reduce the engine size and emissions of the machines. Numerous studies have been published about improving the efficiency of off-road machinery.

Excavators are ordinarily equipped with conventional, centralized hydraulic system, which consists of one or two main pumps that supply volumetric flow for the whole system. This flow is directed from the pump to actuators through control valves, and the returning flow is directed into the tank. Conventional hydraulic system has numerous disadvantages. Many supportive functions are required, including pressure control and load-sensing functions. The power demand of the system changes, which prevents the engine from running at its optimal speed. Even in idle mode, flow losses are present due to continuous circulation of fluid through valves. In addition, the distance between pumps and actuators may be long, which causes pressure loss and an additional weight of long hoses filled with fluid.

Load-sensing (LS) system is common an example of the conventional hydraulics. In a load-sensing (LS) system, a load-sensing circuit monitors the load pressures on all actuators, and adjusts the system pressure to match the highest load. If several actuators operate at the same time, which often is the case, the excess pressure is decreased by throttling. According to Zimmerman *et al.* /1/, these throttle losses may be responsible for as much as 35% of total energy losses during a typical digging cycle. Knowing the energy distribution of the machine is vital in order to steer the research towards the most relevant targets.

This study concentrates on improving the energy efficiency and performance of a JCB micro excavator. In the beginning of project, the 14 kW diesel engine of the excavator was replaced with a 10 kW electric motor and a lithium-titanate battery. This electric system showed performance of same level as the previous diesel powered version. In addition, the noise level decreased, and the emissions of diesel engine were eliminated, both of which are influential factors, especially when working indoors. However, due to low battery capacity and long charging time, the operation time was dramatically lower than of a diesel powered version. /2/. The excavator was further improved with a start-stop system that was able to save energy as much as 32%, but demand for further improvements still exists /3/. The original hydraulic system of the excavator controlled by manually operated directional valves was replaced with the electro-hydraulic proportional valves, which were installed parallel to the original valves /4/. The great amount of power is wasted in throttling losses in the hydraulic circuit, and novel solutions for the issue have been developed. Direct-driven or valveless hydraulics, in particular, have demonstrated encouraging potential to eliminate a large share of hydraulic losses in off-highway mobile machinery. /5/, /6/. Therefore, in this project, the efficiency of the hydraulic system of the excavator is under detailed investigation. Boom, arm and bucket actuation are included in the scope of this work.

The objective of this study is to resolve the actual energy consumption and power distribution of the front hoe of the micro excavator (Figure 1), including boom, arm and bucket actuators. This leads to creation of a simulation model in Matlab/Simulink environment of excavator and experimental validation of model. Excavator is fitted with pressure and position sensors, and the simulation model was verified with laboratory measurements. The verified model was utilized to calculate the power consumption of the excavator during a digging and loading and a levelling cycle.

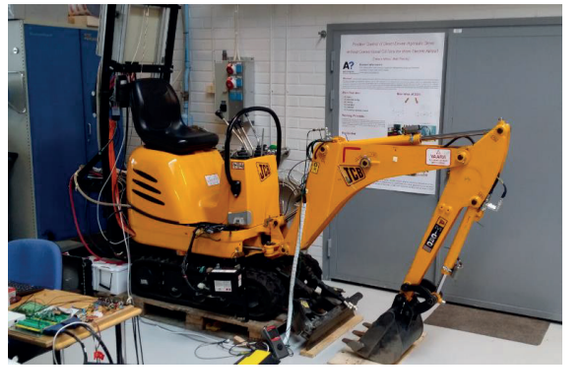


Figure 1: JCB Micro excavator

This structure of this paper is as follows. The excavator and the simulation model is presented in chapter 2. In chapter 3, the simulation model is utilized to study the power consumption of the excavator during two standardized working cycles. The final conclusions, together with suggestions concerning the upcoming research, are presented in chapter 4.

2. Excavator test case

JCB excavator is one of study cases in EL-Zon project. JCB excavator utilizes LS system. It is noteworthy, that the term ‘LS system’ is commonly used to describe a system with a variable-displacement pump. The hydraulic system of this excavator, however, has a fixed-displacement pump with constant rotational speed. It senses the load pressure, and adjusts the system pressure accordingly, by directing the excess volume into the tank, via the pressure adjustment valve.

For clarity in this paper, the conventional hydraulic system refers to the current setup, which is powered by an electric motor, and controlled with electrical valves (for modification in excavator refer to /2-4/. In contrast, the

factory-made system, with diesel engine, and manually controlled directional valves, is referred to as original system. The current hydraulic system of the excavator is illustrated in Figure 2.

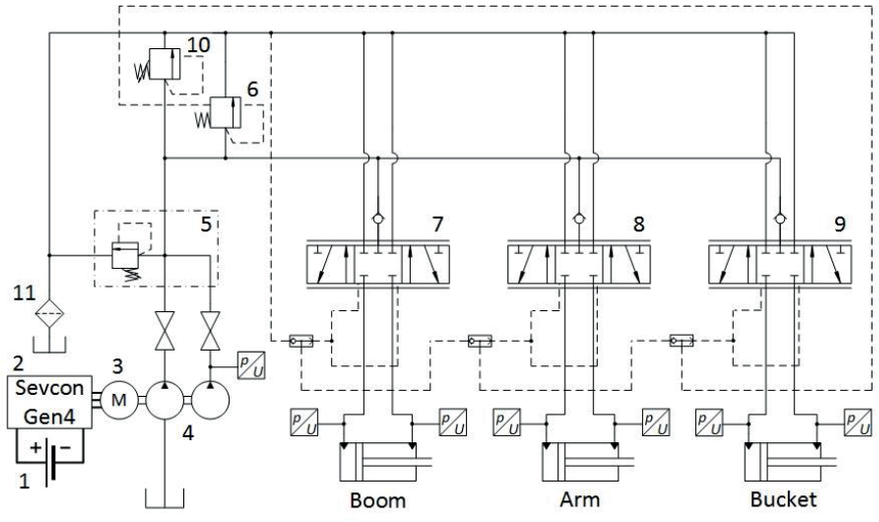


Figure 2: Simplified hydraulic schematic of the hydraulic system of the excavator

Number	Component	Details
1	Battery pack	
2	Motor controller	
3	Electric motor	
4	Pump	Parker PGP511 gear pumps, with a fixed volume of 2 x 6 CC /7/
5	Junction block with PRV	
6	Pressure adjustment valve	
7-9	Directional valves	
10	Pressure relief valve	
11	Return oil filter	

Table 1: Main components of the hydraulic system

Excavator is fitted with additional sensors and data acquisition system. As Figure 2 demonstrates the excavator is fitted with pressure sensors in all cylinder ports and in the pump outlet port, and position sensors at the cylinder rods. The measurement data, combined with dependable, measure-based dynamic model, gives access to otherwise hard-to-find parameters, such as cylinder friction forces and volumetric losses of the system. The measurement signals are collected and recorded at a target-pc, which is operated by Matlab/Simulink Real-time. A simple position feedback controller is established to control the front hoe.

2 Simulation model

A simulation model of micro excavator is created in Matlab/Simulink environment. Developed model is utilized to study the energy consumption of the micro excavator. This work is focused in the hydro-mechanical system of the excavator front hoe, and excluding powertrain. The developed hydraulic model contains the hydraulic pump, directional valve group, auxiliary valves, hydraulic cylinders, the mechanical model of the front hoe, and the connecting hoses. The electric motor and the motor controller are assumed to be ideal, with 100% efficiency and constant rotational speed. In developed multibody model of excavator is created with Simscape Multibody toolbox. Following sub-sections will introduce in short realizations for the modelled components. For detail explanation please refer to /16 /.

2.1 Hydraulic pump model

Two hydraulic pumps in the excavator are Parker PGP511 gear pumps, with a fixed volume of 2 x 6 CC. According to manufacturer data /7/, the PGP511 pump has a 12-tooth gear profile and optimized flow metering to provide reduced pulsation and quiet operation. Therefore, the output flow is assumed “flat” and modelled with a simple lookup table, producing the flow according to the curve provided by manufacturer /7/.

2.2 Hose model

The pressure drops of the hoses are estimated by mathematical formulas. A hose model consists of the pipe friction, orifice, and volume sub-models. In the transition phase between laminar and turbulent flow, the friction factor is modelled with a simple continuous function, which is also continuously differentiable. The accordant friction factor is selected based on the Reynold’s number. In addition to pipe friction, there are flow losses in the system, which are related to change of speed or direction of the flow. These losses are present in joints and bends, for example /8/. Values listed in Kauranne *et al.* /8/ have utilized for friction factor ζ.

2.3 Proportional valve model

Danfoss PVG 32 proportional valve group consists of three main module types: pump side module (PVP), basic modules (PVB), and actuation modules (PVED-CC). The PVP connects to the pump and tank ports, and it has different functions depending on the application. In this valve group, the PVP is an open-centre version, which is to be used with fixed displacement pumps. The manufacturer part number is 157B5110, and the operation is explained in detail in /10/.

The pressure adjustment spool is modelled with a lookup table, result of which corresponds the graph given by the manufacturer, with some adjustments made to make the simulation model match the measured data. A rate limit block is added to limit the transition speed of the spool, and the flow is saturated to minimum of 0 l/min and maximum of 140 l/min. The pressure relief valve is modelled based on the manufacturer data. The nominal set point for the valve block PRV is 18 MPa. However, the system pressure is, based on the measurements, limited to 12-13 MPa. Thus, the pressure limit of the valve block is never reached, and only the junction block PRV activates when the pressure rises up to the limit. The PVB module has a manufacturer part number 157B6100 for the PVB module and 7005 for the spool. The model is controlled with a spool position command u, and it outputs the flow for each valve port (P, A, B, T). It also compares the load pressure of the active port against the loads on other spools, and passes forward the highest pressure. The spool dynamics, consisting of a transfer function and a saturation block, based on the work of Bak & Hansen, which studied the dynamic behaviour of a PVG 32 valves /11/. It must be noted, that this valve has different spool size and different components, so the transfer function parameters serve only as an estimation of the actual spool dynamics. The spool position is converted into the relative openings of the control edges of the spool, which are modelled with four lookup tables, based on the measurement data. Oil flow through the ports was calculated with four separate orifice blocks. Orifice model was utilized to calculate a volumetric flow, caused by a pressure difference over a flow path, and it takes the flow type (laminar, turbulent or transient) into consideration. Ellman & Piche equation for a polynomial laminar flow formula is utilized for the pressure difference is below the transition pressure /12/.

The piecewise equation for volumetric flow q [m^3/s] can be written as:

$$\boldsymbol{q(P)} = \begin{cases} \boldsymbol{K_V\, sgn(p_1 - p_2)\sqrt{|p_1 - p_2|}} & (\boldsymbol{|p_1 - p_2| > p_{tr}}) \\ \boldsymbol{\dfrac{K_V(p_1 - p_2)}{2\sqrt{p_{tr}}}\left(3 - \dfrac{|p_1 - p_2|}{p_{tr}}\right)} & (\boldsymbol{|p_1 - p_2| \le p_{tr}}) \end{cases} \quad (1)$$

where p_1 and p_2 are the pressures before and after the orifice [Pa], p_{tr} is the transition pressure [Pa]. The flow coefficient K_v is calculated for each valve port from equation:

$$K_V = \frac{q_{nom}}{\sqrt{p_{nom}}}, \tag{2}$$

where q_{nom} is the nominal flow [m^3/s], and p_{nom} is the nominal pressure differential [Pa]. The values are determined for each spool separately, based on the measurement data. Used values are collected in Table 2 at the pressure difference of 1 MPa.

Spool	Nominal flow (P-AB) [l/min]	Nominal flow (AB-T) [l/min]
Boom	5.6	6.1
Arm	5.3	6.2
Bucket	5.4	6.1

Table 2: Nominal flow rates of the control spools

2.4 Cylinder model

The cylinder model transforms the introduced volumetric flow into chamber pressures and output force. Output force is a product of chamber pressure and the piston area on that side. Cylinder friction consists of forces between surfaces of the cylinder and the seals, which includes seals of piston and piston rod. Jarf /13/ exploited a dynamic friction model, proposed by Canudas de Wit *et al.* /14/. The utilized model takes into account most of the dynamical friction behaviour, including Stribeck effect, hysteresis, stick, and varying break-away force. In developed model, also known as the LuGre model, the contact is thought as bristles moving against each other. When applied to the cylinder friction, the bristles can be seen as representatives of cylinder seals. The average deflection of the bristles is marked z and its time derivative is modelled by:

$$\frac{dz}{dt} = v - \frac{\sigma_0|v|}{g(v)}z\ , \tag{3}$$

where

$$g(v) = F_c + (F_s - F_c)e^{-\left(\frac{v}{v_s}\right)^2}, \tag{4}$$

$$F_\mu = \sigma_0 z + \sigma_1 \dot{z} + \sigma_2 v\ , \tag{5}$$

where F_μ is the friction force [N], z is the average deflection of bristles [m], and v is the relative velocity between sliding surfaces [m/s]. The friction parameters, demonstrated in Table 3, are based on the literature, and adjusted according to the performed measurements.

Notation	Explanation	Boom cylinder	Arm cylinder	Bucket cylinder	Unit
v_s	Stribeck velocity	0.001	0.001	0.001	m/s
F_c	Coulomb friction	200	200	200	N
F_s	static friction	800	400	400	N
σ_0	stiffness of bristles	$1.6 \cdot 10^6$	$1.6 \cdot 10^6$	$1.6 \cdot 10^6$	N/m
σ_1	damping coefficient	$5 \cdot 10^3$	$5 \cdot 10^3$	$5 \cdot 10^3$	Ns/m
σ_2	viscous friction coefficient	$5 \cdot 10^3$	$5 \cdot 10^3$	$2 \cdot 10^3$	Ns/m

Table 3: Friction coefficients of the cylinders

2.5 Simscape Multibody model

In order to simulate the physical response of the mechanical system, a multibody model is created with Simscape Multibody toolbox. Table 4 shows the utilized weights of the mechanical system of the micro excavator. In this work, it is assumed that all joints are ideal, and provide only certain degree of freedom. No friction acts on the joints accept friction in cylinder model. Bodies are considered to rigid, no deflections or vibrations applied. In addition further simplification have been implemented. The attachment point of the front hoe, the kingpost, is modeled with welded connection to the world frame, whereas the actual excavator provides some degree of movement.

Component	Weight of component [kg]
Boom	59.50
Arm	28.00
Bucket	30.00
Linkages	10.00
Boom cylinder	16.67
Arm cylinder	11.57
Bucket cylinder	9.41
Hoses	1.70
Pins 1, 3, 4, 6	1.08
Pin 2	0.63
Pins 5, 7	0.66
Pins 8, 10	0.83
Pins 9, 11	0.74

Table 4: Weights of the components of the front hoe

2.6 Model verification

The simulated cylinder pressures verified against the measured ones. In order to acquire the necessary measurement data, the excavator is controlled to move the arm cylinder from fully retracted position to fully extracted position and back on full speed. The valve flow signal (AVEF) is recorded and utilized as an input for the spool position in the simulation model. Measured cylinder position, pressures in chambers A and B, and the system pressure at pump outlet port are plotted together with simulated values, and are shown in Figure 3.

Neglectable fluctuation is visible in transition states, namely at 17.5 s, is due to the properties of the electric motor and the controller. In the simulation model, the motor speed is assumed constant, which results in different pressure curves. However, after the transition phase, the pressures are settling on the correct level. The chamber pressures correlate with the cylinder movement appropriately. Despite a minor difference in the trajectories on the position curve, the simulated average speed of the actuator corresponds to the measured speed.

Other actuators (boom and bucket) were driven in predetermined positions, to ensure corresponding inertial properties, but were not subject to control, to prevent any unwanted disturbance for the system pressure. The bucket and boom actuations are evaluated in a similar manner. The simulated system pressure matches the measured values, the chamber pressures are on adequate level, and the cylinder position curves are nearly identical.

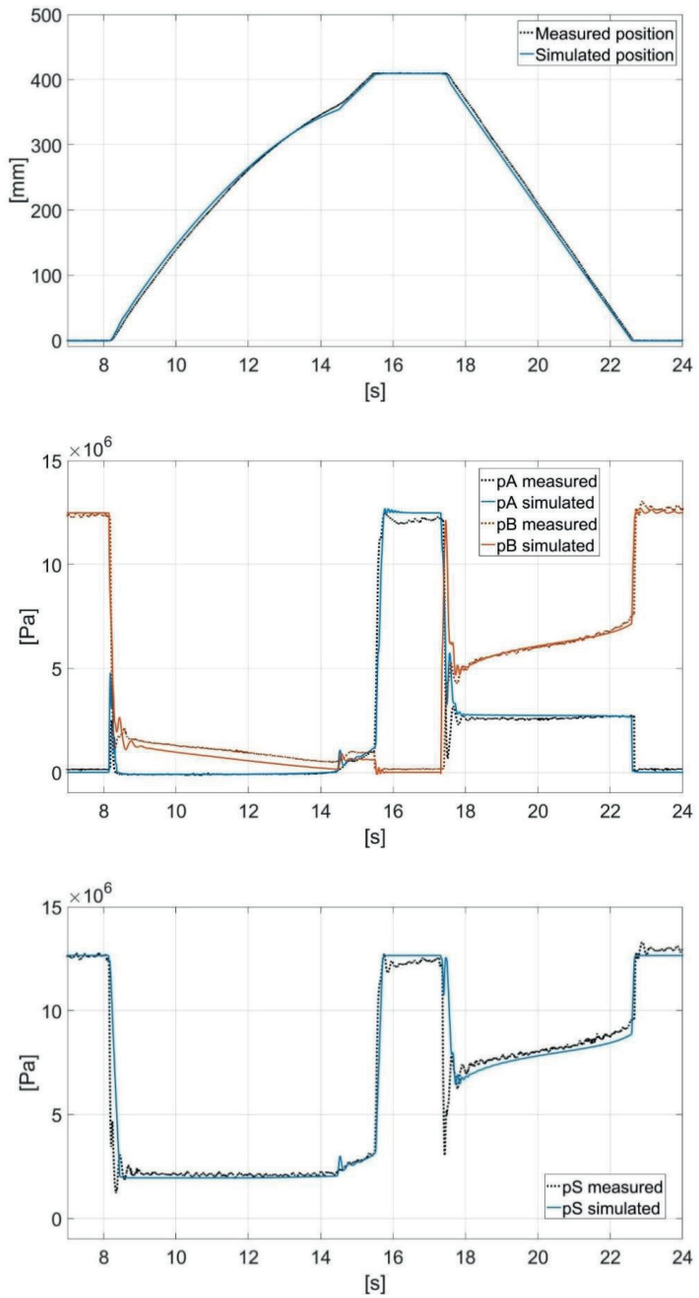


Figure 3: top: Measured and simulated arm position; middle: Measured and simulated arm cylinder chamber pressures; bottom: Measured and simulated system pressures during arm movement

According to the verification tests, all three actuators exhibit a realistic behaviour. The simulated system pressure, during the boom movement, fluctuates more than the measured pressure. This is due to minor difference between the dynamics of simulated and actual pressure adjustment valve. Pressures settle in correct levels and the simulation converts the valve opening signals into precise actuator positions. Therefore, the simulation model is now verified with simple single-actuator manoeuvres.

3 EFFICIENCY ANALYSIS

In this section, the verified simulation model is utilized to study the total energy consumption and power distribution of the micro excavator, and the results are compared and discussed.

In order to evaluate the performance or efficiency of an excavator, it is necessary to determine the actual use of such a machine. Digging movement is common to all duty cycles found in the literature. However, the varying loading conditions make standardizing a difficult task, as the excavators are used in very different conditions. The duty cycles used in the study, are based on The Japan Construction Machinization Association (JCMAS) standard for testing the fuel consumption of hydraulic excavators /15/. Cycles are scaled down, due to the physical limitations of the test excavator. In this study, the loading height is 1.2 m and digging depth 0.75 m. Since the swing motion is not included in the scope of this work, only boom, arm and bucket movements are performed. In the levelling cycle, the processing length is 1.7 m. The reference cylinder lengths for each actuator, compared with visualization of the cycle, are illustrated in Figure 4 for the digging and loading cycle.

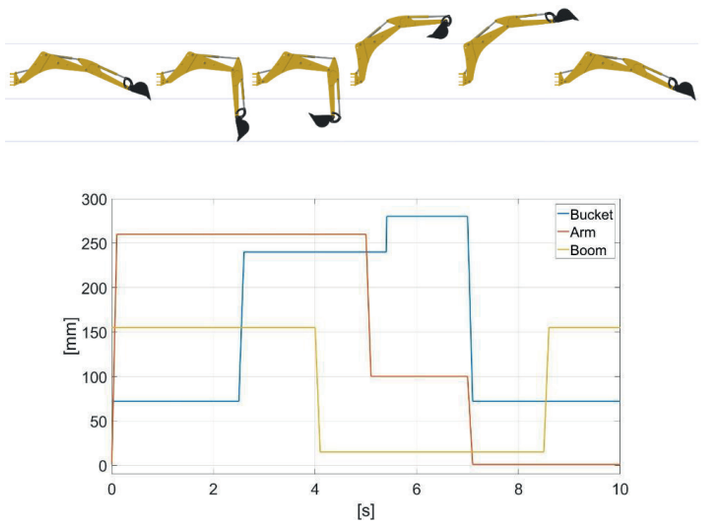


Figure 4: The digging and loading cycle

A similar presentation is displayed in Figure 5 for the levelling cycle.

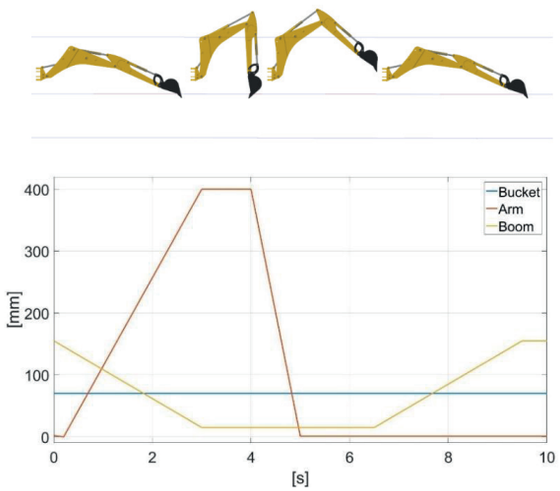


Figure 5: The levelling cycle

First, digging and loading cycle is performed and illustrated in Figure 6. Figure 6 illustrates the power division in seven categories: pump input and output power, pressure adjustment valve (PAV), pressure relief valve (PRV), directional valves, cylinders input and cylinders output.

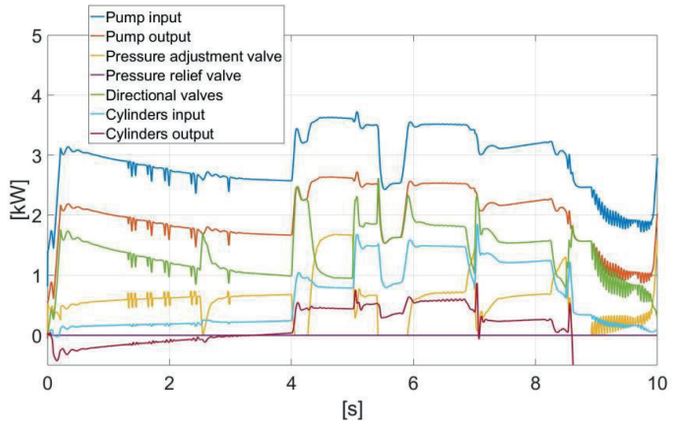


Figure 6: Power distribution during digging and loading cycle

Pump input power, which is the same as the electric motor output, is the mechanical power employed to produce the pressure-dependent torque at the wanted rotational speed. The power model is acquired directly from a data sheet provided by the manufacturer /7/. The pump output power is the hydraulic power leaving the pump, calculated as multiplication of the volumetric flow [m^3/s] and the pressure at the pump [Pa]. The output power was utilized in the directional valves, but a large share of it is lost, mostly in pressure adjustment valve and throttling in directional valves. The power loss of the pump is the difference between input and output power.

The input power of the pressure adjustment valve is the product of pressure at the valve and the flow through the valve. The entire flow returns to tank, so the input power of the PAV is the power loss of the valve. The same applies also for the pressure relief valve, although it is not opening during the test cycles.

Input power of the directional valve group is the product of flow entering the valve and the pressure at the pressure port (P) of the valve. Output power is a combination of outputs of A and B ports, and the power loss is the differential between input and output power.

The hydraulic cylinders transform the hydraulic energy into the actuator work. Losses are caused mainly by the backpressure and mechanical friction. The input power is solely hydraulic power. Output power a combination of mechanical output power and the hydraulic power leaving the cylinder. The volumetric flow out of the cylinder is somewhat problematic. In an ideal system, the leaving flow would jump into the tank in zero pressure. In realistic system, however, the return flow runs through the hoses and valves, which results in a significant pressure rise at the cylinder chamber, the backpressure. It causes a force opposite to working direction, and reduces the net force derived from the actuator. Therefore, using plain net force to calculate the output power gives too disadvantageous picture of the cylinder efficiency. Instead, the leaving flow is count into the output power of the cylinder. The power loss is the differential between input and output power. Power losses are collected in the Table 5.

	Total input	Pump losses	Pressure adjustment valve	Directional valves	Hoses	Actuator losses	Actuator work
Energy, [J]	28 936	9 320	5 852	10 943	2 599	691	10
Share of total loss, [%]	100	32.21	20.22	37.82	8.98	2.39	0.03

Table 5: Energy losses during digging and loading cycle

The actuator work is close to zero as the machine returns to the starting posture in the end of the cycle, where the potential energy is the same as in the beginning.

Second, for levelling cycle Figure 7 demonstrates the power distribution by components.

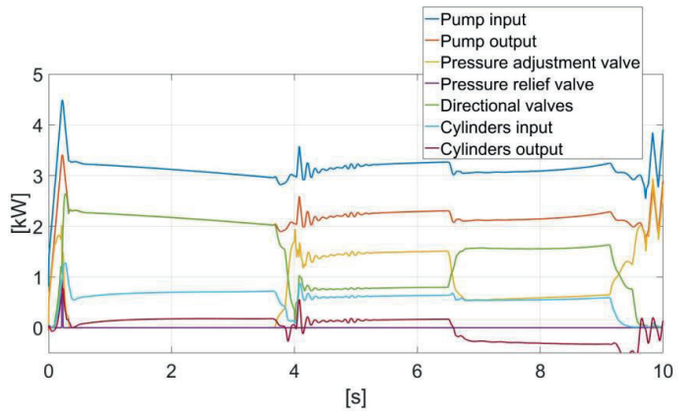


Figure 7: Power distribution during leveling cycle

A similar energy loss calculation is performed for the leveling cycle, and the results are collected in the Table 6

	Total input	Pump losses	Pressure adjustment valve	Directional valves	Hoses	Actuator losses	Actuator work
Energy, [J]	31 251	9 483	7 307	12 089	2 201	646	-7
Share of total loss, [%]	100	30.34	23.38	38.68	7.04	2.07	-0.02

Table 6: Energy losses during levelling cycle

In utilized levelling cycle, the actuator work is on the negative side. Compared to the total input energy, the value is still negligible, denoting that the potential energy at the end position is the same as in the beginning of the cycle. Average values of the two duty cycles are collected in Table 7:

Component	Loss, [J]	Share of total loss, [%]
Pump	9401.5	31.3%
Directional valves	11516.0	38.3%
PAV	6579.5	21.8%
Hoses	2400.0	8.0%
Actuator losses	668.5	2.2%

Table 7: Average energy and loss distribution

The results are consistent between the two cycles. The directional valve is the main energy consumer with 38-39% of total energy. Together with the PAV losses, the total energy lost in the valve group is 58-62%. Pump losses, which include the mechanical and volumetric losses, are 30-32%. Rest of the energy is lost in hose friction (7-9%) and cylinders (2%).

4 Discussion

The developed model is constructed in Matlab/Simulink environment and the parametrization and verification of the simulation model was carried out by measurements on the actual micro excavator. Simulated system consists of the electric motor, hydraulic pump, proportional directional valves and the cylinders. Based on previous studies on the topic /1/, the expectation was that the valves would cause nearly one third of all losses. Efficiency of an excavator was calculated by dividing output power (actuator work) by the total input power. Due to complicated work profile, measuring the total efficiency of a machine is problematic, and knowing the nature and distribution of losses calls for a more detailed information on the dynamic behaviour of the system. The developed model was utilized to simulate a realistic digging-loading cycle of the excavator, and significant sources of energy losses were pointed out. Due to the constant volumetric flow and the open-centre valves, remarkable losses occur whenever the excavator is not moving and during phases of slow movement. During the duty cycles, the throttle losses in valves consume up to 60 % of total input energy.

Therefore, the results indicate a great room for improvement concerning the conventional system. The test case, however, is not completely fair. First, the poor efficiency of a LS system during multiple actuator movement is commonly known. The system pressure was adjusted according to the highest load, and the flow into the other actuators is throttled. In addition, the fixed-volume pump of the micro excavator does not adjust the output flow, as in LS systems, but produces a constant flow. A remarkable portion of the flow is wasted through the pressure adjustment valve, to keep the system pressure level low, according to the low loading condition. According to the simulation, more than 20% of the total power is lost in PAV only. This result calls for more research, and an experimental setup is being prepared to test the excavator in realistic contact with earth. The variable ground contact force will be recorded, and added in to the simulation model, as presented in /5/.

Movement speed of the excavator is dependent on the rotational speed of the electric motor. Increasing the speed would, in this test case, result in more volume lost in PAV. With a more realistic loading condition, in which the PAV would stay unopened most of the time, the additional volumetric flow could be utilized in increased movement speed. This would reduce the cycle time and possibly improve the overall efficiency. The electric motor speed is assumed constant in the simulation model. Additional speed and torque sensor will be fitted for more accurate information on the motor dynamics. A current sensor, which will produce data on the total input energy, will also be prepared for upcoming research.

The actuator losses, which are caused by the frictions in cylinders and the joints of the front hoe, account for only 2% of the total losses in the conventional system. This has given little or no incentive for further research. The friction model could be improved by adding a pressure-dependent component and an angular speed-dependent component, since the current model does not take pressure in to account, and the friction is now a function of cylinder speed only.

5 Summary and Conclusions

A Simulation model of the electro-hydraulic excavator was produced. The model consists of the hydraulic and mechanical systems related to actuation of front hoe, i.e. boom, arm, and bucket. Model parameterization was based on measurement data, when available, and the information found in the literature.

The excavator is fitted with pressure and position sensors, from which the information was collected with a data acquisition system. In addition, a CAN-interface is established in order to communicate with aftermarket directional valves the excavator is fitted with. Comprehensive communication system enables the verification of the simulation model, which gives weight on the obtained results.

The verified simulation model is utilized to study the total energy consumption and power distribution of the micro excavator, and the results are compared and discussed. Two different duty cycles, named digging and loading cycle and levelling cycle, based on the JCMAS standard, was utilized to analyze the power consumption of the excavator.

The results indicate a formidable room for improvement concerning the conventional system, since a power loss of as much as 60% was generated in the directional valve group during two different free-space duty cycles.

Suggested next phase of the research would be the application of external load into the duty cycle. The poor efficiency of a LS-system during unloaded multi-actuator movements is a well-known fact, and operating in this area will give a too negative picture of the efficiency of the conventional system. A ‘sandbox’ for reproducing the ground contact is being planned, and the load-sensing pins will be attached in all cylinders for accurate load measurement.

The simulation model could be improved with a more accurate model of the electric motor. An additional speed-torque sensor will be installed to acquire information on the motor dynamics, and a current sensor, which will produce data on the total input energy, will be prepared for upcoming research. Finally, the friction model could be improved by adding pressure-dependent and angular-speed-dependent variables.

6 Acknowledgements

This research was enabled by the financial support of Tekes, the Finnish Funding Agency for Technology and Innovation (project EL-Zon), internal funding at the Department of Mechanical Engineering at Aalto University and support from Department of Automation and Hydraulic Engineering at Tampere University of Technology.

Nomenclature

Variable	*Description*	*Unit*
B_{eff}	Effective bulk modulus	Pa
d	Pipe inner diameter	m
F_c	Coulomb friction	N
F_s	Static friction	N
F_μ	Friction force	N
K_v	Flow coefficient	-

l	Length	m
P	Power	W
p	Pressure	Pa
Δp	Pressure differential	Pa
p_{tr}	Transition pressure	Pa
p_{nom}	Nominal pressure differential	Pa
q	Volumetric flow	m^3/s
q_{nom}	Nominal flow rate	m^3/s
Re	Reynold's number	-
v	Velocity	m/s
V_t	Total volume of the system	m^3
v_s	Stribeck velocity	m/s
z	Average deflection of bristles	m
λ	Friction factor	-
ε	Relative roughness of a pipe	-
ρ	Fluid density	kg/m^3
σ_0	Stiffness of bristles	N/m
σ_1	Damping coefficient	Ns/m
σ_2	Viscous friction coefficient	Ns/m
ζ	Friction factor (single loss)	-

References

/1/ Zimmerman, J.D., Pelosi, M., Williamson, C.A., Ivantysynova, M. Energy Consumption of an LS Excavator Hydraulic System. Proceedings of IMECE2007, 2007 ASME International Mechanical Engineering Congress & Exposition. November 11-15, 2007, Seattle, Washington, USA.

/2/ Maharjan, D., Mahat, C., Liljeström, J., Vauhkonen, N., Kiviluoma, P., Kuosmanen, P. & Sainio, P. Electrification of Excavator. 9th International DAAAM Baltic Conference, Industrial Engineering, 24-26th April 2014, Tallinn, Estonia.

/3/ Hassi, T., Korva, A., Markkula, S., Partanen, T., Sourander, T., Kiviluoma, P., Korhonen, A. & Kuosmanen, P. Improving Energy Efficiency of an Electric Mini Excavator. 11th International DAAAM Baltic Conference, Industrial Engineering, 20-22th April 2016, Tallinn, Estonia.

/4/ Kiviranta, J. Instrumentation of an Automated Excavator. Master's Thesis. Helsinki University of Technology, 2009. Helsinki, Finland.

/5/ Williamson, C., Zimmerman, J., Ivantysynova, M. Efficiency Study of an Excavator Hydraulic System Based on Displacement-Controlled Actuators. Purdue University, Department of Agricultural and Biological Engineering, West Lafayette, Indiana, USA.

/6/ Hippalgaonkar, R., Ivantysynova, M. A Series-Parallel Hydraulic Hybrid Mini-Excavator with Displacement Controlled Actuators. The 13th Scandinavian International Conference on Fluid Power, SICFP2013, June 3-5, 2013, Linköping, Sweden.

/7/ Parker Hannifin Corporation. Gear Pumps/Motors, Series PGP/PGM Fixed Displacement Pumps, Cast-Iron and Aluminium Designs. Catalogue HY30-3300/UK. 2017 Parker Hannifin Corporation.

/8/ Kauranne, H., Kajaste, J., Vilenius, M. Hydraulitekniikka. 1.Painos. WSOY Oppimateriaalit Oy. 2008, Helsinki, Finland.

/9/ Avci, A., Karagoz, I. A Novel Explicit Equation for Friction Factor in Smooth and Rough Pipes. Journal of Fluids Engineering, Vol. 131. 2009, ASME

/10/ Danfoss. Proportional Valve Group PVG 32, Technical Information. 520L0344. Danfoss. March 2016.

/11/ Bak, M.K., Hansen, M.R. Modeling, Performance Testing and Parameter Identification of Pressure Compensated Proportional Directional Control Valves. University of Agder, Norway.

/12/ Ellmann, A., Piché, R. A Modified Orifice Flow Formula for Numerical Simulation of Fluid Power Systems. FPST-Vol. 3, Fluid Power Systems and Tevhnology: Collected Papers. ASME 1996.

/13/ Järf, A. Flow compensation using hydraulic accumulator in direct driven hydraulic differential cylinder application and effects on energy efficiency. Master's thesis. Aalto University, School of Engineering. Espoo, 2016.

/14/ Canudas de Wit, C., Olsson, H., Åström, K. J., Lischinsky, P. A New Model for Control of Systems with Friction. IEEE Transactions on Automatic Control, vol. 40, no. 3, March 1995.

/15/ JCMAS H 020:2007. Japan Construction Mechanization Association. Earth-moving-machinery – Fuel consumption on hydraulic excavator – Test procedures.

/16/ Ville Salomaa, Efficiency study of an electro-hydraulic excavator, Tampere University of Technology, 2017. Helsinki, Finland.

Wireless Control of an Electro-hydraulic Robotic Manipulator

Željko Šitum, Dalibor Žgela and Juraj Benić

University of Zagreb, Faculty of Mechanical Engineering and Naval Architecture
Ivana Lučića 5, HR-10000 Zagreb, Croatia
E-Mail: zeljko.situm@fsb.hr

This paper deals with the design, practical realization and wireless control of a prototype of an electro-hydraulic robotic manipulator (EHROM) suitable for handling heavy weight objects in industrial environment. The EHROM has been designed in the Laboratory for Automation and Robotics at the Faculty of Mechanical Engineering and Naval Architecture, University of Zagreb. The prototype has been completely built in cooperation with two Croatian companies and is fully open to implementations of various control methods. The robotic manipulator has three-degrees-of-freedom (spherical or polar kinematic configuration) with a hydraulic gripper at the end of the mechanical structure. The manipulator uses a load sensing hydraulic system that provides superior controllability regardless of the load and also contributes to the energy efficiency. Originally the manipulator had no advanced way of being operated, other than the use of joystick or levers on the hydraulic valve block itself. The control system has been upgraded with an assembly suitable for wireless control of the manipulator using a mobile device on iOS platform. This multidisciplinary task involved skills in mechanical engineering, electronics and electrics, as well as computing. The paper focuses on the wireless control of the manipulator using a low-cost microcontroller and custom made controlling interface.

Keywords: Robotic manipulator; electro-hydraulics; wireless control
Target audience: New & Special Applications (Robotics), Digitalization, Connectivity & Communication

1 Introduction

Technological improvements and innovations within modern robotic systems as well as in artificial intelligence, communication and control techniques have made possible some new modalities in traditional robotic system applications [1]. The conventional industrial robots and manipulators are successfully applied for repetitive and relatively simple manufacturing tasks that require organized work space and little interaction between robot and its environment. More recently, the scope of robots is rapidly expanding, and they are increasingly being applied in more complex cases, which generally require faster and more accurate motions and at the same time greater interaction with the environment in which they operate. Owing to the fact that hydraulic drives provide high force multiplication they were used as preferred actuators for industrial robots during the early stages of robotics development. The first prototype of the industrial robot known as Unimate, created by American inventor G. Devol, was produced in 1961 in the world's first robot manufacturing company Unimation founded by J. Engelberger. The Unimate was a hydraulically powered robot. The first robot was installed at a GM's plant and it was programmed to handle hot metal parts used in die casting and for spot welding on auto bodies. The primary purpose of the first robots was to replace humans for the heavy, dangerous and monotonous tasks and they were mostly used for simple pick and place tasks. Despite the fact that at the beginning the first industrial robots had a hydraulic or pneumatic drive, they have undergone a huge change since the first prototypes, so the robots with fluid power drives are rare today. At the beginning of robots development, electric motors did not have satisfactory performance for practical use in many applications. But nowadays, electric drives are by far the most widely used actuators for industrial robots, because they are reliable and accurate. Modern industrial robots with electric drives can lift really large loads as well (payloads over 2 tons), so they dominate in all segments of application [2]. In the last three decades, enormous interest was focused on industrial robots. The automotive companies were, and still are, an important customer, but industrial robots are used in a wide variety of industries, including the mechanical, electronic and chemical industries among others. After having studied robots for decades, we are now witnessing a real interest in robotics and today there is a multitude of teams creating different robots worldwide for special applications such as: agricultural robots, hostile territory exploration, inspection robots, military robots, cleaning robots, service robots, robots for helping the handicapped, medical robots etc. We live in exciting times and the change in robotics technology has never been more rapid. Thus the question arises: are there niche applications for greater use of robots with hydraulic drives? Example of state-of-the-art application of electro-hydraulic drives is remote handling of critical equipment in nuclear fusion reactor [3]. Reliable and robust control strategies are crucial for such applications.

Electro-hydraulic servo systems have desirable features for application in highly automated production facilities as they are characterized with small size-to-power ratio, ability to produce large hydraulic power and large forces, all together in combination with simple processing/transmission of control signals in electrical components. However, precision motion and force control on high power levels are far from trivial. Significant nonlinearities of hydraulic components and complex phenomena of fluid dynamics make control of electro-hydraulic systems extremely challenging task, especially in cases of simultaneous motion of several controlled links of a robotic system. These difficulties are even more emphasized in plants with a large number of control variables and high performance requirements in terms of rapid responses and high accuracy in a wide range of working conditions, smooth and noiseless operation, all in conditions of dynamically changing structure of the robotic system [4].

This paper presents a prototype of the electro-hydraulic robotic manipulator (EHROM) which was developed at the Faculty of Mechanical Engineering and Naval Architecture at the University of Zagreb, Croatia. The robotic manipulator can be used in various industrial applications e.g. assembly lines, CNC machines, welding tasks, in serving foundries, automobile industry etc. The EHROM represents a complex, nonlinear, multivariable system comprised of production components and various features in order to be able to manipulate with objects weighing up to 200 kg. Furthermore, specific for such systems is a large number of parameters which vary depending on the system's operational point. Load-sensing technology is used for the manipulator operation, enabling simultaneous motion of all controlled axes. The robotic manipulator is completely open system and currently is being used as an educational platform for the development of advanced control algorithms [5].

2 Specifications of the electro-hydraulic manipulator

The robotic manipulator, shown in Figure 1, has three-degrees-of-freedom (RRT - polar or spherical kinematic structure). Rotational degrees-of-freedom are used for the rotation of the arm of the manipulator and the rotation of the arm carrying a prismatic joint, while the linear degree-of-freedom is represented through an extendable arm which carries a gripper at the end of the mechanical structure. All degrees-of-freedom are hydraulically actuated, as well as the gripper itself. Rotation of the arm is performed using a hydraulic motor combined with a worm drive, while the rotation of the extendable arm is performed using a double acting hydraulic cylinder. The linear movement of the arm has been enabled using a telescopic hydraulic cylinder. A small double acting hydraulic cylinder is used for the movement of the gripper. The manipulator weighs approximately 515 kg and when the telescopically extendable arm is fully extended its workspace is described with an operating diameter of 3.6 m and height of 2.7 m while its payload capacity is up to 200 kg. This configuration allows the manipulator to reach a wide working area, still being reasonably affordable and flexible. Systems like EHROM can provide a large torque and fast response of actuators with the possibility of simultaneous movement of all the controlled axes of the plant. The system is equipped with sensors allowing the control unit to acquire angular position of two revolute joints and the extension of a linear joint. Furthermore, pressure and force sensors can be used to determine forces exerted upon a specific degree-of-freedom of the manipulator.

The manipulator was built in close cooperation with two Croatian companies: Hidraulika Kutina – The factory of hydraulic and pneumatic equipment and components, Inc. from town Kutina and Rasco – The factory of communal equipment Ltd. from municipality Kalinovac.

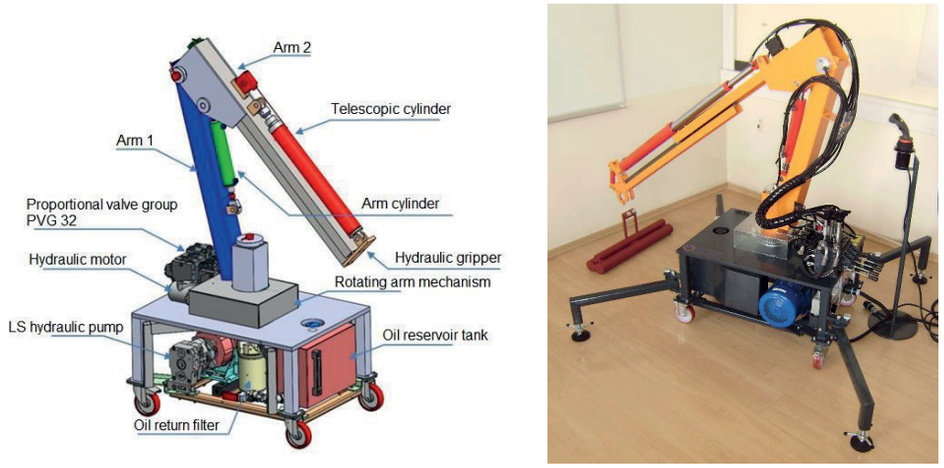


Figure 1. Prototype of an electro-hydraulic robotic manipulator (EHROM)

2.1 Hydraulic power unit

The hydraulic power unit of the EHROM consists of an axial piston pump, a tank containing 60 litres of oil, filters and proportional valve block. Installed axial piston pump, shown in Figure 2, with variable displacement is produced by Parker Hannifin (model PV023), and it is equipped with a load-sensing system which allows the pump to detect the need for oil supply and change the flow rate accordingly. The displacement of the pump is 23 cm^3 with the nominal rotational speed of 1410 l/min which translates to the nominal flow of 32.5 l/min. Maximum pressure the pump can operate at is 120 bar, while the maximum achievable pressure in the system has been reduced to 100 bar by using a pressure regulator. The oil pump is driven by a three-phase squirrel cage induction electric motor, rated 5.5 kW at 1410 rpm. Distribution of the supplied oil is being made by a load-sensing proportional valve group PVG32 with PVEH actuation modules (cross-section shown in Figure 3), produced by Sauer-Danfoss. Characteristic for this valve group is the independence of the flow rate with the pressure in the system and extremely low hysteresis alongside with the compact design and easy installation options.

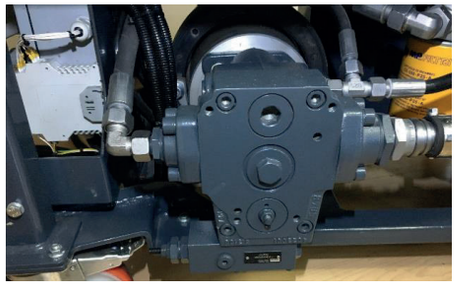


Figure 2. Hydraulic power unit with variable displacement axial piston pump

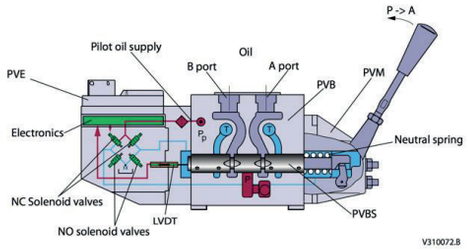


Figure 3. Cross-section of a segment of PVG32 proportional valve group [6]

Maximum working pressure is set to 160 bar and the supply voltage of the valve group is 24V DC. The flow of each of the segment of the valve group is voltage controlled according to the valve characteristics. The flow of the proportional valve group depends on the supply voltage and the signal voltage applied to each individual segment of the group. Flow rates for the actuators of each of three degrees-of-freedom and the gripper have been decided upon during the design process in order to achieve the desired specifications of the system. Therefore, the segment of valve group intended for the oil supply to the double acting hydraulic cylinder raising the arm has been chosen to be able to deliver up to 40 l/min of oil, while the valve segments supplying the torque motor and the telescopic hydraulic cylinder are rated at 20 l/min. Lastly, the flow rate for the small hydraulic cylinder intended for opening and closing the gripper has been chosen to be 5 l/min at most.

2.2 Hydraulic actuators

For allowing the rotary motion of the arm, a torque motor paired with a worm drive with the reduction of 1:50 has been chosen. The torque motor shown in Figure 4 is produced by Parker (model TE0036). With its fixed displacement of 36 cm^3 and the nominal flow rate of the axial piston pump, the maximal rotational speed can be calculated to 917 1/min which translates to rotational speed of the arm itself to be 18.34 1/min. Maximum pressure the torque motor can operate under is 120 bar while the maximum speed is rated at 1167 1/min, which is well under the possible values of the both variables.

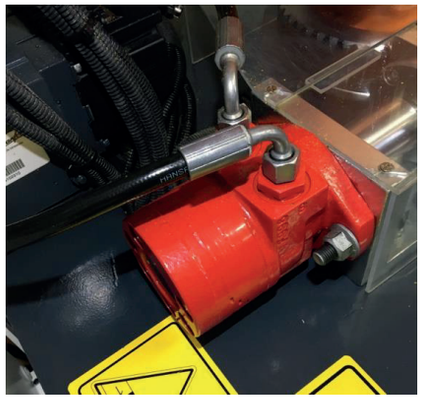


Figure 3. Hydraulic torque motor paired with a worm drive



Figure 4. Double acting hydraulic cylinder used for the rotation of the telescopic arm

Double acting hydraulic cylinder used for the rotation of the extendable arm (Figure 5.) is manufactured by Hidraulika Kutina d.d. The diameter of the piston is 50 mm, while the diameter of the piston rod is 25 mm with maximum stroke of 210 mm. The cylinder is mounted on the manipulator with spherical G-bearings, allowing the proper installation of force sensor on the lower part of the cylinder.

Manufactured by Hidraulika Kutina d.d. as well, telescopic cylinder is used for the linear movement of the extendable arm, the third degree-of-freedom of the manipulator. The diameter of the outer shell of the cylinder is 75 mm, while the diameters of the two pistons are 63 mm and 45 mm (with respective piston rods diameters of 55 mm and 35 mm). Maximum stroke of the telescopic cylinder has been set to 1000 mm.

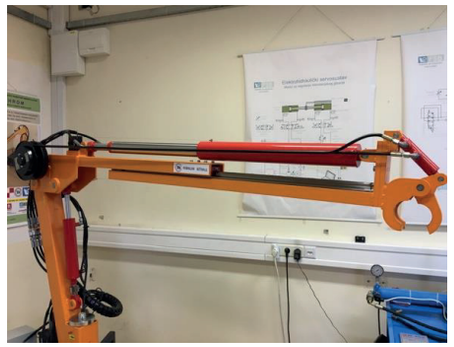


Figure 5. Telescopic hydraulic cylinder used for the linear movement of the extendable arm

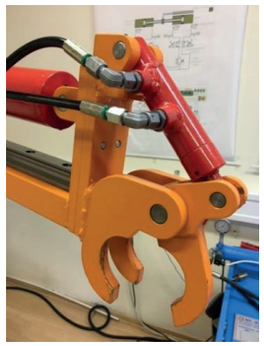


Figure 6. Open gripper

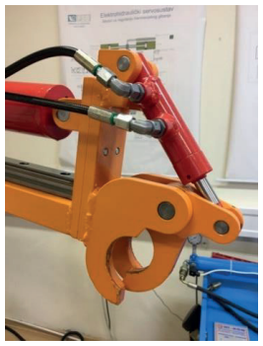


Figure 7. Closed gripper

As well as the other two hydraulic cylinders, small double acting hydraulic cylinder (Figure 7 and 8) actuating the gripper is manufactured by Hidraulika Kutina d.d. The outer diameter of the cylinder is set to 35 mm with 5 mm thick side wall. The maximum stroke of the cylinder (30 mm) has been calculated in a way to enable the full opening and closing of the gripper. Considering the weight of the objects the manipulator can handle, the gripper was designed in simple but effective way, allowing the manipulator to firmly and safely grasp the desired object. The grip is ensured by the overlapping jaws of the gripper itself.

2.3 Sensory part of the system

The manipulator has been equipped with various sensors allowing the control unit to acquire important data regarding the state of the system. In order to measure the angle of the rotation of the arm and telescope, rotary encoders, produced by RLS, have been used. Range of the rotary encoder connected to the base of the arm (Figure 9.) has been chosen to be 360°, considering the achievable angle span of the base of 270°. On the other hand, for measuring the angle of the telescopic arm (Figure 10.), a similar rotary encoder has been used, but with reduced range of 180 ° in order to achieve greater resolution. Both of the chosen rotary encoders are of incremental type, but the voltage output of the encoder to the user is in the range of 0 to 10 V DC thus excluding the need for the additional calculations on the user side. The function describing the voltage in respect to the angle of the rotary encoder is linear which makes the reverse conversion of the voltage signal to the respective angle relatively easy. Given the voltage signal V_m, the angle of the telescopic arm φ can be calculated according to the expression:

$$\varphi(V_m) = 20{,}4489 \cdot (V_m - 3{,}95) \quad [°]\,, \tag{1}$$

or given in radians:

$$\varphi(V_m) = 0{,}3569 \cdot (V_m - 3{,}95) \quad [rad]\,. \tag{2}$$

Linear position of the extendable arm is measured with a linear position sensor manufactured by Micro-epsilon (draw-wire sensor type WPS-2100) and it is based on the working principle of a trimmer. With its range of up to 2100 mm the linear position sensor has been chosen as suitable considering the length of the retracted arm and its maximum elongation. Since the sensor is based on the principle of a voltage divider, its output is directly tied to the supplied voltage. In case of a 24 V DC supply, the following expression can be used to describe the length of the telescopic arm s:

$$s(V_m) = 88{,}5740 \cdot (V_m - 2{,}57) \quad [\mathrm{V}], \tag{3}$$

where V_m stands for the output voltage signal of the linear position sensor.



Figure 8. Rotary encoder for measuring base rotation

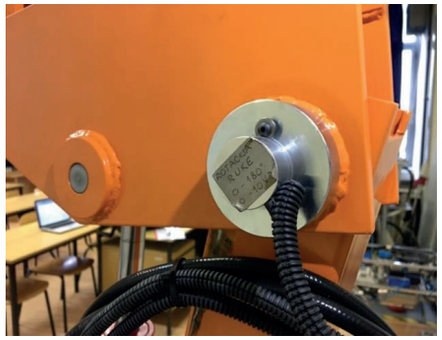


Figure 9. Rotary encoder for measuring telescopic arm rotation



Figure 10. Force sensor for measuring payload

For measuring the oil pressure in the chambers of the telescopic hydraulic cylinder and the torque motor, Siemens pressure sensors SITRANS P220 have been used. This type of pressure sensor is suitable for measuring pressures up to 250 bar which corresponds to the voltage signal output in range from 0 to 10 V DC. Considering the linear characteristic of the sensor, pressure in the chamber p can be calculated using the following expression:

$$p = 25 \cdot 10^5 \cdot V_m \quad [\mathrm{Pa}]\,, \tag{4}$$

where V_m represents the measured output voltage signal.

In order to be able to directly measure force exerted upon the double acting hydraulic cylinder used for the rotation of the telescopic arm, HBM force sensor 1-U9C (Figure 11) is used, combined with RM4220 amplifier. The force that can be measured with the chosen sensor ranges from 2 kN to 50 kN. Value of the output voltage signal ranges from 0 to 10 V DC, or for the output current signal in range from 4 to 20 mA.

3 Wireless control assembly

In order to achieve wireless control of the EHROM over Bluetooth, the existing system had been thoroughly analysed after which the solution was designed and finally built and tested. In the process of the development of the wireless control assembly (Figure 12.), it was necessary to establish a wireless communication between the manipulator and the control device of choice. For that purpose, an iPhone 6s mobile device in addition to the easily acquirable and user-friendly Arduino microcontroller and appropriate Bluetooth module were used. Aside from enabling the wireless communication, it was necessary to program the microcontroller in a way to understand the received messages coming from the mobile device and forward them to the signal conversion board. The self-made signal conversion board is intended for the conversion of low voltage and low energy TTL signals coming from the Arduino into appropriate signals for the installed proportional valve block. Additionally, safety features ensuring the safe process of switching the control system on and off have been designed and developed.



Figure 11. Designed and manufactured wireless control assembly

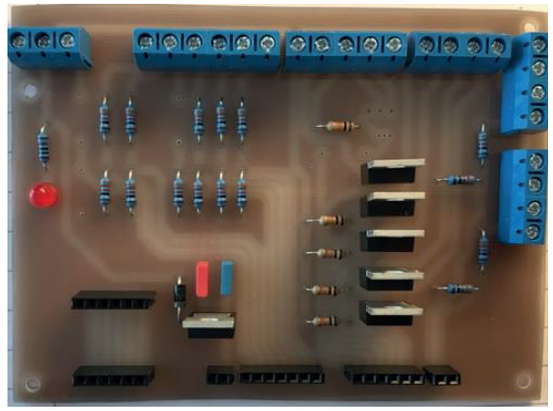


Figure 12. Self-made signal conversion board

3.1 Design and manufacturing of the conversion board

A conversion board shown in Figure 13, is used in order to convert low voltage signals (0 - 5 V DC) arriving from Arduino microcontroller to higher level voltage signal (0-24 V DC) needed for the control of the individual segments of proportional valve block. The way of converting the signals has been chosen regarding the defined voltage signals and the input impedance of the valve block control electronics. For that purpose a MOSFET transistor IRLZ44N was used, combined with 10 kΩ resistor. The transistor is controlled by the logic level voltage of the Arduino microcontroller with the use of pulse-width-modulation (PWM). In order to be able to control all

three degrees-of-freedom of the manipulator, as well as the motion of the gripper four transistor circuits were used, all of which are controlled by four PWM outputs of the Arduino microcontroller. Additionally, the board includes the connection for the Bluetooth module, and the circuitry needed for adjusting the 24V DC voltage coming from the manipulator to the voltage suitable for supplying the microcontroller. The board has been self-made using the conventional etching process.

3.2 Mobile app for wireless control of the manipulator

For the control of all three degrees-of-freedom and the gripper, mobile app named EHROM has been developed. Running on iOS platform it is suitable for installation on devices such as iPhone, iPad or iPod. The development and the testing have been made using an iPhone 6s device running on iOS 10. The app features a welcome screen, Bluetooth connection screen, control screen with the corresponding sliders for the control of the manipulator and screen containing basic information regarding the project.

After successfully establishing the Bluetooth connection between the Bluetooth module connected to the Arduino microcontroller and the mobile device, user is automatically forwarded to the control screen (Figure 14.). Control screen contains sliders corresponding to each of three degrees-of-freedom, as well as a slider for controlling the gripper.

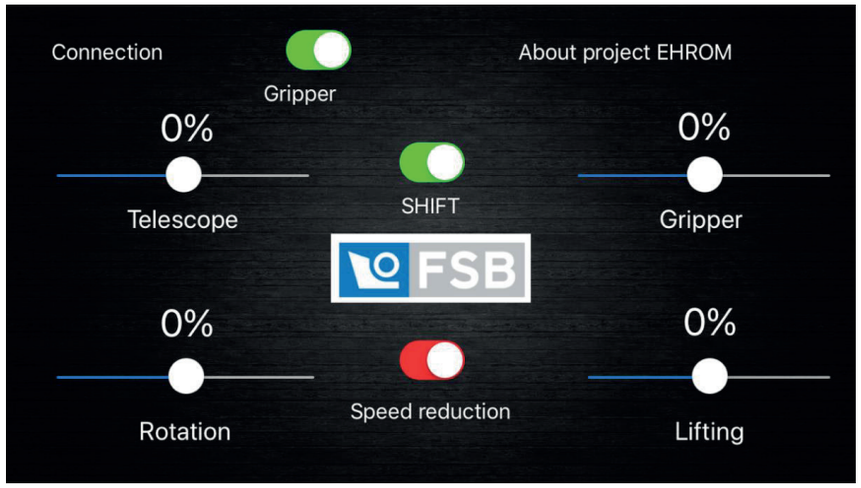


Figure 134. Control screen of the EHROM app

Following the standards of conventional robot teach pendants, safety feature regarding the unintentional movement of the control sliders has been implemented. In order for the control command to be transferred to the Arduino microcontroller and the manipulator respectively, it is necessary for the SHIFT button, shown in Figure 14, to be enabled. By releasing the control commands, the SHIFT button returns automatically to switched off state thus preventing transfer of unwanted commands. Additionally, in order to change the state of the gripper, it is necessary to enable the SHIFT button as well as the gripper enable button. This security feature was added in order to completely reduce unintentional drop of heavy objects the manipulator could be carrying.

3.3 Transfer of data via Bluetooth

The transfer of the control commands from the mobile device running the EHROM app and the Arduino microcontroller is being done using a HM-10 Bluetooth module compatible with Bluetooth 4.0 standard. The command sent from the mobile device is in a form of an integer number followed by a letter. The letter is used to distinguish the element the command will be applied to (Table 1.), while the integer number ranging from -100 to 100, gives the microcontroller the information regarding the opening of the proportional valve segment thus controlling the oil flow and speed of the controlled element.

The Letter	Element the letter corresponds to
A	Rotation of the arm
B	Rotation of the telescopic arm
C	Linear movement of the telescopic arm
D	Movement of the gripper

Table 1. Letter mark for addressing a specific part of the manipulator

It is possible to limit the maximum oil flows to 50% of the unrestricted value by pressing the appropriate button (Speed reduction) on the control screen. This feature allows the user to perform fine movements of the manipulator when such positioning is needed.

3.4 Control logic

For the purpose of receiving the control commands from the Bluetooth HM-10 module and forwarding the PWM signal according to the received commands, Arduino MEGA 2560 microcontroller has been used. Having more than enough of PWM ports, as well as analogue input ports for the future development of data acquisition from the sensors, MEGA 2560 microcontroller has presented itself as an ideal candidate for this application. The main task of the microcontroller is the interpretation of the data received through Bluetooth module. Depending on the received letter and an integer value, PWM duty cycle is assigned to the corresponding output thus determining the voltage of the proportional valve block input. Integer numbers in the Bluetooth message determine the requested direction of the oil flow, and its intensity in such way that 0 marks the state of no flow, while values -100 and 100 represent a request for maximum oil flow but in opposite directions.

3.5 Assembly housing

In order to protect the user and the equipment, developed and assembled electronics have been enclosed in a housing with IP66 level of protection (Figure 12. and Figure 15.). In addition to the housing mounted on the robot itself, a control box has been developed. Control box, shown in Figure 16, is essential for enabling the movements of the manipulator since the power supply of the proportional valve group derives from it, containing two buttons for turning the power supply on or off, alongside with the emergency stop button. Being connected to the central housing with 5 m long cable it enables the user to safely start or stop the system without the risk of being injured by the unexpected movement of the manipulator.

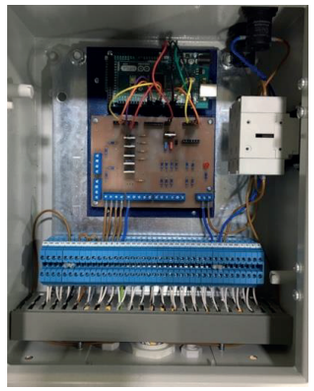


Figure 145. Interior of the housing containing the Arduino microcontroller, HM-10 Bluetooth module and signal conversion board



Figure 156. Control box for the additional safety in turning the system on and off

4 Further development of the control system

Further development of the system should take part in two directions. Considering the computing power and diverse features of smartphones currently available on the market, a valuable approach would be to investigate the potentials of using such devices as wireless and compact yet powerful controllers. By establishing a feedback connection of the data acquired from the sensors, a smartphone could be used as a portable device with a software that can be quickly adjusted to the specific needs of a specific system.

The other direction of the development should involve an implementation of a commercially available control device, such as programmable logic controller (PLC), programmable automation controller (PAC) or industrial PC (IPC) based data acquisition system. In the end a comparison between the systems would be advisable, involving comparison in flexibility, robustness and accuracy of the mentioned systems.

5 Conclusions

Based on the given specifications, an assembly for wireless control of an electro-hydraulic robotic manipulator is proposed. The assembly consists of an Arduino microcontroller with Bluetooth module and a signal conversion board, housed in IP66 protective case. Additional control box has been implemented in order to achieve highest safety standards for the user of the device. Proposed controller of the system is a mobile device with touch screen, allowing the user to use sliders in order to determine the speed of a desired element corresponding to a degree-of-freedom actuator or the gripper. Additional safety features have been implemented on the software side as well, thus eliminating the transfer of unintentionally given commands. Guidelines for the further development of the system have been proposed which offer great potential for further research.

6 Acknowledgment

The authors would like to thank Mr. Ante Bazina and Mr. Darije Miloš from Hidraulika Kutina – The factory of hydraulic and pneumatic equipment and components, Inc. from town Kutina and Mr. Frane Franičević and Mr. Ivica Ivanic from Rasco – The factory of communal equipment Ltd. from municipality Kalinovac for supplying the experimental setup components and for their assistance in the design, construction and implementation of the test system.

Nomenclature

Variable	*Description*	*Unit*
p	Pressure	[bar]
s	Displacement	[m]
V_m	Measured voltage	[V]
φ	Angle of the telescopic arm	[deg]

References

/1/ Wilcox, B., Ambrose, R., Kumar, V., *Robotics: State of the Art and Future Challenges*, WTEC Panel on International Assessment of R&D in Robotics, http://www.wtec.org/robotics/, pp. 39-68, 2008.

/2/ Brochures of Fanuc's product: Super Heavy Payload Robot, Fanuc M-2000iA/2300, http://fanuc.co.jp, visited on November 20, 2017.

/3/ Dubus, G., Davida, O., Nozais F., Meassona, Y., Friconneaua, J.-P., Palmer, J.: Assessment of a wat hydraulic joint for remote handling operations in the divertor region; Fusion Engineering and Desig Vol. 83, pp. 1845–1849, 2008.

/4/ Sirouspour, M. R., Salcudean, S. E., *Nonlinear control of hydraulic robots,* IEEE Transactions Robotics and Automation*,* Vol. 17, No. 2, pp. 173-182, 2001.

/5/ Šitum, Ž., *Fluid power drives in robotic systems*, In: 11th International Conference Fluid Power 2(Maribor, Slovenia, pp. 11-23, September 14-15, 2017.

/6/ Sauer-Danfoss Technical Information: Proportional Valve Group PVG 32, Valve section with nami standard mounted, http://files.danfoss.com/documents/520L0344.pdf, visited on November 27, 201

A new type of hydraulic swing drive with integrated motion sensor for narrow spaces

Wei Cai*, Jingyi Zhao* , Ruixin Zhang and Hao Sun*

Hebei Provincial Key Laboratory of Heavy Machinery Fluid Power Transmission and Control, Yanshan University, Hebei str. 438, Qinhuangdao, China*
E-Mail: chenmochiwei@163.com

The automation of mobile hydraulic machinery, such as bionic robot, requires high power-to-volume ratio and high performance control solutions, which means miniaturized, integrated, and intelligent hydraulic systems. The purpose of the paper is to present a new type of hydraulic swing drive for narrow spaces, where the position sensor is integrated as a part of hydraulic system. The structural characteristics of this hydraulic swing drive as well as its functionality are presented in detail. Through the comparison with the traditional hydraulic motor, position resolution and power-to-volume ratio have been further improved, therefore the application of hydraulic systems has been expanded, especially in some kinds of bionic robots.

Keywords: Narrow spaces, swing drive, flexible rope, digitalization
Target audience: Mobile Hydraulics, New & Special Application

1 Introduction

Due to the high power-to-weight ratio of the hydraulic system, it has a wide range of applications in many fields, such as aircraft, transport vehicles, robots and so on /1/. The automation of mobile hydraulic machinery, such as bionic robot, requires high power-to-volume ratio and high performance control solutions, which means miniaturized, integrated, and intelligent hydraulic systems /2/. In particular, traditional hydraulic components and systems are difficult to be applied to the current field of robots /3/. Currently, the swing of the axis is known to use hydraulic motor directly, or use linkage mechanism driven by hydraulic cylinder. It is difficult to meet the requirements from the host for response and installation dimensions. Wen desheng et al. studied the leakage and volumetric efficiency and seal improvement for double-stator swing hydraulic motor, and a new type of double-stator swing hydraulic motor is put forward, which combines the structure of vane swing hydraulic motor and the thought of double-stator /4/. Zhu Zhichao et al. used a door-shaped sealing structure to decrease the frictional force and improve the movement efficiency and stability of the hydraulic swing vane cylinder /5/. Tao Yong et al. presented a hydraulic swing arm-driven robot hydraulic arm, which driven by the hydraulic swing cylinder. This invention gets more output torque, and the carrying capacity gets improved /6/. This paper presents a new type of hydraulic swing drive for narrow spaces, where the position sensor is integrated as a part of hydraulic system, which can overcome the problems of response and installation dimensions. The research results show that the position resolution and power-to-volume ratio have been further improved, therefore the application of hydraulic systems has been expanded, especially in some kinds of bionic robots.

2 Structure and Principle of the Swing Drive

2.1 Structure of the swing drive

This hydraulic swing drive mainly consists of a servo motor, two hydraulic cylinder, carbon fiber rope, manifold block, the outer tube and some screws. Its 3D structure diagram shows in the Figure 1.

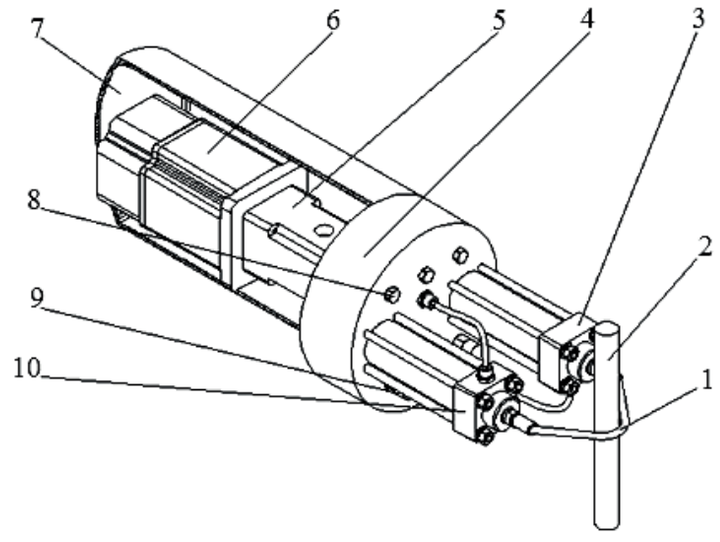


Figure 1: The 3D structure diagram of the swing drive.

The flexible rope structure includes a carbon fiber rope (1) and a swing shaft (2), the midpoint of the carbon fiber rope (1) is fixed on the swing shaft (2), both ends of the carbon fiber rope (1) are fixed on the output rod of the hydraulic cylinder (3), the flexible rope The structure can translate the linear motion of the hydraulic cylinder (3) into the rotation of the swing shaft. The hydraulic drive structure comprises a hydraulic cylinder (3) and a hydraulic cylinder (10) with an integrated position sensor, a manifold (4), a small axial piston pump (5), a servomotor (6), a tank (7), a check valve (8) and a relief valve (9).By controlling the rotation speed of the servo motor (6), the output flow of the pump (5) can be controlled. Because of the working mode of the pump control cylinder, the pump (5) can supply oil in both directions and control the extension and retraction of the hydraulic cylinder (3) and the hydraulic cylinder (10).Thereby achieving the pivot shaft (2) is rotated.

2.2 Principle of the swing drive

Figure 2 shows the hydraulic system diagram of the swing drive.

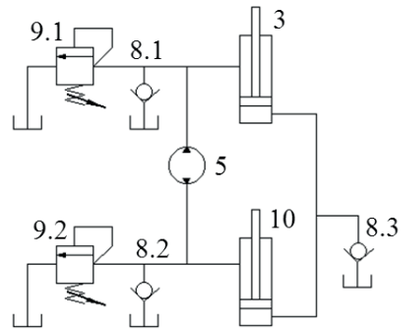


Figure 2: The hydraulic system diagram of the swing drive.

The working principle of the swing drive is that when the oil enters the rod chamber of the hydraulic cylinder (7), the swing shaft rotates counter clockwise and the swing angle α of the swing shaft can be obtained by the Equation (1):

$$\alpha = (\tau \times 360) \div (D \times \pi) \quad (1)$$

The unit of angle is degrees. When oil enters the rod chamber of the cylinder (3), the swinging shaft (2) rotates clockwise. Due to the traction of the carbon fiber rope (1), the cylinder (3) and the rodless chamber of the cylinder (10) communicate with each other, so that the cylinder (3) and the cylinder (10) are synchronized in opposite directions, that is, the moving distances are equal. Because the system is a closed loop, considering the system has a leakage effect, the swing drive through the one-way valve 8.3 access rodless chamber oil-way, one-way valves 8.1 and 8.2 access to the small axial piston pump inlet and outlet oil, to achieve the lack of hydraulic oil through the valve block (4) on the oil hole in time to fill the oil. When the working pressure of the system exceeds the set pressure of the relief valve, the oil is relieved through the oil hole in the valve block (4) through the relief valve 9.1 or the relief valve 9.2 to prevent the traction of the carbon fiber rope (1) from being broken.

The integrated position sensor, the digital controller and the control method also have a significant influence on the oscillating drive capability of the oscillating shaft (2). The hydraulic cylinder (3) and the hydraulic cylinder (10) in the system are each integrated with a position sensor for providing the position information of the hydraulic cylinder to the digital controller. The difference between the measured displacement signal of the hydraulic cylinder (3) and the hydraulic cylinder (10) is the elongation of the carbon fiber rope (1), which is used for the controller to control the servo motor (6) to compensate the variation of the carbon fiber rope (1).

2.3 Design parameters

The tensile strength of Carbon fiber rope can reach 3000Mpa, while the tensile strength of wire rope is about 1770Mpa. The structure which transforms the linear drive into a swing drive by flexible rope increases the power-to-volume ratio of the drive device and the response. Table 1 gives some of the main parameters of an implementation case of this scheme.

Physical quantity	Operating hours	Frequency	Amplitude	Torque	Shaft diameter	Rated pressure
Symbol	t	f	θ	T	d	p
Unit	h	Hz	°	N·m	mm	bar
Value	200	1.2	45	1200	52	200

Table 1: The main parameters of an implementation case of this scheme.

The design parameters of the swing drive designed according to the above data are shown in Table 2, which includes working pressure, material density, cylinder thickness, piston diameter, piston rod diameter and force arm. According to the material density, we can see that the main material selected in this design case is aluminum alloy.

Physical quantity	Working pressure	Material density	Cylinder thickness	Piston diameter	Piston rod diameter	Force arm
Symbol	p	ρ	Δ	D	d	l
Unit	bar	g/cm^3	mm	mm	mm	mm
Value	170	2.7	5	50	25	40

Table 2: The design parameters of the swing drive.

Through some basic formulas, we calculated the data, which is shown in Table 3, which we are very concerned about in the design process, such as hydraulic cylinder load, stroke, rod cavity area and rodless cavity area. The thickness of the force arm and the length of hydraulic cylinder rod are closely related to the dimensions and weight of the actuator. Table 3 also shows the design values.

Physical quantity	Load	Stroke	Rod cavity area	Rodless cavity area	Thickness of force arm	Length of rod
Symbol	F	L	A_B	A_A	$\triangle'$	$1.5L$
Unit	kN	mm	cm^2	cm^2	mm	mm
Value	33.38	31.42	14.73	19.63	28	47.124

Table 3: The intermediate data of interest.

The swing drive input flow is:

$$q = \frac{(2 \times f \times 60 \times L \times A_B)}{10} / 1000 \quad (2)$$

Hydraulic pump power is:

$$P = \frac{(p \times q)}{\eta} / 60 \quad (3)$$

The volume of two hydraulic cylinders is:

$$V = \left(\frac{\pi \times (D + 2\Delta)^2}{4} - \frac{\pi \times D^2}{4} \right) \times 2L / 1000 \quad (4)$$

The weight of two hydraulic cylinders is:

$$G = \frac{\rho \times V}{1000} \quad (5)$$

The weight of two hydraulic cylinders' rods is:

$$G_r = \frac{\pi \times d^2}{4} \times 1.5L \times \frac{2\rho}{1000} / 1000 \quad (6)$$

Table 4 gives the results of the data above.

Physical quantity	Input flow	Hydraulic pump power	Volume of hydraulic cylinders	Weight of hydraulic cylinders	Weight of hydraulic cylinders' rods	Efficiency of hydraulic cylinder
Symbol	q	P	V	G	G_r	η
Unit	L/Min	kW	cm3	kg	kg	---
Value	6.66	1.89	54.28	0.15	0.13	Assumed to be 100%

Table 4: The final parameters of the system.

3 Test System

The simulation system shows in Figure 3. The parameters of each component in the system are set according to Table 3 and Table 4. In order to test the feasibility of the system, the simulation system uses a sinusoidal load. Figure 4 provides the load curve. The peak load is 1200N·m. The flow rate of the pump shows in Figure 5. The pressure of the pump's right port gives in Figure 6. And its peak pressure is 210bar. Simulation system runs 10s, the sampling period is 0.01s.

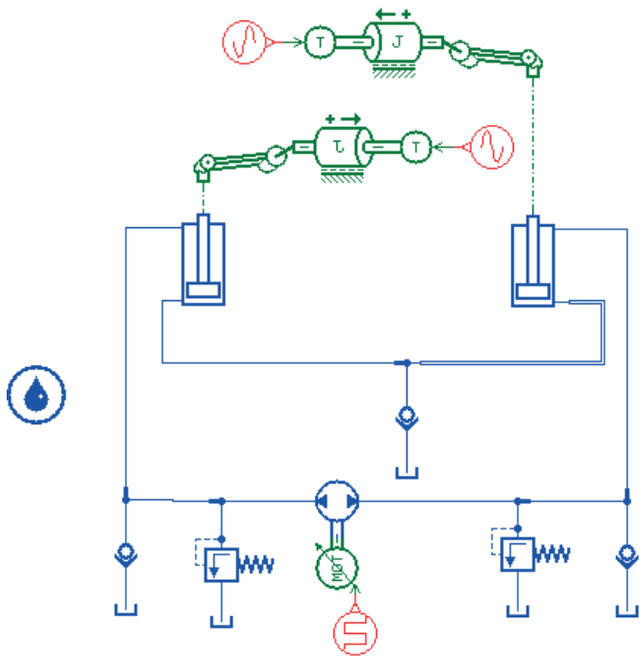


Figure 3: The simulation system of the swing drive.

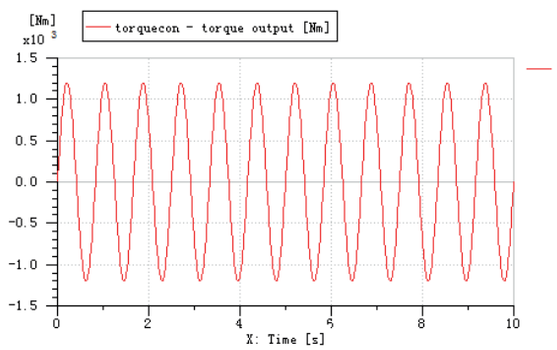


Figure 4: The load curve.

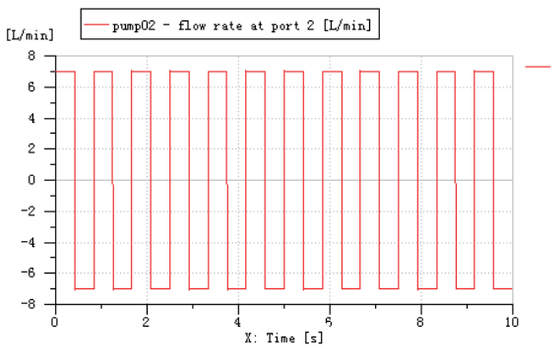


Figure 5: The flow rate of the pump.

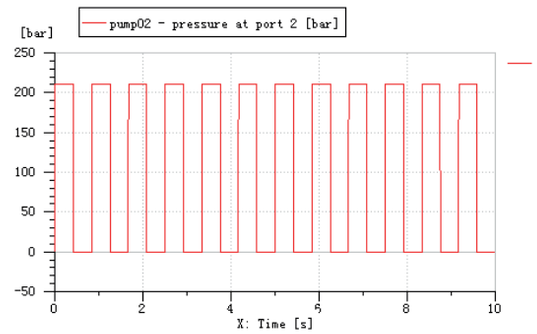


Figure 6: The pressure of the pump's right port.

4 Experimental Results

The displacement of the two actuators shows in the Figure 7, which illustrates the two actuators completed alternating telescopic movement. The results show that the design meets the requirements.

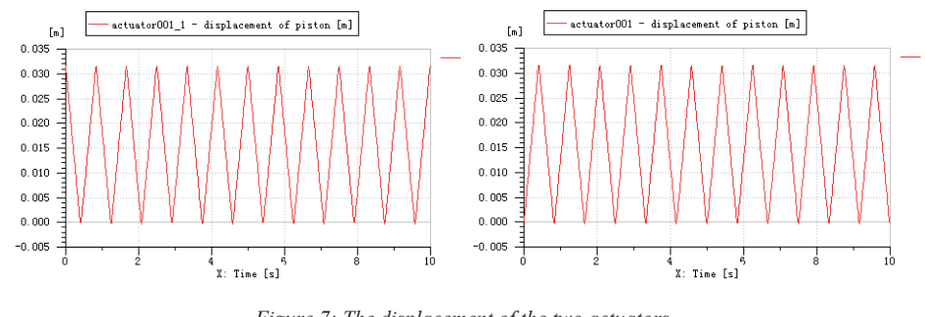


Figure 7: The displacement of the two actuators.

5 Conclusion

The new type of hydraulic swing drive with integrated motion sensor for narrow spaces can increase the power-to-volume ratio of the drive device and the response, and be applied to special robots. Compared with the hydraulic motor, this swing drive overcomes the problem of bulky and inflexible layout. At the same time, the noise of this swing drive is very small compared to mechanical drives such as rack and pinion. Because there is none direct contact between the structures. The simulation system proves the feasibility of the design, but the response of the swing drive needs to be further studied.

6 Acknowledgements

The authors are sincerely grateful to the supports of National Natural Science Foundation of China (Grant No.51405424, 51675461, 11673040).

Nomenclature

Variable	*Description*	*Unit*
α	Swinging angle	[°]
τ	The distance the cylinder moves	[mm]

D	Diameter of the swing axis	[mm]

References

/1/ Adj. Prof. Matti Lijama, Dr.-Ing. Mikko Huova, M.Sc. Otso Karhu & Prof. Kalevi Huhtala, *High-Performance Digital Hydraulic Tracking Control of a Mobile Boom Mockup*,In: 10th International Fluid Power Conference, 10. IFK, Aachen, Germany, pp. 37-47, March 8-10, 2016.

/2/ Ba Kaixian, Kong Xiangdong, Zhu Qixin, Li Chunhe, Zhao Hualong, Yu Bin, *Position/Force-based Impedance Control and Their Experimental Research on Hydraulic Drive Unit*, Journal of Mechanical Engineering, Vol. 53, No. 12, pp. 172-183, 2017.

/3/ Tan Min, Wang Shuo, *Research Progress on Robotics*, Acta Automatica Sinica, Vol. 39, No. 7, pp. 963-972, 2013.

/4/ Wen Desheng, Shang Xudong, Gu Pan, Pan Weiyuan, Shi Zizhou, Zheng Wei, *Analysis of Leakage and Volumetric Efficiency and Seal Improvement for Double-stator Swing Hydraulic Motor*, Transactions of the Chinese Society of Agricultural Engineering, Vol. 33, No. 12, pp. 74-81, 2017.

/5/ Zhu Zhichao, Jiang Lin, Guo Chen, Cheng Wenkai, *Design and Sealing Performance Analysis of a Door-shaped Sealing Structure of Hydraulic Swing Vane Cylinder*, Lubrication Engineering, Vol. 42, No. 5, pp. 102-116, 2017.

/6/ Tao Yong, Hu Lei, Sun Bei, Gao Pengpeng, Liu Hui, *A robot hydraulic manipulator based on a hydraulic oscillating cylinder driving a joint*, Beijing: CN105945989A, 2016-09-21.

Hydraulic Multi-axial Levelling Control for Turbine Access System of Offshore Wind Farm

Mao-Hsiung Chiang, Bo-Yen Chen, Chung-Lung Lo, and Ming-Chun Hsu

Department of Engineering Science and Ocean Engineering, National Taiwan University,
No.1, Sec.4, Roosevelt Rd., Taipei 10617, Taiwan

E-Mail: mhchiang@ntu.edu.tw

Offshore wind energy has become the most important green energy globally. Due to the wave the working point of the vessel oscillates and cannot be kept in a fixed position so that the maritime or underwater construction become difficult and dangerous. Therefore, an active levelling controlled multi-axial hydraulic Turbine Access System (TAS) system for offshore wind farms is necessary for improving this problem. This study aims to investigate a new active levelling control multi-axial hydraulic system for Taiwan offshore wind farms including design, dynamic modelling and simulation of TAS mechanism, hydraulic driving system, control system, and test rig set up for dynamic simulation and experiment. The vertical height, the rolling angle and the vertical acceleration of the end effector of TAS can be effectively reduced through the active motion compensation control of TAS for improving the access safety of the offshore wind turbine. For simulation, the dynamic modelling and co-simulation can be implemented by software ADAMS (Automated Dynamic Analysis of Mechanical Systems) for mechanism integrated with MATLAB/SIMULINK for the hydraulic driving system and the closed-loop control system of the active motion compensation control in order to verify the effect of active compensation control system of TAS. Besides, a full-scale test rig of the TAS is set up for verifying the effect of active compensation control system of TAS experimentally.

Keywords: offshore wind turbine access system, active motion compensation control, kinematics analysis, dynamic simulation, experiment.

Target audience: Mobile hydraulics, Marine Hydraulics, Motion control

1 Introduction

Offshore wind energy has been developed soon and become the most important green energy worldwide since the past decade. The industries in Taiwan have organized a Marine-Team to develop the localized marine engineering for offshore wind energy development in Taiwan. Due to the wave the working point of the vessel oscillates and cannot be kept in a fixed or stable position so that the maritime or underwater construction become difficult and dangerous. The safety assurance for the maintenance of offshore wind turbines becomes an important issue. In order to prevent maintenance staff from the risk of accessing the offshore wind turbines, the turbine access system (TAS) is one of the necessary equipment. Therefore, it is imperative to develop the TAS of offshore wind turbines, which can not only ensure the safety of maintenance, but also effectively enhance the attendance of maritime ship and reduce the installation cost of maritime works. Thus, this study aims to investigate a new offshore wind turbine access system, including design, dynamic modeling and simulation of TAS mechanism, hydraulic driving system, control system, and test rig set up for dynamic simulation and experiment. The vertical height, the rolling angle and the vertical acceleration of the end effector of TAS can be effectively reduced through the active motion compensation control of TAS for improving the access safety of the offshore wind turbine.

2 System Layout of TAS

Considering manufacturing cost, function and the feasibility of practical application, the TAS is installed in the bow of vessel to compensate the shaking motion of ship. When the ship is docked, it is pushed onto the tower with the thrust of the propeller, which can reduce the freedom of motion of the hull from six-DOF to three-DOF, such as heave, roll and pitch, as shown in Figure 1. Hence, the TAS only requires to achieve the motion compensation control of the three DOF.

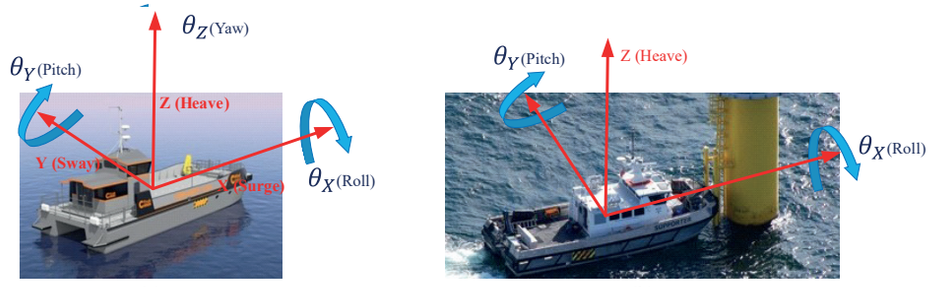


Figure 1: Ship Motions
(a) Six-Degrees of Freedom (b) Three-Degrees of Freedom

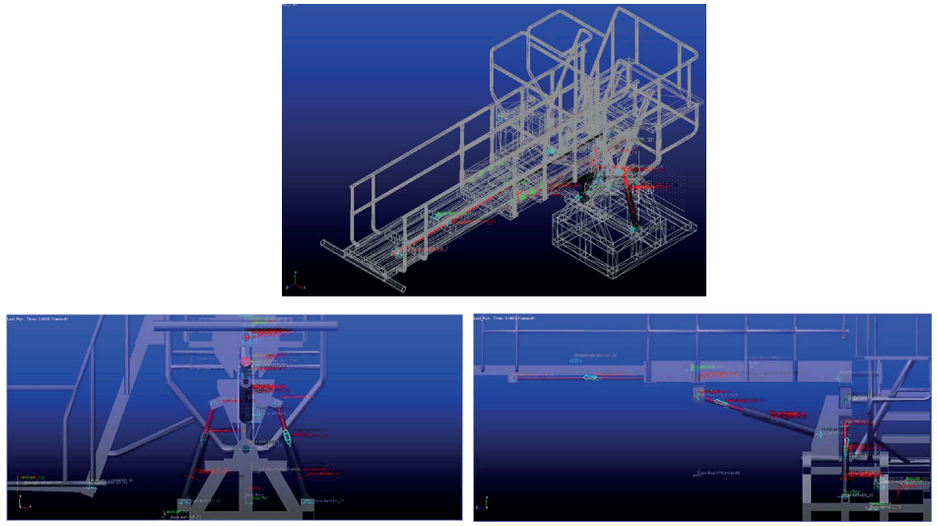


Figure 2: Configuration of TAS.

Figure 2 shows the configuration of the developed TAS. Based on the DOFs of the ship, the design of TAS contains three compensating systems, such as roll, pitch and heave. The roll compensating system consists of a pair of symmetrical hydraulic cylinders moving at same time to balance the motion of ship rolling. In the pitch and heave compensating systems, the hydraulic cylinder is used to balance the motion of ship pitching and heaving simultaneously. In the actual situation, the maintenance staff will go from the side ladder to the upper aisle, with handrails on both sides. The TAS test rig is driven and controlled by the hydraulic servo system. Position sensors are fitted at the cylinders. The A/D and D/A interface cards are used to link the sensors and computer to control the TAS.

3 Kinematic Analysis

In order to decrease the vertical displacement of the end effector, the end effector should be maintained on the initial position possibly. Therefore, it is necessary to obtain the relationship between the end effector and the actuators by kinematics and then implement leveling control. In the study, the geometric analysis of inverse kinematics is adopted to analyze the geometric relationship between the ship motions and the vertical displacement of the end effector in order to obtain the compensative angles and each required hydraulic cylinder elongation, as shown in Figure 3.

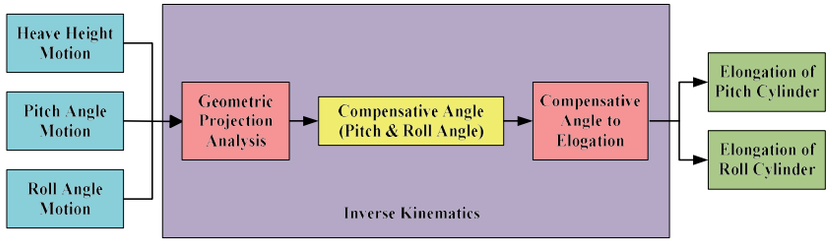


Figure 3: Flow Chart of Inverse Kinematics

Similarly, the forward kinematics, as shown in Figure 4, is to explore the relationship between the elongation of each hydraulic cylinder and the roll angle, the vertical displacement, and the vertical acceleration of the end effector in order to verify the effect of leveling control by TAS.

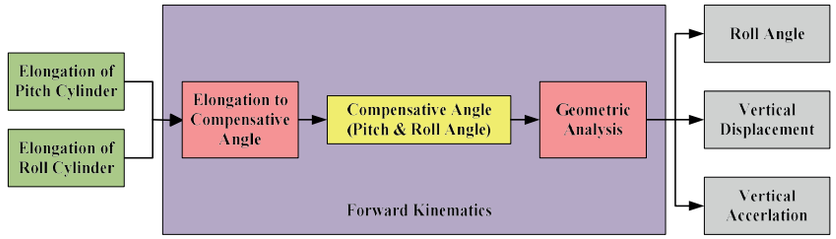


Figure 4: Flow Chart of Forward Kinematics

4 Control System of TAS

The overall control system block diagram of TAS is shown in Figure 5. According to the input ship motion, the target displacement of hydraulic cylinders, X_{roll}, target and X_{pitch}, target can be obtained by the inverse kinematics. The path control of TAS can perform via controllers according to the feedback signals of each sensor. Through kinematics the heave height, roll angle and pitch angle of the end point can be obtained.

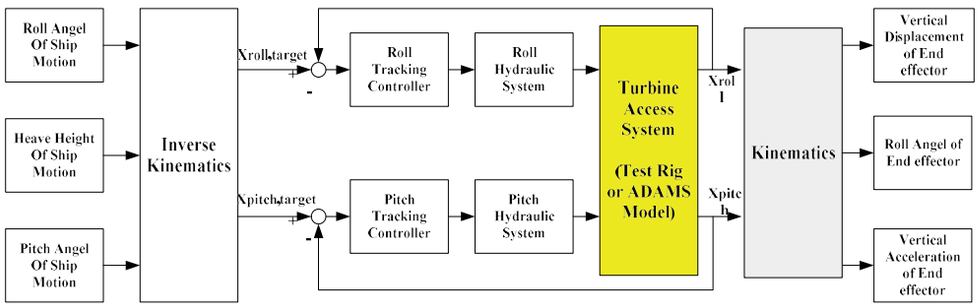


Figure 5: Block diagram of TAS control system.

5 Simulation of TAS

The simulation of TAS contains the mechanism dynamic simulation by ADAMS, hydraulic system by MATLAB/SIMULINK and control system by MATLAB/SIMULINK. The hydraulic system contains two subsystems, including roll compensating system and pitch compensating system. The ship motion which input to the TAS simulation is under the significant wave height 1 m, wave period 7.5sec, and inflow angle 45 degree. Figure 6 shows the direction relation between the ship and the wave. The ship motion under the input sea wave is shown in Figure 7. Figure 8 and Figure 9 show the simulation response of tracking control of pitch and roll compensation system. Finally, the end effector motion simulation comparison between active compensation and uncompensated can be shown in Figure 10, including (a) vertical height of end effector, (b) roll angle of end effector, and (c) vertical acceleration of end effector.

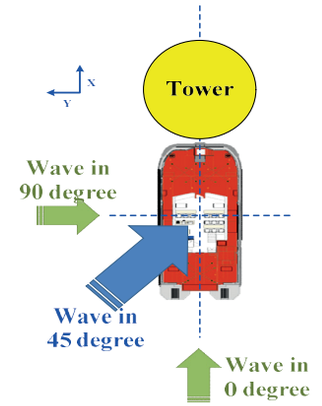


Figure 6: Direction relation between ship and wave.

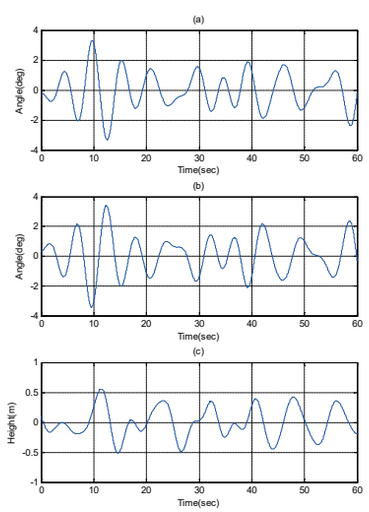


Figure 7: Ship motion under the input sea wave (a) roll angle, (b) pitch angle, (c) Heave position.

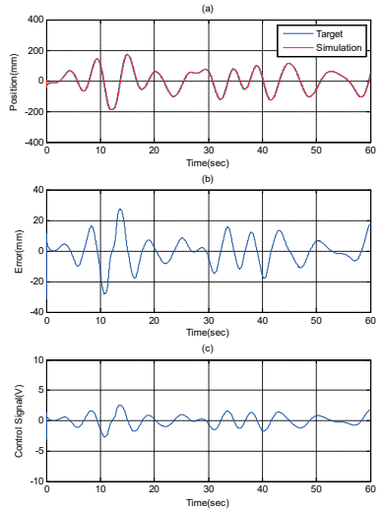


Figure 8: Simulation response of tracking control of pitch compensation system (a) tracking control response, (b) control error, (c) control signal.

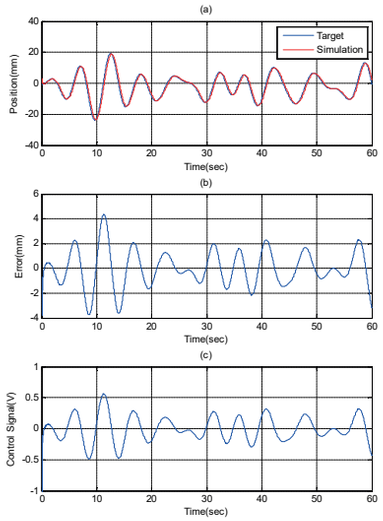


Figure 9: Simulation response of tracking control of roll compensation system (a) tracking control response, (b) control error, (c) control signal.

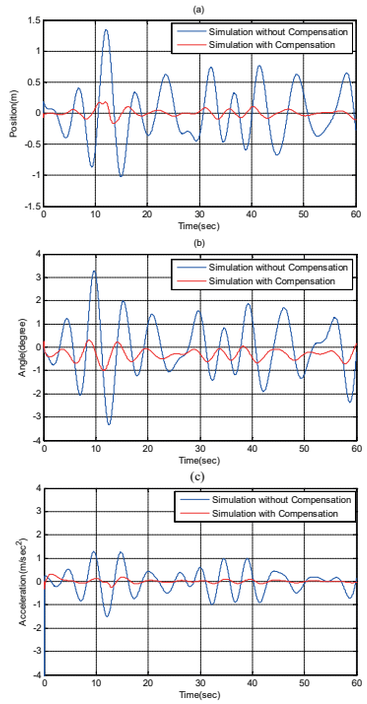


Figure 10: Simulation comparison between active compensation and uncompensated (a) vertical height of end effector, (b) roll angle of end effector (c) vertical acceleration of end effector.

6 Experiment of TAS

The control strategies validated in simulation can be implemented in the test rig of TAS. The condition of wave is the same as that in simulation with the significant wave height 1m, wave period 7.5 sec, and inflow angle 45 degree. The ship motion under the input sea wave is the same as that in Figure 7. Figure 11 and Figure 12 show the experimental response of tracking control of pitch and roll compensation system. Consequently, the end effector motion experimental comparison between active compensation and uncompensated can be shown in Figure 13, including (a) vertical height of end effector, (b) roll angle of end effector, and (c) vertical acceleration of end effector. The maximum cylinder tracking error of pitch and roll compensation systems is about 58mm and 5.4mm. The end effector for the staff can be compensated within $\pm$ 0.35m of vertical height instead of $\pm$ 1.35m without compensation; $\pm$ 1.1^o of roll angle instead of $\pm$ 3.3^o without compensation; $\pm$ 0.04G of vertical acceleration instead of $\pm$ 0.15G without compensation.

7 Conclusions

This study developed a hydraulic multi-axial active motion compensation system of TAS for offshore wind turbines, which is achieve both in the dynamic simulation via ADAMS and MATLAB/ SIMULINK and the practical experiment in the full-scale test rig. The simulation and experimental results show that the TAS can effectively reduce the vertical height, roll angle and pitch angle and the vertical acceleration of the end point.

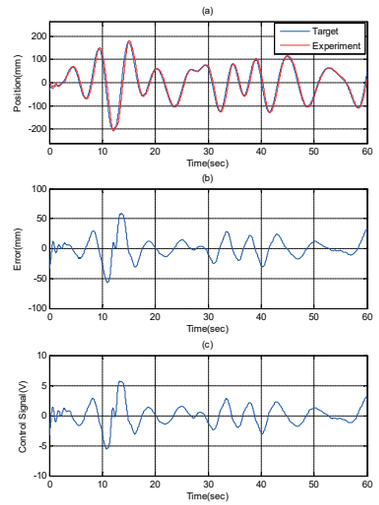


Figure 11: Experimental response of tracking control of pitch compensation system (a) tracking control response, (b) control error, (c) control signal.

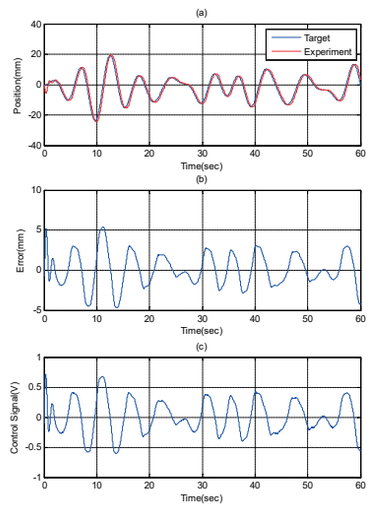


Figure 12: Experimental response of tracking control of roll compensation system (a) tracking control response, (b) control error, (c) control signal.

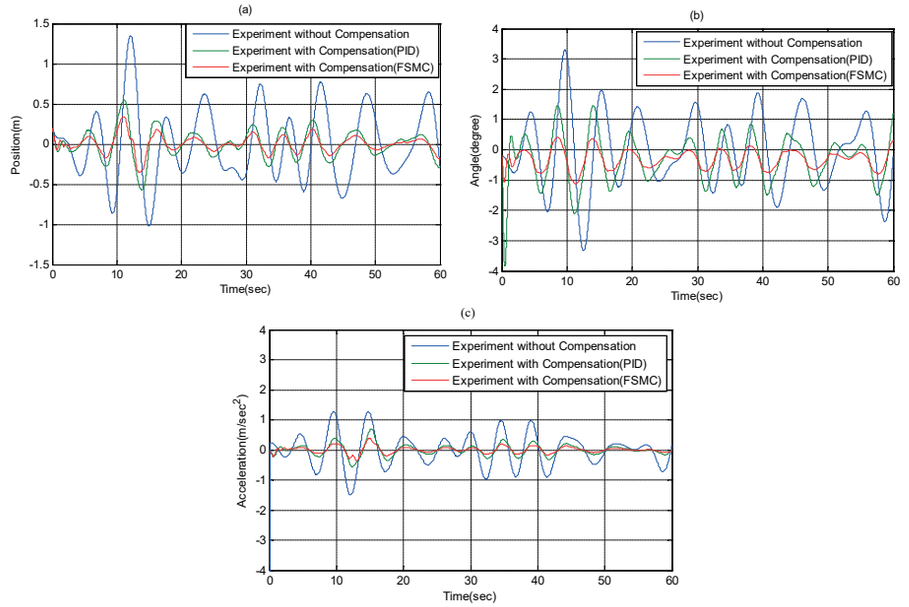


Figure 13: Experimental comparison between active compensation and uncompensated (a) vertical height of end effector, (b) roll angle of end effector (c) vertical acceleration of end effector.

Acknowledgements

This research was sponsored by the Ministry of Science and Technology, Taiwan under the grant MOST 105-2221-E-002-114 and MOST 106-2221-E-002-109-MY3.

References

/1/ J. Twidell and G. Gaudiosi, "Offshore Wind Power", 1. ed., Multi-Science Publishing Co. Ltd., 2014.

/2/ D. J. Cerda Salzmann, "Development of the Access System for Offshore Wind Turbines," Ph.D. dissertation, Delft University of Technology, 2007.

/3/ CTruk, 'Products and Systems-MPC22', 2015. [Online]. Available: http://www.ctruk.com/products-and-systems/MPC22.

/4/ S. W. Bedford, "Access Apparatus for Transferring from Vessels to Fixed Structures," U.S. Patent 8 925 130 B2, Jan. 6, 2015.

/5/ Houlder, 'TAS steps up to turbine access challenge - Houlder', 2014. [Online]. Available: http://houlderltd.com/newsroom/tas-turbine-access-system-steps-access-challenge/.

/6/ Sine.ni.com, 'Control of a Hydraulic Motion Compensated Gangway to Improve Access to Offshore Wind Turbines - Solutions – National Instruments', 2015. [Online]. Available: http://sine.ni.com/cs/app/doc/p/id/cs-14813.

/7/ E. R. P. Dudson and F. V. Perdrix, "Transfer Apparatus for Vessels," U.S. Patent 2013/0198979 A1, Aug. 8, 2013.

/8/ Momac-robotics.de, 'Download MOTS - Momac Offshore Access System', 2015. [Online]. http://www.momac-robotics.de/Download-MOTS.html.

Application of Pneumatic Muscle Actuator to Pulse Diagnosis System of Chinese Therapy

Jyh-Chyang Renn

National Yunlin University of Science and Technology, Department of Mechanical Engineering,
No. 123, University Rd., Sec. 3, Douliou, Yunlin 640, Taiwan
E-Mail: rennjc@yuntech.edu.tw

In this paper, a rotational pneumatic muscle actuator (PMA) is applied to build a brand new pulse diagnosis system for the traditional Chinese therapy (TCT). In traditional Chinese therapy, a doctor uses his/ her fingers to press the patient's artery on the radial bone in order to feel the pulse signal of the patient. Based on empirical judgment, the doctor can realize and point out what kind of physical condition the patient is suffering from. However, this kind of pulse-sensing diagnosis technique relies mainly on the subjective feeling from the doctor's fingers. Therefore, it is possible that different doctor might have a different viewpoint for the same pulse signal. In this study, a well-accepted hypothesis of Organ-Resonance will be introduced to build the complete pulse diagnosis system for TCT. The rotational PMA proposed in this paper serves to imitate the finger motion of a TCT doctor. In addition, the spectrum theory and Fast Fourier Transform (FFT) are also employed to compute and acquire the biological message hidden behind the detected time-domain pulse signal. Finally, experimental results prove the validity of the presented automatic pulse diagnosis system for TCT.

Keywords: Pneumatics, Pneumatic Muscle Actuator, Chinese Therapy, Pulse Diagnosis, Fast Fourier Transform
Target audience: Pneumatic Industry, Welfare Industry, System Integration

1 Introduction

The pneumatic muscle actuator (PMA) is a soft, deformable fluid actuator able to contract and to exert a tension force when supplied with a given air pressure. One advantage of the PMA is its ability to simulate the real human muscle behaviours and motions. Therefore, it has been widely discussed and researched during the past several years [2-8]. On the other hand, due to its soft surface, the PMA can work with human, contact the human body and handle fragile objects. Consequently, such an actuator already finds many applications in the field of medical engineering, medical welfare system and so on. In this paper, an automatic pulse diagnosis system for traditional Chinese therapy (TCT) is designed and implemented. The main idea of this design is depicted in Fig. 1. More details will be described as follows. In the TCT, a doctor uses his/ her fingers to press the patient's artery on the radial bone in order to feel the pulse signal of the patient as shown in Fig 1 (b). Based on empirical judgment, the doctor can realize and point out what kind of physical condition the patient is suffering from. Though this kind of pulse-sensing diagnosis technique is quite popular because it is non-invasive, such a diagnosis, however, relies mainly on the subjective feeling from the doctor's fingers. Therefore, it is possible that different doctor might have a different viewpoint for the same pulse signal. It is also worth mentioning that such a questionable situation has been lasting for hundreds of years. Nowadays, scientists are still trying to establish an objective and quantitative standard for those TCT doctors. In this study, a well-accepted hypothesis of Organ-Resonance /1/ will be introduced to build the complete pulse diagnosis system for TCT. In addition to this hypothesis, the proposed rotational PMA shown in Fig 1 (a) also plays an important role in designing the automatic pulse diagnosis system. It serves to imitate the finger motion of a TCT doctor as shown in Fig 1 (c). The spectrum theory and Fast Fourier Transform (FFT) are also used to compute and acquire the biological message hidden behind the detected time-domain pulse signal. In the following, the introduction of PMA will firstly be outlined.

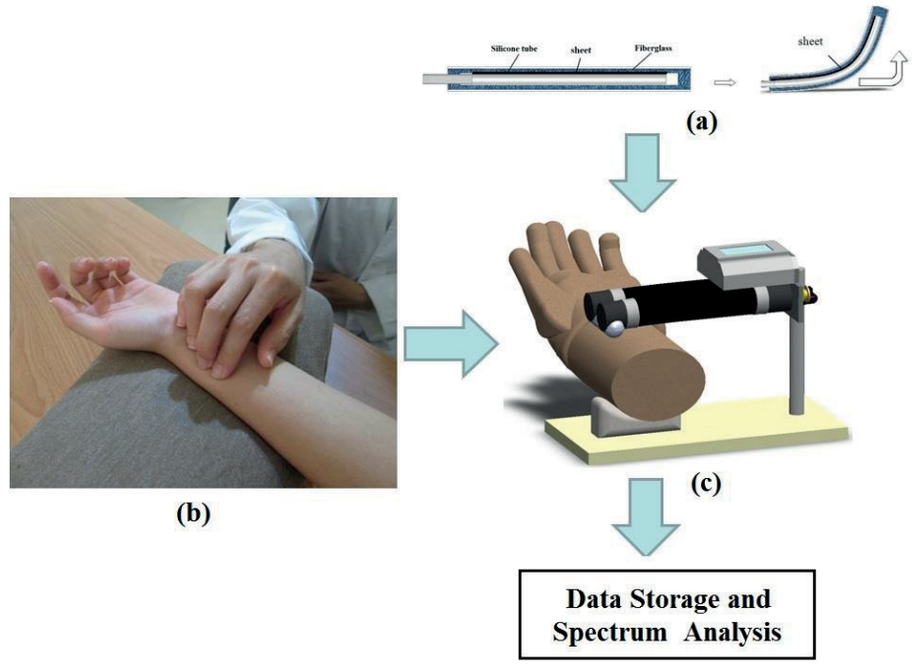


Figure 1: Main idea of this study - Scheme of the pulse diagnosis system of traditional Chinese therapy.

2 Translational and Rotational PMA

Figure 2 shows the basic translational type of PMA. It consists of silicon rubber tube covered with a thin fiber-glass layer. When the compressed air is supplied to the PMA, it contracts in the axial direction as shown in Fig. 2. The contraction length reaches 10 mm corresponding to maximal inlet pressure of 6 bar. Another commonly used PMA is the rotational type as shown in Fig. 3. Compared to scheme shown in Fig. 2, an extra thin metal sheet is inserted between the silicon rubber tube and fiber-glass surface. Since the metal sheet is not deformable, the PMA rotates when the compressed air is supplied as shown in Fig. 3. The rotational angle reaches 30^{o} when the inlet pressure is the maximal 6 bar as shown in Fig. 4.

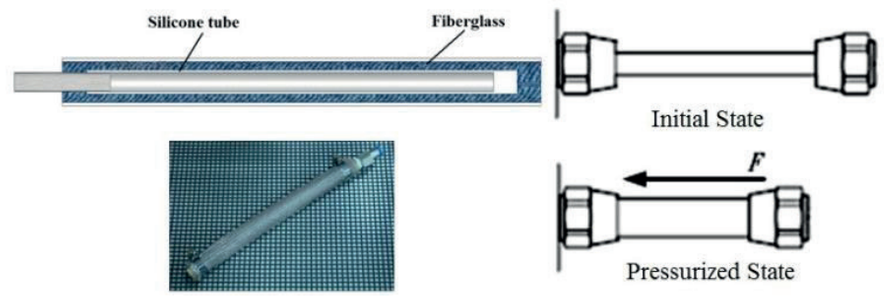


Figure 2: Translational PMA.

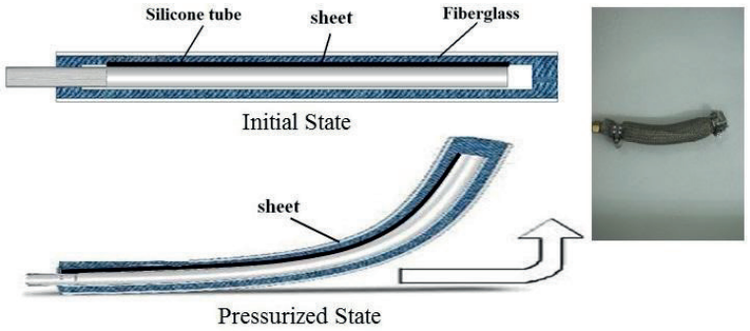


Figure 3: Rotational PMA.

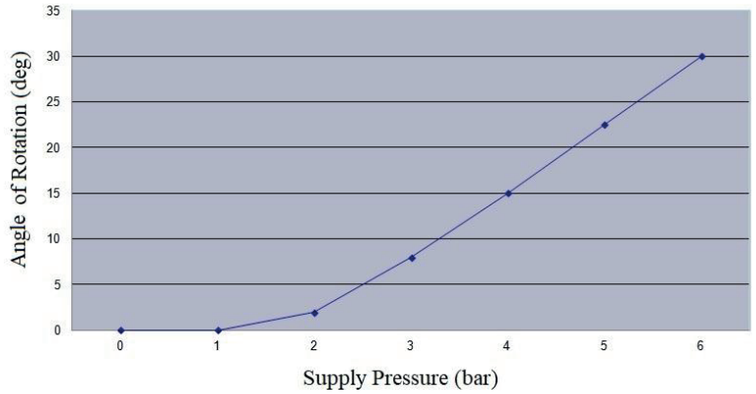


Figure 4: Rotational angle as a function of supply pressure.

3 The Automatic Pulse Diagnosis System

Figure 5 shows the schematic hardware of the developed automatic pulse diagnosis system for TCT, in which a proportional pressure control valve together with a LabVIEW software control program are utilized. Through the precise control of the proportional pressure control valve, the rotational PMA is able to simulate three operations in TCT, including the Light Touching (155 mmHg), Moderate Feeling (165 mmHg) and Heavy Pressing (175 mmHg) as shown in Fig. 6. Finally, the Fast Fourier Transform (FFT) package provided by LabVIEW toolbox is used to compute and acquire the biological message hidden behind the detected time-domain pulse signal.

In this study, a well-accepted hypothesis of Organ-Resonance is introduced to build the complete pulse diagnosis system for TCT. In addition to this hypothesis, as mentioned previously, the proposed rotational PMA also plays an important role in designing the automatic pulse diagnosis system as shown in Fig. 5. It serves to imitate the finger motion of a TCT doctor. Figure 7 depicts the details of the hypothesis of organ resonance. It is proposed that every organ in human body has a corresponding resonance peak in the spectrum diagram derived from the time-domain pulse signal. For example, the first resonance peak represents the heart and the second resonance peak represents the liver, and so on. Thus, it is basically possible to diagnose the health condition of a human by evaluating the change of peak value of these resonant waves.

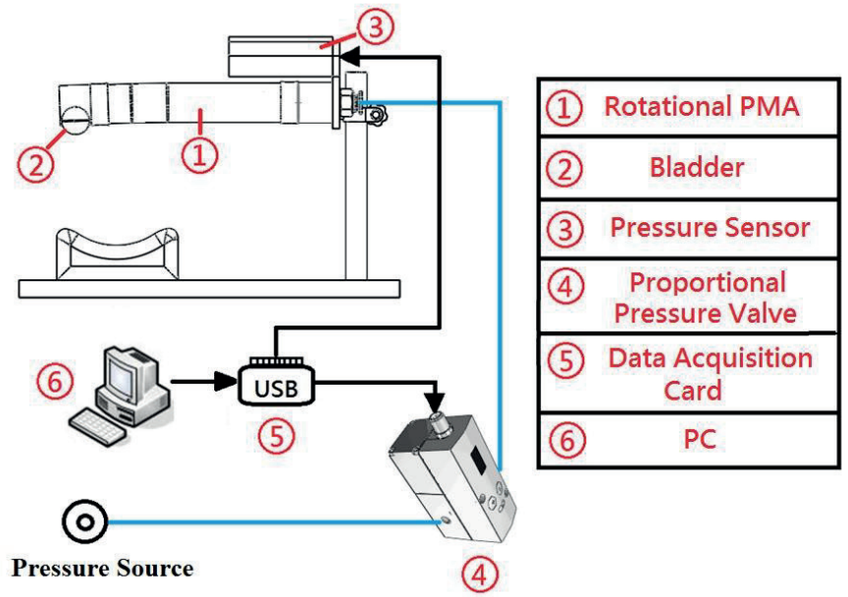


Figure 5: Hardware of the developed automatic pulse diagnosis system.

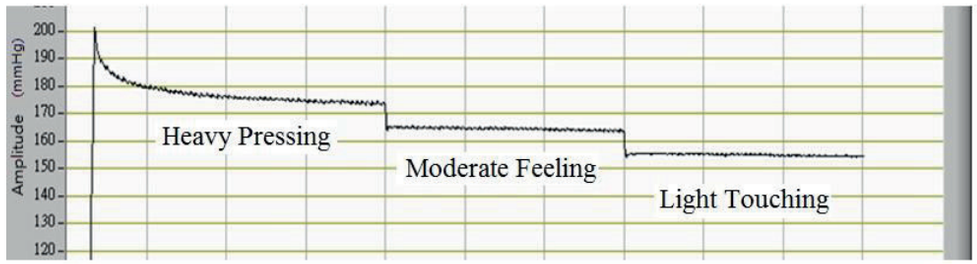
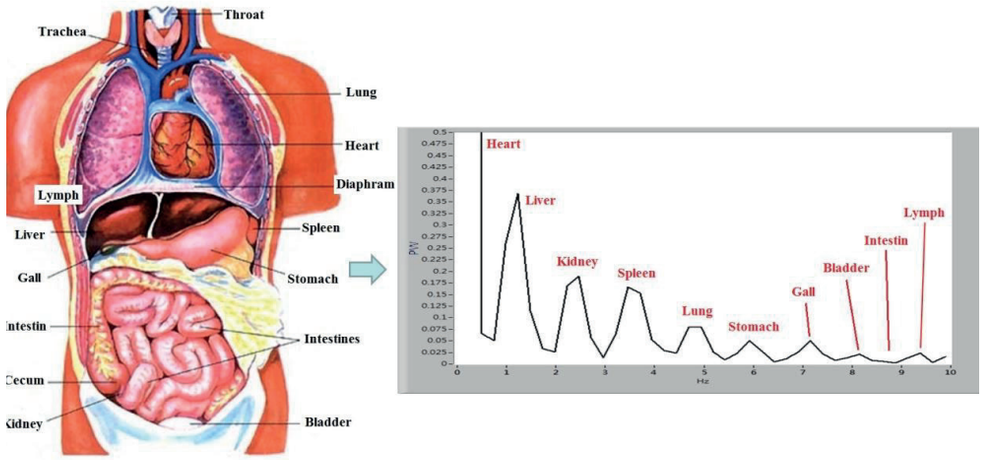


Figure 6: Three operations in traditional Chinese therapy.

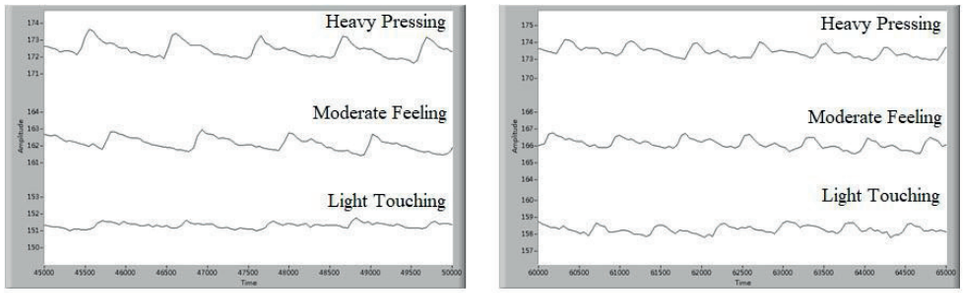


4 Experimental Test Results

Due to the medical law that prohibits any medical experiment on a sick person without prior permission, an alternative simple test program for a healthy person is utilized to examine the validity of the proposed automatic pulse diagnosis system for TCT. The detailed test program is described as follows. At the beginning, a first measurement of the time-domain pulse signal for a healthy person is executed. Then the tested healthy person runs continuously for 30 minutes. After the running, the tested healthy person takes a rest for 10 minutes. Finally, the second time-domain pulse signal is measured. Through the FFT analysis, the spectrum diagrams of the first and second measurements can be derived. The basic idea of these tests is trying to diagnose the health/organ condition of the tested healthy person by evaluating the changes of peak value of the resonant waves between the first and second spectrums. Figure 8 shows the measured first and second time-domain pulse signals. Clearly, it is quite difficult to tell the differences between these two time-domain pulse signals. However, through the spectrum analysis and FFT technique, the differences of the resonant peak values are quite obvious as shown in Table 1. It is worth mentioning that the peak value of the first resonance (representing the heart) is normalized to be unity, and the other peak values are relative and dimensionless.

After careful examination of the experimental results shown in Table 1, it is observed that the peak value of the second resonance (representing the liver) increases significantly after the test program. In the meantime, all other peak values change slightly only. From the viewpoint of TCT, the change of one resonant peak value indicates that the condition of its corresponding organ changes as well. As a matter of fact, the reason why a TCT doctor uses his/ her fingers to press the patient's artery on the radial bone is exactly the effort to acquire these resonant peak values. Consequently, the doctor can precisely point out what kind of physical condition the patient is suffering from.

On the other hand, it has to be explained why only the peak value of the second resonance changes significantly. It is well-known that, during any body exercise like the running, the liver glycogen has to be consumed and converted to energy for supporting the body exercise and to maintain the blood-sugar balance. Thus, it is reasonable to believe that the liver is a very busy organ to do such energy or calorie transformation. Therefore, among all resonant peak values, the second one representing the liver changes significantly.



(a) (b)

Figure 8: (a) The first time-domain pulse signals (before running), (b) the second time-domain pulse signals (after running).

	Heavy Pressing	Moderate Feeling	Light Touching
Heart	1.000	1.000	1.000
Liver	0.454	0.469	0.501
Kidney	0.377	0.341	0.401
Spleen	0.179	0.224	0.246
Lung	0.111	0.151	0.134
Stomach	0.128	0.121	0.212
Gall	0.073	0.085	0.143
Bladder	0.049	0.065	0.156
Intestin	0.052	0.049	0.168
Lymph	0.014	0.082	0.117

(a)

	Heavy Pressing	Moderate Feeling	Light Touching
Heart	1.000	1.000	1.000
Liver	0.628	0.609	0.896
Kidney	0.476	0.395	0.446
Spleen	0.170	0.186	0.193
Lung	0.051	0.108	0.190
Stomach	0.091	0.200	0.183
Gall	0.115	0.151	0.131
Bladder	0.065	0.070	0.200
Intestin	0.056	0.112	0.107
Lymph	0.053	0.082	0.052

(b)

Table 1: Resonant peak values after FFT, (a) before running and (b) after running.

5 Summary and Conclusion

In this paper, a brand new pulse diagnosis system for the traditional Chinese therapy using a soft rotational pneumatic muscle actuator is developed. After real tests, this system is proved to be successful and satisfactory. Besides, three conclusions may also be drawn from this research.

1. Using the spectrum theory and Fast Fourier Transform together with the hypothesis of Organ-Resonance, it is possible and successful to acquire the biological message hidden behind the measured time-domain pulse signal.
2. A feasible, objective and quantitative model for the traditional Chinese therapy is proposed and successfully implemented, which is expected to overcome the inherent disadvantages of traditional Chinese therapy, such as over-subjective dilemma and not precise diagnosis.

3. The soft pneumatic muscle actuator is again proved to be very suitable for the welfare and medical applications.

6 Acknowledgements

The financial support of the Ministry of Science and Technology under grant number *MOST- 105- 2622- E- 224- 016- CC3* is greatly appreciated.

References

/1/ Huang, J. M., Spectrum Diagnosis of Chinese Therapy, Chi-Yin Publishing Company, Taiwan (in Chinese), 2001.

/2/ Renn, J. C., Li, B. H., "A Robot Arm Based on Parallel Pneumatic Flexible Muscle Actuators," Proc. of the 2nd International Conference on Precision Machinery and Manufacturing Technology (ICPMMT), Paper No.: 29, Kenting, Taiwan, 2017.

/3/ Masaya, A., 2008, "Power Assist Wear for Upper Limb Driven by Sheet-Like Pneumatic Rubber Muscle," Proceedings of 7th JFPS International Symposium on Fluid Power, Vol. 1, pp. 787-792, Toyama, Japan.

/4/ Caldwell, D.G., Tsagarakis, N., Medrano-Cerda, G. A., Schofield, J., and Brown, S., 2001, "A pneumatic muscle actuator driven manipulator for nuclear waste retrieval, "Control Engineering Practice, Vol. 9, pp. 23-36.

/5/ Sasaki, D., Noritsugu, T. and Takaiwa, M., 2011, "Development of wearable master-slave training device for upper limb constructed with pneumatic artificial muscles," Proceedings of 8th JFPS International Symposium on Fluid Power, paper No.: 1A2-2, p. 18, Okinawa, Japan.

/6/ Tadano, K., Araya, H., Kawashima, K., Youn, C. and Kagawa, T., 2011, "Development of jump assist system using pneumatic artificial rubber muscle," Proceedings of 8th JFPS International Symposium on Fluid Power, paper No.: 2D3-3, p. 91, Okinawa, Japan.

/7/ Liu, H., Zhang, D., Zhao, Y. and Li, Z., 2014, "Design and control of an upper-limb power-assist exoskeleton driven by pneumatic muscles,' Proceedings of 9th JFPS International Symposium on Fluid Power, paper No.: 3C2-1, p. 125, Matsue, Japan.

/8/ Mori, K., Wakimoto, S., et al., 2014, "Development of thin McKibben artificial muscle and its application to biomimetic mechanism," Proceedings of 9th JFPS International Symposium on Fluid Power, paper No.: 1B2-3, p. 26, Matsue, Japan.

Fault Diagnosis of Pneumatic Actuator Based on Virtual Prototype Fault Simulation

Wanlu Jiang[1,2], Zhenbao Li [1,2], Yong Zhu [1,2], Lei Wang [1,2]

1. Hebei Provincial Key Laboratory of Heavy Machinery Fluid Power Transmission and Control, Yanshan University, Qinhuangdao Hebei, 066044, China
2. Key Laboratory of Advanced Forging & Stamping Technology and Science, Yanshan University, Qinhuangdao Hebei, 066044, China

E-Mail: wljiang@ysu.edu.cn

Aiming at the difficult problem of obtaining typical fault samples of pneumatic actuators in engineering practice and basing on the working principles of pneumatic diaphragm actuator, a model of pneumatic diaphragm actuator system was established by using DAMADICS. Then we simulated its common and typical faults and obtained a lot of samples. In this research, using KPCA to reduce the date dimension that obtained by the established system. We use the method of fault detection and diagnosis based on artificial immune algorithm to pneumatic diaphragm actuator's fault diagnosis. The experimental results indicate that the fault detection method based on artificial immune algorithm performs well.

Keywords: Virtual prototype; Pneumatic diaphragm actuator; Fault diagnosis; Artificial immune algorithm
Target audience: *Pneumatic Transmission, Fault Diagnosis, Fault Simulation*

1 Introduction

As the process control systems are becoming larger and more complex, its work environment is usually in high temperature and pressure, low temperature vacuum or flammable and explosive extreme conditions. If there is a fault in such a system, it will cause significant security incidents and serious environmental pollution. The actuator (also called the regulating valve) is the terminal execution device that executes the automatic control command in the process control system. Its performance is directly related to the fact that whether automatic control system can run smoothly and safely or not. Pneumatic diaphragm actuator, for example, once fault in operation is likely to cause major security incidents such as stopping production or a leakage of toxic substances. With the extensive application of pneumatic actuators, the fault diagnosis problem will become more and more prominent. So this research has a wide range of practical prospects.

In the engineering practice, the typical fault samples of the pneumatic actuators are difficult to obtain. Not only because the research on fault diagnosis of the pneumatic actuators often requires a lot of manpower and material resources, but the fault simulation method is limited. Therefore the research cannot be carried out. Establishing a virtual prototype to simulate the operating state of the real pneumatic actuator system. It can overcome the problems that fault samples are difficult to be obtained in practical engineering and the typical fault of the actuator is difficult to be simulated. This has higher application value.

2 The Establishment Principle of Virtual Prototype of Pneumatic Actuator

Pneumatic actuator systems are essentially non-linear systems. It is difficult to establish accurate mathematical models of pneumatic actuators due to the facts that gas inherent compressibility, low damping characteristics of pneumatic systems, non-linearity of valve port flow and some time-varying factors. Traditional modeling method cannot simulate typical faults of pneumatic actuators. As shown in Figure 1, the pneumatic actuator system consists of pneumatic actuators, regulating valves and valve positioner.

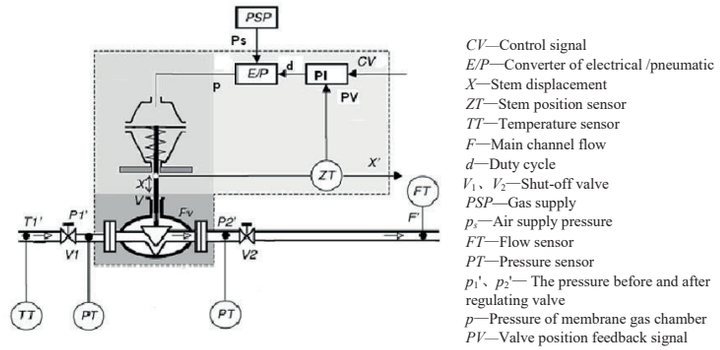


Figure 1. Composition of the pneumatic actuator system

In order to simulate the conditions of pneumatic actuator system in normal and under the faults and obtain the experimental data, the virtual prototype model of pneumatic actuators is built by using DAMADICS simulation platform under the environment of MATLAB/Simulink.

The simulation platform of DAMADICS is an actuator model library based on MATLAB / Simulink, which is developed by European Training Foundation (ETF). The model can effectively simulate the operation process as well as the input and output data of the pneumatic actuator. Each module has an interface of fault input. By connecting to the fault generation module, 19 typical faults of pneumatic actuator can be simulated that listed in Table 1.

Table 1. Typical faults of pneumatic actuator

NO.	Failure mode	Fault type	NO.	Failure mode	Fault type
1	Valve body obstruction	Jump failure	11	Spring failure	Jump failure
2	Core or seat deposits	Gradual failure	12	Electric/Pneumatic converter failure	Jump failure
3	Core or seat corrosion	Gradual failure	13	Position feedback signal sensor failure	Slow drift fault
4	The friction increases of the valve or bushing	Gradual failure	14	Pressure signal sensor failure	Jump failure
5	External leakage	Gradual failure	15	Locator spring failure	Jump failure
6	Internal leakage	Gradual failure	16	Air supply pressure drop	Gradual failure
7	Medium evaporation or critical flow	Jump failure	17	Valve body differential pressure abnormal change	Gradual failure
8	Stem bending	Jump failure	18	The bypass valve open	Jump failure
9	Membrane cap too tight	Random failure	19	Flow sensor failure	Jump failure
10	Membrane damage	Jump failure			

Pneumatic actuator system consists of three parts. We can divide the model into three basic functional units, namely pneumatic servo actuator unit, regulating valve unit and valve positioner unit. Then we can establish serval sub-modules according to the typical parts. Each sub-modules will be connected according to the relationship between input and output. Finally, we set up a complete virtual prototype model of pneumatic actuator. As shown in Picture 2.

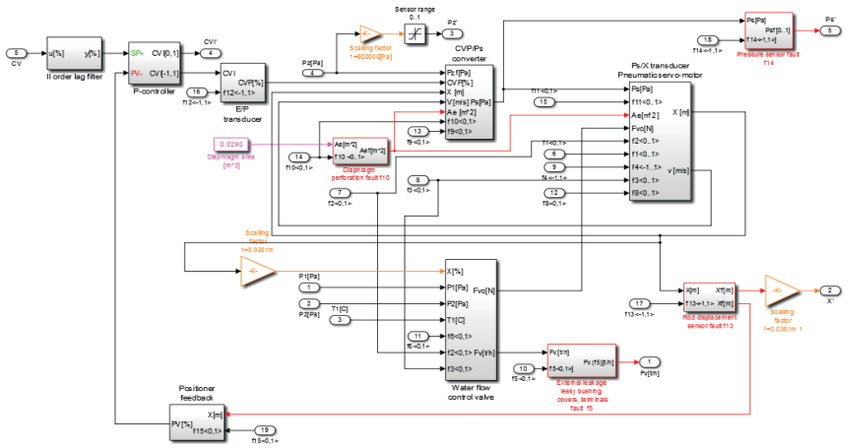


Figure 2. Virtual Prototype Model of Pneumatic Actuator

3 Typical Fault Simulation of Pneumatic Actuator

The entire pneumatic actuator system as shown in Figure 2 is packaged into a subsystem. The input and output parameters are set. Then the fault simulation model as shown in Figure 3 is established. The input of the simulation model is the control signal CV=25sin(0.02π)+50. The upstream pressure of regulating valve is p_1=3.5MPa. The downstream pressure of regulating valve is p_2=2.6MPa. The fluid temperature in regulating valve is T_1=20℃. The output is set as a control signal CV. The stem displacement is X'. The difference pressure between front and rear of regulating valve is p_1'-p_2'. The fluid flow in regulating valve is F'. The control deviation is E.

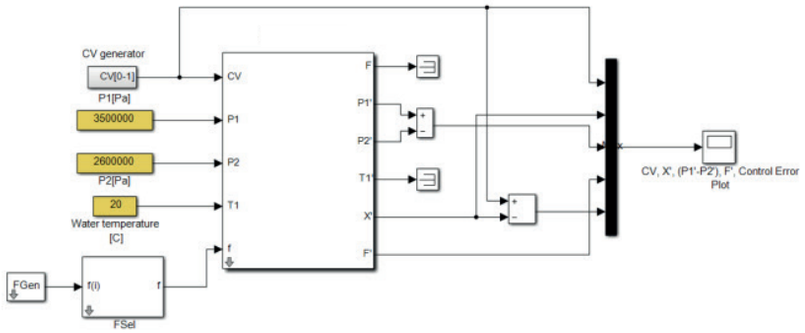
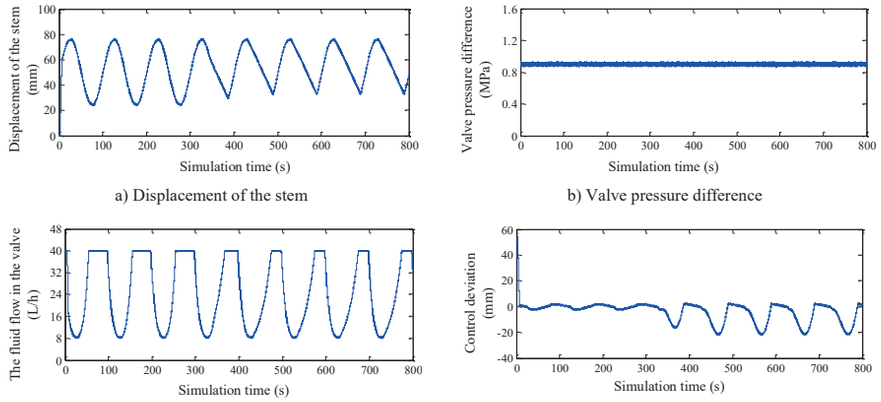


Figure 3. Failure Simulation Model of Virtual Prototype of Pneumatic Actuator

Setting the simulation time to 800 seconds. The fault type of the actuator system is selected by FSel module. The occurrence time and strength of the fault is set by FGen module.

In this paper, we have selected five conditions for fault diagnosis. They are the condition of normal operation condition, electrical/pneumatic converter blockage, position feedback sensor failure, valve body blockage and valve pressure difference abnormal. The fault occurred at the time of 300 seconds. The strength of fault is fs = 0.8. The simulation data of each fault mode is output to the working space of MATLAB. And 50 fault samples are extracted for each output variable after the fault. The corresponding fault sample set is formed. At the same strength of fault (fs = 0.8) for each failure mode to do two simulations. The sample set get from the first failure simulation serves as a training set for the production and training of antibodies. The sample set get from the second failure simulation serves as a test set for fault diagnosis.

Figure 4 shows the waveforms of the four output signals of the simulation results of the electrical/pneumatic converter blockage. The pneumatic actuator is often operated in dusty and polluted conditions. If the gas source is not effectively filtered, there will be large particles of impurities in the air. The impurities will accumulate at the nozzle of the electrical/pneumatic converter, which will eventually lead to nozzle clogging. When this fault occurs, the gas cannot pass through the nozzle of the electrical/pneumatic converter into the membrane chamber. The valve stem of the pneumatic actuator cannot normally follow the control signal to do reciprocating motion. The valve fluid flow is also affected and the control deviation will become larger.



a) Displacement of the stem

b) Valve pressure difference

c) The fluid flow in the valve

d) Control deviation

Figure 4. Simulation results of electrical/pneumatic converter blockage fault

4 The Dimension Reduction of Actuator Failure Sample Based on KPCA

Tests are taken by using five kinds of data samples of the condition of normal operation condition, electrical/pneumatic converter blockage, position feedback sensor failure, valve body blockage and valve pressure difference abnormal. Each type of data samples contain control signals CV, stem displacement X', pressures p_1', p_2' before and after the valve, fluid flow F' in the control valve and fluid temperature T_1' in the regulating valve. The number of samples sampled in each state is 50.

The Kernel Principal Component Analysis (KPCA) method is used to process the fault sample data of the pneumatic actuator. The fault feature is extracted to reduce the dimension of the fault sample data [2]. The KPCA method uses the radial basis function as the kernel function. Selecting σ=10, and the result of the data processing is shown in Table 2:

Table 2. The processing results of KPCA

Eigenvalue number	λ_i	$\lambda_i \Big/ \sum_{i=1}^{n} \lambda_i$	Cumulative contribution rate
1	4.967	0.706	0.706
2	1.832	0.193	0.899
3	0.764	0.041	0.94
4	0.218	0.037	0.977
5	0.091	0.021	0.998
6	0.013	0.002	1.000

According to the results in the table, the cumulative contribution rate of the first two eigenvalues has exceeded 85%. Then the first and second principal elements are selected as the fault feature information. Finally, the fault sample data is reduced from six to two dimensions.

Figure 5 shows the projection of the first and second principal elements extracted by the KPCA method. The KPCA method not only greatly reduces the dimension of the feature set, but also makes a clear distinction between the samples of each fault state of the pneumatic actuator. It lays the foundation for the next fault diagnosis.

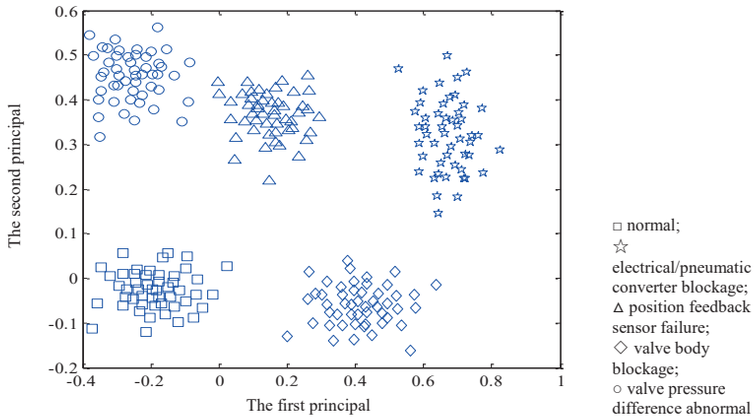


Figure 5.The projection of first and second principal elements extracted by KPCA

5 Fault Diagnosis of Pneumatic Actuator Based on Artificial Immune Mechanism

Inspired by the biological immune system, in recent years, the academic community setsup the artificial immune system (AIS) research boom which is more and more widely used to solve practical problems [3, 4]. The immune system has a strong information processing capabilities and many excellent features. The artificial immune system can enrich the theoretical system of fault diagnosis and engineering application and expand the research idea. The artificial immune system provides new theoretical and technical support for the research and development of fault diagnosis.

5.1 Antibody training

5.1.1 The design and coding of antigen and antibody

In an n-dimensional state space $\boldsymbol{S}^n$, the antibody and antigen are described by n normalized variables, ie, the antigen $\boldsymbol{Ag}=\{x_1,x_2,\cdots, x_n\}$ and the antibody $\boldsymbol{Ab}=\{y_1,y_2,\cdots, y_n\}$. x_i and $y_i(i=1,2,\cdots,n)$, respectively, known as the antigen $\boldsymbol{Ag}$ and antibody $\boldsymbol{Ab}$ gene, corresponding to the n eigenvalues of the state in fault diagnosis. The antigen and antibody sets are shown below: $\boldsymbol{AG}=\{\boldsymbol{Ag}_i|i=1,2,\cdots,M\}$, $\boldsymbol{AB}=\{\boldsymbol{Ab}_i|i=1,2,\cdots,N\}$. M and N are the number of antigens and antibodies.

Firstly, the fault feature samples after dimension reduction by KPCA method are normalized so that the values of all samples are between[0,1]. Each feature of each fault is defined as a different kind of antigen. In this paper, the antigens and antibodies are used in the form of real-number coding.

5.1.2 The calculation of affinity

In the n-dimensional state space $\boldsymbol{S}^n$, the affinity between the antigen $\boldsymbol{Ag}_i$ and the antibody $\boldsymbol{Ab}_i$ is expressed by the formula (1):

$$aff(\boldsymbol{Ag}_i, \boldsymbol{Ab}_i) = e^{-D_E} \tag{1}$$

D_E is the Euclidean distance of $\boldsymbol{Ag}_i$ and $\boldsymbol{Ab}_i$:

$$D_E = \sqrt{\sum_{i=1}^{n}(x_i - y_i)^2} \quad (1 \leqslant i \leqslant n) \tag{2}$$

By the formulas (1) and (2), it can be concluded that the amaller the Euclidean distance D_E, the greater the value of the affinity. The degree of matching of the antigen $\boldsymbol{Ag}_i$ with the antibody $\boldsymbol{Ab}_i$ will be better.

5.1.3 The definition of fitness function

The fitness function is a criterion for evaluating the quality of antibodies determined by the objective function. The fitness function is always nonnegative. The greater the value, the better the trained antibody. The fitness of antibody is the driving force of antibody in training process. While it's also one of the bases for natural selection of antibodies. In this paper, the fitness function is defined as:

$$f = \frac{1}{1 + D_E} \tag{3}$$

It can be seen from the formula (3) that the value of the fitness function f approaches the maximum value 1 when the value of the Euclidean distance D_E approaches zero.

5.1.4 The operation of genetic operator

To make the antibodies produced by the algorithm covering the areas of each type of antigen in the state space as much as possible, we introduced the selection, crossover and mutation operator operations from the genetic algorithm to accelerate the speed of antibody training and to increase the diversity of the antibody.

1. Selection

The antibodies that need to be cross-operated are selected from the initial antibody population . Firstly, the fitness value f_i of each initial antibody Ab_i was calculated according to the formula (3). In this paper, the Monte Carlo method is used to assign a

selection probability p_i to each antibody Ab_i in the initial antibody set. The probability that the antibody Ab_i is selected is expressed as:

$$p_i = \frac{f_i}{\sum_{i=1}^{N} f_i} \tag{4}$$

Where N is the size of the initial antibody population. $\sum_{i=1}^{N} f_i$ is called the cumulative fitness of N initial antibodies.

In this paper, the roulette selection method was used to select the initial antibody to be crossed. The fitness value f_i, the selection probability p_i of each antibody and the cumulative fitness in the initial antibody group were calculated. In order to select the cross individuals, multiple rounds of selection are required. Each round produces a uniform random number in the interval [0,1] as the selection pointer to determine the selected primary antibody.

2. Crossover

Crossover refers to the process of selecting any two parent individuals to produce new individuals by exchanging their partial genes. The real-coded chromosomes of the algorithmic training are used to obtain new antibodies by intermediate cross:

$$\boldsymbol{Ab}^{n+1} = \boldsymbol{Ab}_1^n + \alpha\left(\boldsymbol{Ab}_2^n - \boldsymbol{Ab}_1^n\right) \tag{5}$$

Where $\boldsymbol{Ab}_1^n$ and $\boldsymbol{Ab}_2^n$ represent the parent antibody 1 and 2. $\boldsymbol{Ab}^{n+1}$ represents the offspring antibody. α is a scale factor, which is generated by a random number evenly distributed over [0,1]. And a new α value is selected for each pair of cross antibodies.

3. Mutation

Mutation is a localized random search, which enables the immune algorithm to have a local random searching ability. Improving the diversity of antibody populations to prevent premature convergence (early maturity). According to the distance between any antibody $\boldsymbol{Ab}_i$ and the center of a certain antigen $\boldsymbol{Ag}_i$, take the antigen $\boldsymbol{Ag}_i$ as the center, take R_1 and R_2 as the radiuses. The antibody $\boldsymbol{Ab}_i$ was divided into three different areas of A, B and C. As shown in Figure 6.

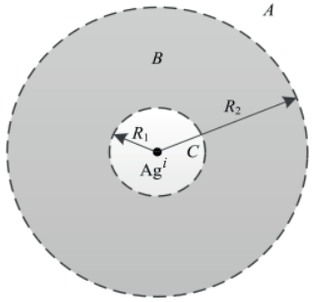


Figure 6. Division of antibody region variable

When the antibody $\boldsymbol{Ab}_i$ is located in the region A or C, The mutation operation does not performed; When the antibody $\boldsymbol{Ab}_i$ is located in the region B, according to formula (6) to perform mutation operation:

$$\boldsymbol{Ab}_i^{n+1} = \boldsymbol{Ab}_i^n + \beta(\boldsymbol{Ag}_i - \boldsymbol{Ab}_i^n) \tag{6}$$

Where β is the mutation rate. $\boldsymbol{Ag}_i$ is the antigen. $\boldsymbol{Ab}_i^n$ is the pre-mutation antibody. $\boldsymbol{Ab}_i^{n+1}$ is the antibody after mutation.

5.1.5 The promotion and inhibition of antibody

In the biological immune system, the number of each type antibodies will change dynamically with the stimulation of the antigens. When the concentration of some kind of antibodies is too high, the amount of the antibody will be inhibited. Whereas the amount of antibodies will be promoted so that the immune response can maintain a suitable strength[5].

The distance between the antibody $\boldsymbol{Ab}_i$ and any other antibody $\boldsymbol{Ab}_j$ in the antibody population (population number N) is D_E. Given a constant a_1 and a_1>0 as a similarity threshold. If $D_E > a_1$, the antibody $\boldsymbol{Ab}_i$ and antibody $\boldsymbol{Ab}_j$ are similar. In this paper, the concentration of antibody $\boldsymbol{Ab}_i$ is defined as L_i. The formula is as follows:

$$L_i = \frac{1}{N}\sum_{j=1}^{N} C_{ij} \tag{7}$$

In this formula, $C_{ij} = \begin{cases} 1, D_E \le a_1 \\ 0, D_E > a_1 \end{cases}$

The desired reproduction rate for the antibody $\boldsymbol{Ab}_i$ is defined as e_i, which can be expressed by:

$$e_i = I_{div}\frac{f_i}{L_i} \tag{8}$$

In the formula, I_{div} is the diversity index of antibody population and $I_{div}=B/N$. B is the number of groups after grouping of antibody group. N is the individual number of the antibody population. f_i is the fitness value of antibody $\boldsymbol{Ab}_i$.

From the formula (8), it can be concluded that the expected reproductive rate e_i of the antibody is proportional to the fitness f_i and is inversely proportional to the antibody concentration L_i. By introducing the expected reproductive rate of the antibody, both the antibody diversity can be maintained and the convergence speed of immune algorithm can be increased.

5.1.6 The update of memory antibody

Immune memory characteristic is an important feature of the immune system, which ensures that the host clears pathogens in the fastest and most effective way when re-infected. According to this characteristic, a memory threshold f_0 is set during the update of each generation of antibody population. When there is excellent individual and its fitness value $f_i > f_0$ in the population. It is added to the memory subgroup and the same individual in the original population are deleted. During each time the memory antibody is renewed, if the memory antibody population is full, the antibody with the worst fitness is replaced. And then check whether there is a good individual in the original population or not, if any, continue to add, otherwise stop the memory update operation.

5.1.7 The steps of antibody training

Antibody training process is shown in Figure 7, the specific steps are:

1. Initialization

Setting the size of antigen set $\boldsymbol{AG}$ and antibody set $\boldsymbol{AB}$ as N_{ag} and N_{ab}. The maximum cyclic algebra is g_{max}. The antigen and the antibody are encoded.

2. Creating the initial antibody

The initial antibody set $\boldsymbol{AB}^1$ is generated. If the number of memory antibodies is less than N_{ab}, the initial antibody is randomly produced to fill the memory antibody population. The antigen set $\boldsymbol{AG}$ consists of some type of training data.

3. The calculation of the indexes

For each antigen $\boldsymbol{Ag}_i$ in $\boldsymbol{AG}$, the affinity of antigen $\boldsymbol{Ag}_i$ and all antibodies $\boldsymbol{Ab}_i$ in $\boldsymbol{AB}^1$ are calculated according to formula (1). Calculating the fitness, antibody concentration and expected reproductive rate of antibodies and antigens,.

4. Producing new antibodies

The initial antibodies in $\boldsymbol{AB}^1$ are first determined by the selecting operator. The antibodies in $\boldsymbol{AB}^1$ are then executed crossover operator operation according to formula(5). Determining the parameters R_1 and R_2. Calculating the Euclidean distance D_E between antibody $\boldsymbol{Ab}_i$ and antigen $\boldsymbol{Ag}_i$. When $D_E<\mathrm{R}_1$ or $D_E>\mathrm{R}_2$, the antibody $\boldsymbol{Ab}_i$ is not executed a mutation operation. When $\mathrm{R}_1\leqslant D_E\leqslant\mathrm{R}_2$, the antibodies in $\boldsymbol{AB}^1$ are mutated according to the formula (6) to obtain the progeny antibodies $\boldsymbol{AB}^2$ of size N_{ab} are added to the parent antibodies to obtain the set $\boldsymbol{AB}^1$ of size $2N_{ab}$.

5. Antibody promotion and inhibition

The value of the expected reproductive rate of the antibodies in $\boldsymbol{AB}^1$ is calculated according to formula(8). Removing antibodies with low expected reproductive rates until N_{ab} antibodies are remained in $\boldsymbol{AB}^1$.

6. Update the memory antibody group

The value of the fitness f_i of the antibody $\boldsymbol{Ab}_i$ is recalculated to determine the memory threshold f_0. When $f_i>f_0$, it is added to the subgroup $\boldsymbol{M}_i$ corresponding to the i -th antigen $\boldsymbol{Ag}_i$, while the same individual in the original population are deleted.

7. Termination discrimination

Determine the termination condition, that is, whether to reach the maximum cyclic algebra $\mathrm{g}_{\max}$ or not. If the condition is satisfied, stop the calculation. Otherwise, perform steps 3 to 6 until the termination condition is met.

8. The memory bank $\boldsymbol{M}_i$ corresponding to the antigen $\boldsymbol{Ag}_i$ are combined to obtain the antibody memory bank $\boldsymbol{M}$.

9. Output the result $\boldsymbol{M}$.

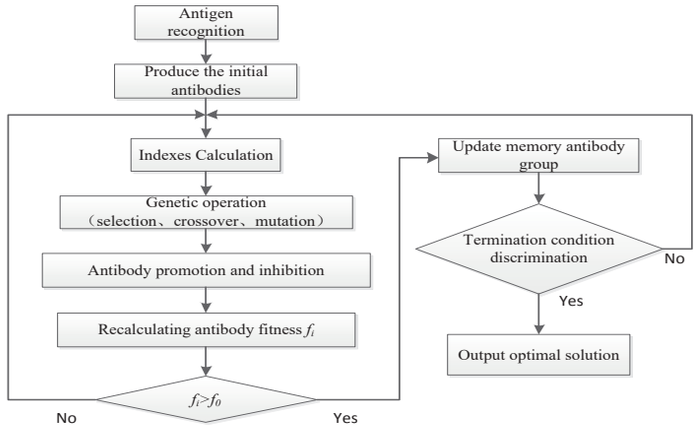


Figure 7. Antibody training process

The initial parameters of the algorithm are finally determined, as shown in Table 3:

Table 3. Initial parameters of the artificial immune algorithm

N_{ab}	$\mathrm{g}_{\max}$	α	f_0	β	R_1	R_2
500	200	0.1	0.96	0.3	0.025	0.15

The set of fault samples generated by the first simulation is extracted by KPCA method as a training set for the generation and training of antibody. Then the memory antibody library is obtained.

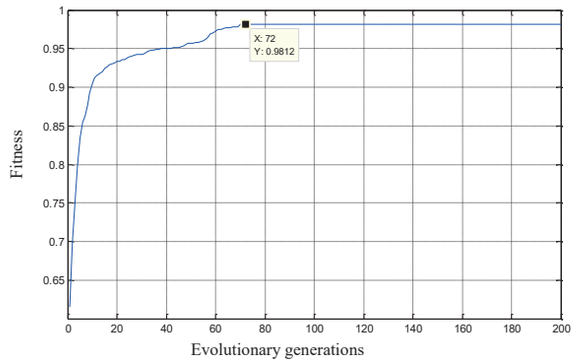


Figure 8 Antibody fitness function values for each generation

Figure 8 shows the changes of the fitness function value of each generation with the evolutionary algebra. It can be seen from the figure that when the algorithm is circulated to the 72nd generation, the value of the antibody fitness function reaches and in the maximum value of 0.9812. Indicating that the algorithm has a better ability to search for antibodies with the highest fitness less evolutionary algebra.

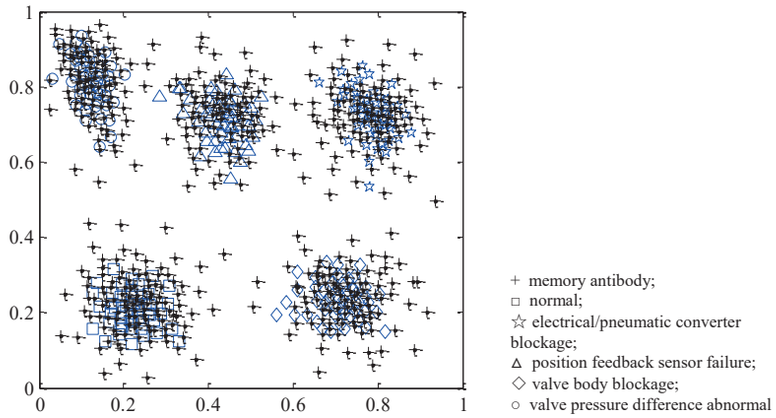


Figure 9 Memory antibody training results

Figure 9 illustrates that the algorithm is effective in learning the training samples and that the resulting memory antibodies can effectively cover the antigens. Besides, there is a clearer classification between each type antibodies.

5.2 The identification and diagnosis of faults

Fault identification and diagnosis are the second phase of the artificial immune algorithm, which is equivalent to the secondary immune response of the biological immune system.

The fault diagnosis concrete steps are as follows:

1. Getting and normalize the fault test samples. And the preprocessed test samples are set as antigens for input;

2. Setting a threshold upper limit y_0 based on the fault samples. Calculate the Euclidean distance D_E between each antigen and the memory antibodies of all fault types. If $D_E<y_0$, the memory antibody is considered to be activated by the antigen and copied into set ***D***. Circulating in this way, until all the activated memory antibodies are obtained in set ***D***;

3. The type of input fault is identified and diagnosed according to the type of failure to which the vast majority of the memory antibodies in set ***D*** belongs. The membership degree of the antigen belongs to a failure mode i is taken as the diagnostic accuracy of the corresponding fault [6];

$$\eta_i = \frac{C_i}{N_i} \tag{9}$$

In this formula, C_i is the number of antibodies that are activated by the antigen in the memory antibody set in failure mode i. N_i is the total number of antibodies in the memory antibody set in failure mode i.

Combining the memory antibody bank ***M*** of each type of failure. The KPCA method is used to extract the fault characteristics of the data generated by the second simulation. And then normalizing and constituting the test sample set as the antigen input. Identifying and diagnosiing it according to the above method. Setting the threshold is y_0=0.08. The final results are shown in Table 4:

Table 4 the results of troubleshooting

Working state	The number of test samples	Correct diagnosis number	Correct diagnosis rate
Normal	50	49	98%
Electrical/Pneumatic converter blockage	50	47	94%
Position feedback sensor failure	50	49	98%
Valve body blockage	50	45	90%
Valve pressure difference abnormal	50	46	92%

The diagnosis results show that the fault diagnosis algorithm based on artificial immune can effectively study the various types of fault samples of pneumatic actuators, generate the memory antibody group, and can accurately detect the type of fault that the test samples belongs to.

6 Conclusion

Based on the operation principle and characteristics of the pneumatic diaphragm actuator, a virtual prototype model of the pneumatic diaphragm actuator system is established under the DAMADICS software environment. The typical faults of the pneumatic diaphragm actuator are simulated according to the simulation. Obtaining a large number of fault samples. solving the problem that typical failure samples are difficult to be obtained in engineering practice.

The artificial immune algorithm is analyzed systematically and the KPCA technique is combined with the artificial immune algorithm. A method of artificial immune complex diagnosis is proposed, which is successfully applied to the fault diagnosis of pneumatic actuators. The validity of the method was verified by using the fault sample data of the virtual prototype of the pneumatic actuator. The experimental results indicate that the fault detection method performs well.

Acknowledgement

This work is supported by the National Natural Science Foundation of China (51475405).

References

/1/ Kocielny J M, Batty M K. Application of Information Theory for Actuators Diagnosis[J]. IFAC Symposium SAFEPROCESS, 2000: 949-1054.

/2/ Li Rongyi. Research on Fault Detection and Diagnosis Based on Kernel Principal Component Analysis[D]. Nanjing: Master 's degree thesis of Nanjing Normal University. 2011:35-51.

/3/ S Forrest, Perelson A S, L. Allen. Self-Nonself Discrimination in a Computer[J]. Proceedings of the IEEE Symposium on Research in Security and Privacy, 1994: 202-212.

/4/ Laurentys C A, Palhares R M. Design of Artificial Immune System Based on Danger Model for Fault Detection[J]. Expert Systems With Applications, 2010, 37(2010): 5145-5152.

/5/ Tong Xiaoling. Research on Function Optimization Based on Artificial Immune Algorithm[D]. Wuhan: Master 's degree thesis of Wuhan University of Technology. 2006:14-39.

/6/ Yu Zongyan. Research on Fault Diagnosis Based on Artificial Immune Algorithm[D]. Daqing: Master 's degree thesis of Northeast Petroleum University. 2006:35-41.

/7/ Wang lei. Research on virtual prototype based AI fault diagnosis method of pneumatic actuator[D]. Qinhuangdao: Master 's degree thesis of Yanshan University. 2013:50-61.

On Stability of the Two Stage Piloted Gas Pressure Control Unit

Dmitry Stadnik, Viktor Sverbilov, Gopalakrishna Gangisetty and Maxim Balyaba

Samara National Research University, 34 Moskovskoye shosse,
443086 Samara, Russian Federation
E-Mail: v.sverbilov@mail.ru

This paper presents the modeling and model validation of a gas pressure control system with a two stage pressure reducing unit. Such regulator structures are in routine use if requirements of high accuracy are coupled with a large pressure drop. Dynamic behavior of such systems drastically depends on performances of the pipe section in between two control valves. In the paper, two system modifications are considered. The initial system has a heating unit installed between two control stages and connected with them by long pipe lines. The field operation of the system at low temperature requires moving the heating unit upstream the first control valve. So the section volume between two stages decreases, and the system is prone to unstable behavior. The both modifications of the system are compared, its dynamic performances are studied on the simulation model and the critical volume of the intermediate section is defined. The experimental results revile reasonable agreement with theoretical analysis.

Keywords: Gas pressure control system, piloted pressure reducing valve, stability
Target audience: Pneumatics, Control System Design

1 Introduction

The gas pressure reducing valves are widely used in industry for various applications. They are main control units of the natural gas transportation and distributing stations in the network from gas extraction to the consumer end-user. The pressure reducer is a normally open valve that keeps outlet pressure nearly constant at a wide range of higher inlet pressure. To provide a high quality of static performances, the pilot operated regulators are widely used. The dynamic behaviour of such complicated units becomes very sensitive to the system configuration and operation conditions. In some cases instabilities are observed downstream the pressure regulator: the outlet pressure oscillates around the set point with very high amplitude.

Many studies were carried out in the past in order to characterize the regulators behavior. The procedure of forming nonlinear dynamic model of a gas pressure regulator was studied in [1]. The model showed a possibility of self-exciting oscillations in the system without outside disturbances. The results reported the effect of each design parameter for self-exciting oscillations and suggested methods to correct them. It was proposed that a linear model is sufficient for evaluation of stability and transient response if flow through the valve is laminar, dry friction is negligible, and the motion of valve and diaphragm is not constrained.

Some experimental and numerical simulations were performed in [2 and 3] to identify the relative influence of several parameters on stability and amplitude of oscillations.

Dynamic simulation of high pressure regulator was studied in [4] with the assumption of adiabatic process in the pressure regulator. The model was simulated using numerical tools and verified experimentally. It was found that as outlet volume increases, the stability of outlet pressure increases too.

The stability characteristics were investigated in [5]. It was found out the cause of vibration and proposed possible design modification for eliminating the unstable vibrations. It was concluded that damping coefficient, the diaphragm area, and upper and lower volumes are most important design parameters that affect the stability.

The comprehensive review of the past works in the area is presented in [6]. A nonlinear mathematical model of pressure regulator used to pressurize liquid propellant rocket tanks was developed. An analytical solution based on constant mass low rate assumption was compared with nonlinear formulation and the results demonstrated a high degree of confidence.

A mathematical model of the piloted gas regulator was developed in [7]. On the basis of modeling, experimental analysis and measured performances the operating conditions were found that increase stability. The numerical and experimental results were in good agreement with respect to each other. It was concluded that oscillations in downstream pressure increase for small volumes and higher upstream pressure.

As shown in the past works no generalized model of the gas pressure regulator exists. The structure and parameters of the regulator and connected network have a differential effect on the system stability. In this paper the two-stage piloted gas pressure regulator is considered. Dynamic behavior of such systems drastically depends on performances of the section in between two control valves. In the paper, two system modifications are considered. The initial system has a heating unit installed between two control stages and connected with them by long pipe lines. The field operation of the system at low temperature requires moving the heating unit upstream the first control valve. So the volume between two stages decreases, and the system is prone to unstable behavior. The both modifications of the system are compared, its dynamic performances are studied on the simulation model and the critical volume of the intermediate section is defined.

2 Modelling and simulation

A diagram of the gas pressure control system is shown in Figure 1. It includes two similar reducing unites installed up- and downstream the heater. The heater is located in a separate housing at a distance around 15 m connected by long pipes with the gas distributing station where both reducing unites are mounted. In this initial structure of the system, a cool gas is admitted to the input of the first reducing unite then goes out to the heater unit and comes back to the second reducer input. In the modified system both reducing valves are connected in series and the heater is located upstream the first stage. So the volume between two stages became much smaller being formed by a short connecting pipe.

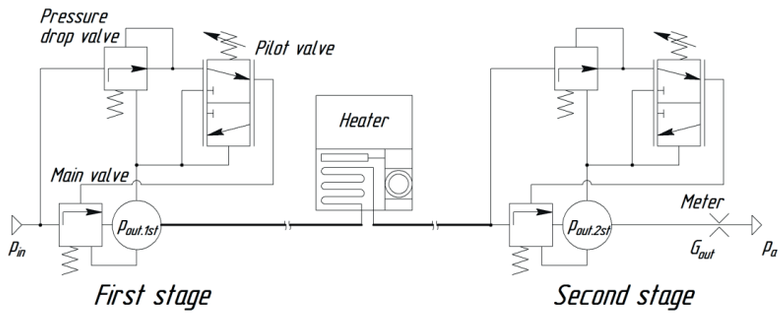


Figure 1: Diagram of the gas pressure control system

Each pressure reducing unit presents a pilot controlled regulator. It is composed of three control valves. The diagram of the regulator is shown in Figure 2. The main valve is positioned in the flow path to restrict the flow rate. The valve is driven by an actuator – a diaphragm, dividing a casing into two chambers K and L. Chamber K is connected to the downstream volume V_{out} through a pressure transmitting pipe. The pressure in other chamber L is controlled by the pilot valve. So the net force required to move the actuator is supplied by the pilot. The pressure induced force exerted on the diaphragm is balanced by the set value of the downstream pressure. The pilot compares downstream pressure p_{out} with a preset value and operates on the main valve by using an auxiliary pressure from the pressure drop valve. The pilot valve moving up and down can respectively decrease

or increase the main valve opening. The role of the pressure drop valve is to provide an independency of the pressure differential across the diaphragm from the upstream pressure p_{in} and the main valve displacement x_m. As the outlet pressure increases to the preset value, the pilot valve moves up such closing lower throttling orifice. The main valve opening interrupts. If pressure p_{out} continues to increase the pilot is moving upper and the upper throttling orifice is opening. The chamber L is connected with the outlet volume V_{out}, the main valve starts closing to decrease the flow rate and to prevent increasing of pressure p_{out}. At a steady state operation the pilot and pressure drop valves are closed; the main valve opening corresponds to the flow rate required to keep constant preset p_{out} value.

2.1 Mathematical model

To simplify mathematical model following assumptions are admitted: a fluid is an ideal gas; dry friction in mechanical units is negligible, lifting forces are independent of the lift, and the motion of valve and diaphragm is not constrained. Some of these assumptions are significantly contradictory to actual operations and are only acceptable in preliminary studies.

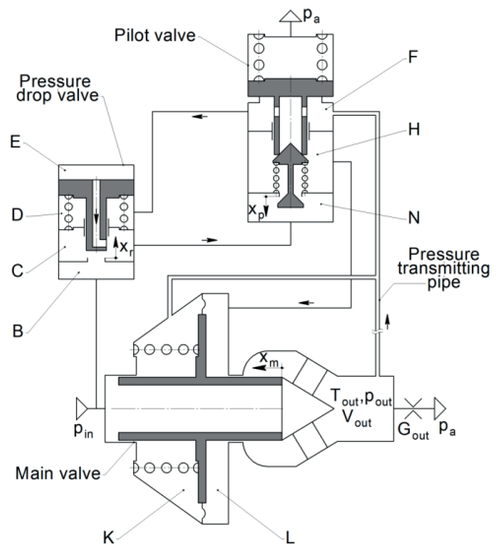


Figure 2: Diagram of the gas pressure reducing valve (one stage)

Mathematical model consists of differential equations including force balance equations for each moving shaft, gas equations for each chamber and mass flow rates for each throttle.

2.1.1 Main valve

Equilibrium equation for the main valve is

$$M\frac{d^2x_m}{dt^2}+D\frac{dx_m}{dt}+Jx_m+F_0+(p_K-p_L)A_m=0\,, \tag{1}$$

where F_0 is a spring pretension at x_m =0, A_m is an equivalent area of the membrane.

Assuming polytropic process for the gas in corresponding volumes, one obtains

$$\frac{V_K}{\gamma RT_K}\frac{dp_K}{dt}=A_m\frac{p_K}{RT_K}\frac{dx_m}{dt}+G_{pipe},$$

$$\frac{V_L}{\gamma RT_L}\frac{dp_L}{dt}=G_{HL}-A_m\frac{p_K}{RT_K}\frac{dx_m}{dt},$$

$$\frac{V_{out}}{\gamma RT_{out}}\frac{dp_{out}}{dt}=G_m-G_{pipe}-G_{out},$$

where G_{HL} is a mass flow rate from volume H to L, G_{pipe} is a mass flow rate in the pressure transmitting pipe from V_{out} to the branch point of pipes to volumes F and K.

Mass flow rate at the valve lift x_m at subcritical flow

$$G_m=C_d\pi d_{seat}x_m p_{in}\sqrt{\frac{2}{RT_{in}}\frac{\gamma}{\gamma-1}\left[\left(\frac{p_{out}}{p_{in}}\right)^{\frac{2}{\gamma}}-\left(\frac{p_{out}}{p_{in}}\right)^{\frac{\gamma+1}{\gamma}}\right]}$$

and at critical pressure drop

$$G_m=C_d\pi d_{seat}x_m p_{in}\sqrt{\frac{\gamma}{RT_{in}}}\left(\frac{2}{\gamma+1}\right)^{\frac{\gamma+1}{2(\gamma-1)}}.$$

2.1.2 Pressure transmitting pipe

For a laminar flow

$$(p_{out}-p_K-Z_{pipe}G_{pipe})\frac{A_{pipe}}{l_{pipe}}=\frac{dG_{pipe}}{dt},$$

where impedance $Z_{pipe}=\frac{RT_{out}}{p_{out}}\frac{32\mu l_{pipe}}{A_{pipe}d_{pipe}^2}$

for a turbulent flow

$$(p_{out}-p_K-Z_{pipe}G_{pipe}^2)\frac{A_{pipe}}{l_{pipe}}=\frac{dG_{pipe}}{dt},$$

where impedance

$$Z_{pipe}=f\frac{RT_{out}}{p_{out}}\frac{l_p}{2d_{pipe}A_{pipe}^2},\quad f=\left(-1.8\log_{10}\left(\frac{6.9}{\mathrm{Re}}+\left(\frac{e}{3.7d_{pipe}}\right)^{1.11}\right)\right)^{-2}$$

- friction factor, e – surface roughness.

2.1.3 Pressure drop valve

Equilibrium equation for the pressure drop valve

$$M\frac{d^2x_r}{dt^2}+D\frac{dx_r}{dt}+Jx_r+F_0+(p_E-p_D)A_{piston}=0. \tag{9}$$

Assuming polytrophic process for the gas in volumes V_C, V_D and V_E one obtains:

$$\frac{V_C}{\gamma RT_C}\frac{dp_C}{dt}=G_r-G_{CN}, \tag{10}$$

$$\frac{V_D}{\gamma RT_D}\frac{dp_D}{dt}=G_{FD}-A_{piston}\frac{p_D}{RT_D}\frac{dx_r}{dt}, \tag{11}$$

$$\frac{V_E}{\gamma RT_E}\frac{dp_E}{dt}=A_{piston}\frac{p_E}{RT_E}\frac{dx_r}{dt}-G_{EC}. \tag{12}$$

For a subcritical and supercritical flow, consequently

$$G_r=C_d\pi d_{seat}x_r p_{in}\sqrt{\frac{2}{RT_{in}}\frac{\gamma}{\gamma-1}\left[\left(\frac{p_C}{p_{in}}\right)^{\frac{2}{\gamma}}-\left(\frac{p_C}{p_{in}}\right)^{\frac{\gamma+1}{\gamma}}\right]}, \tag{13}$$

$$G_r=C_d\pi d_{seat}x_r p_{in}\sqrt{\frac{\gamma}{RT_{in}}\left(\frac{2}{\gamma+1}\right)^{\frac{\gamma+1}{2(\gamma-1)}}}. \tag{14}$$

2.1.4 Pilot valve

Equilibrium equation for the pilot valve

$$M\frac{d^2x_p}{dt^2}+D\frac{dx_p}{dt}+Jx_p+F_0+(p_F-p_a)A_{piston}=0. \tag{15}$$

For a polytropic processes in the valve volumes

$$\frac{V_N}{\gamma RT_N}\frac{dp_N}{dt}=G_{CN}-G_p, \tag{16}$$

$$\frac{V_H}{\gamma RT_H}\frac{dp_H}{dt}=G_p-G_{HL}, \tag{17}$$

$$\frac{V_F}{\gamma RT_F}\frac{dp_F}{dt}=G_{pipe}-A_{piston}\frac{p_F}{RT_F}\frac{dx_p}{dt}-G_{FD}. \tag{18}$$

2.2 Simulation results

Simulation study of nonlinear equations (1) - (18) is carried out using software MatLab/SimuLink at the parameters of the regulator and operating conditions given in Table 1. The parameters presented in Table 1 correspond to the initial system. The modified system is different from the initial one by the intermediate section between two regulators. Instead the heater, a chamber is installed, and the length of each pipe is reduced to 3.25 m. The effect of the chamber volume is studied during simulation.

Parameter	Value	Parameter	Value
Spring stiffness *J, kN/m*		Mass *M*, kg	
• Main valve	25	• Main valve	2
• Pressure drop valve	18	• Pressure drop valve	0.2
• Pilot valve	90.3	• Pilot valve	0.2
Spring pretention F_0, *N*		Seat diameter *d, mm*	
• Main valve	500	• Main valve	50
• Pressure drop valve	270	• Pressure drop valve	2
		• Pilot valve	3
Pipe upstream the heater:		Pipe downstream the heater:	
• length l_{p1}, *m*	18.25	• length l_{p1}, *m*	24.2
• diameter d_{p1}, *m*	0.057	• diameter d_{p1}, *m*	0.057
Specific gas constant *R, J/kg/K*	519	Adiabatic exponent γ	1.4
Volumetric flow rate *Q, nm/h*	0...2000	Kinematic viscosity *v*, m^2/sec	$3.5*10^{-4}$
Input pressure p_{in}, *MPa*	8.0	Temperature *T, K*	306
Output pressure p_{out}, *MPa*		Volume	
• first stage	5.5	• heater V_{heater}, *l*	100
• second stage	1.2	• downstream the main valve V_{out}, *l*	25

Table 1 Simulation input data

Time responses of the regulator to a step change in the output flow rate are shown in Figures 3 and 4. The process starts with a slow increasing the system input pressure up to the nominal value at the meter's diameter 13mm. When the controller reaches standard conditions, the flow rate changes by the meter's diameter step increase from 13 to 15 mm at the 30th second. A step input - the volumetric flow rate - is presented in Figure 5.

The Figures 3 and 4 illustrates instability of the modified system. As can be seen, the initial system shows a stable behaviour but the modified system having a small volume (10 *l*) between two stages of the controller, is unstable from the very beginning. The amplitude of oscillations of the main valve (first stage) is equal to the steady state lift value for initial system. The oscillation amplitude of the second stage regulator is much smaller.

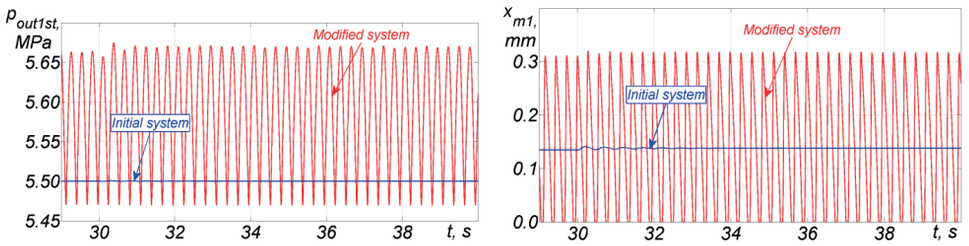


Figure 3: Output pressure and the main valve displacement for the first stage

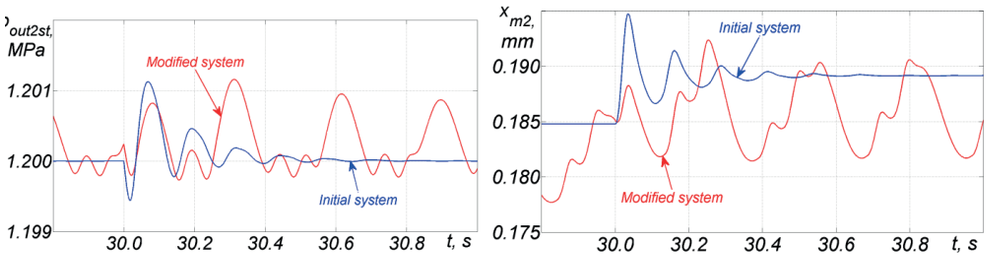


Figure 4: Output pressure and the main valve displacement for the second stage

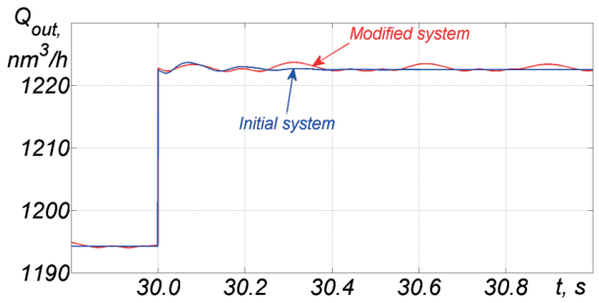


Figure 5: Time response of volumetric flow rate at the system output

An effect of chamber volume downstream of the first stage on the system stability is shown in Figures 6 and 7. A step disturbance of a volumetric flow rate at the system output is presented in Figure 8.

As the chamber volume increases from 20 *l* to 35 *l* the oscillations disappeared, and the system becomes stable.

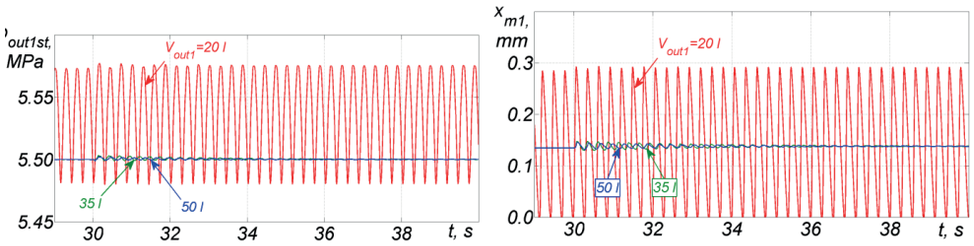


Figure 6: Output pressure and the main valve displacement for the first stage at various volumes (modified system)

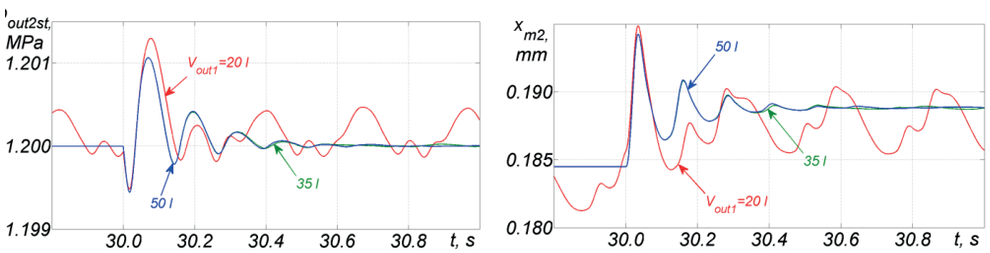


Figure 7: Output pressure and the main valve displacement for the second stage at various volumes (modified system)

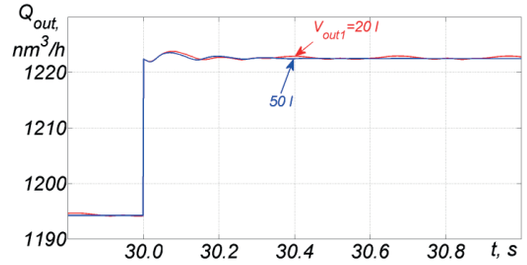


Figure 8 – Time response of volumetric flow rate at the system output

3 Experimental Results

The results of simulations were generally confirmed during operation in the framework of the gas distributing station. The initial system having the heater unit between two reducing stages demonstrated stable behaviour over all range of flow rates. After modification of the system the pressure oscillations downstream the first stage were registered. The range of oscillations was around 10 bars at the set point 50 bars. The oscillations were accompanied with noise. The instability was cut off with a decrease of the input pressure and an increase of the chamber volume. The tests will be continued in the laboratory conditions to find out stability domains in the regulator parameters.

4 Summary and Conclusion

Mathematical model of the two-stage gas pressure reducer was developed and simulated in the paper. The reference system with the heater unit installed between two stages and modified system without heater were compared and their dynamic behaviour was considered. The research revealed the definite and strong effect of the chamber volume in between two reducing stages on the system stability. The critical volume required for a stable behaviour was determined as result of simulation. The results were generally confirmed during operation in the framework of the gas distributing station. The research will be continued with the goal to improve the dynamic performances of the reducer and to widen its stability margin. It will be pointed out to updating the reducer design, its mathematical model and to carrying out laboratory tests of the regulator and its components.

5 Acknowledgements

The authors would like to express their gratitude to the Russian Ministry of Education and Science for the financial support of the investigations (Project # 9.1517.2017/4.6).

Nomenclature

Variable	*Description*	*Unit*	*Variable*	*Description*	*Unit*
A	Area	[m^2]	Q	Volumetric flow rate	[m^3/s]
C_d	Discharge coefficient		R	Specific gas constant	[J/kg/K]
D	Viscous drag coefficient	[N*s/m]	T	Temperature	[K]
d	Diameter	[m]	V	Volume	[m^3]
F	Force	[N]	x	Displacement	[m]
G	Mass flow rate	kg/s	γ	Adiabatic exponent	

J	Spring stiffness	N/m	μ	Dynamic viscosity	[kg/m/s]
l	Length	m	v	Kinematic viscosity	[m^2/s]
M	Mass	kg	ρ	Fluid density	[kg/$m^{3]}$
p	Pressure	[bar]	ω	Frequency	[1/s]

References

/1/ Vujic, D. and Radojkovic, S., *Dynamic model of gas pressure regulator,* In: Mechanics, Automatic Control & Robotics, vol. 3, no. 11, pp. 269–276, 2001.

/2/ Delenne, B. and Mode, L., *Modelling and Simulation of Pressure Oscillations in a Gas Pressure Regulator,* Proceedings of American Society of Mechanical Engineers, Vol. 7, Orlando, 2000.

/3/ Delenne, B., Mode, L. and Blaudez, M., *Modelling and Simulation of a Gas Pressure Regulator,* In: European Simulation Symposium, Erlangen, Germany, 26-28 October, 1999.

/4/ Shahani, A.R., Esmaili, H., Aryaei, A., Mohammadi, S. and Najar, M., *Dynamic simulation of high pressure regulator*, In: Journal of Computational and Applied Research in Mechanical Engineering, vol.1, no.1, pp.17–28, 2011.

/5/ Zafer, N. and Luecke, G. R., *Stability of gas pressure regulators,* In: Applied Mathematical Modelling, vol. 32, no.1, pp. 61–82, 2008.

/6/ Ramzan, M. and Maqsood, A., *Dynamic Modeling and Analysis of a High Pressure Regulator, In: Mathematical Problems in Engineering, Volume 2016, Article ID 1307181, Hindawi Publishing Corporation,* http://dx.doi.org/10.1155/2016/1307181

/7/ El Golli Rami, Bezian Jean-Jacques, Grenouilleau Pascal, Menu François, *Stability Study and Modelling of a Pilot Controlled Regulator*, In: Materials Sciences and Application, 2011, Vol. 2, pp. 859-869, doi:10.4236/msa.2011.27116, Published Online July 2011 (http://www.SciRP.org/journal/msa)

Principle and Application in FAST of Parallel Reliability Test Bench

Jingyi Zhao*,Wei Cai*, Hao Sun* and Shaochen Wang*

Hebei Provincial Key Laboratory of Heavy Machinery Fluid Power Transmission and Control, Yanshan University, Hebei str. 438, Qinhuangdao, China*
E-Mail: chenmochiwei@163.com

The traditional hydraulic components reliability test method has a long test time, low test efficiency and high energy loss, and can not meet the requirements of the reliability test of the core hydraulic components in the hydraulic system. This paper designed a parallel energy-saving method and equipment to test the reliability indexes of key hydraulic components for the hydraulic actuator of FAST. The calculated results met the lifetime request of the gear pump and the relief valve for hydraulic actuator of FAST. The reliability model based on small sample test can be used to estimate the lifetime desperation of components accurately under the status of the limit for the number of sample.

Keywords: Reliability test, parallel energy-saving, FAST, small sample test
Target audience: Systems, Energy Management, Components

1 Introduction

Hydraulic system is at the core of control and power transmission. It is widely used in metallurgical industry, engineering machinery, aerospace, shipbuilding and other important fields. Therefore, the reliability of hydraulic components and systems has become the core factor to ensure product quality /1/. As an important part of the reliability research, the reliability test aims at discovering various defects in product design, material and workmanship, determining the failure mode and failure mechanism of the product, proposing improvement measures for the weak link and further improving the level of product reliability /2/.The 500-meter spherical radio telescope FAST (Five-hundred-meter Aperture Spherical radio Telescope) is China's major science and technology foundation project, which is the world's largest and most sensitive single-aperture radio telescope simultaneously /3/. FAST is composed of six systems, including site survey and excavation system, active reflector system, feed support system, measurement and control system, receiver and terminal system and observation base /4/.Figure 1 shows the effect of the FAST.

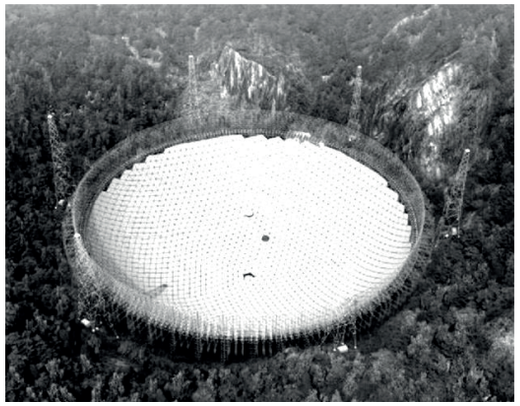


Figure 1: The effect of the FAST.

The main active reflector, as one of the three independent innovations of FAST, is implemented through the initiative configuration of the cable-net. The cable is connected to the actuator via 2225 pull-down cables. The actuator is a telescopic mechanism, one end of which is hinged to the earth anchor and the other end of which is hinged to the pull-down cable which connects the active nodes of the cable net. According to the control signal command, the actuator overcomes the internal force of the cable to generate the pull cable tension, and changes the distance between the anchor point and the end of the pull cable at the active node of the cable net by changing its own length. So as to adjust the position of the active node of the cable net and realize the shape adjustment center of the active reflecting surface of the FAST. The schematic diagram of actuator shows in Figure 2.

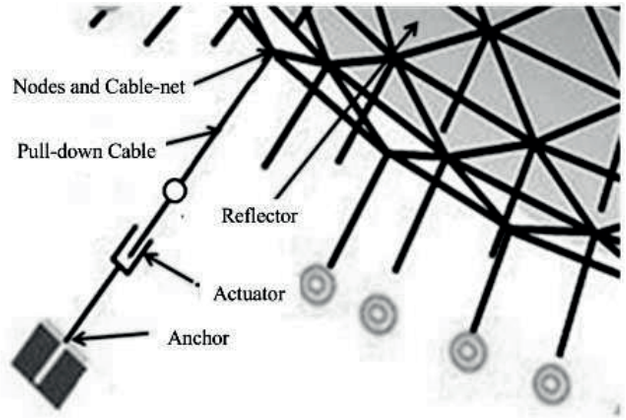


Figure 2: Schematic diagram of actuator.

FAST used the hydraulic actuators. There are thousands of hydraulic actuators operating simultaneously in the telescope observation operation. Therefore, FAST actuator, with a large number of poor working conditions, requires long-term stability and other characteristics, it requires high reliability. The reliability of the actuator core hydraulic components is the basis of the overall hydraulic system reliability. The reliability test of the hydraulic components can be carried out in advance, and the materials and process defects of components not exposed in the design can be found in advance to verify and improve the reliability level, and increase the reliability of the weak links in the system to ensure high reliability of the system /5/. Through the analysis of the failure modes and the hazards of the FAST hydraulic actuator, it is found that the relatively fatal parts of the actuator are the gear pump, the relief valve and the non-return valve. The FAST hydraulic actuator aims at the life expectancy of key hydraulic components is 5 years, so we need to accelerate the reliability test of these three components, judging from the experimental point of view whether the components can meet the requirements. The traditional reliability test bench, each one can only test one type of hydraulic components, and each test can only test one sample component. When testing multiple types of components, it is necessary to manufacture a plurality of different test benches. Testing a number of sample elements of the same type requires multiple tests, resulting in high test costs, time-consuming energy consumption, and waste of manpower. At the same time, the hydraulic components have the advantages of large power and long life, which require a large amount of energy and time to carry out the reliability test /6/. The test cycle of traditional reliability test bench is long. The traditional reliability test bench only reuses the energy after it is used once, and does not really use the energy more than once. Energy-saving effect is not satisfactory /7/. In order to solve these problems, a parallel energy-saving accelerated life test bench for key components of FAST hydraulic actuators was designed and manufactured. The test bench is an accelerated test bench that incorporates parallel energy-saving technologies. It accelerates multiple gear pumps, relief valves and non-return valves at the same time. It enables multiple utilization of energy, shortens test time, energy-saving and efficient.

2 Principle of the Test Bench

FAST hydraulic actuator parallel energy-saving accelerated life test bed was developed to establish a harsh laboratory environment, thereby accelerating the destruction of hydraulic components tested. Test bench tests the life of the gear pump, while the non-return valve and relief valve open-close movements to achieve the effect of accelerating energy-saving. In a short time, the test bench simulate the number of pressure shocks or opening and closing times in 5 years. According to the acceleration life curve, the average lifetimes of three hydraulic components under accelerated stress level are used to extrapolate their average life under rated conditions to evaluate the performance of gear pumps, relief valves and non-return valves. The test provides a reliable guarantee of the normal operation of the FAST hydraulic actuator.

2.1 Technical requirements

Under rated conditions, gear pump and check valve working pressure is 160 bar, the impact pressure is 20 bar, the relief valve population pressure is 50 bar. According to the rated working conditions of gear pump and hydraulic valve, the impact load is determined as accelerating factor, the impact frequency is dimension. Finally, the life data is calculated in terms of time. Respectively, the gear pump, relief valve and non-return valve performance degradation data are volumetric efficiency, cracking pressure and reverse leakage. The test can be carried out in a variety of stress levels, the minimum stress level should be close to normal working stress in the selection of stress, in order to improve the accuracy of extrapolation. The maximum stress level should be selected as large as possible, but not change the failure mechanism of hydraulic components under test, with the safe use of the system as a precondition, the other test stress should be reasonable distribution.

During the test, if any of the following failure criteria appear, the gear pump, relief valve and non-return valve can be considered as failed.

1. Gear pump volumetric efficiency decreased by more than 10% or less than 80%.
2. Relief valve opening pressure lower than 10% of the set value.
3. The reverse leakage of non-return valve exceeds the specified value.
4. Hydraulic components appear noise, temperature rise, stuck, abnormal wear and other phenomena.

The performance parameters of test bench refer to the current national machinery industry standards, the oil temperature is controlled at 50℃±4℃, the oil is 46# hydraulic oil, oil cleanliness is at NAS 9.

2.2 Fundamental

The experiment proposed a multi-component reliability experiment method using parallel energy-saving principle, and designed an accelerated life test bed based on the parallel energy-saving principle. Each experiment can complete shock life test of two gear pumps, two relief valves and two non-return valves. The schematic diagram shows in Figure 3. The motors 1.1 and 1.2 respectively drive two tested gear pumps. When the left side of the electromagnetic reversing valve 4 is energized, the non-return valve sample 5.1 and the relief valve sample 6.1 are opened. The two gear pump samples complete an impact from no-load to load. When the solenoid valve 4 is in the middle, the entire system is under pressure relief to form a pressure shock waveform. When the right side of the electromagnetic reversing valve 4 is energized, the non-return valve sample 5.2 and the relief valve sample 6.2 are opened, and the two gear pump samples are subjected to a no-load-to-load impact process once again. As a result, the gear pump samples were able to complete as many as 2 times the number of check and relief valve open- close attempts.

The test bench sets the flow meter 12.1 and 12.2 at the drain port and inlet port of the gear pump 1.1 to check the output flow of gear pump 1.1. The temperature sensor 13.1 is disposed in the leakage port of the gear pump 1.1 to detect the internal temperature of the gear pump 1.1. The pressure sensor 14.3 is set at the entrance of the test relief valve 6.1 to check its cracking pressure. By controlling the opening and closing of several shut-off valves, the flow meter 12.5 detects the reverse leakage of the non-return valves 5.1 and 5.2 respectively. The tested relief valves 6.1 and 6.2 and the solenoid valve 4 constitute a loading section. The peak pressure is set by the test relief valves 6.1 and 6.2, and the shock load is switched by the oil path of the solenoid valve 4. The cooler 7 and the heating meter 11 constitute the temperature control section. And the temperature of the system fuel tank is monitored by the temperature sensor 13.3 in real time.

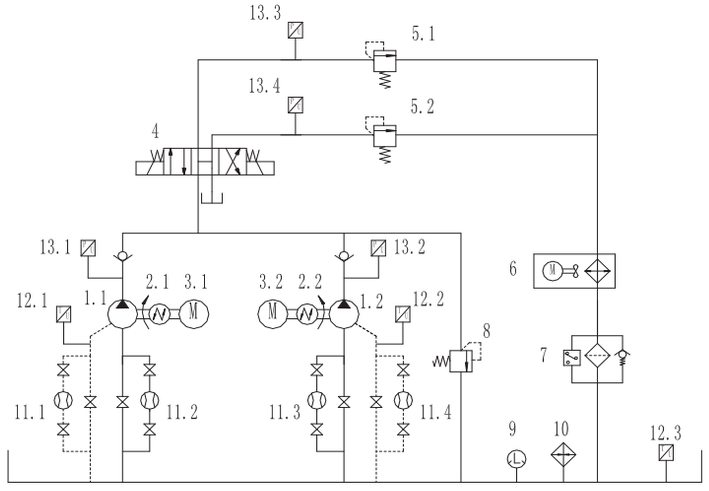


Figure 3: Principle scheme of test platform.

2.3 Experimental Features

The test bench is a typical electromechanical incorporate equipment designed for reliability weaknesses in FAST hydraulic actuators. The test bench shows in figure 4. As the test acceleration factor is a cyclic impact load, and there are three kinds of tested hydraulic components, the test bench compared with the general test stand in the mechanical and electrical design has its own characteristics, mainly in the following four aspects:

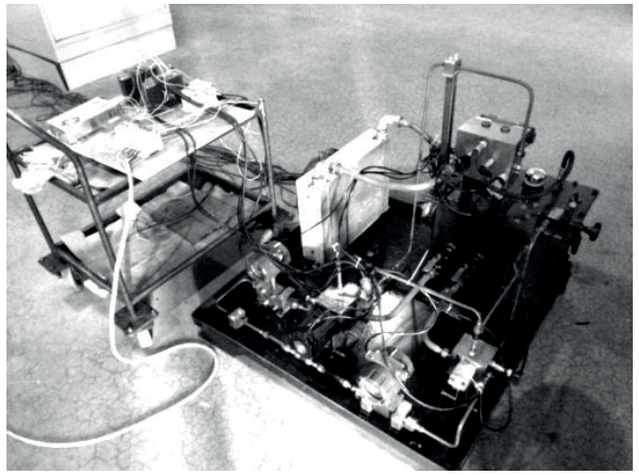


Figure 4: The test bench.

1. The test bench uses the concept of parallel energy-saving. Parallel is not only the same type of multiple components at the same time running, but also a number of different types of components at the same time running, so that energy is being used many times. The use of new components, new technologies

to achieve hydraulic system of energy saving, reduce system installed power and failure rate. In the test, adjusting the pressure relief valve under test can create different pressure levels of impact. These impacts completed the accelerated life test of the gear pump and the non-return valve, and the life test of the relief valve itself at the same time. These enable multiple efficient use of energy instead of simple power recovery. The test bench was designed with this concept. The reliability test of two gear pumps, two relief valves and two one-way valves can be carried out simultaneously in the test. The number of samples in one test is large, the number of types is various, and the time is short, with high efficiency and energy saving.

2. Test bench uses accelerated life test method. It refers to obtain failure data through the life experiment, which ensures the same failure mechanism of the sample, beyond normal stress levels. Using these data, the experimenters can infer the reliability characteristics of the samples. Gear pumps, relief valves and non-return valves are all high-reliability, long-life components. In order to shorten the test period, the test bench is designed based on the principle of accelerated life test, which can test the impact stress, temperature and motor speed as accelerated stress to ensure the smooth running of the test.

3. High degree of automation. The test bed adopts the state monitoring and control system based on PLC and MCGS. All temperature, pressure, flow and other data can be collected using the sensor and recorded in memory, enabling the visualization of the running status of the relevant test hydraulic components, automatic fault diagnosis and playback. The test bench can deal with the abnormal conditions that occur during the test, record the contents of the alarm, and manage the test process and equipment parameters.

3 Result Analysis

Built FAST hydraulic actuator gear pump, relief valve and non-return valve parallel energy-saving accelerated life test bench, in accordance with the above design. The test bench completed 500000 impacts on the gear pump, relief valve and non-return valve in the impact test. Measured pressure shock waveform shown in Figure 5. In the process of debugging, the test rig is also used to deal with the reliability assessment of other components besides the tested components, such as:

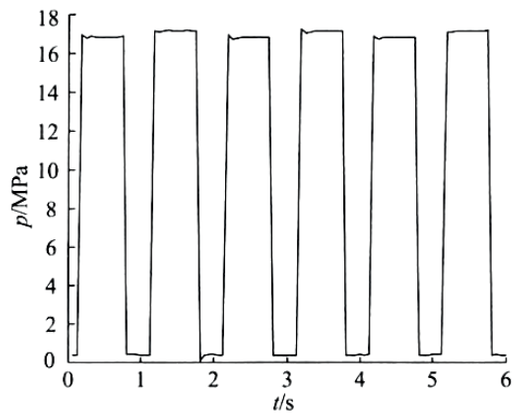


Figure 5: The shock waveform of gear pump pressure.

1. At the beginning of the experiment, both servo motors showed irregular vibration. After demolition, the reason is that the output speed and torque less than the rated speed requirements. It is because the motor drive and the selection of PLC models do not match. The servo motor works back to normal by replacing PLC.

2. After the operation of the test bench, one of the gear pumps abnormal noise, flow meter shows instability, the more obvious when the pressure is loaded. The reason for this phenomenon is the different between gear pump installation screws preload force, resulting in gear pump and installation of valve block joints lax, air inhalation. After adjusting the gear pump mounting screws, the fault is eliminated.

The above problems did not reappear in the test of the following 4 weeks, and the whole test bench operated smoothly and steadily. According to FAST hydraulic actuator test requirements, the test bench stands to complete the gear pump impact life test and relief valve, non-return valve opening and closing accelerated test. The test bench is used to test the reliability indexes of many kinds of hydraulic components at the same time. The test results show that this parallel mode has a short test period and obvious energy-saving effect, which greatly reduces the total power of the test bench and worth popularizing.

4 Conclusion

In view of the weak points in the reliability of FAST actuator hydraulic system, a parallel energy-saving accelerated life test bed is developed from the viewpoint of shortening the test period and reducing the waste of resources. It is capable of performing reliability tests on two gear pumps, two relief valves and two non-return valves simultaneously. The test bench is used to simulate the operating environment of the three hydraulic components under test in the laboratory to accelerate the test process and evaluate the performance indexes of gear pumps, relief valves and check valves. The design method of this test bench is of guiding significance to the development of an accelerated life energy saving test stand for hydraulic core components.

5 Acknowledgements

The authors are sincerely grateful to the supports of National Natural Science Foundation of China (Grant No.51405424, 51675461, 11673040).

References

/1/ Zhao Jingyi, Yao Chengyu, *Progress of reliability research on hydraulic system*, Hydraulics Pneumatics & Seals, Vol. 3, pp. 50-52, 2006.

/2/ Zhao Jingyi, Yao Chengyu, *Overview of China's Hydraulic Reliability Technology*, Vol. 10, pp. 1-7, 2013.

/3/ Nan Rendong, Ren Gexue, Zhu Wenbai, et a1 . *Adaptivecable Mesh Reflector for the FAST. ActastronomieaSinica*, Vol. 44, pp. 13-18, 2003.

/4/ ZHU M., WANG Q.M., LEI Z., WU M.C., *Research for reliability of the actuator of FAST reflector based on FMECA*,10.1109/ICRMS.2014.7107271.2014,Guangzhou,1-6..

/5/ YAO C.Y., ZHAO J.Y., *Research on Fuzzy Fault Tree Analysis Method for Hydraulic System Based on T-S Model*. China Mechanical Engineering, vol.20, no.16, pp.1913-1917,2009.

/6/ ZHANG X.P., CHEN X., ZHANG C.H., *Lifetime assessment method for products with dependent competing failures based on copula theory*. Proceedings of the Institution of Mechanical Engineers, Part C: Journal of Mechanical Engineering Science, vol.228, no.9, pp.1-7, 2016.

/7/ Angadia S.V., Jacksona R.L., et al., *Reliability and life study of hydraulic solenoid valve*. Part 1: A multi-physics finite element model. Engineering Failure Analysis. Vol.16, no. 3, pp.874–887, 2009.

Oil film characteristics and failure mechanism analysis of one kind of mechanical seal under the effect of fluid-structure-thermal coupling

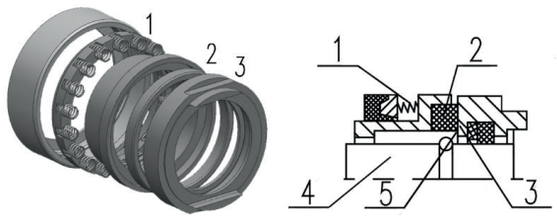
Yuheheng Song*, Shengrong Guo**, Sheng Liu** and Jiming Ma***

Beihang University, School of Reliability and System Engineering, 37#, Xueyuan Rd, Beijing, P.R. China *
Nanjing Engineering Institute of Aircraft System Jincheng, AVIC, 33#,Shuige Rd, Nanjing, P.R.China **
Beihang University, Sino-French Engineering School37#, Xueyuan Rd, Beijing, P.R. China***
E-Mail: songyh125@buaa.edu.cn

A method aims at analysing the fluid-solid-thermal coupling effect of one type of mechanical seal on failure is proposed. The method considers the coupling effects among fluid, solid and heat into one numerical simulation procedure. The deformations of one specific seal are calculated by ANSYS. Samples collected form workshop and field are used for validation of the analysis. Results show that excessive stress is the main reason for the internal ring fractures of the stationary graphite ring. The method proposed in this paper can well predict the location of the fractures. This analysis method is helpful for exploring the failure mechanism, and designing optimization of mechanical seal with longer lifetime and higher reliability.

Keywords: Fluid-structure-thermal coupling, mechanical seal, oil film, failure mechanism, impregnated graphite
Target audience: Hydraulic source, Design Process

1 Introduction



1-compression spring; 2-stationary ring; 3-rotating ring; 4-shaft; 5-liquid space

Figure 1 Structure of mechanical seal

Malfunction of mechanical seal is one of the main causes resulting in failure of electromechanical equipment. Analysis and research on the mechanical failure mechanism is beneficial to improve the performance and life of mechanical seal. The selected mechanical seal by this research, one type of external mechanical seal with specific structure (see Figure 1), is constituted by stationary ring (impregnated graphite with furan resin), rotating ring (mold steel 25Cr3Mo3VNb), compression spring and some accessories. Table 1[1] gives the material and properties of the components and oil.

Component and material	Description	Value	Unit
Rotating Ring (25Cr3Mo3VNb)	Density	7810	kg/m^3
	Specific heat capacity	4.60E+02	J/(kg.K)
	Thermal conductivity	44	W/(m.k)
	Coefficient of thermal expansion	1.01E-05	K^-1
	Reference temperature	20	°C
	Young's modulus	2.20E+11	MPa
	Poisson's ratio	0.28	/
Stationary Ring (M298K)	Density	1650	kg/m^3
	Specific heat capacity	710	J/(kg.K)
	Thermal conductivity	129	W/(m.k)
	Coefficient of thermal expansion	6.50E-06	K^-1
	Reference temperature	200	°C
	Young's modulus	4.04E+04	MPa
	Poisson's ratio	0.27	/
Oil	Density	889	kg/m^3
	Specific Heat capacity	1845	J/(kg.K)
	Heat conductivity	0.145	W/(m.k)
	Coefficient of thermal expansion	1.06	kg/(m.s)
	Reference temperature	25	°C
	Susurlands constant	124	K

Table 1 Material and properties of the components and oil

Statistics of the mechanical seals failure mode from field data, collected by the manufacturer, show that the most common failure is fracture of the graphite stationary ring, see Figure 2. The fracture becomes more serious in inner ring than the outer ring. The purpose of this paper is to analyze the causes of the failure of graphite ring in mechanical seals by simulation method.

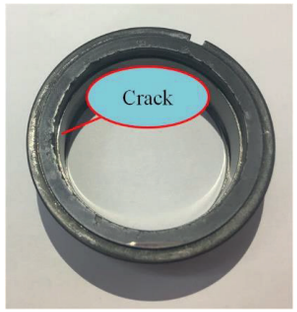


Figure 2 Fracture of stationary ring

Many researches on performance and life prediction of mechanical seal have been carried out. Gu [2] summarized the failure modes of mechanical seals as wear, blister and thermocrack. Wear and blisters cause pits and scratches on the surface, and thermocrack means radial crack under excessive thermal stresses. None of the failure modes matches the one shown in Figure 2. The purpose of this paper is to propose a method to reveal the mechanism of this special failure mode.

The numerical analysis method on behavior of mechanical seal has the most outstanding achievements. Mayer [3] systematically expounds the fluid mechanics and lubrication, friction, wear theory and design methods of mechanical seals. Buck [4, 5] proposed a method to calculate the temperature distribution of the seal ring: the fin method. The heat transfer and the efficiency of the seal were calculated by establishing a fin model of the seal ring. Pascovici [6] studied the thermodynamic properties mechanical seal. The effects of Nusselt number, flow direction and the thermal conductivity on the temperature distribution of the ring were analyzed by solving the heat energy equation.

For validation of the numerical results, there are some researchers focusing on the experiment of mechanical seals. Lebeck [7] used experimental methods to measure and predict the oil film coefficient of mechanical seal.

Several tests with varying speed, temperature and running time were performed to obtain temperature distribution data. Through the temperature distribution of the seal ring, the oil film coefficient of the mechanical seal was predicted, and the result was compared with the measured value. Parviz [8] built the similar experimental equipment to validate the results of a computational model for flow and thermal analysis of mechanical seal. The computational model adequately predicts the temperature distribution within the stator of a mechanical seal. these above studies focused only on the seal rings and their thermal and mechanical behaviors, and did not reveal the characteristics of the flow in the seal chamber.

Thermohydrodynamic(THD) has gradually become the focus of researches in recent decades. Brunetière[9] analyzed the thermal performance of lubrication by establishing the three-dimensional THD model of the sealing face. The factors, which affected lubricating property, such as the sealing ring material, fluid flow type, heat transfer conditions of the seal face, were considered in the model. In the following study [10, 11], numerical models for thermal effects was investigated and the influence of the design and running parameters on the TEHD behavior of Mechanical Face Seals (MFS), in steady dynamic tracking mode, was analyzed. Then, Erwan [12] applied the same model to a specific seal used in reactor coolant pumps, and obtained similar results. Luan [13-15] discussed flow behavior and cooling effect of oil in the seal chamber by means of numerical simulation method. In recent years, researchers began to use analytic method gradually to establish the heat transfer equations of seal rings. [16-18]

Above researches' solutions were obtained based on some assumptions, such as uniform temperature and constant viscosity of the fluid film, neglect of the cooling effect of the oil and so on. These assumptions caused errors in the results.

Under the condition of high temperature, mechanical and thermal deformations are the main factor leading to seal failure. Deformations will aggravate wear, leading to high temperature on seal rings' surfaces. Thermal stress on the seal rings may exceed the stress limit of the material, resulting in fracture. Therefore, the study of mechanical and thermal deformation of mechanical seals is the most important part of failure analysis.

Zhu [19] established the mechanical equation for seal of ship stern shaft, and verified the deformation equation by a certain type of seal. Brunetière [20] proposed a semi-analytical method of non-contact seal considering the thermal deformation. Wang [21] established finite element model of rotating and stationary ring with ANSYS, results indicated that the thermal deformation of the rotating and stationary ring leads to the formation of gap in the seal chamber, resulting in the increase of leakage.

In conclusion, fluid-structure-thermal coupling analysis on mechanical seal has made some progress. However, there are few studies on the pressure distribution of the oil film and the elastic deformation of seal rings caused by inhomogeneous oil pressure distribution. Theoretical researches focused on structure-thermal coupling deformation analysis are also few. The purpose of this study is to propose a method to analyze the temperature and pressure distribution of oil film in seal chamber and deformations of seal rings under fluid-structure-thermal coupling effect. Based on this method, failure mechanism analysis is carried out on one specific type of mechanical seal.

2 RESEARCH CONTENTS AND SCHEME

This research presents a fluid-structure-thermal coupling analysis method on behaviors of oil film in the seal chamber. The oil film characteristics (thickness, temperature distribution, pressure distribution) are obtained by simulation. Then, temperature and pressure distributions are used to calculate the structure-thermal coupling deformation and the temperature contour of seal rings. Thanks to the simulation result, the effect of oil film characteristics on the fracture creating process could be revealed efficiently. By comparing the surface morphology of broken seal, the possible failure showed by the analysis results could be validated. The research scheme is shown in Figure 3.

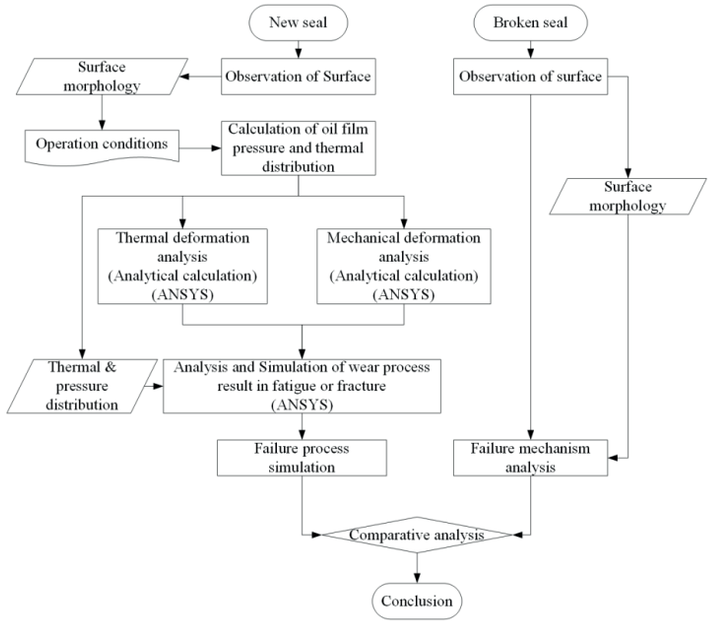


Figure 3 Research Scheme Diagram

3 THEORETICAL MODEL FOR CACULATION OF OIL FILM PRESSURE AND THERMAL DISTRIBUTION UNDER FLUID-STRUCTURE-THERMAL COUPLING EFFECT

3.1 Fluid flow model

The structure of studied mechanical seal and cross section of the seal is shown in Figure 1. The following assumptions are made:

1. Ignore the all body force (gravity or magnetic force).
2. Fluid at the interface is not sliding, that is to say the fluid flow affixed to the rotating ring and stationary ring surface has the same velocity with the rings.
3. Because the oil film thickness is only a few microns or even smaller, the pressure does not change along oil film thickness. So the pressure distribution has only two dimensions, circumferential and radial.
4. Comparing with the oil film thickness, the oil film curvature radius is very large, so the influence of oil film curvature is neglected, and the translational speed is used instead of the rotational speed.
5. Oil in the chamber is Newton fluid.
6. The flow is laminar, there is no turbulence.
7. Comparing with the viscous force, the influence of inertia force can be neglected.

On the basis of the above assumptions, the Reynolds equation can be used to solve the pressure distribution. The general form of the Reynolds equation is shown in the Equation (1). [22]

$$\frac{\partial}{\partial\theta}\left(\frac{h^3}{\mu}\frac{\partial p}{\partial\theta}\right)+\frac{\partial}{\partial r}\left(\frac{h^3}{\mu}\frac{\partial p}{\partial r}\right)=6\left[\frac{\partial}{\partial\theta}\left(\left(U_h-U_0\right)h\right)+\frac{\partial}{\partial r}\left(\left(V_h-V_0\right)h\right)\right]+12\frac{\partial h}{\partial t} \tag{1}$$

In this study, oil film thickness h in one specific time step is constant. U_h is the circumferential velocity of the rotating ring, the value is ω_r, and U_h stay constant in circumference. U_0 is the circumferential velocity of the stationary ring, the value is 0. V_h is the radial velocity of rotating ring and V_0 is the radial velocity of the stationary ring, the values of both are 0. Equation (1) can be simplified and rewritten as Equation (2).

$$\frac{\partial}{\partial\theta}\left(\frac{h^3}{\mu}\frac{\partial p}{\partial\theta}\right)+\frac{\partial}{\partial r}\left(\frac{h^3}{\mu}\frac{\partial p}{\partial r}\right)=12\frac{\partial h}{\partial t} \tag{2}$$

3.2 Temperature distribution equation of the fluid film

For the condition of hydrodynamic lubrication, the variation of kinetic energy and potential energy of fluid flow can be neglected, so that the energy is only a function of temperature. Suppose that the flow is in a stable state, so all variables do not change with time. Under the circumstance of hydrodynamic lubrication, heat convection is much more than heat conduction. So heat conduction along the direction of the film thickness z is negligible. The temperature changes only along direction θ and direction r.

Under these conditions, the energy equation applicable to hydrodynamic lubrication is Equation (3).

$$\frac{\mu_k U^2}{J\rho_0 c_0 h_k}+\frac{{h_k}^3}{12\mu_k J\rho_0 c_0}\left[\left(\frac{\partial p_{k+1}}{\partial\theta}\right)^2+\left(\frac{\partial p_{k+1}}{\partial r}\right)^2\right]-\lambda\left(T-T_{\text{ref}}\right)=q_\theta\frac{\partial T_{k+1}}{\partial\theta}+q_r\frac{\partial T_{k+1}}{\partial r} \tag{3}$$

In which, q_θ and q_r are volume flow of micro-unit in direction θ and r respectively, U is the circumferential velocity of the flow, $U=\omega\dfrac{R_1+R_2}{2}$.

The dynamic viscosity of oil varies with pressure and temperature, the calculation of dynamic viscosity requires reference viscosity, pressure and temperature. The dynamic viscosity is given by Equation (4).

$$\mu=\mu_0\exp\left(\alpha p+\beta\left(T-T_{\text{ref_o}}\right)\right) \tag{4}$$

3.3 Calculation of oil film thickness

The rotating ring has no movement in the axial direction, while the stationary ring can move in the axial direction under the action of the spring. Therefore, the oil film thickness is only related to the motion of the stationary ring and the oil pressure.

Movement analysis on the stationary ring is mainly determined by the force analysis on the stationary ring. According to the structure of seal in the piston pump, the forces acting on the stationary ring include spring force and bearing force of oil film. In addition, the stationary ring is also subjected to a damping force due to the viscous action of the oil. According to the parameters listed in Table 2, the spring force F_N depends on the oil film thickness h_k. The spring force is given by Equation (5).

$$F_N=F_{N_0}+K\left(h_k-H_0\right) \tag{5}$$

The supporting force of oil film is related to the pressure distribution. The supporting force of the oil film on the contact surface between the stationary ring and the oil can be obtained by Equation (6).

$$F_{\text{o}}=\sum_i\sum_j p_{k+1}(i,j)\cdot\left[\left(R_1+j\cdot d_r\right)\cdot d\theta\cdot dr\right] \tag{6}$$

The damping force is one of the main forces that cannot be neglected. It is only related to the motion. The coefficient K_f is an experimental value. In this paper, K_f = 526. The damping force can be calculated by Equation (7).

$$F_f=-K_f\cdot v_k \tag{7}$$

After force analysis of the stationary ring, according to Newton's second law, the acceleration a, velocity v_{k+1} of stationary ring, and the next step time oil film thickness h_{k+1} are obtained.

$$\begin{cases} a=\dfrac{F_N-F_{\text{o}}-F_f}{M_s+M_t} \\ v_{k+1}=v_k+a\cdot dt \\ h_{k+1}=h_k-v_{k+1}\cdot dt \end{cases} \tag{8}$$

4 FLUID-STRUCTURE-THERMAL COUPLING ANALYSIS PROCEDURE

A fluid-structure-thermal coupling analysis procedure for the oil film in the seal chamber is introduced in this section. The oil film thickness, temperature and pressure distribution, which all effect the deformation of seal structure, are studied. All the equations in the previous section are solved based on the finite element method and boundary element method, the temperature and pressure characteristics of oil film are simulated in order to investigate their influences on the wear process. The analysis procedure is shown in Figure 4.

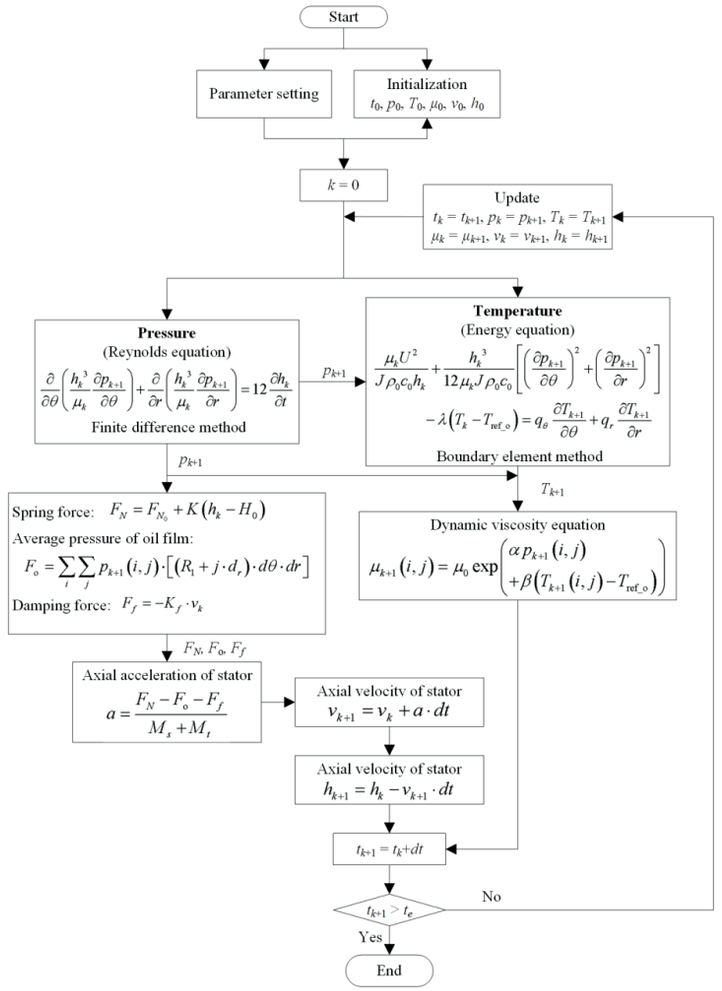


Figure 4 Flow chart of analysis procedure

The instructions for the calculation process are as follows:

1. Parameter setting

The parameters used in the whole calculation process are determined in this step. Most of the values of parameters are theoretical or measured, there is a small amount of them are obtained by experiential hypothesis, such as K_f.

2. Initialization

The time, pressure distribution, temperature distribution, dynamic viscosity of oil film, axial velocity of stationary ring and oil film thickness are initialized for the calculation of the starting state.

3. Calculation of pressure distribution

The Reynolds equation is solved by finite difference method. The calculation requires the pressure distribution, the dynamic viscosity distribution, the axial velocity of stationary ring and the oil film thickness at the previous time step. The first calculation of the initial time takes the initializations as inputs, and then the results obtained at the previous time step can be used at next time step.

4. Calculation of temperature distribution

The energy equation considering the heat conduction is solved by boundary element method. This equation is applicable to the mixed lubrication state. It must be solved after the calculation of pressure distribution because of the need of pressure distribution as input.

5. Calculation of dynamic viscosity of oil film

The dynamic viscosity equation is solved.

6. Calculation of oil film thickness between the stationary and rotating ring

The oil film thickness between the two rings is determined by the axial movement of stationary ring. The motion analysis requires force analysis of stationary ring. After the calculation of the spring force, the oil film pressure and damping force which are the three forces acting at the stationary ring, the axial velocity of stationary ring and the oil film thickness can be calculated.

7. Update the values of variables

Variables (pressure distribution, temperature distribution, dynamic viscosity, stationary ring speed, oil film thickness) are updated to the calculation results of previous time step.

The procedure is repeated until the time t_e has reached the scheduled simulation time. Then the overall calculation is completed.

5 RESULTS AND DISCUSSION

The numerical calculations were performed in order to determine the effect of selected parameters characterizing the seal operation, i.e. the inlet oil temperature (40°C, 100°C and 200 °C), on the distributions of pressure and temperature in the oil chamber.

Table 2 and Figure 5 show the analyzed geometrical and operational parameters of the seal.

Type	Parameter name	Symbol	Value	Unit
Time	Time step	d_t	1e-4	s
	Simulation time	t_e	300	s
Structure & Operation Parameters	Inner radius	R_1	18.3e-3	m
	Outer radius	R_2	20.85e-3	m
	Oil pressure in chamber	P_{oil}	4.5e5	Pa
	Pressure atmosphere	P_{air}	1e5	Pa
	Ambient temperature	T_{ref}	25	°C
	Angular velocity	ω	4200*2*pi/60	rad/s
	Initial velocity of stationary ring	v_0	0	m/s
	Mechanical equivalent of heat	J	4.1840	J/cal
	Spring pretightening force	F_{N0}	88	N
Material	Mass of stationary ring	M_s	0.002022	kg
	Mass of sleeve of stationary ring	M_t	0.025	kg
	Spring stiffness coefficient	K	3460	N/m
	Density of oil	ρ_0	889	Kg/m^3
	Specific heat capacity of oil	c_0	1845	J/(kg·°C)
	Coefficient of heat transfer	λ	475	W/(m^2·°C)
	Thermal conductivity of oil	k_0	0.145	W/(m·°C)
	Pressure viscosity coefficient	α	2.2e-8	/
	Thermal viscosity coefficient	β	-0.03	/
	Reference oil viscosity	μ_0	15e-6	N.s/m^2(Pa·s)
	Reference temperature	T_{ref_o}	50	°C

Table 2 Parameters setting for numerical calculations

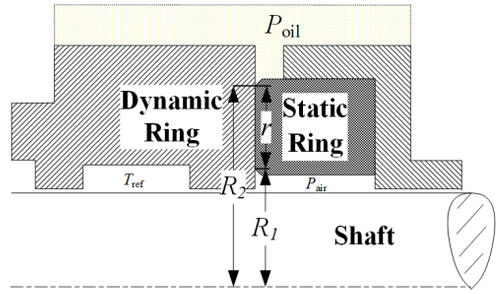


Figure 5 Diagram of operational parameters

After the simulation under the condition of different inlet oil temperature, the calculation results were presented in the graphical form. Figure 6 shows distributions of temperature in the oil chamber for three values of rotational speed of the inlet oil temperature: 40°C, 100°C and 200 °C along the radius. Figure 7 shows the distributions of pressure.

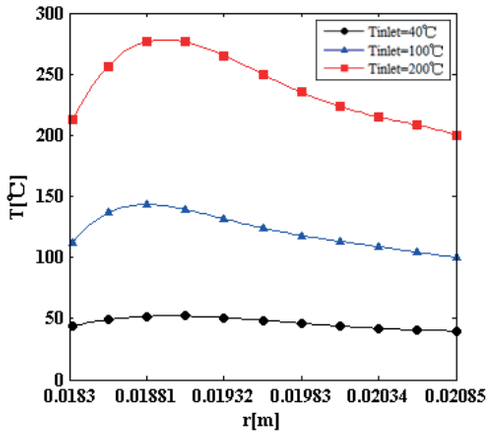


Figure 6 Temperature distribution in oil chamber for different values of inlet oil temperature

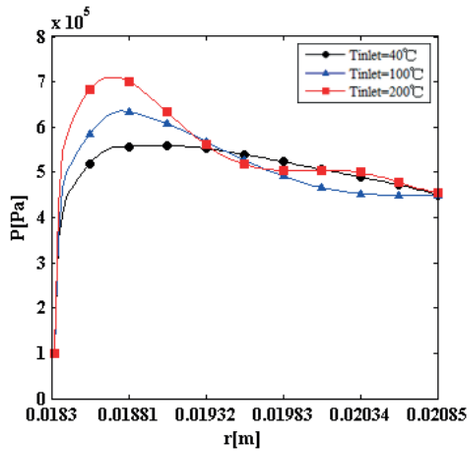
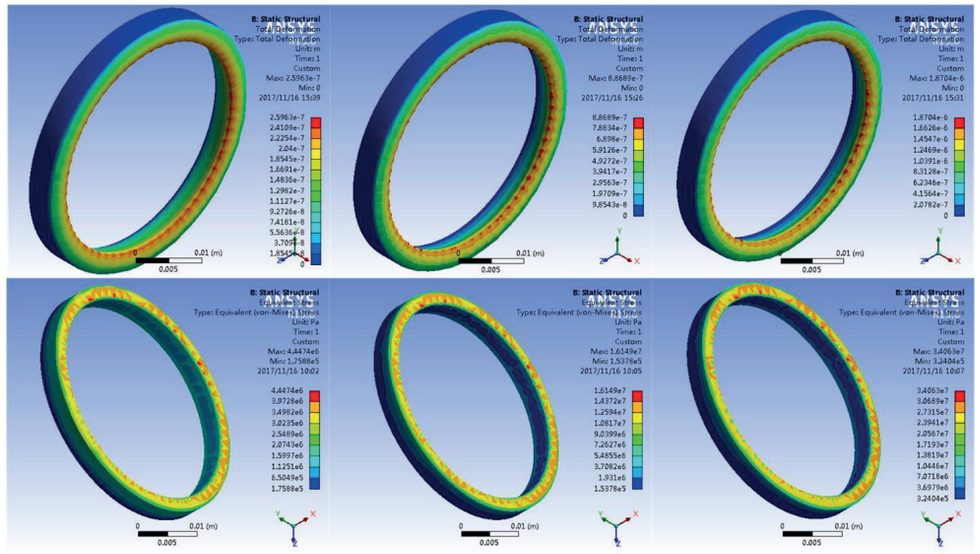


Figure 7 Pressure distribution in oil chamber for different values of inlet oil temperature

It can be seen from Figure 6 and Figure 7, the higher temperature of inlet oil will cause the more significant difference in temperature in the chamber. The position of the higher temperature in the oil chamber is also the position of higher pressure. The temperature and pressure results obtained by simulation are used as input conditions and analyzed in the commercial software ANSYS to determine whether the graphite seal ring will be damaged under the action of the temperature and pressure loads.

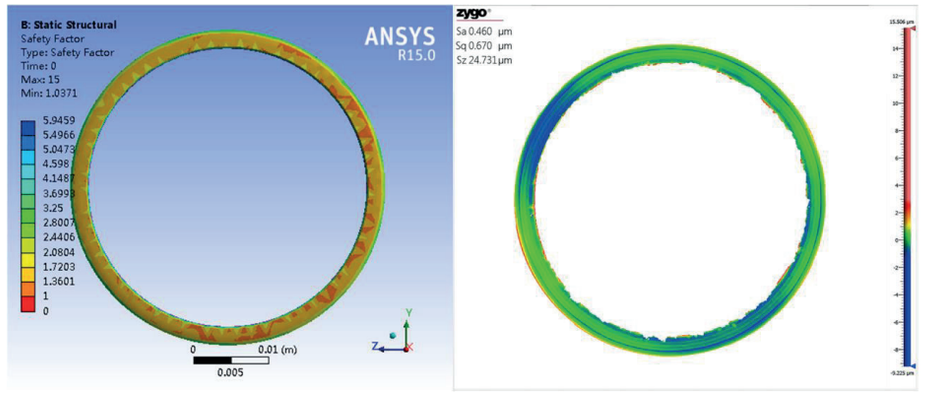


(a) 40°C *(b)100°C* *(c)200°C*

Figure 8 Total deformation and Equivalent (von-Mises) stress results in ANSYS

According to Figure 7, the inner side protrudes and bears tensile stress. The inner side of the graphite ring is subjected to larger stress, and the weak parts are distributed on the inner side. With the increase of the inlet oil temperature, the inner side is subjected to more tensile stress. Under the condition of temperature of 40°C, 100°C and 200°C, the maximum stresses are 4.45MPa, 16.15MPa and 34.06MPa respectively. According to the description of [1], the compressive strength of the graphite material M298K is 120MPa, the shear strength is 57MPa, and the tensile strength is only 0.57 of the shear strength, which is 32.5MPa. When the inlet oil temperature is up to 200 degrees, the stress of the weak part of the inner side has slightly exceeded the tensile strength of the material, and the fracture may appear in the continuous operation process.

The comparison between the measured results and the simulation results is shown in Figure 9. According to Figure 9, the positions of simulated damage (where safety factor are less than 1) are consistent with the position of actual damage in the seal using in the outfield.



(a) *(b)*

Figure 9 Comparison of (a) simulated damage and (b) actual damage

6 CONCLUSION

In this paper, the failure mode of one type of graphite-steel mechanical seal is analyzed. A numerical model under the effect of fluid-structure-thermal coupling, which is suitable for describing the thermal and mechanical behavior of oil in the chamber, has been developed. This model incorporates the Reynolds equation for fluid-flow, energy equation considering the heat conduction for fluid and force analysis of the stationary ring. The effect of the inlet oil temperature on the distributions of pressure and temperature in the oil chamber is analyzed using this model. Results show that the higher the inlet oil temperature is, the more intense the temperature difference is in the oil chamber and the intense temperature difference in the oil chamber will lead to strong squeeze effect of oil, then the pressure in the chamber will increase.

Analysis of Equivalent (von-Mises) stress in ANSYS under the pressure and temperature loads calculated by proposed model of graphite ring indicates that under the condition of inlet oil temperature at 200°C, the graphite bears the stress which exceeds the strength limit of the material. The damage locations predicted by the model are consistent with the observed damage locations. Based on the failure analysis results, excessively high inlet oil temperature is the fundamental cause of failure, and the mechanical seal should avoid long-term operation at high temperature.

The method proposed in this paper is appropriate to describe structural behavior of graphite ring used in mechanical seal in case of inner ring fractures. Indeed, the model proposed is appropriate to calculate the loading details and predict the effects caused by the loading details, which markedly influence the failure mechanism of this type of structures.

References

/1/ X. Shen, *Handbook of sealing materials*. Beijing, China: China Petrochemical Press, 1993.

/2/ Y. Gu, "Sealing Failure Modes and Critical Balance Ratio for Mechanical Seals," *Journal of the*

University of Petroleum, vol. 20, no. 6, pp. 52-56, 1996.

3/ E. Mayer, *Mechanical Seals*. Dusseldorf, Germeny: VDI-Verlag, 1966.

4/ B. GS, "Heat Transfer In Mechanical Seals," presented at the Proceeding of 6th internation pump user symposium, Baton rouge, LA, USA, 1989.

5/ B. GS, "Estimating Heat Generation, Face Temperature and Flush Rate for Mechanical Seals. ," presented at the PumpUsers Expo'99, Baton rouge, LA, USA, 1999.

6/ M. D. Pascovici and I. Etsion, "A Thermo-Hydrodynamic Analysis of a Mechanical Face Seal," Journal *of Tribology,* vol. 114, pp. 639-645, 1992.

7/ A. O. Lebeck, M. E. Nygren, S. A. Shirazi, and R. Soulisa, "Fluid Temperature and Film Coefficient Prediction and Measurement in Mechanical Face Seals--Experimental Results," *Tribology Transactions,* vol. 41, no. 4, pp. 411-422, 1998.

8/ P. Merati, O. Nori Aki, P. Robert L, and J. Larry E, "Experimental and Computational Investigation of Flow and Thermal Behavior of a Mechanical Seal," *Tribology Transactions,* vol. 42, no. 4, pp. 731-738, Oct 1999.

9/ B. Tournerie, J. C. Danos, and J. Frêne, "Three-Dimensional Modeling of THD Lubrication in Face Seals," *Journal of Tribology,* vol. 123, no. 1, pp. 196-304, 2001.

10/ N. l. Brunetièree, B. Tournerie, and J. Frêne, "TEHD Lubrication of Mechanical Face Seals in Stable Tracking Mode: Part 1-Numerical Model and Experiments," *Journal of Tribology,* vol. 125, no. 3, pp. 608-616, 2003.

11/ N. l. Brunetièree, B. Tournerie, and J. Frêne, "TEHD Lubrication of Mechanical Face Seals in Stable Tracking Mode: Part 2- Parametric Study," *Journal of Tribology,* vol. 125, no. 3, pp. 617-627, 2003.

12/ E. Galenne and I. Pierre-Danos, "Thermo-Elasto-Hydro-Dynamic Modeling of Hydrostatic Seals in Reactor Coolant Pumps," *Tribology Transactions,* vol. 50, no. 4, pp. 466-476, 2007.

13/ Z. Luan and M. M. Khonsari, "Numerical Simulations of the Flow Field Around the Rings of Mechanical Seals," *Journal of Tribology,* vol. 128, no. 3, pp. 559-569, 2006.

14/ Z. Luan and M. M. Khonsari, "Computational Fluid Dynamics Analysis of Turbulent Flow Within a Mechanical Seal Chamber," *Journal of Tribology,* vol. 129, no. 1, pp. 120-128, 2007.

15/ Z. Luan and M. M. Khonsari, "Heat transfer correlations for laminar flows within a mechanical seal chamber," *Tribology International,* vol. 42, no. 5, pp. 770-778, 2009.

16/ G. Zhu, "Computer Prediction of Mechanical Seal Performance and Experimental Validation," *Proceedings of the Institution of Mechanical Engineers. Part J: Journal of Engineering Tribology,* vol. 213, no. 6, pp. 433-449, 1999.

17/ S. Błasiak, C. Kundera, and J. Bochnia, "A Numerical Analysis of the Temperature Distributions in Face Sealing Rings," *Procedia Engineering,* vol. 39, pp. 366-378, 2012.

18/ S. Blasiak, "An analytical approach to heat transfer and thermal distortions in non-contacting face seals," *International Journal of Heat and Mass Transfer,* vol. 81, pp. 90-102, 2015.

19/ Z. Hanhua, L. Zhenglin, and W. Shizhu, "Mechanical Deformation of Ship Stern-shaft Mechanical Face Seals," *Tsinghua Science and Technology,* vol. 9, no. 3, pp. 299-302, 2004.

20/ N. Brunetière and A. Apostolescu, "A Simple Approach to the ThermoElastoHydroDynamic Behavior of Mechanical Face Seals," *Tribology Transactions,* vol. 52, no. 2, pp. 243-255, 2009.

21/ W. Heshun and D. Lin, "Research on Thermal Deformation of Hydrostatic Pressure Mechanical Seal," *Energy Education Science and Technology Part A: Energy Science and Research,* vol. 31, no. 1, pp. 473-476, 2013.

/22/ W. Shizhu and H. Ping, *Principle of Tribology*. Tsinghua university press, 2012.

Innovative Structural Design and Coupled Vibration Analysis of the Bionic Hydraulic Pipeline

Changhong Guo*, Shaodong Wu*, Lingxiao Quan* and Ruxia Bai*

Yanshan University, College of Mechanical Engineering, Qinhuangdao, China*
E-Mail: lingxiao@ysu.edu.cn

Aiming at the vibration produced by the hydraulic pipeline system during operation, a bionic hydraulic pipeline with three layers of structure is developed based on the animal biological mechanism. The 14 - equation of hydraulic pipeline is perfected and the fluid-structure interaction dynamic model suitable for the bionic hydraulic pipeline is deduced. The two-way fluid-structure interaction analysis of the ANSYS simulation software shows the bionic hydraulic pipeline has better effect on absorbing pulsation and suppressing vibration. The results will provide a new technical approach for obtaining better vibration control effect.

Keywords: Absorption pulsation, Suppression vibration, bionic, Fluid-structure interaction, 14 - equation
Target audience: Hydraulic system, Fluid-structure interaction, Bionic

1 Introduction

High speed and high pressure will be one of the main development trends of hydraulic transmission system in the next twenty years[1]. It will aggravate the vibration of hydraulic pipeline system and reduce the working performance and reliability of the hydraulic control system. Axial piston pump is considered as one main source of the hydraulic system[2], and more than 50% of the vibration is generated by it. Most of the flow pulsation and mechanical vibration generated by axial piston pump will transmit to the system through the hydraulic pipeline[3]. Therefore, absorbing flow pulsation to suppress vibration has become an important direction in the research of hydraulic pipeline vibration control in recent years.

Several common pulsation elimination devices in hydraulic pipeline system, such as the accumulator, H filter, high frequency on-off valve and pipeline attenuator, can be divided into passive control, semi-active control and active control according to the control mode. These devices and vibration control ideas lay a good foundation for the flow pulsation absorption of axial piston pump[4]. But these devices have the following deficiencies. Most of the devices are installed in the pipeline in parallel, which will excite the broadband secondary pulsation wave which is not conducive to absorption. Most devices have the characteristics of complex structure, many fault points and low reliability.

Comparing the hydraulic power system and the animal blood circulatory system, it can be found that there are many similarities between them. If the hydraulic pump is regarded as the heart of the system, then the hydraulic pipeline is the blood vessel of the system. The research results of absorption flow pulsation and vibration control of hydraulic pipeline at domestic and foreign are summarized in this paper. Referring to the biological mechanism that the left ventricular outflow vessels of the cheetah can tolerate blood pulsation with high pressure and high frequency, a bionic hydraulic pipeline is proposed, which provides a new idea for the vibration control of the hydraulic pipeline.

2 Structure and principle of the bionic hydraulic pipeline

Study on cardiovascular biology has found that when a quadruped, such as a cheetah, is chasing a prey, the heart beats violently and the blood pulsation amplitude and frequency increase instantaneously. The blood vessels are undamaged under blood flow pulsation with high frequency and high pressure, which benefits from the unique physiological structure. The cardiac outlet vessels of cheetah are composed of three layers: intima, media and adventitia. The structure is shown in figure 1. The intima is smooth and the resistance is smaller. The media with better structure adaptability can greatly improve the ability of blood vessel to absorb blood pulsation with high frequency and large amplitude. The adventitia contains large amounts of collagen fibrils that protect the vessel from breaking under high pressure[5]. The structure adaptability study of bionic blood vessels has shown that viscoelasticity of blood vessel has obvious effect on decreasing blood pulsation[6, 7, 8].

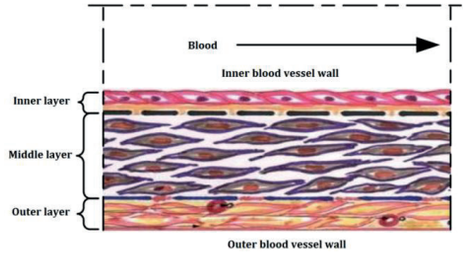
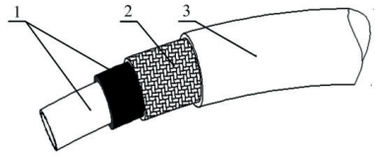


Figure 1 Schematic diagram of blood vessel wall



1. Inner layer 2. Middle level 3. Outer layer

Figure 2 Structure schematic diagram of the bionic hydraulic pipeline

The rubber, a kind of viscoelastic material, has physical and chemical properties which are different from metallic materials. Its mechanical properties are obviously nonlinear[9, 10], and it is mainly used for vibration reduction and sealing in engineering applications. Therefore, according to the cardiovascular biological achievement that the cardiac outlet vessels can tolerate the blood pulsation with high frequency and large amplitude, a bionic hydraulic pipeline with three layers structure is proposed in this paper to absorb the flow pulsation at the hydraulic pump outlet and to suppress the pipeline vibration. The structure schematic diagram of the bionic hydraulic pipeline is shown in figure 2. The inner layer composed of nanometre coating materials and coating matrix is quite smooth and has a good ability to stabilize the flow of oil. The middle layer with good structure adaptability is woven from viscoelastic material, such as rubber, silica gel and so on. The outer layer is a high strength protective layer.

3 The fluid-structure interaction dynamic model

Fluid-structure interaction (FSI) is characterized by friction coupling, Poisson coupling, junction coupling and Bourdon coupling[11], in which Poisson coupling and junction coupling have greater influence[12]. According to the solution of the control equation, it can be divided into the strong coupling of the direct solution and the weak coupling of the partitioned iterative solution[13]. A single straight pipeline is studied as the research object in this paper, so the friction coupling, junction coupling and Bourdon coupling can be neglected, and the Poisson coupling problem is mainly discussed. The strong coupling of direct solution is used during research.

The inner layer of bionic hydraulic pipeline is smooth. If the inner surface of the rubber material is set as smooth, the inner layer cannot be added to the model. The outer layer is a high strength protective layer of stainless steel. Therefore, the bionic hydraulic pipeline model is divided into two layers, as shown in figure 3. As a comparison, the ordinary stainless steel pipeline has only one layer, and the pipeline model is shown in figure 4.

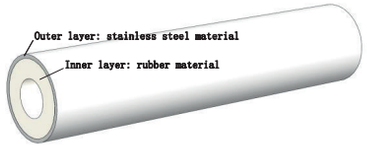


Figure 3 The model diagram of bionic hydraulic pipeline



Figure 4 The model diagram of ordinary stainless steel pipeline

The coordinate system of the straight pipeline with a silica gel layer in figure 3 is established according to the right-hand rule. The force schematic diagram of bionic hydraulic pipeline is shown in figure 5.

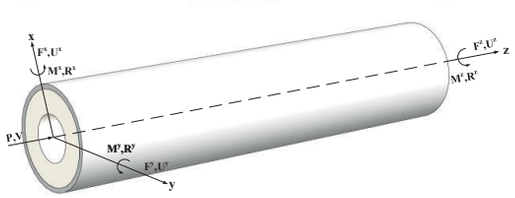


Figure 5 Force schematic diagram of bionic hydraulic pipeline

In order to establish the dynamic model, we assume that the pipeline is installed parallel to the horizontal plane and consider the influence of the gravity inertia and the fluid viscous friction. Referring to the 14 - equation model of fluid-structure interaction[14], the dynamic model of bionic hydraulic pipeline is as follows:

3.1 The motion of the axial pipeline and the fluid

3.1.1 The fluid motion differential equation

A motion element of fluid dz is shown in Fig. 6 and its fluid motion differential equation is expressed as

$$\left(P+\frac{\partial P}{\partial z}dz-P\right)A_f+f=-\rho_f A_f dz\frac{\partial V}{\partial t}, \tag{1}$$

in which $f=2\pi r_r \tau \mathrm{d}z$.

After simplification, the fluid motion equilibrium equations along the axial direction are as follows.

$$\frac{\partial V}{\partial t}+\frac{1}{\rho_f}\frac{\partial P}{\partial z}=-\frac{2\pi r_r \tau}{\rho_f A_f}. \tag{2}$$

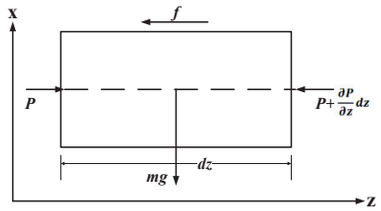


Figure 6 A motion element of fluid

3.1.2 The relationship between pipeline deformation and fluid pressure

If the fluid pressure is P, the pressure on the inner wall of the rubber layer is also P. Supposed that the pressure on the stainless steel layer is P_P. The relationship between P_P and P is

$$2\pi r_r P-k_r\frac{\partial \lambda}{\partial t}-\zeta_r\frac{\partial^2 \lambda}{\partial t^2}-2\pi r_P P_P=0. \tag{3}$$

So,

$$P_P=\frac{r_r}{r_P}P-\frac{k_r}{2\pi r_P}\frac{\partial \lambda}{\partial t}-\frac{\zeta_r}{2\pi r_P}\frac{\partial^2 \lambda}{\partial t^2}. \tag{4}$$

The equation (4) shows that the pressure on the outer wall of the bionic hydraulic pipeline is less than the fluid pressure, while the pressure on the outer wall of the stainless steel pipeline is equal to the fluid pressure. So, compared with the ordinary stainless steel pipeline, the Poisson coupling effect of bionic hydraulic pipeline is smaller.

The stainless steel layer is considered as thin shell. For the thin-walled pipeline, the stress state of pipeline wall is two directional. On the one hand, the pressure can cause circumferential normal stress σ_θ; on the other hand, it can also cause the axial normal stress σ_z. The σ_θ and σ_z can be described as

$$\sigma_\theta=\frac{P_P r_P}{e}, \tag{5}$$

$$\sigma_z=\frac{F^z}{A_P}. \tag{6}$$

And

$$\frac{\partial \sigma_z}{\partial t}=\frac{E}{1-\mu^2}\left(\frac{\partial \varepsilon_z}{\partial t}+\mu\frac{\partial \varepsilon_\theta}{\partial t}\right), \tag{7}$$

$$\frac{\partial \sigma_\theta}{\partial t}=\frac{E}{1-\mu^2}\left(\frac{\partial \varepsilon_\theta}{\partial t}+\mu\frac{\partial \varepsilon_z}{\partial t}\right). \tag{8}$$

In the formula (8),

$$\frac{\partial \varepsilon_z}{\partial t}=\frac{\partial U^z}{\partial z}, \tag{9}$$

$$\frac{\partial \varepsilon_\theta}{\partial t}=\frac{1}{r_P}\frac{\partial H}{\partial t}. \tag{10}$$

Assuming $k_r=0$ and $\zeta_r=0$, by analysing equations (5) - (8), the relationship can be expressed as

$$\frac{\partial U^z}{\partial z}-\frac{1}{EA_P}\frac{\partial F^z}{\partial t}+\frac{\mu r_r}{Ee}\frac{\partial P}{\partial t}=0. \tag{11}$$

3.1.3 The axial motion equation of pipeline

A motion element of fluid dz is shown in figure 7, and the axial motion equation of pipeline is

$$\left(F^z+\frac{\partial F^z}{\partial z}dz-F^z\right)+f=\frac{\partial U^z}{\partial t}(\rho_P A_P+\rho_r A_r)dz, \tag{12}$$

in which $f=2\pi r_r \tau \mathrm{d}z$.

The axial motion equation of the pipeline is simplified as follows.

$$\frac{\partial U^z}{\partial t}-\frac{1}{\rho_P A_P+\rho_r A_r}\frac{\partial F^z}{\partial z}=\frac{2\pi r_r \tau}{\rho_P A_P+\rho_r A_r} \tag{13}$$

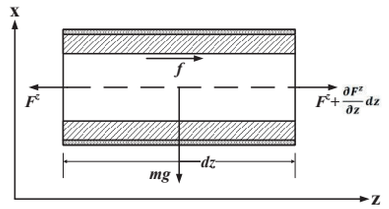


Figure 7 A motion element of pipeline

3.1.4 The continuity equation of fluid

The fluid volume in the pipeline element increases ΔV per unit time, and the ΔV is

$$\Delta V = -A_f \frac{\partial V}{\partial z} dz. \tag{14}$$

The increased fluid is filled into the three parts of the space.

ΔV_1 means the change of volume due to fluid compressibility, which is expressed as

$$\Delta V_1 = \frac{1}{K_f} A_f dz \frac{\partial P}{\partial t}. \tag{15}$$

ΔV_2 is the change of volume caused by compression of rubber layer, which is

$$\Delta V_2 = 2\pi r_r^2 \frac{\partial \lambda}{\partial t} dz. \tag{16}$$

ΔV_3 is the change of volume caused by deformation of stainless steel layer, which is described as

$$\Delta V_3 = 2\pi r_P \frac{\partial Y}{\partial t} dz. \tag{17}$$

The volume change can be expressed as $\Delta V = \Delta V_1 + \Delta V_2 + \Delta V_3$, so the equation is

$$\frac{\partial V}{\partial z} + \left(\frac{1}{K_f} + \frac{2R(1-\mu^2)}{eE}\right)\frac{\partial P}{\partial t} - \frac{2\mu}{EA_P}\frac{\partial F^z}{\partial t} + 2\frac{\partial \lambda}{\partial t} = 0. \tag{18}$$

3.2 Shear and bending in the y-z plane:

The rotation angle of pipeline is caused by two aspects: one is the bend R^z of the pipeline itself; the other is pipeline deformation β^z due to shearing force.

The rotation angle of pipeline caused by shearing force is:

$$\beta^z = \frac{F^y}{A_P G_P + A_r G_r}. \tag{19}$$

So,

$$\frac{dy}{dz} = -R^z - \beta^z. \tag{20}$$

The next equation can be obtained by differentiating the two sides of formula (20) with respect to time.

$$\frac{\partial F^y}{\partial t} - (A_P G_P + A_r G_r)\left(\frac{\partial U^y}{\partial z} + R^x\right) = 0 \tag{21}$$

The relationship between the rotation angle and the bending moment of the pipeline around the X-axis is as follows:

$$\frac{M^x}{E_P I_P + E_r I_r} = \frac{\partial R^x}{\partial z} \tag{22}$$

The two sides of formula (22) is differentiated with respect to time, obtaining the result

$$\frac{\partial M^x}{\partial t} - (E_P I_P + E_r I_r)\frac{\partial R^x}{\partial z} = 0 \tag{23}$$

According to the Newton's second law, the force balance in the Y direction is deduced.

$$\frac{\partial F^y}{\partial z} - \left(\rho_P A_P + \rho_f A_f + \rho_r A_r\right)\frac{\partial U^y}{\partial t} = 0 \tag{24}$$

The moment balance equations of pipeline in the X direction can be expressed as

$$\frac{\partial M^x}{\partial z} - F^y - (\rho_P I_P + \rho_f I_f + \rho_r I_r)\frac{\partial R^x}{\partial t} = 0. \tag{25}$$

When deducing the relationship between shearing force and bending moment in the y-z plane, some parameters of rubber, such as shear modulus and inertia moment, are included in the formula because there is a rubber layer in the bionic pipeline.

3.3 Shear and bending in the x-z plane

The derivation process of formula is the same as 3.2 and the results are shown as

$$\frac{\partial M^y}{\partial z} + F^x - (\rho_P I_P + \rho_f I_f + \rho_r I_r)\frac{\partial R^y}{\partial t} = 0 \tag{26}$$

$$\frac{\partial M^y}{\partial t} - (E_P I_P + E_r I_r)\frac{\partial R^y}{\partial z} = 0 \tag{27}$$

$$\frac{\partial F^x}{\partial z} - \left(\rho_P A_P + \rho_f A_f + \rho_r A_r\right)\frac{\partial U^x}{\partial t} = 0 \tag{28}$$

$$\frac{\partial F^x}{\partial t} - (A_P G_P + A_r G_r)\left(\frac{\partial U^x}{\partial z} - R^y\right) = 0 \tag{29}$$

3.4 The torque at the pipeline wall

The constitutive relationship between the rotation angle and torque can be obtained.

$$\frac{\partial R^z}{\partial z} - \frac{1}{G_P J_P + G_r J_r}\frac{\partial M^z}{\partial t} = 0 \tag{30}$$

According to the axial torque balance equation, there is

$$\frac{\partial M^z}{\partial z} - (\rho_P J_P + \rho_r J_r)\frac{\partial R^z}{\partial t} = 0. \tag{31}$$

Similarly, the shear modulus and polar inertia moment of the rubber are included in the formula because of the rubber layer in the pipeline.

3.5 The compression of the rubber layer

The rubber layer of the bionic hydraulic pipeline is hollow cylinder[10]. The relationship between the cross sectional compression λ and the fluid pressure P under pressure is

$$\lambda = \frac{P(r_P^2 - r_r^2)}{K_r r_r}. \tag{32}$$

The Mooney-Rivlin model with two parameters is used as the constitutive model of the rubber layer in the bionic pipeline. If $C_{10} = 0.2\text{MPa}$ and $C_{01} = 1.4\text{MPa}$, the bulk modulus of rubber material is approximately

$$K_r = 5.487 \times 10^6 \lambda + 1.334 \times 10^8. \tag{33}$$

The bulk modulus of rubber is much smaller than that of stainless steel, so it is easier to deform under compression. The outlet pressure curve of axial piston pump is approximately a sine curve. When the pressure of the fluid increases, the compression of the rubber layer in the bionic hydraulic pipeline becomes larger; the fluid region in the pipeline becomes larger and the velocity of the fluid becomes smaller relatively. When the pressure decreases, the rubber expands; the fluid region in the pipeline becomes smaller and the velocity of the fluid becomes larger than before. If the fluid flows through the bionic hydraulic pipeline, its flow fluctuation will be smaller. In addition, the Poisson coupling effect of the outer layer in the bionic hydraulic pipeline is weakened. Therefore, the bionic hydraulic pipeline can achieve the purpose of absorbing the flow pulsation and suppressing the system vibration.

4 The frequency domain characteristics solution for fluid-structure interaction dynamic model of bionic hydraulic pipeline

The frequency components of the pipeline can be found out by solving the frequency domain characteristics of the hydraulic pipeline so as to provide reference for avoiding the resonance failure of the pipeline. The frequency domain solution of Laplace transform proposed by Zhang Lixiang has good generality. So the Laplace transform will be used in this paper to convert the partial differential equation of the fluid-structure interaction dynamic model into the frequency domain equation that can be solved further.

If $\Phi(z,t)$ means a vector composed of kinetic parameters of medium and pipeline along the axis, it can be expressed as

$$\Phi(z,t) = (V, P, U^z, F^z, U^y, F^y, R^x, M^x, U^x, F^x, R^y, M^y, R^z, M^z, \lambda)^T \tag{34}$$

The relationship of state variables between the pipeline at any position z and at the position 0 can be represented by the domain transfer matrix $\boldsymbol{M}(z,s)$.

$$\bar{\boldsymbol{\Phi}}(z,s) = \boldsymbol{M}(z,s)\bar{\boldsymbol{\Phi}}(0,s) \tag{35}$$

For the pipeline with length L, its state variables at any position can be solved by using the domain transfer matrix and boundary conditions. There are seven boundary conditions respectively for the two ends of a single pipeline (z=0 and z=L), and the general expressions are as follows.

$$[\boldsymbol{D}_0(s)]_{7\times14}[\bar{\boldsymbol{\Phi}}(0,s)]_{14\times1} = [\boldsymbol{Q}_0(s)]_{7\times1} \tag{36}$$

$$[\boldsymbol{D}_L(s)]_{7\times14}[\bar{\boldsymbol{\Phi}}(L,s)]_{14\times1} = [\boldsymbol{Q}_L(s)]_{7\times1} \tag{37}$$

Among them, $D_0(s)$ and $D_L(s)$ are the boundary matrix at both ends of the pipeline; $Q_0(s)$ and $Q_L(s)$ are the excitation matrix at both ends of the pipeline; the subscripts outside square brackets are for rows and columns of matrix respectively.

According to the formula (35) - (37), the state variable of the pipeline at the end of z=0 is

$$\bar{\boldsymbol{\Phi}}(0,s) = \begin{bmatrix} \boldsymbol{D}_0(s) \\ \boldsymbol{D}_L(s)\boldsymbol{M}(L,s) \end{bmatrix}^{-1} \begin{bmatrix} \boldsymbol{Q}_0(s) \\ \boldsymbol{Q}_L(s) \end{bmatrix} \tag{38}$$

5 Solution of dynamic model

If the ends of pipeline are free and full of oil; both ends are blocked; the friction between the inner wall of silica gel layer and the fluid is ignored, the physical parameters of pipeline and fluid are shown in table 1.

	Stainless steel	Silica gel	Fluid	Plug
length (m)	0.5	0.5		
inner radius (m)	0.02	0.005		
wall thickness (m)	0.002	0.015		
Poisson ratio	0.3	0.49		
density (kg/m^3)	7930	1100	872	
Young modulus (Pa)	1.94×10^{11}			
C_{10} (MPa)		0.2		
C_{01} (MPa)		1.4		
quality (kg)				0.25

Table 1 Structural and material parameters of pipeline model

A mechanical shock excitation is applied to the initial end of the pipeline. The average size is F=15000N; the time is T=0.002s, and the expression is

$$F = [1(t) - 1(t-T)] \tag{39}$$

The corresponding excitation vector is:

$$\begin{cases} \boldsymbol{Q}_0(s) = \left[0 \quad -\left(\frac{F}{s}\right)(1-\mathrm{e}^{-s\mathrm{T}}) \quad 0 \quad 0 \quad 0 \quad 0 \quad 0\right]^{\mathrm{T}} \\ \boldsymbol{Q}_L(s) = [0 \quad 0 \quad 0 \quad 0 \quad 0 \quad 0 \quad 0]^{\mathrm{T}} \end{cases} \tag{40}$$

The fluid-structure interaction dynamic model of bionic hydraulic pipeline is programmed and solved in MATLAB. The radial pressure frequency characteristic curve and the axial velocity frequency characteristic curve at the initial end of pipeline are shown in figure 8 and figure 9.

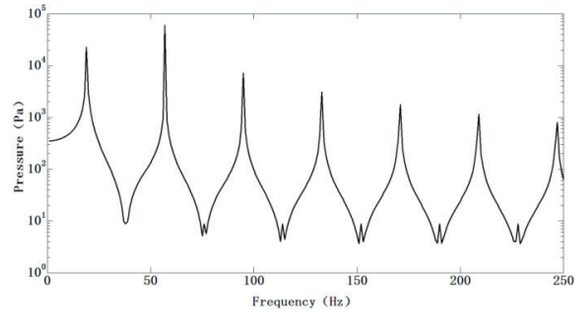


Figure 8 The radial pressure frequency characteristic curve

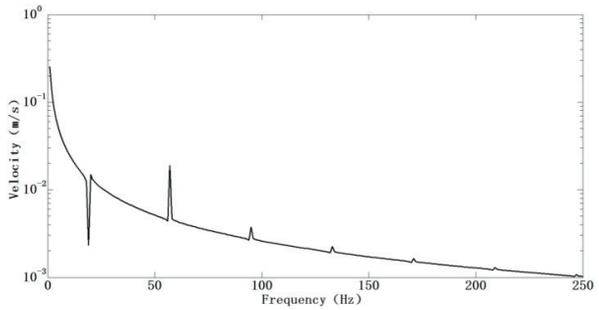


Figure 9 The axial velocity frequency characteristic curve

6 Simulation analysis

The pipeline models of figure 3 and figure 4 are imported into the ANSYS WORKBENCH software respectively to analyse the two-way fluid-structure interaction. The parameters of pipeline model are shown in table 1. The two ends of the pipeline are clamped and the friction between wall and fluid is neglected. The fluid is 10# aviation hydraulic oil; the density is 870 kg/m^3; the kinetic viscosity is 0.0087 kg/ (m·s). The fluid is modelled by a standard k-ε turbulence model

When the outlet pressure of axial piston pump is 9MPa, the flow pulsation curve is shown in figure 10.

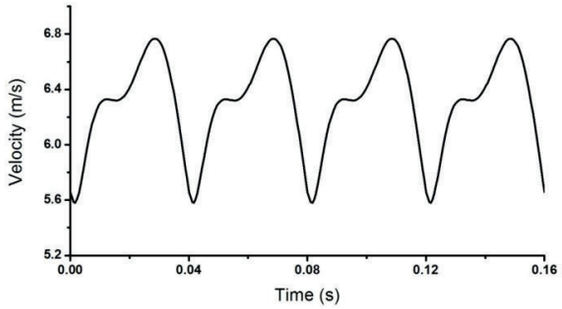


Figure 10 The flow pulsation curve of axial piston pump outlet

The flow pulsation shown in figure 10 is used as the inlet flow condition of the pipeline, and the outlet pressure of the pipeline is set to 9MPa.

The fluid-structure interaction vibration characteristics of the above model are analyzed. The flow pulsation curve at the outlet of bionic hydraulic pipeline and common stainless steel pipeline is shown in figure 11. The vibration amplitude curves of the wall middle joint of the bionic hydraulic pipeline and common stainless steel pipeline are shown in figure 12.

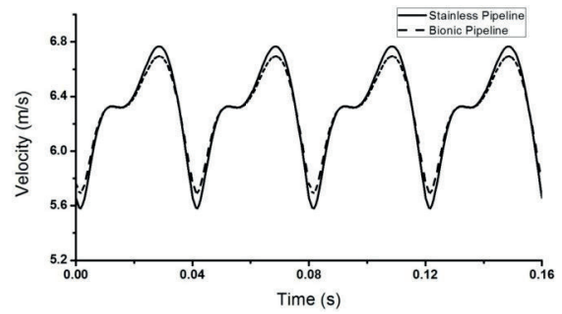


Figure 11 The velocity pulsation curve of different pipelines outlet

It can be seen from figure 11 that the outlet flow of the two pipelines is still periodic pulsation. The flow pulsation amplitude of bionic hydraulic pipeline outlet decreases after absorbed by pipeline, while the flow pulsation amplitude of stainless steel hydraulic pipeline outlet is basically the same as the inlet flow amplitude. It is shown that the pulsating amplitude will decrease when the pulsating fluid flows through the bionic hydraulic pipeline. The bionic hydraulic pipeline has good effect on the absorption of flow pulsation.

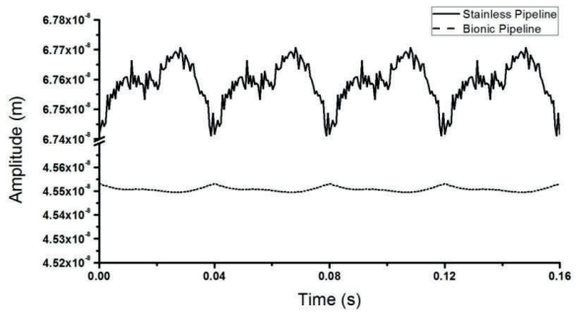


Figure 12 The vibration amplitude curves of the wall middle joint of different hydraulic pipelines

It can be seen from figure 12 that the vibration amplitude of the wall middle joint of the bionic hydraulic pipeline is smaller than that of the stainless steel hydraulic pipeline. It shows that the bionic hydraulic pipeline can suppress the pipeline vibration while absorbing the flow pulsation.

7 Summary and Conclusion

Based on the mechanism of animal biology, a bionic hydraulic pipeline with three layers is created. It is directly connected with the hydraulic pump, so it will not excite the secondary high frequency pulsation, which makes up for the shortcomings of the traditional vibration control means. The research results provide a new technical way to break through the mechanism that absorption pulsation to suppress vibration and to obtain better vibration control effect.

On the basis of the original 14 - equation, the 14 - equation suitable for the bionic hydraulic pipeline is derived in this paper. The equation is successfully solved and the correctness of the new equation is verified. In addition, the simulation analysis shows that the bionic hydraulic pipeline has better capacity of absorbing flow pulsating and suppressing pipeline vibration than the ordinary stainless steel pipeline.

Nomenclature

Variable	*Description*	*Unit*
A	Cross-sectional area	[m^2]
E	Modulus of elasticity	[Pa]
e	Thickness of outer layer	[m]
F	Force	[N]
G	Shear modulus of rigidity	[Pa]
I	Moment of inertia	[m^4]
J	Polar moment of inertia	[m^4]
K	Bulk modulus of elasticity	[Pa]
M	Moment	[N·m]
P	Pressure	[Pa]
R	Rotational velocity	[rad/s]
r	Radius of cross-section	[m]
U	Velocity of pipeline	[m/s]
V	Velocity of liquid	[m/s]
ρ	Mass density	[kg/m^3]
μ	Poisson ratio	[-]
z	Principal directions	[-]
t	Time	[s]
τ	Friction between fluid and inner layer	[-]
Y	Radial variable of outer layer	[m]

λ	Deformation of inner layer	[m]
k	Linear stiffness	[N/m]
ζ	Linear damping	[N·s/m]
C_{10}, C_{01}	Material constant	[MPa]

Superscripts

x, y, z	Principal directions	[-]

Subscripts

f	Fluid	[-]
P	Outer layer	[-]
r	Inner layer	[-]

References

/1/ China Hydraulics Pneumatics & Seals Association, 流体动力传动与控制技术路线图, Science and Technology of China Press, Beijing, China, 2012.

/2/ Lingxiao Quan, Hongliang Luo, Jin Zhang, 斜轴式轴向柱塞泵壳体结构振动谐响应分析, In: Chinese Hydraulics & Pneumatics, pp. 33-39, 2014.

/3/ Zhanlin Wang,飞机高压液压能源系统, Beijing University of Aeronautics and Astronautics Press, Beijing, China, 2004.

/4/ Lingxiao Quan, Xiangdong Kong, Yingjie Gao, 不考虑进口特性的蓄能器吸收冲击理论及试验, In: Journal of Mechanical Engineering, Vol. 43, No. 7, pp. 28-32, 2007.

/5/ George Zorbas, Theodoros Samaras, *A study of the sink effect by blood vessels in radiofrequency ablation*, In: Computers in Biology and Medicine, pp. 182-186, 2015.

/6/ Venkatraman S, Boey F, Lao LL, *Implanted cardiovascular polymers: Natural, synthetic and bio-inspired*, In: Progress in Polymer Science, Vol. 33, No. 9, pp. 853-874, 2008.

/7/ Yu Y, Perdikaris P, Karniadakis G E, *Fractional modeling of viscoelasticity in 3D cerebral arteries and aneurysms*, In: Journal of Computational Physics, pp. 219-242, 2016.

/8/ Lukáčová-Medvid'Ová M, Rusnáková G, Hundertmark-Zaušková A, *Kinematic splitting algorithm for fluid–structure interaction in hemodynamics*, In: Computer Methods in Applied Mechanics & Engineering, Vol. 265, No. 3, pp. 83-106, 2013.

/9/ Liao K, Hu C, Sueyoshi M., *Free surface flow impacting on an elastic structure: Experiment versus numerical simulation*, In: Applied Ocean Research, pp. 192-208, 2015.

/10/ Sahu R K, Patra K, *Estimation of Elastic Modulus of Dielectric Elastomer Materials Using Mooney-Rivlin and Ogden Models*, In: Advanced Materials Research, Vol. 685, No. 1, pp. 331-335, 2013.

/11/ Richter T., Wick T., *Finite elements for fluid-structure interaction in ALE and fully Eulerian coordinates*, In: Computer Methods in Applied Mechanics and Engineering, Vol. 199, No. 41, pp. 2633-2642, 2010.

/12/ Li S, Karney B W, Liu G, *FSI research in pipeline systems – A review of the literature*, In: Journal of Fluids & Structures, pp. 277-279, 2015.

/13/ Ruojun Qian, Shilin Dong, Xingfei Yuan, 流固耦合理论研究进展, In: Spatial Structures, Vol. 14, No. 1, pp. 6-18, 2008.

/14/ Wiggert D C, Hatfield F J, Stuckenbruck S, *Analysis of Liquid and Structural Transients in Piping by the Method of Characteristics*, In: Journal of Fluids Engineering, Vol. 109, No. 2, pp. 161-165, 1987.

/15/ Lixiang Zhang, Ke Yang, 流体结构互动理论及其应用, Science Press, Beijing, China, 2004.

Experimental Researches to Measure the Total Resistance Forces that Appear at the Switching Process of Directional Control Valves

Corneliu Cristescu*, Catalin Dumitrescu*, Radu Radoi* and Petrin Drumea*

Hydraulics and Pneumatics Research Institute INOE 2000-IHP, 14 Cutitul de Argint Street, district 4, 040558, Bucharest, Romania*
E-Mail: cristescu.ihp@fluidas.ro

The paper presents some results obtained in an experimental research, in order to measure the total resistant forces which appear during the switching process of directional control valves. After some theoretical considerations regarding the possibility to calculate the resistant forces, in the second part of the paper there are presented the research infrastructure, the way in which the experimental research was conducted, and also the main results obtained, as well as some conclusions drawn after analyzing the graphical evolution of the total resistant forces, results which have allowed to determine the total resistant forces, needed for dimensioning of the electric coils or the switching mechanism.

Keywords: Tribology, directional control valve, dynamic seals, frictional forces, test bench
Target audience: Tribology & Fluid, Mobile Hydraulics, Industrial Applications

1 Introduction

Increasing energy efficiency of hydrostatic drive systems involves activities of redesign and experimental testing of each core component of the power transmission flow.

While hydrostatic pumps and motors within classic hydrostatic drive systems are the first target in this respect, there are other components, too, that influence energy losses in the system, among which hydraulic directional control valves play an important role. By their functioning mode / scheme that implies sudden changes in the direction of flow and large variations of the flow sections, there results a turbulent flow, with significant energy losses, which requires optimizing the size of the flow paths of the pressurized working fluid.

Changes in the direction of flow at the input of hydraulic directional control valves and sudden variations of section when switching from a working position to another, in addition to classical mechanical forces, give rise to fluidic forces that need to be measured / assessed as accurately as possible, both by theoretical means through classical calculations or hydrodynamic modelling and computer simulations, and especially by experimental means, which allow accurate determination of their value, and the results thus obtained can be used to validate the mathematical models developed.

Assessing as accurately as possible the total resistance forces which occur when switching the hydraulic spool valves from a working position to another is of a great importance to the design activity, when one determines the force required for switching, especially when this force is generated by an electric coil, and it is even more important for large flow dimensions (rated diameters) directional valves, which by design are to be crossed by higher flow rates.

Directional control valves are some of the most important parts in a hydraulic transmission, Figure 1. It is known that in order to carry out the process of directing pressurized fluid or to stop it, there is required a certain method to generate the switching force of the directional spool valve, and this force can be generated in various ways: in a manual, hydraulic, pneumatic, electric etc. way.

Generally speaking, a directional valve, Figure 2, comprises the following main components: body of the directional valve (1), spool (2), compression springs (3) and, depending on the drive type, various subparts are attached, for example two electromagnets (4) or a drive mechanism (5) /1/.

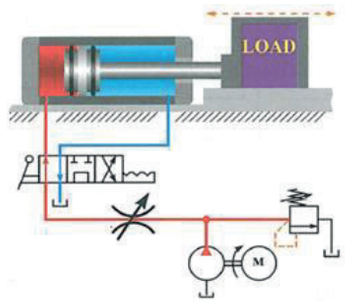


Figure 1: Hydrostatic driving system.

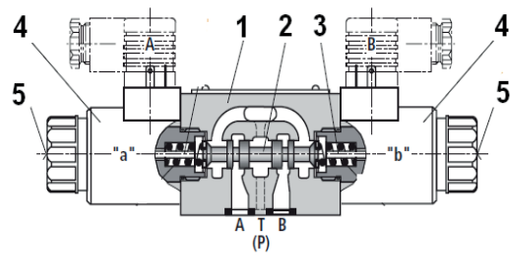


Figure 2: Schematic diagram of a directional control valve /1/.

The spool (or distributor) is the mobile part that connects the inlet port (P) to the outlet ports (A, B); the outlets, and in some versions also the port *P*, are connected to the tank (outlet port T) as well.

There are directional valves with 2, 3 or 4 ports or ways, and 2 or 3 working positions (e.g. 4/2, 4/3).

Figure 3 and Figure 4 below present two flow schemes / sections for the fluid across the body of the hydraulic spool valve, when switching the pressurized fluid flow towards the consumer connected to the port *A*, Figure 3, and Figure 4, when switching the fluid flow towards the port *B*. When performing the switching stroke (-x or +x), the fluid enters the body of the directional valve at an angle of about 69^0, and it develops an **impulse force** upon the spool, and then it goes out through the port *A* or *B*, as appropriate. The initial flow of pressurized oil *Q* reaches the controlled port, *A* or *B*, with a value of Q_l, decreased slightly because of volume losses q_1 and q_2 occurred through the *metal-to-metal* sealing between the spool valve and the body of the directional valve, and a drive flow Q_{mi}, different from the input one, reaches the input of the hydraulic motor; the difference in flow can be found in the flow leakage at the tank q_{sd}, and partly in the flow Q_{me} discharged by the motor to the tank, which is also decreased because of internal flow losses q_{sm} of the hydraulic motor.

From the above one can note that when the fluid crosses the hydraulic directional valve there occurs a series of oil volume losses, and also pressure losses, and energy efficiency is thus diminished; that is why this aspect requires special attention with the purpose of constructive and energy optimization.

At most hydraulic equipment, **flow forces** occur as a **consequence of the local change of the flow sections**, and thus a consequence of acceleration or deceleration of fluid masses, or a consequence of **changing direction** of flow. The variable flow sections are generated between a cylindrical spool with radial channels and a bush / body of directional control valve with radial channels or slots, most often of circular section /2/. The spool of the directional control valve, by its axial position, controls the flow of fluid *Q* which enters the directional control valve, and respectively the flow of fluid Q_{mi}, which leaves the directional control valve and goes to the consumer.

The research conducted highlights the fact that **the flow force** actually has two components: a **stationary** component and a **dynamic** one. The **dynamic** component**,** which occurs as a **consequence of the change in flow over time**, acts upon the spool valve in the direction of opening the flow section, in the first case, and in the direction of closing it, in the second case (in the same sense of direction as the stationary flow force), according to equation (2).

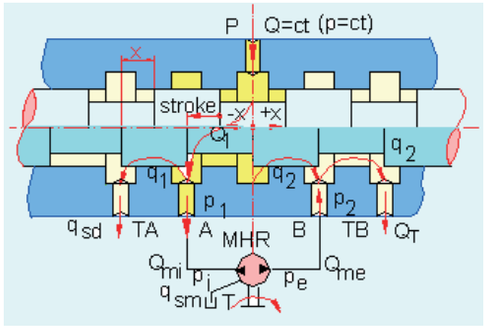


Figure 3: Fluid flow when switching the pressurized flow to the port A.

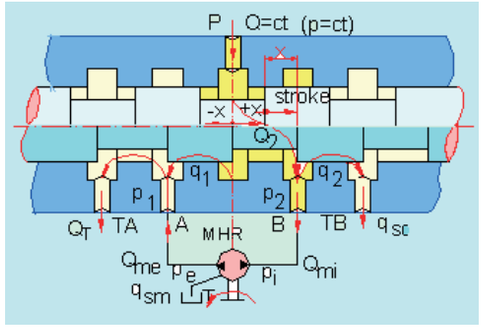


Figure 4: Fluid flow when switching the pressurized flow to the port B.

In paper /3/, the authors aim to analyse the behaviour of the flow force peak values in the initial spool opening of an open center directional control valve and to establish a connection to the behavior of a closed center valve. Finally, a numerical analysis of the flow is performed to confirm and theoretically explain the experimental results. In paper /4/ the authors provided a procedure to analytically estimate the flow force peak value at different pressure drops and flow rates.

The paper /5/ presents an experimental investigation on the significance of the pressure transient flow force acting on hydraulic spool valves. Long time, this flow force effect has been routinely neglected due to its assumed small size. Through analytical and experimental methods, this research shows that flow forces due to pressure transient effects can be comparable in magnitude to the steady flow forces acting on the valve and that the past tradition of neglecting this effect may not always be justified. The paper also shows that the traditional steady flow force model does a fairly good job predicting the steady flow forces on the valve, but more research must be done to develop a good model for pressure transient flow forces.

During the switching operation, which is performed by the movement of spool, the drive mechanism (actuating mechanism) must develop the force required to overcome the **total resistance forces**.

It is known that single stage directional valves are preferred because they are cheaper and most reliable, but increasing the rated size of coils / solenoids, electric actuators, they no longer cope, no longer develop the force required to switch the spool, so for large sizes, i.e. high flow rates, there are preferred multistage directional valves /6/.

That is why, it is very important to determine the resistance forces in both theoretical and the experimental way, especially when a drive electromagnet must be designed.

2 Some theoretical considerations regarding the switching processes

In switching processes of the hydraulic directional control valve from one position to another, Figure 5, for example to achieve the flowing of the fluid Q under the pressure p transmitted by the pump through the port P to the hydraulic consumer connected to the port A of the directional valve where the flow rate Q_1 reaches, as a low flow rate q_a drains through the metal-to-metal sealing of the spool, as shown in Figure 6, the actuator must develop an axial force F_{ax} at least equal to or greater than the sum of forces opposing the movement of the spool /7/.

There are some theoretical considerations regarding the calculation of forces which are acting on the spool when the fluid flow goes through the directional spool valves, Figure 6.



Figure 5: Hydraulic directional control valve [1].

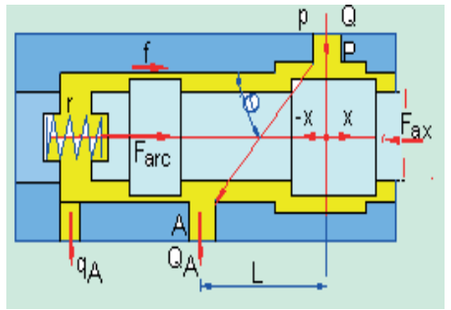


Figure 6: The fluid flow when switching the spool [8].

From Figure 6 one can note that in addition to the **mechanical** forces related to the movement of the spool valve of mass m, there is actuated a quantity of fluid existing along the length L between the ports P and A, which varies over time, and also a **frictional viscous force** that depends on the speed of movement v and the viscous friction coefficient f. In addition to these **dynamic forces** that vary over time, there also occur **static forces** represented by the force in the spring which **varies with spool stroke *x***, a spring constant r, and also the **hydrodynamic force** of the **flow of fluid stream** through the hydraulic spool valve, which is calculated on the basis of theorems of impulse and kinetic momentum (Euler's theorems), finally leading us to the equation:

$$F = pvQ = \rho v^2 S \tag{1}$$

where: ρ is the fluid density, v is the velocity of flow through the directional valve, S is the section through which flow rate Q of the fluid is flowing. As shown in Figure 2, the flow takes place at an angle θ of about 69° (established by **Von Mises)**, so that the projection of the axis of directional valve is given by the following equation, according to /2/:

$$F = \rho vQ \cdot \cos\theta \pm \rho L . \frac{dQ}{dt} \tag{2}$$

By writing the balance equation through projection of the direction of travel, on the X axis, of **all static and dynamic** forces mentioned above, there is obtained the required axial force to be developed by the actuator of the directional valve (solenoid, etc.) according to the equation below:

$$F_{ax} = F_{din} + F_{st} = \left(m\frac{d^2x}{dt^2} + f\,\frac{dx}{dt} + pL\,\frac{dQ}{dt}\right) + \left(p\,\cdot v \cdot Q \cdot cos\theta\, \pm \rho L . \frac{dQ}{dt}\right) + rx\, + \mu\,(mg) \tag{3}$$

In addition to the forces considered, in spool switching there also occur other forces, of which the bonding force, commonly called stick-slip, is of greater relevance and it is important to the long stay of the spool on a certain position /8/.

Generally, these forces are difficult to be theoretically assessed, so it is **necessary to determine experimentally** the total resistance forces that occur when switching the spool of hydraulic directional valve. Such an experimental determination is presented in the following.

3 Presentation of the experimental research infrastructure

In order to determine the total resistance forces occurring during the functioning of directional valves, there has been designed and developed an experimental device able to simulate, in the laboratory, the real operating conditions of a directional valve, and also a testing methodology. To conduct the experimental research, in the Laboratory of Tribology within INOE 2000-IHP, there was arranged a test bench which includes a data acquisition and IT system, meant to register and process the evolution of parameters, thoroughly presented in /8/.

3.1 Presentation of the experimental device

The principle at the basis of developing the experimental device has consisted in using a manual directional control valve, being in the current manufacturing of the company REXROTH BOSCH GROUP, from its market documents /4/, shown in Figure 7. Since the internal structure of an electrical control directional valve, Figure 8, may be similar or even identical to that of a manual control directional valve, the results of experimental research can be used in calculation and design of electric control coils.

The basic idea used is that, in order to measure the resistance forces in switching of hydraulic directional valves, there should be used the original actuating mechanism for switching, and between the actuating mechanism and the spool of the hydraulic valve there should be interposed a force transducer /8/.



Figure 7: Manual directional control valves /9/.

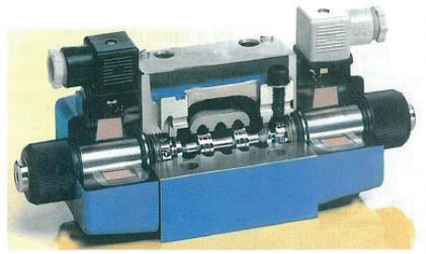


Figure 8: Electric directional control valves.

In order to develop the experimental research aiming at the measurement of total resistance forces that occur in the switching of hydraulic directional control valves, there has been designed a constructive solution shown in Figure 9, based on the use of a manual control hydraulic directional control valve, size 10, /9/, part of the infrastructure of the Laboratory of Tribology within INOE 2000-IHP.

To achieve the experimental device, there has been detached the body of the directional control valve (*1a*) from the mechanism for manual control (*1b*), for placing a force transducer *FT* between the axis of the directional spool valve and the original control mechanism of the directional valve. Physical development of the test device is shown in Figure 10, where one can see the actual technical solutions for developing it.

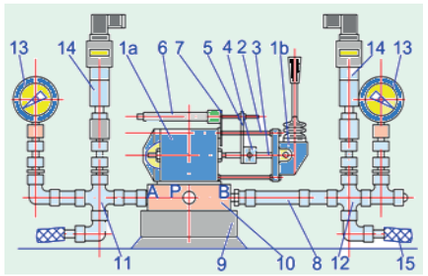


Figure 9: Layout of the experimental device.

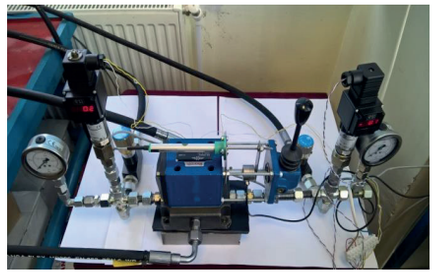


Figure 10: Physical development of the experimental device.

For connecting / coupling the two parts of the main directional control valve, *1a* and *1b*, there were used four threaded rods (2) which have replaced the original screws, thus achieving a space between the two parts of the main directional control valve. In this way, there is created the possibility to insert, by means of threaded sleeves (3), a force transducer (4) between the control rods of the directional spool valve. To measure the stroke achieved by the spool, a rigid blade (5) is attached to the force transducer (4), which drives the rod of a potentiometric stroke transducer (6) that is fixed to the body of the directional valve by a supporting plate (7). The directional control valve is mounted by means of screws on a compatible distribution plate (8) which is placed on another supporting plate (9). From the ports *A* and *B* of the distribution plate (8), pressurized fluid crosses via the two manifolds (11) and (12) to the gauges (13) allowing direct reading of pressure, and also to the pressure transducers (14), by which pressure variations are acquired by the computer system, and through the flexible hoses / piping (15) the fluid reaches the hydraulic motor actuated by the directional control valve /8/.

3.2 Presentation of the experimental test bench

Performing of the experimental research to determine the forces of total hydraulic resistance at switching directional valves has required the design and development of an experimental test bench, inside of the Laboratory of Tribology within INOE 2000-IHP.

The experimental test bench was designed in accordance with the diagram shown in Figure 11 below.

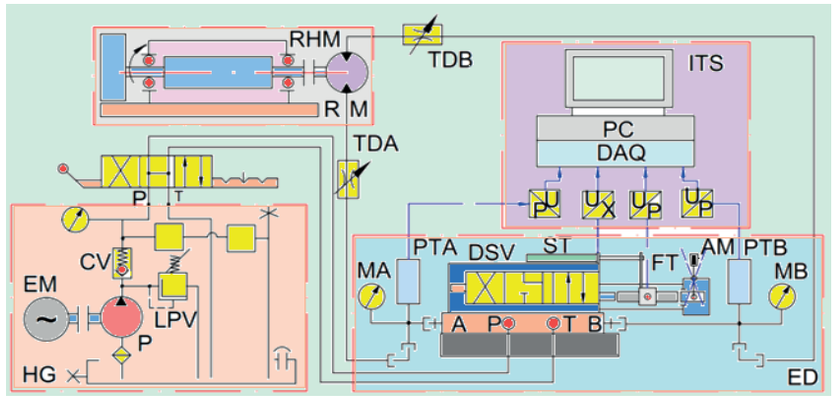


Figure 11: Concept diagram for arranging the experimental test bench.

Besides the experimental device *ED* which contains a force transducer *FT*, a stroke / displacement transducer *ST*, two pressure transducers *PTA* and *PTB*, and two manometers *MA* and *MB*, the test bench also includes a hydraulic mini-station for generating pressurized fluid *HG*, a rotating mechanism *RM* driven by a hydraulic rotary motor *RHM* and a data acquisition and processing system *ITS*, consisting of a data acquisition board *DAQ*, National Instruments type, and a PC type computer. The hydraulic generator *GD* is composed of a gear pump *P* driven by an electric motor *EM*, and assisted by a pressure limiting valve *LPV*, a check valve *CV* and a manual directional valve *MDV* through which pressurized fluid is sent to the ports *A* or *B* of the test device, and from here, through the throttles *TDA* and *TDV*, it reaches the hydraulic rotary motor *RHM*.

Figure 12 presents an overview of the experimental stand, and in Figure 13 one can see in detail the data acquisition and IT system.

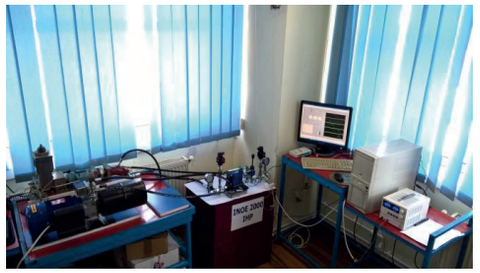


Figure 12: Overview of the experimental test bench.



Figure 13: View of the IT system.

All the signals provided by the transducers reach the data acquisition board *DAQ* installed on the computer, by means of special electric cables, and the *DAQ*, based on specialized software, performs capturing, storage and processing of the measured data.

4 Presentation of some experimental results

The object subjected to this experimental research was a hydraulic directional spool valve, directly operated, with manual actuation, size 10, code 4 WMM 10 J 31/, manufactured by Rexroth Bosch Group, which is a four-way distributor, with three operating positions, the central position providing communication of ports *A* and *B* to the tank *T* and the pump port *P*, closed /10/.

To this end, there has been necessary to set the parameters of interest and define a testing methodology.

With respect to the switching process in hydraulic directional spool valves, the parameters of interest are:

- the spool stroke *x*, measured by the stroke transducer *ST* in Figure 11, item 6 in Figure 9;
- the resistive force *Fax* that opposes the spool movement, which is measured by the force transducer *FT* in Figure 11, item 4 in Figure 9;
- pressure at the port *A*, p_A, which occurs when opening the port *A*, measured by the pressure transducer *PTA* in Figure 11, item 14 in Figure 9;
- pressure at the port *B*, p_B, which occurs when opening the port *B*, measured by the pressure transducer *PTB* in Figure 1, item 14 in Figure 9.

The experimental methodology, thoroughly presented in /8/, consists of performing all the necessary sequences to manually command of the hydraulic directional valve, in order to acquire the signals from all the transducers, and then process them on a computer to obtain variations of interest parameters in numerical and graphical forms.

Following the experimental research, there have been obtained a lot of complete sets of experimental results, for 4 steps of pressure: 25 bar, 50 bar, 75 bar and 100 bar. For each pressure step, each measurement had 3 complete working cycles, for each half of cycle - 3 determinations, which means 6 determinations per cycle, and also for each quarter of cycle - 3 determinations, which means 12 determinations per cycle. In total, there were 21 experimental determinations for each pressure step. For 4 pressure steps there resulted 4x21 = 84 determinations.

After each experimental determination the computer screen displays the complex graphic for all the parameters of interest, as shown in Figure 14. The software especially developed allows one to process and save data in both numerical and graphical forms.

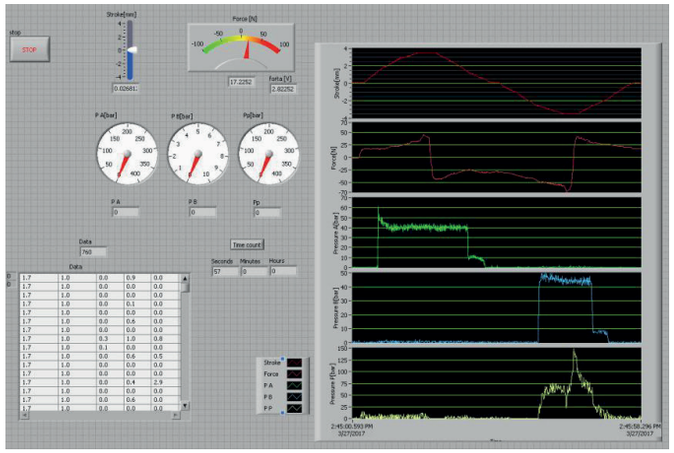


Figure 14: Variation of the interest parameters on the computer screen.

Two examples of complex graphics achieved are presented in Figure 15, for the pressure step of 50 bar, and in Figure 16, for the pressure step of 100 bar.

After analyzing the complex graphs obtained some important conclusions have been drawn, namely:

- the graphs of variation of each parameter of interest have a logical progression, normal and repeatable;
- the pressure values correspond to those directly read on the gauges *MA* and *MB*. They are slightly lower than the pressure values set at the pressure limiting valve (*LPV*) because of pressure losses along the circuits of the hydraulic rotary motor (*RHM*);
- the overall shape of the graph of **spool stroke** corresponds to a full work cycle in the drive / control mechanism with positive or negative values corresponding to the direction of movement of the control handle. Imperfections, small variations on the graph are due solely to the uneven manual drive done by the human operator;

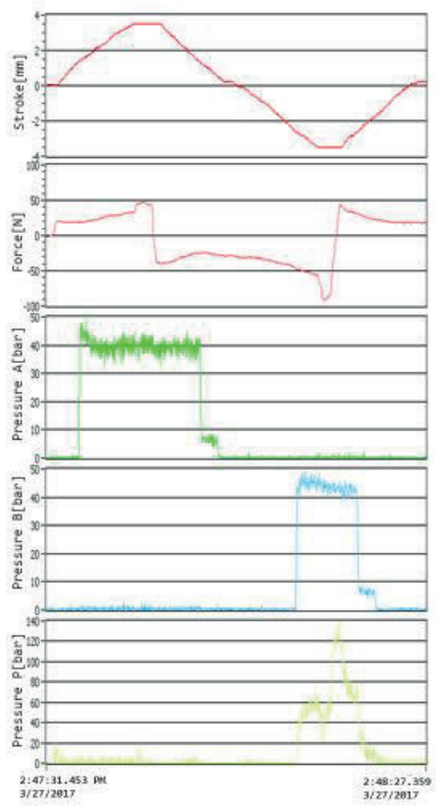


Figure 15: Complex graphs for the pressure step of 50 bar.

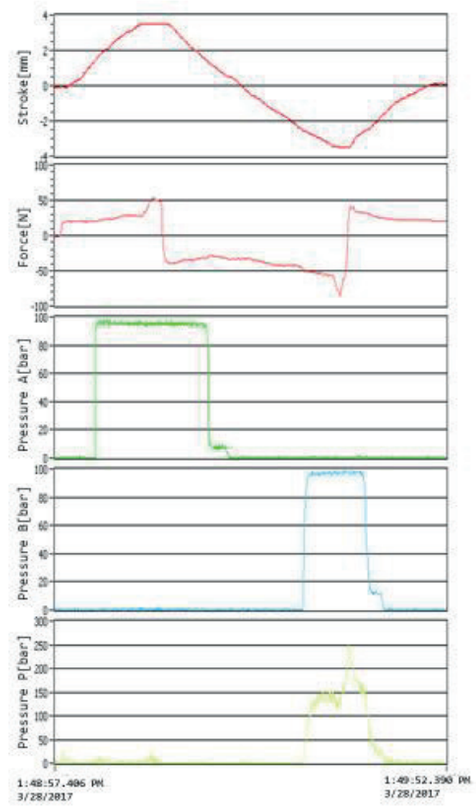


Figure 16: Complex graphs for the pressure step of 100 bar.

- with the exception of the peaks, mean values of the resistance forces over a quarter of a stroke, are within the range (20 - 30) N /10/, when extending the spool, and within the range (30 - 40) N, when retracting the spool, respectively the force transducer, which seems logical and corresponds to the recommendations in the literature /11/;
- comparing the evolution graphs of the resistance forces displayed in Figure 15 and Figure 16, one can notice that, although **the working pressure is doubled**, the resistance forces vary in the same range of minimum and maximum forces (– 50 N, + 50 N), and this is valid for all the pressure steps in the range (25 – 100) bar;

- from a comparative analysis of the graphs of variation of the resistance forces for the **four pressure levels, no significant differences appear** in direct proportion to the increase of pressure value. This may be due to internal pressure balances based on special profiles of surfaces of elements in motion;
- the final conclusion is that the total resistance forces do not depend on the working pressure, and the variation of these forces needs to be investigated in the variation of the fluid flow, research which will further be conducted in the next period.

5 Summary and Conclusion

The paper presents an experimental study developed in INOE 2000-IHP with respect to the assessment of total resistance forces occurring in the switching of a directional control valve, taking into account various pressure levels. There have been presented the research infrastructure and the main results obtained during the progress of this experimental research, and finally some useful and interesting conclusions.

It has been necessary to design and development an experimental device and a test bench, which led to obtaining of several complex variation graphs for the parameters of interest, and this enabled the assessment of resistance forces that occur during the switching process of the directional spool valves.

Following the analysis of the numerical data and complex graphics obtained, it was concluded that the graphs of variation of parameters of interest, especially resistive force, have a normal shape, and their mean values fall in a range of values close to the values mentioned in the technical literature of reference /10/, /11/.

A very important conclusion is that we cannot talk about a significant variation in the resistance forces with increasing pressure, the pressure having a small influence on the switching force of the directional spool valves.

Through the numerical and graphics results, especially through the conclusions reached following the comparative analysis, this paper has special scientific value, and further research on this topic is required.

6 Acknowledgements

This paper has been developed in INOE 2000-IHP, with financial support of the Ministry of Research and innovation (MCI), under the national research *Programme NUCLEU-2016,* project title: *Physics of processes for reducing energy losses and developing renewable energy resources by use of high-performance equipment,* project code PN 16 40.03.01, financial agreement no. 5N/2016.

Nomenclature

Variable	*Description*	*Unit*
x	Spool Stroke	[m]
r	Spring Constant	[N/m]
F	Hydrodynamic Force	[N]
ρ	Fluid Density	[kg/m^3]
v	Velocity of the Flow	[m/s]
Q	Flow Rate	[m^3 /s]
S	Area / Section of Flowing	[m^2]
θ	Flowing Angle	[^{0}]
L	Length of Fluid Volume	[m]
t	Time	[s]
F_{ax}	Axial Force	[N]
F_{dyn}	Dynamic Force	[N]
F_{sta}	Static Force	[N]
m	Spool Masse	[kg]
f	Viscous Friction Coefficient	[Ns/m]
μ	Dry Friction Coefficient	[-]

References

/1/ Rexroth Bosch Group, *Spool hydraulic directional control valve direct-operated / 4/3-way WExx73xxA12*, http://www.directindustry.com/prod/bosch-rexroth-industrial-hydraulics/product-9143-1268489.html, visited on September 29, 2017.

/2/ Ghiță, Al. M., *Forțe hidraulice și pneumatice*, https://prezi.com/xmk0j-zdijwd/forte-hidraulice-si-pneumatice/, visited on October 9, 2017.

/3/ Amirante, R., Del Vescovo, G., Lippolis, A., *Flow forces analysis of an open center hydraulic directional control valve sliding spool*, In: Energy Conversion and Management, Vol. 47, No. 1: pp. 114-131, 2006.

/4/ Borghi, M., Milani, M., Paoluzzi, R., *Stationary axial flow force analysis on compensated spool valves*, In: Int Journal Fluid Power, Vol. 1, No. 1: pp.17–25, 2000.

/5/ Manring, N. D., *Pressure Transient Flow Forces for Hydraulic Spool Valve*, http://dynamicsystems.asmedigitalcollection.asme.org/article.aspx?articleid=1415331, visited on October 12, 2017.

/6/ Qinghui, Y., Perry, Y. L., *Using Steady Flow Force for Unstable Valve Design: Modelling and Experiments*, In: Journal of Dynamic Systems, Measurement, and Control, Vol. 127, No. 3: pp. 451-462, 2004.

/7/ Marin, V., Moscovici, R., Teneslav, D., *Sisteme hidraulice de actionare si reglare automata*, Editura Tehnică, București, pp. 46-61, 1981.

/8/ Cristescu, C., Dumitrescu, C., Radoi, R., Chirita, P., *Determining the resistant friction forces that occur during switching process of directional control valves used in hydrostatic drives*, In: 15th International Conference on Tribology – SERBIATRIB '17, Kragujevac, Serbia, pp. 244 – 250, May 17-19, 2017.

/9/ Rexroth Bosch Group, *Directional spool valves, directly operated, with manual actuation*, https://www.boschrexroth.com/en/us/products/product-groups/goto-products/goto-hydraulics/directional-valves/4wmm-and-4wmr/index, visited on September 22, 2017.

/10/ Rexroth Bosch Group, *Directional spool valves, directly operated, with manual and fluid logics actuation (size 10)*, https://dc-us.resource.bosch.com/media/us/ products_13/product_groups_1/ industrial_hydraulics 5/ pdfs_4/ re22334.pdf, visited on September 27, 2017.

/11/ Rexroth Bosch Group, *Directional spool valves, directly operated, with manual and fluid logics actuation (size 6)*, https://dcus.resource.bosch.com/media/us/products_13/product_groups_1/ industrial_hydraulics_5/pdfs_4/re22280.pdf, visited on September 27, 2017.

REVIEWED

Surface tension of fuels – Analysis of measurement methods and applicability on rail-pressure environments

Marcel Rückert*, Olivier Reinertz* and Katharina Schmitz*

RWTH Aachen University, Institute for Fluid Power Drives and Systems (IFAS), Campus-Boulevard 30,
D-52074 Aachen, Germany*
E-Mail: Marcel.Rueckert@ifas.rwth-aachen.de

Spray characteristics during the injection process of a combustion system, bubble formation in chemical reactors or hydraulic fluids all share surface tension as a key variable regarding aforementioned behaviours. Depending on the system liquid-liquid or liquid-gas interphases play a defining role. In this work, the most relevant measurement methods are discussed. Based on the Du Noüy method, the surface tension of common fuels and mixtures is measured and presented. The measurements do illustrate the influence of mixture components on surface tension as the behaviour can be strongly non-linear. Additionally, the applicability of the aforementioned measurement methods on high-pressure environments is investigated and a possible solution for measurements up to multiple 100 MPa is introduced. With liquid-air interphases being quite difficult to handle at high pressures, an assessment is made for nitrogen regarding it´s properties und extreme conditions.

Keywords: Surface tension, Fuel, High-pressure, Fluid properties
Target audience: Tribology & Fluids, Design Process

1 Introduction

Within the cluster of excellence “Tailor-Made Fuels from Biomass” at RWTH Aachen University, a team of researchers is investigating new biofuel candidates from production to propulsion. The main foci of research are the chemical reaction paths for an industrial scale production, fluid analytics and simulation as well as necessary adaptions and improvements of the combustion system.

Amongst others, a suitable biofuel candidate combines advantageous rheological properties regarding the combustion process many of which are in direct opposition to each other. Volumetric losses in common-rail injection pumps, which are lubricated by the fuel itself, can be reduced by using a fuel with elevated viscosity. Looking at the injector, a higher viscosity leads to a limited performance, effectively reducing the overall combustion efficiency and increasing soot emissions. The reason for this phenomenon is the increased friction of the fluid, causing reduced mass flow. Another vital factor for fluid properties regarding injector performance is the spray distribution behaviour. One way to characterise spray is the dimensionless Ohnesorge number *Oh*, see equation (1) /1/. Here, the internal viscosity dissipation is related to the surface tension energy. For lower Ohnesorge numbers, the friction losses due to viscous forces are weak and the energy converts into surface tension energy enabling the formation of droplets /2/. Figure 1 shows the Ohnesorge number plotted over the Reynolds number *Re* to distinguish different spray areas: Rayleigh breakup, windinduced breakup, which accounts for two different areas depending on jet velocity and oscillation, and atomisation /3/. In order to ensure a homogeneous spray distribution in the combustion chamber, injectors work with Ohnesorge numbers far below 0.1, see Figure 1.

$$Oh = \frac{\eta}{\sqrt{L \cdot \sigma \cdot \rho}} \tag{1}$$

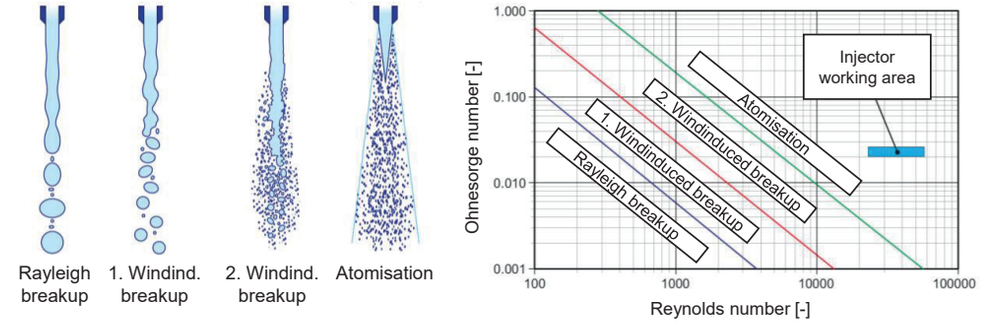


Figure 1: Different spray areas depending on Ohnesorge- and Reynolds number after /3/.

In order to design new injection systems or tune existing technology to perform in an optimal way using innovative biofuel candidates, fluid characteristics need to be known. Especially surface tension is a key property not only for the design of injectors, but also for chemical reactors, see /4/.

Looking at hydraulics, cavitation as a whole has been a defining and relevant topic. Damages or reduced performance due to cavitation are subject to current research, see /5/ and /6/. The ascension speed of a bubble inside hydraulic oil can be described with Equation (3) using the Young-Laplace Equation (2) to substitute the bubble radius with the surface tension, see /7/. Here, the speed has a quadratic dependency on surface or interface tension between bubble and oil. This phenomenon is highly relevant for design and simulation of hydraulic reservoirs, where air bubbles need to leave the oil as fast as possible. Additionally, latest and more sophisticated modelling of cavitation requires surface tension as an input parameter. In order to increase simulation accuracy, this parameter needs to be known over a wide range of pressure and temperature.

$$\left(p_{bubble} - p_{fl}\right) = \frac{2 \cdot \sigma}{r} \tag{2}$$

$$v = \frac{2}{9}\left(\rho_{fl} - \rho_{bubble}\right)\frac{r^2 g}{\eta} = \frac{8}{9} \cdot \frac{\left(\rho_{fl} - \rho_{bubble}\right) \cdot g \cdot \sigma^2}{\eta \cdot \left(p_{bubble} - p_{fl}\right)^2} \tag{3}$$

Looking at binary mixtures, surface tension can be highly non-linear, see Figure 2. Here, a mixture of water and different weight fractions w_2 of sulfuric acid and Diethylene-glycol-diethyl-ether (dgde) respectively was investigated at 293 K and ambient pressure /8, 9/. Since the mixture-behaviour strongly differs depending on the partners, analytical modelling is only possible to a certain extent. Therefore, empirical data is needed to provide accurate input for simulation and design purposes.

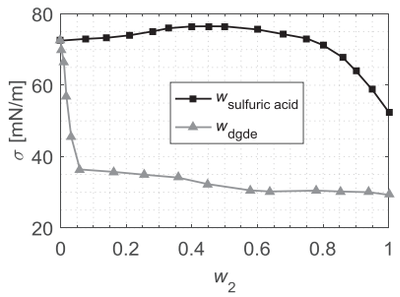


Figure 2: Surface tension of water-sulfuric acid and water-dgde mixture over the mass fraction after /8, 9/.

1.1 Pressure dependency

For combustion systems, chemical reactors and fluid power systems in general, the assumption that the effects of surface tension only play a role at ambient pressure is hardly true. Depending on the operational strategy of an engine and the pressure level of chemical reactors and fluid power systems, surface tension is relevant at a wide range of pressures and temperatures. The pressure dependency of surface tension can be seen in Figure 3. Here, diesel was measured with a gaseous nitrogen atmosphere at pressure levels up to 9.4 MPa using the capillary wave method, see /10/. The change in surface tension at 9.4 MPa compared to ambient pressure can be computed to 28%. For natural water in a methane atmosphere, see /11/, the change of surface tension at 21 MPa compared to ambient conditions is 21%. For measurements up to 40 MPa, the pendant drop method was used. The measurements were done at 298 K. Both values indicate a highly pressure-dependent behaviour of surface tension. In order to do high-pressure measurements, a suitable technique has to be identified. In the following, prominent methods for measuring surface tension are introduced and advantages as well as disadvantages of each method are discussed.

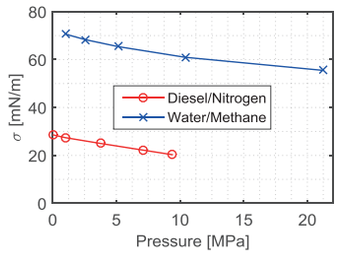


Figure 3: Pressure-dependency of surface tension for water in a methane atmosphere and diesel in an nitrogen atmosphere after /10, 11/.

2 Measurement methods

The determination of surface tension can be done using different methods. In the following, the most relevant methods will be introduced and an evaluation regarding the applicability in high-pressure measurements is done. First of all, the measurement principles are categorised in four groups: Resistance, droplet, capillary and frequency based methods.

2.1 Resistance based measurements

The measurement of surface tension can be done by dragging a body through the surface of the fluid in question. Figure 4 shows the different principles of measurement: Wilhelmy plate method, Du Noüy ring method and wire method.

The Wilhelmy method uses a thin plate mostly made of roughened platinum-iridium alloy or platinum which is cleaned and flamed before every measurement. Then, the plate is put in a fixed position relative to the horizontal liquid surface. A vertical force F is applied to the plate while it is being lifted from the liquid. Due to surface tension, a liquid meniscus originates. The weight of the meniscus equals the pulling force in equilibrium. With knowledge of force F, thickness t and length L of the plate as well as the meniscus angle φ, the surface tension can be calculated using equation (4) /12/.

$$\sigma = \frac{F}{2(L+t)\cdot\cos\varphi} \tag{4}$$

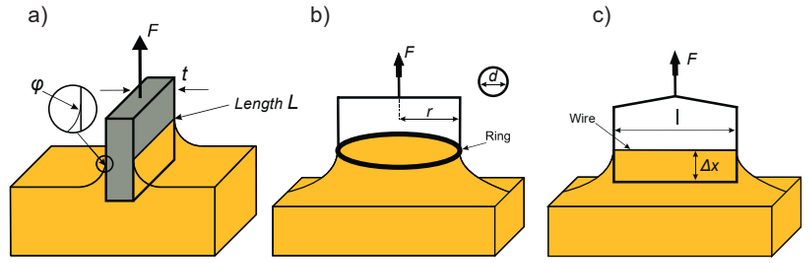


Figure 4: Surface tension measurement methods: Wilhelmy method a), Du Noüy method b), wire method c).

Using the Du Noüy method, the force F is measured which is required to pull a ring made of platinum-iridium alloy or platinum out of a liquid surface. The ring has a wire diameter d and a radius r. Pulling the ring through the liquid surface, a meniscus rises with the ring. Using a microscale, force F equals the weight of the liquid meniscus. Surface tension can be calculated at the point where the meniscus collapses, using equation (5). At the point of a collapsing meniscus, the angle φ is approximately zero which results in $cos\ \varphi$ being unity. Additionally, a correction factor f is needed, which can be calculated after the measurement, see equation (6). For measurement purposes, smaller rings are favoured due to bigger correction factors /12/. The wire method works with the same principle than the Du Noüy method. Instead of a ring, a straight, thin wire is used. The forces measured therefore are smaller and finer microscales are needed.

$$\sigma = \frac{F}{4\pi r\cdot\cos\varphi}\cdot f \approx \frac{F}{4\pi r}\cdot f \tag{5}$$

$$f = 0.725 + \left(\frac{9.075\cdot 10^{-4}F}{\pi^3\Delta\rho g r^3} - \frac{1.679d}{2r} + 0.04534\right) \tag{6}$$

In general, all the above mentioned methods are applicable in high-pressure surroundings, since the measurements do not take up much space and can be integrated into pressure chambers. Additionally, the force measurements do not rely on optical evaluation and can be completely immersed in the test fluid. For the Wilhelmy method, a sensor to evaluate the angle between meniscus and plate needs to be incorporated in the pressure chamber as well. Here, pressure limits are set due to the optical nature of this measurement. Additionally, not all liquids can be measured with the Wilhelmy method, since the surface energy of the plate can be influenced by non-ionic surfactants for example. The Du Noüy method on the other hand only needs a force measurement due to the meniscus angle being approximately zero. Compared to the wire method, the force sensor has to detect approximately three times higher forces. With forces being in the order of mN, higher forces equal higher accuracy. When done correctly, the Du Noüy method provides the highest accuracy out of the aforementioned methods /12/.

2.2 Droplet-based measurements

Droplet based measurements can range from simply to set up methods to highly complex test rigs. Figure 5 shows the three primary methods: Pendant drop method, spinning drop method and drop volume method.

For the pendant drop method, the equatorial diameter d_e and the additional diameter d_s at the drop height d_e need to be measured, see Figure 5 *a)*. Calculation of the surface tension can be done using equation (7). Here, the shape dependent parameter H needs to be calculated using empirical data /13/. The pendant drop method requires high cleanliness and a capillary which is adjusted to the drop geometry. The recommended capillary diameter is less than 0.5 d_e but should not be too small, since d_s is directly influenced by the capillary diameter.

$$\sigma = \frac{\Delta\rho g d_e^2}{H} \tag{7}$$

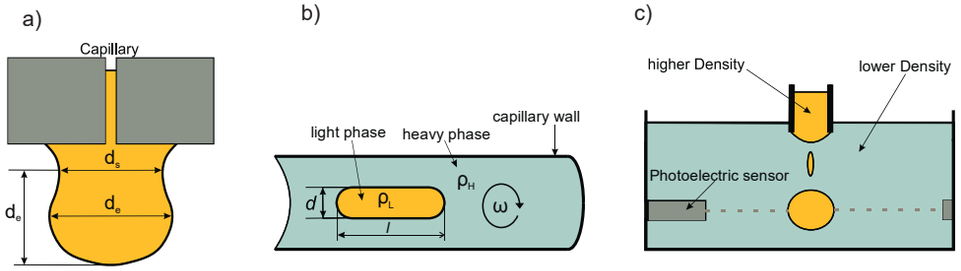


Figure 5: Surface tension measurement methods: Pendant drop method a), spinning drop method b), drop volume method c).

The spinning drop method, as presented in Figure 5 *b)*, is a method to study ultralow surface tension values down to 10^{-6} mN/m /14/. In a horizontal tube, a droplet of lower density than the surrounding fluid is spun with rotational velocity ω. At sufficiently high speeds, the droplet becomes cylindrical. The resulting diameter d is a result of the surface tension, which can be calculated using equation (8).

$$\sigma = \frac{1}{32} d^3 \Delta\rho \omega^2 \tag{8}$$

For the drop volume method, seen in Figure 5 *c)*, the volume V of a drop falling from a capillary with a radius r is determined by using a photoelectric sensor for example. With the drop volume and the capillary radius, the surface tension can be calculated using equation (9) with f being a correction factor as a function of $r/V^{1/3}$, see equation (10) /15/. A weak point of this method is the vulnerability to minor vibrations. These can cause the premature ejection of droplets before reaching the critical mass resulting in inaccurate measurements.

$$\sigma = \frac{V \Delta\rho g}{2\pi r^2 f\left(\frac{r}{\sqrt[3]{V}}\right)} \tag{9}$$

$$f\left(\frac{r}{\sqrt[3]{V}}\right) = 0.167 + 0.193\left(\frac{r}{\sqrt[3]{V}}\right) - 0.0489\left(\frac{r}{\sqrt[3]{V}}\right)^2 - 0.0496\left(\frac{r}{\sqrt[3]{V}}\right)^3 \tag{10}$$

The applicability of droplet-based measurements to high-pressure surroundings highly depends on the method in question. The spinning-drop-method for example requires a transparent tube to evaluate the drop geometry. Using specific material, a transparent pressure tube could be manufactured. Nevertheless, this cannot compensate the drawback only liquid-liquid measurements can be conducted with this method. The drop volume method requires high precision sensors to determine the volume of the droplets. With such a precision sensor integrated into high-pressure, only certain pressure-levels can be reached without damaging the sensor itself or influencing the principle on which the sensor is based. Measurements at elevated pressures based on the pendant-drop-method have been conducted already, see /11/. Here the pressure range is also limited due to the optical nature of the method. Additionally, depending on viscosity and surface tension, a change of capillaries at higher pressure levels might be necessary. This means, that the equilibrium is disturbed and measurement in itself can be questioned.

2.3 Capillary-based measurements

The surface inside a capillary can also be used to evaluate surface tension. Figure 6 shows two options: Capillary rise method and capillary flow method.

With the capillary rise method the height h of a meniscus in a round glass tube with inner diameter d is measured. If the tube diameter is small compared to the tube height, the meniscus has an almost spherical shape, making the cosine of the contact angle between meniscus and tube unity. In case of a spherical meniscus, equation (11) can be applied. For non-spherical menisci, equation (12) applies /12/. The challenge using the capillary rise method is the uniformity of the inner diameter of the glass tube. Additionally, this method is not suitable for liquid-liquid interfaces.

$$\sigma = \frac{\Delta\rho g h d}{4\cos\varphi} \tag{11}$$

$$\sigma = \frac{1}{2}\Delta\rho g r h \cdot \left(1 + \frac{r}{3h} - 0.1288\frac{r^2}{h^2} + 0.1312\frac{r^3}{h^3}\right) \tag{12}$$

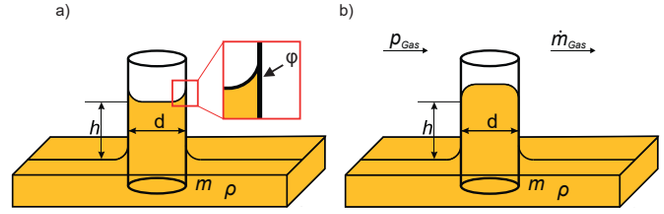


Figure 6: Surface tension measurement methods: Capillary rise method a), capillary flow method b).

Based on the same principle, the capillary flow method, see Figure 6 b), uses a gas which flows over a glass tube. Inside the tube, the geometry of the meniscus can be evaluated and the surface tension calculated. The same problems regarding manufacturing apply to this method as well, which means that liquid-liquid measurements are challenging to realise.

Both of the above mentioned methods do show significant problems regarding high-pressure applicability. With glass being highly brittle, hydrostatic loads can cause cracking of the glass tube. The manufacturing challenges regarding a uniform glass tube also add to this list. Additionally, the capillary flow method requires a fluid flow over the capillary. At high pressures, this flow is difficult to realise. Without possibility of measuring liquid-liquid surfaces, these methods are not suited for the aspired high-pressure measurements.

2.4 Frequency-based measurements

In order to measure the dynamic surface tension, two different approaches can be made: Oscillating drop method and the capillary wave method, shown in Figure 7.

The oscillating drop method evaluates the surface tension of an expanding and collapsing droplet hanging from a capillary. Using a pump, the pressure of the droplet can be varied and different pressure drops can be evaluated while continuously monitoring geometry and pressure of the droplet. The capillary wave method on the other hand uses a needle to create waves on the surface of a liquid. The wave frequency and length can be measured to calculate the surface tension. This method was already used for measurements of different fuel candidates at pressures up to 9.4 MPa, see /11/.

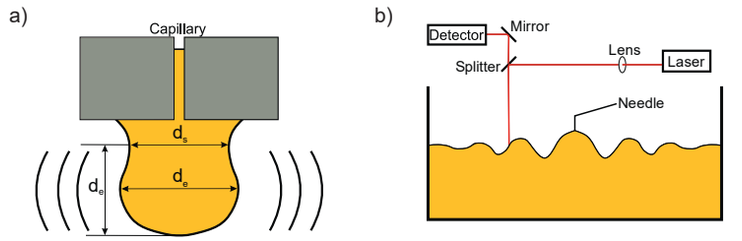


Figure 7: Surface tension measurement methods: Oscillating drop method a), capillary wave method b).

Nevertheless, usability of these methods for high-pressure measurements is limited due to the required optical measurement devices. Additionally, this method is difficult to realise with a liquid-liquid interphase.

2.5 Evaluation

After presenting the most prominent measurement methods for surface tension and analysing applicability for high-pressure surroundings, only a few candidates stand out: Wilhelmy plate, Du Noüy ring and pendant drop. Comparing these methods with the others, the first advantage is their simplicity. This is a great advantage when thinking about the integration into high-pressure chambers. Ideally, measurements can be conducted without optical sensors, since high-pressures of more than 100 MPa require robust systems and transparency of all test liquids at high pressures cannot be ensured. Additionally, high precision force detection of less than 1 mN and reproducibility is required and a change in set up during the measurements should be avoided (e.g. changing the capillary due to changing surface tension). With the Du Noüy ring-method, all requirements for high-pressure applicability are fulfilled. With the assessment, this method is selected for further design recommendations regarding the applicability to high-pressure environments.

3 Measurements

The following measurements were done using the Du Noüy ring method at ambient conditions of 0.1 MPa and 295.15 K. Every measurement was conducted three times. All deviations within each measurement routine were below 2.3% from each other, causing the error bars to be within the dimensions of the marker itself. A calibration measurement was done using neat water with a surface tension around 72.5 mN/m. Compared to literature values in /9/, where the values of surface tension are in the range of 72.44 mN/m, the deviation is in the order of 0.1%.

The nonlinear behaviour of binary mixtures can be seen in Figure 8. Here, the surface tension is plotted over the amount of substance of ethanol. Measured values and data from literature show fairly good agreement, see /9/.

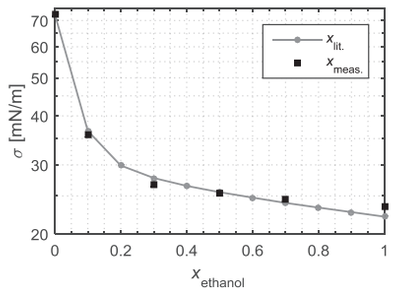


Figure 8: Comparison of literature- with measurement-data of a water-ethanol mixture after /9/.

3.1 Liquid-gas Measurements

During the injection process, a low surface tension is advantageous for a homogeneous spray distribution in the combustion chamber. The fuel is injected into air. Therefore, surface tension measurements were conducted using a fuel/air interphase. Figure 9 shows the results for common fuels after /16, 17, 18/ (left) and biofuel candidates (right). Since the commercially available fuels are mixtures and blended with additives that can vary depending on the location, the measurement results do only yield a tendency.

ROZ 95 (Super) and E10 fuel display an advantageous low surface tension between 20 and 22 mN/m, while EN 590 (Diesel) lies around 30 mN/m. These values indicate a better combustion performance for Otto-fuels in comparison with EN 590. Looking at the emissions, surface tension might be a factor for the higher soot emissions with EN 590. The range of promising fuel candidates regarding surface tension for neat components is smaller. Here, 2-Methyltetrahydrofuran, 2-MTHF, has a value of around 27 mN/m, while Di-n-Butylether, DnBE, displays a value of around 25 mN/m. The highest value can be found for 1-Octanol with 29.3 mN/m. Using a blend of 50 volume-percent 1-Octanol with DnBE and 2-MTHF respectively, the values are well within the neat fuel numbers. Almost linear behaviour can be observed using neat biofuels and blends.

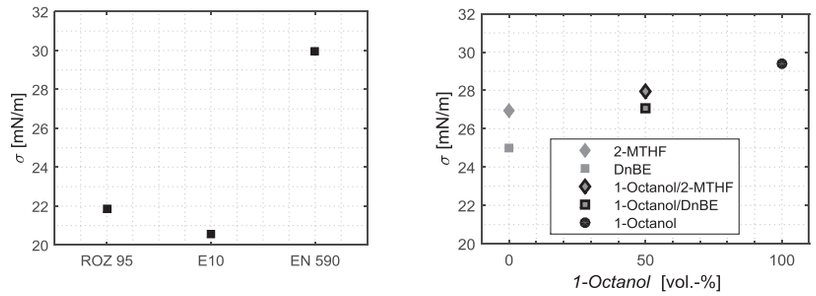


Figure 9: Surface tension values for standard fuels (left) and biofuel candidates and blends (right).

3.2 Liquid-liquid measurements

For cavitation, the interfacial tension between water and hydraulic oil can play an important role. Therefore, measurements were conducted for three hydraulic oils of differing viscosity: HLP46, HLP22 and HLP15. All HLP oils are mineral based with additives to enhance ageing-resistance, prevent corrosion and raise high-pressure usability, see /19/. Figure 10 shows the results. All oils do show surface tension values around 32.5 mN/m with an air atmosphere. If water is added and the interfacial tension between water and oil is investigated, the results vary drastically compared to the oil/air measurements. Starting from just below 20 mN/m for HLP46 and water, interfacial tension decreases with the oil viscosity. This yields 14 mN/m for HLP22 and water down to 7 mN/m for HLP15 and water. This interesting tendency can play a major role for choosing the right hydraulic oil. Nonetheless, the influence of additives within the oils which potentially react with water can also cause the behaviour seen in Figure 10. Due to a limited knowledge of the additives and their volume fraction within each respective oil, a general statement cannot be made.

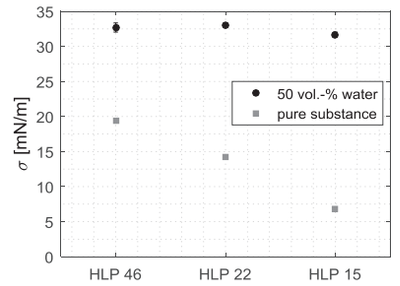


Figure 10: Influence of water on the surface tension between water and different hydraulic oils.

4 Derivation of an operational principle for high pressure tensiometers

4.1 Requirements

The presented literature survey and the investigation of the benefits and weaknesses of the different measurement approaches have shown, that the aspired measurement of surface tension under high pressure should be preferably realised by the Du Noüy ring method. Furthermore, measured surface tension of diverse fuels and biofuel candidates in figures 8 and 9 indicate a required measurement range in the order of 1-100 mN/m. Herein, a minimum resolution of 1% should be achieved. For the targeted high pressure tensiometer (IFAS HPT), the complete measurement device will probably be arranged in the high-pressure chamber of the

high pressure viscometer at IFAS, see /20/, leading to additional requirements due to confined space. Table 1 shows a comparison of different state of the art devices for ambient pressure and the resulting design parameters for the IFAS HPT to be developed.

Manufacturer and Device	**Lauda TD3 /21/**	**IMETER V6 /22/**	**Krüss K100 /23/**	**IFAS HPT**
Footprint	250 x 120 mm²	270 x 400 mm²	300 x 390 mm²	Ø 40 mm
Height	250 mm	560 mm	585 mm	200 mm
Stroke	80 mm	135 mm	110 mm	50 mm
Pressure range	Ambient pressure			up to 750 MPa
Surface tension measurement with Du Noüy ring method				
Min. surface tension	0.75 mN/m	0.5 mN/m	1 mN/m	1 mN/m
Max. surface tension	300 mN/m	1000 mN/m	2000 mN/m	100 mN/m
Resolution	0.01 mN/m	0.01 mN/m	0.001 mN/m	0.01 mN/m
Precision weighting				
Max. force	5 g / 50 mN	220 g / 2.2 N	210 g / 2.1 N	Not feasible
Resolution	0.1 mg / 1 µN	0.01 mg / 0.1 µN	0.01 mg / 0.1 µN	
Liquid density measurement				
Measurement body	External			Internal
Max. density	2000 kg/m³	1600 kg/m³	2200 kg/m³	1500 kg/m³
Resolution	1 kg/m³	1 g/m³	1 kg/m³	0.1 kg/m³

Table 1: Comparison of different state of the art devices /21, 22, 23/ and IFAS HPT under development.

Thereof, the required resolution of the force sensing device can be deduced. The simplified correlation of surface tension σ and force F_{ST} on the Du Noüy ring in equation (13) enables the definition of the required forces /24/.

$$\sigma = \frac{F_{ST}}{4\pi \cdot r} \tag{13}$$

Employing a Du Noüy ring according to DIN EN 14370 with a radius r of 9.75 mm results in tension forces of 0.123 mN to 12.25 mN in the aspired surface tension regime. The weight of the Du Noüy ring and the movable part of the force detecting device adds to the tension force, leading to a significant offset. Thus, huge demands on the precision of the force sensing device result whether the smallest values for surface tension have to be measured with reasonable accuracy.

To allow for precise measurements, commercially available devices possess electromagnetically compensated weigh cells. Therein, a voice coil actuator (VCA) holds the load in constant position, which is fed-back by a contactless position sensor. As the VCA possesses a completely linear force/current characteristics in fixed position the load is proportional to the measured current through the VCA's coil. Recalibration is achieved by one or more integrated calibration weights in the weigh cell assembly, so that changes in current/force gain can be automatically corrected /25/. Unfortunately, such devices do not fit in the high pressure chamber of the high pressure test rig and the change in density of the surrounding medium over pressure interacts with the measurement and calibration devices and thus leads to strong deviations of the measured values and calibration.

Hence, the key challenge in designing a high pressure tensiometer for liquid/liquid and liquid/gas applications lies on the one side in the confined space and required measurement accuracy and on the other side in the ability of remote recalibration under high pressure. The last challenge will be discussed in the following subchapter.

4.2 Recalibration strategy

Supposing an ideal sensor which possesses a completely linear force current relationship with force gain k, the effect of changing density on measurement results still prohibits an exact determination of the surface tension. Taking into account a volume of the moving measurement device V_M with a mean density ρ_M, and the density of the surrounding fluid ρ_{fl}, the measured force yields

$$F = k \cdot i = V_M \cdot g \cdot (\rho_M - \rho_{fl}) + F_{ST} \tag{14}$$

Supposing a volume V_M of 5 cm³, a small inaccuracy in density ρ_{fl} or ρ_M of 1 kg/m³ already leads to a deviation in measured force signal of 49.05 µN, which equals a change in surface tension of 0.4 mN/m. Hence, to achieve sufficient measurement accuracy over a wide pressure and temperature span, a continuous in situ recalibration of the fluid density ρ_{fl} by the tensiometer is required.

As the accuracy of the measurement device is also highly affecting measurement accuracy, the force gain of the measurement device should also be recalibrated under operating conditions. Recalibration of sensor and fluid density can be achieved by use of two incompressible calibration weights (volumes V_1 and V_2) of different densities ρ_1 and ρ_2 inside the tensiometer. Assuming, that the second calibration weight can only be added to the system if the first one is applied and calibration is achieved without surface tension acting on the Du Noüy ring, the equations describing the system with (index "1" and "12") and without (index "0") calibrations weights are:

$$F_0 = k \cdot i_0 = g \cdot V_M \cdot (\rho_M - \rho_{fl}) \tag{15}$$

$$F_1 = k \cdot i_1 = g \cdot \left(V_M \cdot (\rho_M - \rho_{fl}) + V_1 \cdot (\rho_1 - \rho_{fl})\right) \tag{16}$$

$$F_{12} = k \cdot i_{12} = g \cdot \left(V_M \cdot (\rho_M - \rho_{fl}) + V_1 \cdot (\rho_1 - \rho_{fl}) + V_2 \cdot (\rho_2 - \rho_{fl})\right) \tag{17}$$

As a result, the force gain of the sensor k and the fluid density ρ_F can be determined as:

$$k = \frac{g \cdot V_2 \cdot (\rho_1 - \rho_2)}{(i_1 - i_0) \cdot \frac{V_2}{V_1} - (i_{12} - i_1)} \tag{18}$$

$$\rho_{fl} = \frac{V_1 \cdot \rho_1 \cdot (i_{12} - i_1) - V_2 \cdot \rho_2 \cdot (i_1 - i_0)}{V_1 \cdot (i_{12} - i_1) - V_2 \cdot (i_1 - i_0)} \tag{19}$$

Thus, online recalibration of the sensing device and the surrounding density is feasible. Nevertheless, a technology to implement a highly linear and stroke independent sensor, the actuator to move the Du Noüy ring and the actuators to apply two calibration weights in the confined cylindrical space still pose a challenge, which has to be met in the future. A promising way could be the integration of a VCA as sensing and driving element and two electromagnetic actuators holding the at least partially ferromagnetic weights. There for, subsequent studies on linearity of suitable VCA's and on a frictionless linear bearing for its coil are necessary. Also, a stroke sensor or at least velocity estimation using the VCA's voltage has to be considered for surface tension measurement.

5 Summary and Conclusion

The paper illustrates the necessity of high-pressure surface tension measurements. With a first concept, some challenges are addressed. In order to investigate the applicability of the proposed method, a first prototype needs to be developed.

In this paper, the importance of surface tension measurements was shown to support design processes as well as the understanding of fluid flow phenomena. First, an introduction was given with examples regarding injector-technology, chemical reactors and hydraulics. With the introduction to pressure dependent surface tension, common measurement methods were introduced and evaluated concerning the applicability in high-pressure environments. As a result, the Du Noüy ring method was identified as a suitable candidate for the adaption to high-pressure. Afterwards, measurements results for ambient conditions were presented for different fuel and biofuel candidates as well as different hydraulic oils. Moreover, the tendency for a lower interfacial tension between water and oil for lower viscosity oils was shown. Afterwards, an analysis of current commercial Du Noüy ring tensiometers was performed and requirements for a high-pressure application were derived. With these requirements a first concept was presented.

6 Acknowledgements

This work was performed as part of the Cluster of Excellence "Tailor-Made Fuels from Biomass", which is funded by the Excellence Initiative by the German federal and state governments to promote science and research at German universities.

Nomenclature

Variable	*Description*	*Unit*
d	Diameter	[m]
F	Force	[N]
f	Correction factor	[-]
g	Gravitation	[m/s²]
H	Shape dependent parameter	[-]
h	Height	[m]
i	Current	[A]
k	Calibration factor	[N/A]
L	Length	[m]
Oh	Ohnesorge number	[-]
p	Pressure	[Pa]
R	Radius	[m]
r	radius	[m]
Re	Reynolds number	[-]
t	Thickness	[m]
V	Volume	[m³]
v	Speed	[m/s]
w	Weight fraction	[-]
η	Dynamic viscosity	[Pa s]
ρ	Density	[kg/m³]
σ	Surface Tension	[N/m]
φ	Meniscus angle	[°]
ω	Rotational velocity	[1/s]

Index	*Description*
0	Initial
1	Calibration weight 1
2	Calibration weight 2
12	Calibration weights 1 and 2 together
$bubble$	Properties of a bubble
e	Equatorial
fl	Fluid
M	Moving measurement device
s	Additional
ST	Acting on Du Noüy ring

Abbreviation	*Description*
$2-MTHF$	2-Methyltetrahydrofuran
$E10$	Unleaded fuel with 5-10 vol.% ethanol
$EN\ 590$	Diesel fuel
$dgde$	Diethylene glycol diethyl ether
$DnBE$	Di-n-Butylether
$E10$	Gasoline with 10% ethanol
HLP	Minreal based hydraulic oil with corrosion and high-pressure additives
HPT	High-pressure tensiometer
$IFAS$	Institute for fluid power drives and controls
$ROZ\ 95$	Unleaded fuel (Super)
VCA	Voice coil actuator

References

/1/ Ohnesorge, W., *Formation of drops by nozzles and the breakup of liquid jets* – Journal of Applied Mathematics and Mechanics 16, p. 355-358, 1936

/2/ Li, D., *Encyclopedia of Microfluidics and Nanofluidics* – Springer, New York, United States, 2015

/3/ Schneider, B.M., *Experimentelle Untersuchungen zur Spraystruktur in transienten, verdampfenden u nicht verdampfenden Brennstoffstrahlen unter Hochdruck* – Dissertation, ETH Zürich, 2003

/4/ Kreutzer, M.T. et al., *Multiphase monolith reactors: Chemical reaction engineering of segmented flo microchannels* – Chemical Engineering Science 60, p. 5895-5916, 2005

/5/ Longhitano, M., Murrenhoff, *H., EXPERIMENTAL INVESTIGATION OF AIR BUBBLE BEHAVIOU IN STAGNANT MINERAL OILS* – Proceedings of the ASME/BATH 2015 Symposium on Fluid Powe Motion Control, Chicago, Illinois, USA, 2015

/6/ Krahl, D., et al., *Visualization of cavitation and investigation of cavitation erosion in a valve* - Proceedings of the 10th International Fluid Power Conference, Dresden, Germany, 2016

/7/ Murrenhoff, H., *Fundamentals of Fluid power – Part 1: Hydraulics* - 8th Edition, Shaker, Aachen, 20

/8/ Nielsen, C.J., *Density and Surface Tension of Aqueous H2SO4 at Low Temperature* – Journal of Chemical Engineering Data 43, p. 617-622, 1998

/9/ Wohlfarth, C., Surface Tension of Pure Liquids and Binary Liquid Mixtures – Group IV: Physical Chemistry Volume 24, Supplement to IV/16, Springer, Berlin, Germany, 2008

/10/ Dechoz, J., Roze, D., *Surface tension measurement of fuels and alkanes at high pressure under differe atmospheres* - Applied Surface Science 229, p. 175-182, 2004

/11/ Sachs, W., Meyn, V., *Pressure and temperature dependence of the surface tension in the system natu gas/water* – Colloids and Surfaces A: Physicochemical and Engineering Aspects 94, p. 291-301, 199

/12/ Drelich, J., et al., *MEASUREMENT OF INTERFACIAL TENSION IN FLUID-FLUID SYSTEMS* – Encyclopedia of Surface and Colloid Science, Marcel Dekker Inc., New York, 2002

/13/ Misak, M.D., *Equations for determining 1/H versus S values in computer calculations of interfacial tension by pendent drop method* – J. Colloid Interface Science 27, p. 141-142, 1968

/14/ *Manual of the Spinning Drop Tensiometer Site 04*, Krüss GmbH, Hamburg, Germany, 1995

/15/ Harkins, W.D., Brown, F.E., *The determination of surface tension (free surface energy), and the weig of falling drops: the surface tension of water and benzene by the capillary height method*, J. Am. Che Soc. 41, p. 499-525, 1919.

/16 N, N., *DIN EN 228 - Automotive fuels - Unleaded petrol - Requirements and test methods* – Beuth, Berlin, Germany, 2017

/17 N, N., *DIRECTIVE 2009/28/EC OF THE EUROPEAN PARLIAMENT AND OF THE COUNCIL of 2. April 2009 on the promotion of the use of energy from renewable sources* – Brussels, Belgium, 2009

/18 N, N., *EN 590 – Automotive fuels - Diesel - Requirements and test methods* – Brussels, Belgium, 201

/19/ N, N., *DIN 51524-2 - Druckflüssigkeiten – Hydrauliköle – Teil2: Hydrauliköle HLP, Mindestanforderungen* – Deutsches Institut für Normung e. V., Berlin, Deutschland, 2017

/20/ Drumm, S.M., *Entwicklung von Messmethoden hydraulischer Kraftstoffeigenschaften unter Hochdru* Dissertation, RWTH Aachen University, Shaker, Aachen, 2012.

/21/ N, N., *Operating Instructions - TD3*, LAUDA DR. R. WOBSER GmbH & Co. KG, 2009.

/22/ N, N., *IMETER V6*, http://www.imeter.de, visited on November 10, 2017.

/23/ N, N., *FORCE TENSIOMETER – K100 – SPECIFICATIONS*, KRÜSS, 2018.

/24/ N, N., *DIN EN 14370 - Grenzflächenaktive Stoffe – Bestimmung der Oberflächenspannung*, Beuth, Berlin, Germany, 2004.

/25/ Burkhard, H.-R., Schneider, F., *EP 2533024 A1 - Force transferring device with attachable calibratic weight*, Patent, 2011